# INTEGRATED GROUND-BASED REMOTE SENSING STATIONS FOR ATMOSPHERIC PROFILING

## COST Action 720 – Final Report

Edited by
DIRK A.M. ENGELBART
German Meteorological Service, Richard-Aßmann-Observatory, Lindenberg, Germany

WIM A. MONNA
Royal Netherlands Meteorological Institute (KNMI), De Bilt, The Netherlands

JOHN NASH
UK MetOffice, Exeter, United Kingdom

CHRISTIAN MÄTZLER
Institute for Applied Physics, University of Bern, Bern, Switzerland


Luxembourg: Publications Office of the European Union, 2009

# CONTENTS

# FOREWORD / EXECUTIVE SUMMARY

## INTRODUCTION

COST Action 720 started October 4, 2000. With an extension because of some delay resulting from the transition of the COST Office, and in order to allow some additional research connected to field experiments, the Action ended June 3, 2006. 12 EU countries participated: Austria, Finland, France, Germany, Greece, Italy, The Netherlands, Poland, Portugal, Spain, Switzerland and the United Kingdom. Also non-COST Institutions participated from Macao and Ukraine.

The aim of the Action is the development of cost-effective integrated ground-based remote-sensing stations for atmospheric profiling and the assessment of their use for meteorological analysis and forecast as well as climate research and climate monitoring.

The rationale for this Action is the lack of vertical profile data of temperature and water in all three phases with adequate quality, resolution and availability. These data are particularly important for short-range forecasts and nowcasting, including boundary-layer evolution and pollution dispersion. Although there are already remote-sensing instruments that in principle can measure these parameters, the resolution needs further improvement, and real operational use is hardly possible yet. COST-720 was therefore proposed because integration of ground-based remote-sensing techniques on one location are expected to yield better vertical profiles for all potential users.

## ORGANISATION

Two Working Groups were established:

Working Group 1, **Basic techniques and algorithms**

Tasks were the assessment of the state of the art of individual techniques in view of their potential for integration. Where necessary and possible, work has been done here on improvements, especially with respect to basic algorithms but also with respect to an assessment of the usability of basic techniques for the scope of users. Considered measurement systems were in particular: Microwave and infrared radiometer, lidar, wind profiling radar, cloud radar and C-band weather radar.

Working Group 2, **Integration**

Tasks were the derivation of profiles of temperature, humidity, wind and clouds by using various combinations of systems.

Additional activities were carried out on data use, such as the assessment of assimilation techniques for humidity and cloud profiles, impact studies on ground-based networks of high-resolution profiling stations, and a proposal for a BUFR code for integrated profiling stations.

## USER NEEDS

We refer to results from a detailed review of user requirements performed by S. Stringer in the UK Met Office in 2006 for the various atmospheric variables required by all types of users in the Met Office. This review was performed at the end of the COST-720 period, but allows some amplification of results from the earlier workshop in L'Aquila. Here the review will be used to indicate suitable performance targets for the development of integrated profiling systems.

## NUMERICAL WEATHER PREDICTION

COST 720 agreed that numerical weather prediction was one of the primary users for the integrated profiling stations which were to be developed. Observations would have to be assimilated for use in the forecasts produced, but would also be required to validate the products from the models. In both operational and research models there is a trend towards much finer grids, with spacing between grid points less than 2 km being necessary to represent some types of severe weather. In addition, the number of levels at which data are input into NWP models is increasing with time. In general, better temperature accuracy, vertical and horizontal resolution is required in the boundary layer than in the rest of the lower troposphere due to its greater variability in space and time. We concentrate here on the requirements for regional NWP. These are generally more stringent than other applications - requiring higher resolution observations in time and space and it is here that ground-based remote sensing instruments are likely to have most impact.

Needs for *regional numerical weather prediction* were

- More comprehensive wind, temperature, and moisture observations in space and time, especially in the boundary layer; wind profiles closer together

- More accurate estimates of precipitation

- More comprehensive observations of cloud base, cloud thickness and other cloud properties

And for *global numerical weather prediction*

- Wind profiles up to and including stratosphere/mesosphere
- Temperature profiles of adequate vertical resolution in cloudy areas
- Precipitation observations

## NOWCASTING

The primary needs for *nowcasting / very short range numerical weather prediction* were

- More frequent 3-dimensional wind field with closer horizontal and vertical spacing
- More frequent 3-dimensional humidity field with closer horizontal and vertical spacing
- Clouds and precipitation profiles
- Cloud amount and base height from remote sites and marine areas
- More frequent 3-dimensional temperature field with closer horizontal and vertical spacing

In the case of nowcasting the requirements for atmospheric parameters was larger reflecting the larger range of applications than for regional NWP.

## CLIMATE MONITORING

*Climate monitoring* requires a network of very stable instruments sampling in the same configuration over periods >10 years to detect small changes. As for new observing systems the absolute calibration has not yet been demonstrated over these timescales, it is unlikely that their data will contribute significantly to the climate monitoring requirements for some time.

## WHY SENSOR SYNERGY?

The rationale for sensor synergy follows from the different interaction mechanisms between electromagnetic radiation and atmospheric phenomena. This interaction depends on the wavelength used, and whether signals are scattered, reflected, absorbed and/or emitted. Passive instruments, like radiometers, measure the radiation emitted by the atmosphere itself. They measure either path-integrated values of the full atmospheric vertical column between

surface and space, or, when multiple frequencies are used and assuming idealized models of the radiative absorption of the atmosphere, have a limited capability of profiling. Active instruments like radars or lidars, on the other hand are profiling instruments that can measure spatial structures in the atmosphere by emitting its own radiation.

The most common remote-sensing instruments for operational and scientific use are described, in view of their potential for sensor synergy and operational applicability: microwave radiometer and FTIR, advanced lidars and ceilometers, windprofiler/RASS, sodar, cloud radar and weather radar. A combination of these instruments, each measuring different aspects of the atmospheric phenomena by e.g. using different frequencies, viewing angles, and by combining active and passive techniques may offer a wide range of new possibilities, which have been investigated in considerable detail throughout the action. Ways of combining instruments can either be integration of additional *hardware* into a basic system (e,g, combining a wind profiler system with RASS hardware in order to obtain improved measurements (winds) or additional parameters (temperature), or integrating remote-sensing *data* from several systems via sophisticated algorithms in order to enhance vertical resolution, all-weather capabilities, data quality or even to enable the measurement or retrieval of new (additional) parameters. Examples of integrated (combined) systems which have been investigated throughout COST-720 are:

- Dual frequency radar: combining high and low frequencies makes observation of e.g. raindrop size distribution feasible;

- The radar/lidar combination, which utilizes differences in scattering mechanisms of each basic technique enables improved discrimination of signal targets, the detection of e.g. aerosols below cloud base and cloud droplets, or the determination of particle sizes in ice clouds;

- Wind profiler radar combined with RASS or a sodar combined with radar-signal-generation hardware is used to estimate temperature profiles or improved wind profiles within the PBL;

- Active wind profiler and passive microwave radiometers can estimate humidity profiles.

## FIELD EXPERIMENTS

In order to test combinations of ground-based remote-sensing techniques, five field experiments were carried out.

## TUC-2003 (TEMPERATURE, HUMIDITY AND CLOUD PROFILING CAMPAIGN)

This field experiment was held in Payerne (Switzerland) from $15^{th}$ Nov. 2003 until $15^{th}$ Feb. 2004. It was a COST-720 initiative, broadened into the field of weather nowcasting and automatic cloud cover detection. Single ground-based temperature and humidity profiling systems were tested and automatic cloud detection systems and algorithms were assessed. The dataset shows how the remote-sensing systems behave at various weather conditions with a focus on fog related phenomena. It also enables the study of possibilities for system integration in order to improve temperature and humidity profiling. Finally, the usefulness of these data for the detection of PBL phenomena for weather nowcasting can be assessed.

## INTERNATIONAL RADIOSONDE INTERCOMPARISON IN MAURITIUS, FEBRUARY 2005

Information on the accuracy that can be achieved with the new operational high-quality radiosondes was required by COST 720 for experimental validation of ground based remote sensing measurements. Referencing the quality of radiosonde relative humidity measurements between daytime and night conditions is difficult without independent observations of water vapour. After discussion with the delegate from WMO it was decided to participate at the intercomparison as this is seen as of mutual benefit for WMO and COST-720. COST 720 suggested that GPS water vapour measurements be used as a reference, and that a combination of 78 GHz FM-CW cloud radar and laser ceilometer is used to record the clouds conditions associated with the radiosonde measurements. The GPS water-vapour measurements proved useful in identifying day-night differences in the radiosonde relative humidity measurements, and should always be used in supporting WMO test in future. Both cloud radar and laser ceilometer deployed in Mauritius experienced difficulties in observing with the moist conditions and it was clear that systems need to be improved or higher specification equipment used to cope with the tropical conditions in Mauritius.

## CONVECTIVE STORMS INITIATION PROJECT CSIP

This experiment was conducted by the CCLRC Chilbolton Observatory, UK Universities, the UK Met Office and colleagues from various institutes in Germany. The campaigns (July 2004, June–August 2005) were based at Chilbolton Observatory. A microwave radiometer and laser ceilometer were deployed alongside a 1290 MHz windprofiler at Linkenholt, Hampshire, UK. Remote-sensing from these instruments was supplemented by measurements from the Chilbolton 25 m radar scanning across the top of the site. Hourly

radiosondes were performed for 6 day periods. This will allow integration studies to continue on summertime boundary layer conditions.

## LAUNCH[1]

More than 20 institutions participated in the LAUNCH field experiment from August 29, 2005, until the end of October. The first major objective was related to improvements in NWP modelling. This refers on one hand to a 4D-data set for the validation of model output as well as on the other hand for further developments of physical parametrisations and numerics. Data were provided by a large set of different remote-sensing systems and two complete integrated stations for monitoring wind, temperature, water vapour and clouds. The second major objective was related to the realization of an assessment of water-vapour lidar and microwave systems providing input for mesoscale NWP assimilation experiments in Eastern Germany and in middle and Southern Italy. Furthermore, the LAUNCH campaign enabled an assessment of new (basic) remote-sensing techniques for atmospheric profiling, particularly a quasi-operational water-vapour Raman-lidar system, a new single-photon-counting high-range ceilometer and an FTIR spectrometer for atmospheric temperature and humidity sounding.

## HELSINKI TESTBED

August 2005 meteorological measurement campaigns started in Southern Finland. Aim is to provide input and experience for mesoscale weather research, forecast and dispersion model development and verification, information systems integration, end-user product development and data distribution for public and research community. The Finnish weather observation network was supplemented in 2005 with nearly 60 stations equipped with Vaisala WXT510 weather transmitters, of which 42 were located at cell-phone base-station masts. New ground-based remote-sensing measurements in the Testbed domain included a 1.3 GHz windprofiler/RASS, a dual-polarization weather radar in Helsinki, and five laser ceilometers.

[1] INTERNATIONAL LINDENBERG CAMPAIGN FOR ASSESSMENT OF HUMIDITY AND CLOUD PROFILING SYSTEMS AND ITS IMPACT ON HIGH-RESOLUTION MODELLING

# INTEGRATED PROFILING TECHNIQUES

## RADAR-LIDAR SYNERGY FOR THE RETRIEVAL OF THE LIQUID-WATER CONTENT OF WATER CLOUDS

No single instrument is sufficient to completely measure liquid water clouds, because:

- lidar signals do not reach the cloud top and are therefore not representative for the whole cloud,
- radars are not always sensitive enough to detect the cloud base, and suffer from the 'large droplet issue', where a few small drizzle-like droplets dominate the radar signal and obscure reflections of smaller cloud droplets,
- standard microwave radiometers are not range-resolving and can only give estimates of the integrated liquid water path of a cloud; details of the vertical distribution of the cloud water are not resolved.

So only a combination of sensors can lead to satisfactory results. The combination of radar and lidar to retrieve the liquid water content (*LWC)* is very beneficial for the operational observation of liquid water clouds. It is useful for:

- The detection and parametrisation of the drizzle fraction in water clouds,
- the classification of water clouds into three types: 'non-drizzling clouds', 'clouds-in-transition' and 'drizzling clouds', and/or for
- the retrieval of profiles of the liquid water content.

The proposed technique for the *LWC* retrieval has been applied to the dataset collected in the framework of the CloudNet project on four European remote-sensing sites: Chilbolton (UK), Cabauw (The Netherlands),Lindenberg (Germany), and Palaiseau (France), together 1784 days of observation.

## DETECTION OF FOG AND STRATUS BY COMBINING CEILOMETER AND CLOUD RADAR INFORMATION

An automatic detection algorithm combining a ceilometer CT25K and a 78 GHz FM-CW cloud radar allowed, under conditions without precipitation, the detection of fog situations in two third of the cases. Low stratus cloud without precipitation situations were detected in more than half of the cases. The ceilometer turns out to be an excellent instrument for cloud base detection, although the vertical precision was not investigated. Cloud tops were determined by the cloud radar for about 41-69% of the time, mainly depending of the presence of precipitation. The difficulties of the cloud top detection with

the FMCW radar may be due to its lack of sensitivity to small droplets and to saturation at the first gates in presence of very thin fog layers. A combination of both ceilometer and cloud radar could be a good alternative for human observations to monitor low clouds evolution e.g. on airports. In addition, cloud amount (sky coverage in octas) could automatically be estimated using incoming long-wave radiation and surface parameters.

## AN EXAMPLE OF INTEGRATION OF UHF WINDPROFILER AND MICROWAVE RADIOMETER

Atmospheric humidity high-resolution profiles can be derived by synergetic use of MicroWave Radiometer Profiler (MWRP) and windprofiler (WPR). Key of the proposed technique is the processing of WPR data for estimating the potential refractivity gradient profiles and their optimal combination with MWRP estimates of potential temperature profiles. The algorithm uses recent developments in WPR signal processing, computing the zeroth, first, and second order moments of WPR Doppler spectra via a fuzzy logic method, which provides quality control of radar data in the spectral domain. The application of a neural network to brightness temperatures, measured by a multichannel MWRP, can provide continuous estimates of tropospheric temperature and humidity profiles. Results are compared with simultaneous radiosonde observations. The WPR and MWRP data were collected at the Atmospheric Radiation Measurement (ARM) Programme Southern Great Plains (SGP) site. Combined microwave radiometer and windprofiler measurements show encouraging results and significantly improve the vertical resolution of atmospheric humidity profiles, preserving the big advantage of being independent from in-situ measurements.

## INTEGRATION OF MICROWAVE AND THERMAL-INFRARED RADIOMETERS

Integrating microwave and infrared radiometers extends the observations to a very large frequency range of thermal radiation. Multiband systems, covering this wide spectrum, are able to yield significantly more independent information than either system alone. It is important that the observation directions, beam widths and observation times are the same for all channels. The following examples reveal interesting feasibilities.

- *Potential to measure cloud-base height*

From the temperature profile obtained with the microwave radiometer and the cloud-base temperature obtained from the infrared radiometer we can determine the height of the cloud base. This method was tested with ASMUWARA supported by cloud radar, laser ceilometer and radiosonde data. Cloud-base heights agree well for periods of low IR temperature variability when measured at short (5 s) intervals.

- *Potential to detect very thin and high clouds*

Because it is difficult to accurately determine the radiation level of the cloud-free atmosphere, a high accuracy is required to detect very thin clouds such as high cirrus. Approximate profiles of temperature and humidity are needed. These can be obtained from microwave radiometers. For thin clouds, infrared radiometers can be used to estimate the amount of integrated liquid water or integrated ice water.

- *Distinction between liquid water, ice clouds and supercooled liquid water clouds*

The combination of microwave and infrared radiometry allows to classify ice and liquid-water clouds. Especially it is possible to identify supercooled water clouds if integrated liquid water is non zero and if the cloud-base temperature is below zero degrees. The microwave radiometers determine the amount of cloud-liquid water, and the presence of clouds and the cloud base temperature are determined by the infrared radiometer. Ice clouds are identified if integrated liquid water is zero with a non-negligible cloud signal in the infrared.

- *Boundary-layer and air-sea temperatures*

Over a surface with a well-defined emissivity, the combination of microwave and infrared radiometers allows the monitoring of surface temperature and atmospheric boundary layer. The data are important for the determination of latent and sensible heat flux and of the atmospheric stability.

- *Model physics and sensor validation*

Synergisms also help in the validation of instruments. Microwave and infrared radiometers are combined to address the need for more accurate measurements of micro-physical properties of clouds with low liquid water paths.

## COMBINING UHF RADAR WINDPROFILER AND MICROWAVE RADIOMETER FOR THE ESTIMATION OF ATMOSPHERIC HUMIDITY PROFILES

Humidity profiles in the lower troposphere measured by ground-based microwave radiometers have poor vertical resolution. Windprofilers are very sensitive to changes in the humidity. When these instruments are combined, the complementary characteristics could yield improved vertical resolution of the humidity profile. Methods were tested to solve the humidity equation. It was found that in principle the use of windprofiler data can significantly improve the automatic estimation of humidity in the troposphere. The only conditions are the availability of a temperature profile, which need not to be very accurate, and a good estimate of humidity either at a single point or on a given integrated layer not exceeding the profiler range coverage.

## INVESTIGATION OF THE RELATIONSHIP BETWEEN WINDPROFILER SIGNAL TO NOISE RATIO AND TEMPERATURE, HUMIDITY AND CLOUD PROFILES

Though designed to provide measurements of wind, wind profiler signals also contain information about the vertical distribution of temperature, water vapour and clouds. Bragg, Fresnel and Rayleigh scattering contribute to the signal to noise ratio, which is related to the mean gradient of the refractive index. The spectral width can in principle be used to quantify the turbulence. The variation of the refractive index in the vertical derived from radiosondes was compared with observations of signal to noise from the various experiments. Finally, recommendations were developed on utilizing wind profiler signal to noise in a quantitative manner to improve the accuracy of relative humidity profiles.

## 1D-VAR RETRIEVAL OF TEMPERATURE AND HUMIDITY PROFILES FROM GROUND-BASED MICROWAVE RADIOMETERS

A one dimensional variational (1D-VAR) retrieval method has been developed to combine observations from ground-based microwave and infrared radiometers and surface sensors with background information from an NWP model to provide retrievals of temperature, humidity and cloud profiles using a total water control variable. The use of NWP data has been shown to be advantageous over methods taking their background from statistical climatology, while variational methods also provide error estimates of the retrieved parameters. In the future the 1D-VAR retrievals will be extended to include observations from other instruments, such as the cloud base height from a ceilometer, cloud base/top from cloud radar and refractive index gradient from a wind profiler.

## DATA ASSIMILATION

The impact of the assimilation of profiles of water vapour mixing ratio from a small network of Raman lidar systems, obtained from the LAUNCH experiment, has been evaluated using the 4DVAR OSE technique.

The PSU/NCAR mesoscale model (MM5) has been used, because it provides a 4DVAR system that is considered to be most suitable for the assimilation of high-resolution data from ground based Raman lidar systems. The essential difference between 4DVAR and 3DVAR is that the measured data is assimilated at observation time, rather than on prescribed moments in time. These lidar systems provided observations of water-vapour mixing ratio and temperature, which are at the same time the prognostic variables used in MM5. The first assimilation experiments, using only observations of water vapour,

show a clear impact on the water vapour mixing ratio and temperature fields even long after the end of the assimilation window. The high vertical resolution of the lidar data allows to considerably correct the vertical distribution of tropospheric water vapour as given by the ECMWF analysis on the standard pressure levels. This is a remarkable result, because it shows that lidar measurements enable a substantial improvement of the high-resolution initial fields. This improvement is most effective when the driving ECMWF analysis is already a good representation of the observed situation.

Moreover, the assimilation of vertical profiles from water-vapour lidars obviously produces a small impact on the quantitative precipitation forecasts, but this result has still to be further investigated.

## CONCLUSIONS

## MANAGEMENT ASPECTS

The original memorandum of understanding proposed three working groups to cover five Scientific Programme topics, but this did not prove feasible in practice. Thus, the work was split into two working groups concentrating on improving the basic systems identified as useful for integrated profiling and on performing initial investigations into integration. Cooperative field experiments were initiated, leading to the development of new international areas of cooperation. 10 papers were published in the *Meteorologische Zeitschrift*. At the Final Symposium, about 60 papers were presented.

## BASIC TECHNIQUES AND ALGORITHMS

**Microwave Radiometers** Recommendations were developed as to the best adjustment methods for using the radiometer measurements in subsequent comparisons with theoretically modelled radiance produced from radiosonde observations. During COST 720 the design of commercially available radiometers progressed so that observations became available at a high temporal resolution necessary to resolve cloud structure. This new generation of radiometers seems ready for more extensive testing and the development of associated integration techniques.

**Lidars (*water vapour, wind, clouds*, and *aerosol*)** Within the LAUNCH campaign, a large number of lidars contributed high-resolution water-vapour measurements to the campaign data set and for use in subsequent data assimilation experiments. Manufacturers contributed in the final COST workshop.

**Wind profiler radars** The use of complex signal processing has improved the detection of the atmospheric signal and the reliability of the reported winds.

**Cloud radar** Cloud radars were purchased and evaluated at several of the potential integrated profiling sites. They seem to be an important component of future integrated profiling sites.

**C-band weather radar** In Finland, the use of C-Band weather radar measurements for deriving vertical profiles of cloud layers was investigated and quantified.

## PROGRESS WITH INTEGRATION OF INDIVIDUAL SYSTEMS INTO ONE PROFILING STATION

**Derivation of drizzle fraction and cloud liquid water content** In association with the CLOUDNET project, Doppler cloud radar (35 or 94 GHz), laser ceilometer or Doppler lidar measurements were combined to determine the amount of drizzle in the water cloud, and hence the liquid water content of the clouds as a function of time. The Integrated Profiling Technique (IPT) for profiles of temperature, humidity, and clouds, developed in Germany has integrated measurements of microwave radiometer, laser ceilometer, cloud radar, and the closest available radiosonde. A combination of these two techniques has also been developed.

**Derivation of cloud top and base** A combination of a cloud radar with high vertical resolution and a laser ceilometer to determine the vertical extent of cloud have been tested. In many cases a cloud radar can reliably measure the top of low cloud or fog as long as there are larger water drops towards the top of the fog or cloud. The technique was used to verify satellite measurements of the depth of fog/low cloud. This method would be beneficial for future operational observing systems.

**Detection of layers associated with maximum refractive index gradient** The heights of layers associated with maximum vertical refractive index gradient in clear air can be identified from maxima in the signal to noise of UHF or VHF profilers. As the change in refractive index is mostly associated with changes in water vapour in the vertical, it has been proposed that these heights be assimilated into NWP models to improve the heights of inversions in the lower troposphere, or alternatively used as an additional element in integrated profiling techniques associated with microwave radiometer measurements.

The reproducibility of wind profiler signal to noise and spectral width measurements has been examined in view of the identification of the atmospheric processes associated with the signals. Different algorithms were examined on the moment estimation from the wind profiler spectra, with recommendations for future applications.

**Temperature and humidity profiles inferred from wind profiler signals** Initial tests were performed in Switzerland in the winter on combining UHF wind profiler signals with microwave radiometer measurements of vertical temperature and water vapour to produce more reliable retrieval of atmospheric structure than could be obtained from the microwave radiometer alone. The wind profiler signals were not strong enough to allow humidity to be constrained over a very deep layer. It is expected that this technique would work better in summer when the vertical extent of reliable signal to noise measurements would have a better match with the vertical resolution of the microwave radiometer. Proposals for future combinations of systems were generated. Using a similar technique, a case study was done on combining layers of high wind profiler signal to noise identified with a fuzzy logic algorithm with microwave radiometer measurements.

## DATA RETRIEVAL/ASSIMILATION TECHNIQUES

Data assimilation for numerical weather prediction and retrieval techniques for combining information from microwave radiometers with various other sources of information were investigated. Further work is required if integrated profiling based on the techniques suggested above is to be fully exploited in future.

## INITIATION OF A EUMETNET OBSERVATORY TYPE NETWORK PROJECT

The work of COST 720 and CLOUDNET on improving or implementing new observing systems into a level of reliability where they can be operated at sites where staff are available to support operation, has led to a proposal for a EUMETNET- OBSNET network based on a network of stations for integrated profiling in Europe. This was not implemented but further cooperation has been sought within EU Framework Programmes.

## COST-EFFECTIVE PROFILING FOR OPERATIONAL NETWORKS

Understanding of the potential of the integrated profiling techniques has reached a stage where potential combinations of systems for unmanned operation can be identified. The most cost-effective combinations of systems to be used in the operational integration have yet to be identified, since this also requires a better knowledge of the atmospheric processes that need to be observed at high temporal resolution. Future observing systems will need to satisfy both the requirements of operational meteorology and the requirements of more generalised cross-cutting environmental monitoring activities. Thus, a proposal to co-ordinate future operational developments and associated scientific studies and data assimilation activities in a new COST Action,

EG-CLIMET (European Ground-based observations of essential variables for CLImate and operational METeorology) has been prepared. This proposal was accepted, and the Action started in May 2008.

**Wim A. Monna**
Chairman COST-720, KNMI
De Bilt, The Netherlands, June 2008

# ACKNOWLEDGEMENTS

For the success of this COST Action the enthusiastic participation of many delegates in the Management Committee, in the Working Groups, and in writing this Final Report was of vital importance. With participants from Weather Services, the scientific community, and industry, COST 720 was fortunate to receive contributions from a variety of experts. Below we mention explicitly those that played a key-role in some specific activities.

The first Workshop was held in L'Aquila (Italy) at the Scuola Superiore Guglielmo Reis Romoli. We gratefully acknowledge Prof. Guido Visconti and Prof. Frank Marzano from the CETEMPS of the Università di L'Aquila for inviting us, and Laura Bianco and Nico Cimini for organising the local arrangements and the publication of the Volume of Abstracts.

For the "'Final Workshop"' we were kindly invited by Météo France in Toulouse. Here, we gratefully acknowledge the Local Organising Committee, in particular Vladislav Klaus, Michel Mauprivez, Jean-Louis Maridet, Guy Lachaud, Pierre Caille, Sylviane Balland, and Isabelle Varin. They also facilitated the publication of the Volume of Abstracts to this final workshop.

Two successive Scientific Secretaries from the EC, Zoltan Dunkel, and Pavol Nejedlik, took care of organisational and administrative matters throughout the whole action. Here, we gratefully acknowledge their support.

We finally acknowledge Dr. U. Görsdorf for his thorough final reading and checking of the total report as well as Mrs. Heidrun Pisch and Mr. Krispin Bisek, all from the Remote-Sensing Section of the DWD's Richard-Aßmann Observatory at Lindenberg for their arduous work on translation of numerous documents into La*TeX*, figure editing, and combining all documents into this Final Report. Without all their diligent work, the report would never have reached its objective to become a legible up-to-date source of remote-sensing techniques and its associated potential for sensor synergy.

Chapter 1

# INTRODUCTION

Wim A. Monna

*Royal Netherlands Meteorological Institute (KNMI), De Bilt, The Netherlands*
Wim.Monna@knmi.nl

## 1.1 BACKGROUND

Atmospheric research and weather forecasting use models at increasingly smaller spatial and temporal scales. Therefore aerological measurements with better resolution are needed. With respect to wind COST-76 results demonstrated that wind profilers can measure wind with adequate resolution, and are sufficiently developed to be used operationally. This has led to the EUMETNET programme WINPROF, with the objective to maintain and develop the know-how of COST-Action 76 on wind profiling radars and to organize the exchange of their data. The second phase, WINPROF-II started May 2005.

However, there still is a lack in adequate measurements of vertical profiles of other essential meteorological parameters, in particular of temperature and water (solid, liquid and vapour). Measurements of these parameters are particularly important for short-range forecasts and nowcasting, including boundary-layer evolution and pollution dispersion. Although there are already instruments such as radiometers, lidar and cloud radar that in principle can measure these parameters, the resolution needs further improvement, and real operational use is hardly possible yet.

Realising that integration of these techniques on one location can yield better vertical profiles, the concerted Action COST-720 was proposed. The main objective of the action is the development of cost-effective integrated ground-based remote-sensing stations for atmospheric profiling and the assessment of their use for meteorological analysis and forecast as well as climate research and climate monitoring. Advantages of integrated remote-sensing systems are:

- integration of various techniques in one profiling station will enable the derivation of additional parameters and the improvement of the quality control procedures

- reduced efforts and cost of manual service and maintenance of the stations, in particular under operational conditions, also allowing cost-effective operation in remote areas

- increase interest of the industry to reduce the costs of remote-sensing instruments

It is stressed here that ground-based remote-sensing techniques are, and will remain, complementary to already existing upper-air observing systems for various reasons:

- radiosondes can provide high-resolution vertical profiles, but they cannot economically provide the high-time resolution data needed for the new fine-scale models and very short-range forecasts

- commercial aircraft measurements may provide high-time resolution data, but they are limited in profiling to regions around airfields

- geostationary-satellite measurements can meet timeliness and areal requirements, but they cannot supply profiles with sufficient vertical resolution and accuracy, particularly in the critical lower 2 km. Moreover, in most cases satellite sounding instruments have poor performance under cloudy conditions. Polar-orbiting satellites have better sounding capacities than geostationary ones but provide poor temporal resolution.

## 1.2 THE COST FRAMEWORK

Founded in 1971, COST is an intergovernmental framework for European Co-operation in the field of Scientific and Technical Research, allowing the co-ordination of nationally funded research on a European level. COST Actions cover basic and pre-competitive research as well as activities of public utility.

COST has clearly shown its strength in non-competitive research, in pre-normative co-operation and in solving environmental and cross-border problems and problems of public utility. It has been successfully used to maximise European synergy and added value in research co-operation.

The member countries participate on an "'a la carte"' principle and activities are launched on a "bottom-up" approach. One of its main features is its built-in flexibility. This concept clearly meets a growing demand and in addition, it complements the other Community programs.

COST has developed into one of the largest frameworks for research co-operation in Europe and is a valuable mechanism coordinating national research activities in Europe. Today it has almost 200 Actions and involves nearly 30,000 scientists from 34 European member countries and more than 80 participating institutions from 11 non-member countries and non-governmental organisations.

## 1.3 OBJECTIVES AND ORGANISATION

The aim of the action is is the development of cost-effective integrated ground-based remote sensing stations for atmospheric profiling and the assessment of their use for meteorological analysis and forecast as well as climate research and climate monitoring.

A COST Action was proposed to realize these goals as it is the best framework in view of the following: In practice, remote-sensing tools are often exploited by institutions that have specific knowledge and expertise in a limited number of techniques. Moreover, cooperation between data users (e.g. numerical modellers) and the instrumental community is currently rather weak. This COST action, inter alia, addresses this weakness through proposing a well-structured international project, in which experts from National Weather Services, Universities and Industry cooperate.

COST-720 started October 4, 2000 for a period of 5 years. However, because of the delay resulting from the transition of the COST Office, and in order to allow some additional research connected to field experiments, the Action was extended until June 3, 2006. 12 EU countries participated: Austria, Finland, France, Germany, Greece, Italy, The Netherlands, Poland, Portugal, Spain, Switzerland and the United Kingdom. Also non–COST institutions participated from Macao and Ukraine.

Though originally three Working Groups were foreseen, it was decided to establish only two:

**Working Group 1:** *Basic techniques and algorithms*

Tasks were the assessment of the state of the art of individual techniques in view of their potential for integration. Where necessary and possible work has been done on improvements, especially with respect to algorithms. Considered measurement systems were in particular: Microwave and infrared radiometer, lidar, wind profiling radar, cloud radar and C-band weather radar.

**Working Group 2:** *Integration*

Tasks were the derivation of profiles of temperature, humidity and clouds. Some additional activities on data use were carried out, such as the assessment of assimilation techniques for humidity and cloud profiles, impact studies on ground-based networks of high-resolution profiling stations, and a proposal for a BUFR code for integrated profiling stations.

## 1.4 RESULTS

Key activities were the following five field experiments:

- TUC-2003 (Temperature, Humidity and Cloud Profiling campaign)

This field experiment held in Payerne from November 15, 2003 until February 15, 2004. It was a COST-720 initiative, broadened into the field of weather

forecasting and automatic cloud cover detection. The experiment was designed to test single ground-based temperature profiling systems and humidity profiling systems. Additionally, automatic cloud detection systems were assessed. A dataset was provided which on one hand shows how the remote sensing systems behave at various weather conditions with a focus on fog related phenomena. Moreover this dataset enables the study of possibilities for system integration for improved temperature and humidity profiling. Finally, the usefulness of these data for the detection of PBL phenomena for weather forecasting can be assessed. In the mean time these data were explored at several meetings. The research led to 10 publications in a special issue of *Meteorolog.Zeitschr.*, Vol.**15**, No. 1, Febr. 2006.

- International Radiosonde Intercomparison in Mauritius, February 2005

After discussion with the delegate from WMO it was decided to participate with GPS water vapour, cloud radar and laser ceilometer, as this is seen as of mutual benefit for WMO and COST-720. A WMO report has been completed and can be found on the WMO web page at:
http://www.wmo.int/pages/prog/www/IMOP/publications/IOM-83_RSO-Mauritius/IOM-83_Radiosondes_Vacoas2005.pdf .

- Convective Storms Initiation Project CSIP

The CSIP experiment (July 2004, June–August 2005) was conducted by several UK universities, the Met Office, CCLRC (who own the Chilbolton Observatory where the experiment was based) and colleagues from various institutes in Germany. The aim was to improve the understanding of how convective storms are initiated. A wide variety of instruments were deployed at Chilbolton and across the surrounding area. A microwave radiometer and laser ceilometer were deployed alongside a 1290 MHz windprofiler at Linkenholt, Hampshire, UK. Remote sensing from these instruments was supplemented by additional measurements from the Chilbolton radar scanning across the area of the experiment. Hourly radiosondes were performed for 6 day periods. This will allow integration studies to continue on summertime boundary conditions.

- LAUNCH[1]

More than 20 institutions participated in the LAUNCH field experiment from August 29, 2005, until the end of October. The first major objective is related to improvements in NWP modelling. This refers on one hand to a 4D-data set for the validation of model output as well as for further developments of physical parametrisations. Data were provided by a large set of different remote-sensing

[1] International Lindenberg campaign for assessment of humidity and cloud profiling systems and its impact on high-resolution modelling

systems and 2 complete integrated stations for monitoring wind, temperature, water vapour and clouds. The second major objective is related to the realisation of an assessment of water-vapour lidar and microwave systems providing input for mesoscale NWP assimilation experiments in Eastern Germany as well as middle and Southern Italy. Furthermore, the LAUNCH campaigns enabled an assessment of new (basic) remote-sensing techniques for atmospheric profiling, particularly a new single-photon-counting high-range ceilometer and a FTIR spectrometer for atmospheric temperature and humidity sounding.

- Helsinki Testbed

August 2005 meteorological measurement campaigns started in Southern Finland. Aim is to provide input and experience for mesoscale weather research, forecast and dispersion model development and verification, information systems integration, end-user product development and data distribution for public and research community. The Finnish weather observation network has been supplemented with nearly 60 stations equipped with Vaisala WXT510 weather transmitters, of which 42 are cell-phone base-station masts. New ground-based remote-sensing instruments in the testbed domain are a 1,3 GHz wind profiler/RASS, a dual-polarization weather radar in Helsinki, and five laser ceilometers.

These field experiments and the subsequent research with the data obtained, partly facilitated by Short Term Scientific Missions and Expert Meetings, enhanced the networking and cooperation between European scientists in these fields and with existing research programmes such as CloudNET and BBC, broadening the expertise within the Action and increasing its momentum. These networks will be profitable for future research.

This volume reports on the results of the experiments and research in detail in the following chapters. In this Introduction we only mention some key items:

➢ Cloud geometry and structure

Instruments: Radar (estimation of radar reflectivity), lidar, (extinction profile), microwave radiometer and first guess.

➢ Fog, low level clouds, cloud top and cloud base.

Instruments: Ceilometer, FM-CW radar, present-weather sensor.

➢ Humidity profile.

Instruments: Microwave radiometer, wind profiler (S/N ratio, spectral width), cloud radar, ceilometer, GPS, ASMUWARA (all-sky multi-wavelength radiometer, Uni-Bern).

➢ Temperature profile 1.

Instruments: Microwave radiometer, infrared radiometer, cloud radar, ceilometer, wind profiler. A variational method has been developed to integrate observations from these instruments with *a priori* information from an NWP model. The required forward models and error characteristics have been developed and validated for some of these observations. The same technique can be applied to the retrieval of humidity profiles.

➢ Temperature profile 2.

Instruments: Wind profiler (VHF), RASS.

## 1.5 OUTREACH ACTIVITIES

COST-720 organised two workshops.

The first workshop was held in L'Aquila (Italy) on invitation by the *Scuola Superiore Guglielmo Reiss Romoli* (SSGRR), June 18-21, 2002. The main aim was to discuss ways forward in the field of integrating ground-based remote-sensing techniques.

The COST-720 Final Symposium was held in Toulouse on invitation by Météo France, May 15-18, 2006. Its aim was the dissemination of COST-720 results, and discussions on future research and project proposals. Abstracts are available at Météo France. The presentations can be found at:
http://www.cnrm.meteo.fr/cost720/gb/program/program_detail.html

Results of the TUC field experiment were published in a special issue of Meteorologische Zeitschrift, Volume 15, No 1, February 2006 (see at:
http://www.ingentaconnect.com/content/schweiz/mz/2006/00000015/00000001;jsessionid=13vllawg2ultw.victoria ).

At the $7^{th}$ International Symposium on Tropospheric Profiling: Needs and Technologies, Boulder, Co, USA, June 11-17, 2006, many COST-720 results were presented, as well as, on invitation, an overview of the action as a key-note lecture.

Chapter 2

# USER NEEDS

John Nash[1], Tim Hewison[2], and Catherine Gaffard[2]

[1] *UK MetOffice, Exeter, United Kingdom*
✉ John Nash@meto.gov.uk

[2] *UK Met Office, Reading University, Reading, UK*

## 2.1 USER CATEGORIES

User needs for integrated profiling were reviewed at the first COST-720 workshop held in L'Aquila in 2002, At that time , a wide range of atmospheric variables were considered for the action. To concentrate the manpower resources available in the project it was decided to limit investigations primarily to profiles of temperature, water vapour, and wind and profiles of cloud properties, with some limited considerations associated with lidar measurements of aerosol profiles.

As the action progressed, the requirements of users were gradually changing as numerical weather prediction techniques developed, along with the data assimilation techniques in use. The observations available from commercial aircraft increased and there was a rapid increase in upper air observations from new satellite observing systems. Hence, most users primarily paid attention to these new data sources and data assimilation techniques were developed to exploit the large data sets available from satellites. Thus, whilst the influence of wind profiler measurements were investigated, assimilation techniques were not centred on optimizing the high temporal resolution available from such systems, and the limited number of integrated profiling systems were not the first priority for the numerical weather prediction users during most of the action.

In planning for the future, priorities for the national weather services have often been to ensure exploitation of the data available from satellites, and then to invest in ground based systems for information which was not readily available with suitable resolution from most current satellites, e.g. upper wind, and for systems observing at heights where the vertical resolution required could not be met from satellites e.g. temperature and humidity structure in the lower

troposphere and cloud profiles at low and mid levels as might be provided from integrated profiling systems..

In this chapter we will refer to results from a detailed review of user requirements performed by Stringer (2006) in the UK Met Office for the various atmospheric variables required by all types of users in the Met Office. This review was performed at the very end of the COST-720 period, but allows some amplification of results from the earlier workshop. Within the Met Office, this review was used to check which variables could be derived from space based satellite systems and then to establish which measurements still needed to be performed by ground based observing systems. The result of this review within the Met Office was that integrated profiling systems would be tested along with in-situ observing systems and weather radar observations within a new development project, lasting at least until 2011, to establish the best mix of observing systems to fill the requirements for more upper wind and associated temperature, humidity and cloud profiles than are currently provided by the operational observing networks. Here the review will be used to indicate suitable performance targets for the development of integrated profiling systems.

### 2.1.1 NUMERICAL WEATHER PREDICTION

COST 720 agreed that numerical weather prediction (whether for operational meteorology or for research and development of different types of numerical models) was one of the primary users for the integrated profiling stations which were to be developed. Observations would have to be assimilated for use in the forecasts produced, but would also be required to validate the products from the models and hence to help identify current weaknesses in the numerical models. In both operational and research models there is a trend towards much finer grids, with spacing between grid points less than 2 km being necessary to represent some types of severe weather. In addition, the number of levels at which data are input into NWP models is increasing with time. For instance, in the current Met Office model with 50 levels the pressure level are separated by about 50m in height near the surface, 400m at about 3 km above the surface and about 1 km at 10 km above the surface. However, a 70 level configuration is now being implemented with smaller spacing between levels in the lower troposphere. Thus, the averaging in the vertical applied to observations with high vertical resolution (such as from radiosondes) is becoming lower with time and NWP users may benefit more from these high resolution profiles.

Some arbitrary classification of models into global, regional and fine scales was used in the review of user requirements because this allows some decisions to be made on the observations needed to optimize forecasts in the immediate vicinity of the observing network and its region. The requirements for this observation are more stringent than when concerned with the forecast accuracy in an area remote from a given observing network.

In the latter part of the COST 720 Action enough observations were being produced from integrated profiling systems that it was possible to start data assimilation experiments and to evaluate forecast impacts, but in practice most of these studies required further effort following COST 720.

### 2.1.2 NOWCASTING AND VERY SHORT-RANGE NWP

Nowcasting and very short-range numerical weather prediction have different user requirements to the regional numerical weather prediction. Again these users were considered of primary importance within COST-720. Here the use of the observations tends to be targeted for particular applications e.g. forecasting fog clearance, forecasting convection (instability index, capping inversions), forecasting dispersion of pollutants (stability and vertical speed), mesoscale precipitation, thermal outflows from convection, leading to early warnings for significant /severe weather.

In general, the requirements are more stringent than for regional NWP for vertical resolution, observing cycle and delay in availability and much more so for horizontal resolution, because accurate vertical stability, the depth of the boundary layer and the heights and strength of the capping inversions, the location of intrusions of dry air near the ground are significant for many applications.

However, some nowcasting applications in the Stringer review have lower accuracy requirements than those for regional NWP. It is not obvious why this is the case, since some of the uses requiring lower accuracy temperatures are for instability indices which require good consistency in the vertical. In any case, the upper air temperature fields need to be consistent between different types of observing system if they are to be useful for a wide range of use. Thus, the user requirements show there is a need for further investigations. A variety of observing techniques need to be investigated in field experiments to find cost-effective mixtures of observing systems for the observing networks, particularly for regions specified nowcasting applications are of greatest importance. So the main application in a given area will also influence the choice of equipment. This will also be influenced by the weather climatology of the area. Observing systems that will not function very well with low cloud or rain may not be very useful in areas which have large amounts of low cloud, but may be the optimum choice for areas which are mostly sunny.

In future, although nowcasting will be supported largely by numerical weather prediction, there will be needs to monitor trends in some observations at high temporal resolution, e.g. trends in inversion height, cloud top height, etc., so that some of these observations will still be required to be displayed independently for the foreseeable future.

## 2.2 USER REQUIREMENTS

The requirements of all the users of upper air observations in the Met Office were reviewed by Stringer (2006). The requirements are expressed in terms of the accuracy, vertical and horizontal resolution, observing cycle and delay required for profiles of temperature, humidity, wind (horizontal and vertical), cloud liquid, ice, snow, precipitation and aerosol, as well as column integrated water vapour, boundary layer top, cloud base and top heights. In most cases these requirements are the same for the upper and lower troposphere, although the temperature requirements for the boundary layer are more stringent. Although different tables of requirements have been compiled for climate monitoring, global and regional NWP, synoptic, aeronautical and nowcasting applications, we concentrate here on the requirements for regional NWP. These are generally more stringent than other applications – requiring higher resolution observations in time and space and it is here that ground-based remote sensing instruments are likely to have most impact.

The requirements are defined in terms of the *minimum* threshold for an observations to have any impact on each application, the *breakthrough* threshold at which the observations could provide a significant advance in forecast capability (relative to that currently available), and the *maximum* threshold, above which no significant benefit will be felt.

In these user requirements *accuracy* is defined as the 2-sigma uncertainty due to random and systematic errors in the observations. When there is only one data source for each variable the specification of the accuracy may be less important. However, this becomes more critical when multiple systems are involved to ensure they can be integrated optimally.

### 2.2.1 REGIONAL NUMERICAL WEATHER PREDICTION

The user requirements are shown in table 2.1 for regional numerical weather prediction. Note, the minimum horizontal resolution required is not provided even by the current radiosonde network and the breakthrough values require a big change in the way upper air measurements are produced. It is here that observations from ground-based remote sensing systems are expected to have most beneficial impact, with certain types of wind profiler fulfilling the requirements for helping to track potential vorticity anomalies in the upper troposphere lower stratosphere and intrusions for dry stratospheric air into the middle troposphere. Information from surface based radiometers and UHF wind profilers is concentrated in the lower troposphere, which often has high temporal variability and needs to be observed at high temporal resolution. Aircraft and weather radars will also provide useful measurements to improve the horizontal resolution of the observing networks. In general, better temperature accuracy, vertical and horizontal resolution is required in the boundary layer than the rest of the lower troposphere due to its greater

variability in space and time.

*Table 2.1:* User requirements of temperature and humidity profiles for Regional NWP – minimum, breakthrough and maximum thresholds

| WMO Parameter | Vertical Region | Horizontal Resolution (km) | | | Vertical Resolution (km) | | | Observing Cycle (h) | | | Delay of Availab. (h) | | Accuracy | | |
|---|---|---|---|---|---|---|---|---|---|---|---|---|---|---|---|
| | | Min | Brk | Max | Min | Brk | Max | Min | Brk | Max | Min | Max | Min | Max | Units |
| Atmospheric temperature profile | Boundary Layer | 50 | 10 | 1 | 0.5 | 0.3 | 0.01 | 3 | 1 | 0.17 | 3 | 0.08 | 1.5 | 0.5 | K |
| Atmospheric temperature profile | Lower & Upper Troposphere | 200 | 30 | 3 | 2 | 1 | 0.1 | 12 | 3 | 0.5 | 5 | 0.25 | 1.5 | 0.5 | K |
| Specific humidity profile | Lower & Upper Troposphere | 200 | 30 | 3 | 2 | 1 | 0.1 | 12 | 3 | 0.5 | 5 | 0.25 | 10 | 5 | % |
| Specific humidity | Column | 100 | | 10 | | | | 1 | | 0.5 | 0.5 | 0.1 | 5 | 1 | $kg/m^2$ |
| Wind profile (horizontal comp.) | Lower & Upper Troposphere | 200 | 30 | 3 | 2 | 1 | 0.1 | 12 | 3 | 0.5 | 5 | 0.25 | 3 | 1 | m/s |
| Wind profile (vertical comp.) | Lower & Upper Troposphere | 200 | | 3 | 2 | 1 | 0.1 | 12 | | 0.5 | 5 | 0.25 | 5 | 1 | cm/s |
| Boundary Layer Height | Boundary Layer | 50 | 10 | 3 | | | | 3 | 1 | 0.5 | 3 | 0.25 | 300 | 100 | m |
| Cloud base height | Column | 50 | 10 | 3 | | | | 3 | 1 | 0.5 | 3 | 0.25 | 1 | 0.05 | km |
| Cloud top height | Column | 50 | 10 | 3 | | | | 3 | 1 | 0.5 | 3 | 0.25 | 1 | 0.5 | km |
| Cloud cover | Column | 50 | 10 | 3 | | | | 3 | 1 | 0.5 | 3 | 0.25 | 20 | 5 | % |
| Cloud water profile (<100µm) | Lower & Upper Troposphere | 200 | 30 | 3 | 2 | 1 | 0.1 | 12 | 3 | 0.5 | 5 | 0.25 | 50 | 5 | % |
| Cloud Water Snow profile | Lower & Upper Troposphere | 200 | | 3 | 2 | 1 | 0.1 | 12 | | 0.5 | 5 | 0.25 | 50 | 5 | g/kg |
| Cloud ice profile | Lower & Upper Troposphere | 200 | 30 | 3 | 2 | 1 | 0.1 | 12 | 3 | 0.5 | 5 | 0.25 | 50 | 5 | % |
| Precipitation profile | Boundary Layer, Lower & Upper Trop | 200 | 10 | 1 | 2 | 1 | 0.1 | 3 | 1 | 0.08 | 3 | 0.25 | 1 | 0.1 | mm/h |
| Aerosol profile | Lower & Upper Troposphere | 200 | 30 | 3 | 2 | 2 | 0.1 | 24 | 6 | 1 | 5 | 0.25 | 20 | 10 | % |
| Ozone profile | Lower & Upper Troposphere | 200 | | 3 | 2 | 1 | 0.1 | 24 | | 3 | 5 | 0.25 | 20 | 5 | % |

The most significant changes in observations for regional numerical weather prediction were summarised as

- More comprehensive wind and moisture observations in space and time, especially in the boundary layer. Wind profiles closer together.
- More accurate estimates of precipitation
- More comprehensive observations of cloud base, cloud thickness and other cloud properties

And for the global numerical weather prediction

- Wind profiles up to and including stratosphere/mesosphere
- Temperature profiles of adequate vertical resolution in cloudy areas

Precipitation observations

### 2.2.2 NOWCASTING

The primary observing network changes required for nowcasting/very short range numerical weather prediction were summarised as

- More frequent 3-dimensional wind field with closer horizontal and vertical spacing
- More frequent 3-dimensional humidity field with closer horizontal and vertical spacing
- Clouds and precipitation profiles
- Cloud amount and base height from remote sites and marine areas
- More frequent 3-dimensional temperature field with closer horizontal and vertical spacing

In case of nowcasting, the requirements for atmospheric parameters reflecting the large range of applications were larger than for regional NWP and included:

- Total column amounts of aerosol and ozone,
- airborne toxic material,
- black carbon,
- $CH_2O$,
- effective radius of cloud droplets, smoke, sand and dust location,
- fog top,
- overshoot of connective cloud,
- electric field,
- height of melting layer,
- lightning detection,
- profiles of the concentration of pathogens,
- petroleum products,

- PM10 aerosol,
- radionuclides,
- CO, NO, $NO_2$,
- volcanic ash,
- volcanic ash,
- eruptions and plumes,
- slant visibility.

### 2.2.3 GLOBAL CLIMATE MONITORING

The horizontal and vertical resolution required for global climate monitoring is much lower than for regional NWP, while the observing cycle and delay in availability is much longer. However, the accuracy requirements are similar to those in table 2.1. In addition to the quoted accuracy, figures for bias and decadal stability are also given for temperature, humidity and wind. For temperature a decadal stability of measurements of 0.05K is required, for water vapour 0.3% per decade and wind about 0.1 $ms^{-1}$ per decade. These requirements are difficult to meet with any observing system and are not straightforward for ground-based instruments due to the variable nature of their operating environment.

Global climate monitoring requires additional observations of profiles of temperature, humidity, cloud water ice and wind in the stratosphere as well as the column amount of liquid water and lighting location, which are not required for regional NWP.

Climate monitoring requires a network of very stable instruments sampling in the same configuration over periods $>$10 years [IPCC:01] to detect small changes. As new observing systems the absolute calibration has not yet been demonstrated over these timescales, it is unlikely that their data will contribute significantly to the climate monitoring requirements for some time.

## 2.3 DISCUSSION

All observing systems have strengths and weaknesses – none meet the breakthrough levels for all aspects (accuracy, vertical and horizontal resolution, observation cycle and delay). However, it may be hoped that the solution to these requirements could be best met by a composite of different observing systems. For this reason procurement specifications for instruments may be different from the ideal requirements.

In table 2.2, a specification is suggested for a useful integrated profiling system which is an interpretation of the information in table 2.1 for an observing instrument or group of instruments which ought to have positive

impact when in use. In some cases, e.g. horizontal wind, the requirements have been tightened to exclude faulty instrument performance.

*Table 2.2:* Interpretation of table 2.1 giving more specific requirements for measurements that should prove useful and reducing the ranges suggested to those which should be useful

| Parameter | Horizontal resolution | Vertical resolution | Observing cycle | Accuracy |
|---|---|---|---|---|
| **Wind** (u,v) | 1 - 30 km<br>Min 100 km | 100m [300m]<br>- 1 km | 0.5 - 3h<br>[0.25h] | 0.5 - 1.0 m $s^{-1}$ |
| **Humidity** | 1 - 30 km<br>Min 100 km | 150m [100m]<br>- 1 km [300m] | 0.5 - 1h | 4 - 10 % |
| **Temperature profile** | 1 - 30 km<br>Min 100 km | 100 - 300m | 0.5 - 3h | 0.5 K |
| **Aerosol profile** | 10 - 30 km<br>Min 200 km | > 2 km | 1 - 6h | 20 % |
| **Cloud base height** | 3 - 30 km<br>Min 100 km | > 100m | 5min - 3h | 90 m |
| **Cloud cover** | 1 - 30 km<br>Min 100 km | | 5min - 3h | 10 % |
| **Cloud top height** | 1 - 10 km<br>Min 50km | 100m | 10min - 3h | 100 m |
| **Vertical wind** (w) | 500m - 30 km<br>Min 200km | 50m - 1 km | 10min - 3h | 1 - 10 cm $s^{-1}$ |
| **Column water vapour** | 10 - 50 km<br>Min 100 km | | 0.5 - 1h | 1 kg $m^{-2}$ |
| **Boundary layer height** | 3 - 10 km<br>Min 50 km | 100 - 300m | 0.5 - 3h | 100m |
| **Cloud ice profile** | 3 - 30 km<br>Min 200km | 100m - 1 km | 0.5 - 12h | 5 % |
| **Cloud water profile** | 3 - 30 km<br>Min 200km | 100m - 1 km | 0.5 - 12h | 5 % |
| **Height of melting layer** | 5 - 10 km | | 0.25 - 1h | 100m |
| **Precipitation profile** | 1 - 5 km<br>Min 50 km | 100m - 1 km | 5min - 3h | 0.1 mm / h |

### 2.3.1 RANDOM VS. SYSTEMATIC ERRORS

In these user requirements *accuracy* is defined as the 2-sigma uncertainty due to random and systematic errors in the observations. For climate monitoring applications the bias component becomes more important as typically many observations are averaged spatially and temporally to reduce the random error of their mean. Whereas for NWP applications, the random component is often more important as the bias is assumed to vary slowly and may be

corrected as part of the assimilation cycle by comparing time series of observations against model backgrounds.

### 2.3.2 IMPLICATIONS FOR NETWORK DENSITY

If the user requirement for the *minimum* horizontal resolution of boundary layer temperature profiles is taken at face value, then ground-based observations will have no impact in regional NWP, unless they can be deployed in a dense network of $\sim$100 in the UK or $\sim$1000 across Europe. It would be prohibitively expensive to deploy a network of ground-based instruments that essentially take spot measurements (i.e. do not cover a significant area) capable of exceeding the stated *minimum* threshold for horizontal resolution of regional NWP. However, it may be possible to exploit the observations' high time-resolution as a proxy for horizontal sampling within 4D-VAR.

### 2.3.3 DIRECT VS. INDIRECT OBSERVATIONS?

Many systems do not provide direct observations of these variables. In these cases it is difficult to compare the benefit of each observation. Many of these observations need *a priori* information from the NWP model because the retrieval of geophysical parameters is *ill-posed*. These systems often apply empirical bias corrections to the observations as part of the assimilation cycle to ensure there is no systematic difference between the observations and the model and account for any long term drifts in the instrument's calibration.

When assessing different observations it is necessary to specify whether each system is capable of providing observations independent of NWP. It is important that some direct observations are maintained in the Global Observing System to ensure the models do not diverge from the true state of the atmosphere, as well as the ongoing requirements for direct observations that are stable enough that the bias does not change significantly on decadal timescales. It is also important that direct observations are maintained to be co-located with remote sensing observations to allow monitoring of their absolute calibration.

## Bibliography

IPCC: Climate Change 2001: The Scientific Basis, *Intergovernmental Panel on Climate Change*, Cambridge University Press, 2001.

Stringer, S.: User Requirements for Upper Air Observations, *Observation Supply* Met Office Internal Report, Available from Met Office, FitzRoy Road, Exeter, 2006.

Chapter 3

# INSTRUMENTS FOR ATMOSPHERIC PROFILING

## 3.1 THE RATIONALE FOR SENSOR SYNERGY

Herman W. J. Russchenberg[1] and Dirk A. M. Engelbart[2]

[1] *Delft University of Technology – IRCTR, Delft, The Netherlands*
✉ H.W.J.Russchenberg@irctr.tudelft.nl

[2] *German Meteorological Service, Richard-Aßmann-Observatory, Lindenberg, Germany*

Atmospheric processes are complex. Many parameters are involved and non-linear feedback mechanisms are linking changes in atmospheric states. Observation of these processes is not easy. Existing instruments are only suited to measure a limited number of parameters; they will never display the full picture. A broader view on all interacting processes can only be achieved when observations of different sensors are combined, and when the synergistic use of these observations leads to additional atmospheric parameters that are otherwise not retrieved. As an example for an additional parameter, which may not be retrieved by a single system, the radio-acoustic sounding system (RASS) may be quoted. While the use of a simple wind profiler radar system (WPR) will only provide vertical profiles of the three-dimensional wind vector, the addition of a sound source to the WPR as well as a modified data processing and evaluation will beneficially provide high-quality profiles of the atmospheric temperature and potentially enables furthermore to reduce the influence of ground clutter on WPR wind measurements by provision of an alternative method for wind measurements.

The following chapter 3 here, describes the merits of the most important basic techniques for atmospheric profiling in view of their potential for sensor synergy as being useful for data assimilation in NWP models, for research on climate processes in high time resolution or as a means for a reference to satellite remote sensing and/or numerical models' output. – The rationale for sensor sensor synergy follows from the different interaction mechanisms

between electromagnetic radiation and atmospheric phenomena. This depends on the wavelength used, and whether signals are scattered, reflected, absorbed and/or emitted.

Passive instruments, like radiometers, measure the radiation emitted by the atmosphere. In their simplest form, radiometers measure path-integrated values. Advanced radiometers, using multiple frequencies, have a limited capability of profiling. Active instruments on the other hand, like radars or lidars, are profiling instruments and can measure spatial structures in the atmosphere. The advantage of the combined use of such instruments can be exemplified by the following case of water clouds:

The water content and droplet size in stratocumulus increases with its depth. Ceilometers or generally lidars are very efficient in detecting the cloud base, but the increasing attenuation of the lidar signal, as it penetrates the cloud, often prevents it from reaching the cloud top. Cloud radars on the other hand, have the opposite shortcoming: often they are not sensitive enough for detection of the small droplets at the cloud base, but most adequate for cloud top detection. Combination of these instruments is therefore highly beneficial to obtain the cloud boundaries. Radar and lidar are both differently sensitive to droplet size: radar to the larger droplets, and lidar to the smaller ones. When combined, better insights are obtained in the micro-structure of the clouds. Finally, when combined with a microwave radiometer which gives the total liquid water path in the cloud, properties like mean droplet size, number concentration and liquid-water size can be derived.

This chapter describes the most common remote-sensing instruments for operational and scientific use: the microwave radiometer, advanced lidars and the ceilometer, the wind profiler/RASS, SODAR, the FTIR method, cloud radar and weather radar. Whilst these instruments are often used in standalone mode, their combination offers a wide range of new possibilities. What are the most important aspects of these instruments to make synergistic use fruitful?

- They should measure different aspects of the atmospheric phenomena under consideration. This can be achieved by using significantly different frequencies, viewing angles and/or by combination of active and passive instruments. Examples are:
  - Dual frequency radar: combining high and low frequencies makes observation of different aspects of, for instance, the raindrop size distribution feasible;
  - The radar/lidar combination, where the differences in scattering properties enable the detection of, for instance, aerosols below cloud base and cloud droplets, or the determination of particle sizes in ice clouds;
  - Wind profiler and RASS systems in which Doppler-shifted radar backscattering caused by acoustic wavefronts is used to estimate temperature profiles;

  - Active wind profiler and passive microwave radiometers to get an rough estimation on humidity profiles.

- In case sensor synergy is used to get more details about the microstructure of atmospheric phenomena, an accurate common observation volume has to be achieved.

*Table 3.1.* Potential of sensor synergy, discussed in Chapter 4. The top line lists the instruments. The *application* boxes shows which combinations are suited for certain areas

| *instrument* | cloud radar | lidar | radiometry | wind profiler/RASS | sodar |
|---|---|---|---|---|---|
| *application* | cloud microstructure and geometry | | | | |
| | fog layer detection | | | | |
| | | | wind, temperature, humidity | | |
| | | cloud base temperature | | | |

The table above gives an overview of typical application fields of sensor synergy. They are discussed in detail in chapter 4. This chapter however, describes the different instruments separately and in depth. – The driving force behind the efforts to combine instruments on the one hand was to derive *additional parameters* by combining single remote-sensing techniques for atmospheric profiling. On the other hand, the motivation for an investigation of the potential of sensor synergy was related to the demand of a *maximized data quality* of measured parameters, in order to enable and to facilitate proofs of climate change by measurements.

Generally, the demand on high-quality data as well as on detailed information about the vertical structure of the atmosphere is of crucial importance to understand the energy balance of the atmosphere, i.e. how is incoming solar radiation affected by gases, clouds and aerosols, and how is heat radiation emanating from the Earth absorbed and emitted by those same atmospheric phenomena? Such questions can not be answered without an integral view of atmospheric processes and the links between them. In this field, ground-based remote sensing provides useful options and tools to help understanding these processes by real measurements with known error characteristics, being always an invaluable advantage compared to re-analysis data of numerical models or to satellite remote sensing as long as referred to atmospheric profiling using passive space-borne sensors and their related parameter-retrieval techniques.

Parallel to this, improvements in numerical weather prediction have also stimulated new technological developments. Especially the need for parameterizations of small-scale phenomena, e.g. clouds, in weather prediction models is required. In this field, the subsequent chapter 4 will later describe techniques to assimilate data, derived from sensor synergistic techniques, in numerical weather prediction models.

# 3.2 GROUND-BASED MICROWAVE REMOTE SENSING OF THE TROPOSPHERE

Christian Mätzler[1], Ed R. Westwater[2], Domenico Cimini[3,2], Susanne Crewell[4], Tim Hewison[5], Jürgen Güldner[6], and Frank S. Marzano[7]

[1] *Institute for Applied Physics, University of Bern, Bern, Switzerland*
✉ matzler@iap.unibe.ch

[2] *Cooperative Institute for Research and Environmental Sciences, University of Colorado / NOAA ESRL Physical Science Division, Boulder(Colorado), USA*

[3] *IMAA/CNR, Tito Scalo(Potenza), Italy. email: cimini@imaa.cnr.it*

[4] *University of Cologne, Institute for Geophysics and Meteorology, Cologne, Germany*

[5] *UK MetOffice, University of Reading, Meteorology Building, Reading, UK*

[6] *Richard-Aßmann Observatory Lindenberg, German Meteorological Service, Lindenberg*

[7] *University "La Sapienza", Rome, Italy*

## 3.2.1 INTRODUCTION

Surface-based radiometric measurements of atmospheric thermal emission are useful in a variety of applications, including meteorological observations for nowcasting and forecasting, atmospheric physics (boundary layer physics and turbulence, formation of clouds and precipitation), climate studies, air-sea interaction, validation of complementary methods, satellite-data validation, communication, geodesy and long-baseline interferometry, and fundamental molecular physics. One reason for the utility of these measurements is that with careful design, radiometers can be operated in a long-term unattended mode in nearly all weather conditions (Hogg et al., 1983; Liljegren, 2000; Ware et al., 2003; Revercomb et al., 2003; Ingold and Mätzler, 2000; Barbaliscia et al., 1998; Elgered and Jarlemark, 1998; Morland et al., 2005). An important feature is the nearly continuous observational capability on time scales of seconds to minutes. Measurements have enabled the continued development of absorption and radiative transfer models of the atmosphere since the 1940's, (Liebe, 1989; Rosenkranz, 1998, 1999; Hewison et al., 2006; Pardo et al., 2001, 2004; Dicke et al., 1946). This development has been greatly aided by long-term, carefully calibrated radiometer measurements, supplemented by frequent radiosonde releases using active sensors for cloud identification (Turner et al., 2003; Clothiaux et al., 2000). Last, but not least, is the development of retrieval and data assimilation algorithms (Rodgers, 1976; Han et al., 1997) with

which radiometer data can be combined with external data sources, such as forecasts or soundings from active sensors.

Assuming sky-looking microwave radiometers situated at the earth surface, the key atmospheric parameters that can be measured are the vertically Integrated amounts of Water Vapour (IWV) and of Liquid Water (ILW), sometimes also called Water-Vapour Path (WVP) and Liquid-Water Path (LWP), respectively. In addition, profile information can be obtained for temperature and humidity, but with limited vertical resolution. However, the measurement of cloud height requires additional sensors, such as lidars, radars or infrared radiometers. Although, microwave radiometers are very sensitive to rain, the complications arising from precipitation have not yet been fully exploited; some of the few studies on rain observations by microwave radiometers were reported by Marzano et al. (2002) and Sheppard (1996). On the other hand ice clouds are highly transparent, and thus not detectable, at frequencies below 100 GHz. Therefore, we confine our attention to radiometric measurements of water vapour, temperature, and cloud liquid water in the troposphere. Similar extensive reviews are given in Westwater et al. (2004b, 2005a,b), and some of the material in this overview has been extracted from these documents.

### 3.2.2 PHYSICAL PRINCIPLES OF MICROWAVE RADIOMETRY

The basic ideas of radiative transfer and thermal emission are given in Goody and Yung (1995) and their application to microwave radiometric remote sensing is outlined in Janssen (1993), Ulaby et al. (1981), Mätzler et al. (2006). From the concept of an ideal black body and *Kirchhoff's Law*, it is known that the emission from a black body depends only on its temperature, and that the higher the temperature of the body, the more is its emission. The idea is made quantitative by calculating the spectral distribution of a blackbody emission from *Planck's Law*, which expresses the radiance $B_\nu(T)$ emitted from a blackbody at temperature $T$ and frequency $\nu$ as

$$B_\nu(T) = \frac{2h\nu^3}{c^2}\frac{1}{(\exp(h\nu/kT)-1)} \tag{3.1}$$

where $h$ = Planck's constant, and $k$ = Boltzmann constant. The radiance expresses the emitted power per unit projected area per unit solid angle per unit frequency interval. The second consideration is to relate the emission from a real body, sometimes called a "grey" body, to that of a blackbody at the same temperature. The fraction of incident energy from a certain direction absorbed by the grey body is called absorptivity, $A(\nu)$. By Kirchhoff's Law of thermal radiation, the emitted radiance is $A(\nu)\cdot B_\nu(T)$ , which means that absorptivity and emissivity are equal. For a perfectly reflecting or transmitting body, the emissivity is zero, and incident energy may be redirected or pass through the body without being absorbed. In the situation considered here, namely upward-

looking radiometers viewing a non-scattering medium, the equation that relates our primary observable, brightness temperature, $T_b$, to the atmospheric state is the radiative transfer equation (RTE)

$$B_\nu(T_b) = B_\nu(T_c)\exp(-\tau_\nu) + \int_0^\infty B_\nu(T(s))\ \alpha_\nu(s)\exp(-\int_0^s \alpha_\nu(s')ds')\ ds\ , \tag{3.2}$$

or in the Rayleigh-Jeans Approximation

$$T_b = T_c\exp(-\tau_\nu) + \int_0^\infty T(s)\ \alpha_\nu(s)\exp(-\int_0^s \alpha_\nu(s')ds')\ ds\ , \tag{3.3}$$

where $s$ = path length in m, $T(s)$ = Temperature (K) at the point $s$, $T_c$ = Cosmic background brightness temperature of 2.75 K, $\tau_\nu$ = opacity = total optical depth along the path

$$\tau_\nu\ =\ \int_0^\infty \alpha_\nu\ (s)\ ds, \tag{3.4}$$

where $\alpha_\nu(s)$ = absorption coefficient in 1/m at the point $s$. The use of the blackbody source function in (3.2) is justified by the assumption of local thermodynamic equilibrium in which the population of emitting energy states is determined by molecular collisions and is independent of the incident radiation field (Goody and Yung, 1995).

Equation (3.2) and its simplified form in the Rayleigh-Jeans approximation (3.3) are discussed in textbooks such as Janssen (1993) and Ulaby et al. (1981), and its more general form including scattering is discussed in Gasiewski (1993) and Mätzler et al. (2006). Scattering, although neglected here, may arise from liquid, ice, or melting ice, depending on the size distribution of the particles. For our purposes, we note the dependence on the temperature profile $T(s)$ and the implicit dependence on pressure, water vapour, and cloud liquid through the absorption coefficient $\alpha$. For a plane-parallel atmosphere, s and the height h are related by $s{\cdot}\cos(\theta){=}\ h$, where $\theta$ is the zenith angle. Information on meteorological variables is obtained from measurements of $T_b$ as a function of $\nu$ and/or $\theta$. Equation (3.4) is used: (3.2) in forward model studies in which the relevant meteorological variables are measured by radiosonde in-situ soundings, (3.3) in inverse problems and parameter retrieval applications, in which meteorological information is inferred from measurements of $T_b$ or $\tau$, and (3.4) in system modelling studies for determining the effects of instrument noise on retrievals and optimum measurement ordinates, such as $\nu$ and $\theta$. Calculations of $T_b$ for a warm (surface temperature $T_s$ =293 K) atmosphere are shown in figure 3.1. The region around 22.235 GHz is used for sensing of water vapour,

while the transmission windows near 30-50, 70-100, and 130-150 GHz are used primarily for remote sensing of clouds. The strong absorption regions near 60 and 118 GHz are used for temperature sensing. Finally, the strong absorption region near 183 GHz is used to study very low amounts of water vapour such as are found during Arctic winter conditions.

### 3.2.3 MICROWAVE ABSORPTION AND EMISSION

The principal sources of atmospheric microwave emission and absorption are water vapour, oxygen, and cloud liquid. In the frequency region from 20 to 200 GHz, water-vapour absorption arises from the weak electric dipole rotational transition at 22.235 GHz and the much stronger transition at 183.31 GHz. In addition, the so-called continuum absorption of water vapour arises from the far wing contributions from higher-frequency resonances that extend into the infrared region. Again, in the frequency band from 20 to 200 GHz, oxygen absorbs due to a series of magnetic dipole transitions centred around 60 GHz and the isolated line at 118.75 GHz. Because of pressure broadening, i.e., the effect of molecular collisions on radiative transitions, both water vapour and oxygen absorption extend outside of the immediate frequency region of their resonant lines. There are also resonances by ozone that are important for stratospheric sounding (Klein and Gasiewski, 2000). In addition to gaseous absorption, scattering, absorption, and emission also originate from hydrometeors in the atmosphere. Our focus is on non-precipitating clouds for which emission and absorption are of primary importance.

**3.2.3.1 Gaseous Absorption Models.** Detailed calculations of absorption by water vapour and oxygen were first published by J. H. Van Vleck (van Vleck, 1947a,b). The quantum mechanical basis of these calculations, including the Van Vleck-Weisskopf line shape (van Vleck and Weisskopf, 1947), together with laboratory measurements, has led to increasingly accurate calculations of gaseous absorption. Both these historical- and recent- developments are discussed in Rosenkranz (1993). Currently, there are several absorption models that are widely used in the propagation and remote-sensing communities. Starting with laboratory measurements that were made in the late 1960s and continuing for several years, H. Liebe developed and distributed the computer code of his Microwave Propagation Model (MPM). One version of the model (Liebe and Layton, 1987) is still used extensively, and many subsequent models are compared with this one. Liebe later made changes to both water-vapour and oxygen models, especially to parameters describing the 22.235 GHz $H_2O$ line and the so-called water-vapour continuum (Liebe et al., 1993). More recently, Rosenkranz (Rosenkranz, 1998, 1999) developed an improved absorption model that also is extensively used in the microwave propagation community. However, there are many issues in the determination of parameters that enter into water-vapour-absorption modelling, and clear discussions

of several of these issues are given in Rosenkranz (1993) and Chapter 2 of Mätzler et al. (2006). Relevant to the discussion is the choice of parameters to calculate the pressure-broadened line width, which, in the case of water vapour, arises from the collisions of $H_2O$ with other $H_2O$ molecules (self broadening), or from collisions of $H_2O$ molecules with those of dry air (foreign broadening). In fact, Rosenkranz (1998, 1999) based his model on using Liebe and Layton's (Liebe and Layton, 1987) values for the foreign-broadened component, and those from Liebe et al. (1993) for the self-broadened component. Another model that is used extensively in the US climate research community is the Line-by-Line Radiative Transfer Model (LBLRTM) by S. Clough and his colleagues (Turner et al., 2003; Clough et al., 2005). An extension of the model, called MONORTM, is most appropriate for millimetre wave and microwave RTE studies (Clough et al., 2005). One feature of the Clough models is that they have been compared extensively with simultaneous radiation and radiosonde observations near 20 and 30 GHz. Recently, some refinements of absorption models have occurred. This first is the Rosenkranz (Rosenkranz, 2004; Tretyakow et al., 2005; Tretyakov et al., 2003) refinement of his 1998 codes. Another one is by Liljegren et al. (2005), which incorporates the line width parameters of the 22.235 GHz model from the HITRAN data base (Rothman et al., 2005) with a different continuum formalisation. Both of these new models showed initial promise in calculating emission from radiosonde data (Mattioli et al., 2005), but the change proposed by Liljegren et al. was not confirmed by observations in a winter climate by Hewison et al. (Hewison et al., 2006).

**3.2.3.2 Cloud Absorption Models.** For spherical particles, the classical method to calculate scattering and absorption coefficients is through the *Lorenz-Mie Equations* (Van de Hulst, 1981; Deirmendjian, 1969; Bohren and Huffman, 1983); for sufficiently small particles, the Rayleigh approximation can be used. For a given wavelength and single particle, the particle contribution is calculated; the total coefficients are then obtained by integration over the size distribution of particles. An important physical property for the calculations is the complex dielectric constant of the particle. The dielectric constant of liquid water is described by orientational relaxation of water molecules in the liquid phase, see Debye (Debye, 1929).

The strong temperature dependence of the relaxation frequency is linked to the temperature-dependent viscosity of liquid water; therefore the cloud-absorption coefficient also shows significant temperature sensitivity. Above $0^oC$, the dielectric constant can be well measured in the laboratory, and a variety of measurements have been made from 5 to 500 GHz (Liebe et al., 1991). However for super-cooled water, below $0^oC$, the situation is less certain, and, for example, models of Liebe et al. (1991), Grant et al. (1957), or Rosenberg

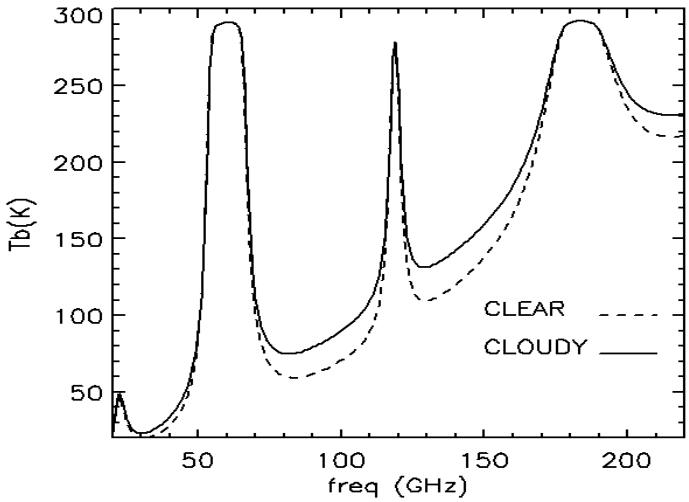


*Figure 3.1.* Calculated brightness temperatures (K) from 20 to 220 GHz for clear and cloudy conditions. The clear calculations are based on a standard atmosphere with the surface values (S) of $P_S$ *=1013 mb,* $T_S$ *=293 K,* $\rho_S$ *= 10 gm*$^{-3}$*, and IWVH = 23.4 mm. The cloudy atmosphere contains 1 mm of integrated cloud liquid with a cloud layer of liquid density of 0.1 gm*$^{-3}$ between 1 and 2 km. The absorption models used are given in figure 3.2.

(1972) differ by 20 to 30% in this region (Westwater et al., 2001). A recent evaluation of dielectric data of water by Ellison in chapter 5 of Mätzler et al. (2006) presents a new analytic model, but also stresses the need for more experimental investigations, especially at low temperatures. This is relevant for cloud remote sensing, because measurements of super-cooled liquid are important for detection of aircraft icing (Rasmussen et al., 1992). When calculating absorption for nonprecipitating clouds, we assume Rayleigh absorption, for which the liquid absorption depends only on the total liquid amount and does not depend on the drop size distribution, and scattering is negligible. The Rayleigh approximation is valid when the size parameter $\beta = |n(2\pi r/\lambda)| << 1$ (Deirmendjian, 1969). Here, $r$ is the particle radius, $\lambda$ is the free space wavelength, and $n$ is the complex refractive index. For rain and other situations for which the size parameter is greater than roughly 0.1, the full Mie equations, combined with a proper size distribution, must be used. Due to the nonspherical shape of ice hydrometeors, the situation is more complicated when scattering plays a role. Although this situation is beyond the scope of the present discussion, the particle size of cirrus clouds can be on the order of 100 microns, and scattering may be important near transmission windows at millimetre wavelengths. On the other hand, the dielectric properties of ice (Hufford, 1991; Mätzler, 1998; Mätzler et al., 2006) are very different from those of liquid water. The dielectric losses of ice have a minimum near 1 GHz, and ice is an almost perfectly loss-free medium over a large frequency range. Therefore microwave emission of pure ice particles can be neglected in most

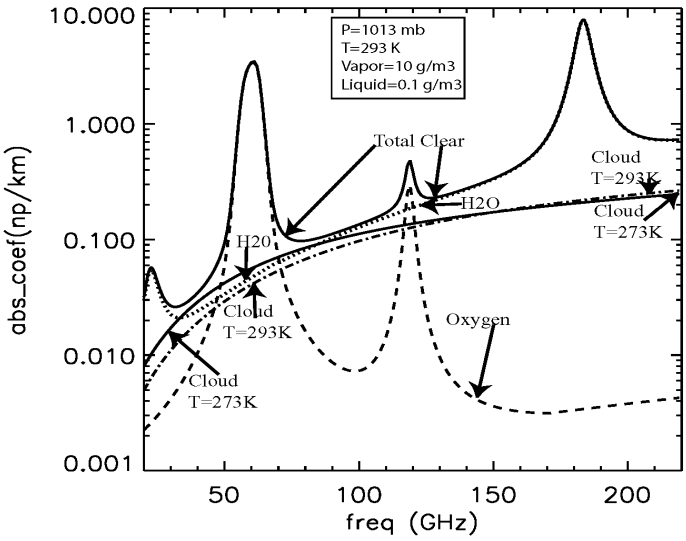


*Figure 3.2.* Microwave absorption spectra from 20 to 220 GHz. The absorption models used were Liebe (Liebe, 1989) for clear absorption, and Liebe et al. (Liebe et al., 1991) for cloud liquid. P = pressure, T = temperature, $\rho_V$ = *absolute humidity, and* $\rho_L$ = cloud liquid density.

cloud situations. Special situations occur when ice particles start to melt. A very thin skin of liquid water can be sufficient to cause significant absorption and thus emission. Usually, these conditions apply to precipitating clouds or in the so-called radar "bright band."

**3.2.3.3 Calculations of Absorption Spectra.** For standard conditions at sea level, we calculated the water vapour ($H_2O$), oxygen ($O_2$), and total clear ($H_2O + O_2$) contributions to the absorption coefficient. In addition, we calculated the liquid absorption coefficient for $\rho_L = 0.1$ gm$^{-3}$ at $T$= 293 and 273 K. From the results shown in figure 3.2, we note the strong oxygen absorption regions near 60 and 118 GHz and the large absorption near 183 GHz due to water vapour. For a given frequency, location and altitude, the oxygen absorption is relatively constant, with variations of 10 to 20%, while both the 22.235 and the 183.31 GHz absorptions can vary by a factor of 10 to 20 because of the variable density of water vapour. Note also the temperature dependence of cloud absorption, and the reversal of this dependence at around 150 GHz near the effective relaxation frequency of liquid clouds as described in chapter 5 of Mätzler et al. (2006).

**3.2.3.4 Radiometric Response to Atmospheric Profiles: Weighting Functions.** Equations (3.2)(3.3)(3.4) describe the theoretical radiometric response to atmospheric temperature T(s) and absorption coefficient $\alpha_v(s)$as a function of the path coordinate s. Since the absorption coefficient also depends

on the atmospheric state, the brightness temperature is a non-linear functional of the profiles of temperature, pressure, vapour density and liquid density.

However, it is quite revealing to consider the brightness-temperature response to small changes in an initial state or background profiles. Thus, if we denote these background profiles as $\{T_0, P_0, \rho_{V0}, \rho_{L0}\}$, then we can write

$$\delta T_b = \int_0^\infty (W_T(s)\,\delta T(s) + W_P(s)\delta P(s) + W_{\rho_V}(s)\delta\rho_V(s) + W_{\rho_L}(s)\delta\rho_L(s))\,ds \quad , \tag{3.5}$$

where the weighting functions W can be explicitly calculated from the dependence of $\alpha_v(s)$ on the background profiles. For simplicity in notation, we have suppressed the frequency dependence of W. Further discussion on the calculation of weighting functions and their significance can be found in Gasiewski (1993) and Westwater (1993).

**Temperature Weighting Functions Near 60 GHz.** The temperature weighting functions of the Radiometrics Microwave Radiometer Profiler (to be described below) are representative to other radiometer systems that use the 60 GHz $O_2$ emission band and are shown in figure 3.3a. Note the significantly different response of the first four channels to temperature in the first 2 km, and the lack of significantly different response above this altitude.

**Water Vapour Weighting Functions Near 22.235 GHz.** The MWRP also contains 5 channels for water vapour and cloud liquid density sensing; the corresponding water-vapour weighting functions are shown in figure 3.3b. We note that the 22.235 and 22.035 GHz weighting functions increase with height, while the 23.835 GHz function is almost constant with height. The constant response with height implies that the channel is the most appropriate to derive the vertically Integrated Water Vapour (IWV), the total amount of water vapour in a column of unit cross section:

$$IWV = \int_0^\infty \rho_V\, dh \tag{3.6}$$

where the atmospheric path variable is the height $h$ above the surface. The natural units of IWV are kg/m$^2$. However, it is customary to deal with IWV in terms of IWV-equivalent Height (IWVH) of condensed water, defined as IWVH= IWV/$\rho_w$ where $\rho_w$ is the density of liquid water ($\rho_w$ =1 g/cm$^3$). Both quantities have the same numerical values if IWV is expressed in kg/m$^2$ and IWVH in mm. The same reasoning, mutatis mutandis, applies to the Integrated Liquid Water (ILW) of clouds.

Measurements of $T_b$ from different frequencies can be used to infer coarse vertical features of the water-vapour profile (see below).

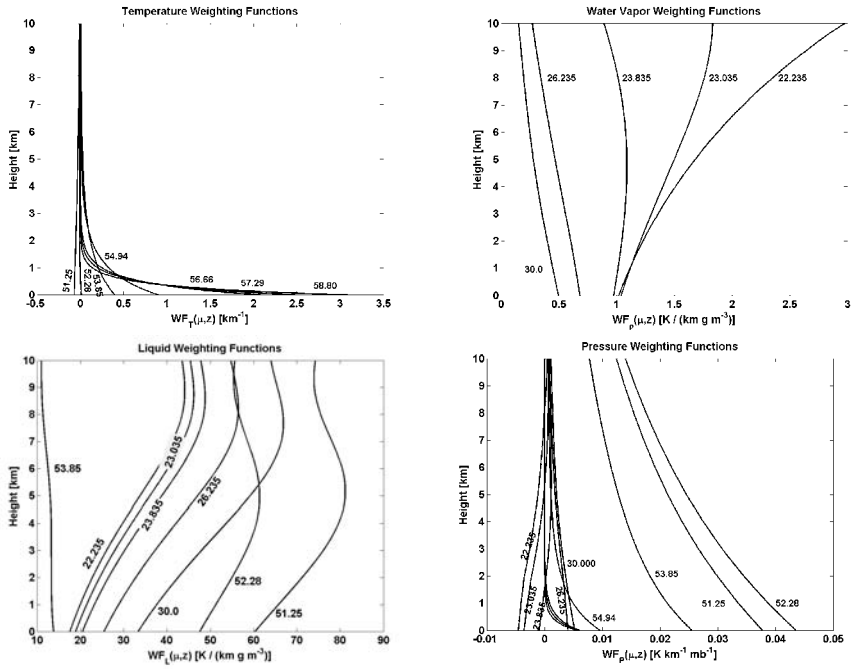


*Figure 3.3.* Weighting functions for the Radiometrics Profiler. (Top left) Temperature weighting functions and centre frequencies for V-band channels. High sensitivity to boundary layer temperatures is shown. (Top right) Vapour density weighting functions and centre frequencies for K-band channels. In conjunction with typical vapour density scale height of approximately 2 km, the vapour density weighting functions provide substantial constraints in the boundary layer. (Bottom left) Liquid density weighting functions for K1-5 and V1-3. (Bottom right) Pressure weighting functions for all 12-channel. Note that for V1-3, pressure fluctuations are not negligible

**Pressure Weighting Functions Below 60 GHz.** Because of pressure broadening, the variations in pressure from an initial state can also give rise to changes to $T_b$ (see figure 3.3c). Although changes in surface pressure of, say 1 hPa, give a maximum of 0.045 K, a not uncommon 10 hPa change gives a 0.45 K change in brightness temperature which is not generally negligible. This suggests that when considering a background state, that represents an entire month of observations, supplementing $T_b$ with surface pressure measurements would be useful.

**Cloud Liquid Weighting Functions Below 60 GHz.** As shown in figure 3.3d, both the lower five channels of the MWRP and two of the upper seven channels contain significant response to cloud liquid water density. These functions, derived for cloud-droplet sizes in the Rayleigh region, indicate that brightness temperature measurements can be used to infer coarse vertical features of the liquid water profile. However, such measurements supplemented

with additional measurements of cloud base and top from active sensors (Löhnert et al., 2001) or from thermal infrared radiometers sensing the cloud-base temperature can be used for profiling of $\rho_L$.

**Temperature and Water Vapour Weighting Functions at Millimetre Wavelengths.** For low temperature (-10 to -40$^o$C) and dry conditions (IWV $< \sim 3$ kg/m$^2$), the sensitivity of brightness temperature measurements near 22.235 GHz to water vapour is not high. A way to overcome this lack of sensitivity is to measure brightness temperature near 183.31 GHz. As shown in figure 3.2, the absorption near 183.31 GHz is significantly larger (from 10 to 100 times greater, depending on the exact frequency). However, because of the strength of the 183.31 GHz line, the response to water vapour and temperature is nonlinear and can change significantly depending on the amount of water vapour present in the atmosphere. Thus, instead of weighting functions that are linear over a broad range of atmospheric conditions, the response functions depend markedly on the amount of water vapour present. This nonlinear response is illustrated in figure 3.4, where both $W_T$ and $W_{\rho v}$ are shown for several ranges of IWV.

### 3.2.4 FREQUENCY ALLOCATIONS

An issue of concern for microwave radiometry is the active use of the electromagnetic spectrum by men for communication, radar and other technical and commercial applications. The spectral power density of man-made radiation can be much higher than for natural radiation. Useful radiometer measurements rely on spectral bands, which are kept free of man-made noise. For all uses, the frequency allocations are controlled by the International Telecommunication Union (ITU) in the Radio Regulations. They are updated every three years. A number of frequency bands are allocated to passive services, the name for radiometry in ITU. New commercial applications develop a high pressure to use the "free" bands. It is not easy to defend the continued interests required by radiometer operations. Pioneering steps were made by radio astronomers. In Europe the Committee on Radio Astronomy Frequencies (CRAF) of the European Science Foundation (ESF) has been very active in the past. The earth observation community began to defend its requirements some years ago.

### 3.2.5 RETRIEVAL TECHNIQUES

Since a special chapter is devoted to retrieval methods, see 4.4, here we only give some brief notes on the special situation of microwave radiometers. Techniques to derive meteorological information from radiation measurements are generally based on equations (3.2)(3.3)(3.4) or its perturbation form equation (3.5). Because only a finite number of imperfect radiation measurements are available, and a continuum of parameters is needed to describe profiles of temperature, water vapour, and cloud liquid, a rigorous mathematical solu-

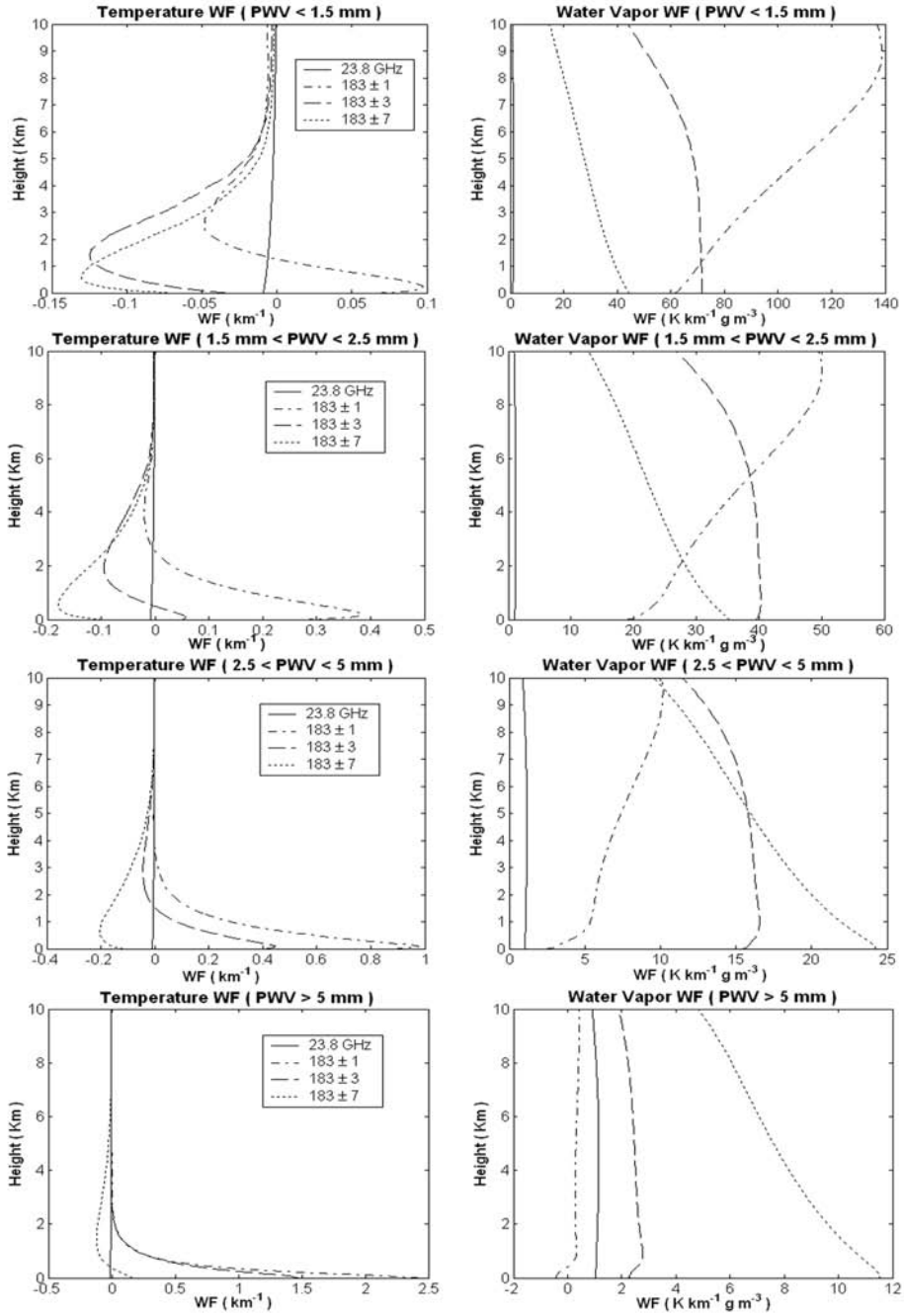


*Figure 3.4.* Average vapour density and temperature weighting functions for four ranges of IWV. The absorption model used is Rosenkranz (1998, 1999). After Racette et al. (2005).

tion does not exist and the inverse problem is said to be ill-posed (Twomey, 1977; Tikhonov and Arsenin, 1977). Therefore, it is better to regard the measurements as constraints and to blend them with supplementary sources of information or to drastically reduce the dimensionality of the inverse problem by projecting the profiles onto their linear functionals. Useful supplementary information can be provided by numerical meteorological forecasts, or by a priori information obtained from past data. Examples of profile linear functionals are PWV and LWP for moisture variables and geopotential height for temperature profiles (Westwater, 1993). We briefly discuss algorithms that are commonly used in meteorological remote sensing.

Equations (3.2),(3.3) can be approximated by a Fredholm integral equation of the first kind (Rodgers, 1976; Westwater, 1993) and in its discrete form is written

$$g_e = Kf + \varepsilon \tag{3.7}$$

where $g_e$ is a vector composed of $n$ measurements, $f$ is an $m$-vector whose components represent the profile that we want to determine, $K$ is an $n$ x $m$ matrix relating the measurements to the unknown profile, and the $n$-vector $\varepsilon$ explicitly denotes that the measurements have an unknown error component that will affect the solution to some degree. For mildly nonlinear problems, the perturbation form expressed by equation (3.5) is frequently used as the basis of subsequent iterations. The K matrix is the discrete approximation to the weighting functions of equation (3.5). If one is working in a spectral region where, for example, humidity, clouds, and pressure contributions to $T_b$ are negligible, then $f$ is a m-vector representing only temperature. In the more general case, f could represent all relevant variables: $f^T = [(\delta T)^T, (\delta \rho_V)^T, (\delta \rho_L)^T, (\delta P)^T]$ where the superscript denotes matrix transpose. Retrieval algorithms that require calculations of $K$ for their implementation are called "physical." An excellent review article discussing techniques for solving equation (3.7) was written by Rodgers (1976). A general algorithm for solving equation (3.7) in the linear case is given by

$$\hat{f} - f_0 = \left[S_f^{-1} + K^T S_\varepsilon^{-1} K\right]^{-1} K^T S_\varepsilon^{-1} (g_e - K f_0) \quad . \tag{3.8}$$

This method is used to incorporate a priori statistics, including means and covariance matrices of $f$, $S_f$ , and $\varepsilon$, $S_\varepsilon$, into the retrieval process (Rodgers, 1976; Westwater, 1993). The matrices $S_f$ and $S_\varepsilon$are defined as $S_f = E\{f - f_0\}\{f - f_0\}^T$ and $S_\varepsilon = E\{\varepsilon\varepsilon^T\}$, where the expectation value E ranges over a joint probability distribution of f and $\varepsilon$. Choices of the function $f_0$can include a climatological average, an initial guess based on a forecast, or an estimate derived from another remote sensor, and thus $S_f$ is a measure of the uncertainty in the guess. In some cases, the matrix could be diagonal, with $(\sigma_f)_i^2$ describing the uncertainty at the $i^{th}$level, or even scalar, with $S_f = (\sigma_f)^2 I$, where I is the identity matrix. Similarly, $S_\varepsilon$is composed of two terms: the first describes the instrumental uncertainty and the second contains and estimate of the forward

model errors. If both $S_f$ and $S_\varepsilon$are scalar, then the ratio $\gamma = (\sigma_\varepsilon)^2 / (\sigma_f)^2$ yields the regularization parameter $\gamma$ of Twomey (Twomey, 1977) and Tikhonov and Arsenin (Tikhonov and Arsenin, 1977). Iterative extensions of equation (3.8) are also discussed by Rodgers (Rodgers, 1976).

Although equation (3.8) is general, and many retrieval methods are its special cases, we mention a few other frequently used methods: neural network inversion (Churnside et al., 1994; Del Frate and Schiavon, 1998), Kalman filtering (Han et al., 1997; Ledskam and Staelin, 1978; Moteller et al., 1995; Askne and Westwater, 1986), and regression (Phillips et al., 1979); Kalman Filtering is also a general technique and is described in excellent books (Gelb, 1988; Brown and Hwang, 1997). Another technique of great promise is to combine radiometer data with a numerical forecast model, as has been done successfully in satellite meteorology (Derber and Wu, 1998; Ohring et al., 2002), and demonstrated for ground-based radiometers (Cimini et al., 2006b).

### 3.2.6 RADIOMETER TECHNIQUES

The pioneer in the development of microwave radiometry was Robert Henry Dicke (1916-1997). The radiometer type named after him was a great invention in 1944 to measure the low power levels associated with thermal microwave radiation (Dicke, 1946). A first radiometer operated at the MIT in Massachusetts at a wavelength of 1.25 cm; this is close to the 22 GHz water-vapour line. Dicke introduced the concepts of antenna temperature $T_A$, of the mean atmospheric temperature $T_m$ relevant for the observed radiation, and the tipping-curve method for calibration (Dicke, 1946; Dicke et al., 1946).

Today measuring downwelling thermal emission by microwave and millimetre wavelength radiometers from surface-based platforms is routinely performed on an operational basis (Liljegren, 2000; Ware et al., 2003). Some long-term data bases have been obtained (Revercomb et al., 2003; Ingold and Mätzler, 2000; Barbaliscia et al., 1998; Elgered and Jarlemark, 1998; Morland et al., 2005) and their continuations are becoming useful for climate studies. In addition, surface-based radiometers are frequently deployed in campaigns specifically designed to study water vapour (Revercomb et al., 2003; Racette et al., 2005; Cimini et al., 2006b; Martin et al., 2006b), clouds (Crewell et al., 2002), and temperature (Kadygrov and Pick, 1998; Trokhimovski et al., 1998; Westwater et al., 1999). In some deployments, specifically designed to measure water vapour and clouds in combination with other zenith-looking sensors, zenith observations are of primary interest. In others, particularly those used to measure boundary-layer temperature profiles, elevation-scanning radiometers are frequently used. More recently, radiometers scanning in both azimuth and elevation have also been used to observe clouds and other structural features.

The fundamentals of microwave radiometers were discussed in (Janssen, 1993; Ulaby et al., 1981; Skou, 1989). Radiometers measure the thermal radiance $B_\nu$, usually expressed by the antenna temperature $T_A$, and when used

to observe the atmosphere they are comprised of a highly directional antenna, a sensitive receiver, followed by a detector unit and a data-acquisition system. To produce meteorologically important information, the total system requires calibration. In this section, we briefly discuss general techniques common to ground-based systems, and then give examples of contemporary radiometers.

**3.2.6.1 Antennas.** An antenna receives the power that is associated with the antenna temperature, $T_A$, which is the integration over 4 $\pi$ steradians of the product of the scene radiance (or brightness temperature $T_b$) and the power pattern of the antenna (see below). Usually, the antennas have symmetric beam patterns with typical widths from 1 to 10°. Because many remote-sensing systems perform scanning in a vertical plane, low side lobes are required to minimize contamination from ground emission. In addition, because surface-based antennas are deployed in rain and snow, protection from and reduction or elimination of environmental effects is of primary concern.

**Antenna Parameters.** The spectral power density received by an antenna can be expressed by the following integral, using the effective antenna area $A_e$ as

$$\frac{dP(\mathbf{r},\theta_0,\phi_0)}{d\nu} = \frac{1}{2}\int_{4\pi} I_\nu(\mathbf{r},\theta,\phi)A_e(\theta,\phi,\theta_0,\phi_0)d\Omega \tag{3.9}$$

or, the antenna temperature in the Rayleigh-Jeans approximation, using the antenna directivity D

$$T_A(\mathbf{r},\theta_0,\phi_0) = \frac{1}{4\pi}\int_{4\pi} T_b(\mathbf{r},\theta,\phi)D(\theta,\phi,\theta_0,\phi_0)d\Omega \tag{3.10}$$

where $I_\nu$ is the radiance and $T_b$ the Rayleigh-Jeans brightness temperature of the radiation received from directions $(\theta,\phi)$. The effective area $A_e$ and the directivity D of the antenna depend on the orientation of the antenna axis in direction $(\theta_0,\phi_0)$. The directivity and the effective area are related (here for negligible antenna losses):

$$A_e(\theta,\phi) = \frac{\lambda^2 D(\theta,\phi)}{4\pi} \tag{3.11}$$

with the normalisation

$$\frac{1}{4\pi}\int_{4\pi} D(\theta,\phi)d\Omega = 1$$

A simple and robust antenna used to observe the atmosphere is a horn, either scalar or corrugated, that has a suitable beam pattern. Such antennas have very low losses and low sidelobes. If a multi-frequency and equal-beamwidth

system is desired, the dimensions of the horns can be scaled appropriately. For some systems, the entire electronics package is rotated with the antenna. A more common system is to direct the antenna beam from the primary antenna onto a flat or parabolic reflecting mirror that is scanned. In this configuration, only the flat reflector is moved. An example of this type of system is shown in figure 3.5 (Martin et al., 2003). Another common method is to use a lens antenna with or without a reflector. The main problems of dielectric lenses are inevitable absorption and reflection losses and the related emission. More sophisticated scanning designs are also possible, such as the use of subreflectors, multiple reflectors, and mirrors. Frequently, to protect the system from the environment, the electronics package and the antenna are enclosed within a radome.

It is important to consider the losses from radomes and from dielectric lens antennas. Lenses for remote sensing are usually constructed from low-loss material (loss tangent less than $\sim 10^{-3}$). A lossy antenna attenuates an incoming signal and adds noise due to its own physical temperature. If the loss factor and the lens temperature are known, the unwanted signal can be corrected from the measured brightness temperature. The effect can be calibrated out by external targets or tipping curves, and a limitation is imposed by the time spent between valid calibration observations.

**3.2.6.2 Receivers.** A variety of receiver designs are also common in surface-based radiometry and several involve Dicke modulation-type radiometers in which the input to the receiver is alternatively switched between the scene (sky) and an internal calibration load (Skou, 1989). In the original NOAA radiometer (Hogg et al., 1983), the receiver was based on the Hach (Hach, 1968) design in which the signal was sequentially switched between the scene and two internal blackbody targets (hot = $145^o$C and reference = $45^o$C). These targets were simply waveguide terminations kept at strictly controlled and measured temperatures.

In the Radiometrics Corporation design (http://www.radiometrics.com), a signal generated by a noise diode is alternatively turned off and on and added to the signal from the scene at each angle, including the internal blackbody target (Liljegren, 2000). The Russian-designed scanning radiometers for boundary-layer temperature measurement (Kadygrov and Pick, 1998; Trokhimovski et al., 1998; Westwater et al., 1999) are total-power radiometers but have been modified to include the signal from a noise generator. Both the NOAA Dual Channel radiometer and the NOAA Ground-based Scanning Radiometer receivers use either conventional Dicke or Hach switches that alternate between internal reference loads and the scene. Finally, all of the above receivers are of double-side-band design in which the signal from a stable local oscillator is mixed with the incoming radio-frequency signal emanating from the scene; the intermediate-frequency (IF) signal is then amplified and detected. With IF bandwidths usually around 200 MHz to 1 GHz, 1-sec radiometric sensitivities

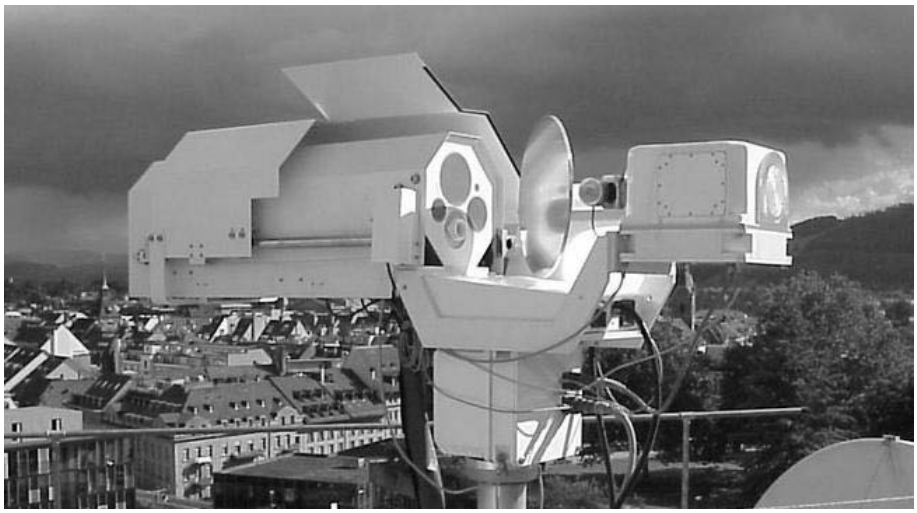

*Figure 3.5.* ASMUWARA in operation in Bern. The openings of the 4 horns appear as grey disks at the left of the flat rotatable mirror, while the IR radiometer looks through the white cylinder below the largest horn. The picture also shows on the left the protecting rain roof. During precipitation the roof is moved over the mirror. Also visible is the webcam located to the right of the mirror.

of 0.1 K are common. Also noteworthy is a specially constructed high-stability radiometer (Tanner and Riley, 2003). Based on tip-cal analysis, this unit gave rms errors of less than 0.05 K over time periods of a month, and stabilities of better than 0.01 K over time scales of 1000 to 10000 s. Another possibility is to use direct detection at the radio frequency of interest, thus eliminating the mixer and local oscillator. As improvements are made in radio frequency amplifiers, increasing use of direct detection is expected. The use of Dicke or Hach switching overcomes the effect of receiver-gain variations, but reduces the sensitivity of the receiver. As improvements are made in temperature and other environmental controls, total-power radiometers may become more common. RPG-HATPRO illustrates one of these more recent developments as will be shown below.

**3.2.6.3 Calibration.** To derive quantitative information from radiometric measurements, accurate radiometric calibration with accuracies of 0.5 to 1.0 K is required. In addition, the shape and direction of the radiometer antenna beam have to be known to a high accuracy, and the beam efficiency must be sufficiently close to 1 (more than 99%), in order to avoid uncertainties about the origin of the radiation. Here we will concentrate on the radiometric aspects. Most radiometers have one or two internal noise sources that provide some measure of radiometric calibration. However, waveguide losses, lack of complete knowledge of radiometric parameters, and a host of other causes (of-

ten related to limited beam efficiency) dictate that some external calibration method also be employed. We assume that the radiometer uses a square law detector, in which the output voltage is proportional to the input power; i. e., voltage is linear with the antenna temperature. We will briefly describe three commonly used calibration techniques.

**External Blackbody Reference Targets.** A seemingly straightforward calibration method is to view two external blackbody targets that are kept at two widely separated temperatures (Skou, 1989). If $T_2$ and $T_1$ are the two target temperatures with respective output voltages of $U_2$ and $U_1$, then the antenna temperature $(T_A)_S$ of the scene (Rayleigh-Jeans approximation) is given by

$$(T_A)_S = T_1 + \frac{T_2 - T_1}{U_2 - U_1}(U_S - U_1) \tag{3.12}$$

where $U_S$ is its corresponding voltage. Preferably, the target temperatures bracket the range of antenna temperatures. Also, it is important to construct targets with high emissivity such that reflections from external sources are negligible, and to have the targets sufficiently large that at least $1\frac{1}{2}$ to 2 projected antenna diameters are captured by the target system. Targets are frequently constructed with a surface having high thermal conductivity covered with a thin layer of strongly absorbing material. Often, a corrugated pyramidal surface with wavelength-dependent spacing and depth ratios, is constructed to reduce reflections and hence to increase emissivity. The target is frequently embedded in a thermal insulator that is transparent to incoming radiation to enhance thermal homogeneity of the radiator. Finally, when a target is placed in an environment in which the temperature differs greatly from the desired target temperature, measurements of temperatures at several locations within the target are essential. The target calibration methods are most useful when the atmospheric brightness temperatures are within the range of easily achieved target temperatures; e.g., near the centre of the 60 GHz $O_2$ absorption or near the 183.31 GHz water vapour line.

**Internal Reference Targets.** To monitor the stability and properties (gain and noise temperature) of the receiver, internal reference targets are used. These are either matched waveguide terminations at known and controlled temperature or stable noise diodes. The calibration signal is either switched or injected into the radiometer signal path. A radiometer that switches alternatively between the antenna signal and an internal reference is called a Dicke radiometer (Dicke, 1946). With the extension to a second internal reference at a different temperature (Hach radiometer (Hach, 1968)), it is possible to monitor both the receiver noise temperature and the radiometer gain. Effects resulting from the antenna cannot be calibrated by internal targets. Critical components are the calibration targets, the switches and couplers, whose absorption and

reflection losses must be negligible or at least well known. For non-negligible losses the temperature must be controlled.

**The Tipping Curve Calibration Method.** In the transmission windows, clear-sky $T_b's$ can be in the 10 to 50 K range and, hence, operational deployment of targets whose temperatures are in this range is difficult. In this high transmission case (small optical depth), the so-called tipping-curve calibration method (tip cal) can give a high degree of accuracy (Liljegren, 2000; Han and Westwater, 2003) and has been commonly used throughout the microwave community. In this method, brightness temperatures are measured as a function of zenith angle $\theta$, and are then converted to opacity $\tau o\theta)$ using the mean radiating temperature approximation (Westwater, 1993). For each angle $\theta$, a mean radiating temperature $T_{mr}(\theta)$ is used to derive the optical depth $\tau(\theta)$ by

$$\tau(\theta\ ) = \frac{\tau_0}{\cos\theta} = \ln\left(\frac{T_{mr}(\theta\ ) - T_c}{T_{mr}(\theta\ ) - T_b(\theta\ )}\right) . \tag{3.13}$$

where $\tau_0$ is the zenith opacity, and the dependence of $T_{mr}$ on $\theta$ is rather weak and may be neglected (Martin et al., 2006a). We assume in this equation that the antenna temperature has been adjusted to the brightness temperature $T_b$ (Han and Westwater, 2003). If the system is in calibration, then the linear fit of $\tau(\theta)$ as a function of (normalized) air mass $m$=1/cos$\theta$, will pass through the origin; conversely, if $\tau(m) = m{\cdot}\tau(m{=}1){+}b$ does not pass through the origin (b$\neq$0), then a single parameter in the radiometer equation is adjusted until it does. Note that when the calibration is achieved, then the slope of the line is equal to the zenith opacity. Several of the factors affecting the accuracy of tip cals were analyzed in (Han and Westwater, 2003). The most serious of these errors are those caused by non-stratified atmospheric conditions and can occur due to clouds and horizontal variations in the water vapour field. Various criteria, based on symmetric scans, are available to determine the quality of a tip cal (Liljegren, 2000; Han and Westwater, 2003). In summary, the tip cal method, when applicable, can give absolute accuracies of 0.3 to 0.5 K rms over to 20 to 200 GHz frequency range.

**Brightness Temperature Calculations to Calibrate.** For a highly stable radiometer such as the NOAA prototype (Hogg et al., 1983) that was operated at a radiosonde launch facility, radiosonde data that are taken during clear-sky conditions can be used with a forward radiative transfer model equations (3.2)(3.3)(3.4) to calculate $T_b$s. If the $T_b$s are taken over a variety of zenith angles, or over a representative range of meteorological conditions, the measured data can be used as calibration points. This method assumes implicitly the correctness of the forward model and also of the radiosondes. The technique is most applicable near highly absorbing spectral regions, such as in the 60 GHz oxygen region, for which the calculated $T_b$s are insensitive to choice of forward model. When applied to all channels of a multi-frequency radiometer that de-

rives meteorological information, it also ensures internal consistency between radiometric data and the forward model used in retrievals.

**Cryogenic Loads to Calibrate.** The use of blackbody targets immersed in cryogenic fluids, such as liquid nitrogen (LN2), is another method of establishing a single calibration point (McGrath and Hewison, 2001; Cimini et al., 2003a). In this method, a blackbody target is immersed in the cryogen, and the antenna looks directly at the target. Allowance for the reflection of the ambient scene must be made, and the reflection coefficient of the cryogen must also be known. For example, the apparent brightness temperature of LN2 at 290 K at a wavelength of 2.2 mm is 79.05 K (McGrath and Hewison, 2001). In (Cimini et al., 2003a), a series of LN2 calibrations were done, and the Tb differences between the Radiometrics Corporation Microwave Radiometer and the predicted value of Tb emitted from LN2 was within 0.7 K. Frequently a transparent enclosure, such as polystyrene, surrounds the LN2-immersed blackbody, and care must be taken to avoid condensation on the polystyrene and to account for its losses.

**Calibration Accuracy.** The calibration accuracy can be estimated from detailed error assessments using a radiative model of the entire radiometer system. As an example of such a model, see the report for TROWARA (Morland, 2002). Other information is obtained by direct comparison of results from collocated radiometers. Several intercomparison campaigns have been realised in the past, and relevant information is available (Cimini et al., 2006a; Martin et al., 2006c; Crewell, 2002).

## 3.2.7 EXAMPLES OF RADIOMETER SYSTEMS

In this section, we discuss several types of contemporary ground-based radiometers. Since some of these are commercially available, we, of course, do not endorse any particular instrument.

**3.2.7.1 NOAA Dual Channel Radiometer.** The U.S. National Oceanic and Atmospheric Administration (NOAA) designed, constructed, and currently operates several dual-frequency radiometers at (20.6 or 23.87 GHz, 31.65 GHz) that are used for measuring Integrated Water vapour (IWV) and Integrated Liquid Water (ILW) (Hogg et al., 1983). For each of the radiometers, the electronics, the antenna and the feed are all housed in a benign environment, such as a seatainer (a cargo container that can be deployed either on a ship or on the land). In this enclosed environment, the radiometer is free from precipitation and the internal temperature of the seatainer is controlled to about 5 degrees. The antenna is an offset paraboloid with a hybrid-mode feed, which avoid obstructions of the antenna aperture and results in high-quality radiation patterns that minimize the effect of extraneous sources of noise. The antenna

has the same beamwidths at both frequencies (the full width at half power – FWHP– is either 2.5 or $4.0^o$), thus minimizing differential beam-filling during inhomogeneous cloud conditions. The parabolic antenna is housed internally in the seatainer and views an external flat reflector through a transparent (mylar) window. By rotating the external reflector, the beam is steerable in a vertical plane. A complete description of the antenna configuration is given in Hogg et al. (1983). In addition, some NOAA systems have rapidly rotating reflectors to reduce the effects of rain (Jacobson and Nunnelee, 1997). The radiometer is triple switched in the Hach (Hach, 1968) mode; this results in continuous internal calibration and high stability. External calibration is accomplished on approximately a weekly basis using the tip cal method in which the external flat reflector is rotated symmetrically through three air masses.

**3.2.7.2 Radiometrics Corporation Microwave Radiometer (MWR).** Radiometrics Corporation (http://www.radiometrics.com) has designed, constructed, and delivered several dual-frequency (23.8 and 31.4 GHz) MWRs for measuring IWV and ILW (Liljegren, 2000). Each radiometer is easily portable and all electronics, antenna, and calibration targets are enclosed in a radome. The antenna is a corrugated horn with a dielectric lens that views a stepping mirror for scanning the atmosphere and a blackbody target. The FWHP beamwidths of the system are $5.9^o$ at 23.8 GHz and $4.5^o$ at 31.4 GHz. The gain of the system is determined by viewing the target with and without noise injected by a noise diode. Calibration of the system consists in determining the effective noise diode temperature $T_{ND}$ and is done by the tip cal method. When tip cals can't be done, $T_{ND}$is estimated by an averaging procedure described in (Liljegren, 2000). The MWR is equipped with a heated blower and a moisture detector to minimize the effects of rain and dew. Data from several MWR's have been used extensively by the U. S. climate community (Westwater et al., 2003; Ackerman and Stokes, 2003).

**3.2.7.3 Tropospheric Water Vapour Radiometer (TROWARA).** At the Institute of Applied Physics (IAP) at the University of Bern, a first generation radiometer system for continuous measurements of IWV and ILW has been operated since 1994. The instrument, called TROWARA, (http://www.iapmw.unibe.ch/research/projects/TROWARA/) was designed and built at the IAP, operating at 21 and 31 GHz (Martin et al., 2003) with internal calibration (Hach Type (Hach, 1968)), and supplemented by hourly tipping curves (Mätzler, 1992). The limitation to two channels requires an estimate of the effective tropospheric temperature (Ingold et al., 1998). Over the years TROWARA has provided a large data set, which has been used for validating other remote-sensing methods (Ingold et al., 2000) and for climate monitoring (http://www.iapmw.unibe.ch/research/projects/STARTWAVE/). The positive IWV bias of 2 mm observed by Ingold and Mätzler (Ingold and Mätzler, 2000) over the 1995 to 1998 period was eliminated by radiometer improvements.

Since December 2002 the instrument has been working with improved stability and with complete protection against raindrops, thus allowing measurements during all-weather conditions (Morland, 2002).

**3.2.7.4 Meteorological Temperature Profiler (MTP5).** Kipp & Zonen BV is marketing a radiometer that was originally designed and deployed by the Russian firm ATTEX (Kadygrov and Pick, 1998; Westwater et al., 1999). This radiometer is designed to measure temperature profiles in the boundary layer from 0 to 600 m above ground level (AGL). The radiometer is a single-channel (61 GHz) solid-state Dicke-type super-heterodyne receiver that is electronically chopped at 1 KHz between the sky and a reference noise source. The antenna is a scalar horn with a FWHP beam width of $6^o$ and scans by viewing a flat reflector at each of 11 scanning angles. Because of the 2 GHz bandwidth and a low receiver noise temperature of 600 K, a high sensitivity of 0.04 K is achieved. Calibration of the receiver is achieved by $0.1^o$C temperature control and a switched internal noise generator. A one-point absolute calibration is achieved either by viewing an external target or by knowing the emission temperature in the horizontal direction. A variation of this radiometer, developed at NOAA, scans continuously in a $360^o$ vertical plane, and, in addition to temperature profiles, can also be used to measure air-sea temperature difference (Trokhimovski et al., 1998; Cimini et al., 2003b). Another version of the MTP5 with a lower centre frequency is designed to retrieve temperature profiles up to 1 km.

**3.2.7.5 Radiometrics Corporation Microwave Profiler (MWRP).** Radiometrics Corporation (http://www.radiometrics.com) has also developed a multi-frequency microwave radiometer that is based on a highly stable, tunable, and synthesized, local oscillator in the receiver. This design overcomes errors caused by receiver frequency drift, while allowing observation of a large number of frequencies across wide tuning ranges. The total power receiver has a highly stable noise diode that is used as a gain reference. The radiometer observes atmospheric brightness temperatures in five frequency channels from 22 to 30 GHz, and in seven channels from 51 to 59 GHz (Ware et al., 2003; Solheim et al., 1998; Liljegren, 2004) to allow retrieval of humidity and temperature profiles as well as IWV and ILW. Weighting functions for these channels were shown in figure 3.3. The feed horns of the two bands are coupled onto a common axis and scan a range of elevation angles by reflection in a planar mirror. The system also measures zenith infrared temperature, surface temperature, humidity, and pressure. The radiometer has optional automated azimuth-scanning capability. The observation interval can be as short as several seconds. The instrument is portable, with 0.12 $m^3$ volume and 32 kg mass.

**3.2.7.6 Microwave Radiometer for Cloud Cartography (MICCY).** MICCY is an 19 frequency 22-channel radiometer that was built by Radiome-

ter Physics GmbH (http://www.radiometer-physics.de) and is operated by the University of Bonn (http://www.meteo.uni-bonn.de), (Crewell et al., 2001), which is capable of high temporal (0.1 s) and spatial (< 1 km) resolution. The radiometer has 10 channels on the high-frequency side of the 22.235 GHz water vapour line, 10 channels on the low-frequency side of the 60 GHz $O_2$ absorption band, and two channels at 90 GHz; at 25.235, 54.8 and 90 GHz both H and V polarization are measured. MICCY is a single sideband total power radiometer that is based on a heterodyne receiver filter-bank design (parallel detection of all frequency channels). The thermal stability of the receivers is less than 20 mK, which implies that the instrument is capable of maintaining its radiometric accuracy for several minutes without recalibration. Both targets and inserted noise from highly stable diodes are used in calibration. With FWHP beam widths of about $0.9^o$ the radiometer is capable of full $360^o$ scanning in azimuth and a zenith scan of 0 to $90^o$. For mapping of clouds, the entire system can be scanned in azimuth and elevation. The latter is performed by a planar mirror that reflects the incoming radiation into a fixed 1 m Cassegrain system. The system comprises a quasi-optical multiplexer for three frequency bands. Internal ambient and cold blackbodies are used for absolute calibration, while internal noise calibration standards are used in between absolute calibrations. The entire system is mounted on a transportable trailer, and all parts are enclosed in a radome.

**3.2.7.7 Radiometer Physics GmbH-Humidity and Temperature Profiler (RPG-HATPRO).** Because the implementation of an operational network of microwave radiometers is presently hampered by the cost and complexity of available instruments, it was a major objective of the European CLIWA-NET project (Crewell et al., 2002) to develop a network-suitable low-cost microwave radiometer (Rose et al., 2005). The radiometer, RPG-HATPRO, was developed and built by the German company Radiometer Physics GmbH (http://www.radiometer-physics.de). The RPG-HATPRO comprises total-power radiometers utilizing direct detection receivers at all frequencies (14 channels from 22 to 60 GHz). This approach avoids any problems that might arise from mixers or local oscillators (standing waves, frequency drifts, insufficient isolation, sideband suppression, higher system complexity and cost). Thus, the stability and accuracy of the system are drastically improved. Furthermore, possible interferences caused, for example, by communication systems that frequently operate near the IF frequencies, are eliminated. The receivers of each frequency band are designed as filter-banks in order to acquire each frequency channel in parallel. In addition, the flexibility to adjust each channel bandwidth individually allows for optimizing temperature profiling for both boundary layer and full troposphere. Feed horns covering the two bands are reflected in a parabolic mirror to scan the elevation angle. This reduces the FWHP beamwidth from 3.5° to 2.5°. The radiometer is enclosed

in a radome and protected by a rain-activated shutter to allow rapid recovery after precipitation.

**3.2.7.8 All-Sky Multi-Wavelength Radiometer (ASMUWARA).** ASMUWARA, shown in figure 3.5, is a radiometer system designed for remote sensing of tropospheric water vapour, cloud liquid water, and temperature profiles (http://www.iapmw.unibe.ch/research/projects/ASMUWARA/) (Martin et al., 2003, 2006a). It was designed and built at the IAP. The instrument consists of nine microwave channels in the frequency range from 18 to 151 GHz, a thermal infrared radiometer (wavelength band: 8 to 14 $\mu$m), meteorological sensors, including a rain detector, and an optical camera. The radiometers are housed in a temperature-controlled cylinder with all beams aligned in a horizontal direction pointing to a flat, rotating mirror that scans the sky and two calibration loads. The entire instrument can be rotated around its vertical axis. The beams perform a rosette-like pattern to map the sky hemisphere within 15 to 20 minutes. All channels have the same view and a common full beam width of 9°, formed by corrugated horns. The beam width is a compromise between angular resolution and sky coverage within the time scale of atmospheric variations. All horns are vertically polarized. The mirror reflection rotates the polarization during the scan from vertical (at the horizon) to horizontal (at nadir and zenith). A special challenge was to design the optics to cover the broad frequency range, spanning from 18 GHz to the thermal infrared. The solution was to construct a sufficiently large flat aluminium mirror that allowed parallel beams for each spectral range, and to avoid any sort of radome. In this way the instrument works well in periods without precipitation. An extension to all-weather operability includes a movable roof with a limited sky view during periods of rain (Martin et al., 2006a); rain drops on the mirror and calibration load are mostly eliminated. A second IR radiometer, covering the narrower range of 9.6 to 11.5 micrometer, was added to get an additional range indication for clouds. Figure 3.5 shows the weather-exposed parts of ASMUWARA in operation on the roof at IAP. In principle, ASMUWARA is similar to other recently developed radiometer systems for the troposphere (Ware et al., 2003; Solheim et al., 1998; Liljegren, 2004). The main difference is the availability of and the concentration on the hemispheric imaging mode for all channels, including the infrared (Martin et al., 2006b).

**3.2.7.9 NOAA Ground-Based Scanning Radiometer (GSR).** For purposes of Arctic deployments, NOAA designed and constructed a multi-frequency scanning radiometer (http://www.etl.noaa.gov/technology/gsr/) operating from 50 to 380 GHz. The radiometers are installed into a scanning drum or scan head (see figure 3.6). The GSR uses a sub-millimetre scan head with 11-channels in the 50-56 GHz region, a dual-polarized measurement at 89 GHz, 7-channels around the 183.31 GHz water vapour absorption line, a dual-polarized channel at 340 GHz, and three channels near 380.2 GHz. It also has

a 10.6 micrometer infrared radiometer within the same scan head. All of the radiometers use lens antennas and view two external reference targets during the calibration cycle.

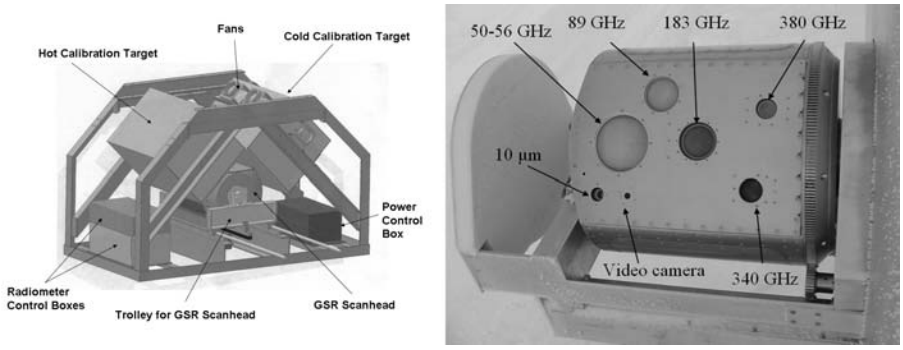


*Figure 3.6.* Left. Schematic diagram of the GSR calibration and scanning system. The GSR scan head periodically moves out of the framework for atmospheric viewing on a trolley system, and shares time observing the atmosphere and the two thermally controlled blackbody reference targets. Right. Photograph of the scan head of the GSR.

In addition, each of the radiometers' design includes two internal reference points for more frequent calibration. The GSR instrument is a modification of a similar instrument that operated at the North Slope of Alaska/Adjacent Arctic Ocean site in 1999 (Racette et al., 2005). A substantial improvement in radiometer calibration for ground observation in the Arctic environment has been achieved. Based on experience from the 1999 experiment, a new set of thermally stable calibration targets with high emission coefficients were also designed, constructed, and deployed. The primary use of the instrument is to measure temperature, water vapour, and clouds, at cold (-20 to -55 $^{\circ}$C) and dry (IWV $<$ 5 mm) conditions. A schematic of the GSR is shown in figure 3.6. The GSR, along with the MWR and the MWRP, was deployed in the NSA/AAO Arctic Winter Radiometric Experiment that was conducted in Barrow, Alaska, USA, during March-April 2004 (Westwater et al., 2004a) (see figure 3.7). The beam widths of the GSR channels range from 3.5 to 1.8$^{\circ}$ and can be averaged to given beam-widths that are consistent with the MWR (4.5$^{\circ}$ to 5.5$^{\circ}$). The GSR performs a scan sequence that includes viewing both the atmosphere and calibration targets. Each scan begins and ends with the radiometer viewing the hot and cold calibration targets. The scan head then moves out of the calibration housing where it views the atmosphere with a series of continuous and dwell movements. Each scan takes about 2-min to complete. Data from the 26 channels of the GSR should lead to unprecedented information on the evolution of temperature, water vapour, and clouds in the Arctic.

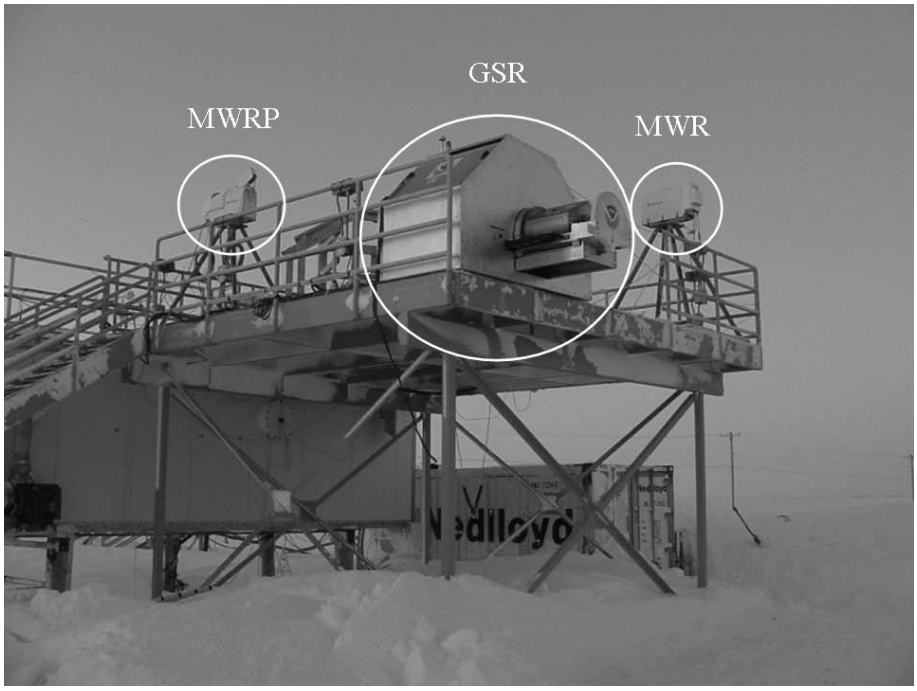


*Figure 3.7.* Photograph of the deployment of the GSR, MWRP, and MWR at the NSA/AAO Arctic Winter Radiometric Experiment that was conducted in Barrow, Alaska, USA, during March-April 2004.

## 3.2.8 COMPLEMENTARY SENSORS

As shown by the described examples, microwave radiometers usually are complemented with additional sensors to aid in the data interpretation and to protect the instruments from certain disturbances.

**3.2.8.1 Standard Meteorological Sensors.** Surface-air temperature, pressure and humidity are most useful to define the lower boundary condition of the atmosphere. The barometric pressure is also used to determine the liquid nitrogen boiling temperature, which is used for absolute calibration. Furthermore temperature and humidity can be useful for tuning the calibration parameters because some properties of microwave components are sensitive to these variables.

**3.2.8.2 Rain Protection.** Rain sensors detect periods when water droplets hit the instrument, and thus modify the transmission properties of lenses and radomes or the reflection properties of the exposed mirrors. The sensor may initiate an automatic process to protect or clean the exposed surfaces, e.g. by dry air. An alternative way to protect the radiometer is to set up

the system in a covered room from where the atmosphere is observed through an open or microwave-transparent window that is not exposed to rain at all. See also (Marzano et al., 2002) for rain mitigation.

**3.2.8.3 Infrared Radiometer.** Infrared radiometers extend the wavelength range of microwave radiometers to the 10-micrometer range. The additional information mainly includes the identification of clouds and the measurement of cloud-base temperature, see also 4.4. In contrast to the microwave range, both ice and water clouds have similar radiometer signatures in the thermal infrared range. A typical cloud gets optically thick at $\lambda$=9-12 $\mu$m whenever its ILW reaches or exceeds 20 to 30 g/m$^2$ (Bloemink et al., 1999). For ice clouds infrared radiometers are even slightly more sensitive. Note that optically thick clouds are very good black bodies in the thermal infrared, and that scattering effects are negligible. The combination of microwave and infrared radiometry allows to classify ice and liquid-water clouds. Especially it is possible to identify supercooled water clouds if ILW is non zero and if the cloud-base temperature is $< 0^o$C. For this purpose it is important to have the same view direction at all channels as realised by ASMUWARA.

**3.2.8.4 Cloud Radar.** Cloud radars are active microwave sensors to detect and to monitor the development of clouds and precipitation. See chapter 3.7 in this report.

**3.2.8.5 Lidars, Ceilometers.** Cloud lidars are active optical sensors to detect and monitor the development of clouds and aerosols. A simplified version designed to detect the base height of clouds, is called ceilometer. See chapter 3.3 in this report.

## 3.2.9 FINANCIAL CONSTRAINTS

**3.2.9.1 Costs.** The costs for a dual channel microwave radiometer (23.8/31.4 GHz) suitable for continuous, high temporal resolution (1s) observation of integrated liquid water (ILW) and integrated water vapour (IWV) is about 80 k€. These kinds of systems are extremely well thermally stabilized and achieve an absolute accuracy of about 0.5 K and an RMS of 0.1 K. They include rain detection/blower systems to allow accurate observations in non-precipitation situations. Further additions are GPS clock, temperature, humidity and pressure sensors (Rose et al., 2005). Optionally, an additional channel at a higher frequency, e.g. 90 or 150 GHz can be added to improve ILW estimates (Löhnert and Crewell, 2003) for a total of $\sim$105 k€. In order to go from vertical pointing to a better spatial coverage an azimuth scanner for about 15 k€ can be added. Microwave profilers with several frequencies along the water vapour (22-31 GHz) and oxygen (50-60 GHz) can provide the tempera-

ture and humidity profiles as well as improved LWP (by 5-10 $gm^{-2}$) estimates. The price of these systems is about 125 k€ in 2005.

**3.2.9.2 Potential for Cost Reduction and for Wider Use of Microwave Radiometers.** The price for a microwave profiler has decreased from nearly 300 k€ to 125 k€ within the last decade. At the same time new technologies (for example direct detection) have improved the accuracy. The further integration of microwave components, chip development and improved automation of the production process are expected to lead to a further reduction. Recent advances in the application of millimeter-wave integrated circuit (MMIC) technology to reduce the cost, mass and volume of microwave radiometers has demonstrated that a water vapour profiler (22-28 GHz) can be implemented for a parts cost of only 32 k€ for the first instrument and 9 k€ for each additional unit (Iturbide-Sanchez et al., 2004; Reising et al., 2005). Therefore, if 4-5 units are manufactured each year, the per-unit price for the profiler is expected to fall below 60 k€ in the next 3 years. Mass production would lead to further cost reduction, to improved stability, ruggedness and lifetime. Under such circumstances surface-based microwave radiometers could develop to standard instruments at weather stations.

## 3.2.10 LONG-TERM MONITORING

Operation of surface-based microwave radiometers over many years has been performed at the Onsala Space Observatory in Sweden (Elgered and Jarlemark, 1998), at the University of Bern in Switzerland (Ingold and Mätzler, 2000), and at the Richard-Aßmann Observatory at Lindenberg, Germany (Güldner and Leps, 2005). Here we report on the experience gained at Lindenberg. It describes operational aspects of microwave radiometer applications with a focus on long-term and continuous observations.

**3.2.10.1 Continuous evaluation of retrieval accuracy.** Microwave radiometers have demonstrated their capability to operate in unattended mode and in nearly all weather conditions. Therefore it represents an indispensable component for any reference site established for atmospheric research. Providing of data for NWP models and climatological applications are the foremost task of such validation sites. Work at the Richard-Aßmann Observatory at Lindenberg was directed on the use of microwave radiometer to fulfil this goal.

The observatory has operated a Radiometrics 12-channel microwave radiometer profiler TP/WVP 3000 for about seven years. An evaluation of retrieval accuracy has been provided continuously for 3 months periods since summer 2002. The assessment includes temperature and water vapour profiles calculated with a neural network (Solheim et al., 1998) and a measurement-based regression method (Güldner and Spänkuch, 2001).

Any evaluation requires quality-proved measurements and retrieval results. Detecting and eliminating faulty observations is not easily accomplished and require targeted algorithms. Nevertheless, concurrent measurements employing independent techniques are needed for intercomparisons. The reference site at Lindenberg is well equipped to assess the data quality of its monitoring products. It provides aerological in-situ observations and several active and passive ground-based remote-sensing measurements. In order to accomplish the quality control of microwave data and of the corresponding retrieved profiles an algorithm has been developed which takes into account radiosonde and GPS data. The control scheme realized at Lindenberg operates partly automatically. Its last step is archiving measurements and results in a databank to complement the "Lindenberg column" (Güldner and Leps, 2005). With respect to microwave data, measurement errors mostly caused by rain have to be identified and eliminated. Therefore the IWV calculated from rain-independent radiosonde observations and GPS measurements as well as the variability of consecutive microwave data for the 12 channels are included in the comparison. The evaluation scheme is performed every month after corrected high quality observations of radiosondes are available.

The recurrent estimation of retrieval accuracy is a vital component of sounding systems aimed at obtaining long-term observations. For statistical investigations data from radiometers and radiosondes at Lindenberg are compared. The Neural Network (NN) and an observation-based regression method, which applies inter-related radiometer and radiosonde measurements, were included in the intercomparisons. Figure 3.8 shows the results of comparisons for three one-year periods from 2002 to 2005 for 684, 868 and 1171 cases respectively. The mean differences (solid line) and the rms errors (dashed line) between radiometer retrievals and radiosondes are displayed for the regression method and the NN approach. Two different regression methods representing a real-time version with operators calculated from in-situ observations in the past ($\mathrm{REG}_{old}$) and an adjusted variant where actual measurements are included in the calculation ($\mathrm{REG}_{new}$). These retrievals are harmonized with contemporary radiosonde observations and well qualified for climatological applications. Furthermore, the second operator can be used as real-time operator for the succeeding period.

Regularly it is confirmed that the neural network overestimates water vapour and generates systematic deviations for the temperature sounding as well. Due to uncertainties in the radiative model used for the training of the neural network (NN) or as a result of calibration errors, biases are evident permanently. In figure 3.8 it is shown that the height of the wet bias of NN retrievals is different but always located in the range of 0.5 g/m$^3$. During the first period 2002/03 the bias has a maximum at altitudes from 2 to 4 km. In contrast to this year for the periods 2003/04 and 2004/05 most significant bias was detected for the levels from 500 m to 3 km. The bias of the humidity profiles estimated by regression methods is negligible. Between 0.5 and 3 km the rms errors of

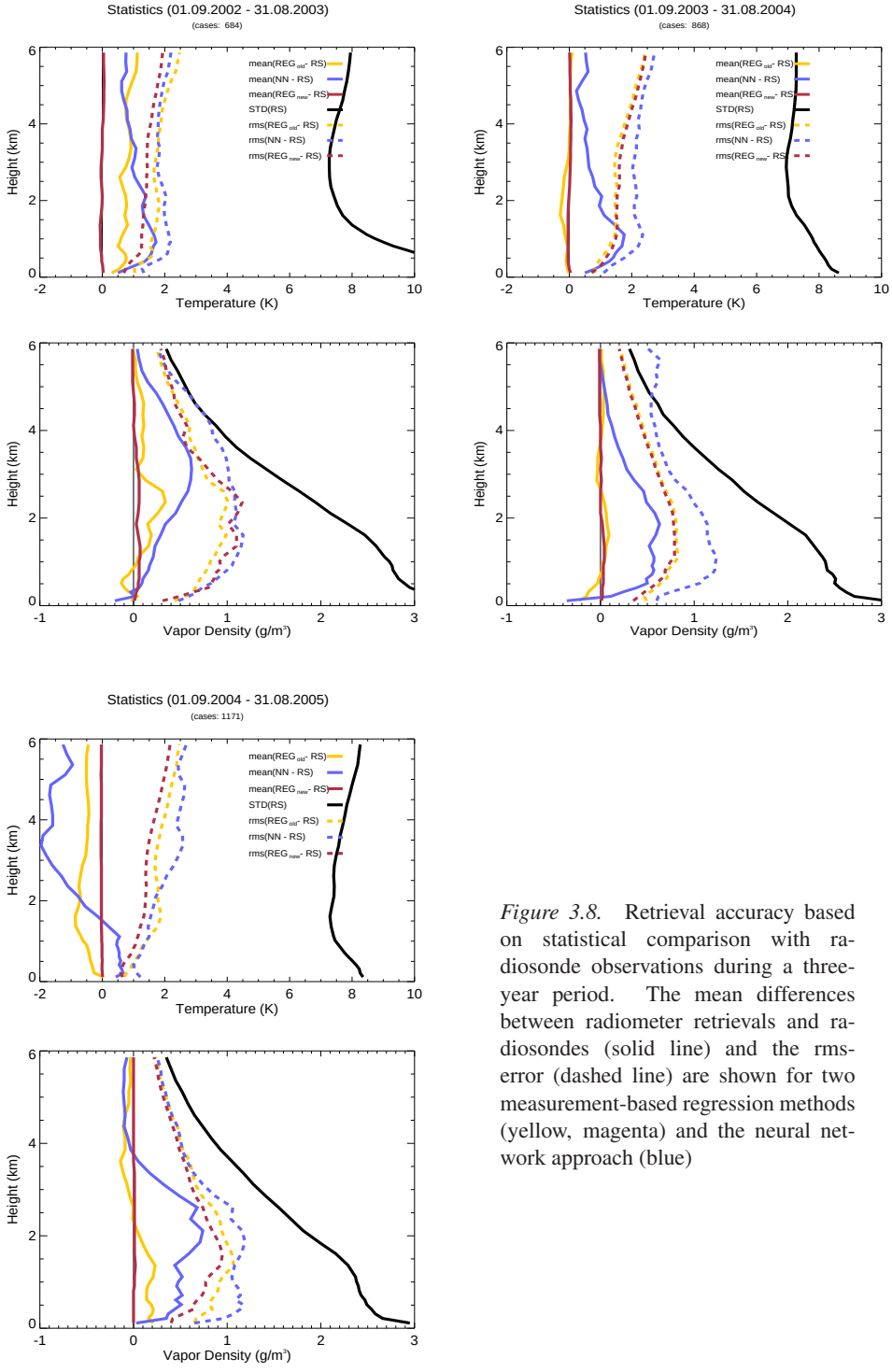


*Figure 3.8.* Retrieval accuracy based on statistical comparison with radiosonde observations during a three-year period. The mean differences between radiometer retrievals and radiosondes (solid line) and the rms-error (dashed line) are shown for two measurement-based regression methods (yellow, magenta) and the neural network approach (blue)

water vapour retrievals reaches a broad maximum with about 1 g $m^{-3}$ for the regression methods. The error is about 0.3 g $m^{-3}$ higher for the neural network approach at some heights. The temperature rms error is about 0.5 K near the surface due to the incorporation of the direct surface values, and reaches about 1 K between 0.5 and 1 km. The error is less than or equal to about 1.5 K up to 3 to 4 km.

The results document that microwave radiometers are well suitable to provide basic information about the atmospheric state. Temperature and humidity profiles are available with a high degree of availability as has been proved by the number of comparisons in the accuracy assessments shown in figure 3.8. During the considered three-year period the microwave profiler was in operation at Lindenberg for almost every time. About 80 percent of the data were archived in the local database after passing different quality checks and rain screening applied to every observation.

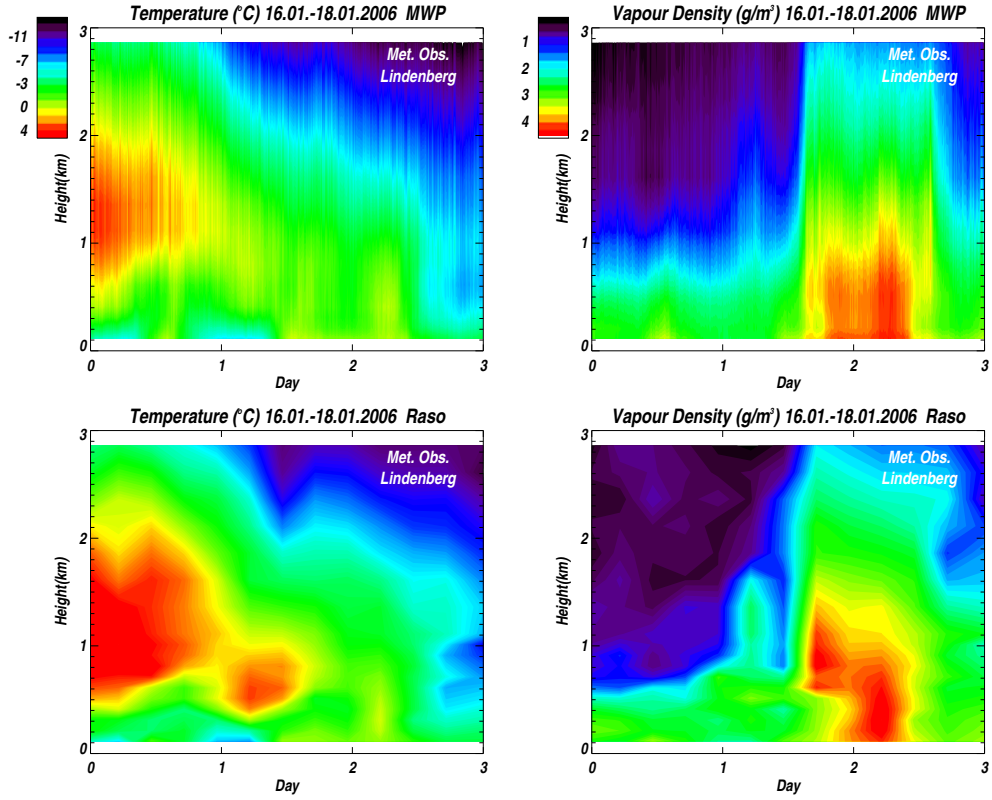


*Figure 3.9.* Temperature and humidity profiles at Lindenberg observed by radiometer (top) and radiosonde (bottom)

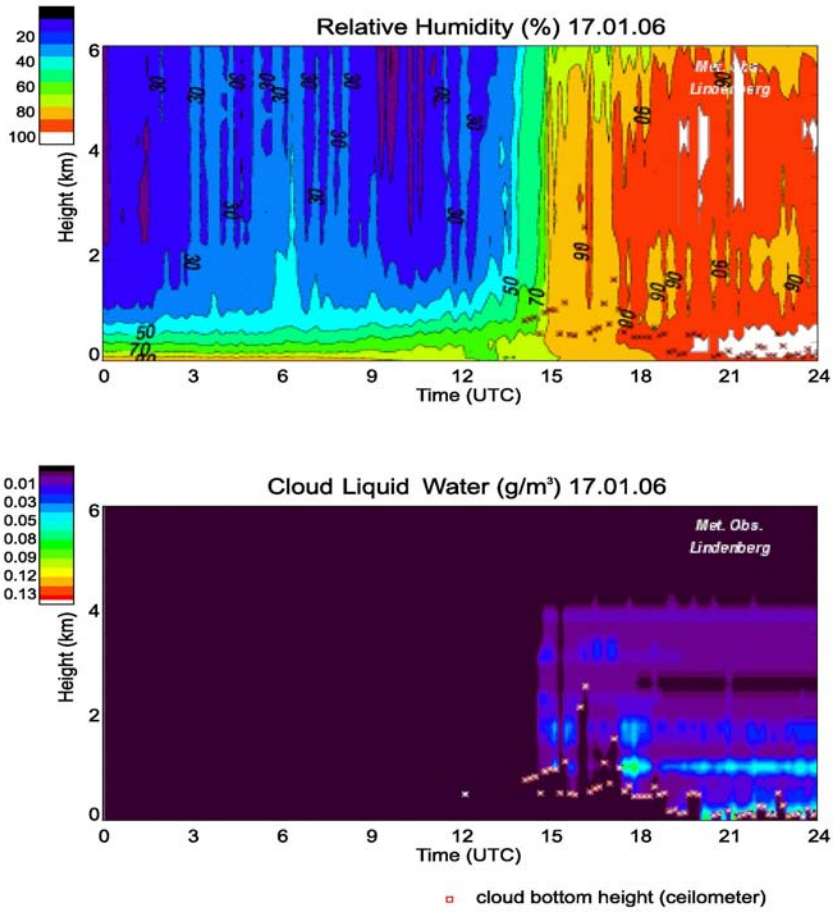


*Figure 3.10.* Relative humidity and cloud liquid water derived from microwave measurement on 17 Jan 2006. The values below the cloud bottom height (provided by a ceilometer) are set to zero.

**3.2.10.2 Real-time capabilities of microwave profiling .** In addition to the unattended operation a fast access to measurements and derived profiles is an important object for any operational application. This advantage of microwave radiometers is demonstrated by hourly and daily updated websites showing comparisons of microwave retrievals versus other measurements observed at Lindenberg. The illustration is addressed to potential users to familiarise themselves with the type of information which is provided. Advantages and limitations of derived vertical profiles are more comprehensible if they are shown in conjunction with traditional techniques.

The continuously updated figures substantiate operational capabilities as demonstrated on the basis of a three-day time series from 16 to 18 January 2006. Figure 3.9 offers a comparison of temperature and humidity profiles derived from microwave profiler measurements versus radiosonde observations.

Both the temperature inversion on 16 January and the rapid increase and passage of moist air on 16/17 January are comprehended by the microwave retrievals. The smoothing of structures inherent in passive sounding methods cause that a temperature increase of 11.5 K observed by radiosondes is calculated as a 9.5 K increase by means of microwave measurements. Moreover, cloudiness is observed at 14 UTC and derived as liquid water as can be seen in figure 3.10. The cloud bottom heights provided by a ceilometer confirm the observation, but were not included in the retrieval procedure. The snowfall starting at 16 UTC did not influence the measurements of the radiometer because the blower prevented the formation of a water film on the radome.

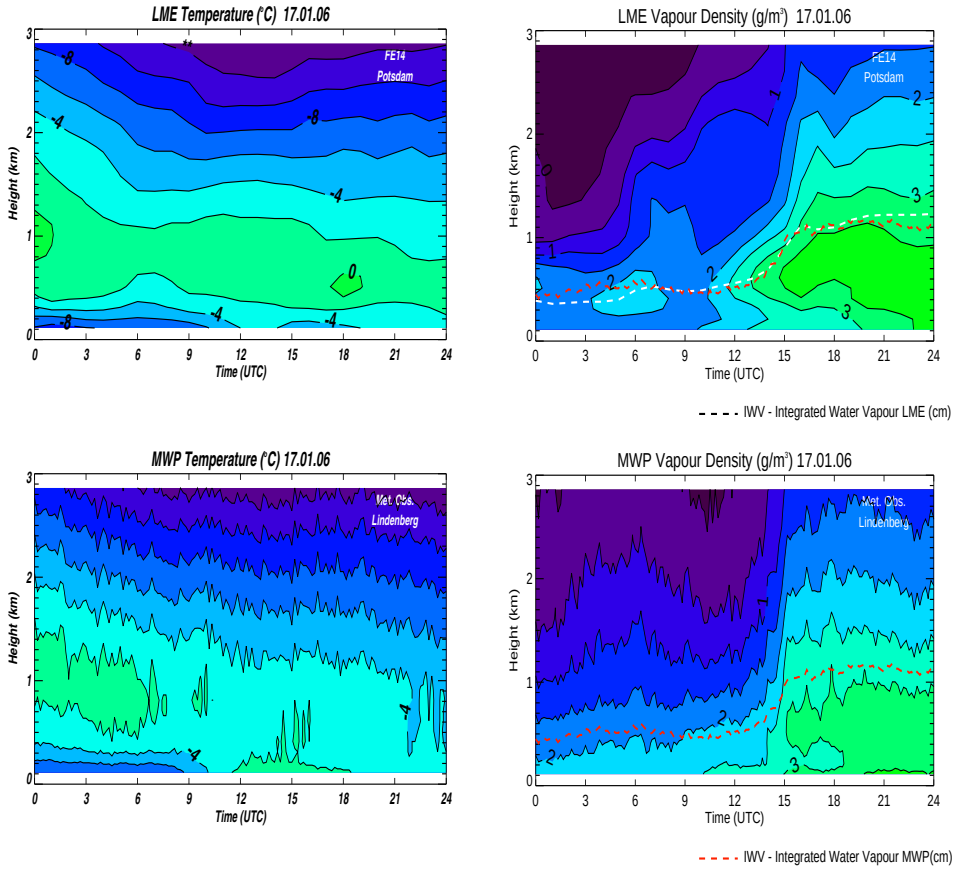


*Figure 3.11.* Comparison of operational local model forecast of the DWD model (upper panel) and microwave profiler measurements (lower panel). Displayed are height-time sections of temperature (left) and vapour density (right) on 17 Jan 2006 at Lindenberg.

In spite of complicated weather conditions the microwave measurements are capable to display humidity increase observed by the radiosonde launched on 17 January at 17 UTC with a maximum at a height between 700 and 1200 m.

The moisture increase is reproduced noticeably weaker and at lower heights, but are apparent in the retrieved profiles as shown in figure 3.9.

In addition to the illustration of observations from different sounders the operational capability of microwave profiling offers the possibility to show comparisons with the operational *Local model* (LM) forecast of DWD's NWP system at gridpoint Lindenberg. Corresponding views are realised for the previous day as well as for the actual NWP model forecast enabling a real-time evaluation of model outputs. Referring to the discussed period, figure 3.11 shows a height-time section of LM/MWP comparisons for temperature and water vapour on 17 January. A permanent temperature inversion was predicted by the model for this day. A temperature increase of 10 K at the initial time decreased to about 4 K at 11 UTC and to 2 K at 23 UTC. The height of the temperature maximum declined from 1 km at the beginning to 500 m. The radiosonde at 11 UTC observed a lifted inversion. It could not be resolved by the microwave radiometer and the retrieved profile has a constant temperature up to 1.2 km height. The inversion disappeared at the end of the day. The diagram of the humidity profiles shows a suitable agreement of model and observed data regarding the time and the amount of moisture increase.

The examples demonstrate that microwave measurements provide continuous basic information about the atmospheric state for nearly all-weather conditions in an unattended mode. The observations can be prepared in real time as indispensable precondition for operational use.

## Bibliography

Ackerman, T. P. and G. M. Stokes, 2003: The Atmospheric Radiation Measurement Program. *Physics Today*, **56**, 1, pp. 38-44.

Askne, J. and E. R. Westwater, 1986: A Review of Ground-Based Remote Sensing of Temperature and Moisture by Passive Microwave Radiometers. *IEEE Transactions on Geoscience and Remote Sensing*,**G3-24**, pp.340-352.

Barbaliscia, F., E. Fionda and P. G. Masullo, 1998: Ground-based radiometric measurements of atmospheric brightness temperature and water contents in Italy. *Radio Science*, **33**, pp.697-707.

Bloemink, H. I., A. C. A. P. van Lammeren, A. J. Feijt and S. C. H. M. Jongen, 1999: Active-passive sensor synergy for cloud observation; IR cloud properties and cloud liquid water. **in:** *Remote Sensing of Cloud Parameters*, Proc. of the Symposium, 21-22 Oct. 1999, IRCTR, Delft University of Technol., ISBN 90-804551-6-4, The Netherlands.

Bohren, C. F. and D. R. Huffman, 1983: *Absorption and Scattering of Light by Small Particles*. New York, John Wiley.

Brown, R. G. and P. Y. C. Hwang, 1997: *Introduction to Random Signals and Applied Kalman Filtering*. New York, J. Wiley & Sons.

Cermak, J., M. Schneebeli, D. Nowak, L. Vuilleumier, and J. Bendix, 2006: Characterization of low clouds with satellite and ground-based remote sensing systems. *Meteorol. Zeitschr.*, TUC special issue, **15**, No. 1, pp.65–72.

Churnside, J. H., T. A. Stermitz and J. A. Schroeder, 1994: Temperature Profiling with Neural Network Inversion of Microwave Radiometer Data. *Journal Atmosph. Ocean. Technol.*, **11**, pp.105-109.

Cimini, D., E. R. Westwater, Y. Han and S. J. Keihm, 2003: Accuracy of ground-based microwave radiometer and balloon-borne measurements during the WVIOP2000 field experiment. *IEEE Transactions on Geoscience and Remote Sensing*, **41,** 11, pp.2605-2615.

Cimini, D., J. A. Shaw, Y. Han, E. R. Westwater, V. Irisov, V. Leuski and J. H. Churnside, 2003: Air Temperature Profile and Air-Sea Temperature Difference Measurements by Infrared and Microwave Scanning Radiometers. *Radio Science*, **38**(3), 8045, doi:10.1029/2002RS002632.

Cimini, D., T. J. Hewison and L. Martin, 2006: Comparison of brightness temperatures observed from ground-based microwave radiometers during TUC. *Meteorol. Zeitschr.*. TUC special issue, **15**, No. 1, 19–25.

Cimini, D., T. Hewison, L. Martin, J. Güldner, C. Gaffard and F. S. Marzano, 2006: Temperature and humidity profile retrievals from ground-based microwave radiometers during TUC. *Meteorol. Zeitschr.*, TUC special issue, **15**, No. 1, pp.45–56.

Clothiaux, E. E., T. P. Ackerman, G. G. Mace, K. P. Moran, R. T. Marchand, M. A. Miller, and B. E. Martner, 2000: Objective Determination of Cloud Heights and Radar Reflectivities Using a Combination of Active Remote Sensors at the ARM CART Sites. *Journal of Applied Meteorology*. **39,** 5, pp.645–665.

Clough, S. A., M. W. Shephard, E. J. Mlawer, J. S. Delamere, M. J. Iacono, K. Cady-Pereira, S. Boukabara and P. D. Brown, 2005: Atmospheric radiative transfer modeling: A summary of the AER codes. *Journal of Quantitive Spectroscopy and Radiative Transfer*, 9, 233-244.

Crewell, S., H. Czekala, U. Löhnert, C. Simmer, Th. Rose, R. Zimmermann and R. Zimmermann, 2001: Microwave Radiometer for Cloud Carthography: A 22-Channel Ground-Based Microwave Radiometer for Atmospheric Research. *Radio Science*, **36**, pp.621-638.

Crewell, S., 2002: Bodengebundene Fernerkundung der bewölkten Atmosphäre und deren Nutzung zur Evaluierung dynamischer Atmosphärenmodelle". Habilitationsschrift der Math. Naturw. Fakultät, Rheinische Friedrich-Wilhems-Universität Bonn.

Crewell, S., M. Drusch, E. van Meijgaard and A. van Lammeren, 2002: Cloud Observations and Modeling within the European BALTEX Cloud Liquid Water Network. *Boreal Environmental Res.*, **7**, pp.235-245.

Crewell, S. and U. Löhnert, 2003: Accuracy Of Cloud Liquid Water Path from Ground-Based Microwave Radiometry. Part II. Sensor Accuracy and Synergy. *Radio Science*, **38**(3), 8042, doi:10.1029/2002RS002634.

Debye, P., 1929: *Polar Molecules*, New York, Dover.

Deirmendjian, D., 1969: *Electromagnetic Scattering on Spherical Polydispersions*. New York, American Elsevier Publishing Company, Inc.

Del Frate, F. and G. Schiavon, 1998: A Combined Natural Orthogonal Functions/Neural Network Technique for Radiometric Estimation of Atmospheric Profiles. *Radio Science*, **33**, pp. 405-410.

Derber, J. C. and W.-S. Wu, 1998: The Use Of TOVS Cloud-Cleared Radiances in the NCEP SSI Analysis System. *Monthly Weather Review*, **126**, pp.2287-2302.

Dicke, R. H., 1946: The measurement of thermal radiation at microwave frequencies. Rev. Sci. Instr., Vol. 17, pp. 268-275.

Dicke, R. H., Beringer R., Kuhl R. L. and Vane A.B. 1946: Atmospheric absorption measurements with a microwave radiometer. *Phys. Rev.* Vol. 70, pp. 340-348.

Elgered, G. and O. J. Jarlemark, 1998: Ground-based microwave radiometry and long-term observations of atmospheric water vapor. Radio Science, Vol. 33, pp. 707-717.

Frisch, A. S., G. Feingold, C. W. Fairall, T. Uttal and J. B. Snider, 1998: On Cloud Radar and Microwave Measurements of Stratus Cloud Liquid Water Profiles. *Journal of Geophys. Res.*, **103**, pp. 23195-23197.

Gaikovich, K. P., E. N. Kadygrov, A. S Kosov and A. V. Troitskiy, 1992: Thermal Sounding of the Boundary Layer of the Atmosphere at the Center of the Line of Oxygen Absorption. *Izvestia vuzov, Radiophysica,* **35**, 2, pp. 130-136.

Gasiewski, A. J., 1993: Microwave Radiative Transfer in Hydrometeors. **in**: Michael A. Janssen (ed.), *Atmospheric Remote Sensing by Microwave Radiometry*. New York, J. Wiley & Sons Inc., pp.91-144.

Gelb, A., 1988: *Applied Optimal Estimation*. Cambridge, MA, The M. I. T. Press.

Goody R. M. and Y. L. Yung, 1995: *Atmospheric Radiation, Theoretical Basis*. Oxford University Press, 2nd Edition, 544 pages.

Grant, E. H., J. Buchanan and H. F. Cook, 1957: Dielectric Behavior of Water at Microwave Frequencies, *Journal of Chemical Physics,* **26**, pp. 156-161.

Güldner, J. and D. Spänkuch, 2001: Remote Sensing of the Thermodynamic State of the Atmospheric Boundary Layer by Ground-Based Microwave Radiometry. *Journal Atmosph. Ocean. Technol.*, **18**, pp. 925-933.

Güldner, J. and J.-P. Leps, 2005: Analysis of CLIWA-NET intensive operation period data as part of the monitoring activities at the German Meteorological Service Site Lindenberg. *Atmospheric Research*, **75**, pp. 151-166.

Hach, J., 1968: A Very Sensitive Airborne Radiometer using Two Reference Temperatures. *IEEE Transactions on Microwave Theory and Techniques*, **MTT-16**, 9, pp. 629-636.

Han, Y. and E. R. Westwater, 1995: Remote sensing of tropospheric water vapor and cloud liquid water by integrated ground-based sensors. *Journal Atmosph. Ocean. Technol.*, **12,** 5, pp.1050-1059.

Han, Y., E. R. Westwater, and R. A. Ferrare, 1997: Applications of Kalman Filtering to Derive Water Vapor from Raman Lidar and Microwave Radiometers". *Journal Atmosph. Ocean. Technol.*, **14**, 3, pp.480-487.

Han, Y. and E. R. Westwater, 2003: Analysis and Improvement of Tipping Calibration for Ground-Based Microwave Radiometers. *IEEE Transactions on Geoscience and Remote Sensing*, **38**, pp. 1260-1277.

Hewison, T., D. Cimini, L. Martin, C. Gaffard and J. Nash: 2006: Validating clear air absorption models using ground-based microwave radiometers and vice-versa. *Meteorol. Zeitschr.*, TUC special issue, **15**, No. 1, pp.27–36.

Hogg, D. C., M. T. Decker, F. O. Guiraud, K. B. Earnshaw, D. A. Merritt, K. P. Moran, W. B. Sweezy, R. G. Strauch, E. R. Westwater, and C. G. Little, 1983: An Automatic Profiler of the Temperature, Wind and Humidity in the Troposphere. *Journal of Applied Meteorology*, **22**, 5, pp. 807-831.

Hufford, G., 1991: A Model for the Complex Permittivity of Ice at Frequencies below 1 THz. *International Journal of Infrared and Millimeter Waves*, **12**, pp. 677-682.

Ingold, T., R. Peter and N. Kämpfer, 1998: Weighted Mean Tropospheric Temperature and Transmittance Determination at Millimeter-Wave Frequencies for Ground-Based Applications. *Radio Science*, **33**, pp. 905-918.

Ingold, T., B. Schmid, C. Mätzler, P. Demoulin and N. Kämpfer, 2000: Modeled and Empirical Approaches for Retrieving Columnar Water Vapor from Solar Transmittance Measurements in the 0.72, 0.82 and 0.94 $\mu$m Absorption Bands. *Journal Geophys. Res.*, **105(D19)**, pp. 24327-24343.

Ingold, T. and C. Mätzler, April 2000: Four Years of Columnar Water Vapor Measurements Above the Swiss Central Plain Using Radiosondes and a Microwave Radiometer. IAP Research Report No. 2000-02, Institute of Appl. Physics, University of Bern, Bern, Switzerland.

Iturbide-Sanchez, F., S. C. Reising and R. W. Jackson, September 2004: Design and Implementation of a Miniaturized Water Vapor Profiling Radiometer. *Proc. IEEE Internat. Geoscience and Remote Sensing Symposium*, Anchorage, Alaska.

Jacobson, M. D. and W. M. Nunnelee, 1997: Design and Performance of a Spinning Flat Reflector for Millimeter-Wave Radiometry. *IEEE Transactions on Geoscience and Remote Sensing*, **35**, pp. 464-466.

Janssen, M. A., 1993: An Introduction to the Passive Remote Sensing of Atmospheres. *in*: Michael A. Janssen (ed.), *Atmospheric Remote Sensing by Microwave Radiometry*, New York, J. Wiley & Sons Inc., pp.1-36.

Kadygrov, E. N. and D. R. Pick, 1998: The Potential Performance of an Angular Scanning Single Channel Microwave Radiometer and some Comparisons with in Situ Observations. *Meteorological Applications, UK*, **5**, pp. 393-404.

Klein, M. and A. J. Gasiewski, 2000: Nadir Sensitivity of Passive Millimeter and Submillimeter Wave Channels to Clear Air Temperature and Water Vapor Variations. *Journal Geophys. Res.*, **105**, D13, pp.17481-17511.

Ledskam, W. M. and D. H. Staelin, 1978: An Extended Kalman-Bucy Filter for Atmospheric Temperature Profile Retrieval with a Passive Microwave Sounder. *Journal of Applied Meteorology*, **17,** pp. 1023-1033.

Leuskii, V., V. Irisov, E. Westwater, L. Fedor and B. Patten, 2000: Airborne measurements of the sea-air temperature difference by a scanning 5-mm wavelength radiometer. *Proc. IGARSS2000*, July 24-28, Honolulu, Hawaii, USA, pp.260-262.

Liebe, H. J. and D. H. Layton, 1987: Millimeter Wave Properties of the Atmosphere: Laboratory Studies and Propagation Modeling. National Telecommunications and Information Administration (NTIA) Report *87-24*, 74 pp. (available from the National Technical Information Service, 5285 Port Royal Road, Springfield, VA, 22161).

Liebe, H. J., 1989: MPM, An Atmospheric Millimeter Wave Propagation Model. *International Journal of Infrared and Millimeter Waves*, **10**, 6, pp. 631-650.

Liebe, H. J., G. A. Hufford, and T. Manabe, 1991: A Model for the Complex Permittivity of Water at Frequencies Below 1 THz. *International Journal of Infrared and Millimeter Waves*, **12**, 7, pp. 659-675.

Liebe, H. J., G. A. Hufford and M. G. Cotton, 1993: Propagation Modelling of Moist Air and Suspended Water/Ice Particles at Frequencies below 1000 GHz. **in:** *AGARD Conference Proceedings 542, Atmospheric propagation effects through natural and man-made obscurants for visible through MM-wave radiation*, pp. 3.1 to 3.10 (available from NASA Center for Aerospace Information, Linthicum Heights, MD).

Liljegren, J. C., 2000: Automatic Self-Calibration of ARM Microwave Radiometers. **in**: P. Pampaloni and S. Paloscia, (eds.), *Microwave Radiometry and Remote Sensing of the Earth's Surface and Atmosphere*, Utrecht, VSP Press, pp. 433-441.

Liljegren, J. C., 2004: Improved Retrievals of Temperature and Water Vapor Profiles with a Twelve-Channel Radiometer. **in:** *2004 Proc. of the Eighth Symposium on IOAS-AOLS*, Am. Meteorol. Soc., 11-15 Jan. 2004, Seattle, WA.

Liljegren, J. C., S. A. Boukabara, K. Cady-Pereiria and S. A. Clough, 2005: The Effect of the Half-Width of the 22-GHz Water Vapor Line on Retrievals of Temperature and Water Vapor Profiles with a Twelve-Channel Microwave Radiometer. *IEEE Transactions on Geoscience and Remote* Sensing, **43**(5), pp. 1102-1108.

Löhnert, U., S. Crewell, A. Macke and C. Simmer, 2001: Profiling Cloud Liquid Water by Combining Active And Passive Microwave Measurements with Cloud Model Statistics. *Journal Atmosph. Ocean. Technol.*, **18**, pp. 1354-1366.

Löhnert, U. and S. Crewell: 2003: Accuracy of cloud liquid water path from ground-based microwave radiometry. Part I. Dependency on cloud model statistics. *Radio Science*, **38**, No. 3, 8041, doi:10.1029/2002RS002654.

Löhnert, U., S. Crewell and C. Simmer, 2004: An Integrated Approach towards Retrieving Physically Consistent Profiles Of Temperature, Humidity and Cloud Liquid Water. *Journal of Applied Meteorology,* **43**, 9, pp. 1295-1307.

Lüdi, A., L. Martin and C. Mätzler, Sept. 2003: The Retrieval of Temperature Profiles with the Ground-Based Radiometer System ASMUWARA. IAP Research Report, No. 2003-13.

Martin, L., August 2002: ASMUWARA - The All-Sky Multi Wavelength Radiometer: Documentation. IAP Research Report, No. 2002-12, University of Bern.

Martin, L., A. Lüdi and C. Mätzler, 2003: Tropospheric Monitoring with ASMUWARA. Proc. *6$^{th}$ International Symposium on Tropospheric Profiling (ISTP): Needs and Technologies*, Leipzig, Germany, Sep. 14-20, 2003.

Martin, L., M. Schneebeli and C. Mätzler, 2006: ASMUWARA, a ground-based radiometer system for tropospheric monitoring. *Meteorol. Zeitschr.*, TUC special issue, **15**, No. 1, pp.11–17.

Martin, L., M. Schneebeli and C. Mätzler, 2006: Tropospheric water and temperature retrieval for ASMUWARA. *Meteorol. Zeitschr.*, TUC special issue, **15**, No. 1, pp.37–44.

Martin, L., C. Mätzler, T. Hewison and D. Ruffieux, 2006: Intercomparison of integrated water vapour measurements. *Meteorol. Zeitschr.*, TUC special issue, **15**, No. 1, pp.57–64.

Marzano, F. S., E. Fionda, P. Ciotti and A. Martellucci, 2002: Ground-based multi-frequency microwave radiometry for rainfall remote sensing. *IEEE Trans. Geosci. Rem. Sens.*, **40**, pp. 742-759.

Marzano, F. S., D. Cimini, P. Ciotti and R. Ware, 2005: Modeling and Measurement of Rainfall by Ground-based Multispectral Microwave Radiometry. *IEEE Transactions on Geoscience and Remote Sensing,* **43**, 5, pp.1000-1011.

Mattioli, V., E. R. Westwater, S. I. Gutman and V. R. Morris, 2005: Forward Model Studies of Water Vapor using Scanning Microwave Radiometers, Global Positioning System, and Radiosondes during the Cloudiness Inter-Comparison Experiment. *IEEE Transactions on Geoscience and Remote Sensing*,. **43**(5), pp. 1012-1021.

Mätzler, C., 1992: Ground-Based Observations of Atmospheric Radiation at 5, 10, 21, 35 And 94 GHz. *Radio Science*, **27**, pp. 403-415.

Mätzler, C., 1998: Microwave Properties of Ice and Snow. **in:** B. Schmitt et al. (eds.), *Solar System Ices,* Astrophysics and Space Science Library,**227**, Dordrecht, Kluwer Academic Publishers, pp. 241-257.

Mätzler, C., P. W. Rosenkranz, A. Battaglia and J. P. Wigneron (eds.), 2006: Thermal Microwave Radiation - Applications for Remote Sensing. IEE Electromagnetic Waves Series 52, London, UK.

McGrath, A. and T. Hewison, 2001: Measuring the Accuracy of MARSS—An Airborne Microwave Radiometer. *Journal Atmosph. Ocean. Technol.*, **18**, *pp. 2003–2012*.

Morland, J., November 2002: TROWARA – Tropospheric water vapour radiometer: Radiometer review and new calibration model. *IAP Res. Rep.*, No. 2002-15, Institute of Appl. Physics, University of Bern, Bern, Switzerland.

Morland, J., B. Deuber, D. G. Feist, L. Martin, S. Nyeki, N. Kämpfer, C. Mätzler and L. Vuilleumier, 2005: The STARTWAVE atmospheric water vapour database, Atm. Chemistry and Physics Discussions, **5**, 10839-10879, 2005, and in press in Atmospheric Chemistry and Physics, textbf6.

Moteller, H. E., L. L. Strow, L. McMillin, and J. A. Gualtieri, 1995: Comparison of Neural Networks and Regression-Based Methods for Temperature Retrievals, *Appl. Optics*, **34**, pp. 5390-5397.

Nehrkorn, T. and C. Grassotti, 2004: Mesoscale Variational Assimilation of Profiling Radiometer Data. $16^{th}$ *Conference on Numerical Weather Prediction*, Seattle, WA, Am. Meteorol. Soc..

Ohring, G., K. Michell, M. Ji, S. Lord and J. Derber, 2002: Applications of Satellite Remote Sensing in Numerical Weather and Climate Prediction. *Advances in Space Research* **30**, pp. 2433-2439.

Pardo, J. R., J. Cernicharo and E. Serabyn, 2001: Atmospheric transmission at microwaves (ATM): An improved model for millimeter/submillimeter applications. *IEEE Trans. Antennas Propag*. **49,** 1683-1694.

Pardo, J. R., M. C. Wiedner, E. Serabyn, C. D. Wilson, C. Cunningham, R. E. Hills and J. Cernicharo, 2004: Side-by-side comparison of Fourier Transform Spectroscopy and Water Vapor Radiometry as tools for the calibration of mm/submm ground-based observatories. *Astrophys. J. Suppl.*, **153**, 363-367.

Peter, R. and N. Kämpfer, 1992: Radiometric Determination of Water Vapor and Liquid Water and its Validation with other Techniques, *Radio Science,* **97** ,D16, pp. 18173-18183.

Phillips, N. A., L. M. McMillin, D. Wark and A. Gruber, 1979: An Evaluation of Early Operational Temperature Soundings from TIROS-N. *Bulletin of the Am. Meteorol. Soc.*, **60**, pp. 1188-1197.

Racette, P. E., et al., April 2005: Measurement of Low Amounts of Precipitable Water Vapor Using Ground-Based Millimeterwave Radiometry. *Journal Atmosph. Ocean. Technol.*, **22**(4), pp. 317 - 337.

Rasmussen, R. M., M. K. Politovich, J. Marwitz, W. Sand, J. McGinley, J. Smart, R. Pielke, S. Rutledge, D. Wesley, G. Stossmeister, B. Bernstein, K. Elmore, N. Powell, E. Westwater, B. B. Stankov and D. Burrows, 1992: Winter Icing and Storms Project (WISP). Bull. Am. Meteorol. Soc., **73**(7), 951–974.

Reising, S. C., F. Iturbide-Sanchez and R. W. Jackson, October 2005: A Miniaturized Water Vapor Profiling Radiometer for Network-based 3-D Measurements of the Tropospheric Water Vapor Field. Paper F08.3, *Proc. 28th General Assembly of the International Union of Radio Science (URSI)*, New Delhi, India.

Revercomb, H. E., et al., 2003: The ARM Programs's Water Vapor Intensive Observation Periods: Overview, Initial Accomplishments, and Future Challenges. *Bull. Am. Meteorol. Soc.*, **84**,1, pp. 217-236.

Rodgers, C. D., 1976: Retrieval of Atmospheric Temperature and Composition From Remote Measurements of Thermal Radiation. *Reviews of Geophysics and Space Physics,* **14**, pp.609-624.

Rose, T., S. Crewell, U. Löhnert and C. Simmer: 2005: A network-suitable microwave radiometer for operational monitoring of the cloudy atmosphere. *Atmos. Res.*, *Special issue: CLIWA-NET: Observation and Modelling of Liquid Water Clouds*. **75**(3), pp. 183–200, doi:10.1016/j.atmosres.2004.12.005.

Rosenberg, V. I., 1972: *Scattering and Extinction of Electromagnetic Radiation by Atmospheric Particles*. Leningrad, Gidrometeoizdat, (in Russian).

Rosenkranz, P. W., 1993: Absorption Of Microwaves By Atmospheric Gases. Chapt. 2, **in**: Michael A. Janssen (ed.), *Atmospheric Remote Sensing by Microwave Radiometry*, New York, J. Wiley & Sons Inc., pp.37–90.

Rosenkranz, P. W., 1998: Water Vapor Microwave Continuum Absorption: A Comparison of Measurements and Models. *Radio Science,* **33,** 4, pp. 919-928.

Rosenkranz, P. W., 1999: Correction to "Water Vapor Microwave Continuum Absorption: a Comparison of Measurements and Models". *Radio Science*, **34**, 4, pp. 1025.

Rosenkranz, P. W., March 2004: Massachusetts Institute of Technology, Cambridge, MA, private communication.

Rothman, L. et al., 2005: The HITRAN 2004 Molecular Spectroscopic Database. *Journal of Quantitat. Spectroscopy and Radiat. Transf.*, **96**, pp. 139-204.

Sheppard, B. E., 1996: Effect of rain on ground-based radiometric measurements in the 20-90 GHz. *J. Atmosph. Ocean. Technol.*, **13**, pp. 1139-1151.

Skou, N., 1989: *Microwave Radiometer Systems: Design and Analysis*. Norwood, MA, Artech House Inc..

Solheim, F., J. Godwin, E. Westwater, Y. Han, S. Keihm, K. Marsh and R. Ware, 1998: Radiometric Profiling of Temperature, Water Vapor, and Liquid Water using Various Inversion Methods. *Radio Science*, **33**, pp. 393-404.

Stankov, B. B., B. E. Martner and M. K. Politovich, 1995: Moisture Profiling of the Cloudy Winter Atmosphere using Combined Remote Sensors. *Journal Atmosph. Ocean. Technol.*, **12**, pp. 488-510.

Stankov, B. B., E. R. Westwater and E. E. Gossard, 1996: Use of Wind Profiler Estimates of Significant Moisture Gradients to Improve Humidity Profile Retrieval. *Journal Atmosph. Ocean. Technol.*, **13**, 6, pp.1285-1290.

Stokes, G. M. and S. E. Schwartz, 1994: The Atmospheric Radiation Measurement (ARM) Program: Programmatic Background and Design of the Cloud and Radiation Testbed. *Bulletin of the American Meteorological Society,* **75**, pp.1201-1221.

Tanner, A. B. and A. L. Riley, 2003: Design and Performance of a High-Stability Water Vapor Radiometer. *Radio Science*, **38**, 3, 8050, doi:10.1029/2002RS002673.

Tikhonov, A. N. and V. Y. Arsenin, 1977: *Solutions of Ill-Posed Problems*. Washington, DC, V.H. Winston and Sons.

Tretyakov, M. Yu., V. V. Parshin, M. A. Koshelev, V. N. Shanin, S. E. Myasnikova and A. F. Krupnov, 2003: Studies of 183 GHz water line: broadening and shifting by air. $N_2$and $O_2$ and integral intensity measurements *Journal of Molecular Spectroscopy*, **218,** pp. 239-245.

Tretyakov, M. Yu., M. A. Koshelev, V. V. Dorovskikh, D. S. Makarov and P. W. Rosenkranz, 2005: 60-GHz oxygen band: precise broadening and central frequencies of fine-structure, absolute absorption profile at atmospheric pressure, and revision of mixing coefficients. *Journal Molec. Spectrosc.*, **231**, pp. 1–14.

Trokhimovski, Yu. G., E. R. Westwater, Y. Han and V. Ye. Leuskiy, 1998: The Results of Air and Sea Surface Temperature Measurements using a 60 Ghz Microwave Rotating Radiometer, *IEEE Transactions on Geoscience And Remote Sensing*, **36**, 1, pp. 3-15.

Turner, D., B. Lesht, A. Clough, J. Liljegren, H. Revercomb, and D. Tobin, 2003: Dry Bias and Variability in Väisälä RS80-H Radiosondes: The ARM Experience. *Journal Atmosph. Ocean. Technol.* , **20**, 1, pp.117-132.

Twomey, S., 1977: *Introduction to the Mathematics of Inversion in Remote Sensing and Indirect Measurements*. New York, Elsevier.

Ulaby, F. T., R. K. Moore and A. K. Fung, 1981: *Microwave Remote Sensing, Active and Passive*, Volume 1: *Microwave Remote Sensing Fundamentals and Radiometry*. Reading, MA, Addison-Wesley Publishing Company.

Van de Hulst, H. C., 1981: *Light Scattering by Small Particles*. New York, Dover Publications Inc..

van Vleck, J. H. and V. F. Weisskopf, 1947: On the Shape of Collision Broadened Lines. *Reviews of Modern Physics*, **17**, 227-236.

van Vleck, J. H., 1947a: The Absorption of Microwaves by Uncondensed Water Vapor. *Physical Review*, **71**, 425-433.

van Vleck, J. H., 1947b: The Absorption of Microwaves by Oxygen. *Physical Review*, **71**, 413-424.

Ware, R., R. Carpenter, J. Güldner, J. Liljegren, T. Nehrkorn, F. Solheim, and F. Vandenberghe, 2003: A Multi-Channel Radiometric Profiler of Temperature, Humidity and Cloud Liquid. *Radio Science*, **38**, 4, pp. 8079-8032.

Westwater, E. R., 1965: Ground-based Passive Probing Using the Microwave Spectrum of Oxygen. *Radio Science Journal of Research of the NBS,* **9D**, 9, pp. 1201-1211.

Westwater, E. R., J. B. Snider and A. C. Carlson, 1975: Experimental Determination of Temperature Profiles by Ground-Based Microwave Radiometry. *Journal of Applied Meteorology*. **14,** 4, pp. 524-539.

Westwater, E. R., 1993: Ground-based Microwave Remote Sensing of Meteorological Variables. **in:** Michael A. Janssen (ed.), *Atmospheric Remote Sensing by Microwave Radiometry*, New York, J. Wiley & Sons, Inc., pp. 145-213.

Westwater, E. R., Y. Han, V. G. Irisov, V. Leuskiy, E. N. Kadygrov and S. A. Viazankin, 1999: Remote Sensing of Boundary-Layer Temperature Profiles by a Scanning 5-mm Microwave Radiometer and RASS: Comparison Experiment. *Journal Atmosph. Ocean. Technol.*, **16**, 7, pp. 805-818.

Westwater, E. R., Y. Han, M. D. Shupe and S. Y.Matrosov, 2001: Analysis of Integrated Cloud Liquid and Precipitable Water Vapor Retrievals from Microwave Radiometers during SHEBA. *Journal of Geophys. Res.*, **106**, 23, pp.32019-32030.

Westwater, E. R., B. B. Stankov, D. Cimini, Y. Han, J. A. Shaw, B. M. Lesht and C. N.Long, 2003: Radiosonde Humidity Soundings and Microwave Radiometers during Nauru99 *Journal Atmosph. Ocean. Technol.*, **20**, 7, pp.953-971.

Westwater, E. R. et al., 2004: Initial Results from the 2004 North Slope of Alaska Arctic Winter Radiometric Experiment. *Proc. IGARSS'04*, Anchorage, AK, USA, Sep. 20-24, 2004.

Westwater, E. R., S. Crewell, C. Mätzler, 2004: A Review of Surface-based Microwave and Millimeter wave Radiometric Remote Sensing of the Troposphere. *Radio Science Bulletin of URSI*, RSB-310. **59-80**, ISSN 1024-4530.

Westwater, E. R., S. Crewell and C. Mätzler, March 2005: Surface-based Microwave and Millimeter wave Radiometric Remote Sensing of the Troposphere: A Tutorial. *IEEE Geoscience and Remote Sensing Newsletter*, **16-33**. ISSN 0161-7869.

Westwater, E. R., S. Crewell, C. Mätzler and D. Cimini, 2006: Principles of surface-based microwave and millimeter wave radiometric remote sensing of the troposphere. *Journal of the Società Italiana di ElettroMagnetismo*, **1**, 3, pp. 50-90.

## 3.3 LIDAR

Ulla Wandinger

*Leibniz Institute for Tropospheric Research, Leipzig, Germany*
ulla@tropos.de

Light detection and ranging (lidar) is an active remote-sensing technique based on the emission of short laser pulses and the time-resolved detection of scattered laser light. In principle, lidar allows the time- and range-resolved retrieval of the basic atmospheric state parameters (temperature, humidity, and wind), the observation of aerosols and thin clouds, as well as the measurement of atmospheric trace gases. In general, lidar observations have the benefit of high temporal and spatial -especially high vertical- resolution. The measurements are performed in a well-defined atmospheric volume determined by the width and divergence of the laser beam.

Nowadays, the lidar technique is widely applied in atmospheric research (Weitkamp, 2005). However, most of the instruments represent individual developments and require expert's knowledge in operation and data evaluation. Advanced systems are relatively complex and, therefore, man-power intensive and mostly non-autonomous. Besides relatively simple backscatter lidars (such as the widely used ceilometer) which give a more or less qualitative information on the atmospheric layering in terms of aerosols and clouds, so far only a few advanced systems are routinely applied, e.g., for long-term water-vapour observations (Goldsmith et al., 1998). Nevertheless, the status of technical and technological development in the field of lasers, optics, and data acquisition systems, in principle, allows the construction of robust lidar systems for unattended operation.

In the following, we focus on four basic lidar techniques which are applied to obtain profiles of the major parameters and constituents of the troposphere and which have the highest potential for the use in integrated profiling:

- The **elastic-backscatter lidar technique** gives information on the vertical structure of the atmosphere in terms of the particle backscatter coefficient and is applied to identify aerosol and cloud layers and to determine their boundaries.

- Inelastic molecular scattering processes are used in the **Raman lidar technique** to obtain profiles of water vapour and temperature as well as aerosol and cloud extinction.

- The **differential-absorption lidar or DIAL technique** takes advantage of the absorption properties of atmospheric trace gases and is mainly ap-

plied to measure water-vapour and ozone concentration with high spatial and temporal resolution.

- Horizontal and vertical wind velocities are obtained with the **Doppler lidar technique** by determining the frequency shift of scattered radiation caused by the collective motion of atmospheric molecules and particles.

Table 3.2 gives an overview on meteorological parameters that can be retrieved with these lidar techniques and the typical achievable measurement ranges under consideration of the latest technical developments. The techniques are described in more detail in the following subsections. Their status with respect to routine application and their potential for integrated profiling is discussed. Special emphasis is put on water-vapour profiling, because it is expected that lidar can especially well contribute to the observation of the spatially and temporally highly variable humidity field.

| Technique | Measured quantity | Typical achievable measurement range |
|---|---|---|
| Elastic-backscatter lidar | Aerosols and clouds<br>→ layer boundaries,<br>→ backscatter coefficient | Throughout troposphere (day and night) |
| Raman lidar | Water vapour | Throughout troposphere (night), 0–5 km (day) |
| | Temperature | Throughout troposphere (day and night) |
| | Aerosols and clouds<br>→ layer boundaries,<br>→ backscatter coefficient | Throughout troposphere (day and night) |
| | → extinction coefficient,<br>→ lidar ratio | Throughout troposphere (night), 0–5 km (day) |
| Differential-absorption lidar | Water vapour | (Lower) troposphere (day and night) |
| Coherent Doppler lidar | Wind velocity | Boundary layer (day and night) |

*Table 3.2.* Overview of tropospheric lidar techniques with a potential for integrated profiling

## 3.3.1 STATUS OF SELECTED LIDAR TECHNIQUES

**3.3.1.1 Elastic-backscatter lidar for aerosol and cloud profiling.** The elastic-backscatter lidar as the basic lidar type measures the light elastically backscattered by particles and molecules with a single detector at the wavelength that is emitted with a pulsed laser source. Elastic scattering is the primary interaction process of light with atmospheric constituents, so that, in principle, any lidar can serve as an elastic-backscatter lidar.

Commercially available laser ceilometers for routine and unattended operation represent the simplest type of an elastic-backscatter lidar. They are based on InGaAs laser diodes which emit laser pulses with a repetition rate of several kHz at a wavelength of about 900 nm. The backscattered light is usually detected with Si avalanche photodiodes. In the infrared wavelength region, particle backscattering dominates the lidar return signal. Therefore, layer boundaries, especially cloud base heights, are easily derived from signal gradients. Ceilometers are also well suited to atmospheric visibility measurements (Werner et al., 2005).

A quantitative evaluation of the lidar return signal in terms of atmospheric scattering parameters requires more sophisticated signal detection and data evaluation schemes than typically applied in the ceiling technique. Detector linearity over a dynamic signal range of several orders of magnitude, adequate data acquisition either based on $\geq$12-bit analog-to-digital conversion rate or on photon counting, and sufficient background suppression by using small receiver fields of view belong to the technical requirements. Micropulse lidars (MPL) are applied among other instruments, e.g., in the Atmospheric Radiation Measurement (ARM) program for autonomous, long-term observation of geometrical and optical aerosol and cloud parameters (Campbell et al., 2002) and in the Asian Dust Network (Murayama et al., 2001). These systems are based on a diode-pumped, frequency-doubled Nd:YLF laser with 2.5 kHz repetition rate and 20 $\mu$J pulse energy, a 20-cm telescope, and a photon-counting Geiger-mode avalanche photodiode.

The majority of research instruments that apply the elastic-backscatter lidar technique is nowadays based on the Nd:YAG laser operating with 20–50 Hz repetition rate and pulse energies of up to 1.5 J. Its primary wavelength of 1064 nm can be converted to 532 or 355 nm by nonlinear frequency generation, so that a broad spectral range from the ultraviolet to the infrared region can be covered. Most of the stations within the European Aerosol Research Lidar Network EARLINET, the first aerosol lidar network with continental coverage, apply this type of laser (Bösenberg et al., 2002). It is also used for space-borne lidar instruments, such as the Lidar In-space Technology Experiment (LITE) onboard the Space Shuttle and the Cloud-Aerosol Lidar with Orthogonal Polarization (CALIOP) on the recently launched Cloud-Aerosol Lidar and Infrared Pathfinder Satellite Observation (CALIPSO) satellite, which

demonstrate the potential of elastic-backscatter lidars for global monitoring (McCormick, 2005).

The elastic lidar return signal is described by the lidar equation (see Wandinger (2005a) for a detailed explanation):

$$P(R,\lambda_0) = P_0 \frac{c\tau}{2} A\eta \, \frac{O(R)}{R^2} \, \beta(R,\lambda_0) \exp\left[-2\int_0^R \alpha(r,\lambda_0)\mathrm{d}r\right]. \qquad (3.14)$$

$P(R,\lambda_0)$ is the signal power from distance $R$ at the wavelength $\lambda_0$ of the transmitted laser light, $P_0$ is the average power of a single laser pulse, $\tau$ is the pulse duration, and $c$ the speed of light. $A$ is the area of the primary receiver optics responsible for the collection of backscattered light, and $\eta$ is the overall system efficiency. $O(R)$ describes the laser-beam receiver-field-of-view overlap function. $O(R) < 1$ close to the lidar, and $O(R) = 1$ for larger distances for which the volume illuminated by the laser beam is completed imaged onto to the detector surface.

The backscatter coefficient $\beta(R,\lambda_0)$ is the primary atmospheric parameter that determines the strength of the lidar signal. It describes how much light is scattered into the backward (180°) direction, i.e., towards the lidar receiver. The laser light is scattered by air molecules and particulate matter, i.e., $\beta(R,\lambda_0)$ can be written as

$$\beta(R,\lambda_0) = \beta_{\mathrm{mol}}(R,\lambda_0) + \beta_{\mathrm{par}}(R,\lambda_0). \qquad (3.15)$$

Molecular or Rayleigh scattering (index mol), mainly occurring from nitrogen and oxygen molecules, primarily depends on air density and thus decreases with height. Furthermore, it shows a strong wavelength dependence proportional to $\lambda^{-4}$ and thus dominates lidar signals in the ultraviolet. Particle scattering (index par) depends on the content of aerosol and cloud particles in the atmosphere and is therefore highly variable in space and time. Its wavelength dependence is strongly influenced by the particle size.

The final term in equation (3.14) is the transmission term which describes the fraction of light that gets lost on the way from the lidar to the scattering volume and back. The sum of all transmission losses is called light extinction, and $\alpha(R,\lambda)$ is the extinction coefficient. Extinction of light occurs because of scattering and absorption by molecules and particles. The extinction coefficient therefore can be written as the sum of four components,

$$\begin{aligned} \alpha(R,\lambda_0) \;=\; & \alpha_{\mathrm{mol,sca}}(R,\lambda_0) + \alpha_{\mathrm{mol,abs}}(R,\lambda_0) \\ & + \alpha_{\mathrm{par,sca}}(R,\lambda_0) + \alpha_{\mathrm{par,abs}}(R,\lambda_0), \end{aligned} \qquad (3.16)$$

where the indices sca and abs stand for scattering and absorption, respectively.

Molecular absorption is often negligible if the laser wavelength is appropriately chosen. Molecular scattering is sufficiently well known from (standard or actual) pressure and temperature profiles. Thus the elastic-backscatter lidar

equation contains two unknown atmospheric quantities, the particle backscatter and extinction coefficients. The attempts to solve the lidar equation in order to retrieve trustworthy extinction profiles and the discussion of achievements and limitations of these methods fill entire text books (see, e.g., Kovalev and Eichinger (2004)). However, all the procedures suffer from the fact that two unknown physical quantities must be determined from only one measured signal. Therefore, the usual approach is to introduce the extinction-to-backscatter ratio, or lidar ratio, for particles,

$$S_{\mathrm{par}}(R,\lambda_0) = \frac{\alpha_{\mathrm{par}}(R,\lambda_0)}{\beta_{\mathrm{par}}(R,\lambda_0)}, \tag{3.17}$$

and for molecules,

$$S_{\mathrm{mol}} = \frac{\alpha_{\mathrm{mol}}(R,\lambda_0)}{\beta_{\mathrm{mol}}(R,\lambda_0)} = \frac{8\pi}{3}\,\mathrm{sr}. \tag{3.18}$$

For the sake of simplicity, in the following equations we do not explicitly write down the dependence of the parameters on wavelength anymore. Furthermore, we define

$$Y(R) = S_{\mathrm{par}}(R)\left[\beta_{\mathrm{par}}(R) + \beta_{\mathrm{mol}}(R)\right] \tag{3.19}$$

and assume that $O(R) \equiv 1$, i.e., we consider only regions where the overlap of laser beam and receiver field of view is complete. Now, equation (3.14) can be written as

$$\begin{aligned} X(R)S_{\mathrm{par}}(R)\exp\left\{-2\int_0^R \left[S_{\mathrm{par}}(r) - S_{\mathrm{mol}}\right]\beta_{\mathrm{mol}}(r)\,\mathrm{d}r\right\} \\ = KY(R)\exp\left[-2\int_0^R Y(r)\,\mathrm{d}r\right]. \end{aligned} \tag{3.20}$$

$X(R)$ is the range-corrected lidar signal $P(R)R^2$, and the factor $K$ comprises the range-independent parameters. Taking the logarithms of both sides of equation (3.20) and differentiating them with respect to $R$ gives the Bernoulli differential equation

$$\begin{aligned} \frac{\mathrm{d}\ln\left(X(R)S_{\mathrm{par}}(R)\exp\left\{-2\int_0^R \left[S_{\mathrm{par}}(r) - S_{\mathrm{mol}}\right]\beta_{\mathrm{mol}}(r)\,\mathrm{d}r\right\}\right)}{\mathrm{d}R} \\ = \frac{1}{Y(R)}\frac{\mathrm{d}Y(R)}{\mathrm{d}R} - 2Y(R), \end{aligned} \tag{3.21}$$

the solution of which, for the boundary condition

$$Y(R_0) = S_{\mathrm{par}}(R_0)[\beta_{\mathrm{par}}(R_0) + \beta_{\mathrm{mol}}(R_0)], \tag{3.22}$$

is (Sasano et al., 1985):

$$\beta_{\mathrm{par}}(R) + \beta_{\mathrm{mol}}(R) = \frac{A(R,R_0)}{B(R_0) - 2\int_{R_0}^R S_{\mathrm{par}}(r)A(r,R_0)\mathrm{d}r}, \tag{3.23}$$

with

$$A(R,R_0) = X(R)\exp\left\{-2\int_{R_0}^{R}\left[S_{\mathrm{par}}(r) - S_{\mathrm{mol}}\right]\beta_{\mathrm{mol}}(r)\,\mathrm{d}r\right\} \tag{3.24}$$

and

$$B(R_0) = \frac{X(R_0)}{\beta_{\mathrm{par}}(R_0) + \beta_{\mathrm{mol}}(R_0)}. \tag{3.25}$$

The profile of the particle extinction coefficient can be estimated from the solution $\beta_{\mathrm{par}}(R)$ by

$$\alpha_{\mathrm{par}}(R) = S_{\mathrm{par}}(R)\beta_{\mathrm{par}}(R). \tag{3.26}$$

Equation (3.23) is integrated by starting from the reference range $R_0$, which may be either the near end ($R > R_0$, forward integration) or the remote end of the measuring range ($R < R_0$, backward integration). Numerical stability, which is not to be mistaken for accuracy, is given only in the backward integration case. The latter procedure is often called the Klett method (Klett, 1981). The reference range $R_0$ in equation (3.23) is usually chosen such that at $R_0$ the particle backscatter coefficient is negligible compared to the known molecular backscatter value.

The most critical input parameter in the Klett method is the particle lidar ratio $S_{\mathrm{par}}(R)$. This quantity depends on the microphysical, chemical, and morphological properties of the particles and on the laser wavelength. For water clouds and typical laser wavelengths in the ultraviolet to visible wavelength region lidar ratios of 18–20 sr are typical. In contrast, ice clouds show a wide range of values between about 2 sr (if falling, oriented crystals are observed with a vertically pointing lidar) and 50 sr. The lidar ratio of aerosol particles varies between 20–25 sr for sea-salt particles and 100 sr for strongly absorbing aerosol particles. Dust and less-absorbing urban aerosols show typical lidar ratios between 40 and 80 sr. Because of this wide range of values it is almost impossible to estimate trustworthy extinction profiles after equation (3.26). With accompanying Sun photometer observations, which deliver the spectral optical depth (integral over the extinction-coefficient profile), a column-related lidar ratio for the wavelength of interest can be estimated from the ratio of the optical depth to the column-integrated backscatter coefficient determined from equation (3.23). This lidar ratio can be considered as a first guess. However, the true lidar-ratio profile always remains unknown in the case of elastic-backscatter observations.

An additional option for elastic-backscatter lidars is the implementation of a polarization-sensitive measurement capability in order to obtain information on particle shape. Usually, linearly polarized laser light is emitted and the perpendicular and parallel polarized components of the backscattered light are detected (Sassen, 2005). The linear depolarization ratio

$$\delta(R) = C_\delta \frac{P^{\perp}(R)}{P^{\parallel}(R)} \tag{3.27}$$

is easily calculated from the ratio of the two signal components $P^{\perp}(R)$ and $P^{\parallel}(R)$. The constant $C_{\delta}$, which accounts for the different detection efficiencies of the two measurement channels, can be determined by calibrating the $\delta$-profile in height regions of dominating molecular scattering. The molecular depolarization ratio is of the order of a few percent and can be calculated in dependence on wavelength and filter bandwidth. If the molecular contributions to the signal components are subtracted, one obtains the particle depolarization ratio

$$\delta_{\mathrm{par}}(R) = \frac{\beta_{\mathrm{par}}^{\perp}(R)}{\beta_{\mathrm{par}}^{\parallel}(R)}, \tag{3.28}$$

with the coefficients $\beta_{\mathrm{par}}^{\parallel}$ and $\beta_{\mathrm{par}}^{\perp}$ for parallel and cross-polarized particle backscattering, respectively.

The depolarization ratio is especially helpful in distinguishing spherical and non-spherical scatterers. Whereas backscattering by cloud droplets and small aerosol particles does not depolarize the linearly polarized laser light, 180°-scattering from non-spherical ice crystals or comparably large mineral dust particles causes a considerable light depolarization. The measurement of the linear depolarization ratio can therefore be used to discriminate the water and ice phases in clouds or to distinguish mineral-dust layers from anthropogenic pollution.

Another effect that has to be taken into account in cloud measurements with lidar is multiple scattering. If the scatterers are large compared to the laser wavelength, approximately half of the scattered light is diffracted into the forward direction and remains in the field of view of the instrument. The effective extinction is decreased (less of the radiation gets lost) and the transmission (exponential term in equation (3.14)) is increased accordingly. Furthermore, if the multiply scattered light is backscattered by droplets, the backscattering process, which occurs under angles slightly different from 180°, leads to a depolarization of the scattered light. The absolute contribution of multiple scattering and its influence on quantities derived from the lidar signals depends in a complex way on the actual measurement geometry (laser beam divergence, receiver field of view, distance to the cloud) and on the cloud particle size and can only be treated with the help of specific models (Bissonnette, 2005). Further details of elastic-backscatter lidar data evaluation are discussed on the basis of a measurement example in section 3.3.2.2.

**3.3.1.2 Raman lidar for aerosol and cloud profiling.** The major deficit of the elastic-backscatter lidar, i.e., that two unknowns must be determined from a single signal, has been overcome with the introduction of the Raman lidar technique (Ansmann et al., 1990, 1992). By detecting a pure molecular backscatter signal in addition to the standard elastic backscatter signal, an independent retrieval of the particle extinction and backscatter coefficients becomes possible. A pure molecular signal can be obtained in different

ways. The simplest and most robust method is the spectral separation of the vibration–rotation Raman signal of nitrogen with an interference filter. This Raman signal is shifted by 2331 $\mathrm{cm}^{-1}$ from the laser wavelength and can easily be separated from the elastic backscatter signal. The limitation is the weak signal strength, because the Raman scattering cross section is about three orders of magnitude smaller than the Rayleigh scattering cross section. Thus Raman lidars require certain instrumental efforts (high-power laser, large telescope, efficient detection and data acquisition) and the measurements have a somewhat limited spatial and temporal resolution and, under daylight conditions, a limited range (see table 3.2). A better signal-to-noise ratio can be obtained if a pure Rayleigh backscatter signal is separated from the elastic-backscatter spectrum. However, this so-called high-spectral-resolution lidar technique requires much higher technical efforts, and only few research instruments have been developed so far (Eloranta, 2005). In contrast, the Raman lidar technique is widely applied nowadays.

The lidar equation for a Raman backscatter signal is written as

$$P(R,\lambda_{\mathrm{Ra}}) = \frac{KO(R)}{R^2}\beta_{\mathrm{Ra}}(R,\lambda_0)\exp\left\{-\int_0^R [\alpha(r,\lambda_0)+\alpha(r,\lambda_{\mathrm{Ra}})]\,\mathrm{d}r\right\}. \quad (3.29)$$

Here, $\beta_{\mathrm{Ra}}$ denotes the Raman backscatter coefficient. The only particle-scattering effect on the signal strength is attenuation. $\alpha(R,\lambda_0)$ describes the extinction on the way up to the backscatter region, $\alpha(R,\lambda_{\mathrm{Ra}})$ the extinction on the way back to the lidar. For a vibration–rotation Raman signal the shift of the wavelength from $\lambda_0$ before to $\lambda_{\mathrm{Ra}}$ after the scattering process must be considered.

The Raman backscatter coefficient is calculated from the molecular number density $N_{\mathrm{Ra}}$, i.e., the nitrogen density here, and the Raman backscatter cross section $\mathrm{d}\sigma_{\mathrm{Ra}}/\mathrm{d}\Omega(\pi,\lambda_0)$:

$$\beta_{\mathrm{Ra}}(R,\lambda_0) = N_{\mathrm{Ra}}(R)\frac{\mathrm{d}\sigma_{\mathrm{Ra}}}{\mathrm{d}\Omega}(\pi,\lambda_0). \quad (3.30)$$

The molecular number density profile is derived from actual radiosonde observations or standard atmospheric temperature and pressure profiles. Then, equation (3.29) can directly be solved for the particle extinction coefficient:

$$\alpha_{\mathrm{par}}(R,\lambda_0) = \frac{\frac{\mathrm{d}}{\mathrm{d}R}\ln\frac{N_{\mathrm{Ra}}(R)}{X(R,\lambda_{\mathrm{Ra}})} - \alpha_{\mathrm{mol}}(R,\lambda_0) - \alpha_{\mathrm{mol}}(R,\lambda_{\mathrm{Ra}})}{1+\left(\frac{\lambda_0}{\lambda_{\mathrm{Ra}}}\right)^{\mathring{a}(R)}}. \quad (3.31)$$

The Ångstrøm exponent $\mathring{a}$ is introduced to describe the wavelength dependence of $\alpha_{\mathrm{par}}$ between the laser and the Raman wavelength. In clouds, $\mathring{a}=0$. For aerosols $\mathring{a}$ usually varies between 0 and 2. Thus $\mathring{a}=1$ is a good estimate in equation (3.31). Overestimation and underestimation of $\mathring{a}$ by 0.5 leads to relative errors of $\alpha_{\mathrm{par}}$ of the order of 5%.

The particle backscatter coefficient $\beta_{\mathrm{par}}(R,\lambda_0)$ can be determined from the elastic backscatter and the Raman signal. By using two measured signal pairs $P(R,\lambda_0)$ and $P(R,\lambda_{\mathrm{Ra}})$ at $R$ and $R_0$ and forming the ratio

$$\frac{P(R_0,\lambda_{\mathrm{Ra}})P(R,\lambda_0)}{P(R_0,\lambda_0)P(R,\lambda_{\mathrm{Ra}})},$$

one obtains:

$$\begin{aligned}\beta_{\mathrm{par}}(R,\lambda_0) \quad &+ \quad \beta_{\mathrm{mol}}(R,\lambda_0) = [\beta_{\mathrm{par}}(R_0,\lambda_0)+\beta_{\mathrm{mol}}(R_0,\lambda_0)] \\ &\times \quad \frac{P(R_0,\lambda_{\mathrm{Ra}})P(R,\lambda_0)}{P(R_0,\lambda_0)P(R,\lambda_{\mathrm{Ra}})}\frac{N_{\mathrm{Ra}}(R)}{N_{\mathrm{Ra}}(R_0)} \\ &\times \quad \frac{\exp\{-\int_{R_0}^{R}[\alpha_{\mathrm{par}}(r,\lambda_{\mathrm{Ra}})+\alpha_{\mathrm{mol}}(r,\lambda_{\mathrm{Ra}})]\mathrm{d}r\}}{\exp\{-\int_{R_0}^{R}[\alpha_{\mathrm{par}}(r,\lambda_0)+\alpha_{\mathrm{mol}}(r,\lambda_0)]\mathrm{d}r\}}. \qquad (3.32)\end{aligned}$$

As in the Klett procedure, a reference value for particle backscattering at $R_0$ must be estimated. The reference height should be chosen in the upper troposphere where particle scattering is typically negligible compared to Rayleigh scattering. Then only the air density, the molecular backscattering, and atmospheric extinction properties must be estimated to solve equation (3.32). Again, meteorological profiles or standard-atmosphere data are used to calculate air density and molecular backscatter terms. The particle transmission ratio for the height range between $R_0$ and $R$ is estimated from the measured particle extinction profile with the assumption on the Ångstrøm exponent $\mathring{a}$ as used in equation (3.31). Finally, the height profile of the particle lidar ratio,

$$S_{\mathrm{par}}(R,\lambda_0) = \frac{\alpha_{\mathrm{par}}(R,\lambda_0)}{\beta_{\mathrm{par}}(R,\lambda_0)}, \qquad (3.33)$$

can be obtained from the profiles of $\alpha_{\mathrm{par}}(R,\lambda_0)$ and $\beta_{\mathrm{par}}(R,\lambda_0)$ with equation (3.31) and (3.32).

If several wavelengths are emitted, spectrally-resolved extinction and backscatter coefficients can be determined. From these data sets, microphysical particle properties such as effective radius, surface and volume concentrations, the complex refractive index and the single-scattering albedo can be derived (Ansmann and Müller, 2005). Therefore, the Raman lidar technique has a wide field of applications in meteorological and climate research. The very robust setup of the instruments allows trustworthy routine and long-term observations. Within EARLINET, Raman lidar measurements represent the backbone in the establishment of an European aerosol climatology. In addition to the aerosol and cloud properties, advanced Raman lidar instruments deliver water-vapour and temperature profiles (see section 3.3.1.3 and 3.3.1.4).

As an example, figure 3.12 shows the setup of the temperature-moisture-aerosol Raman lidar of the Leibniz Institute for Tropospheric Research (IfT) in Leipzig, Germany, one of the EARLINET stations. The instrument also

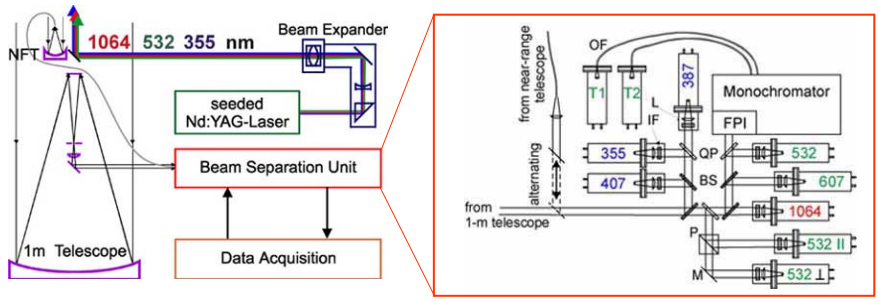


*Figure 3.12.* Setup of temperature-moisture-aerosol Raman lidar of the Leibniz Institute for Tropospheric Research, Leipzig, Germany; BS – beamsplitter, FPI – Fabry–Perot interferometer, IF – interference filter, L – lens, M – mirror, OF – optical fiber, QP – quartz plate, P – polarizer.

contributed to the LAUNCH–2005 campaign (see section 5.2). It applies a seeded Nd:YAG laser which emits light pulses at the wavelengths of 1064, 532, and 355 nm with an overall power of 1.6 J and a repetition rate of 30 Hz. A 15-fold beam expander reduces the beam divergence to less than 0.1 mrad. The backscattered light is alternately collected with a far-range telescope (1-m Cassegrain) and a near-range telescope (10-cm Newton). A 10-channel receiver separates the elastically backscattered signals at the three laser wavelengths and the Raman signals of nitrogen at 387 and 607 nm and of water vapour at 407 nm by the use of dichroic beamsplitters and interference filters. A polarizer discriminates the parallel-polarized and cross-polarized components of the 532-nm backscatter signal. For the temperature measurements (see section 3.3.1.4) two pure rotational Raman signals of nitrogen are separated with a double-grating monochromator. A Fabry–Perot interferometer (FPI) allows the suppression of the daylight background between the pure rotational Raman lines. All signals are detected with photomultiplier tubes and recorded in single-photon-counting mode. From the detected signals, profiles of the backscatter coefficient at the three emitted wavelengths, of the extinction coefficient and the lidar ratio at 355 and 532 nm, of the depolarization ratio at 532 nm, and of the water-vapour mixing ratio and the temperature are determined.

Next to advanced research instruments, smaller, cost-saving devices for autonomous operation were developed recently (Engelmann et al., 2003). *Polly*, shown in figure 3.13, is a portable two-channel mini Raman lidar for the measurement of extinction and backscatter coefficients at 532 nm. A frequency-doubled Nd:YAG laser emits pulses with an energy of 120 mJ and a repetition rate of 15 Hz. A 20-cm Newton telescope collects the backscattered light. The elastic-backscatter signal and the vibration–rotation Raman signal of nitrogen at 607 nm are analyzed. *Polly* is used for quasi-continuous, automated measurements in the lower troposphere at the Leibniz Institute for Tropospheric Research in Leipzig, Germany, and has been applied in various international

field campaigns. The regular measurements are published via the internet in real time (see http://iftwetter.tropos.de/VAP/). Upgraded versions of *Polly* with a larger number of measurement channels are presently under development.

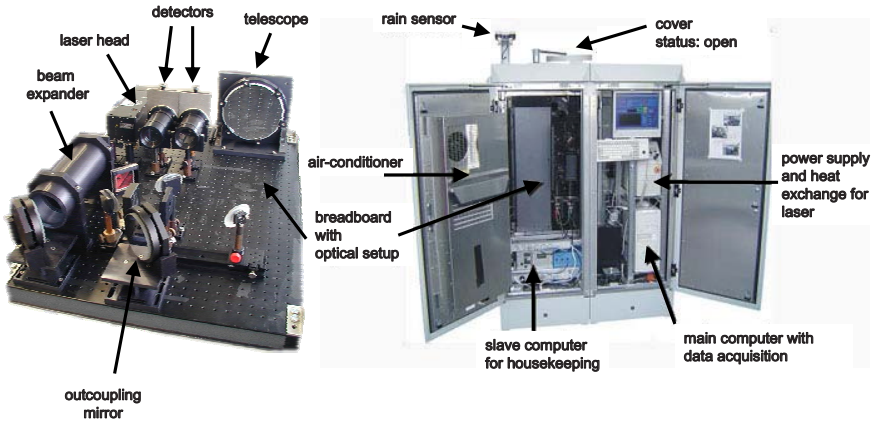


*Figure 3.13.* *Polly* – the portable two-channel mini Raman lidar of the Leibniz Institute for Tropospheric Research, Leipzig, Germany.

**3.3.1.3 Water-vapour Raman lidar.** The detection of water vapour with Raman lidar is a well established method in atmospheric research (Wandinger, 2005b). Water vapour, similar to nitrogen and oxygen, shows a Raman-shifted vibration–rotation band well separated by approximately 3650 $cm^{-1}$ from the exciting wavelength, which can easily be detected by applying small-bandwidth interference filters with sufficiently high suppression at the laser wavelength. The low demands regarding choice of the wavelength, spectral purity of the laser light, and frequency stabilization of the receiver allow the construction of stable and robust water-vapour Raman lidar systems for long-term operational use. The first operational water-vapour Raman lidar for unattended and autonomous operation was set up at the Cloud and Radiation Testbed site of the Atmospheric Radiation Measurement Program of the U.S. Department of Energy in Oklahoma in 1996 (Goldsmith et al., 1998). The German Meteorological Service started operating the water-vapour Raman lidar *RAMSES* (Raman Lidar for Atmospheric Moisture Sensing) at the Richard-Aßmann Observatory in Lindenberg in summer 2005. A variety of research instruments is available, and new instruments are under development or have already been implemented at major European atmospheric research field sites, e.g., at Cabauw (The Netherlands), Chilbolton (United Kingdom), L'Aquila (Italy), and Jungfraujoch (Switzerland). As in the case of aerosol and cloud measurements, the low Raman cross sections require high laser power, a large telescope, and an efficient signal detection and data acquisition technique. Additional efforts, i.e., a small-bandwidth receiver and a narrow telescope field of

view, are necessary for daytime operation. Only then, daytime measurements up to the mid troposphere are possible (see table 3.2).

By measuring the vibration–rotation Raman signals of water vapour and of nitrogen, as a reference signal, and forming the signal ratio $P_{H_2O}/P_{N_2}$ (see equation (3.29)), we directly obtain the mixing ratio of water vapour relative to dry air:

$$m_{H_2O}(R) = C_{H_2O} \frac{P_{H_2O}(R)}{P_{N_2}(R)} \frac{\exp\left[-\int_0^R \alpha(r, \lambda_{N_2}) \mathrm{d}r\right]}{\exp\left[-\int_0^R \alpha(r, \lambda_{H_2O}) \mathrm{d}r\right]}, \tag{3.34}$$

with the calibration constant $C_{H_2O}$. Equation (3.34) assumes identical overlap factors and range-independent Raman backscatter cross sections for the two signals. The difference between the atmospheric transmission at $\lambda_{H_2O}$ and the one at $\lambda_{N_2}$ is mainly caused by Rayleigh scattering and can easily be corrected by using standard-atmosphere profiles of temperature and pressure, or, if available, actual radiosonde data. Differences in the transmissions at the two Raman wavelengths caused by wavelength-dependent particle extinction can be neglected in most cases (see section 3.3.1.2).

The calibration constant $C_{H_2O}$ is usually determined by comparing the profile $m_{H_2O}(R)$ with the data from an accompanying radiosonde ascent. Calibration to the column water-vapour content measured with microwave radiometer, Sun photometer, or GPS is possible as well. The automated calibration procedure used for the *RAMSES* data evaluation is described in section 3.3.2.1.

The optical setup of *RAMSES* is shown in figure 3.14. System parameters are listed in table 3.3. The source of radiation is a frequency-tripled Nd:YAG laser with a total pulse energy of about 1.6 J. Only third-harmonic radiation at 354.7 nm is emitted into the atmosphere. The typical pulse energy at this wavelength chosen for operational conditions is 300 mJ. The pulse repetition rate is 30 Hz. The laser beam is expanded tenfold and directed onto the axis of the far-range telescope with three beam-folding mirrors. The receiving optics is presently optimized for nighttime water-vapour measurements throughout the troposphere. *RAMSES* is operated with two receiver telescopes simultaneously. The far-range Cassegrain telescope with a mirror diameter of 790 mm is preferably used for measurements above 1 km height. The receiver field of view can be chosen between 0.2 and 1 mrad. For measurements in the lower atmosphere a fiber-coupled Newton telescope with a mirror diameter of 200 mm and a fixed receiver field of view of 3 mrad is used. The near-range telescope is installed close to the secondary mirror of the far-range telescope. Its optical axis, which can be tilted against the laser beam, has a distance of 256 mm to the laser beam axis. Two nearly identical receiver boxes for the far-range and the near-range channels are deployed. They are constructed such that identical optical path lengths for all channels are realized. After the beam collimation, dichroic beamsplitters and interference filters separate the elastically backscattered light at 354.7 nm and the vibration–rotation Raman signals

of water vapour at 407.5 nm and of nitrogen at 386.5 nm. The optical signals are recorded with photomultiplier tubes with a diameter of the active area of 22 mm. Data acquisition is performed with analog/photon-counting transient recorders.

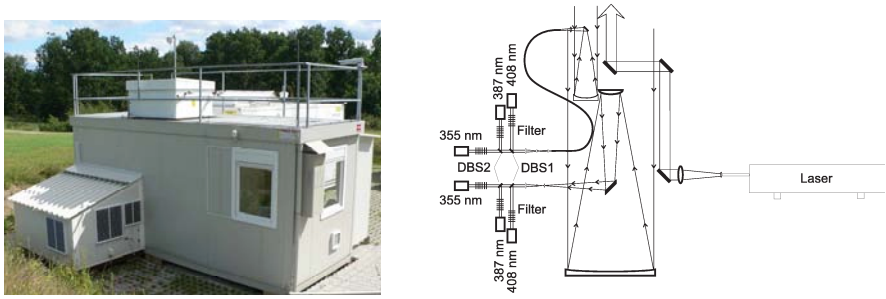


*Figure 3.14.* *RAMSES* at the Richard-Aßmann Observatory in Lindenberg (left) and scheme of its optical setup (right); DBS – dichroic beamsplitter.

A water-vapour measurement taken with *RAMSES* during the LAUNCH–2005 campaign on September 25, 2005, is shown in figure 3.15. The raw data were measured with the far-range telescope and the analog detection channels which allow the extremely high resolution of 7.5 m in height and 30 s in time presented here. Calibration was performed with the Lindenberg radiosonde at 00 UT. Small-scale structures are well resolved up to 5 km height.

Another water-vapour Raman lidar within the COST–720 action is the Chilbolton UV Raman lidar system located at the CCLRC Chilbolton Observatory in the southern UK. The system applies a Nd:YAG laser with a nominal pulse energy of 350 mJ at 355 nm and a 450-mm receiver mirror. The received signal is split between five channels. These are the vibration–rotation Raman channels for water vapour and nitrogen, two rotational Raman channels, and one elastic-scattering channel. The system is capable of measuring aerosol, water vapour, and temperature with the methods described in section 3.3.1.2–3.3.1.4. An analog and photon-counting system is used to cover a large dynamic signal range during day and night. Data are recorded with a resolution of 20 s and 7.5 m and are averaged as required for a particular application. The system is operated on a case study basis, particularly for field campaigns based around Chilbolton Observatory. Recently, it has been an integral part of the Convective Storm Initiation Project (CSIP) which studied the onset of convection with the aim of improving the forecasting of severe weather.

Figure 3.16 presents measurements of the particle backscatter coefficient and the water-vapour mixing ratio during a warm-front approach at the Chilbolton site. The upper panel shows the particle backscatter coefficient with the as-recorded time and height resolution. The cloud-base height decreased from 6 to 2 km as the front approached. The middle panel shows the water-vapour mixing ratio with the same time and height resolution. Sunset

*Table 3.3. RAMSES* system parameters.

| | | | |
|---|---|---|---|
| Laser | | | |
| Pulse energy, 1064 nm | 1600 mJ | | |
| Pulse energy, 355 nm | 650 mJ (300 mJ operational) | | |
| Pulse length, 1064 nm | 5–9 ns | | |
| Pulse length, 355 nm | 3–7 ns | | |
| Repetition rate | 30 Hz | | |
| Beam divergence | 0.5 mrad | | |
| Pointing stability | $\pm 30$ $\mu$rad | | |
| Line width (injection seeded) | 0.003 $cm^{-1}$ | | |
| Beam expander | | | |
| Magnification factor | 10 | | |
| Input aperture | 12 mm | | |
| Output aperture | 120 mm | | |
| Input beam diameter | 8 mm | | |
| Output beam diameter | 80 mm | | |
| Far-range telescope | | | |
| Type | Cassegrain | | |
| Primary mirror diameter | 790 mm | | |
| Secondary mirror diameter | 203 mm | | |
| Effective focal length | 6000 mm | | |
| Receiver field of view | 0.2–1 mrad | | |
| Near-range telescope | | | |
| Type | fiber-coupled Newton | | |
| Primary mirror diameter | 200 mm | | |
| Effective focal length | 560 mm | | |
| Fiber core diameter | 1.7 mm | | |
| Distance to laser beam axis | 256 mm | | |
| Receiver field of view | 3 mrad | | |
| Beamsplitters and filters | | | |
| Channel (wavelength) | 354.7 nm | 386.5 nm | 407.5 nm |
| Reflectivity of dichroic beamsplitter 1 | 1.6% | 0.7% | >99% |
| Reflectivity of dichroic beamsplitter 2 | 0.3% | >99% | – |
| Interference filter bandwidth (FWHM; far range/near range) | 1.98/1.95 nm | 2.08/2.08 nm | 1.74/1.78 nm |
| Interference filter transmission (far range/near range) | 60%/58% | 86%/78% | 88%/84% |

was at approximately 18:25 UT. The noise level in the signal decreased greatly as the skies grew darker. This also allowed an increase in gain to be applied to the water-vapour measurement from 18:40 UT onwards, which improved the sensitivity. Water-vapour data cannot be obtained from above the cloud base. The lower panel of figure 3.16 shows the same water-vapour measurement averaged to 5 min and 22.5 m resolution. This gives a considerable reduction in noise level, however depending on the application, the higher resolution data are sometimes of use.

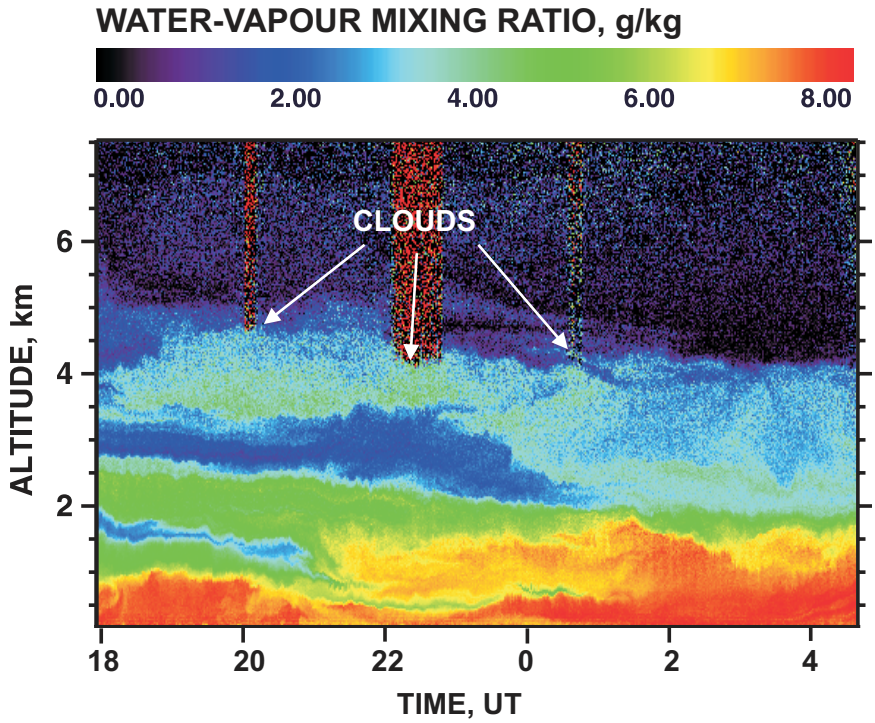


*Figure 3.15.* *RAMSES* water-vapour measurement on September 25–26, 2005.

**3.3.1.4 Temperature Raman lidar.** With some instrumental efforts any water-vapour and aerosol Raman lidar can also be upgraded for temperature measurements. The temperature information comes from the intensity distribution within the pure rotational Raman spectrum of nitrogen and oxygen which is centered at the exciting wavelength and has a width of about 400 $cm^{-1}$. The intensities of rotational Raman lines close to the incident wavelength decrease with rising temperature whereas the intensities of lines with a larger shift increase with temperature. This behavior is a result of the temperature-dependent population of the molecule's rotational energy levels which follows a Boltzmann distribution. By selecting two signals $P_{RR1}(T,R)$ and $P_{RR2}(T,R)$ with opposite temperature dependence out of the rotational Raman spectrum and forming the signal ratio

$$Q(T,R) = \frac{P_{RR2}(T,R)}{P_{RR1}(T,R)} \approx \exp\left(a - \frac{b}{T}\right), \tag{3.35}$$

one obtains the atmospheric temperature profile as

$$T(R) = \frac{b}{a - \ln Q(R)}. \tag{3.36}$$

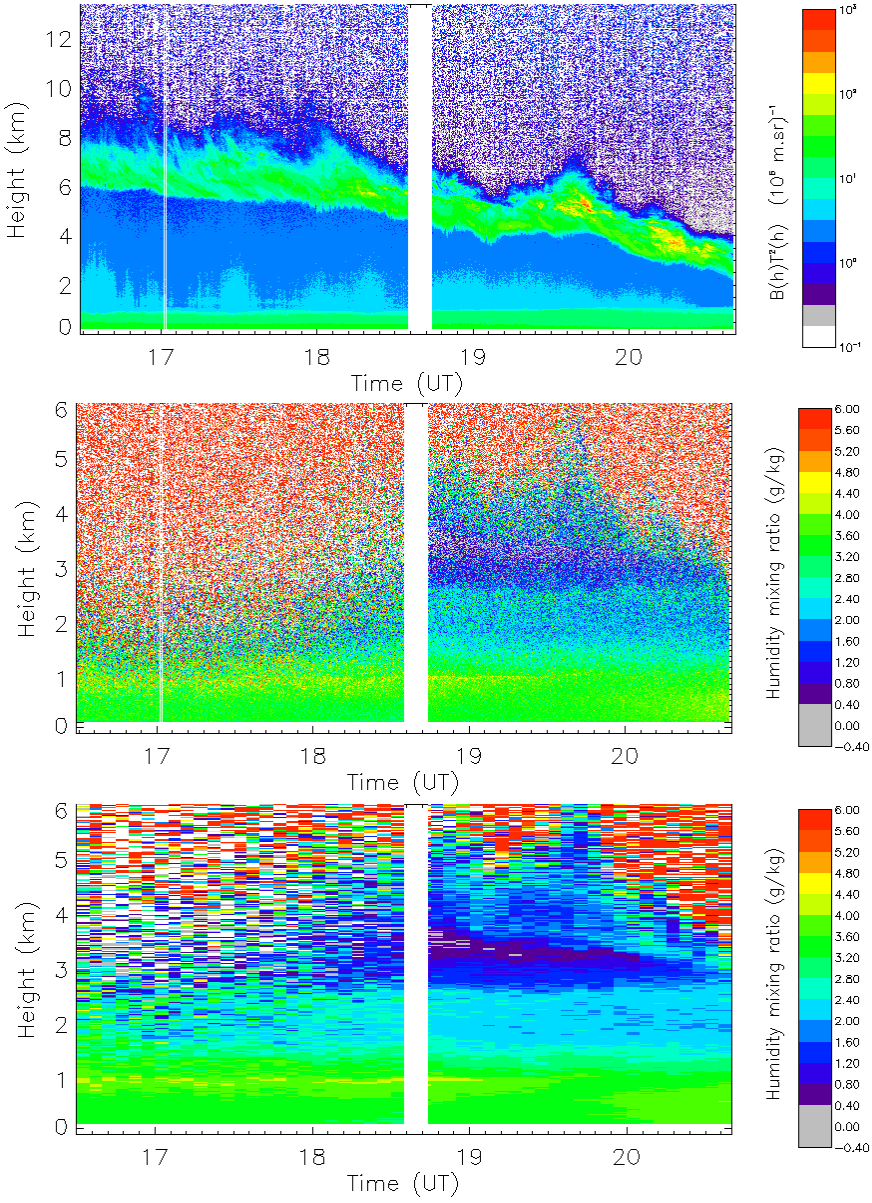


*Figure 3.16.* Backscatter coefficient (upper panel) and water-vapour mixing ratio (middle and lower panel) measured with the Chilbolton UV Raman lidar during the approach of a warm front on March 23, 2006. The resolution is 7.5 m and 20 s in the upper two panels and 22.5 m and 5 min in the lower panel.

The two calibration constants $a$ and $b$ are determined by comparison with an accompanying radiosonde profile. Equation (3.36) is strictly valid only if single rotational Raman lines are selected. If several lines contribute to the signals, second-order calibration functions with three or more calibration constants have to be used. Details can be found in the literature (Behrendt, 2005).

The major technical challenge of the rotational Raman lidar technique results from the necessity to select two spectrally narrow signals in the wavelength region close to the exciting laser line (usually 355 or 532 nm emitted with a Nd:YAG laser). A sufficient blocking of the elastic-backscatter signal of about seven orders of magnitude is required. Double-grating monochromators (see section 3.3.1.2) or advanced narrow-band interference filters, which have become available only in recent years, are used for this purpose. The signal detection with narrow bandwidth is of advantage for daytime operation. An additional background suppression is possible with a Fabry–Perot interferometer (see section 3.3.1.2, Arshinov et al. (2005)). Therefore, temperature profiles can be measured throughout the troposphere at day and night. In addition, an appropriate summation of $P_{\mathrm{RR1}}(T,R)$ and $P_{\mathrm{RR2}}(T,R)$ in order to obtain a temperature-independent pure molecular backscatter signal allows an advanced retrieval of the particle extinction coefficient after the method described in section 3.3.1.2.

**3.3.1.5 Water-vapour DIAL.** Water-vapour measurements with high spatial and temporal resolution and high signal-to-noise ratio under daylight conditions are only possible with the differential-absorption-lidar or DIAL technique (Bösenberg, 2005). This technique makes use of single water-vapour absorption lines in the near infrared. By emitting a pair of wavelengths $\lambda_{\mathrm{on}}$ and $\lambda_{\mathrm{off}}$, with the wavelength $\lambda_{\mathrm{on}}$ at the centre of an absorption line and the wavelength $\lambda_{\mathrm{off}}$ away from the line centre, the differential molecular absorption coefficient

$$\Delta\alpha_{\mathrm{mol,abs}} = \alpha_{\mathrm{mol,abs}}(\lambda_{\mathrm{on}}) - \alpha_{\mathrm{mol,abs}}(\lambda_{\mathrm{off}}) \tag{3.37}$$

is determined. If the differential absorption cross section

$$\Delta\sigma_{\mathrm{abs}} = \sigma_{\mathrm{mol,abs}}(\lambda_{\mathrm{on}}) - \sigma_{\mathrm{mol,abs}}(\lambda_{\mathrm{off}}) \tag{3.38}$$

for the two wavelengths is known from spectroscopic measurements, the number concentration $N_{\mathrm{H_2O}}$ of the water-vapour molecules is deduced from the ratio of the detected lidar signals $P_{\mathrm{on}}(R) = P(R,\lambda_{\mathrm{on}})$ and $P_{\mathrm{off}}(R) = P(R,\lambda_{\mathrm{off}})$:

$$N_{\mathrm{H_2O}}(R) = \frac{\Delta\alpha_{\mathrm{mol,abs}}}{\Delta\sigma_{\mathrm{mol,abs}}} = \frac{1}{2\Delta\sigma_{\mathrm{abs}}}\left[\frac{\mathrm{d}}{\mathrm{d}R}\ln\left(\frac{P_{\mathrm{on}}(R)}{P_{\mathrm{off}}(R)}\right)\right]. \tag{3.39}$$

Actually, in case of water-vapour measurements equation (3.39) is only a rough simplification and does not represent more than the basic idea of the DIAL technique. The equation shows that DIAL is a self-calibrating technique, i.e., all instrument constants are removed by forming the signal ratio and taking the

derivative of its logarithm with respect to range. In reality, a variety of corrections to equation (3.39) is necessary and the requirements regarding laser stability and spectral purity are very strict. The reason is that the water-vapour absorption lines are very narrow and their centre positions and shapes vary with pressure and temperature. Therefore, the transmitted laser radiation and the backscattered radiation undergo a different range-dependent effective absorption, which is determined by the spectral distribution of the laser light, the actual shape of the absorption line, and the Doppler broadening of the Rayleigh backscatter component. Even if the absorption lines are appropriately selected and the laser parameters are carefully controlled, systematic measurement errors must be taken into account, e.g., when steep gradients in the aerosol backscatter coefficient occur. Furthermore, it has to be stated that ground-based water-vapour DIAL observations are practically limited to the planetary boundary layer. Because of the decrease of the absolute humidity with height and the strong light attenuation by water-vapour absorption in the lower layers, the online signal becomes extremely weak after a few kilometers. This situation changes if the atmosphere is sensed from top to bottom, i.e., when the DIAL system is operated on an airborne or space-borne platform.

As a consequence of the technical requirements, so far water-vapour DIAL systems have been based exclusively on specially designed laser transmitters which are not commercially available. Alexandrite and Ti:Sapphire lasers as well as optical parametric oscillators have been used as tunable laser sources in the spectral regions with water-vapour absorption lines around 730, 820, and 940 nm, respectively. A variety of ground-based and airborne water-vapour DIAL instruments has been operated in dedicated research campaigns over the past two decades. Only recently, a container-based water-vapour DIAL for continuous and unattended operation has been developed by the Max-Planck Institute for Meteorology, Hamburg, Germany. Long-term operation for almost one year has been demonstrated so far. The system is based on an injection-seeded Ti:sapphire ring laser pumped with a frequency-doubled Nd:YAG laser. It operates in the 820-nm wavelength region where several water-vapour absorption lines of different strength are available. External-cavity laser diodes are used as separate seeders for the online and offline wavelengths. An electro-optical switch changes the wavelength after each shot. A single-mode polarization-maintaining fibre is used to inject the seed laser radiation into the X-shaped ring cavity of the power oscillator which contains only the absolute minimum number of elements, i.e., the Ti:sapphire crystal, cut at the Brewster angle, and four folding mirrors. One of the mirrors is mounted on a piezo drive to adjust the cavity length to the desired wavelength via a digital lock loop, in which a precise wavemeter based on a set of Fizeau interferometers serves as the reference. With this setup an absolute wavelength stability of $<0.0005$ cm$^{-1}$ and a spectral purity of $>99.9\%$ is realized. The system operates with 10 mJ pulse energy at a repetition rate of 50 Hz. The laser beam is expanded tenfold and transmitted vertically into the atmosphere through a

quartz window. Two separate telescopes are used for near-range and far-range measurements. The backscattered radiation sampled with the near-range telescope mirror of 150 mm diameter is directly coupled into a 1-mm fiber. For the far range a Cassegrain telescope with a primary mirror of 400 mm diameter is used. In both receivers interference filters with 1 nm bandwidth suppress the skylight to permit full daytime operation. The detectors are silicon avalanche photodiodes. Online and offline shots are averaged separately with a two-channel 14-bit data acquisition system with a vertical resolution of 15 m.

An eighty-day measurement campaign, including the complete LAUNCH–2005 period, was performed with the DIAL system at the Richard-Aßmann Observatory in Lindenberg. At this site, four ascents of advanced radiosondes per day are available for intercomparison studies. As an example, figure 3.17 shows the water-vapour profiles from the near-range and far-range channels of the DIAL and from the four radiosondes on October 15, 2005. The figure is a standard output from the automated data evaluation. The near-range channel apparently produces reliable results from 100 or 200 m to 1 km above ground, while the far-range channel can be trusted beyond 600 m. Generally, the DIAL results are slightly lower than the radiosoundings, except for the sondes launched at noontime. Presently this systematic effect is not explained, but nothing is known that could affect the lidar results in such a way. While the atmospheric structure is generally retrieved well with both systems, it is apparent that the DIAL resolution at the far end is too low to reveal small-scale structures.

A 24-hour DIAL measurement in Lindenberg on September 8, 2005, is presented in figure 3.18. The figure shows that even for relatively high humidity, i.e., high signal absorption, a range of 1.5 km is reached. The development of the humid boundary layer from about 10 to 14 UT is clearly visible as well as the subsequent dryout. Fog affected the very near range in the morning, but the lidar obviously penetrated the fog layer and yielded reliable results beyond. Again, the lidar water-vapour measurement shows that the humidity structure is very variable, so that two or even four radiosoundings per day do not capture the distribution sufficiently.

**3.3.1.6 Doppler Lidar.** The Doppler lidar technique makes use of the collective motion of molecules and aerosol particles to measure wind velocity and direction in the atmosphere (Werner, 2005). The method considerably differs from the techniques described above. The optical Doppler effect leads to a frequency shift $\Delta f_{\mathrm{D}}$ of the backscattered radiation with respect to the emitted laser radiation with frequency $f_0 = c/\lambda_0$ of:

$$\Delta f_{\mathrm{D}} = \frac{2 f_0 v_{\mathrm{LOS}}}{c}. \tag{3.40}$$

The Doppler shift $\Delta f_{\mathrm{D}}$ for typical atmospheric line-of-sight velocities $v_{\mathrm{LOS}}$ is seven to ten orders of magnitude smaller than the frequency $f_0$ of the emitted

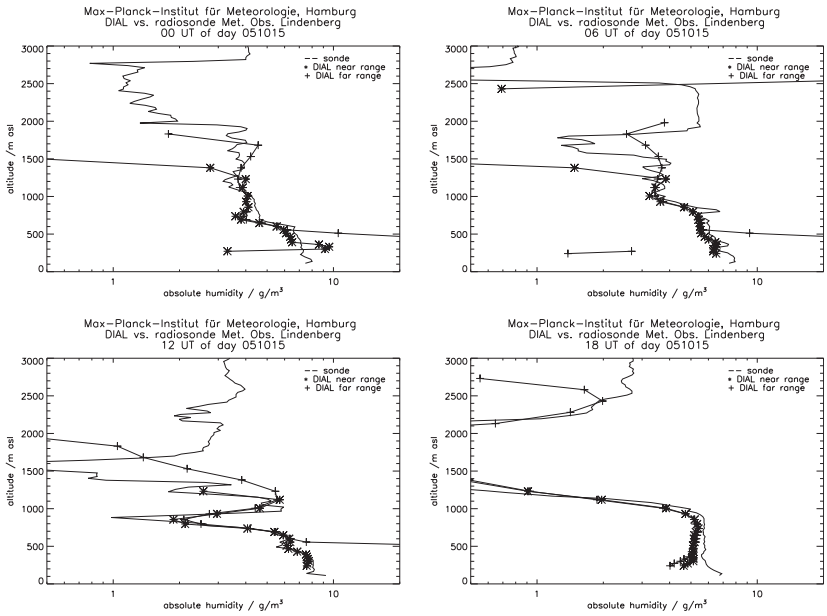


*Figure 3.17.* Comparison of DIAL and radiosonde water-vapour profiles in Lindenberg, Germany, on October 15, 2005.

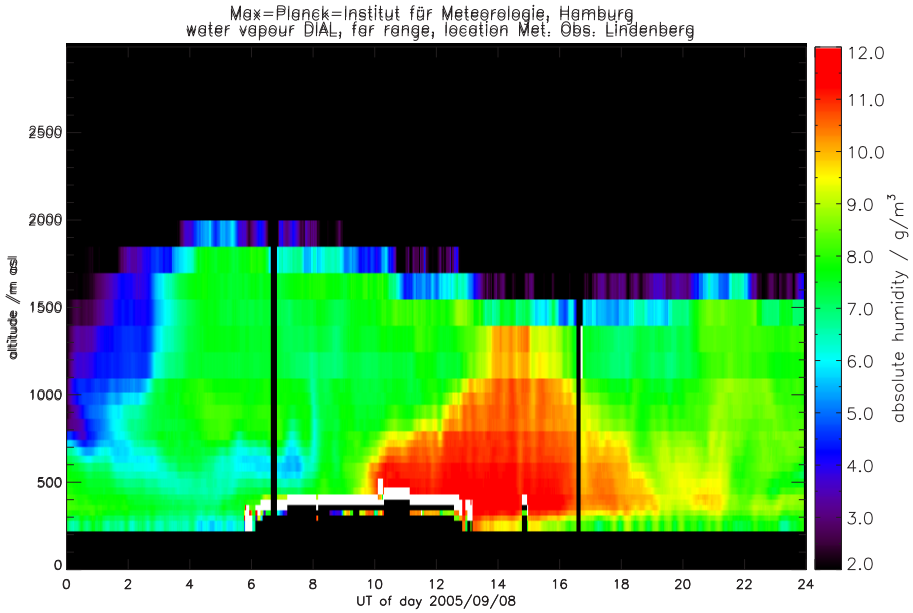


*Figure 3.18.* DIAL water-vapour measurement in Lindenberg, Germany, on September 8, 2005.

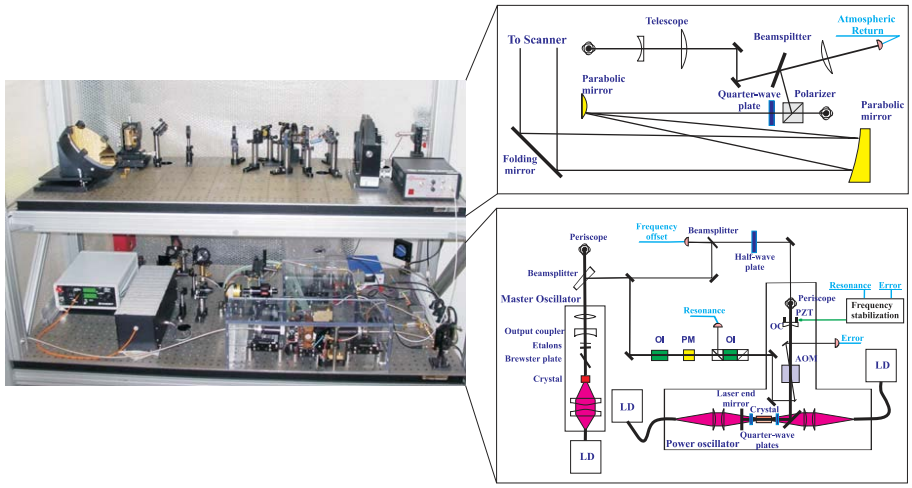


*Figure 3.19.* Setup of the IfT coherent Doppler lidar. Lower level: master-oscillator power-oscillator laser transmitter, upper level: transceiver setup; AOM – acousto-optical modulator, LD – laser diode, OC – output coupler, OI – optical isolator, PM – phase modulator, PZT - piezo translator.

laser radiation. Therefore, its measurement requires specific technical efforts regarding laser frequency stabilization and signal detection. To measure horizontal and vertical wind speeds in the lower atmosphere, the coherent Doppler lidar technique is applied. Here, the Doppler shift is determined by optical heterodyning the frequency of a local oscillator, which serves as a seed laser for the pulsed power laser of the lidar, and the radiation backscattered from atmospheric aerosol or cloud particles. With modern solid-state laser technology in the 1 to 2 $\mu$m wavelength region a compact and user-friendly lidar design can be realized. A variety of research and commercial instruments is available. The systems are usually equipped with a scanning unit. Appropriate scanning of the laser beam permits the reconstruction of the three-dimensional wind vector from the line-of-sight velocities measured with the lidar under certain zenith and azimuth angles.

Lidar wind measurements can be performed with a temporal resolution of 1–10 s, a spatial resolution of 50–100 m, and an accuracy of a few cm/s independent of daylight background. In contrast to radar measurements, the information comes from the well-defined volume illuminated by the laser radiation. Therefore, lidar wind measurements are especially useful to study processes over complex terrain, to measure fluxes in the planetary boundary layer, to obtain three-dimensional wind fields in the vicinity of buildings or other obstacles, or to monitor aircraft wake vortices.

Figure 3.19 shows the IfT Doppler wind lidar *WiLi*. A master-oscillator power-oscillator setup is realized (see figure 3.19, lower level). The master oscillator is a continuous-wave Tm:LuAG laser which produces single-mode,

single-frequency laser radiation at 2.022 $\mu$m. In the L-shaped power oscillator the Tm:LuAG crystal is pumped from both sides with fiber-coupled laser diodes. Q-switched pulse operation is realized with a 80-MHz acousto-optical modulator, which is also used for injection seeding and frequency-offset generation. The frequency offset is needed for heterodyning in order to determine not only the wind speed but also its direction (towards or apart from the lidar). Pulses are generated with an energy of about 2 mJ, a length of 450 $\mu$s, and a repetition rate of 750 Hz. The frequency stability is of the order of 1 MHz. In the transceiving optics (see figure 3.19, upper level) a Glan-Taylor polarizer and a quarter-wave plate are inserted to use the off-axis Mersenne telescope for expanding and transmitting the laser beam as well as for receiving of atmospheric backscattered radiation. The received signal is directed onto an InGaAs detector and optically heterodyned with the reference radiation from the master oscillator. Data acquisition is performed with an 8-bit digitizer PC card with a sampling rate of 250 MS/s. The signal is divided into approximately 200 bins of 1 $\mu$s length each. By applying a window function and half overlapping height intervals a spatial resolution of 75 m is achieved. The signals are transformed to the frequency domain, the resulting power spectra are shifted to correct for the offset frequency and are finally averaged for a fixed time interval. It was found that 3 seconds temporal averaging is sufficient to obtain well analyzable spectra. Afterwards, spectral peak finding and hence wind speed determination is performed by a center-of-mass approach.

Figure 3.20 shows the comparison of profiles of horizontal wind velocity and direction determined with the IfT Doppler lidar and the DWD wind profiler in Ziegendorf, Germany. The measurements were made on September 22, 2005, during the LAUNCH–2005 campaign, when both the IfT multiwavelength Raman lidar and the IfT Doppler wind lidar were located next to the DWD wind profiler. Horizontal wind speed and direction were obtained with the lidar by performing conical scans at $65^{\mathrm{o}}$ zenith angle and by fitting a sine wave as a function of azimuth angle to the line-of-sight wind data. The data were averaged over 26 minutes corresponding to the operational mode of the wind profiler. The vertical resolution of the scanning wind lidar was 30 m, whereas the wind profiler uses 250 m height resolution in its low-mode operation. Excellent agreement of the lidar and the profiler wind data in the upper boundary layer was found. In the time period from 22:30 to 22:56 lt the development of a nocturnal low-level jet is noteworthy. This feature occurred below the vertical measurement range of the wind profiler and was only detected with the lidar.

The development of the planetary boundary layer in terms of the particle backscatter coefficient at 532 nm (measured with the IfT multiwavelength Raman lidar) and the vertical wind speed (measured with the IfT Doppler lidar) in Ziegendorf on September 22, 2005, is presented in figure 3.21. The upward motion of particle-rich air from the ground indicates a growth of the boundary layer from 600 m height at 12:00 lt to about 1300 m around 15:00

lt. The increase of the backscatter coefficient with altitude (see mean profile in figure 3.21) is caused by the hygroscopic growth of particles with increasing humidity. The high-resolved aerosol and vertical-wind measurements can be used, e.g., to calculate vertical particle fluxes in the convective boundary layer.

## 3.3.2 NEW AND IMPROVED METHODS

**3.3.2.1 Automated Lidar Data Analyzer (*ALDA*).** For the operational Raman lidar *RAMSES* of the German Meteorological Service (see section 3.3.1.3) the automated lidar data evaluation software *ALDA* (Automated Lidar Data Analyzer) has been developed at the Leibniz Institute for Tropospheric Research in Leipzig, Germany. *ALDA* is the first lidar software which automatically analyzes lidar signals, performs quality control, and provides the derived product files online for operational weather forecast. The products are the water-vapour mixing ratio, the relative humidity, the backscatter ratio (ratio of elastic backscattering to molecular backscattering), the particle backscatter and extinction coefficients, and the particle lidar ratio (see section 3.3.1.2 and 3.3.1.3).

For routine data analysis, *ALDA* provides three modes of operation. The *online mode* is designed for the automatic analysis of lidar signals during a running or already finished measurement and for the visualization of the current products. All relevant data and information (raw signals, used parameters, protocol entries, and product files) are stored into a zip archive when the analysis of a measurement is finished. The *view mode* allows visualization of already existing lidar products in terms of profiles or time-series plots. The user can optimize, e.g., axis scaling, line style, fonts, or title of a plot interactively. All plots are connected to hierarchical lists which display header information and input parameters of each single profile. The *archive mode* is designed to manage the backup process of analyzed and archived measurements. In addition, a *science mode* is in preparation which shall be used for interactive re-analysis of measurements with, e.g., individual quality control of raw signals and products.

For each integration time interval (typically 30 s) the six signals measured with *RAMSES* (far-range and near-range elastic backscatter signal at 355 nm, nitrogen Raman signal at 387 nm, water-vapour Raman signal at 407 nm, see section 3.3.1.3) and header information of the actual measurement are stored in the netCDF file format. These netCDF raw signal files are analyzed with *ALDA*. The steps of data analysis are as follows:

(1) read raw signals,

(2) control quality of the raw signals,

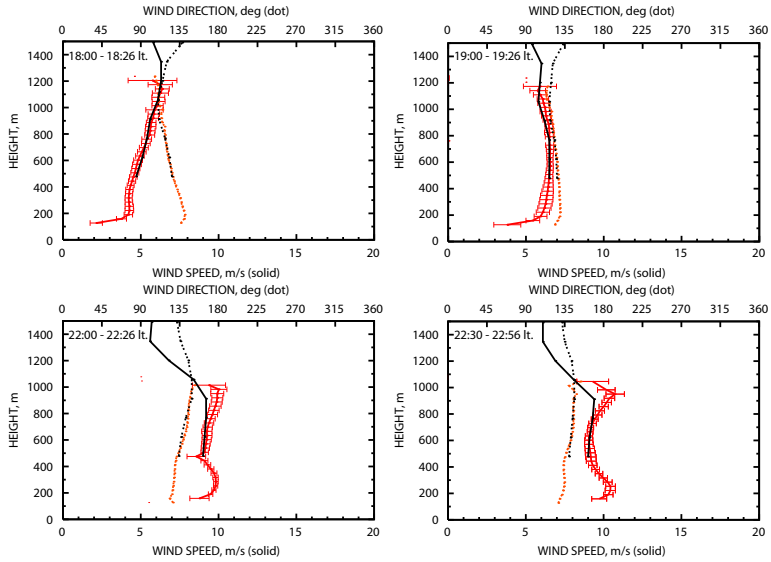


*Figure 3.20.* Comparison of wind profiler (black) and Doppler lidar data (red and orange) of horizontal wind speed (solid) and wind direction (dotted) measured in Ziegendorf, Germany, on September 22, 2005.

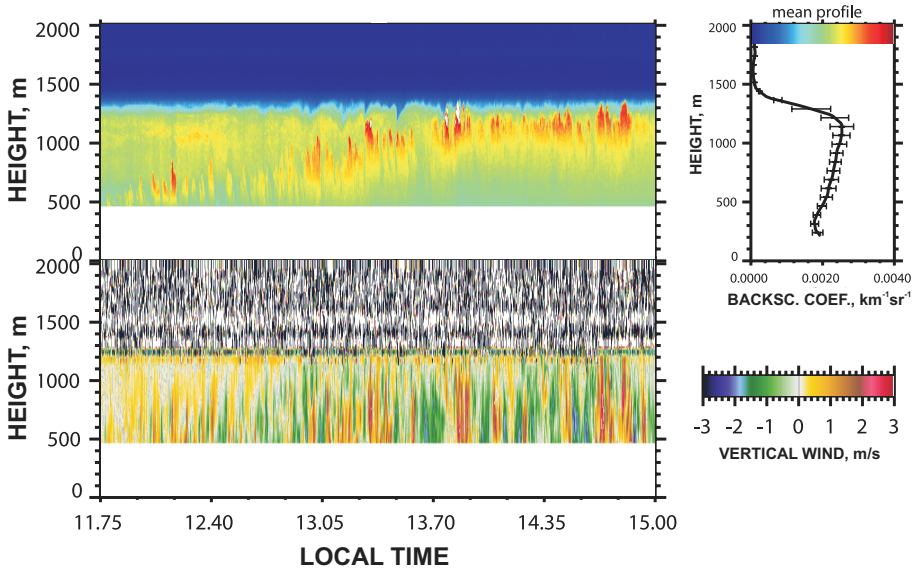


*Figure 3.21.* Particle backscatter coefficient at 532 nm and vertical wind speed measured with the IfT multiwavelength lidar and the IfT Doppler wind lidar, respectively, at Ziegendorf, Germany, on September 22, 2005.

(3) correct the raw signals for range, background, and dead time,

(4) look for a new radiosonde,

(5) average raw signals in time,

(6) correct atmospheric transmission,

(7) smooth profiles spatially,

(8) calculate products from near-range signals and far-range signals independently,

(9) merge the near-range and far-range products,

(10) perform final quality control,

(11) provide final products in netCDF file format,

(12) create a zip archive containing all relevant data and information.

Steps 1 to 11 are repeated until a running measurement is finished or until all raw signals of an already finished measurement are processed.

Automated calibration procedures for water-vapour and particle backscatter profiles have been developed. To determine the water-vapour mixing ratio, individual calibration factors for both telescope ranges can be derived during the measurement from comparisons to mixing-ratio profiles from the on-site operational radio soundings (00, 06, 12, 18 UT). *ALDA* actively checks whether a new sonde is available in the internal Oracle database of the DWD. Then the calibration is performed with those lidar signals which were detected exactly when the sonde flew through the user-defined calibration height range as illustrated in figure 3.22 (left). Only data points that fulfil certain quality criteria (user-defined thresholds) are used in the calibration procedure. The individual calibration factors for both telescope ranges are converted into general calibration constants under consideration of the transmission values of neutral-density filters used in the water-vapour and nitrogen channels during the actual measurement. After a final quality check the general calibration constants are stored in an internal database. If there is no radiosonde profile available during the lidar observation the calibration factors are calculated from the stored calibration constants as illustrated in figure 3.22 (right).

In order to obtain a profile from ground up to the tropopause, the product profiles derived from the near-range and from the far-range signals are merged. The user can define a merging range and select one out of three criterions to find the best contact point of the two sub profiles within the merging range:
1) use the point of smallest difference between the sub profiles,
2) use the sub profile with the lowest uncertainty,
3) use the sub profile with the best height resolution.

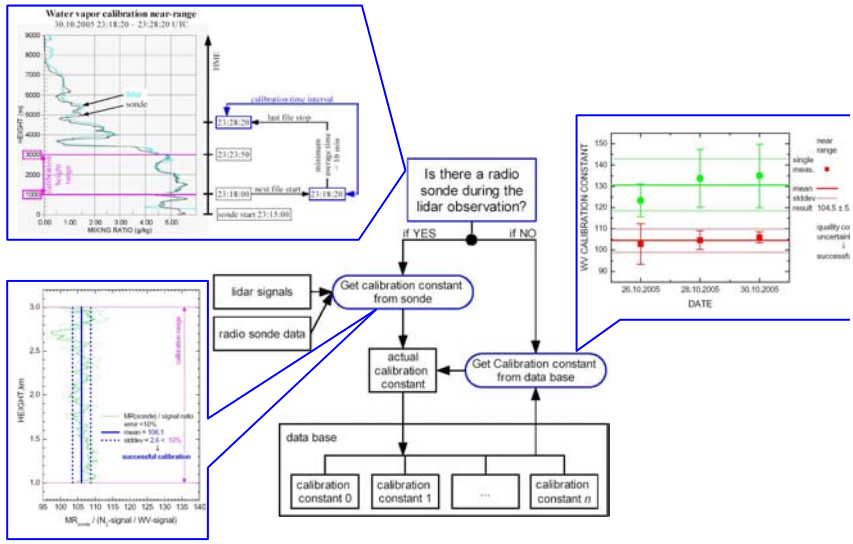


*Figure 3.22.* Illustration of the *ALDA* water-vapour calibration procedure. The *RAMSES* near-range measurement on September 30, 2005, 23:18:20–23:28:20 UT, and the Lindenberg radiosonde launched at 23:15 UT are used as an example. Calibration is successfully performed for the height range between 1000 and 3000 m (left). Calibration constants from previous days stored in the database can be used alternatively (right).

*ALDA* is based on modern, robust, and reliable software development standards. It is built on top an object-oriented multi-threading framework which handles memory management, prevents memory leaks, and provides real-time capability of dataflow, database persistence of configuration data, and easy object-oriented access to the netCDF data file standard. *ALDA* makes extensively use of the power of relational databases.

#### 3.3.2.2 Accurate retrieval of extinction profiles at water-cloud base.

Within the COST–720 experts group on cloud measurements a new retrieval scheme to derive accurate extinction profiles at the base of water clouds from lidar measurements has been developed. Accurate extinction profiles are needed in integrated lidar–radar algorithms for the estimation of microphysical liquid-water cloud properties (see section 4.1). Former schemes applied the Klett method (see section 3.3.1.1) to standard ceilometer output profiles. However, this method did not deliver trustworthy extinction data. It especially suffers from the low power of the instrument and the low dynamic range of the data acquisition which result in a low cloud penetration depth. As shown below, the Klett algorithm requires a certain number of data points within the cloud in order to become independent on the reference value. The new algorithm uses data from a high-power Raman lidar (here *RAMSES*) and combines the Klett and the Raman algorithms (see section 3.3.1.1 and 3.3.1.2) to retrieve

extinction profiles at the cloud base and to account for the multiple-scattering effect.

Figure 3.23 shows the near-range elastic-backscatter signal measured with the 355-nm photon-counting channel of *RAMSES* during the night of September 20–21, 2005. A stratocumulus cloud appeared at the top of the residual layer at 22:40 UT and covered the sky until the end of the measurement in the morning of September 21, 2005. The residual layer is indicated by the green color in the left panel of figure 3.23. The right panel of figure 3.23 shows the signal dynamics for two 10-min periods, one with pure aerosol conditions and one with the cloud. To cover the signal increase at the cloud base as well as the strong attenuation for larger penetration depths a dynamic signal range of approximately five orders of magnitude is necessary. This corresponds to a $\geq$14-bit analog-to-digital conversion rate which is not available, e.g., in state-of-the-art ceilometers.

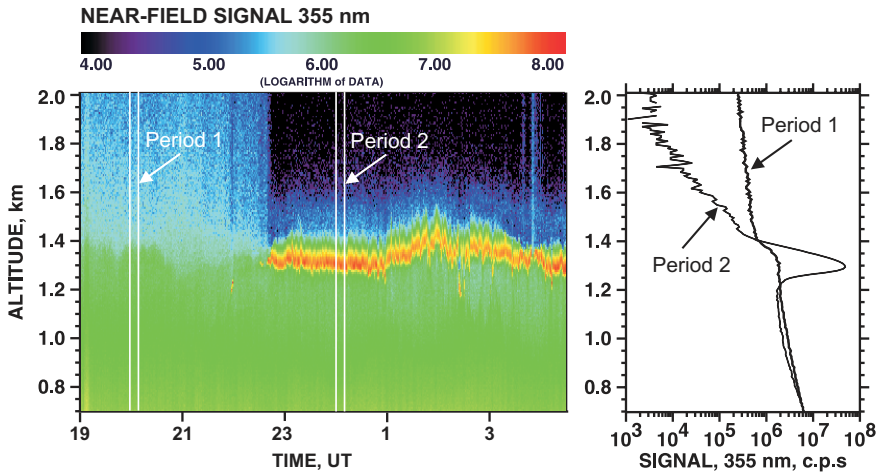


*Figure 3.23.* Near-range elastic-backscatter signal measured with *RAMSES* on September 20–21, 2005. The resolution is 30 s in time and 7.5 m in height. A stratocumulus cloud covered the sky from 22:40 UT until the end of the measurement at 4:30 UT. The right panel shows the signal dynamics for two 10-min periods with and without cloud, respectively.

For the evaluation of the lidar signals with respect to cloud extinction the following items have to be taken into account:

- The cloud extinction coefficient is calculated either from the elastic-backscatter signal after the *Klett method* with equation (3.23)–(3.26) or from the nitrogen Raman signal after the *Raman method* with equation (3.31).
- The *Klett method* requires a reference value and a lidar-ratio profile as input parameters. If a sufficient cloud penetration depth is reached, the reference value set to the far end of the profile does not influence the profiles derived near the cloud base (see below). In contrast, the lidar ratio

is a critical input parameter, because it is used to correct the transmission effect which is large in the case of clouds. For the *Raman method* no critical input parameters are needed. (The Ångstrøm exponent is set to 0.)

- With the *Klett method* the cloud profiles can be calculated with high spatial and temporal resolution (10–30 s, 5–30 m). The *Raman method* requires averaging over 5–10 min in time and 30–100 m in space.

- Lidar signals in clouds are generally influenced by multiple scattering. Multiple scattering leads to an effective decrease of extinction, because a large amount of the multiply scattered light remains in the lidar's receiver field of view (see section 3.3.1.1). Therefore, the *Raman method* and the *Klett method* deliver apparent instead of single-scattering extinction coefficients. However, the multiple-scattering influence on the retrieved extinction profiles is different for the two methods (see below).

- The single-scattering lidar ratio for water clouds is nearly constant for typical droplet size distributions and laser wavelengths in the ultraviolet to visible wavelength region. For 355 nm, a value of $18.9 \pm 0.4$ sr is valid for median droplet diameters between 3 and 17 $\mu$m (O'Connor et al., 2004).

- In the case of the *Klett method* multiple scattering influences the retrieval via the transmission correction and thus via the lidar-ratio input. Using the apparent instead of the single-scattering lidar ratio as the input -provided it is known- one obtains the correct (i.e., single-scattering) backscatter coefficient. Then, the single-scattering extinction coefficient is simply calculated by multiplying the backscatter coefficient with the constant single-scattering lidar ratio of 18.9 sr.

- The apparent extinction coefficient determined with the *Raman method* deviates by 10%–50% from the single-scattering value, because it is directly derived from the (apparent) transmission of the laser light (Wandinger, 1998). The actual deviation depends on the lidar geometry (field of view), the cloud height, and the droplet size.

- The *Raman method* delivers the cloud backscatter coefficient in addition to the cloud extinction coefficient. Because this parameter is calculated from a signal ratio (see equation (3.32)), it is practically not influenced by multiple scattering (Wandinger, 1998). Therefore, the lidar ratio calculated from the extinction and backscatter coefficients after equation (3.33) represents the apparent value due to the multiple-scattering influence on the extinction coefficient.

- The calculation of the backscatter coefficient after the Raman method requires the calibration of the profile (see equation (3.32)). Because wa-

ter clouds usually are not penetrated by the laser beam, a calibration of the profiles in the free troposphere or lower stratosphere, where particle scattering can be neglected, is not possible. Therefore, the profiles must be calibrated below the cloud where the aerosol content is typically high. The calibration is only possible with an assumption on the aerosol lidar ratio below the cloud. This lidar ratio can either be determined in cloud-free periods of the measurement after the Raman method or taken from a database of typical aerosol lidar ratios.

With all these facts in mind, a combined Raman–Klett algorithm can be constructed to retrieve accurate extinction coefficients at the base of water clouds with high temporal and spatial resolution. The scheme is based on the determination of the apparent lidar-ratio profile—and thus of the actual multiple-scattering influence—with low resolution by the use of the *Raman method*. This apparent lidar ratio is applied in the *Klett method* to derive single-scattering backscatter coefficients with high resolution. The single-scattering extinction coefficients are obtained by multiplying the backscatter coefficients with the constant single-scattering lidar ratio of water clouds. In detail, the following steps have to be performed:

(1) Determine the aerosol lidar ratio below the cloud base by either

- applying the Raman method (see equation (3.31)–(3.33), section 3.3.1.2) to cloud-free measurement periods or
- taking a typical value from a database.

(2) Calculate the apparent extinction-coefficient profile(s) with the Raman method after equation (3.31) with adequate temporal and spatial resolution (so that the statistical error is $\leq$10%–20%).

(3) Compute the corresponding backscatter profile(s) after equation (3.32) with the same temporal and spatial resolution. Perform the calibration below the cloud base, so that the mean extinction coefficient divided by the mean backscatter coefficient gives the lidar-ratio value determined in Step 1.

(4) Calculate the apparent cloud lidar-ratio profile(s) after equation (3.33) with the data from Steps 2 and 3.

(5) Determine a mean apparent cloud lidar ratio for the time and height interval of interest (within the cloud).

(6) Apply the Klett method to the high-resolution lidar data and calculate cloud backscatter-coefficient profiles by setting an arbitrary reference value at the far end of the signal profiles and using the mean apparent cloud lidar ratio from Step 5 in the integrals of equation (3.23).

(7) Multiply the cloud backscatter-coefficient profiles from Step 6 with the single-scattering lidar ratio of 18.9 sr (for 355 nm) to obtain the single-scattering extinction-coefficient profiles of the cloud.

(8) A cross check can be performed by comparing the cloud backscatter-coefficient profiles determined with the Raman method and the Klett method for the same time and height averaging intervals.

The cloud measurement on September 20–21, 2005 (see figure 3.23) is used in the following to illustrate the algorithm described above. The aerosol lidar ratio below the cloud was determined in the period from 19:15 to 21:50 UT before the first clouds appeared. A mean value of 53 sr was found in the height region from 800 to 1100 m (Step 1). The time period with the stratocumulus cloud from 22:40 to 4:30 UT was divided into 35 intervals of 10 min length each. Profiles of the backscatter coefficient, the extinction coefficient, and the lidar ratio were determined for the 10-min intervals with a height resolution of 82.5 m with the Raman method (Steps 2–4). The backscatter coefficients were calibrated so that integral values of the corresponding extinction coefficient divided by the integral value of the backscatter coefficient, both between 800 and 1100 m, give the lidar ratio of 53 sr found in Step 1. In order to obtain a mean apparent lidar ratio for the entire cloud measurement period (Step 5), the profiles were normalized to the cloud base height. The cloud base height was arbitrarily chosen as the height at which the backscatter coefficient becomes larger than 0.1 $km^{-1}sr^{-1}$. The profiles normalized in this way are presented in figure 3.24. The thick black lines show the mean backscatter coefficient,

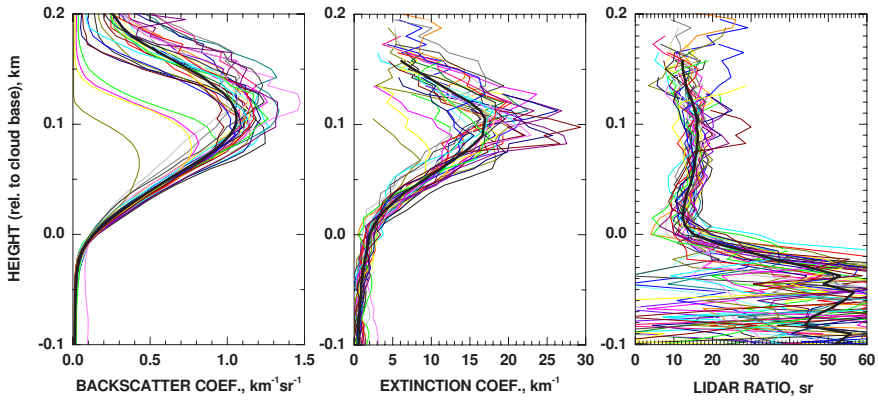


*Figure 3.24.* Profiles of backscatter coefficients, extinction coefficients, and lidar ratios determined after the Raman method and normalized to the cloud base for 10-min intervals (colored lines) from 22:40 to 4:30 UT on September 20–21, 2005. The vertical resolution is 82.5 m. The thick black lines indicate the mean of all 35 profiles.

the mean apparent extinction coefficient, and the mean apparent lidar ratio as a function of penetration depth. As expected, the lidar ratio drops from

typical aerosol values around 50 sr to values smaller than the single-scattering water-cloud lidar ratio of 18.9 sr, indicating the multiple-scattering effect. A penetration depth of >200 m is reached for the backscatter coefficient. The extinction coefficient can, on average, be determined up to 150 m penetration depth or up to a one-way apparent optical depth of 1.4. The mean apparent lidar ratio for that height region is 14.3±1.4 sr. A slight dependence on penetration depth is found, but the values vary between 12.3 and 16.3 sr only. Thus the mean value of 14.3 sr can be used in the Klett method without introducing a large error.

Figure 3.25 shows the extinction coefficients determined with a resolution of 7.5 m and 30 s. First, the Klett method was applied to calculate the backscatter-

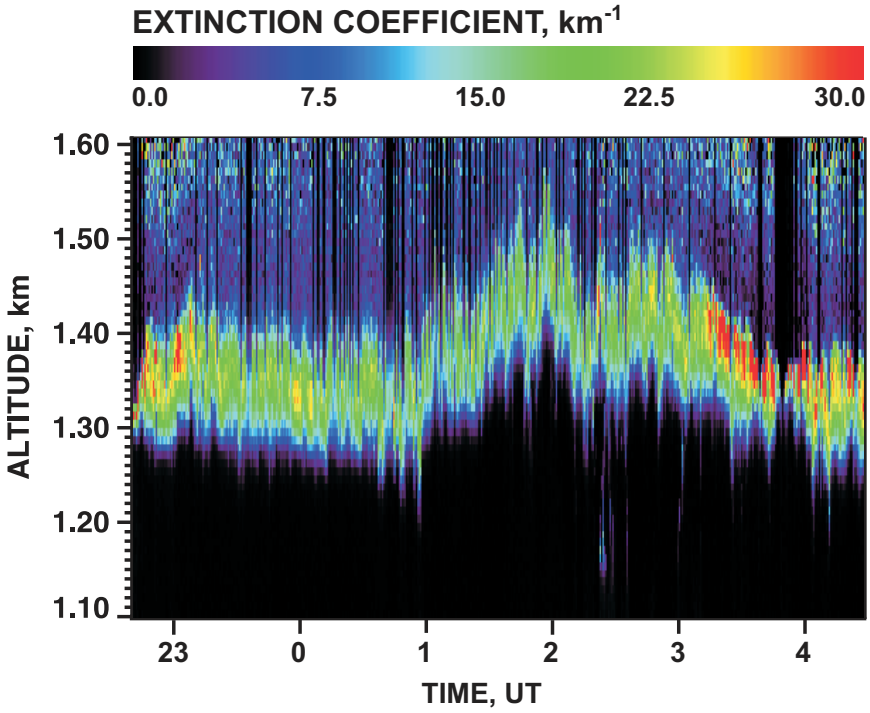


*Figure 3.25.* Cloud extinction coefficients determined with the Klett method from 22:40 to 4:30 UT on September 20–21, 2005. The vertical resolution is 7.5 m, the temporal resolution is 30 s. The reference value was set to 0 $km^{-1}sr^{-1}$ at 1.8 km height. An apparent lidar ratio of 14.3 sr was used in the retrieval of the backscatter coefficient. The backscatter coefficients were converted to extinction coefficients with a lidar ratio of 18.9 sr.

coefficient profiles (Step 6). A reference value of 0 $km^{-1}sr^{-1}$ at 1.8 km height and an apparent lidar ratio of 14.3 sr were used as the input data. Then, the backscatter coefficients were multiplied with the single-scattering lidar ratio of 18.9 sr to obtain the extinction profiles (Step 7). The color scale is chosen such that trustworthy data are given by green to red colors. The bluish colors

above indicate the region of noisy solutions which is strongly influenced by the choice of the reference value.

Figure 3.26 (left panel) shows the variation of the profiles in dependence on the reference value, set at a height of 1.8 km, in the upper part of the cloud for the 10-min time interval from 23:20–23:30 UT. The solutions converge

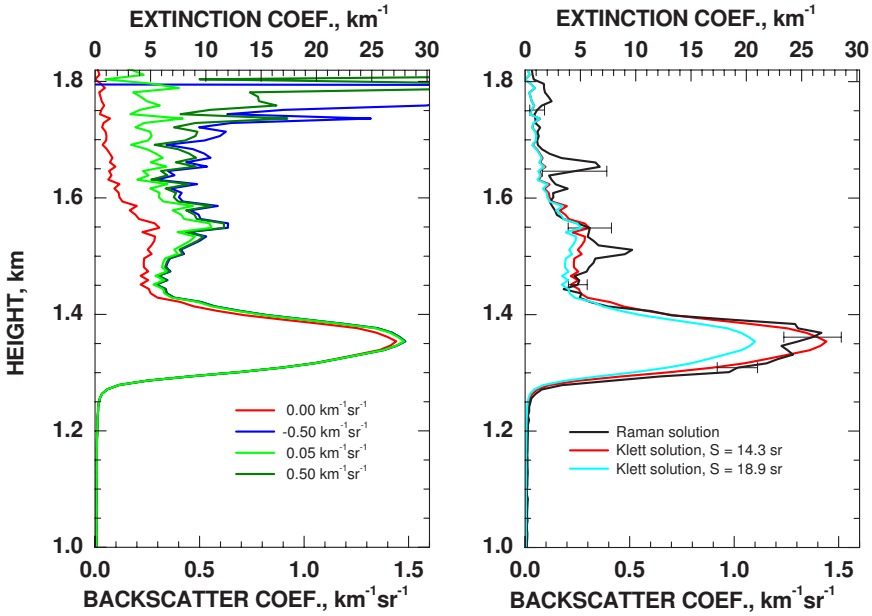


*Figure 3.26.* Backscatter-coefficient profiles for the time interval from 23:20–23:30 UT. Left: influence of the reference value (set at 1.8 km height) on the solution. Right: comparison of Klett and Raman solutions. The Raman profile was smoothed with a gliding average of 37.5 m above 1.30 km and of 82.5 m above 1.45 km. The error bars represent the corresponding statistical uncertainty. The upper axes show the extinction coefficient obtained from the backscatter coefficient by assuming a single-scattering lidar ratio of 18.9 sr.

and become almost independent of the reference value in the lower part of the cloud, i.e., a certain transmission is necessary until the influence of the reference value becomes negligible in the integration of equation (3.23). That is the reason that the Klett method fails when it is applied to data with low signal dynamics, e.g., 8-bit ceilometer data.

The right panel of figure 3.26 presents a comparison of the Klett and the Raman solutions for the same 10-min time interval (Step 8). The Klett solution obtained with a reference value of 0 $km^{-1}sr^{-1}$ and an apparent lidar ratio of 14.3 sr agrees very well with the Raman profile. The error bars show the statistical uncertainty of the Raman solution, which was slightly smoothed for larger penetration depths (see figure caption). If the Klett retrieval is performed without taking multiple scattering into account, i.e., with the single-scattering lidar ratio of 18.9 sr, the extinction coefficients are underestimated by 20%-30% in

the lower part of the cloud in the specific case presented here (see figure 3.26, right panel). In conclusion, it can be stated that the combined Raman–Klett retrieval delivers trustworthy extinction profiles at the base of water clouds which are believed to be accurate within 10% and which can be used in integrated lidar–radar algorithms for the determination of microphysical cloud properties.

## Bibliography

Ansmann, A., and D. Müller, 2005: Lidar and atmospheric aerosol particles. *In:* C. Weitkamp (ed), *Lidar – Range-Resolved Optical Remote Sensing of the Atmosphere*, 105–141, Springer, New York.

Ansmann A., M. Riebesell, and C. Weitkamp, 1990: Measurements of atmospheric aerosol extinction profiles with a Raman lidar. *Optics Letters*, **15**, 746–748.

Ansmann A., U. Wandinger, M. Riebesell, C. Weitkamp, and W. Michaelis, 1992: Independent measurement of extinction and backscatter profiles in cirrus clouds by using a combined Raman elastic–backscatter lidar. *Appl. Optics*, **31**, 7113–7131.

Arshinov, Y.F., S. M. Bobrovnikov, I. B. Serikov, A. Ansmann, U. Wandinger, D. Althausen, I. Mattis, and D. Müller, 2005: Daytime operation of a pure rotational Raman lidar by use of a Fabry–Perot interferometer. *Appl. Optics*, **44**, 3593–3603.

Behrendt, A., 2005: Temperature measurements with lidar. *In:* C. Weitkamp (ed), *Lidar – Range-Resolved Optical Remote Sensing of the Atmosphere*, 273–305, Springer, New York.

Bissonnette, L., 2005: Lidar and multiple scattering. *In:* C. Weitkamp (ed), *Lidar – Range-Resolved Optical Remote Sensing of the Atmosphere*, 43–103, Springer, New York.

Bösenberg, J., 2005: Differential-absorption lidar for water vapor and temperature profiling. *In:* C. Weitkamp (ed), *Lidar – Range-Resolved Optical Remote Sensing of the Atmosphere*, 213–239, Springer, New York.

Bösenberg, J. et al., 2002: EARLINET: Establishing the European Aerosol Research Lidar Network. *In:* L. Bissonnette, G. Roy, and G. Vallée (eds), *Lidar Remote Sensing in Atmospheric and Earth Sciences*, 535–539, Defence R&D Canada – Valcartier.

Campbell, J.R., D. L. Hlavka, E. J. Welton, C. J. Flynn, D. D. Turner, J. D. Spinhirne, V. S. Scott III, and I. H. Hwang, 2002: Full-time, eye-safe cloud and aerosol lidar observation at Atmospheric Radiation Measurement Program sites: instruments and data processing. *J. Atmosph. Ocean. Technol.*, **19**, 431–442.

Eloranta, E., 2005: High spectral resolution lidar. *In:* C. Weitkamp (ed), *Lidar – Range-Resolved Optical Remote Sensing of the Atmosphere*, 143–163, Springer, New York.

Engelmann, R., P. Rhone, and D. Althausen, 2003: The mini Raman lidar Polly – setup and experiments. *In:* U. Wandinger, R. Engelmann, and K. Schmieder (eds), *Sixth International Symposium on Tropospheric Profiling: Needs and Technologies*, 240–242, Leipzig, Germany.

Goldsmith, J. E. M., F. H. Blair, S. E. Bisson, and D. D. Turner, 1998: Turn-key Raman lidar for profiling atmospheric water vapor, clouds, and aerosols. *Appl. Optics*, **37**, 4979–4990.

Klett, J. D., 1981: Stable analytical solution for processing lidar returns. *Applied Optics*, **20**, 211–220.

Kovalev, V.A., and W. E. Eichinger, 2004: *Elastic Lidar*. John Wiley & Sons.

McCormick, M. P., 2005: Airborne and spaceborne lidar. *In:* C. Weitkamp (ed), *Lidar – Range-Resolved Optical Remote Sensing of the Atmosphere*, 355–397, Springer, New York.

Murayama, T., et al., 2001: Ground-based network observations of Asian dust events of April 1998 in east Asia. *J. Geophys. Res.*, **106**, 18345–18359.

O'Connor, E. J., A. J. Illingworth, and R. J. Hogan, 2004: A technique for autocalibration of cloud lidar. *J. Atmosph. Ocean. Technol.*, 21, 777–786.

Sasano Y., E. V. Browell, and S. Ismail, 1985: Error caused by using a constant extinction/backscatter ratio in the lidar solution. *Applied Optics*, **24**, 3929–3932.

Sassen, K., 2005: Polarization in lidar. *In:* C. Weitkamp (ed), *Lidar – Range-Resolved Optical Remote Sensing of the Atmosphere*, 19–42, Springer, New York.

Wandinger, U., 1998: Multiple-scattering influence on extinction- and backscatter-coefficient measurements with Raman and high-spectral-resolution lidars. *Applied Optics*, **37**, 417–427.

Wandinger, U., 2005: Introduction to lidar. *In:* C. Weitkamp (ed), *Lidar – Range-Resolved Optical Remote Sensing of the Atmosphere*, 1–18, Springer, New York.

Wandinger, U., 2005: Raman lidar. *In:* C. Weitkamp (ed), *Lidar – Range-Resolved Optical Remote Sensing of the Atmosphere*, 241–271, Springer, New York.

Weitkamp, C. (ed), 2005: *Lidar – Range-Resolved Optical Remote Sensing of the Atmosphere*. Springer, New York.

Werner, C., J. Streicher, I. Leike, and C. Münkel, 2005: Visibility and cloud lidar. *In:* C. Weitkamp (ed), *Lidar – Range-Resolved Optical Remote Sensing of the Atmosphere*, 165–186, Springer, New York.

Werner, C., 2005: Doppler wind lidar. *In:* C. Weitkamp (ed), *Lidar – Range-Resolved Optical Remote Sensing of the Atmosphere*, 325–443, Springer, New York.

# 3.4 FOURIER TRANSFORM INFRARED RADIOMETER

Jens Reichardt and Jürgen Güldner
*German Meteorol. Service (DWD), Richard-Aßmann Observatory, Lindenberg, Germany*
✉ Jens.Reichardt@dwd.de

## 3.4.1 FOURIER TRANSFORM INFRARED SPECTROSCOPY

Over the years, Fourier Transform Spectroscopy (FTS) has become the method of choice in the near- to far-infrared spectral region, and thus for studies of thermal radiation in the atmospheric sciences. In FTS, the spectrum of interest is determined by measuring its interferogram with a (Michelson) interferometer and subsequently applying the Fourier transformation to the interferogram. This approach to spectral measurements, although seemingly more complicated than direct measurements with dispersive instruments, offers a number of advantages over the latter (Bell, 1972). First, the multiplex advantage. In FTS all frequencies of a spectrum are measured at the same time and not sequentially. Second, Fourier spectrometers have a higher throughput because apertures with larger cross-sectional area can be used. Third, FTS permits much faster measurements and, fourth, the resolving power is higher. A further advantage is the highly precise wavenumber calibration which is easily obtained from the interference pattern of the monochromatic light of a built-in He-Ne laser. Moreover, the high spectral resolution and the large number of observed emission lines of many atmospheric constituents render retrievals possible that are either better vertically resolved (e.g., temperature, water vapor), or yield a larger number of measurement products (e.g., concentrations of several trace gases), than those obtained with infrared radiometers with a limited number of discrete detection channels.

FTS is widely used in the atmospheric and planetary sciences, and Fourier Transform Infrared (FTIR) spectrometers have been deployed on all kinds of platforms. FTIR instruments are on board spacecrafts to explore the atmospheres of other planets (Moroz et al., 1986), are orbiting the Earth on satellites (Milz et al., 2005), are payloads of scientific balloons (Friedl-Vallon et al., 2004), are installed on aircraft (Revercomb et al., 2005), ship, and, of course, ground. Scientific studies using FTIR data encompass evaluation of line-by-line radiative transfer codes (Tobin et al., 1999), atmospheric profiling (Spänkuch et al., 1996; Feltz et al., 2003), measurements of tropospheric and stratospheric trace gases (von Clarmann et al., 1993; Spänkuch et al., 1998), and characterization of aerosols and clouds (Spänkuch et al., 2000; Rathke et al., 2002; Turner et al., 2003; Huang et al., 2004).

This contribution to the COST 720 final report summarizes the FTIR investigations of the German Meteorological Service (DWD), namely work done with the FTIR spectrometer EISAR (Emission Infrared Spectrometer for Atmospheric Research). It would be well beyond its scope to present a general overview of all FTS instrumental aspects, or current retrieval methods. First, a brief description of the EISAR instrument is given. Then the retrieval technique used for boundary-layer temperature and humidity profiling is shortly described, and measurement examples are discussed. Finally, an outlook on future work is given.

### 3.4.2 EISAR

FTS of the atmosphere started in 1994 when EISAR was installed at the Meteorological Observatory in Potsdam, Germany. The early work benefited from decade-long experience with spacecraft-based FTIR instrumentation (Kempe et al., 1980; Moroz et al., 1986; Spänkuch et al., 1987). At that time, measurements were taken during campaigns only. In 2003, EISAR was relocated to the Meteorological Observatory Lindenberg southeast of Berlin, Germany, and an upgrade of the instrument to fully autonomous operation was initiated. This transition has been accomplished recently, and EISAR is now ready to perform its main task, the monitoring of the thermal and moisture structure of the planetary boundary layer.

EISAR consists of a measurement unit which is installed atop a building with free hemispherical view, and data acquisition, control and support hardware in a laboratory below the platform. The core instrument of the measurement unit is a Bruker IFS-55 spectrometer with modifications concerning the internal arrangement of the optical components and the use of a cooled sandwich detector (Bruker, 1996). Considering the limiting noise equivalent radiation, this detector offers an effective spectral range from 600 to 3000 $\mathrm{cm}^{-1}$ with a maximum spectral resolution of 0.3 $\mathrm{cm}^{-1}$. The basic EISAR characteristics are compiled in Tab. 3.4.2. The spectrometer is installed in a dehumidified and temperature-controlled chamber. The dewar for the detector coolant (liquid nitrogen) is refilled every week, the desiccant is replaced every other month. Light from the atmosphere enters the spectrometer via a sky tracking system that allows rapid pointing at any sky position, in particular, it can be used as a sun tracker. For radiometric calibration, the tracker points at a wide-aperture blackbody. Both tracker and blackbody are protected from adverse weather conditions, i.e. precipitation and stormy winds, by a water-proof housing with hatch.

A typical FTIR observation begins with a measurement of the blackbody set to a temperature 5°C above the dew point. Then a series of sky measurements is performed. Finally, the blackbody set to a warm temperature of about 50°C is measured again. The two blackbody reference spectra are necessary to correct for detector nonlinearities and thus to achieve the radiometric preci-

*Table 3.4.* EISAR instrument parameters.

| | |
|---|---|
| interferometer | |
| manufacturer | Bruker Optics GmbH |
| type | modified IFS 55/e (Michelson, autoaligned) |
| spectral range, effective | 600–3000 $cm^{-1}$, 16.7–3.3 $\mu$m |
| spectral resolution, apodized | $> 0.3\,cm^{-1}$ |
| mirror scan rate (standard) | 0.7–3.0 cm/s (1.3 cm/s) |
| beamsplitter | KBr, Ge-coated |
| field of view | 33 mrad |
| blackbody | |
| manufacturer | CI Systems |
| type | SR-80-4A |
| emissivity | $> 0.98$ |
| aperture diameter | 10 cm |
| temperature stability | $\pm 0.01$ K |
| temperature accuracy, absolute | 0.03 K |
| temperature uniformity | better than 0.01 K |
| temperature range | dew point+5 K to 385 K |
| detector | |
| type | HgCdTe/InSb (stacked) |
| photo-active area | $0.1 \times 0.1\,cm^2$ / $0.0079\,cm^2$ (circular) |
| coolant | liquid nitrogen |

sion of 0.1°C and accuracy of 1.0°C required for atmospheric temperature and humidity sounding. Collection of each spectrum takes about 5 s, but averaging is performed to reduce random noise. With this technique, calibrated atmospheric spectra are collected about once every 15 min. However, a rapid sampling mode of about 1 min temporal resolution is also possible. With EISAR's sky tracking system it is anticipated to improve the vertical resolution of these observations by slanting the spectrometer field-of-view and thus increasing the emitting path. EISAR is comparable in spectral coverage and resolution with the Atmospheric Emitted Radiance Interferometer (AERI) which has been installed at several Atmospheric Radiation Measurement (ARM) Program sites of the U. S. Department of Energy (Knuteson et al., 2004a,b).

Aside from monitoring temperature and humidity with EISAR as a standalone instrument, investigations are planned if and to what extent these measurement products can be improved by combining the EISAR observations with data sets of other instruments such as microwave profilers and water-vapor lidars. Each of these systems have different observational advantages and disadvantages (see Tab. 3.4), thus considerable instrument synergy can be expected. The Richard-Aßmann Observatory Lindenberg with its extensive suite of remote-sensing instruments is well equipped for this task.

*Table 3.5.* FTIR performance in comparison with other humidity and temperature profilers.

| *property* | *FTIR* | *microwave profiler* | *water-vapour lidar* |
|---|---|---|---|
| vertical resolution | low to moderate | low | excellent[a] |
| affected by clouds | yes[b] | no | yes[c] |
| liquid water path | no | yes | no |
| other trace gases | column[d] | no | no |
| cloud microphysics | (yes)[e] | no | no |
| retrieval complexity | high | high | low |
| hardware complexity | moderate | low | high |
| maintenance | moderate | low | high |

[a] water vapour; resolution of temperature measurement is moderate.
[b] profiling restricted to heights below clouds.
[c] temperature profiling restricted to heights above clouds.
[d] scanning capability required.
[e] case studies.

### 3.4.3 RETRIEVAL TECHNIQUE AND MEASUREMENT EXAMPLES

A variety of techniques can be used to derive information on the atmospheric state from ground-based observations of the atmospheric emission. Some of them have been analysed in the chapter 3.2 or by Cimini et al. (2006). Independently from the spectral region, the applied algorithms are solutions of an inverse problem deduced from the radiative transfer equation (RTE).

At the Meteorological Observatory Lindenberg atmospheric profiles are derived from microwave measurements applying a neural network approach and a measurement-based regression method (Güldner and Spänkuch, 2001). For the regression method an a priori data set of simultaneous radiosonde profiles and radiometer observations is used to provide information for the RTE solution as follows:

$$\hat{x} = x_o + C_{xy} C_{yy}^{-1}$$

where $C_{xy}$ and $C_{yy}$ represent the covariance matrix of the state vector x and the corresponding observations and the auto-covariance matrix of y. $\hat{x}$ and $x_o$ are the state vector and the initial guess.

According to this measurement-based regression method, which implies the availability of an a-priori data set of simultaneous state vectors $x$ and observations $y$, a simulation-based regression was developed for retrieving profiles from FTIR-spectra measured by EISAR. In contrast to the measurement-based regression, calculated radiance spectra are used instead of observations. In order to provide a representative data set, IR spectra based on radiosonde measurements launched at Lindenberg were calculated using the software FASCOD3P (Anderson et al., 1989).

In the following case study temperature profiles observed by radiosondes and retrieved from radiance measurements with EISAR are compared to demonstrate the capability of the ground-based FTIR technique.

Figure 3.27 shows emission spectra from Lindenberg observed on 18 September 2006 between 5 and 17 UTC under clear sky conditions. Radiosonde data, plotted in Fig. 3.28, show a temperature inversion for the morning ascent which disappeared before the succeeding sonde was launched at 11 UTC. During that period the temperature increases from 15°C to 24°C near the surface and from 18°C to 21°C at 300 m height. During the afternoon hours, the temperature increases by about 2 K between 200 m and 1 km while it remains unchanged at higher levels. A beginning development of a temperature inversion is discernible again for the radiosonde launched at 17 UTC.

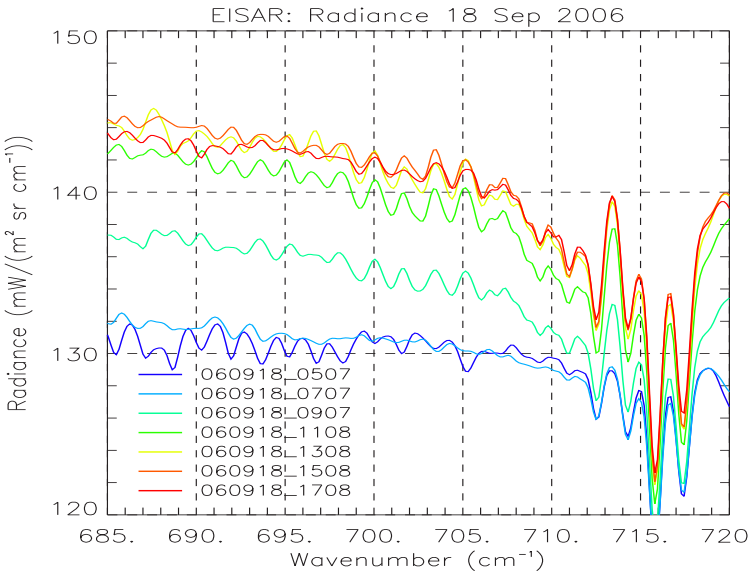


*Figure 3.27.* Time series of zenith radiance spectra between 685 and 720 $cm^{-1}$ at Lindenberg on 18 September 2006.

Figure 3.27 illustrates how the evolution of the temperature profile is reflected by the emission spectra measured with EISAR. The emission spectrum of the temperature inversion measured at 5 UTC displays an inverse curvature for the lines at about 692 and 700 $cm^{-1}$, i.e., lower radiances are measured near the line centres than at the adjacent wavelengths. If there were no inversion, the spectral signature would be the opposite. Then the spectral radiance would decrease from the centre of each line (representing warmer temperatures at lower levels due to the strong atmospheric absorption) to the line wings and between the absorption lines (representing colder temperatures at higher levels due to the weak atmospheric absorption). Following the same line of reasoning, one would also expect to observe a decrease in spectral radiance from the

opaque centre of the $CO_2$ band to its wings, which is indeed the case for the measurements on 18 September from 9 UTC onwards. In contrast, the morning measurements at 5 and 7 UTC affected by the temperature inversion are spectrally flat $< 710\,\mathrm{cm}^{-1}$, indicating the strong dependence of the spectra of downwelling atmospheric radiance on the lapse rate of the atmospheric temperature (Fig. 3.27).

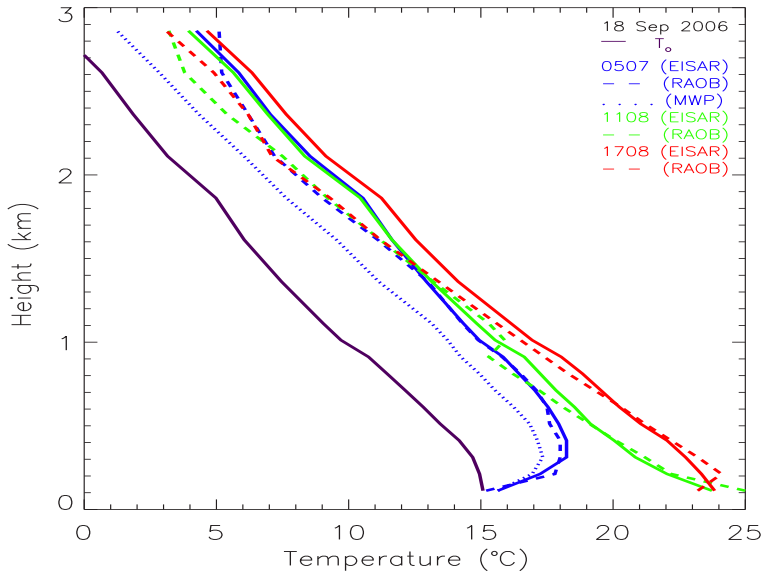


*Figure 3.28.* Intercomparison of temperature profiles as measured with radiosondes (dashed lines), derived from EISAR measurements (solid lines) and retrieved from microwave observations (dotted line) on 18 September 2006. The temperature profile $T_0$ which was used as a first guess in the retrievals is also shown.

For the temperature retrieval with the simulation-based regression method, the spectral region between 685–720 $\mathrm{cm}^{-1}$ of the 15-$\mu$m $CO_2$ band is used because it contains valuable information about the atmospheric thermal structure (as we have shown) and it is only slightly affected by variable atmospheric constituents. A limited number of emission lines is selected for the retrieval to avoid reduncancy, each line is sampled up to three times (at the centre or the slopes). Altogether, 21 channels ranging from 681.6 to 721.2 $\mathrm{cm}^{-1}$ are used. Surface temperature is also input to the retrieval algorithm. The comparison to radiosonde soundings in Fig. 3.28 demonstrates the remarkable profiling capability of EISAR. For the selected clear-sky case, the temperature inversion is much better captured with EISAR than with a microwave profiler operated at the same site.

The simulation-based regression method has also been used successfully for the combined retrieval of temperature and water vapour profiles. Figure 3.29 shows the corresponding height-time cross sections for 18 September 2006. On that day, EISAR measurements were taken every 2 hours only. Smaller

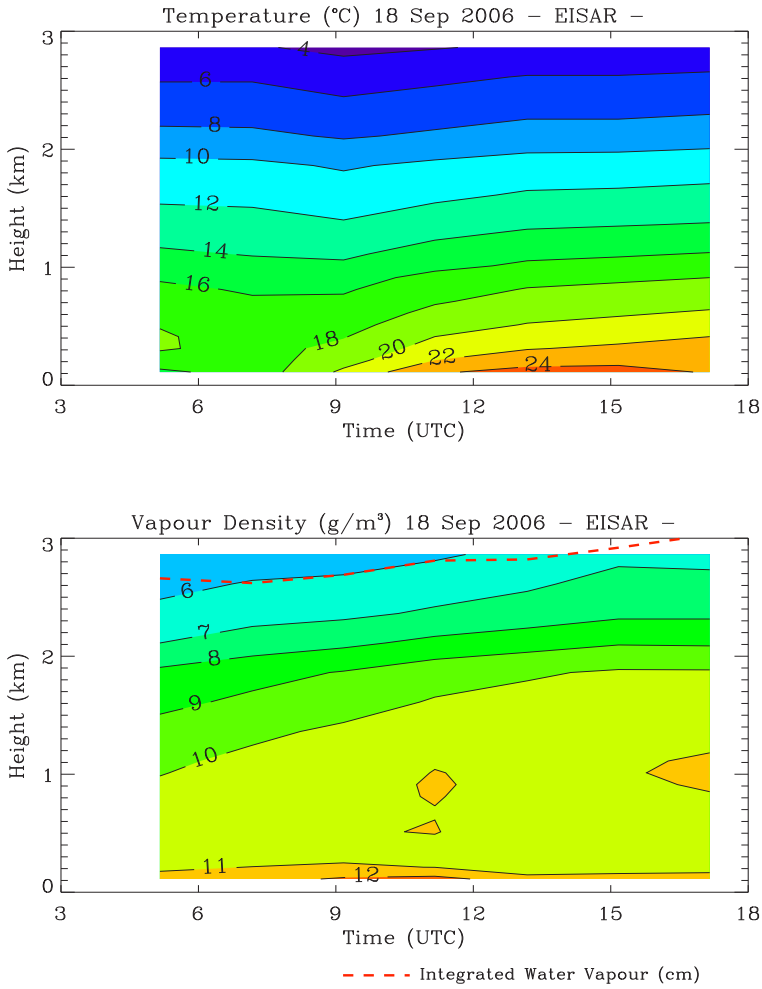


*Figure 3.29.* Height-time cross section of temperature and humidity retrieved from EISAR measurements on 18 September 2006. Integrated water vapor (cm; red dashed curve).

time steps are possible, and so is a quasi-continuous monitoring of the diurnal cycles of the temperature and humidity fields over Lindenberg, which is already achieved with a microwave profiler on a routine basis (see the special section on microwave radiometry, section 3.2).

### 3.4.4 OUTLOOK

Future work will focus on two major objectives. First, routine operation of EISAR has to be established. This endeavour comprises continuous optimization and maintenance of the technical infrastructure, improvement of the retrieval algorithms, and quality assurance of the measurement products. Second, studies of instrument synergy. It is planned to combine the EISAR

observations with data obtained with the co-located microwave profiler (Güldner and Spänkuch, 2001) and the water-vapor Raman lidar RAMSES (Raman lidar for Atmospheric Moisture SEnSing) (Engelbart et al., 2006; Mattis and Jaenisch, 2006).

## Bibliography

Anderson, G. P., S. A. Clough, F. X. Kneizys, E. P. Shettle, J. H. Chetwynd, and L. W. Abreu, 1989: FASCOD3: Update. In Shettle, E. P., and F. X. Kneizys (Eds.): *Proc. 12th Annual Review Conference on Atmospheric Transmission Models, Part 1*. Geophys. Lab. AFSC, Hanscom AFB, MA, October 1989, 163–187.

Bell, R. J.,1972: *Introductory Fourier Transform Spectroscopy*. Academic Press, New York.

Bruker Analytische Messtechnik GmbH, 1996: *Equinox 55 User's Manual*. Ettlingen, Germany.

Cimini, D., T. J. Hewison, L. Martin, J. Güldner, C. Gaffard, and F. S. Marzano, 2006: Temperature and humidity profile retrievals from ground-based microwave radiometers during TUC. *Meteorol. Z.*, **15**, 45–56.

Engelbart, D., J. Reichardt, I. Mattis, U. Wandinger, V. Klein, A. Meister, B. Hilber, and V. Jaenisch, 2006: RAMSES - German Meteorological Service Raman lidar for atmospheric moisture sensing. *Reviewed and Revised Papers*, 23rd International Laser Radar Conference, Nara, Japan, 24–28 July 2004, 683–686.

Feltz, W. F., H. B. Howell, R. O. Knuteson, H. M. Woolf, and H. E. Revercomb, 2003: Near continuous profiling of temperature, moisture, and atmospheric stability using the Atmospheric Emitted Radiance Interferometer (AERI). *J. Appl. Meteorol.*, **42**, 584–597.

Friedl-Vallon, F., G. Maucher, A. Kleinert, A. Lengel, C. Keim, H. Oelhaf, H. Fischer, M. Seefeldner, and O. Trieschmann, 2004: Design and characterization of the balloon-borne Michelson Interferometer for Passive Atmospheric Sounding (MIPAS-B2). *Appl. Opt.*, **43**, 3335–3355.

Güldner, J., and D. Spänkuch, 2001: Remote sensing of the thermodynamic state of the atmospheric boundary layer by ground-based microwave radiometry. *J. Atmos. Oceanic Technol.*, **18**, 925–933.

Huang, H.-L., P. Yang, H. Wei, B. A. Baum, Y. Hu, P. Antonelli, and S. A. Ackerman, 2004: Inference of ice cloud properties from high spectral resolution infrared observations. *IEEE Trans. Geosci. Remote Sens.*, **42**, 842–853.

Kempe, V., D. Oertel, R. Schuster, H. Becker-Ross, and H. Jahn, 1980: Absolute IR-spectra from the measurements of Fourier spectrometer aboard Meteor-25 and 28. *Acta Astronautica*, **7**, 1403.

Knuteson, R. O., and Coauthors, 2004a: Atmospheric Emitted Radiance Interferometer. Part I: Instrument design. *J. Atmos. Oceanic Technol.*, **21**, 1763–1776.

Knuteson, R. O., and Coauthors, 2004b: Atmospheric Emitted Radiance Interferometer. Part II: Instrument performance. *J. Atmos. Oceanic Technol.*, **21**, 1777–1789.

Mattis, I., and V. Jaenisch, 2006: Automated lidar data analyzer (ALDA) for RAMSES - the autonomously operating German Meteorological Service Raman lidar for atmospheric moisture sensing. *Reviewed and Revised Papers*, 23rd International Laser Radar Conference, Nara, Japan, 24–28 July 2004, 215–218.

Milz, M., T. von Clarmann, H. Fischer, N. Glatthor, U. Grabowski, M. Höpfner, S. Kellmann, M. Kiefer, A. Linden, G. Mengistu Tsidu, T. Steck, G. P. Stiller, B. Funke, and M. Lopez-Puertas, 2005: Water vapor distributions measured with the Michelson Interferometer for Passive Atmospheric Sounding on board Envisat (MIPAS/Envisat). *J. Geophys. Res.*, **110**, No. D24, D24307, doi:10.1029/2005JD005973.

Moroz, V. I., D. Spänkuch, and Coauthors, 1986: Venus spacecraft infrared radiance spectra and some aspects of their interpretation. *Appl. Opt.*, **25**, 1710–1719.

Rathke, C., J. Notholt, J. Fischer, and A. Herber, 2002: Properties of coastal Antarctic aerosol from combined FTIR spectrometer and sun photometer measurements. *Geophys. Res. Lett.*, **29**, 2131, doi:10.1029/2002GL015395.

Revercomb, H. E., D. C. Tobin, R. O. Knuteson, F. A. Best, W. L. Smith, Sr., P. F. W. van Delst, D. D. LaPorte, S. D. Ellington, M. W. Werner, R. G. Dedecker, R. K. Garcia, N. N. Ciganovich, H. B. Howell, E. R. Olson, S. B. Dutcher, and J. K. Taylor, 2005: Highly accurate FTIR observations from the scanning HIS aircraft instrument. *Proc. SPIE*, **5655**, 41-53.

Spänkuch, D., J. Güldner, and W. Döhler, 1987: Investigations to temperature soundings with partial interferograms. *Contrib. Atmos. Phys.*, **60**, 103–128.

Spänkuch, D., W. Döhler, J. Güldner, and A. Keens, 1996: Ground-based passive atmospheric remote sounding by FTIR emission spectroscopy - first results with EISAR. *Contrib. Atmos. Phys.*, **69**, 97–111.

Spänkuch, D., W. Döhler, J. Güldner, and E. Schulz, 1998: Estimation of the amount of tropospheric ozone in a cloudy sky by ground-based Fourier-transform infrared emission spectroscopy. *Appl. Opt.*, **37**, 3133–3142.

Spänkuch, D., W. Döhler, J. Güldner, and E. Schulz, 2000: Effect of coarse biogenic aerosol on downwelling infrared flux at the surface.*J. Geophys. Res.*, **105**(D13), 17,341–17,350.

Tobin, D. C., and Coauthors, 1999: Downwelling spectral radianceobservations at the SHEBA ice station: Water vapor continuum measurements from 17 to 26 microns. *J. Geophys. Res.*, **104**(D2), 2081–2092.

Turner, D. D., S. A. Ackerman, B. A. Baum, H. E. Revercomb, and P. Yang, 2003: Cloud phase determination using ground-based AERI observations at SHEBA. *J. Appl. Meteorol.*, **42**, 701–715.

von Clarmann, T., H. Oelhaf, and H. Fischer, 1993: Retrieval of atmospheric $O_3$, $HNO_3$, CFC-11, and CFC-12 profiles from MIPAS-B-89 limb emission spectra. *Appl. Opt.*, **32**, 6808–6817.

# 3.5 WINDPROFILER/RASS

Hans Richner[1], V. Klaus[2], G. Frederick[3], C. Gaffard[4]

[1] *Institute for Atmospheric and Climate Science, ETH Zürich, Zürich, Switzerland*
✉ Hans.Richner@ethz.ch

[2] *Meteo France, CNRM, Toulouse, France*

[3] *Vaisala Inc., Georgetown/TX, USA*

[4] *UK Met Office, Reading University, Reading, UK*

## 3.5.1 BASIC ALGORITHMS FOR WIND PROFILING USING WPR

In this section, the standard algorithms for wind profiling are briefly portrayed. Then, in random sequence, a number of additions and improvements of these basic procedures are described and their effects discussed. A separate subsection then in detail compares the effectiveness of a selection of these extensions. The section ends with a description of recently developed methods for retrieving additional profiles from wind profilers, such as temperature and humidity.

**3.5.1.1 Signal Processing.** (This section is an excerpt of the publication *"Wind Profiling: The History, Principles, and Applications, May 2005"*; with permission of Vaisala)

The basic wind profiler signal processing algorithms were defined at the Middle Atmospheric Program: Workshop on Technical Aspects of MST Radars, 23-27 May 1983, Urbana, Illinois (Strauch, 1983; Carter, 1983; Cornish, 1983; Woodman, 1983). The techniques presented in the workshop have become ubiquitous. The atmospheric return signal is amplified and filtered in the profiler receiver system. For each transmit pulse repetition period, the video receiver output is sampled, using dual analog to digital converters, at specific intervals corresponding to the range of the sample volume from the radar.

In principle, wind velocities of any magnitude, of great accuracy, and from any range could be determined if there were no restrictions on the data. In practice, however, the data are restricted in several ways.

The rate at which pulses are transmitted, the Pulse Repetition Frequency (PRF), limits the range over which heights can be unambiguously determined. Alternately, one can think in terms of the reciprocal of the PRF: the Inter-Pulse Period (IPP). If the IPP is too short, the return signals will overlap. Return signals will begin to be received from a pulse while signals from the previous pulse are still arriving, as shown in figure 3.30. Unless some other information

is available, it is impossible to interpret these signals independently. This is referred to as range aliasing because a return signal from a distant scatter would be attributed to a much closer range gate. The time between pulses must be at least as long as the time delay between transmission of a pulse and reception of a return signal from the greatest height expected for useful return.

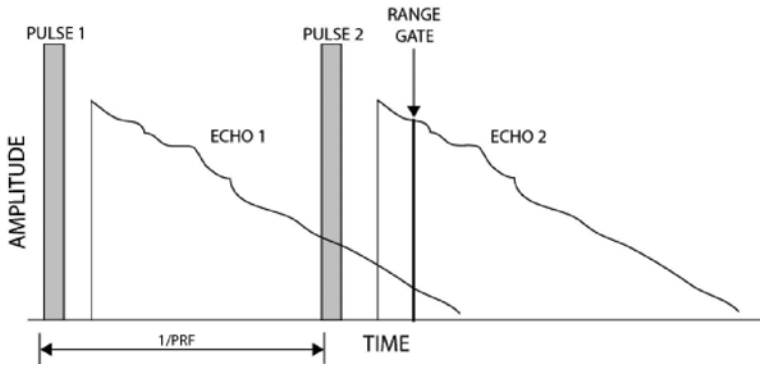


*Figure 3.30.* Pulse Repetition Frequency

Velocities (Doppler shifts) can be determined unambiguously only if they are within limits determined by the radar sampling parameters. Doppler shifts outside these limits will appear at incorrect frequencies and the velocities calculated from them are incorrect. This is referred to as velocity aliasing. The frequency limits over which the Doppler shift can be determined unambiguously for any height depend upon the effective sampling rate. When samples are not averaged, the sampling rate is the same as the rate at which pulses are transmitted, the PRF. To maximize the range of radial velocities that can be determined unambiguously, the effective sampling rate should be as high as possible. This conflict between range and velocity aliasing requires compromise between the related parameters.

For each range gate, several hundred samples are gathered and then converted into a frequency spectrum using a mathematical inversion technique known as the Fast Fourier Transform (FFT). Figure 3.31 is a drawing of such a resulting spectrum. The central frequency corresponds to the transmitted frequency. To the right and left of these are the Doppler shifted frequencies. Positive Doppler shifts correspond to motions toward the profiler and negative shifts to motions away from the profiler. The figure shows a peak to the right of center, or motion toward the profiler. The Doppler frequency shift is converted into the radial velocity component of the wind. The power return and the width of the peak at each range gate are measures of the degree of turbulence in the sampled volume.

For some range gates, a peak is also seen at the center of the spectrum. This is caused by reflections from solid, stationary targets (such as buildings) in the sidelobes of the antenna pattern. This is called ground clutter.

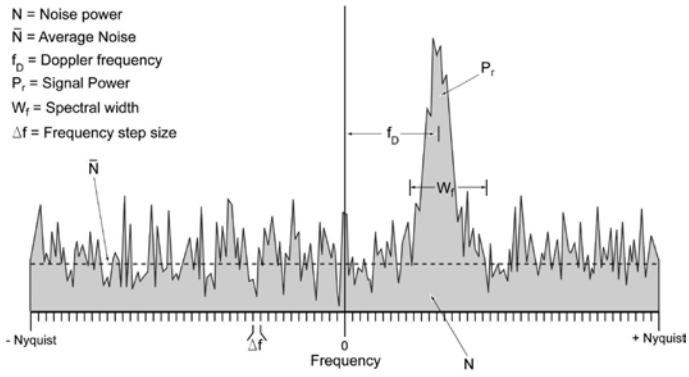


*Figure 3.31.* Typical Power Spectrum

The noise in the spectrum is due to cosmic background radiation (mostly from our own galaxy) and electronic noise in the system. Noise causes uncertainty in the measurements but can be largely compensated for by signal integration techniques. Two types of integration may be used for each range gate, those computed in the time and frequency domains. Time-domain averaging (integration) consists of taking the mean of several consecutive samples in time before the FFT is computed. Alternatively, long time-series or time-domain filtering may be employed.

Frequency domain, or spectral averaging (integration), involves calculating a mean spectrum from several consecutive spectra after the FFT computations have been performed. Figure 3.32 shows the steps commonly involved in reducing the time-series data to moments calculation. Both types of averaging are shown.

Time domain averaging or filtering reduces noise and the computational load of the FFT. An effect of time-domain averaging is that it limits the range of Doppler shifts (and thus radial velocities) that can be determined unambiguously. The effective sampling rate is the PRF divided by number of samples in the time domain average. The number of samples used in the average depends upon the maximum winds expected.

Windowing is used to reduce the influence of certain mathematical artifices associated with the FFT.

Spectral averaging enhances detectability by reducing noise variance. This leads to more reliable determinations of power received, Doppler shift, and spectral width. However, it reduces the time resolution of the final results. If noise were not present, it would take only a few seconds to get reliable spectra. In the presence of noise, many spectra must be averaged, yielding a time resolution of ten seconds to several minutes, depending on the profiler operating frequency.

The noise power density value for each range gate is calculated using the Hildebrand and Sekhon (1974) algorithm. The radial velocity is chosen by,

first, selecting the largest spectral peak. The extent of the peak that exceeds the maximum noise is determined. The power of all the points within the extent of the peak above the mean noise is summed. This is the return power (zeroth) moment. The Doppler (first) moment is determined by dividing the sum of the power times frequency of the points within the extent of the peak, by the sum of the power points. The spectral width is two times the square root of the second moment about the mean velocity, which is the sum of the power times the frequency squared of the points within the extent of the peak above the mean noise divided by the sum of the power points.

Wind values are calculated using radial velocity samples gathered using at least two orthogonal antenna directions and a consensus averaging method (Strauch et al., 1984). Vertical velocity correction requires either a vertical radial velocity sample, or using two opposed orthogonal pairs of radial velocity samples. The averaging period must be adequate to ensure that homogeneity between the separate radial volumes is satisfied. The consensus algorithm identifies a window of valid values and rejects outliers. The radial velocity during the consensus interval is the mean of the Doppler samples that fall within the window. The vector sum of the horizontal components of the wind velocity is the wind speed/direction during the consensus period.

The standard profiler normally incorporates signal processing refinements that have been validated since the original 1983 definition. Complementary pair pulse coding/decoding (Ghebrebrhan, 1990) is implemented during the coherent averaging step. Pulse coding increases the average power by extending the transmit pulse, but maintains range resolution by phase coding segments of the extended pulse. The segments are defined in increments that correspond to the desired range resolution.

Wavelet transforms may be used to reduce the amplitude of stationary and moving ground clutter including ocean wave motion (Jordan et al., 1997). Implemented following the coherent averaging process, the Wavelet transform allows sorting of the averaged time-series by the persistence and/or time characteristics of the signal. Since the clutter interference is typically very persistent, the contaminated samples can be removed from the time-series. See further description of wavelet transform applications in section 3.5.1.2.

A method of reducing the effect of intermittent clutter contamination (Merritt, 1995) may be implemented as an alternative to the mean spectral averaging. Before the point-by-point averaging, the distribution of the collected samples is evaluated using a method similar to the noise calculation, and outliers are rejected.

A module may be provided which identifies multiple spectral peaks in the power spectrum and Doppler moments. They are evaluated according time and height continuity and spectral characteristics (Griesser and Richner, 1998) to reduce contamination of the profiler data from clutter and interference. See further description of this technique in section 3.5.1.3.

Rejection of ground clutter contamination (Riddle and Angevine, 1992) may be performed during the selection of moment values. The method selects a secondary spectral peak if the largest peak falls within a boundary near zero velocity.

A method to evaluate the wind and virtual temperature data using time and height continuity (Weber et al., 1993) may be implemented following the consensus calculation.

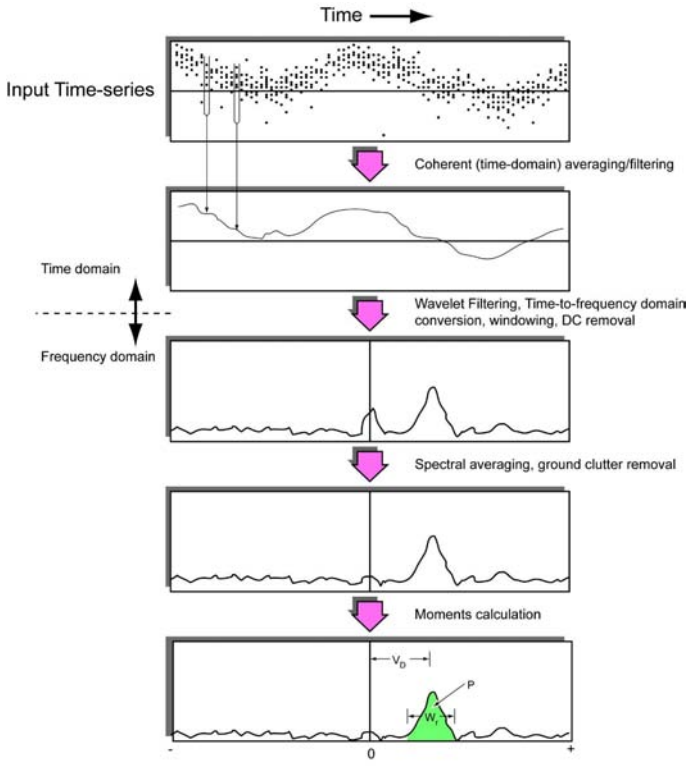


*Figure 3.32.* Processing Steps to Compute Radial Wind Data

### 3.5.1.2 Wavelet packets as tool for profiler data filtering.

**The wavelet packet analysis.** Among several techniques, the wavelet packet analysis has given very encouraging results for removing various types of pollution such as ground clutter or transient echoes due to aircrafts or birds. This is achieved by filtering possible spurious echoes appearing on ST radar data directly from the time series before spectral analysis, keeping in mind that spectral analysis often hides important features characterizing various un-

desirable components of the signal and thus prevents optimum detection and discrimination of the radar echo.

The wavelet packet method is an extension of the wavelet decomposition described by Jordan et al. (1997) and Lehmann and Teschke (2000) for ST radar application. Here, the signal is decomposed in a regular number of wavelet packets which can be assimilated to the outputs of a filter bank. Global energy as well as reconstructing exact features are preserved which is most important for further processing. The entirety of the packets provides another view of the signal showing possible irregularities, and very simple criteria can, subsequently, be applied for removing undesirable features before reconstruction.

The principle is based on the decomposition of the signal into two equal parts called approximation and detail that represent its low and high frequency contents respectively. Each part is split in half so that the total number of points stays constant. Such decomposition can be iterated any number of times, nevertheless, an exact reconstruction of the initial series is always possible through reverse filtering. The basic steps of the decomposition are shown in figure 3.33.

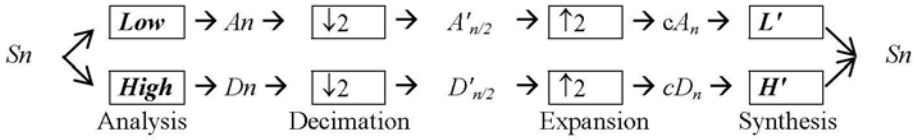


*Figure 3.33.* Wavelet decomposition of a n-point signal Sn into n/2-point approximation $A'_{n/2}$ and detail $D'_{n/2}$ using lowpass and highpass filter, respectively, and removing every second point (Decimation $\downarrow 2$). From the decimated series, the exact initial n-point signal can be restored after inserting zeros between each sample (Expansion $\uparrow 2$) and using the associated reconstruction filters ($L'$ and $H'$)

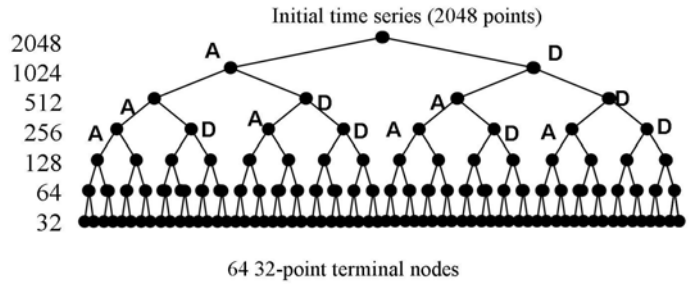


*Figure 3.34.* Decomposition of the VHF radar time series into 64 terminal nodes using wavelet packet analysis. At each level, the signal is divided into an approximation (A) and a detail (D) resulting respectively from lowpass and highpass filtering. The 64 terminal nodes are then analyzed and thresholded before reconstruction

**Description of the method.** The radar raw data consists of a 2048-point time series representing the signal received from a given direction beam during 2 minutes. This signal is decomposed into two 1024-point nodes using a lowpass and its associated highpass filter as described previously. For each resulting series, this process is iterated six more times in order to produce 64 32-point terminal nodes each corresponding to a particular frequency band. As an example, the first left node, which results only from lowpass filters or approximation nodes, is centered around the zero frequency and contains the ground clutter which can be analyzed and thresholded before reconstruction.

In addition, any spurious signal characterized by transient features such as an airplane echo can thus be detected and deleted using well defined thresholds. The time series is then rebuilt before spectral processing.

**Ground clutter removal.** Filtering zero-frequency clutter is most important for low speed signal detection as low speed signals are always intensely mixed with spurious returns from fixed obstacles. Figure 3.35 shows a typical example of clutter pollution. In the upper frame, the signal is well centred on zero frequency (marked at point 128) and the turbulence echo at the base on its right is hardly recognizable. After thresholding the lowest frequency approximation node (first left point in figure 3.34), this signal is easily extracted from the original clutter (lower frame of figure 3.35). Any attempt to discriminate the turbulence echo from the ground clutter using only the spectrum would have been close to impossible in this case.

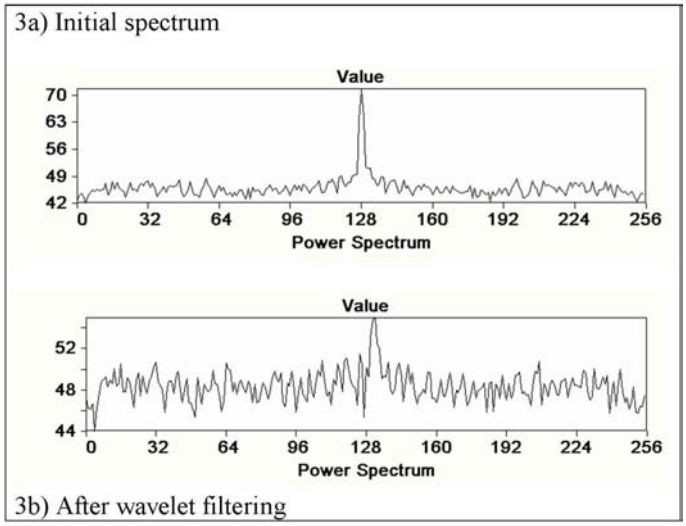


*Figure 3.35.* Clutter removal by thresholding the first approximation node, which corresponds to high-pass filtering

**Aircraft echo filtering.** Another typical application is the removal of aircraft echo. Some specialized techniques already exist in this field based on the convolution by a wavelet pattern well fitted to the aircraft echo signature on the time series (Boisse et al., 1999). However, for this problem, wavelet packets filtering can be just as efficient without extra programming and computation time: The aircraft echo is characterized by its transient feature (figure 3.36, left frame), which distinguishes it from the regular turbulent echo (figure 3.36, right frame). Consequently, it may be useful to divide each terminal node into several segments and to calculate for each of them the maximum absolute amplitude. If a threshold is chosen that corresponds to the lowest among these values and apply it to the remaining segments with a some tolerance, two possibilities may occur: If no transient interference exists, all the points have the same magnitude and nothing needs to be changed. However, if any large variation appears in a given segment, the signal magnitude will automatically be limited. The right frame of figure 3.36 shows the result obtained by using a dynamic thresholding after dividing each node into four segments and applying the thresholding to the whole node. In this example, the ground clutter was already removed with the method described previously. This was necessary because the aircraft echo spectral band was so large as to include also zero-frequency components.

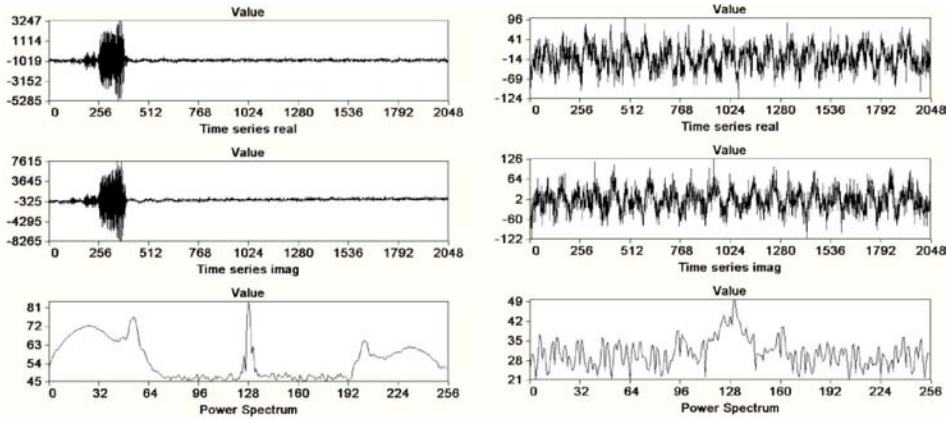


*Figure 3.36.* Time series showing a strong aircraft interference and the corresponding spectrum without wavelet packet filtering (left frame) and after using dynamic thresholding after dividing each node into 4 segments (right frame). Ground clutter filtering is used as described above

**3.5.1.3 Multipeak processing.** Signal processing in most of the profiler systems is based upon the assumption that each spectrum includes only system noise and the radar return from the atmosphere. However, it is known that - in addition to the peak in the Doppler spectrum caused by the wind - additional peaks may appear. These may result from a number of sources in-

cluding external noise (e.g. lightning) in the received spectrum, ground clutter (i.e. echoes from fixed targets), reflections from moving ground targets in the antenna sidelobes, fliers (aircraft, insects and birds), spurious signals received from other transmitters operated at a frequency near that of the radar, and precipitation.

Advanced signal processing methods using spectral data and time series data were developed, leading to an improvement in data quality (Clothiaux et al., 1994; Merritt, 1995; Jordan et al., 1997). These methods are successful in dealing with certain types of contamination. However, there is still a need for a more broadly applicable algorithm using the spectral data which can be applied operationally.

**The peak processing algorithm.** The peak processing algorithm consists of two steps: (a) peak identification and (b) peak selection.

For peak identification, first the mean noise level is calculated according to Hildebrand and Sekhon (1974). Then up to three contiguous regions are determined where the power is above this mean noise level. Subsequently, for each region a spline approximation is carried out, and the local maxima and minima are determined; the smoothing parameter for the spline approximation depending on the width of the region. The local minima of the spline function are used to determine the peak boundaries. The estimation of the moment data is based on the original (i.e. un-smoothed) data set for each peak. For double and triple peaks, i.e. two or three peaks either partly overlapping or close together, a least square parameter estimation technique in the log domain is used for obtaining a better estimation of the moments. Hence, at the end of the peak selection process, for each range gate and beam, the moment data of up to three peaks are available.

For peak selection, a ground clutter check is first applied: All symmetrical peaks with respect to zero velocity are flagged. This ground clutter check is performed up to a specified height level and works quite similarly to the ground clutter check in the single peak algorithm (Riddle and Angevine, 1992). The difference between the two methods is that in the single peak algorithm, the ground clutter algorithm is not applied at a range gate if the signal in the range gate above is near zero velocity.

In a next step, for each range gate and for each peak, the characteristics of the individual peaks are compared in time, height (i.e. range gate), and (with the exception of the signal-to-noise ratio) in mode; an individual weight is calculated for each peak. This weighting factor represents a measure of continuity in space and time. However, the peak with the highest weight in a range gate does not necessarily correspond to the wind peak. Ground clutter peaks are continuous in time and for the lowest gates also in height; as mentioned, these ground clutter peaks were flagged. To select the wind peak, first a check is made for the ground clutter flag. If this is positive, and if there is a second

peak with a high evaluation factor, this second peak is subsequently treated as the wind peak.

In most cases, the estimation of the wind peak is correct. However, there are still problems when the wind peak selection method fails. Sometimes spurious echoes with a high weight are observed. To improve this situation, an algorithm is applied which builds continuous vertical profiles ("chains") from the first to the last range gate. The algorithm was originally developed by Clothiaux et al. (1994). Chains are formed across range gate spectra by connecting those peak locations that satisfy a continuity constraint. In the case when more than one profile is obtained, the most likely profile is selected by favoring the one with the maximum number of peaks, the highest accumulated power density, the minimal peak-to-peak deviation, and the minimal number of ground-clutter-flagged peaks. In the peak selection routine, up to three regions are determined which is sufficient in most cases.

**Assessment of the Multiple Peak Processing Algorithm.** (*For a comparison with other methods for improving wind profiler data quality, see section 3.5.1.7*)

During the development of the multiple peak processing algorithm, the procedure was optimized by testing single case studies. To assess the performance of the multiple peak processing algorithm, a long-term data set was reprocessed using this algorithm. The results obtained are compared with results achieved originally when using the single peak processing algorithm; both data availability and data quality are compared. For verification, this comparison is repeated using a data set from a completely different type of wind profiler.

The data set was obtained with a Radian LAP-3000 boundary layer wind profiler at the meteorological station in Payerne in 1995 and 1996. The profiler is a 1290 MHz system with a phased antenna, which has a size of 2.7 x 2.7 $m^2$. The meteorological station in Payerne is located on the Swiss Plateau, a wide valley embedded between the Alps and the Jura mountains. The meteorological station at an altitude of 491 m ASL is surrounded by trees, houses, power lines, and roads.

The LAP-3000 system offers the possibility to save the raw data (i.e., the averaged Doppler spectra) as well as the moment data computed with the single peak algorithm. All this data was saved for 101 days. Due to interruptions in the measurements, a net recording time of somewhat more than 90 days was realized. The raw data were reprocessed with the new multiple peak processing algorithm. Moment data based on the single peak processing algorithm as well as on the multiple peak processing algorithm were subsequently subjected to a consensus algorithm for calculating 30 min. mean wind values.

Consensed data were checked for quality using an automated continuity algorithm (Weber et al., 1993). About 3 % of the data from both data sets (single peak processing algorithm and multiple peak processing algorithm) were edited in this way; no manual editing was applied.

The multiple peak processing algorithm leads to a visible increase in data availability. For the high mode (long pulse length) the increase is about 9 % and for the low mode (short pulse length) approx. 16 %. Please note that there is a significant increase in availability at the lowest gates of the low mode.

After developing the algorithm for the 1290 MHz system mentioned, it was tested with data of a 482-MHz profiler for a 28-hour period. For this test, none of the parameters in the evaluation procedures was changed, except those representing system characteristics. Because the 482-MHz system suffered of interference with the 50 Hz mains, an additional test was applied to identify 50 Hz main interference peaks. As figures 3.37 and 3.38 illustrate for a period of just over a day, the multiple peak processing algorithm improved the mean data coverage by about 7 % and – more important – reduced the number of unrealistic or suspicious wind data points from originally 8 % to zero!

Multiple peak processing can significantly improve the quality of wind data gathered with wind profiler radar, compared to single peak processing methods. It is obvious that the earlier dubious primary data can be eliminated, the less they will contaminate derived quantities.

While multiple peak processing does improve data coverage (because the quality checking algorithms for the derived winds needs to eliminate less suspicious data), its main advantage lies more in the fact that it replaces virtually all suspicious and unrealistic wind data.

The algorithm introduced here is rather insensitive to instrument characteristics and does not need elaborate tuning. This was demonstrated impressively when the software package which was developed for a 1290 MHz boundary layer profiler was applied to a data set obtained with a 482 MHz profiler: It improved wind data coverage and wind data quality in practically the same way as for the boundary layer profiler without any adaptations (for examples, see Griesser and Richner (1998)).

The algorithm can be applied in real time, hence, no time-delaying off-line reprocessing is necessary. Given a modular structure of profiler software, it is easily introduced between the spectra computation and the wind computation; there is no need for other software modifications or changes in hardware configuration.

Griesser and Richner (1998) gave an example of how the algorithm - developed for a 1290-MHz system - performs on a 482-MHz instrument. Figures 3.37 and 3.38 illustrate the recent improvement of data coverage and data quality applied to an operational wind profiler operating at 64 MHz.

**3.5.1.4 NIMA.** The fuzzy logic method is a relatively new and promising tool applied to ST radars for the first time by Cornman et al. (1998). This method, applied to Doppler spectra profiles, takes advantage of the improved software capabilities gained with computers in recent years by replacing independent analysis at each range gate by a global processing of the whole profile of Doppler spectra in a way similar to image analysis. By this way,

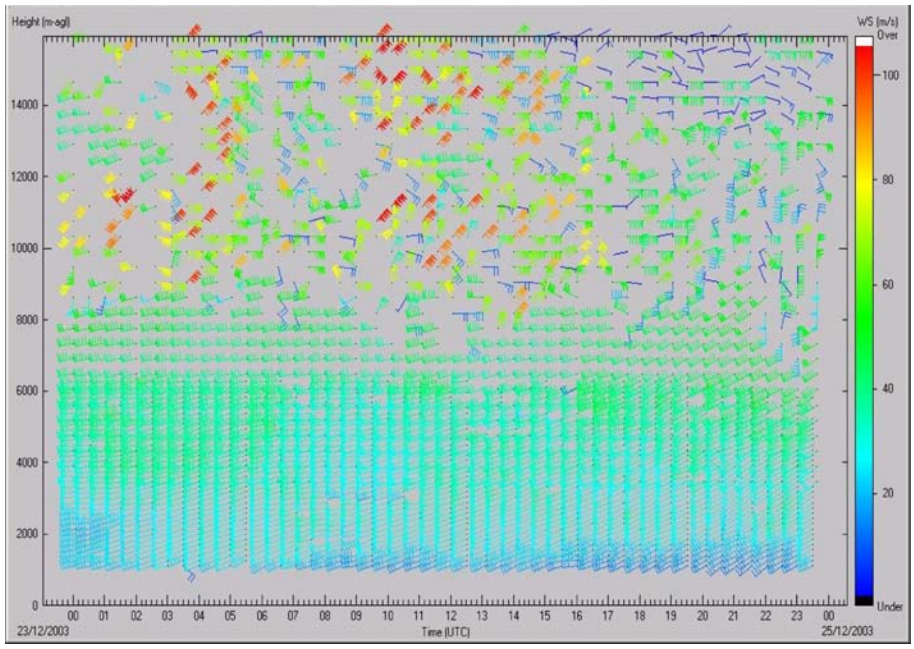


*Figure 3.37.* Example of wind field derived from profiler data using the standard single-peak algorithm (*Courtesy of UK MetOffice*)

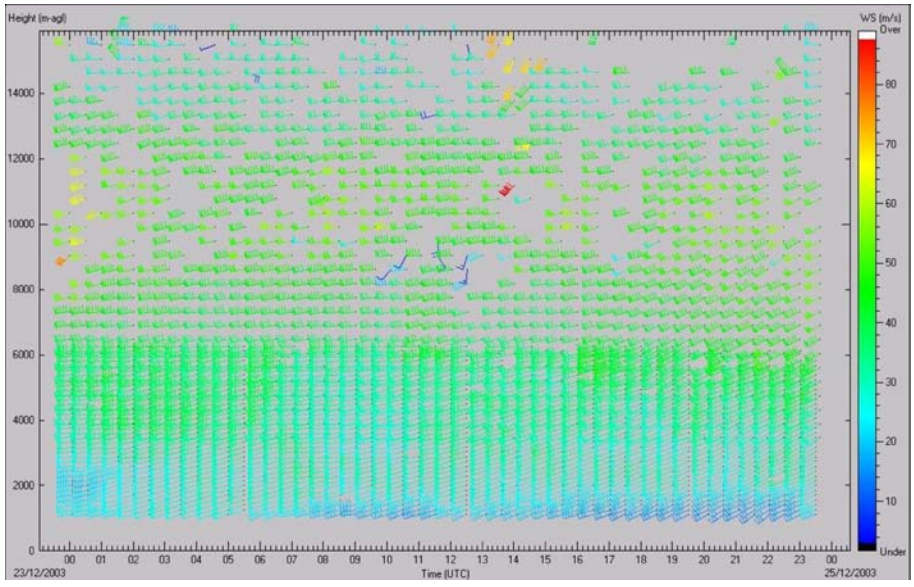


*Figure 3.38.* Wind field derived from the same spectral data as in figure 3.37 but processed with the multi-peak algorithm (*Courtesy of UK MetOffice*)

two-dimensional information (in frequency and in height) is used for improving both the discrimination of good signals among various types of contamination and the accuracy of the Doppler moments. The method, which approaches the skill level of the human expert, has been successfully tested on UHF profilers in China and in USA (COST-76 Final Report, 2003). The NCAR

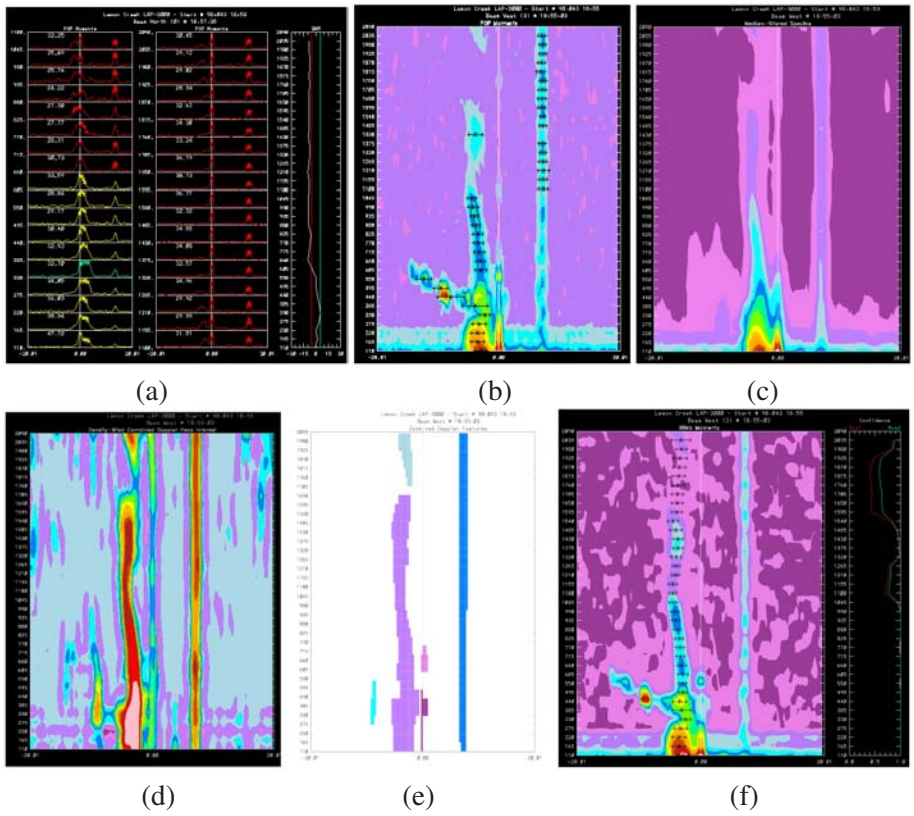


*Figure 3.39.* Steps in the NIMA processing chain [from: Vaisala (2004)]: (a) Stacked spectra(raw data), (b) Equivalent spectral intensity contours (c) 2D median-filtered spectra (d) Membership field values (for improved identification of the atmospheric signal) (e) Resulting Doppler peak feature candidates (f) NIMA moments overlaid on 1D (velocity) median-filtered spectra (sideplot shows confidence)

Improved Moments Algorithm (NIMA) software, developed at the National Center for Atmospheric Research (NCAR), was created to improve the quality of Doppler wind profiler estimations of wind speed, direction, and three-dimensional structure in clutter-rich environments. NIMA uses a combination of mathematical analysis, image-processing techniques, and fuzzy logic algorithms to mimic the human expert's skill in analysing wind profiler spectra data. NIMA software is modelled on data-quality verification practices employed by scientists to identify and eliminate ground clutter, sea clutter, RF-

interference, point targets, and occasional instrument noise (Vaisala, 2004). Figure 3.39 depicts the steps in the NIMA processing chain.

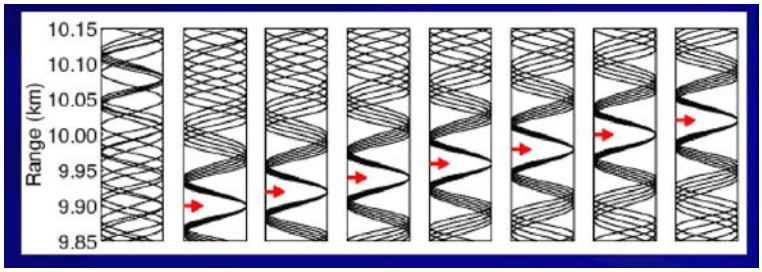


*Figure 3.40.* RIM phase shift technique (*Image courtesy of Phillip.Chilson@noaa.gov*)

The NIMA signal processing method using the fuzzy-logic method, and based on a combination of mathematical analysis, fuzzy-logic synthesis and image-processing technique is an efficient tool to extract a signal in a contaminated spectrum in a way comparable to human expertise. Moreover, it is also able to check the quality of the atmospheric signal and to remove any spurious contribution allowing a better moment estimation. This method can be applied to all kinds of pollutants of ST radar spectra such as aircraft or bird echoes (Richner and Kretzschmar, 2000) or electromagnetic interference. The main task (and one of the drawbacks to the method) is to select a certain number of criteria where a certain difference is observed between the good and the spurious signal (COST-76 Final Report, 2003).

**3.5.1.5 Range Imaging (RIM).** The available range resolution of pulsed radar wind profilers is normally limited by bandwidth. Range Imaging (RIM) has recently been developed as a means of mitigating these limitations by using a technique of combining signals from shifted frequencies to reconstruct the atmospheric structure in range within the radar volume. Signals from shifted frequencies can be added coherently at a specific range by introducing proper phase shifts to the signals. Figure 3.40 graphically portrays this feature. Figure 3.41 depicts the effect of RIM processing on a radar profiler signal. Many features in the planetary boundary layer that escape detection by standard wind profiler processing are readily identified by the higher resolution available with RIM processing. Understanding the vertical exchange of mass and momentum and the generation of turbulence is more readily found using the RIM technique with existing radar wind profiler systems and frequencies. Such RIM-derived features as the height and thickness of the entrainment zone, internal gravity waves in stable stratified flows, and Kelvin-Helmholtz instabilities are important to atmospheric analysis. Range imaging has been developed as a technique for high-range resolution measurements with pulsed radars using a small set of distinct transmitter frequencies. RIM is presently

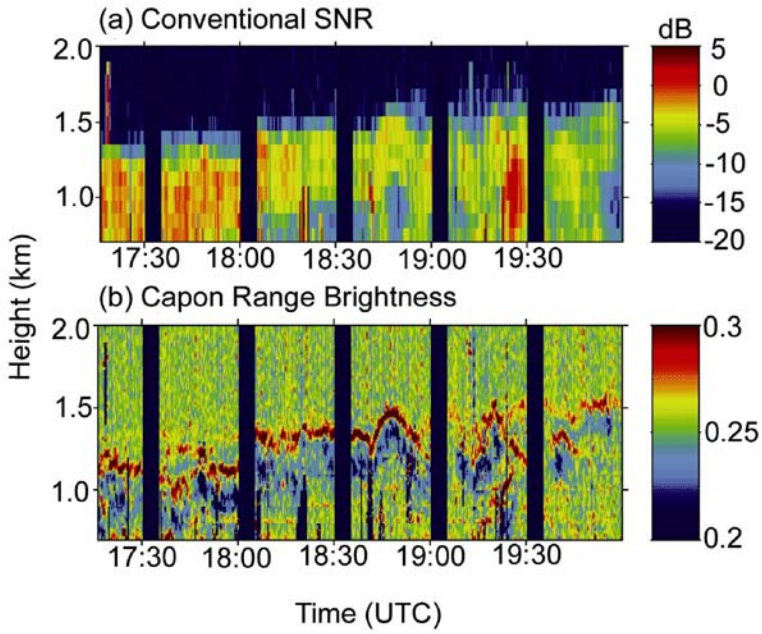


*Figure 3.41.* Wind profiler signal before and after RIM processing (*Image courtesy of Phillip.Chilson@noaa.gov*)

transitioning from research to operations and should be available to the operational community in the near future.

### 3.5.1.6 Neural network and fuzzy logic.

**Migrating birds as problem in wind profiling.** Figure 3.42 shows an example of supposed wind data which, in reality, is showing the velocity of migrating birds during night-time. Particularly for 1 GHz profilers, birds are a serious problem because their signals are much higher than those from clear air turbulence. This is clearly seen in the signal-to-noise ratio plotted in figure 3.43 for the same event.

Migration usually takes place between February and June and between July and November. It is a nocturnal phenomenon. The birds start to fly one hour after sunset. The migratory behaviour of birds is influenced by many factors, among them weather and topography. Most of the migrating birds in Central Europe fly below a height of 2 km (Bruderer, 1996).

**Fuzzy logic and neural networks as a possible solution.** To prevent that bird-contaminated spectra are used in the spectral averaging process, a procedure based on fuzzy logic and a neural network identifies and eliminates contaminated single spectra. Figure 3.44 shows where the software package accomplishing this located in the processing chain. After evaluating several

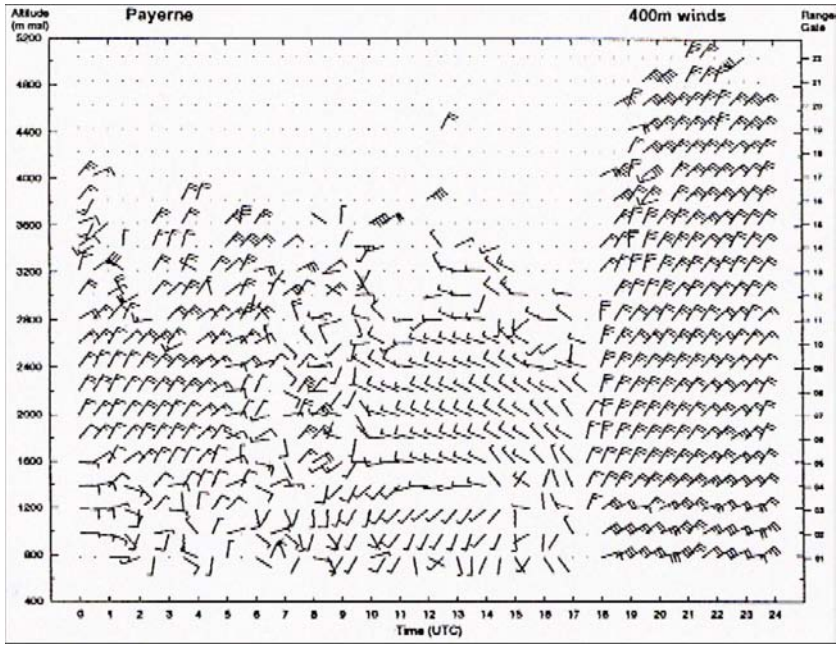


*Figure 3.42.* Example of high-UHF wind profiler "wind" data showing night-time bird migration

neural network types, a multilayer feed forward network was selected for classifying the single-spectrum-profiles. In figure 3.45 a typical architecture is shown. There is an input layer with $k$ nodes, one hidden layer with $j$ nodes and an output layer with $i$ nodes. This architecture implies two layers of weights $w_{jk}$ and $W_{ij}$. input $k$ is set to $\xi_k^\mu$ when pattern $\mu$ is supplied. The activation of the hidden node $V_j^\mu$ becomes

$$V_j^\mu = g(\sum_k w_{jk}\, \xi_k^\mu)$$

and by passing it though the activation function $g$, the outputs becomes

$$O_i^\mu = g\left[\sum_j W_{ij}\, g(\sum_k w_{jk}\, \xi_k^\mu)\right]$$

A common activation function for multilayer feed-forward networks is the sigmoid function

$$g(x) = \frac{1}{1+e^x}$$

The sigmoid function is a smooth version of a step function. It is zero for low inputs. At some point it starts rising rapidly and then, at even higher levels of inputs, it saturates.

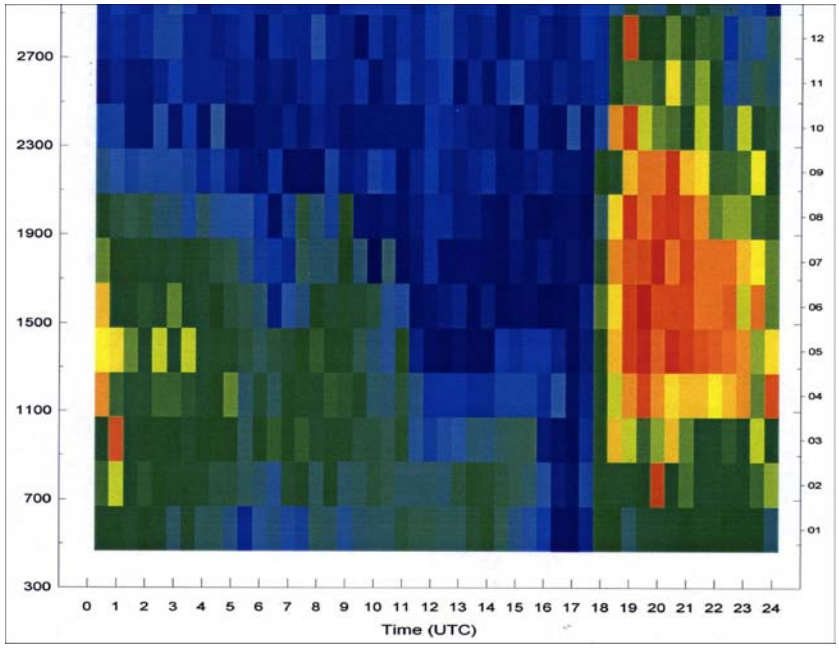


*Figure 3.43.* Signal-to-noise ratio *SNR* of the profiler signal for the same period as in figure 3.42. The warmer the colour, the higher the *SNR*

The feed-forward network finally selected has 5 nodes in the input layer, 25 in the hidden layer and one node in the output layer. Because there are only two classes of interest - birds and no birds - only one output neuron is sufficient. The output value 1 stands for contaminated spectrum and 0 for uncontaminated.

In order to determine the correct weights, so the input is correctly mapped to the output, the neural network must be trained by a set of input features where the output is known. In the period March to April 2002, seven nocturnal campaigns were carried out. Every two seconds, a single-spectrum-profile was recorded, so the total number of the spectra was about 100,000. During this time, about 900 birds were detected by an infrared camera (and, of course, also by the wind profiler). The reason for the relatively small number of birds is that the wind profiler was run in the three-

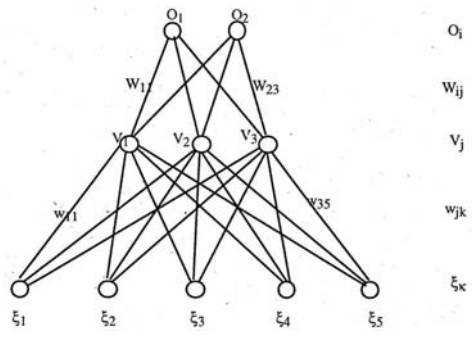


*Figure 3.45.* A two-layer feed-forward network

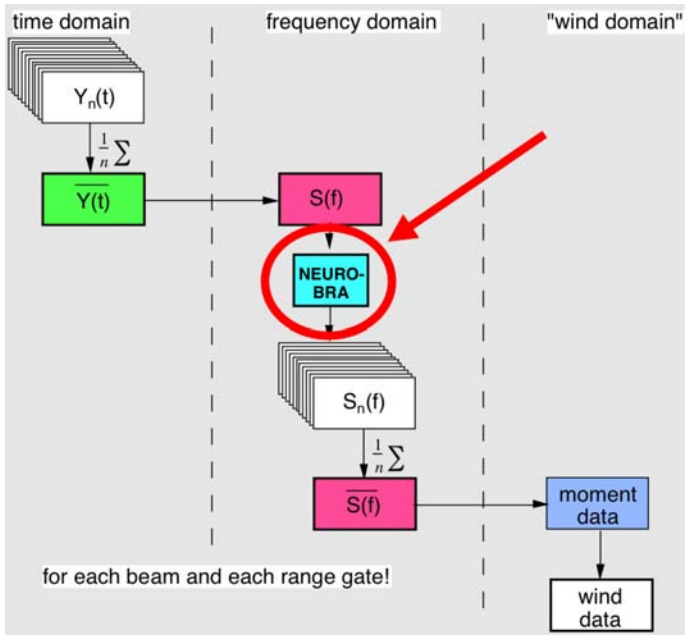


*Figure 3.44.* Processing chain showing the location of fuzzy logic neural-network routine *"neuro-bra"*

beam mode, while the infrared camera was fixed in the vertical. In addition, the infrared system had a smaller aperture angle than the wind profiler, and finally, the weather conditions were not optimal for bird migration. The network was trained with about 6000 data sets and tested with 600 sets.

It turned out that the neural network is "optimally" trained with the following five input features related to the most significant peak in each single spectrum:

- Signal-to-noise ratio
- Signalpower
- Doppler shift
- Skewness
- Kurtosis

**Results and conclusions.** After training the neural network with the roughly 6000 data sets, 96 percent of the test data was correctly classified. This percentage refers to the hit rate.

There are several attempts to increase the quality in wind profiler data. In this project, bird removal is applied to single-spectra-profiles. This method has

the advantage that the loss of data is minimized because a sufficient number of spectra are for averaging.

Haykin (1991) showed, the successes of neural network for classifying birds is much higher than that of purely statistical methods.

The neural network can in principle also be trained to identify rain. In this way wind profilers could be used as rain detectors, estimate the intensity of rain, and - by referring to the vertical velocity profile - measure the height of the melting zone.

Rain-contaminated single-spectrum profiles may show two peaks: one related to the clear-air echo signal, the other to rain. A neural network can be trained to detect the clear-air echo signal and the rain signal separately. First attempts to identify rain were moderately successful, the hit rate was around 75 percent.The main drawback of neural networks is the need for a training data set, i.e., there must be a set of data which allows to teach the software whether there were birds in the beam of the profiler or not. In addition, the training of the network requires a substantial amount of computing efforts, however, once the network is trained, it can easily be integrated into the real-time evaluation software according to figure 3.44.

It is unknown, to which extent instrument characteristics and location influence the performance of a trained network, i.e., it is nor yet clear whether a neural network performing ideally at a given site with a given instrument will function equally well at another site and/or with another instrument.

**3.5.1.7 A comparison of signal processing methods.** Gaffard et al. (2006) used five post-processing methods to estimate moments from spectral data and conducted a comparison of these techniques. The methods used were Vaisala Single Peak (called hereafter SPP), Vaisala Multi-Peak (hereafter MPP), a fuzzy logic method (hereafter FL), a method developed in le Centre de Recherches Météorologiques (hereafter CNRMP), and NCAR Improved Moments Algorithm (hereafter NIMA). Several versions of NIMA were used based on tuning employed. These are hereafter referred to as NIMA_04, NIMA_05, and NIMA_DEFAULT_04.

**Main differences between post-processing methods.** SPP assumes that only ground-clutter contamination can exist in the spectra. Once the ground clutter rejection algorithm has been applied, the maximum in the spectrum is identified as atmospheric signal without taking into account any spatial and time continuities of the solution. No quality control is applied on the high time resolution data. SPP relies solely on the consensus average technique to filter outliers. The other methods (termed advanced post-processing methods in this section) consider other sources of contamination away from the zero Doppler. For MPP and CNRMP more than one maximum in the spectrum are assumed possible atmospheric signals, height and time continuity are used to select the peak. For NIMA and FL, a-priori information about the spectral

| Method | Mode | Field | Bias in $ms^{-1}$ | STD in $ms^{-1}$ | Correl. Coeff. | No. Pts. | Outliers |
|---|---|---|---|---|---|---|---|
| SPP | High | U | - 0.52 | 3.63 | 0.92 | 117 | 8 |
| | | V | 1.21 | 4.34 | 0.79 | | |
| | Low | U | - 0.48 | 4.63 | 0.65 | 329 | 14 |
| | | V | 0.44 | 5.03 | 0.54 | | |
| MPP | High | U | - 0.45 | 2.93 | 0.95 | 110 | 0 |
| | | V | 0.85 | 2.65 | 0.88 | | |
| | Low | U | - 0.23 | 2.10 | 0.89 | 310 | 0 |
| | | V | 0.17 | 2.34 | 0.85 | | |
| NIMA (threshold = 0.5) | High | U | 0.43 | 2.94 | 0.92 | 98 | 0 |
| | | V | 0.76 | 2.73 | 0.86 | | |
| | Low | U | 0.05 | 1.48 | 0.93 | 303 | 0 |
| | | V | 0.40 | 1.68 | 0.89 | | |
| NIMA (threshold = 0.4) | High | U | 0.46 | 2.83 | 0.92 | 108 | 0 |
| | | V | 0.79 | 2.75 | 0.85 | | |
| | Low | U | 0.04 | 1.48 | 0.93 | 322 | 0 |
| | | V | 0.36 | 1.67 | 0.89 | | |
| NIMA_DEFAULT (threshold = 0.4) | High | U | - 0.23 | 3.18 | 0.95 | 60 | 0 |
| | | V | 1.30 | 2.62 | 0.90 | | |
| | Low | U | - 0.14 | 1.67 | 0.94 | 125 | 0 |
| | | V | 0.32 | 2.21 | 0.86 | | |
| CNRMP | High | U | - 0.50 | 2.43 | 0.96 | 94 | 0 |
| | | V | 0.23 | 2.84 | 0.89 | | |
| | Low | U | 0.16 | 1.65 | 0.92 | 251 | 0 |
| | | V | 0.27 | 1.82 | 0.88 | | |
| FL | High | U | - 1.23 | 2.64 | 0.96 | 79 | 2 |
| | | V | 2.03 | 3.16 | 0.83 | | |
| | Low | U | - 0.64 | 2.31 | 0.88 | 296 | 0 |
| | | V | 0.93 | 3.50 | 0.72 | | |

*Table 3.6.* Statistical comparison of all five analyzed post-processing methods in terms of mean error (bias in $ms^{-1}$), standard deviation (in $ms^{-1}$), and correlation coefficient for the horizontal wind components as well as number of matching points available and number of outliers

shape of ground clutter, atmospheric signal, RFI, and height continuity are used to score each element of the spectrum (time continuity is used as well for NIMA). It can viewed at as a generalized multi-peak technique, as to start with, any of the spectrum values can be considered to be atmospheric signal. At the end of the process the part of the spectrum with the maximum atmospheric score is identified as atmospheric signal. The main difference between NIMA and FL is the tuning process. The way FL characterizes the a-priori information and the scoring process is established by a learning database, and it is universal. NIMA offers this possibility as default, and allows the operator to adjust the different weights used in the scoring process to optimize the performance of the method.

**Comparison with rawinsondes.** Table 3.6 shows a statistical comparison of the five analyzed post-processing methods in terms of mean error (bias in $ms^{-1}$), standard deviation (in $ms^{-1}$), and correlation coefficient for the two wind components; number of matching points available and number of outliers are also shown in the table. Outliers are not taken into account in the statistics. The statistics compares the components measured by rawinsonde versus values obtained from the methods investigated (SPP, MPP, NIMA_05, NIMA_04, NIMA_DEFAULT_04, CNRMP, and FL after consensus-average for low mode and high mode, respectively).

**NIMA.** The NIMA algorithm was tuned by NCAR expert. This significantly improved the data availability compared to the un-tuned version (see figures 3.46 and 3.47). However, for a non-expert it is quite difficult to tune this software, i.e., to modify the large number of adjustable parameters in the program.

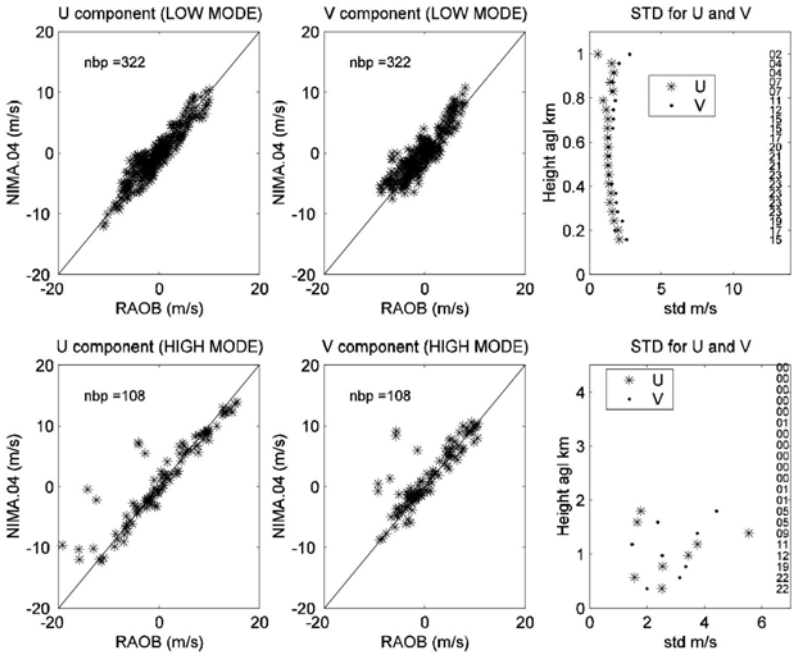


*Figure 3.46.* Statistical comparison for NIMA_04 (tuned version)

**Statistical comparison of consensus winds with rawinsondes.** Figures 3.48 and 3.49 depict a statistical comparison of the consensus averaged wind components obtained from post processing method versus those measured by rawinsonde. Left frames: scatter plot of U component. Centre frames: V com-

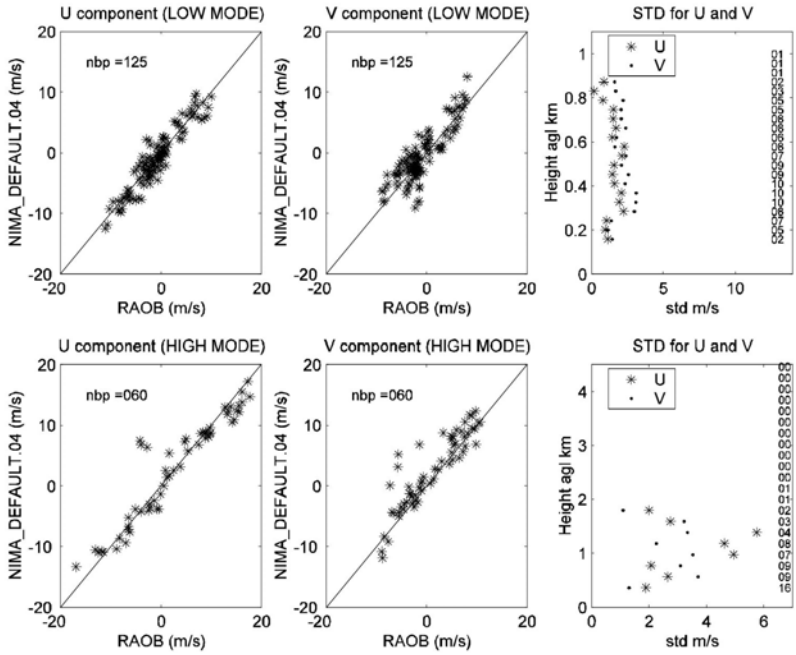


*Figure 3.47.* Statistical comparison for NIMA_DEFAULT_04 (non-tuned version)

ponent. "nbp" is the number of points (number of matching rawinsonde and consensus average winds) in the scatter plot. Right frames: standard deviation of the difference between wind profilers and rawinsonde for each component (stars = U, dots = V) versus altitude above the ground level; numbers on the right indicate the number of matching rawinsonde and consensus average winds used in the comparison for each range gate.

**Conclusions for wind profiling using WPR.** In the data set investigated, all advanced methods performed better than the single peak algorithm SPP, mainly because they were able either to flag the two first gates in the low mode, or to select the true atmospheric signal. Without tuning, NIMA rejected much of the data. The tuning of NIMA increases the data availability and gave the best statistics for the low mode. For the high mode, SPP is performing nearly as well as all the advanced methods in terms of correlation. MPP and CNRMP are very similar and get better statistics than SPP and NIMA for both correlation and standard deviation, however CNRMP retains less data. Because of the limited data set, it is difficult to rank the methods from the best to the worst. this data set shows that, in case of stationary contamination with strong discontinuity in height, all methods using height continuity for selecting the atmospheric signal are able to either reject the wrong signal or find the true one. However,

the limited data set does not show how these methods will perform in cases of strong wind shear. For very noisy data, as was the case for the high mode, only a small improvement was obtained by the advanced methods. The reason might be that the consensus filtering is very efficient for SPP in such cases. However, for high time-resolution data, when the consensus average cannot be applied, it can be expected that advanced post-processing methods perform better than SPP because they use more information from the spectra: multiple peaks as well as height and time continuity. Additional comparisons over longer periods, covering all seasons and different sites, should be performed to truly rank the different post processing methods. In "Combining radar wind profiler and microwave radiometer for the estimation the humidity profile" (Klaus et al., 2006), it is implicitly assumed that the method that gives the best statistical results on the 1st moment estimation also selects the true atmospheric signal, therefore, giving a better estimation of the other moments. Results obtained from MPP, which is better for the high mode, and NIMA_04, which is better for the low mode, have been selected for this purpose. However, the moments estimated by advanced methods have been used in the second step of the work (Klaus et al., 2006), and no significant differences were found. This shows again the difficulties in a reliable ranking of the results obtained for this data set.

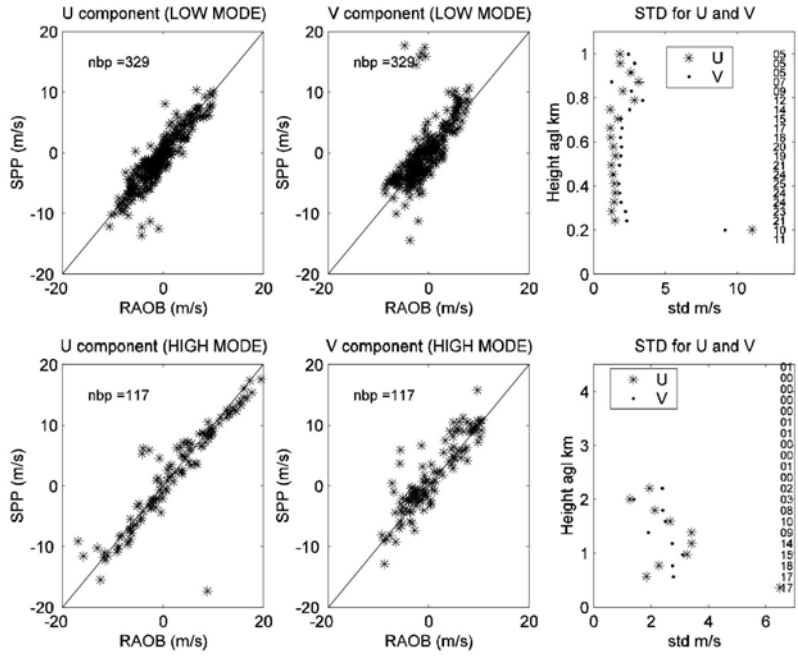


*Figure 3.48.* Statistical comparison for single peak processing (SPP)

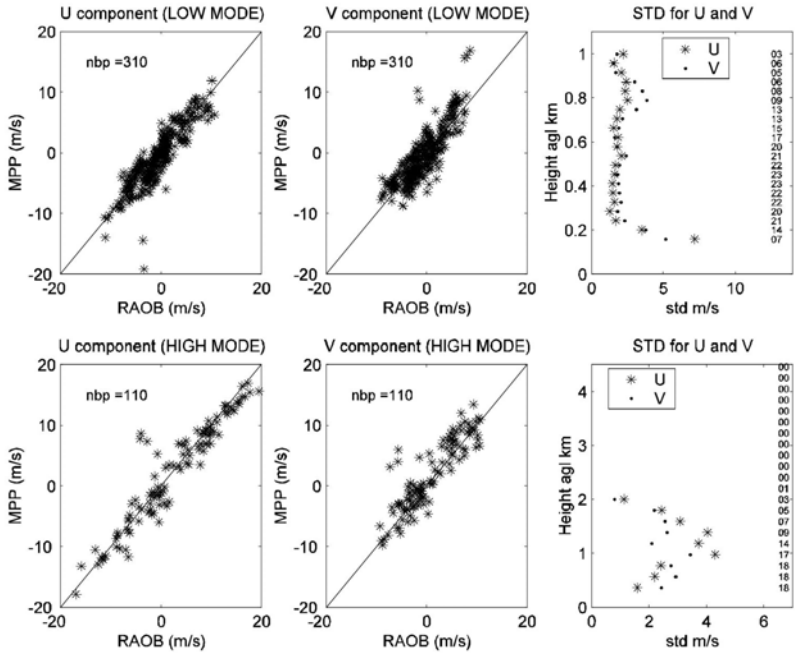


*Figure 3.49.* Statistical comparison for multiple peak processing (MPP)

## 3.5.2 IMPROVED TEMPERATURE PROFILING USING WPR/RASS

The Radio Acoustic Sounding System (RASS) capabilities for measuring virtual temperature profiles have already been widely attested (Angevine et al., 1994). This technology, involving acoustic propagation in the atmosphere can be used both with UHF and VHF radar. However, range coverage is limited to a few kilometers if no advanced and expensive technique, such as the beam ray tracing, is implemented for tracking the acoustic wave advected by the horizontal wind. In studies at CNRM, Toulouse, a RASS was coupled to a 45 MHz VHF radar, and theoretical studies as well as practical observations have shown that the statistical possibility to obtain temperature data decreases sharply above 6 km height (Klaus et al., 2002).

To complement the temperature profile above this range, two other techniques can be exploited when using VHF radar. Both methods make use of the Brunt-Vaisala frequency (N) calculation. The absolute temperature is then extracted by integrating the gradients involved in this equation. Consequently, a reference value is necessary to solve the integral, which makes the technique useful only in the frame of an integrated system where additional instruments

yield at least approximate temperature (and humidity) data for the upper atmosphere.

#### 3.5.2.1 Brunt-Vaisala frequency measurement with a VHF radar.

**Vertical velocity variations.** In this simple technique, variations of the vertical velocity are observed during at least 20 minutes with high temporal resolution (about 1 minute). The capability to determine N from such observations has been mentioned in various studies (Ecklund et al., 1985; Röttger, 1985; Revathy et al., 1996; Mohan et al., 2001). Figure 3.50 shows such an example. The main drawback is the need for vertical beam measurements only during a substantial period which prevents observations in oblique beams that would be necessary for observing horizontal winds.

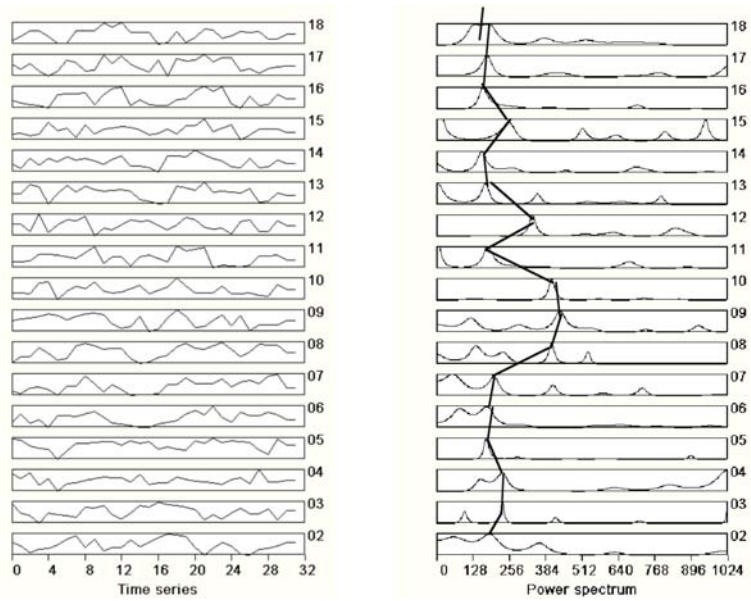


*Figure 3.50.* Example of vertical velocity time series (left frame) and the corresponding spectra showing the Brunt-Vaisala frequency at the highest peaks (right frame). Data were collected by the 45 MHz radar at CNRM, Toulouse

**Using return signal power in the dry atmosphere.** The second technique is more suitable for operational wind profiler because it exploits the return signal power ($P_r$) from oblique beams to calculate the dry refractive index gradient ($M_D$). However, it is limited to ranges where humidity can be neglected. N is calculated using the equation (for details, see Hooper et al. (2004)):

$$N^2 = K' \cdot z \cdot \exp(\frac{z}{H})\sqrt{P_r} \tag{3.41}$$

in the variable $K'$, parameters characterizing the radar as well as the state of the atmosphere are combined. In addition, a constant-lapse-rate atmosphere must be assumed which might complicate the evaluation if both the troposphere and the stratosphere are to be sounded simultaneously.

**3.5.2.2 Temperature retrieval from Brunt-Vaisala frequency.** Having obtained N by either one of the above techniques, basic equation for N needs to be solved for temperature T:

$$N^2 = \frac{g}{T}\left(\frac{dT}{dz} + \Gamma\right) \quad , \tag{3.42}$$

where $\Gamma$ is the adiabatic lapse rate assumed to be constant.

According to Revathy et al. (1996) the equation can be solved as:

$$T(z) = \frac{1}{S(z)}\left[S(z_o)T_o - \Gamma \int_{z_o}^{z} S(x)dx\right] \quad , \tag{3.43}$$

where

$$S(z) = \exp\left[-\int_{z_o}^{z} \frac{N^2(y)}{g}dy\right] \quad . \tag{3.44}$$

$T_o$ is a reference temperature value at $z_o$ height.

The reference temperature $T_o$ can be extracted from the RASS profile at a higher range gate. However, this value may not be precise enough for a good profile estimation, because it is quite sensitive to the radar calibration. Consequently, another temperature point is desirable in order to avoid any major deviation of the profile. Such reference points can be provided, e.g., by commercial jet liners at around 10 km height or by a radiometric profiler giving a mean temperature value for a deeper layer.

**3.5.2.3 Preliminary results for temperature profiling.** During the Mesoscale Alpine Program (MAP) a VHF radar was operated continuously during a two month period in the region of Milano, Italy. At this location also about one hundred radio sondes were launched allowing a good statistical validation and various simulations. As a typical example of the capability of the method, temperature profiles between 6 and 10 km height are compared (figures 3.51 and 3.52). At lower range (6 km), temperature is retrieved from RASS measurements while temperature at higher altitude (10 km) is obtained from a jetliner. For the comparisons with the radiosonde ascents shown in figures 3.51 and 3.52, two sets of data were used: (a) the results obtained by the technique described here, and (b) profile data obtained by simple interpolation of the temperature values between the lower and the higher range (i.e., 6 and 10 km). An improvement in both standard deviation and bias by a factor of

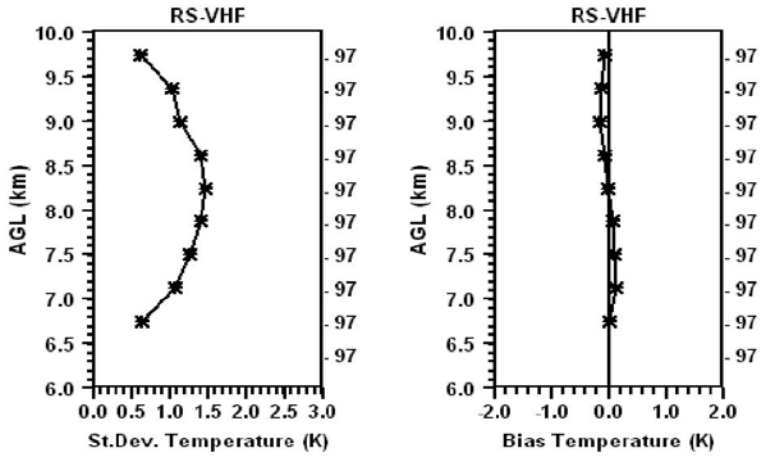


*Figure 3.51.* Statistical comparison (standard deviation and bias) of the temperature profile obtained from the VHF profiler versus the one measured by radiosondes (RS) by using. Here, the return signal power from the VHF radar is used, and the temperature is supposed to be known at 6 and 10 km height. Numbers at right represent the number of cases taken for the statistics at the range gate in question

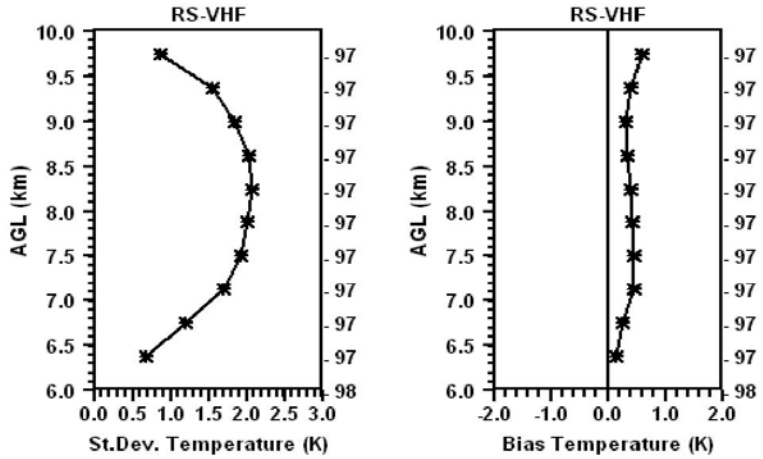


*Figure 3.52.* Same as in figure 3.51 but VHF data being replaced by interpolated values between 6 and 10 km height

about 2 can be noted. Particular examples show that a systematic detection of the tropopause height - which would allow different lapse rates in the retrieval of N - may further improve the capabilities of the technique.

## 3.5.3 ALGORITHMS FOR HUMIDITY PROFILING USING WPR (/RASS)

Two main algorithms have been used to extract humidity gradients from radar data. The first one uses the refractive index gradient $M$ (Tsuda et al., 2001), the second one the potential refractive index $\phi$ (Gossard et al., 1998). Both require the reflectivity data and the turbulent dissipation rate values calculated from the zeroth and the second moment, respectively, of the radar signal spectrum.

### 3.5.3.1 Preliminary calculations from the zeroth and the second moment of the WPR spectra signal: Reflectivity and turbulence dissipation rate.

**Reflectivity.** According to VanZandt et al. (1978), reflectivity $\eta$ can be calculated from

$$\eta = \frac{9\pi}{2} \cdot \frac{c\,kB(T_c + T_{rx}/\alpha)}{\alpha P_t F_r A_e \cos\beta} \left(\frac{z}{\Delta z}\right) \left(\frac{S}{N}\right) \quad , \tag{3.45}$$

with $c$ = velocity of light, $k$ = Boltzmann's constant, $T_c$ = cosmic noise temperature, $T_{rx}$ = receiver noise temperature, $\alpha$ = efficiency of the radar antenna and transmission line, $P_t$ = peak transmitted power, $F_r$ = pulse repetition frequency, $A_e$ = effective antenna area, $\beta$ = antenna beam elevation angle, $z$ = range, $\Delta z$ = range resolution, and $S/N$ = signal-to-noise ratio.

**Turbulence dissipation rate.** There are various equations for deriving the turbulent dissipation rate $\varepsilon$ from the spectral width $\sigma$ of the radar signal spectrum. Hocking (1983) proposed

$$\varepsilon = 0.5 \cdot N\sigma^2 \quad , \tag{3.46}$$

where $N$ = Brunt-Vaisala frequency and

$$N^2 = g\frac{d\ln\theta}{dz} = \frac{g}{T}\left(\frac{dT}{dz} + \Gamma\right) \tag{3.47}$$

while Gossard et al. (1998) suggested

$$\varepsilon = \frac{1}{\delta}\left[\frac{\sigma^2}{\frac{3}{2}\Gamma\left(\frac{5}{3}\right)\alpha\gamma^2}\right] EQ \tag{3.48}$$

with $\alpha$ = Kolmogorov constant ($\approx 1.6$), $\Gamma$ = Gamma function, $a$ = half the diameter of the (circular) beam cross section, and $b$ = half-length of the pulse. For $a \geq b$:

$$\begin{aligned} \delta &= a \\ \gamma^2 &= 1 - 4h/15 - h^2/105... \\ h &= 1 - (b/a)^2 \end{aligned}$$

For $a < b$:

$$\begin{aligned} \delta &= b \\ \gamma^2 &= 1 - 4h/15 - 8h^2/105... \\ h &= 1 - (a/b)^2 \end{aligned}$$

The $\sigma$ values provided by the profiler need to be corrected because of wind shear and other disturbing factors (see for example Jacoby-Koaly et al. (2002).

**3.5.3.2 Humidity via the refractive index gradient.** As mentioned, once reflectivity and turbulent dissipation rate are known, humidity can be computed from the refractive index gradient M. Again there are several relationships in the literature for deriving this value from the radar data ($\eta$ and/or $\varepsilon$). According to Gage and Balsley (1980) it is

$$|M| = K \cdot \sqrt{\eta} \quad , \tag{3.49}$$

while Tsuda et al. (2001) suggests

$$|M| = \frac{1}{\sqrt[3]{\varepsilon}} \sqrt{F\eta} \cdot N \quad . \tag{3.50}$$

Subsequently, the humidity equation can be solved

$$\frac{dq}{dz} + A(z)\, q = B(z) \quad , \tag{3.51}$$

where

$$A(z) = -\frac{2N^2}{g} \tag{3.52}$$

and

$$B(z) = \left( 1.652 \frac{T^2}{p} M + \frac{T}{7800} \frac{N^2}{g} \right) \quad . \tag{3.53}$$

This leads to

$$q(z) = \theta^2 \left[ \int_{z_0}^{z} B(z) \theta^{-2} dz + \frac{q_0}{\theta_0^2} \right] \quad , \tag{3.54}$$

with $\theta$ = potential temperature, $T$ = absolute temperature, $p$ = atmospheric pressure, $g$ = acceleration of gravity, $q_0$ and $\theta_0$ = respectively humidity and potential temperature at boundary-layer height.
As suggested by Hooper et al. (2004), $p/T$ can be approximated as

$$\frac{p}{T} \approx \rho_0 \cdot \exp\left( \frac{-z}{\overline{H}} \right) \quad , \tag{3.55}$$

with $\rho_0$ = mean density at sea level and $\overline{H}$ = mean scale height which may be considered as constant. Hence, for solving the humidity equation, one needs

$M$ and $T$ profiles, ground data ($\rho_0$), and boundary conditions ($q_0$ and $\theta_0$) at a given range or over a defined layer.

In this process, attention must be paid to the sign ambiguity of $M$. In reality, $M$ can become positive in 10 to 20% of the cases. The ambiguity can be avoided, if one realizes that –in general!– $M$ becomes positive whenever $N^2$ is below a certain threshold of a few $10^{-5}$rad$^2$ s$^{-2}$ (Tsuda et al., 2001).

**3.5.3.3 Humidity via the potential refractive index gradient $\phi$.** The second approach uses the expression involving the vertical gradient of the potential refractive index $\phi$. According to Gossard et al. (1998)

$$\left(\frac{d\phi_0}{dz}\right)^2 = \frac{c_\varphi^2}{c_w^2}\left(\frac{L_w}{L_\varphi}\right)^{4/3}\left(\frac{du_0}{dz}\right)^2 \quad , \tag{3.56}$$

where $c_\phi^2$, i.e. the structure parameter of the potential refractive index is defined as

$$c_\phi^2 = \frac{\eta}{0.38}\,\lambda^{1/3} \tag{3.57}$$

and $\lambda$ is the radar signal wave length. $c_w^2$ is the structure parameter of the wind velocity along the vertical direction defined as

$$c_w^2 \approx 2.80 \cdot \varepsilon^{2/3} \quad , \tag{3.58}$$

and $L_w$ is the outer scale of the velocity along the vertical direction, and $L_\varphi$ is the outer scale of the refractive index field respectively.
According to Gossard et al. (1982) it is

$$\frac{L_w}{L_\varphi} \approx 4 \quad , \tag{3.59}$$

with $du_0/dz$ as mean vertical gradient of wind speed. With $u$ as zonal and $v$ as meridional wind component, the this relation becomes

$$\left(\frac{du_0}{dz}\right)^2 = \left(\frac{du}{dz}\right)^2 + \left(\frac{dv}{dz}\right)^2 \quad . \tag{3.60}$$

The humidity gradient equation can then be expressed as

$$\frac{dq}{dz} = \left[\frac{d\phi}{dz} + a_0\frac{d\theta}{dz}\right] b_0 \quad , \tag{3.61}$$

which becomes by integration

$$q(z) = q(z_0) + [\varphi(z) - \varphi(z_0) + a_0\,[\theta(z) - \theta(z_0)]\ ]\, b_0 \quad . \tag{3.62}$$

Here, $a_0$ and $b_0$ are assumed to be constant. They are estimated using approximations based on the standard atmosphere.

**3.5.3.4 Deficits in humidity profiling.** Humidity profiling using WPR cannot work independently of complementary instruments, but can be accomplished by an appropriate integrated system. There are a number of requirements when applying this technique:

- The temperature profile. This parameter -which does not need to be very accurate- can be extracted from radiometric measurements (see (Klaus et al., 2006)).
- The surface air density. From this and the available temperature profile, pressure at the different range gates is derived. Subsequently, the potential temperature profile can be computed; this is needed to solve the humidity equation.
- A humidity value either at a given height or over a larger layer; this is necessary to integrate the absolute humidity values from the gradients.
- A good calibration of the profiler.

## Bibliography

Angevine, W. M., W. L. Ecklund, D. A. Carter, K. S. Gage, and K. P. Moran: Improved radio acoustic sounding techniques, *J. Atmosph. Ocean. Technol.*, **11**, 42–49, 1994.

Bianco, L. and J. M. Wilczak: Convective boundary layer mixing depth: Improved measurement by Doppler radar wind profiler using fuzzy logic, *J. Atmosph. Ocean. Technol.*, **19**, 1745–1758, 2002.

Boisse, J.-C., V. Klaus, and J.-P. Aubagnac: A wavelet transform technique for removing airplane echoes from ST radar signals, *J. Atmosph. Ocean. Technol.*, **16**, 334–346, 1999.

Bruderer, B.: Vogelzugforschung im Bereich der Alpen 1980-1995. *Ornitholog. Beob.*, **93**, 119–193, 1996.

Carter, D. A.: Signal Processing at the Poker Flat MST Radar, *Handbook for Middle Atmosphere Program*, **9**, 532–534, 1983.

Chilson, Ph. B., T.-Y. Yu, R. G. Strauch, A. Muschinski, and R.D. Palmer: Implementation and Validation of Range Imaging on a UHF Radar Wind Profiler, *J. Atmosph. Ocean. Technol.*, **20**, 987–996, 2003.

Chilson, Ph. B.: The Retrieval and Validation of Doppler Velocity Estimates from Range Imaging, *J. Atmosph. Ocean. Technol.*, **21**, 1033–1043, 2004.

Clothiaux, E. E., R. S. Penc, D. W. Thomson, T. P. Ackerman, and S. R. Williams: A first-guess feature-based algorithm for estimating wind speed in clear-air Doppler radar spectra, *J. Atmosph. Ocean. Technol.*, **11**, 888–908, 1994.

Cornish, C. R.: Parameterization of Spectra, *Handbook for Middle Atmosphere Program*, **9**, 535–542, 1983.

Cornman, L. B., R. K. Goodrich, C. S. Morse, and W. L. Ecklund: A Fuzzy Logic Method for Improved Moment Estimation from Doppler Spectra, *J. Atmosph. Ocean. Technol.*, **15**, 1287–1305, 1998.

COST-76 Final Report, Bruxelles, 2003.

Ecklund, W. L., B. B. Balsley, D. A. Carter, A. C. Riddle, M. Crochet, and R. Garello: Observations of vertical motions in the troposphere and lower stratosphere using three closely spaced ST radars, *Radio Sci.*, **20**, 1196–1206, 1985.

Gaffard, C., L. Bianco, V. Klaus, and M. Matabuena: Evaluation of moments calculated from wind profiler spectra: A comparison between five different processing techniques, *Meteorol. Zeitschr.*, **15**, 73–86, 2006.

Gage, K. S. and B. B. Balsley: On the scattering and reflection mechanisms contributing to clear air radar echoes from troposphere, stratosphere and mesosphere, *Radio Sci.*, **15**, 243–257, 1980.

Ghebrebrhan, O.: Full Decoding of Truncated Ranges for ST/MST Radar Applications, *IEEE Trans. Geosci. Remote Sens.*, **28**, 14–18, 1990.

Gossard, E. E., R. B. Chadwick, W. D. Neff, and K. P. Moran: The use of ground-based Doppler radars to measure gradients fluxes and structure parameters in elevated layers, *J. Appl. Meteor.*, **21**, 211–226, 1982.

Gossard, E. E., D. E. Wolfe, K. P. Moran, R. A. Paulus, K. D. Anderson, and L. T. Rogers: Measurement of clear-air gradients and turbulence properties with radar wind profilers, *J. Atmosph. Ocean. Technol.*, **15**, 321–342, 1998.

Griesser, T. and H. Richner: Multiple Peak Processing Algorithm for Identification of Atmospheric Signals in Doppler Radar Wind Profiler Spectra, *Meteorol. Zeitschr.*, **7**, 292–302, 1998.

Haykin, S.: Classification of Radar Clutter Using Neural Networks, *IEEE T NEURAL NETWORK*, **2**, 589–600, 1991.

Hildebrand, P. H. and R. S. Sekhon: Objective determination of the noise level in Doppler spectra, *J. Appl. Meteorol.*, **13**, 808–811, 1974.

Hocking, W. K.: On the extraction of atmospheric turbulence parameters from Radar backscatter Doppler spectra. P.1. Theory, *J. Atmosph. Terr. Phys.*, **45**,No.(2/3), 89–102, 1983.

Hooper, D. A., J. Arvelius, and K. Stebel: Retrieval of atmospheric static stability from MST radar return signal power, *Ann. Geophysicae*, **22**, 3781–3788, 2004.

Jacoby-Koaly, S., B. Campistron, S. Bernard, B. Bénech, F. Ardhuin-Girard, J. Dessens, E. Dupont, and B. Carissimo: Turbulent Dissipation Rate in the Boundary Layer via UHF Wind Profiler Doppler Spectral Width Measurements, *Bound.-Lay. Meteorol.*, **103**, 361–389, 2002.

Jordan, J. R., R. J. Lataitis, and D. A. Carter: Removing Ground and Intermittent Clutter Contamination from Wind Profiler Signals Using Wavelet Transforms, *J. Atmosph. Ocean. Technol.*, **14**, 1280–1297, 1997.

Karayiannis, N. B., R. Kretzschmar and H. Richner: Pattern classification based on quantum neural networks, *in:* S.K. Pal and A. Pal (eds.) *Pattern Recognition: From classical to modern approaches*. World Sci. Publ., Singapore, ISBN No. 981-02-4684-6, 612pp., 301–328, 2001.

Klaus, V., J-P. Aubagnac, J. Van Baelen, G. Cherel, R. Durbe, and A. Frappier: New developments with the CNRM INSU/Meteo VHF radar RASS, FDI and upgraded processing techniques, *Meteorol. Zeitschr.*, **7**, 355–365, 1998.

Klaus, V., G. Chérel, P. Goupil, and N. Pénetier: RASS Developments on the VHF Radar at CNRM/Toulouse Height Coverage Optimization, *J. Atmosph. Ocean. Technol.*, **19**, 967–979, 2002a.

Klaus, V., L. Bianco, C. Gaffard, M. Matabuena, and T. Hewison: Combining radar wind profiler and microwave radiometer for the estimation of atmospheric humidity profiles, *Meteorol. Zeitschr.*, **15**, 87–98, 2006.

Lehmann, V. and G. Teschke: Wavelet based methods for improved wind profiler signal processing. Proc. *9th Workshop on Technical and Scientific Aspects of MST Radar Combined with COST76 Final Profiler Workshop*, Toulouse, France, SCOSTEP & Météo-France, 455–458, 2000.

Merritt, D. A.: A statistical averaging method for wind profiler Doppler spectra, *J. Atmosph. Ocean. Technol.*, **12**, 985–995, 1995.

Mohan, K., D. N. Rao, T. N. Rao, and S. Raghavan: Estimation of temperature and humidity from MST radar observations, *Ann. Geophysicae*, **19**, 855–861, 2001.

Morse, C. S., R. K. Goodrich, and L. B. Cornman: The NIMA Method for Improved Moment Estimation from Doppler Spectra, *J. Atmosph. Ocean. Technol.*, **19**, 274–295, 2002.

Revathy, K., S. R. P. Nair, and B. V. K. Murthy: deduction of temperature profile from MST radar observations of vertical wind, *Geophys. Res. Lett.*, **23**, 285–288, 1996.

Richner H. and R. Kretzschmar: Bird identification on 1290-MHz wind profiler data applying neural networks and neurofuzzy systems, *Phys. Chem. Earth (B),* **26**, 181–186, 2000.

Riddle, A.C. and W.M. Angevine, 1992: Ground clutter removal from profiler spectra. Proc. *5th Workshop on Technical and Scientific Aspects of MST Radar*, SCOSTEP Secr., Urbana, III, 418–420, 1992.

Röttger, J.: Determination of the Brunt-Vaisala frequency from vertical velocity spectra, *Handbook for MAP*, **20**, 168–172, 1985.

Ruffieux, D., J. Nash, P. Jeannet, and J. L. Agnew: The COST-720 Temperature, hUmidity, and Cloud profiling campaign: TUC, *Meteorol. Zeitschr.*, **15**, 5–10, 2006.

Stankov, B. B., E. E. Gossard, B. L. Weber, R. J. Lataitis, A. B. White, D. E. Wolfe, and D. C. Welsh: Humidity gradient profiles from wind profiling radars using the NOAA/ETL advanced Signal Processing System (SPS), *J. Atmosph. Ocean. Technol.*, **20**, 3–22, 2003.

Strauch, R. S.: Data Analysis Techniques: Spectral Processing, *Handbook for Middle Atmosphere Program*, **9**, 528–531, 1983.

Strauch, R. G., D. A. Merritt, K. P. Moran, K. B. Earnshaw, and D. Van de Kamp: The Colorado Wind-profiling Network, *J. Atmosph. Ocean. Technol.*, **1**, 37–49, 1984.

Tsuda, T., M. Miyamoto, and J. Furumoto: Estimation of a Humidity Profile Using Turbulence Echo Characteristics, *J. Atmosph. Ocean. Technol.*, **18**, 1214–1222, 2001.

Vaisala Brochure, NIMA, 2004.

VanZandt, T. E., J. L. Green, K. S. Gage, and W. L. Clark: Vertical profiles of refractivity turbulence structure constant: Comparison of observation by the Sunset radar with a new theoretical model, *Radio Sci.*, **13**, 819–829, 1978.

Weber, B. L., D. B. Wuertz, D. C. Welsh, and R. McPeek: Quality Controls for Profiler Measurements of Winds and RASS Temperature, *J. Atmosph. Ocean. Technol.*, **10**, 452–464, 1993.

Wilczak, J. M., R. G. Strauch, F. M. Ralph, B. L. Weber, D. A. Merritt, J. R. Jordan, D. E. Wolfe, L. K. Lewis, D. B. Wuertz, S. A. McLaughlin, R. R. Rogers, A. C. Riddle, and T. S. Dye: Contamination of wind profiler data by migrating birds: Characteristics of corrupted data and potential solutions, *J. Atmosph. Ocean. Technol.*, **12**, 449–467, 1995.

Woodman, R. F.: Spectral Moment Estimation in MST Radars, *Handbook for Middle Atmosphere Program*, **9**, 548–562, 1983.

# 3.6 SODAR / RASS

Erich Mursch-Radlgruber[1], S. Bradley[2], and D. A. M. Engelbart[3]

[1] *University of Natural Resources and Applied Life Sciences, Institute for Meteorol. and Physics, Vienna, Austria*
✉ Erich.Mursch.Radlgruber@boku.ac.at

[2] *University of Auckland, Physics Department, Auckland, New Zealand*

[3] *German Meteorol. Service (DWD), Richard-Aßmann Observatory, Lindenberg, Germany*

## 3.6.1 INTRODUCTION

Acoustic remote sensing (**sodar** = *sound detection and ranging*) uses characteristics of sound wave propagation to obtain data on atmospheric parameters. The method allows finding wind velocity and direction, and determination of turbulence intensity from fluctuations of amplitude and phase of the sound wave. Acoustic remote sensing is based on the scattering of sound waves from turbulent inhomogeneities in the atmosphere. Because the scattering by temperature and velocity inhomogeneities is more then 1000 times stronger for sound than for electromagnetic waves (table 3.7), and therefore the scattering cross-section about a million times greater, it offers high potential for high-resolution measurements close to the ground. A drawback is the high attenuation of the acoustic waves in the atmosphere. This attenuation increases strongly with increasing frequency, so that the measurement range is limited to maximum heights of about 1000 m. A special limiting factor is the range of useful frequencies which are most of the time between 2 and 6 kHz. This is in the audible range and may close to habitations exhibit quite a problem.

| Variation | Acoustic | Radio | Optic |
|---|---|---|---|
| **1 K temperature** | 1700 | 1 | 1 |
| **1 m/s velocity** | 3000 | $2*10^{-6}$ | – |
| **1 mb vapour pressure** | 180 | 4 | 0.04 |

*Table 3.7.* Refractive index variation (Wesely, 1976)

Sodar technology is well established as a tool for visualising and quantifying atmospheric dynamics in the lowest few hundred meters. For more than thirty years sodars have been used for boundary layer studies (Brown and Hall, 1978; Neff and Coulter, 1985; Singal, 1997). A Doppler sodar is an instrument which measures wind speed and direction within a number of vertically contiguous volumes above the ground. Each measurement is obtained by transmitting a

pulse of sound upward into the atmosphere and then measuring the change in pitch of sound reflected from the combination of turbulent density fluctuations within each distinct volume. Transmission of acoustic pulses is done sequentially into several directions tilted slightly off-vertical so that separate wind vector components can be estimated in these directions and both wind speed and direction estimates can be inferred in each height range. Some post-processing using consistency algorithms may mean that data obtained from each volume are not strictly independent, but essentially a wind profile is obtained.

At each altitude range, the wind speed estimate $\hat{v}$ and the wind direction estimate $\hat{\theta}$ are obtained from inputs comprising

- knowledge of the transmitted sound frequency
- an estimated speed of sound
- an estimate of the angle of transmission from the vertical
- a set of frequencies at which echo strength is measured: the frequency at which peak echo power occurs is a measure of wind speed component in the direction of sound transmission (Doppler analysis)
- an estimation of the compass orientation of the plane containing the transmitted beam and the vertical.

The height range at which $\hat{v}$ and $\hat{\theta}$ are obtained is estimated from

- an estimated speed of sound
- an estimate of the angle of transmission from the vertical.

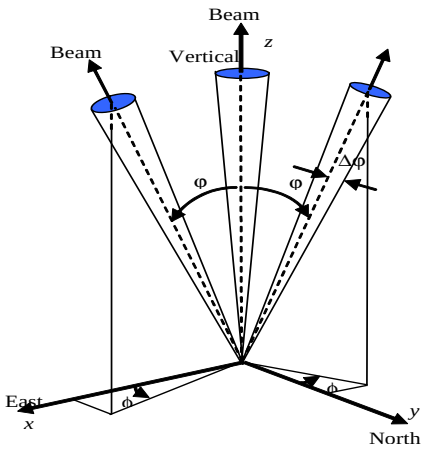


*Figure 3.53.* Mono-static antenna configuration

The most common measurement arrangement is to measure three beams for the three wind components (see Fig. 3.53). Also 5 beams are sometimes used.

When the transmit antenna are also used to receive the scattered sound, it is called a mono-static setup and the scattered signal is pure 180 degree backscatter. Acoustic scattering is unique in that the angular dependence of scattering from temperature and velocity in homogeneities is particularly different (Fig. 3.54). This offers the possibility to discriminate between scattering from temperature and velocity fluctuations (temperature structure parameter $c_T^2$ and velocity structure parameter $c_v^2$. But to measure both structure parameters the transmit and receive antennas must be separated which is called bi-static setup.

All the commercially available sodar systems are mono-static and therefore use only the scattered signals from temperature inhomogeneities. This is another limiting factor since under atmospheric conditions with small temperature changes (neutral atmosphere) the instrument's measurement range will be shorter.

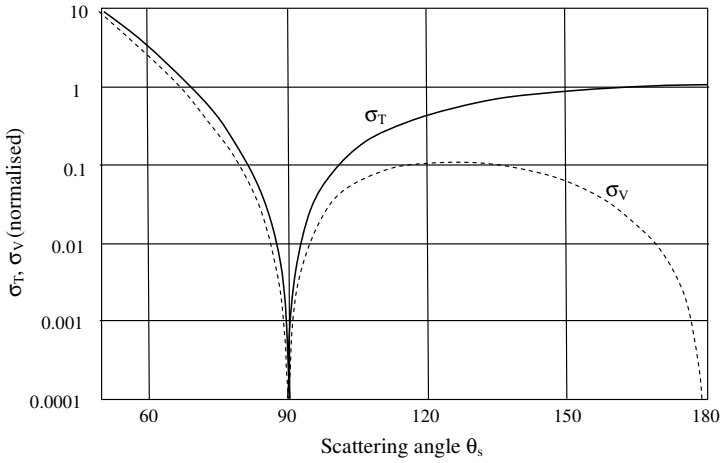


*Figure 3.54.* Angular dependence of scattering

Conventional sodar systems work at 2 to 3 kHz with single or multiple pulses (multiple frequencies) to achieve greater height range. The pulse length is between 50 and 100 ms which is the main limiting factor for range resolution.

To achieve greater range resolution, higher frequencies between 4 and 6 kHz are often used. As a result of attenuation, this limits the useful range to 200 m. Because of their smaller size, such systems are called mini sodar.

Given the above system description, it is easy to understand that a sodar is a useful instrument for boundary-layer applications. The biggest drawback perhaps is, that the systems use frequencies in the human-audible frequency range. Also, as with RADAR systems, sodars have the problem of being sensitive to

reflections from surrounding objects (the clutter problem), which restricts useful measurement sites.

Most of the commercially available systems have array antennas made from piezo tweeters, with phasing of the array to produce the necessary beams. Therefore the instrument is limited to sequential measurements of the beams. Because of the low speed of sound a few seconds are necessary for a complete profile. By using piezo tweeters the antennas are small and light and therefore they are easy to setup.

### 3.6.2 RASS AS AN EXTENSION TO SODAR

RASS (Radio Acoustic Sounding System) was introduced by Marshall et al. (1972) as tracking the acoustic pulse from a sodar with a continuous electromagnetic wave CW-RADAR in order to derive temperature profiles from the measured speed of sound. The speed of sound in the direction of transmission is a function of velocity and temperature. If the velocity in the vertical is known, the temperature can be calculated.

From the travel time of the acoustic pulse the actual measurement height is determined with a first guess sound velocity. From the frequency shift of the electro-magnetic reflected signal the local sound velocity is derived by Doppler analysis. Therefore this type of RASS is called a Doppler-RASS or sodar/RASS (Peters and Kirtzel, 1994a; Peters et al., 1996). The most common RASS is the Bragg-RASS as an extension to a wind profiler (see section 4.5 on Windprofiler/RASS).

To get optimal reflections from the acoustic pulse the wave length of the acoustic pulse has to be half of the electro-magnetic signal (the Bragg condition). Since the acoustic pulse suffers from Doppler shift due to the wind the pulse has to have a certain bandwidth of frequencies to guarantee a Bragg match. Petenko and Bedulin (1994) suggested linear frequency modulation of the acoustic pulses to avoid the problem arising from Bragg mismatch. Some experience with a RASS system with an acoustic chirp is reported by Engelbart et al. (1999).

The reflected Doppler shifted electro-magnetic signal is analysed with the sodar software after mixing with the transmitted electro-magnetic signal.

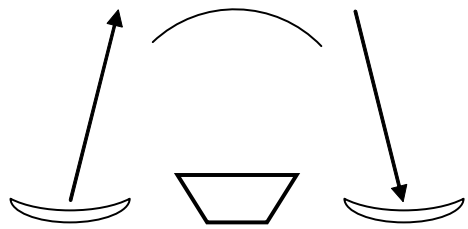

*Figure 3.55.* Antenna of a Doppler-RASS: Sound source in the center and electromagnetic transmitter / receiver on the left and right side, respectively

The separated transmitter and receiver antennas are placed symmetrically around the acoustic antenna (see Fig. 3.55). Since the acoustic wave is moved by the horizontal wind, the focus of the reflected electro-magnetic wave easily moved out of the receiving antenna. This is the biggest problem for RASS systems and is the major factor for height limitations. Stronger horizontal winds mean a smaller height range. Typical height coverage is between 200 m and 500 m with a 1290 MHz RADAR system.

The main use of the sodar/RASS is to measure temperature profiles. By tracing acoustic pulses with different angles it is possible to measure also the wind components. Four independent beams are necessary to get the three wind components and temperature. This has been shown by Marakova (1980) with a double-beam RASS. The signal quality of a RASS is very high and a special benefit is it is clutter-free. Since the target acoustic pulse is moving at the speed of sound it easily can be separated in the signal processing from ground reflections (clutter). Because of the high signal quality, measurement of momentum transport in the lower boundary layer is possible (Peters and Kirtzel, 1994b; Hirsch and Peters, 1998).

### 3.6.3 TYPICAL APPLICATIONS AND LIMITATIONS OF SODAR/RASS

The characteristics of sodar systems limit themselves for the exploration of the atmospheric boundary layer. Also with the RASS extension the height limit is about 500m, mainly because of beam bending by strong wind.

Some of the basic boundary layer parameters are measured directly by sodar with Doppler capability:

- Acoustic scattering cross section
- Horizontal mean wind components
- Vertical wind variance

### 3.6.4 ACOUSTIC CROSS SECTION - BACK SCATTER INTENSITY

The scattered signal is very useful for visualizing vertical structure of the boundary layer. During stable situations it shows the layering of regions with strong temperature fluctuations, which is mainly a consequence of strong temperature gradients. Wave structures from gravity currents associated with drainage flows, land/sea breezes or cold fronts play a key role in generating solitons (Cheung and Little, 1990; Rao et al., 2002), and these can easily be analysed with sodar. An example with the analysis of the vertical velocity is shown in figure 3.56.

With the use of a network of three or more sodar antennas the whole set of wave parameters can be obtained (Bull, 1997; Hünerbein and Bradley, 2004).

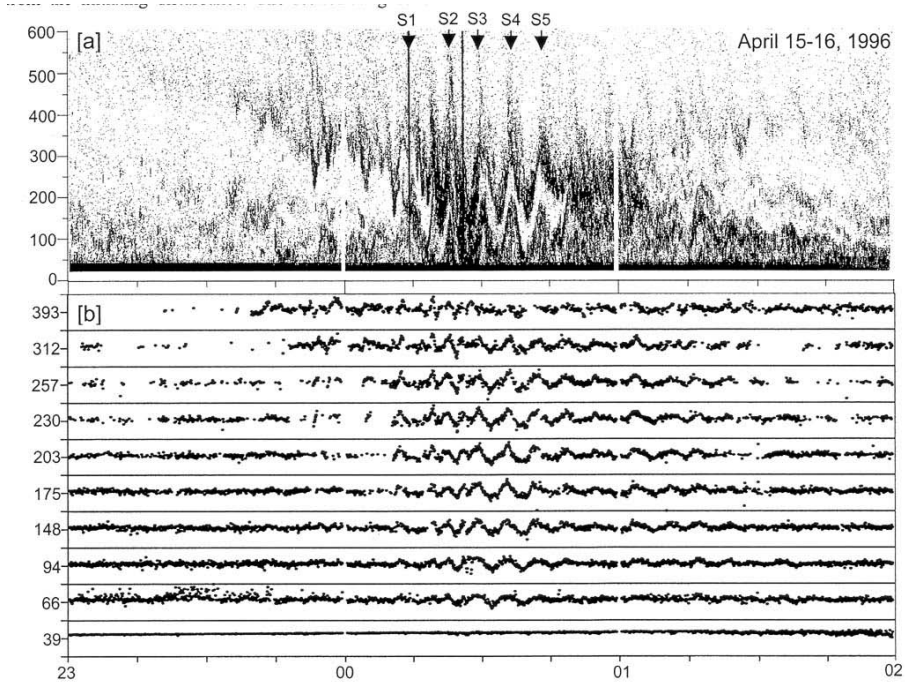


*Figure 3.56.* Sodar facsimile record (a) and (b) time series of vertical wind (+3 m/s) (Rao et al., 2002)

## 3.6.5 MEAN WIND AND VARIANCES

From the many comparative studies done in the past the major conclusion is that sodar provide excellent estimates of mean wind and direction (Kallistratova, 2002). Quite accurate estimates can be made for the vertical variance $\sigma_w$ but rather poor for the horizontal wind variances $\sigma_u$ and $\sigma_v$. This is mainly a consequence of the slightly off-vertical tilted beam directions.

Figure 3.57 shows an example of the mean wind profile (15 min mean) from a mini sodar

## 3.6.6 MIXING HEIGHT

The determination of mixing height is partially a problem of no universally accepted definition of this important scaling parameter. As long as the mixing height does not exceed the range of the sodar, a sodar will be a good tool to estimate it. But during convective conditions very often the useful range of a sodar will not be enough to measure the mixing height directly.

The determination of mixing height can be done by visual inspection of the time-height plot of back scattered intensity (facsimile plot), by using free convection air similarity theory, where $\sigma_w^2$ is related to the mixing height or boundary layer profile fits (Asimakopoulos et al., 2002).

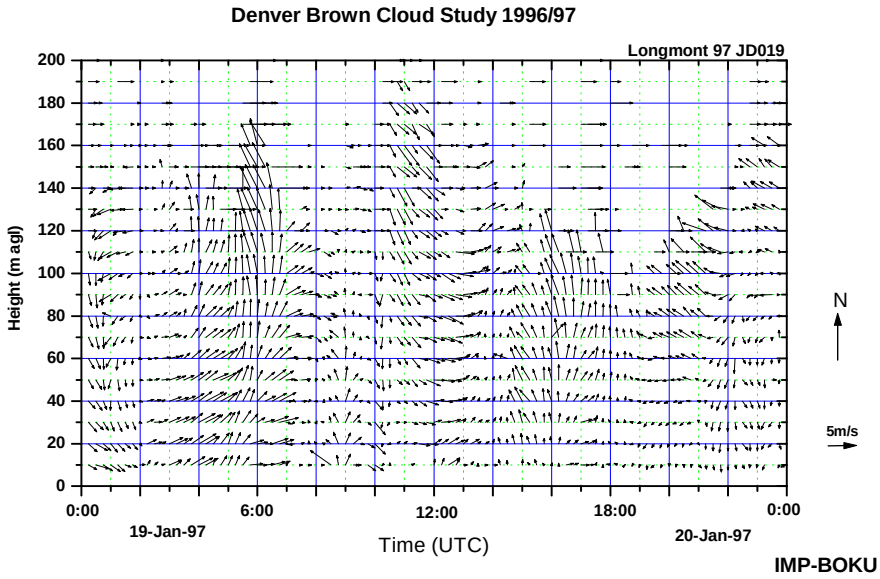


*Figure 3.57.* Mini sodar mean wind profile during measurements of the Denver brown cloud study 1997

## 3.6.7 TURBULENCE VARIABLES AND FLUXES

The signal amplitude of the scattered acoustic signal is proportional to the temperature and velocity structure parameter ($c_T^2$ and $c_v^2$ respectively). To interpret these quantities directly from the scattering cross section requires a well calibrated system, which is only possible with research instruments. The angular dependence of the scattered signal allows separate both quantities in a bi-static measurement. The accuracy of this method is usually limited to about a factor of 2 because of problems such as excess attenuation (Neff, 1978).

The velocity structure parameter defined by

$$c_v^2 = < (v(x+r) - v(x))^2 / r^{2/3} >$$

is directly related to the dissipation rate of turbulence ($\varepsilon$) through

$$e = (c_v^2 / 1.97)^{3/2} \quad .$$

Therefore $e$ can be estimated from the velocity profile measurement (Coulter, 1997).

The vertical velocity variance is a quantity $\sigma_w^2$ is a quantity which can be estimated quite well. An FFT (Fast Fourier Transform) is most of the time used to get the Doppler shift and from the spectral density distribution the velocity

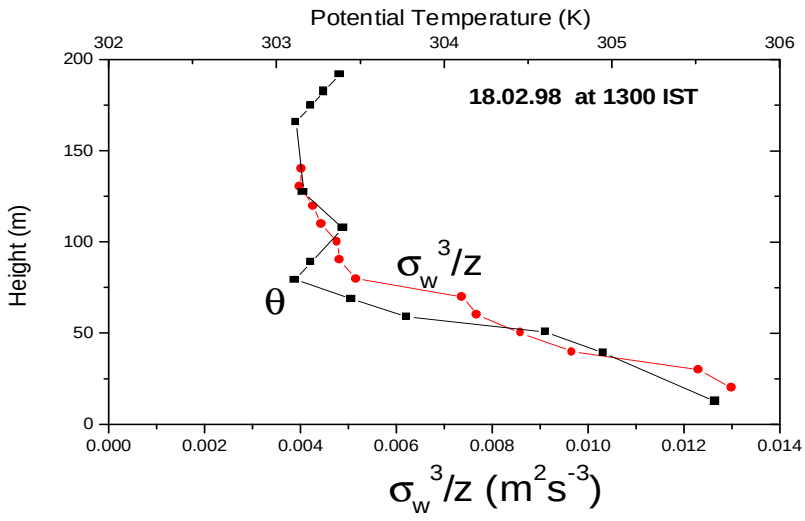


*Figure 3.58.* Comparison of potential temperature profile with buoyancy production (Prabha et al., 2002)

shift. Since the spectral density distribution has a width due turbulence in the finite scattering volume this width also is an estimate of the turbulence state of the scattering atmosphere.

Heat flux measurements in the convective boundary layer are mostly based on similarity theory. Weill et al. (1980) demonstrated the detection of heat flux profiles from measurements of the vertical variance during well mixed conditions.

In figure 3.58, a comparison is shown of convective buoyancy production and the potential temperature profile during a sea breeze event at the Indian coast, as measured by a mini sodar. Also Weill and Alli-Goulam (1990) has shown the potential of momentum flux measurements.

A very interesting application of sodar data is its use for air pollution modelling. For this the most important factor is the estimate of diffusion categories. Since sodar are not able to measure the variance of the wind direction (for which categorization to diffusion classes exist) Ganske et al. (2002) proposed a parameterisation of the directional variance by the vertical velocity variance.

For complex air pollution modelling which use a complex wind field, multiple sodars can be used to get mean wind profiles for wind field calculation using diagnostic or prognostic modelling.

The big advantage of the RASS extension of sodar is to get temperature profiles along with wind and structure information. Figure 3.59 gives an example

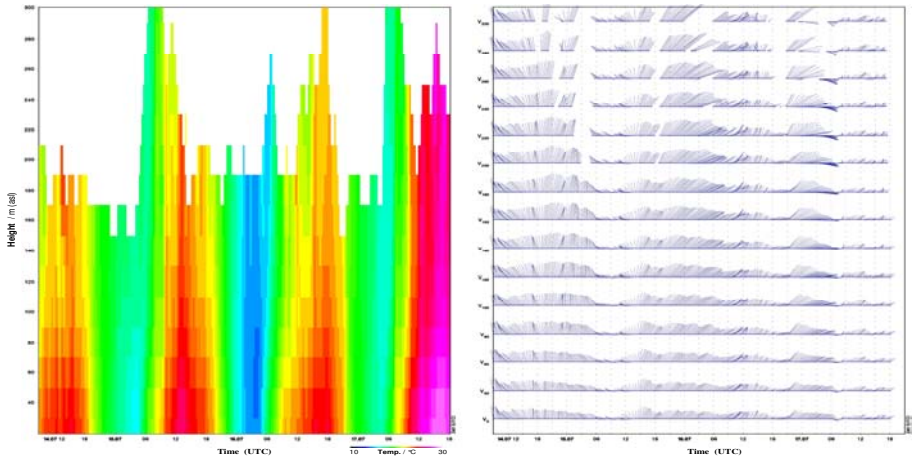


*Figure 3.59.* Example of sodar/RASS measurement – daily courses between July $14^{th}$ and $17^{th}$, 2006 at the Richard-Aßmann-Observatory Lindenberg, Germany

of a temperature and wind profiles from a sodar/RASS.

## Bibliography

Asimakopoulos,D.N., C.G. Helmis and J. Michopoulos: Determination of mixing height with an Acoustic Radar Profilometer. Proc. 11th Internat. Symp. Acoust.Rem. Sens. and Assoc. Techn. of the Atmosph. and Oceans, 229-234, 2002.

Brown, E.H. and F.F. Hall: Advances in atmospheric acoustics. *Rev. Geophys. Space Physics*, **16**, 47–110, 1978.

Singal, S.P. *(ed)*: Sodar investigation of gravity waves by cross spectral analysis. *Acoustic Remote Sensing Applications*, Lect. Notes in Earth Sciences, **69**, Springer, 275–292, 1997.

Cheung, T.K. and Little, C.: Meteorological Tower, microbaraograph array and sodar observation of solitary-like waves in the nocturnal boundary layer. *J. Atmosph. Sci.*, **47**, 2516–2536, 1990.

Coulter, R. L.: Turbulence variables derived from sodar data. Sigal, P.S. *(ed)*, *Acoust. Rem. Sens. Applicat.*, Lect. Notes in Earth Sciences, **69**, Springer, 191–201, 1997.

Engelbart, D., H. Steinhagen. U. Görsdorf, J. Neisser, H. J. Kirtzel, and G. Peters: First results of measurements with a newly designed Phased-Array sodar with RASS. *Meteorol. Atmosph. Phys.*, **71**, 61–68, 1999.

Ganske, A., G. Peters, and B. Fischer: Bestimmung meteorologischer Ausbreitungsparameter mit sodar. *Bericht Zentrum für Meeres- und Klimaforschung*, **34**, Univ. Hamburg, 2002.

Hirsch, L. and G. Peters: Abilities and limitations of a Radar-RASS windprofiler for the measurement of momentum flux in the planetary boundary layer. *Meteorol. Zeitschr.*, N.F. **7**, 336–344, 1998.

Hünerbein, S. and S. Bradley: sodar array for boundary layer evolution studies. *12th Internat. Sympos. on Acoust. Rem. Sens. and Assoc. Technol. of the Atmosph. and Oceans*, Cambridge(UK), 11-16 July, 123–127, 2004.

Kallistratova, M. A.: The role of ISARS symposium in development of acoustic sounding of the atmosphere. *in:* Argentini, S., G.Mastrantonio, I.Petenko (ed): *11th Internat. Sympos. on Acoust. Rem. Sens. and Assoc. Technol. of the Atmosph. and Oceans*, June 24-28, Rome, Italy, 1–14, 2002.

Marakova: Wind velocity measurements with double-beam Radio-aoustic Sounding. Izvestiya, Atmospheric and Oceanic Physics, **16**, No. 5, 366-368, 1980.

Marshall, J.M., A.M. Peterson, and A.A. Barnes Jr.: Combined Radar-Acoustic sounding System. Appl. Opt., **11**, 108-112, 1972.

Neff, W. D.: Beamwidth effects on acoustic echoes from the planetary boundary layer. *Techn. Rep. ERL 322-WPL*, 3834pp., NOAA, Boulder(CO), 1978.

Neff W. D. and R. L. Coulter: Acoustic Remote Sensing. *in:* D. Lenschow (ed.), "Probing the atmospheric boundary layer", *AMS*, 201–236, 1985.

Petenko, I. V. and A. N. Bedulin: Accuracy of RASS measurements and the Bragg condition. *Int. J. Rem. Sens.*, 369–374, 1994.

Peters, G. and H. J. Kirtzel: Complementary wind sensing techniques, sodar and RASS. *Annales Geophysicae*, **12**, 506–517, 1994.

Peters, G. and H. J. Kirtzel: Measurement of momentum flux in the boundary layer by RASS. *J. Atmos. Ocean. Technol.*, **11**, 63–75, 1994.

Peters, G., H. J. Kirtzel, B. Fischer, and T. Schlotfeld: A small RASS – as an extension of a Doppler sodar. Kalistratova, M.A. (ed): *8th Internat. Sympos. on Acoust. Rem. Sens. and Assoc. Technol. of the Atmosph. and Oceans*, 27-31 May, **3.7**, 1996.

Prabha, T.V., R. Venkatesan, E. Mursch-Radlgruber, and N. Jayanti: Thermal Internal Boundary Layer characteristics at a tropical coastal site as observed by a mini-sodar under varying synoptic conditions. Proc. Indian Acad. Sci. (Earth Planet. Sci.), **111**, No. 1, 63-77, 2002.

Rao, M.P., P.Castracane, S.Casadio, D.Fua, and G.Fiocco: Sodar observation of solitons. *in:* Argentini, S., G.Mastrantonio, I.Petenko (ed): *11th Internat. Sympos. on Acoust. Rem. Sens. and Assoc. Technol. of the Atmosph. and Oceans*, June 24-28, Rome, Italy, 55–58, 2002.

Singal, S. P. (ed.): Acoustic Remote Sensing Applications. *Lect. Notes in Earth Sciences*, **69**, Springer, 585pp., 1997.

Weill, A., C. Klapisz, B. Strauss, F. Baudin and C. Jaupart: Measuring heat flux and structure function of temperature fluctuation with an acoustic Doppler sodar. *J. Appl. Meteorol.*, **19**, 199–205, 1980.

Weill, A. and F. Alli-Goulam: Momentum flux measurement with sodar and mini-sodar. *Singal S.P.(ed)*: 5th Int. Symp. on Acoust. Rem. Sens. and Assoc. Technol. of the Atmosph. and Oceans, February 6–9, New Delhi, India, 161–166, 1990.

Wesely, M.L.: The combined effect of temperature and humidity fluctuations on refractive index. *J. Appl. Meteorol.*, **15**, 43–49, 1976.

# 3.7 CLOUD RADAR

Ulrich Görsdorf

*Richard-Aßmann-Observatory Lindenberg (DWD), Lindenberg, Germany*
✉ Ulrich.Goersdorf@dwd.de

## 3.7.1 STATUS OF CLOUD RADARS

**3.7.1.1 Introduction.** Radar technology is applied in various areas of meteorology, either to detect precipitation (weather radars, see section 3.8), to measure vertical wind profiles (wind profiler, see section 3.5) or to detect clouds and provide information on their structure (cloud radars). The first cloud radars have been applied during the 1960s by the US Air Force for cloud observations. Confronted with technical problems, the systems were decommissioned in the beginning of the 1970ies, whereas some technical components were later used for the development of some research systems. During the last two decades of the last century millimeter-wave radars have been established as valuable systems for remote sensing of cloud structure and processes. Cloud radars measure profiles of the intensity of particle-backscattered signals and their Doppler shift which can be used to derive information about the particle size and concentration as well as about their motion. Some radars have the capability for polarimetric measurements which provides additional information about the particle shape and/or their orientation. In combination with other remote sensing systems like lidar and radiometer cloud radar measurements can be used to derive several macro- and microphysical parameters.

Basics of radar principles and their application in meteorology are described in many text books, e.g. Atlas (1990), Doviak and Zrnic (1993), Raghavan (2003) and Meischner (2004). To get a general overview about cloud radars the articles from Kropfli and Kelly (1996) and Kollias et al (2007) can be recommended. The potential of cloud radar data to derive cloud parameters is highlighted for example in Russchenberg and Boers (2003).

This section gives a brief introduction to the principles of cloud radar operation, the measured quantities and about different types of cloud radars. Furthermore, the potential and limitations for cloud parameter retrievals are discussed.

**3.7.1.2 Principles of cloud radars.** A cloud radar transmits electromagnetic waves, which interact with an arbitrary target in the atmosphere from which a small portion of the signal returns to the radar.

**Radar equation and scattering mechanism.** The received power $P_r$ is a function of the technical characteristics of the radar, the distance between

radar and target, the reflectivity of the target and the propagation conditions for waves through the atmosphere. A simple form of the radar equation (e.g. Skolnik (1990)) can be written as:

$$P_r = C\frac{\sigma}{r^2} \tag{3.63}$$

where $C$ is a constant depending on system parameters, $\sigma$ is the radar cross section and $r$ is the range between the radar and the target. For distributed targets within a sampling volume (defined by the pulse length and the beam width) the radar reflectivity $\eta$ is used instead of the cross section $\sigma$ which is used for point targets.

$$\sigma = \eta V \tag{3.64}$$

The following scattering mechanisms can be distinguished for short wavelengths (0.1 - 0.001 m):

- incoherent particle scattering,
- coherent particle scattering,
- coherent clear air scattering.

**Incoherent particle scattering** is the dominant scattering process for millimeter-wave radars and can be described by the Rayleigh-approximation, provided that the particle size is much smaller than the wavelength:

$$\eta = \frac{\pi^5}{\lambda^4}|K|^2\sum_{i=1}^{N} D_i^6 \tag{3.65}$$

where $D_i$ is the diameter of droplet $i$, $|K|^2$ is a constant describing the optical properties that depend on the complex refraction index. For wavelengths between 0.01 and 0.10 m $|K|^2$ is practically independent of temperature and varies between 0.91 and 0.93 for water. An estimation of the complex refractivity index for other wavelengths and as a function of temperature is given in Liebe (1989).

In radar meteorology the term $\sum_{i=1}^{N} D_i^6$ is named the radar reflectivity factor $Z$. For a continuous function of the particle distribution $N$(D), $Z$ can be written as:

$$Z = \int_0^\infty N(D)D^6 dD \tag{3.66}$$

In the atmosphere $Z$ may varies over several magnitudes and therefore the logarithmic scale is used

$$dBZ = 10log_{10}\frac{Z}{Z_0} \tag{3.67}$$

where $Z_0$ is 1 $mm^6m^{-3}$. Thus, the volume reflectivity for incoherent scattering is described by

$$\eta = \frac{\pi^5}{\lambda^4} |K|^2 Z \tag{3.68}$$

$\eta$ is measured by the radar and used to calculate the reflectivity factor $Z$ which is a function only from backscatter properties and independent of frequency, range and radar parameters. Applying eq. 3.68 for all situations, i.e., also when the Rayleigh condition $D << \lambda$ is not fulfilled or for ice crystals (different $|K|^2$) the effective reflectivity factor $Z_e$ is introduced.

Characteristic values for $Z_e$ are given in table 3.8 (see also figure 3.68 of section 3.8).

*Table 3.8.* Typical values of the reflectivity factor $Z_e$ for different cloud types

| Reflectivity | Cloud type |
|---|---|
| -50 .. 0 dBz | cirrus |
| -50 .. -30 dBz | fair weather cumulus |
| -50 .. -30 dBz | non drizzling stratocumulus |
| -30 .. 10 dBz | stratocumulus with drizzle |
| -10 .. 10 dBz | light rain (drizzle) |
| 10 ..30 dBZ | moderate rain |

As already mentioned the relationship between drop sizes and reflectivity defined in eq. 3.65 is only valid in the Rayleigh regime where the backscattered power is proportional to the sixth power of droplet diameter. For larger particles (greater than 1.6 and 0.6 mm for 35 and 95 GHz radars, respectively (Lhermitte, 1990)) the scattering is described by the Mie function, where the backscattered power oscillates with consecutive minima and maxima with increasing droplet diameter. The locations of these minima and maxima can be evaluated from scattering theory and used, for example, for the determination of vertical air velocity from Doppler spectra of cloud radar measurements in rain (Kollias et al., 2002).

**Coherent particle scatter** can occur in turbulent environments where particles are separated by turbulent eddies (Erkelens et al., 2001). It is assumed that this scatter process can be neglected for millimeter-wave radars (Russchenberg and Boers, 2003).

**Coherent clear air scatter** is caused by turbulent fluctuations in the refractive index. In the inertial subrange and for isotropic turbulence the reflectivity can be expressed by (Ottersten, 1969)

$$\eta = \frac{0.38}{\lambda^{1/3}} c_n^2 \tag{3.69}$$

where $c_n^2$ is the refractive index structure parameter. Due to the dependency of $\eta$ on $1/\lambda^{1/3}$ **coherent clear air scatter** (often named as Bragg scatter) does not play a significant role for millimeter-wave radars.

Merely for cloud radars in the X- and S-band clear air and particle scatter can occur and be used for example for cumulus cloud studies (Knight and Miller, 1998).

**Attenuation.** The received power is not only dependent on the reflectivity properties of the target, but is also influenced by the attenuation of electromagnetic waves by gaseous molecules, cloud and rain droplets when propagating through the atmosphere. Generally the attenuation increases with increasing frequency, which should be considered before interpreting Z. A comprehensive theory about attenuation is given in Ulaby et al. (1981). On the base of values and approximation formulas in Lhermitte (1990), table 3.9 lists exemplary attenuation values for the frequency bands: 35 and 94 GHz.

*Table 3.9.* Attenuation coefficient ($dBkm^{-1}$) for 35 and 94 GHz radar separated for absorption by gases ($p = 1013hPa,\ \theta = 0°C,\ abs.\ humidity = 0.25\ and\ 25\ gm^{-3}$), extinction by clouds ($LWC = 0.3\ gm^{-3}\ and\ 5\ gm^{-3}$) and extinction by rain ($rr = 0.3\ mmh^{-1}\ and\ 10\ mmh^{-3}$).

| | Absorption by gases $\rho =$ | | Extinction by clouds $LWC =$ | | Extinction by rain $R =$ | |
|---|---|---|---|---|---|---|
| | $0.25\ gm^{-3}$ | $25\ gm^{-3}$ | $0.3\ gm^{-3}$ | $5\ gm^{-3}$ | $0.3\ mmh^{-1}$ | $10\ mmh^{-1}$ |
| 35 GHz | 0.04 | 0.35 | 0.30 | 0.96 | 0.06 | 2 |
| 94 GHz | 0.042 | 2.1 | 1.47 | 24.5 | 0.35 | 7 |

The extinction by ice clouds is about two orders of magnitude smaller than for water clouds. Due to the frequency dependency of attenuation 94 GHz radars may have more problems in detecting of high level clouds than radars with shorter wavelengths. Independent of frequency, the strong attenuation in heavy rain can yield breaks in measured cloud top heights. Figure 3.60 shows that during the strong rain between 16.00 and 16.15 UT the detectable cloud top height decreased from about 10 km to about 3 km.

**Doppler principle.** Most radars are able to measure the phase of the received signal related to the transmitted signal to determine the Doppler velocity of the targets. The Doppler velocity is the power-weighted mean of the radial velocities $v_r$ and is related to the Doppler frequency $f_d$ by

$$f_d = \frac{2f}{c} v_r \tag{3.70}$$

where $f$ is the frequency of the radar and $c$ the speed of light. The range $r$ between the radar and the target is determined by the time $\tau_s$ the signal needs

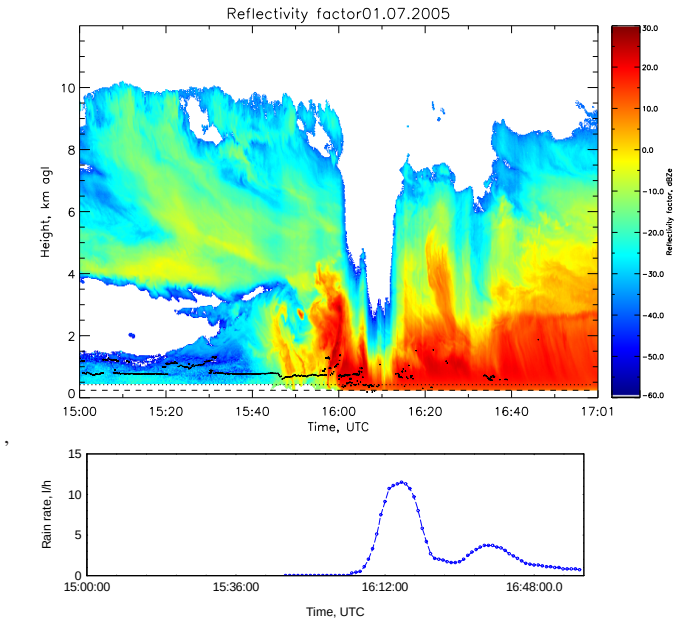


*Figure 3.60.* Time-height cross section of reflectivity and rain rate for the 1 July 2005.

to travel to and back from the target:

$$r = \frac{c\tau_s}{2} \tag{3.71}$$

The range resolution $\Delta r$ is proportional to the pulse length $\tau$ and defined as:

$$\Delta r = \frac{c\tau}{2} \tag{3.72}$$

**Polarisation.** Some radars are capable to control the polarization of the transmitted waves and to receive selected polarization states to determine the depolarization ratio which may give information on the shape, the fall orientation (related to the beam direction), the size, the refractive index and the bulk density of the scatterers. Meteorological radars use horizontally, circularly or elliptically polarized signals realized by different transmitter/receiver designs (Gekat et al., 2003; Illingsworth, 2003). For linear polarization measurements the differential reflectivity

$$Z_{DR} = 10log(\frac{Z_{HH}}{Z_{VV}}) \tag{3.73}$$

is a measure for the anisotropy of the scatterers and their orientation. Additional information on particle shape, orientation and the dielectric constant

(refractive index) provides the linear depolarization ratio:

$$LDR = 10log(\frac{Z_{VH}}{Z_{HH}}) \tag{3.74}$$

where $Z_{VH}$ is the cross-polar return at vertical polarization for horizontally polarized transmission. $Z_{HH}$ is the co-polar return at horizontal polarization for horizontally polarized transmission, and $Z_{VV}$ the co-polar return for the vertical polarisation. As illustrated in figure 3.63 the *LDR* has typical signatures for different targets. Aydin and Singh (2004) used *LDR* with other radar observables and air temperatures for cloud ice crystal classification using a fuzzy logic scheme. Typical values of the vertical pointing $K_a$- band radar at Lindenberg are given in table 3.10.

*Table 3.10.* Typical values of LDR for different particles

| LDR | Particle type |
|---|---|
| -10 .. -30 dBz | mixed phased clouds |
| -10 .. - 25 dBz | ice clouds |
| 0 .. -20 dBz | melting layer |
| 0 .. -10 | insects |

Ellipticall polarization yields, compared to the other polarization types, higher signals in the "weak" polarization channel and is therefore preferably used for the investigation of tenuous cirrus (Matrosov and Kropfli, 1993) or other low reflectivity clouds (Matrosov et al., 2001; Reinking et al., 1997).

**Signal properties.** At the output of the demodulator a complex time series is available for each range gate, which is the sum of the desired atmospheric signal and the white noise of the receiver (figure 3.61). The atmospheric signal contains information not only from cloud particles but also from other targets, which are usually not in the focus of interest. Usually, the power spectrum of the time series is calculated for further signal processing, which is related to the size and the number of particles in the sampling volume.

Assuming that the scatter from meteorological targets can be described by a Gaussian process, the desired atmospheric parameters can be estimated for each range gate by calculating the moments of the power spectrum $S(f)$ (often named as Doppler spectrum), where

- the 0th moment is related to the received power

$$P_r = \int S(f)df = \int S(v)dv \tag{3.75}$$

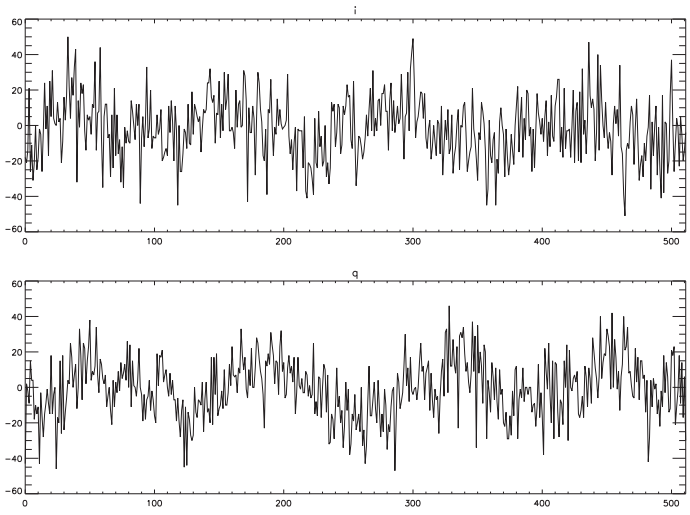


*Figure 3.61.* Time series of the in-phase and quadrature component of a signal measured with the 35.5 GHz cloud radar at the Meteorological Observatory Lindenberg at 27 September 2005.

- the 1st moment is related to the radial velocity

$$\bar{v} = \frac{\int vS(v)dv}{\int S(v)dv} \tag{3.76}$$

- and the 2nd moment is related to the spectrum width

$$\sigma_v^2 = \frac{1}{S}\frac{\int (v-\bar{v})^2 S(v)dv}{\int S(v)dv} \tag{3.77}$$

Figure 3.62 shows examples of Doppler spectra for different targets. Cloud droplets and ice crystals yield well defined spectra with a peak maximum around 0 m/s or with a light motion downwards. Insects or dusts (so-called atmospheric plankton), which are preferably observed in the warm season, yield peaks randomly distributed in space and time. The example for the 09 November 2004 shows the spectra of a stratocumulus (cloud base at about 200 m) where (at least) two droplet regimes, cloud and drizzle droplets, can be observed. The occurrence of two droplet distributions makes it difficult to use the moments for the derivation of microphysical parameters.

For polarized radars the moments can be calculated for both polarization planes, while the 0th moment of the two planes is used for the calculation of the LDR.

Figure 3.63 shows time-height cross sections of the three moments and the LDR, measured with the 35.5 GHz cloud radar at the Meteorological Observatory Lindenberg on 9 September 2004, where several types of targets up to

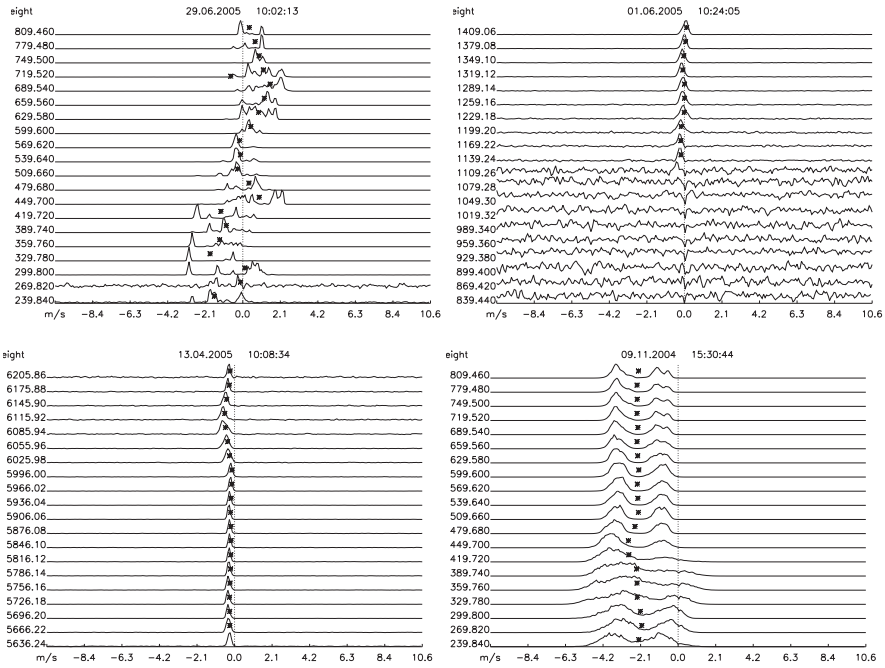


*Figure 3.62.* Doppler spectra of different targets measured with the 35.5 GHz cloud radar at the Meteorological Observatory Lindenberg. 29 June 2005: atmospheric plankton; 1 June 2005: stratocumulus, cloud base at 1140 m; 13 April 2005: Cirrus; 9 November 2004: stratocumulus with drizzle

an altitude of nearly 12 km can be studied. The period from 00 until 09 UTC is dominated by two Cirrus layers at 6 and 10 km and by atmospheric plankton below 2 km, which is indicated by high values of the LDR. At 09 UTC heavy rain began, where the levels below the melting layer at about 2.5 km (observable through the sharp increase of reflectivity and the high LDR-band) are characterized by high values of reflectivity and spectral width as well as by significant values of the vertical velocity. The example demonstrates that the determination of cloud base is complicated by the occurrence of plankton and rain. The given examples are sampled with an averaging interval of 10 s and a vertical resolution of 30 m, which is a compromise of possibly good resolution and acceptable storage requirements. Nevertheless, Kollias et al. (2005) suggest that sampling intervals of 2 s or less are more appropriate especially for studying the turbulent cloud structure.

**Filtering .** The received signal is the sum of the backscattered signal and noise caused by the thermal noise of the receiver and solar radiation. In the frequency domain (power spectrum) the signal can be detected if the signal is greater than the noise level. The noise level can be estimated either by statistic

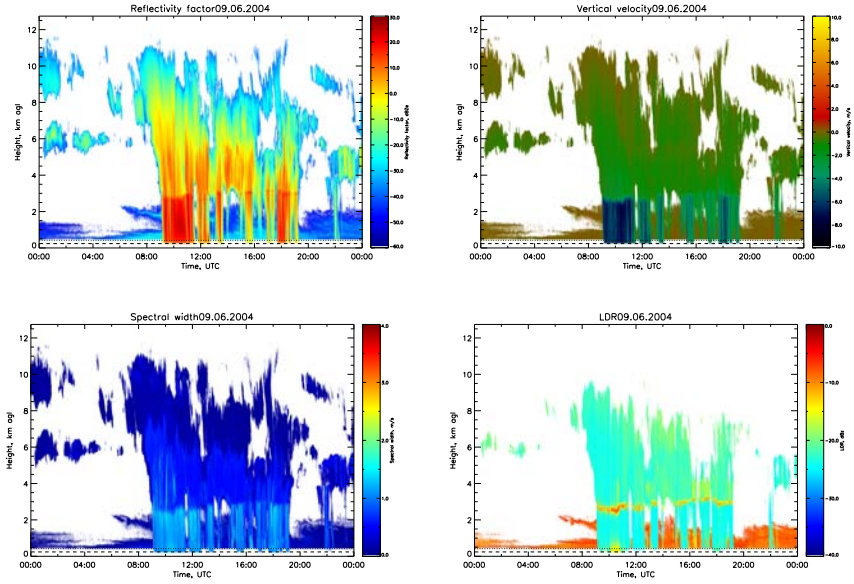


*Figure 3.63.* Time-height cross section of radar reflectivity, Doppler velocity, spectral width and linear depolarization ratio (LDR) measured with a Ka-band cloud radar at the Meteorological Observatory Lindenberg

methods (Hildebrand and Sekhon, 1974) or by determining the averaged power spectra in a reference range gate where no meteorological signal is present. Depending on the selection of the noise level more or less non meteorological signals pass the signal processing. Therefore, the filtering of data belongs to the first steps of data processing. An algorithm applying a median filter on the time-height cloud pixel is described in Clothiaux et al. (1995).

Furthermore, eventual backscattered signals from surface objects (ground clutter) interfering over the side lobes of the antenna have to be removed. Due to their preference for certain heights clutter removal is a feasible task.

Signals not only arise from hydrometeors; also other particles, e.g., insects and/or dust, yield a significant return and make it difficult to identify cloud layers. A separation between the different targets can be done either by combination with other instruments or by filtering techniques.

**3.7.1.3 Types of cloud radars.** Due to the Rayleigh scattering, millimetre-wave radars have a higher sensitivity than centimetre radars. Small antenna sizes yield very narrow beams which allow measurements with high spatial and temporal resolution. Cloud radars can be separated with respect to their

- frequency band
- wave form

- transmitter type
- antenna type and measuring mode

**Frequency band.** The frequency choice for cloud radar operation is restricted to spectral regions in which absorption of the radar signal by atmospheric gases, especially by oxygen and water is minimal. Above about 10 GHz atmospheric windows exists at 35, 90 and 135 GHz (Ulaby et al., 1981), whereas the 35 GHz and 90 GHz band, named also as Ka- and W-band (see figure 3.64) are preferred for cloud radar operation. The residual atmospheric attenuation in these windows is caused by skirts of water vapour absorption lines and increases with shorter wavelengths (Lhermitte, 1990). Therefore, Ka-band radars are more suitable for cloud soundings over the whole vertical range than W-band radars, although W-band systems are by about 17 dB more sensitive than Ka-band systems for the same transmitting power (due to the $\lambda^{-4}$ reflectivity dependence). Further disadvantages of W-band radars are larger losses in the waveguide components and the higher noise figure of the receiver compared to Ka-band radars. Due to their compact design W-band radars are more suitable for airborne and space missions than lower frequency systems. Systems operating in the X- and S-band, particularly used as weather radars, can also be used for cloud observations (see section 3.8). The advantages are the low system costs and/or their wide use in operational services. On the other hand, due to the low sensitivity the detection especially of low non-precipitating clouds is difficult.

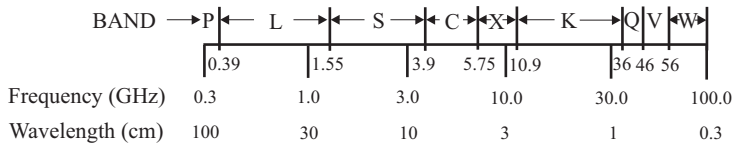


*Figure 3.64.* The microwave spectrum and the band designation

**Wave form.** Frequency-modulated-continuous wave (FMCW) and pulsed wave radars are principally distinguished. FMCW radars have a higher vertical resolution and a lower minimum range than pulsed systems and therefore they are used for measurements of low clouds or fog. Furthermore, FMCW radars can achieve a higher sensitivity compared with pulse radars for the same instantaneous output power. To increase the sensitivity of (short-) pulse radars by about 10-15 dB the phase-coded pulse compression technique is often applied (Schmidt et al., 1979).

**Transmitter type.** Magnetrons and travelling wave tubes (TWT) are generally used as transmitter in 35 GHz cloud radars, while klystrons are the main transmitter type for 94 GHz systems. The advantages of magnetrons are the

high peak power of up to 150 kW, the small size and the higher cost efficiency (at nearly half the cost of the TWT, Hamazu et al. (2003); Skolnik (2002)). Otherwise, the phase from pulse to pulse is random for the magnetron, whereas the TWT is fully coherent. Therefore, Doppler measurements with magnetron radars require the measurement of the transmitting phase. The life time and reliability of the transmitters are an important criterion for operational use of cloud radars, that is why TWT's are often favoured instead of magnetrons (Kollias et al., 2005). But recent experiences in long term operation of magnetrons indicate a much longer life time than primarily expected. The magnetron of the 35 GHz cloud radar at Lindenberg is in continuous operation for more than 2 years with a transmitting power degradation of less than 5 kW.

**Antenna type.** The function of the radar antenna is to concentrate the microwave energy into a beam of required shape, to transmit it into the desired direction and to receive the returned signal. Main parameters of the antenna are the frequency band, antenna pattern, power (or antenna-) gain, beam-width, side-lobe level, polarisation, and power handling capability component to transmit and receive radiated waves. Usually antenna of the reflector of cloud radar is a fixed paraboloid illuminated by a source at the focal point. A moving antenna (scannable radar) improves the functionality of the radar essentially for example for studying the life cycle and the spatial structure of clouds or to detect low clouds or fog (Hamazu et al., 2003). Reinking et al. (2002) investigated the horizontal depolarization ratio as function of antenna elevation angle in order to identifying different hydrometeors.

**3.7.1.4 Sensitivity, calibration, accuracy.** The radar sensitivity and the minimum detectable signal are crucial for the detection of small droplet clouds like stratocumulus or fair weather cumulus with low reflectivities (below -40 dBz) and of high ice clouds composed of small crystals. To detect all clouds with an optical depth of $> 0.05$ a sensitivity of better than -55 dBZ at 1 km is recommended (CLOUD-NET deliverable 13;
http://www.met.rdg.ac.uk/radar/cloudnet/). The minimum detectable signal of a radar essentially depends on its transmitting power, the noise figure of the receiver, and on the signal processing. Figure 3.65 gives an example for the different detection rate of clouds if sensitivity differs by about 4 dB. Measurements were made simultaneously with two 35.5 GHz radars which are nearly identical in construction but slightly different in sensitivity. Significant differences can be seen at heights between 2 and 5 km and above 7.5 km. Due to the lower sensitivity the detection loss is 20% at 4 km and 65% at 8 km. The calibration of the radar, e.g. the minimization of systematic errors, is important, when reflectivity values are used to derive cloud parameters. Normally, radars with a scanning antennas can use a direct method of calibration by measuring the return signal from a calibrated reflector of known cross section (Sekelsky and McIntosh, 1996). Without scanning capability absolute calibration can

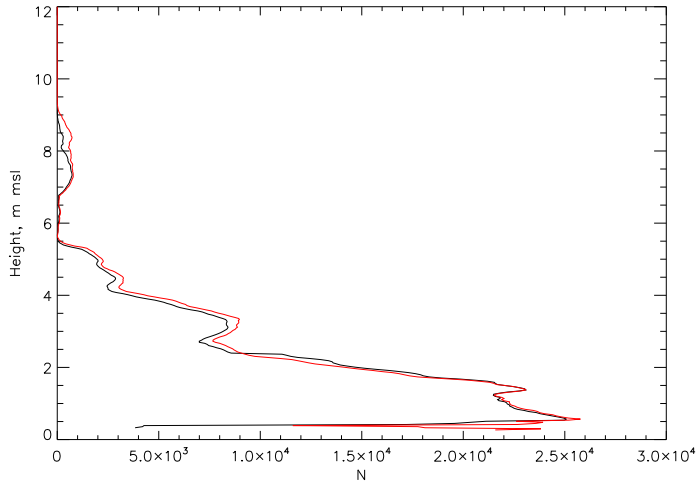


*Figure 3.65.* Absolute number of detectable clouds by the two 35.5 GHz radars MIRA-36 (blue) and MIRA-36-S (red) (see table 3.11 for details) which are nearly identical in construction but slightly different in sensitivity by 4 dB, measured between November 18 and 24, 2005, at Lindenberg.

also be obtained by alignment of the radar beam to the reflector with a mirror (Widener and Mead, 2004). Hogan et al. (2003) describes a calibration method for 94 GHz systems which is based on attenuation in rain. For systems with fixed vertically pointing antenna, calibration can be realized only indirectly by taking into account the gain or the loss of the major radar components. But this so-called budget calibration is afflicted with some inaccuracies. Having at least one calibrated system, intercomparisons can help to adjust other radars.

Such intercomparisons also give an idea about random errors or the precision of radar measurements. Operating two identical systems side by side, the total variance $s^2_{total}$ of any measured parameter is caused by the sum of random errors of the two systems and the variance due to the atmospheric variability.

$$s^2_{total} = s^2_1 + s^2_2 + 2s^2_{Atm.} \tag{3.78}$$

Assuming that $s_1 = s_2$ and the influence of the atmosphere is negligible the precision can be calculated by:

$$s = \frac{s_{total}}{\sqrt{2}} \tag{3.79}$$

For a one-week intercomparison at Lindenberg with two very similar radars the precision (on the base of 10 s values) varies between 2 and 4 dBZ for reflectivity and between 0.2 and 0.4 m/s for vertical velocity (figure 3.66).

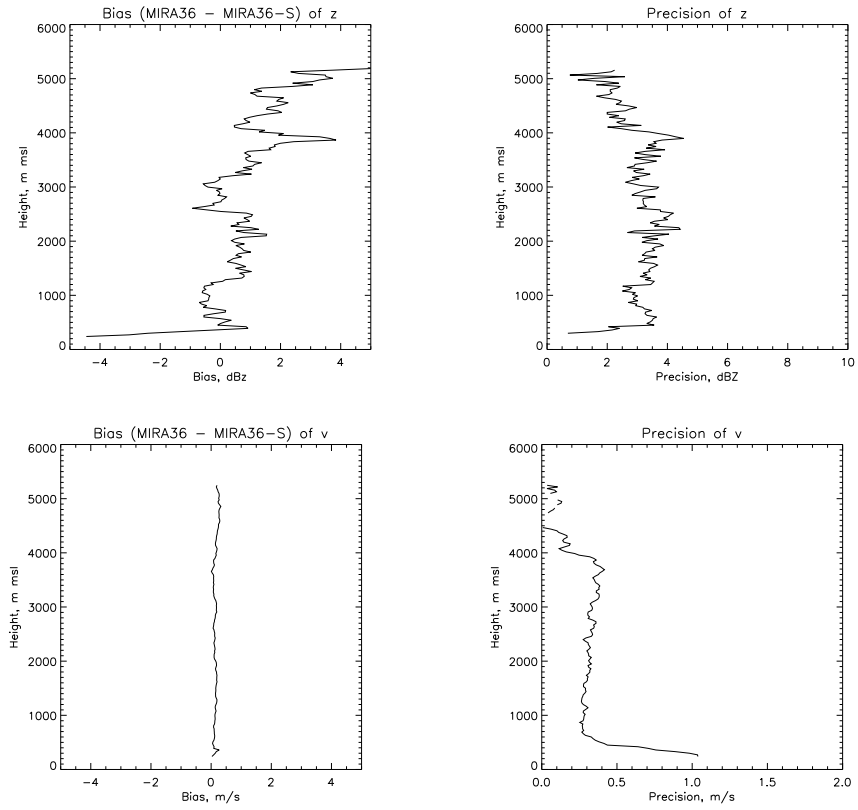


*Figure 3.66.* Bias and precision of reflectivity (top) and velocity (bottom) for collocated operation of two nearly identical 35.5 GHz radars (MIRA36 and MIRA36-S, see table 3.11) at Lindenberg in December 2005

**3.7.1.5 Overview of existing systems.** Table 3.11 contains a selection of currently available cloud radars in Europe and their main characteristics. While some of them are operating mostly in the frame of campaigns, others are in continuous operation.

## 3.7.2 PARAMETERS WHICH CAN BE DERIVED FROM CLOUD RADAR MEASUREMENTS

In principle, cloud radars can provide information about the geometrical dimensions of clouds and about their microphysical properties. Compared to optical systems attenuation of electromagnetic waves in clouds is much smaller than for light and therefore radars have the potential for cloud detection over the whole troposphere. Especially, the determination of cloud top height is valuable for different applications (e.g. satellite validations). Nevertheless, the radar is not only sensitive for cloud or rain droplets but for all particles

| Name, Frequency | Site/User | Characteristics | Operating since, Mode | Reference |
|---|---|---|---|---|
| MIRA-36, 35.5 GHz | Lindenberg, DWD | Magnetron, $P_{peak}$=30 kW, Doppler, polarimetric | 2004, continuously | Görsdorf and Handwerker (2006) |
| MIRA-36-S, 35.5 GHz | Karlsruhe, IMK | Magnetron, $P_{peak}$=30 kW, Doppler, polarimetric | 2005, scannable | Görsdorf and Handwerker (2006) |
| 34.66 GHZ | Cabauw, KNMI | TWT, 100 W peak | 2004, continuously | www.knmi.nl/samenw/cloudnet/realtime/rt-img-radar.html |
| Galileo, 94 GHz | Chilbolton, Uni Reading | Klystron, $P_{peak}$=1.6 KW, bistatic, Doppler | 1994, continuously | www.met.rdg.ac.uk/radar/chilbolton.html |
| 94.92 GHz, RASTA | Palaiseau, CNRS/IPSL, on aircraft | Klystron, $P_{peak}$=1.8 kW, sens. -50 dBz (1km, 1s) | 2002, continuously | Protat et al. (2002) |
| 3.315 GHz, TARA | Cabauw, TU Delft | Solid state, FMCW, Doppler, bistatic,polarimetric, $P_{peak}$=140 W | 2000, continuously | www.tudelft.nl/ |
| 95 GHz | Geesthacht, GKSS | Klystron,$P_{peak}$=1.7 kW, Doppler, polarimetric, scannable | 1996, periodically | Quante et al. (1997) |

*Table 3.11.* Selection of radars used in Europe for cloud studies and some of their characteristics

in the atmosphere as for insects, dust or pollen. Furthermore, corresponding to equation 3.66 the reflectivity is proportional to the 6th power of particle diameter. That means that few relatively large particles in the radar volume can dominate the radar signal. Therefore, the detection of cloud base heights on the base of radar reflectivities is impossible in situations with:

- precipitation,
- clouds with falling drizzle,
- insects (or other particles).

These problems can be overcome simplest by combining radars with optical systems as ceilometer, which has been applied frequently for unambiguous cloud base detection (Uttal et al., 1995; Clothiaux et al., 1995, 2000; Hogan et al., 2001; Sievers et al., 2002; Uttal et al., 2005). A way to insect echoes filter independently of any other system is the use of additional radar parameters as for example the LDR, which is considerable higher for insects than for clouds (Khandwalla et al., 2003; Teschke et al., 2006; Bauer-Pfundstein and Görsdorf, 2007). Also two radars with different frequencies can be very useful either for insect echoes filtering (95 GHz radars are less sensitive to insects than 35 GHz systems (Khandwalla et al., 2003)), or for liquid water retrievals (Hogan et al., 2005).

The strong dependency of reflectivity on droplet diameter, occasionally referred to as large droplet issue (Russchenberg and Boers, 2003), makes it also difficult to derive microphysical cloud properties. For example, the liquid water content (LWC) is proportional to the 3rd power of droplet diameter whereas it is not possible to calculate the LWC directly from reflectivity measurements. Different methods are suggested to derive liquid and ice water content (an overview can be found in Turner et al. (2007) and Comstock et al (2007), respectively). In section 4.1, one LWC-retrieval method is described in detail.

**3.7.2.1 Summary.** Cloud radars can provide valuable information about clouds, which can not be derived with other ground based remote sensing systems. A main advantage is their capability to penetrate clouds up to the cloud top height and their high vertical resolution. The state of the art has reached a level that cloud radars can be used unattended for long term operations to derive cloud parameters for different purposes like model validation or climatological studies. Due to the dependency of the reflectivity to the 6th power of the particle diameter the necessity arises to combine radar measurements with those of ceilometers and radiometers in order to separate between cloud and non-cloud echeos and to derive microphysical parameters.

Due to new developments in radar techniques (increasingly powerful data processing, polarization capability) additional information are available. The LDR for example is helpful for target classification and Doppler spectra give information about different droplet regimes and turbulence.

# Bibliography

Atlas, D. (1990): Radar in Meteorology. *Amer. Meteor. Soc.*, 45 Beacon Street, Boston, MA02176.

Aydin, K. and Singh, J. (2004): Cloud ice crystal classification using a 95-GHz polarimetric radar. *J. Atmos. Oceanic Technol.*, 21:1679–1688.

Bauer-Pfundstein, M and U. Görsdorf (2007): Target separation and classification using cloud radar Doppler-spectra. *33rd International Conference on Radar Meteorology, 6-10 August 2007, Cairns, Australia*.

Clothiaux, E.E., Miller, M.A., Albrecht, B.A., Ackerman, T.P., Verlinde, J., Babb, D.M., Peters, R.M., and Syrett, W.J. (1995): An evaluation of a 94-GHz radar for remote sensing of cloud properties. *J. Atmos. Oceanic Technol.*, 12(2):201–229.

Clothiaux, Eugene E., Ackerman, Thomas P., Mace, Gerald G., Moran, Kenneth P., Marchand, Roger T., Miller, Mark A., and Martner, Brooks E. (2000): Objective determination of cloud heights and radar reflectivities using a combination of active remote sensors at the ARM CART sites. *J. Appl. Meteor.*, 39:645–665.

Comstock, J. M., D'Entremont, R., DeSlover, D., Mace, G. G., Matrosov, S. Y., McFarlane, S. A., Minnis, P., Mitchell, D., Sassen, K., Shupe, M. D., Turner, D. D. and Wang, Z. (2007): An intercomparison of microphysical retrieval algorithms for upper-tropospheric ice clouds. *Amer. Meteor. Soc.*,191–204.

Doviak, Richard J. and Zrnic, Dusan S. (1993): Doppler Radar and Weather Observations. *Academic Press*.

Erkelens, J.S., Venema, V.K.C., Russchenberg, H.W.J., and Ligthart, L.P. (2001): Coherent scattering of microwaves by particles: Evidence from clouds and smoke. *J. Atmos. Sci.*, 58:1091–1102.

Gekat, Frank, Meischner, Peter, Friedrich, Katja, Hagen, Martin, Koistinen, Jarmo, Michelson, Daniel B., and Huuskonen, Asko (2003): The state of weather radar operations, networks and products. *Weather Radar*, chapter 1, pages 1–51. Springer.

Görsdorf, Ulrich and Handwerker, Jan (2006): A 36 GHz high sensitivity cloud radar for continuous measurements of cloud parameters - experiences of 2-years operation and system intercomparison. *Proc. Seventh International Symposium on Tropospheric Profiling: Needs and Technologies (ISTP)*, Boulder(CO), 12-16 June 2006, 2006.

Hamazu, Kyosuke, Hashiguchi, Hiroyuki, Wakayama, Toshio, Matsuda, Tomoya, Doviak, Richard J., and Fukao, Shoichiro (2003): A 35-GHz scanning Doppler radar for fog observations. *J. Atmos. Oceanic Technol.*, 20:972–986.

Hildebrand, Peter H. and Sekhon, R.S. (1974): Objective determination of the noise level in Doppler spectra. *J. Appl. Meteor.*, 13:808–811.

Hogan, Robin J., Francis, P.N., Flentje, H., Illingworth, A.J., Quante, M., and Pelon, J. (2003): Characteristics of mixed-phase clouds Part I: Lidar, radar and aircraft observations from CLARE'98. *Quart. J. Roy. Meteor. Soc.*, 129:1–28.

Hogan, Robin J., Gaussiat, Nicolas, and Illingworth, Anthony J. (2005): Stratocumulus liquid water content from dual-wavelength radar.*J. Atmos. Oceanic Technol.*, 22:1207–1218.

Hogan, Robin J., Jakob, Christian, and Illingworth, Anthony J. (2001): Comparison of ECMWF winter-season cloud fraction with radar derived values. *J. Appl. Meteor.*, 40:513–525.

Illingsworth, Anthony (2003): Improved precipitation rates and data quality by using polarimetric measurements. *Weather Radar*, chapter 5, pages 130–166. Springer.

Khandwalla, A., Sekelsky, S.M., and Quante, M., editors (2003): Algorithms for filtering insect echoes from cloud radar measurements. *Thirteenth ARM Science Team Meeting Proceedings*, Broomfield, Colorado.

Knight, Charles A. and Miller, L. Jay (1998): Early radar echoes from small, warm cumulus: Bragg and hydrometeor scattering. *J. Atmos. Sci.*, 55:2974–2992.

Kollias, Pavlos, Albrecht, B.A., and Jr., F. Marks (2002): Why mie? Accurate observations of vertical air velocities and raindrops using a cloud radar. *Bull. Amer. Meteor. Soc.*, 83(10):1471–1483.

Kollias, Pavlos, Clothiaux, Eugene E., Albrecht, Bruce A., Miller, Mark A., Moran, Kenneth P., and Johnson, Karen L. (2005): The atmospheric radiation measurement program cloud profiling radars: An evaluation of signal processing and sampling strategies. *J. Atmos. Oceanic Technol.*, 22:930–948.

Kollias, Pavlos, Clothiaux, Eugene E., Miller, Mark A., Luke, Edward P., Johnson, Karen L., Moran, Kenneth P., Widener, Kevin B., Albrecht, Bruce A.(2007): The Atmospheric Radiation Measurement Program Cloud Profiling Radars: Second-Generation Sampling Strategies, Processing, and Cloud Data Products. *J. Atmos. Oceanic. Technol.*, 24:1199–1214.

Kropfli, R.A. and Kelly, R.D. (1996): Meteorological research application of MM-wave radar. *Meteorol. Atmos. Phys.*, 59:105–121.

Lhermitte, Roger (1990):Attenuation and scattering of millimeter wavelength radiation by clouds and precipitation. *J. Atmos. Oceanic Technol.*, 7:464–479.

Liebe, Hans J. (1989): MPM-AN atmospheric millimeter-wave propagation model. *Int. J. Infrared Millim. Wawes*, 10(6):631–650.

Matrosov, Sergey Y., Reinking, Roger F., Kropfli, Robert A., Martner, Brooks E., and Bartram, B.W. (2001): On the use of radar depolarization ratios for estimating shapes of ice hydrometeors in winter clouds. *J. Appl. Meteor.*, 40:479–490.

Matrosov, S.Y. and Kropfli, R.A. (1993): Cirrus cloud studies with elliptically polarized Ka-band radar signals: A suggested approach. *J. Atmos. Oceanic Technol.*, 10:684–692.

Meischner, Peter (2004): *Weather radar*, Springer.

Moran, Kenneth P., Martner, Brooks E., Post, M.J., Kropfli, Robert A., Welsh, Davic C., and Widener, Kevin B. (1998): An unattended cloud-profiling radar for use in climate research. *Bull. Amer. Meteor. Soc.*, 79(3):443–455.

Ottersten, Hans (1969): Mean vertical gradient of potential refractive index in turbulent mixing and radar detection of CAT. *Radio Sci.*, 4(12):1247–1249.

Protat, A., Tinel, C., and Testud, J., editors (2002): Dynamic properties of clouds and dynamic/microphysical interaction from 94 GHz cloud radar and lidar. *ERAD 2002*.

Quante, M., Baptista, J.P.V. Poiares, and Raschke, E., editors (1997): *Proceedings of the Workshop on 'Synergy of Active Instruments in the Earth Radiation Mission'*, GKSS Research Centre, Geesthacht.

Raghavan, S. (2003): *Radar Meteorology*, Kluwer Academic Publishers.

Reinking, Roger F., Matrosov, Sergey Y., Bruintjes, Roelof T., and Martner, Brooks E. (1997): Identification of hydrometeors with elliptical and linear polarization $K_a$-band radar. *J. Appl. Meteor.*, 36:322–339.

Reinking, Roger F., Matrosov, Sergey Y., Kropfli, Robert A., and Bartram, Bruce W. (2002): Evaluation of a 45° slant quasi-linear radar polarization state for distinguishing drizzle droplets, pristine ice crystals, and less regular ice particles. *J. Atmos. Oceanic Technol.*, 19:296–321.

Russchenberg, Herman and Boers, Reinout (2003): Radar sensor synergy for cloud studies; Case study of water clouds. *Weather Radar*, chapter 8, pages 235–254. Springer.

Schmidt, Gerhard, Rüster, Rüdiger, and Czechowsky, Peter (1979): Complementary code and digital filtering for detection of weak VHF radar signals from the Mesosphere. *IEEE Trans. Geosci. Electronics*, GE-17(4):154–161.

Sekelsky, S. M. and McIntosh, R. E. (1996): Cloud observations with a polarimetric 33 GHz and 95 GHz radar. *Meteorol. Atmos. Phys.*, 59:123–140.

Sievers, O., Meywerk, J., and Quante, M., editors (2002): Statistics of non-precipitating daytime clouds, based on 95 GHz cloud radar measurements during the BBC campaign. *ERAD 2002*.

Skolnik, Merrill I. (1990): *Radar Handbook*. McGraw-Hill, Inc., second edition.

Skolnik, Merrill L. (2002). *Introduction in radar systems*, McGrawHill.

Teschke, G., U. Görsdorf, Ph. Körner, and Dennis Trede (2006): A new approach for target classification of Ka-band radar data. *Proc. Fourth European Conference on Radar in Meteorology and Hydrology*, Barcelona, 18–22 September 2006, 2006.

Turner, D. D., Vogelmann, A.M., Austin, R.T., Barnard, J.C., Cady-Pereira, K., Chiu, J. C., Clough, S. A., Flynn, C., Khaiyer, M. M., Liljegren, J., Johnson, K., Lin, B., Long, C., Marshak, A., Matrosov, S. Y., McFarlane, S. A., Miller, M., Min, Q., Minnis, P., O'Hirok, W., Wang, Z., Wiscombe, W. (2007): Thin liquid water clouds. Their importance and our challenge. *Amer.Meteor. Soc., 177–190*.

Sekelsky, S. M. and McIntosh, R. E. (1996): Cloud observations with a polarimetric 33 GHz and 95 GHz radar. *Meteorol. Atmos. Phys.*, 59:123–140.

Ulaby, F. T., Moore, R.K., and Fung, A.K. (1981): *Microwave remote sensing Volume I: Microwave remote sensing fundamentals and radiometry*, Artech House. Inc.

Uttal, Taneil, Clothiaux, Eugene E., Ackerman, Thomas P., Intrieri, Janet M., and Eberhard, Wynn L. (1995): Cloud boundary statistics during FIRE II. *J. Atmos. Sci.*, 52(23):4276–4284.

Uttal, Taneil, Frisch, Shelby, Wang, Xuanji, Key, Jeff, Schweiger, Axel, Sun-Mack, Sunny, and Minnis, Patrick (2005): Comparison of monthly mean cloud fraction and cloud optical depth determined from surface cloud radar, TOVS, AVHRR, AND MODIS over Barrow,

Alaska. In Uttal, Taneil, editor, *AMS 8th Conference on Polar Meteorology, San Diego, CA*. Environmental Technology Laboratory, Boulder, CO.

Widener, K. B. and Mead, J. B., editors (2004): *W-Band ARM cloud radar - specifications and design*. Fourteenth ARM Science Team Meeting Proceedings, Albuquerque, New Mexico.

# 3.8 OBSERVATION OF CLOUDS WITH WEATHER RADAR AND CEILOMETER

Jani Poutiainen

*Finnish Meteorological Institute, Helsinki, Finland*
Jani.Poutiainen@fmi.fi

## 3.8.1 INTRODUCTION

Radar has proved to be an important method of observation in meteorology. Traditionally, Doppler weather radars have been used in the study of rain intensity, its spatial distribution and wind field. Many types of meteorological radars have been exploited in various other scientific studies, related for instance to refractive index of air, insects, clouds, boundary layer roll vortices, and backscattering particle types and size distributions. The current work focuses on the detection of non-precipitating clouds.

The first radar observations of clouds were based on 1,25 cm wavelength measurements. These studies concentrated on the classification of cloud types, determination of detection thresholds and description of cloud structures. The essential result was that precipitating clouds (Cumulonimbus and Nimbostratus) were observable while optically thin clouds, and clouds with smaller water or ice content (Cumulus humilis, thin Stratocumulus and Cirrus) went nearly always undetected.

The question whether non-precipitating clouds would be observable with modern weather radars was raised again. After these early studies radar technology, detection sensitivities and display systems have improved significantly. On the other side, weather radars are extensively used in operational services so that many observation products are readily available. The exploitation of modern and routinely measured weather radar data has been obscured with respect to observation of clouds, because revised information on the topic has not been available. That is, what clouds and how reliably they can be seen in weather radar images. In current work, simultaneous ceilometer and visual cloud observation are used to verify cloud observations with weather radar.

## 3.8.2 WEATHER RADAR

**3.8.2.1 Measurement principle.** The operation of weather radar is based on the reception of transmitted electromagnetic pulses backscattered from distributed targets in the atmosphere. The power of the detected signal is proportional both to properties of the radar and of the targets. The radar equation expresses the mean received power from a given range resolution cell

in terms of radar and atmospheric properties:

$$\overline{P_r} = \frac{\pi^3 c}{1024(\ln 2)} \left( \frac{P_t \tau G_0^2 \theta \phi}{\lambda^2} \right) \left( |K|^2 \frac{Z}{r^2} \right) \cdot \kappa, \tag{3.80}$$

where $c$ is the speed of light, $P_t$ the transmitted power, $\tau$ the length of transmitted pulse, $G_0$ the maximum antenna gain, $\theta$ and $\phi$ are the effective full beam widths in perpendicular directions, $\lambda$ is the wavelength, $|K|^2$ dielectric factor, $Z$ the radar reflectivity factor, and $r$ the distance of the observed volume element from the radar. The last term $\kappa = \exp(-2\int_0^r k_L dr)$, where $k_L$ is the extinction coefficient. If some assumptions are not fully valid in deriving the equation, radar reflectivity factor is replaced with an equivalent radar reflectivity factor $Z_e$. In particular, scattering particles are usually assumed to be liquid water, spherical and much smaller in diameter than the radar wavelength. The radar equation is solved for $Z$, and for practical purposes the radar reflectivity factor is usually expressed in decibel form *(dBZ)*:

$$Z(dBZ) = 10 \cdot \log_{10} Z \left( mm^6 / m^3 \right) \tag{3.81}$$

Weather-radar theory has been extensively discussed elsewhere (e.g. Battan, 1973; Doviak and Zrnic, 1984; Sauvageot, 1992).

**3.8.2.2 On the observation of clouds with weather radar.** Radar reflectivity factor values can be calculated if drop size distribution is known.

$$Z = \int_0^\infty N(D) D^6 dD, \tag{3.82}$$

where $D$ is the drop diameter and *N(D)dD* is the number of drops per unit volume in the range *(D,D+dD)*. For mixed-phase clouds, ice and water content may be examined separately. If a cloud is thermodynamically unstable, ice particles will grow quickly on the expense of water particles. Ice crystal maximum size may be in the order of millimeters. As a result, ice content will contribute much more to the radar reflectivity than liquid cloud droplets. According to an approximation (Marshall and Gunn, 1952), the radar backscattering cross section of an irregularly shaped particle equals to the backscattering cross section of a spherical particle with similar mass.

For a radar, the smallest value for detectable radar reflectivity factor *dBZ(min)* can be deduced from the radar equation. It is also clear from the equation that wavelength is not the only factor affecting radar sensitivity. Figure 3.67 presents the smallest detectable radar reflectivity factor for the weather radar used in this study. Depending on the distance, *dBZ(min)* values greatly affect the ability to detect clouds. At the distance of ceilometer and visual cloud observation (12,5 km), the detection limit is about -25 dBZ when using long transmission pulses. Measurement arrangements are described in section (3.8.4).

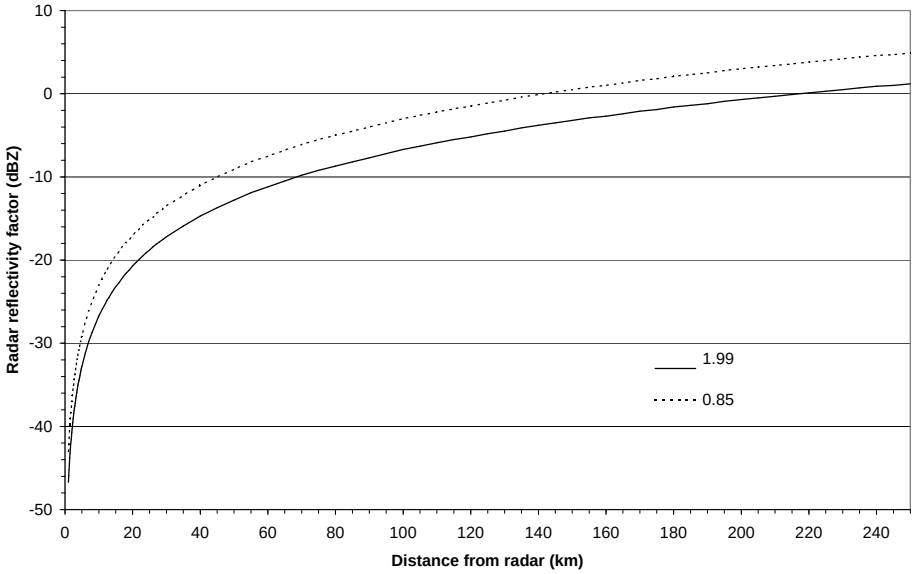


*Figure 3.67.* Minimum detectable radar reflectivity factor versus distance from the Vantaa 5,6 cm wavelength radar. The solid line represents long pulses (1,99 $\mu$s) and dotted line short pulses (0,85 $\mu$m)

Figure 3.68 shows radar reflectivity factors for various clouds, derived from literature. Some of the values are based on relationship between radar reflectivity factor and median diameter (Bartnoff and Atlas, 1951; Gossard and Strauch, 1983), and some have been calculated from drop size distributions. At the distance of ceilometer and visual cloud observation, a part of the clouds are below detection threshold and a part of the clouds are clearly above the limit. In the vicinity of the radar, nearly all clouds should be principally visible whereas far from the radar only Cumulonimbus or Cumulus congestus are expected to be seen. In practice, however, these assumptions are not always valid because non-meteorological radar echoes disturb the interpretation of cloud echoes near radar and the effect of ice particles has not been taken into account.

The radar reflectivity factor depends on the sixth power of the drop diameter. Only a small number of large drops will cause greater radar reflectivity factor values than large amount of small drops. When rain drops start to grow in a cloud, a bimodal drop size distribution forms. The first mode represents small cloud droplets and the other one represents rain drops. Already a few large ice crystals or liquid drops significantly change the ”cloud” radar reflectivity. Therefore estimates calculated solely from cloud liquid droplet size distributions may greatly misjudge the actual reflectivity. For instance, in towering Cumulus and Cumulonimbus there exist nearly always rain drops, and many clouds or parts of clouds reside above the 0 $^{o}$C isotherm. At times, convective clouds are embedded in a uniform cloud deck. In rain, backscatter from rain drops entirely dominates the radar echo.

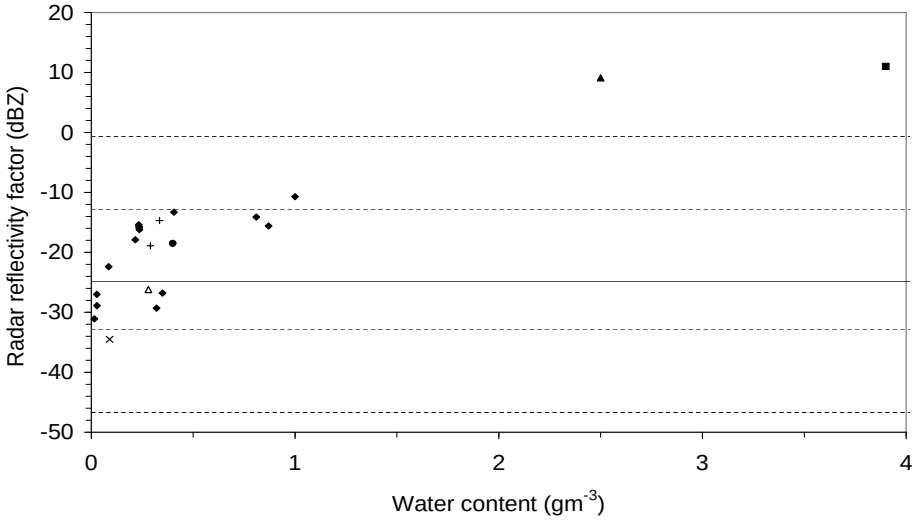


*Figure 3.68.* Estimates of the radar reflectivity factor for various water clouds, cumulus (diamond), cumulus congestus (square), cumulonimbus (filled triangle), stratocumulus (x), nimbostratus (filled circle), stratus (+), and altostratus (open triangle). The solid line represents the smallest detectable radar reflectivity factor at 12,5 km from the radar. Starting from the bottom, the dotted lines represent respective minimum dBZ values at distances of 1, 5, 50 and 200 km

Weak echoes from clouds are often mixed and covered with other non-precipitating echoes such as insects and changes in the air refractive index. Bragg backscatter exists, if the characteristic extent over which these changes occur are in the order of half a wavelength. The frequency of clear-air echoes caused by the above-listed reasons and found in the present study was significant due to the high turbulence intensity during the summer season (June-July).

### 3.8.3 COMPARISONS OF WEATHER RADAR AND CEILOMETER

The functioning of weather radars and ceilometers is based on backscattering of electromagnetic radiation, but with widely different wavelength, and thus different size parameter $x$, defined by the ratio, circumference to wavelength. Backscatter from spherical particles is described by the Lorenz-Mie theory. For $x << 1$ ($D << \lambda$) the much simpler Rayleigh Approximation is applicable. At the wavelength of ($\lambda$=5,6 cm) the Rayleigh Approximation is well suitable for cloud droplets, but this is not the case for the ceilometer ($\lambda$=0,905 $\mu$m). In analogy to the radar equation, received power of a ceilometer can be expressed with lidar equation (Collis, 1969), see also section 3.3.1

In dense clouds multiple scatter may reduce the representativity of the equation. This may be compensated by reducing the effective extinction. The Lidar equation corresponds to the radar equation in an attenuating environment.

*Table 3.12.* Comparison of weather radar and ceilometer properties. Values marked with asterisk (*) are settings specific to the current configuration

| | **Radar** | **Ceilometer** |
|---|---|---|
| Measurement range:<br>Horizontal<br>Vertical | <br>20 km (*)<br>5 or 12 km (*) | <br><br>7,5 km |
| Range resolution:<br>Half beam width<br>Sampling interval in scan<br>Half beam diameter | <br>0,95$^o$<br>0,2$^o$ (*)<br>203 m (1) | 30 m (2) |
| Time between consecutive measurements | 30 min (*) | 30 s (*) |
| Duration of a single measurement | approx. 1 min. (*) | 12 s |
| Wavelength | 5,6 cm | 905 nm |
| Pulse length | 1,99 $\mu$s / 597 m (*) | 0,1 $\mu$s / 30 m |
| Pulse power | 300 kW | 0,016 kW |
| Pulse repetition frequency | 570 Hz (*) | 5 570 Hz |
| Number of samples | 256 (*) | approx. 65 000 |
| Manufacturer and model | Gematronik Meteor 360 AC with signal processor RVP6 by Sigmet Inc. | Vaisala CT25K |
| Application software | IRIS/Open | Ct-View |

(1) 12,5 km distance and 0$^o$ angle.
(2) Vertical resolution of backscatter profile with Ct-View software.

With certain restrictions, weather radars and ceilometers may measure the same group of targets in the atmosphere. However, their temporal sampling and spatial coverage are very different: the radar measurement volume is much larger than that of a ceilometer. The measurement geometries are different, too. The weather-radar concentrates on near horizontal ray paths in all azimuthal directions, leading to a large areal coverage, whereas ceilometers usually observe in only one, near-vertical direction with a limited range of typically 10 km. However, the most important difference results from the different radiation wavelengths. This means both backscatter and extinction of radiation behave differently for each type of instrument. Primary weather radar backscatter is obtained from rain drops while ceilometers detect strong backscatter from cloud droplets.

By combining information from both of sensors it is principally possible to increase the information on clouds. Technical specifications of instruments used here are presented in table 3.12.

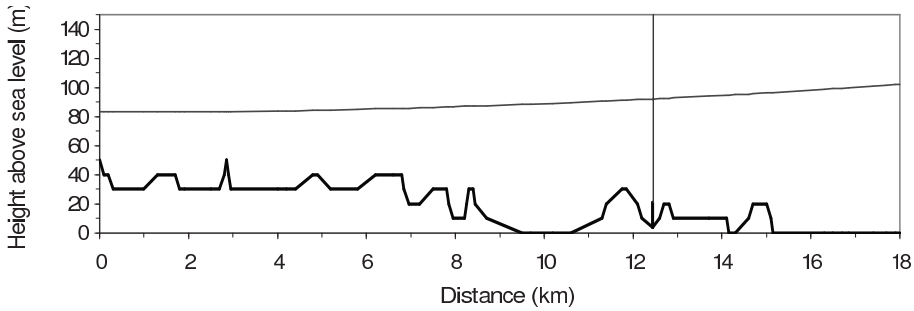


*Figure 3.69.* Arrangements of the near-horizontal radar and the vertical lidar beams together with the surface profile on the connection line between the two sensors. The radar is located on the left edge, its antenna height is 83 m above sea level, and the ceilometer is located at 12,5 km distance on the building roof at a height of 21 m above sea level.

### 3.8.4 MEASUREMENT ARRANGEMENTS

Radar measurements were performed in June-July 1998 with the Finnish Meteorological Institute's (FMI) radar located at Vantaa. Complementary observations were obtained from the roof top of the FMI Observation Unit's building, Sahaajankatu 20, Helsinki. Between the operational azimuthal radar scans, range height scans (RHI, Range Height Indication) were executed. RHI scans were done at a fixed azimuth angle ($129{,}2^o$). Primary ceilometer data consisted of vertical backscatter profiles. Figure 3.69 shows the measurement situation together with the land-surface profile.

The highest possible sensitivity of the radar was pursued because cloud echoes were anticipated to be in the order of detection limit of the radar. This was sought by adjusting radar, signal processor filter and threshold configurations. The sensitivity is better with long pulses than with short pulses. The amount of samples was set to as large as possible. A Doppler filter is useful in removing of stationary targets such as ground clutter. It was anticipated that cloud backscattering particles may be more sensitive to Doppler filtering than rain drops because rain drops have higher vertical velocity than cloud droplets. Therefore, a mild Doppler filtering was used.

In order to enhance weak backscatter signals, CT25K integrates about 65000 echo signals for a single measurement result. Such a measurement lasts about 12 seconds, after which the signal is processed with the ceilometer algorithm and data message containing cloud-layer heights, and the backscatter profile is produced.

In addition to radar and ceilometer observations, the cloud genus was verified by visual cloud observation for each measurement. In these human-made observations all cloud genera, total cloudiness, clouds in the direction of the RHI scan, and for the cloud directly above the ceilometer were determined. If observations were done in several consecutive time steps, also the development of clouds was described in writing. Human cloud observation was done

whether or not clouds were seen in the radar. Observations were usually not performed during rain because it was clear that strong rain echoes dominate over non-precipitating cloud echoes.

## 3.8.5 RESULTS AND CONCLUSIONS

**3.8.5.1 Clouds observed with weather radar.** The primary purpose was to study the ability of modern weather radar to detect clouds. To achieve this, the following criteria were determined to be sure that observed radar echoes really originated from clouds.

(1) The radar echo had to be exactly above the ceilometer location, simultaneously to a visually observed cloud.

(2) Radar echoes had to be from about the same height as the ceilometer echoes, and neither height was allowed to be in disagreement with visually observed cloud genus.

(3) Other cloud echoes mixed with non-precipitating radar echoes (predominantly insects) were subjectively rejected.

If the above requirements were met, it was concluded that a cloud was seen in the radar. The conditions are strict in a sense that among other situations the following cases had to be excluded. The radar echo was seen near the surface, but not exactly above the ceilometer location. Or the ceilometer signal was fully attenuated within a lower cloud while the radar saw the echo at upper heights. The third condition is a remarkable constraint for boundary layer clouds. Exceptions to the rules are situations in which upper clouds are at heights where ceilometer observation could not be expected with Vaisala model CT25K. Very few boundary layer clouds were detected. This is due to low radar reflectivity, but also due to other disrupting echoes at low altitudes. The only stratocumulus case that fulfilled the requirements occurred when 7/8 octas of the sky was covered by the same cloud type, also at the position above the ceilometer. At a closer look, the radar echo seemed to originate in the upper limit of the ceilometer backscatter layer or above. This suggests that the radar signal was caused by Bragg scatter. Whether the radar echo was caused by hydrometeors or Bragg scatter, it implied the existence of a cloud. In all but one case, stratus echoes were due to drizzle. Due to summer time and sea breeze, cumulus clouds at the coast site were relatively rare.

In many of the low cloud situations radar echoes were seen near the heights of the ceilometer echoes, but due to uncertainty related to the origin of low-height echoes, these cases were usually neglected.

Middle clouds were detected more often than low clouds. Noticeably high likelihood for cloud detection was observed in case of altostratus which was detected in all the possible occasions. Middle clouds may include ice crystals

and also precipitation that evaporates before reaching ground. These characteristics are likely to strengthen radar reflectivities.

High clouds were detected better than low or middle clouds. Sudden vanishing of altocumulus and cirrostratus clouds were observed in some radar images, although the clouds existed visually very clearly. As expected, all precipitating nimbostratus and cumulonimbus clouds were detected with radar.

Table 3.13 summarizes the results on weather radar cloud observations and provides comparison with earlier comparable studies.

*Table 3.13.* Comparison of cloud detectability in previous and the present study. Earlier researchers used 1,25 cm (Plank et al., 1955) and 8,6 mm (Harper, 1964) wavelength radars, here 5,6 cm wavelength was used. The table indicates the fraction of observable clouds (%), and the detected maximum equivalent radar reflectivity factor ($dBZ_e$) for each cloud type. Values marked with asterisk (*) were measured in drizzle or rain. Parentheses show the ratio of radar cloud observations and visual cloud observations

| | **Likelihood of cloud detection with radar (%)** | | | **Maximum values for equivalent radar reflectivity factor ($dBZ_e$)** |
|---|---|---|---|---|
| | Plank et al. (1955) | Harper (1964) | Current work | |
| **CUMULUS** | | | 0 (0/9) | - |
| Humilis | 0 | 6 | | |
| Mediocris | - | 57 | | |
| Congestus | 60 | 100 | | |
| **CUMULONIMBUS** | 100 | - | 100 (3/3) | min. +15 (*) |
| **STRATOCUMULUS** | | 62 | 5 (1/20) | -15 |
| Translucidus | 20 | | | |
| Opacus | 80 | | | |
| **STRATUS** | 41 | - | 31 (4/13) | -15, +5 (*), +10 (*) |
| **NIMBOSTRATUS** | 100 | 100 | 100 (2/2) | min. +15(*) |
| **ALTOCUMULUS** | | 68 | 29 (4/14) | -15, +5 |
| Floccus | 50 | | | |
| Translucidus | 22 | | | |
| Opacus | 64 | | | |
| **ALTOSTRATUS** | | 83 | 100 (9/9) | 0- min. +15 |
| Translucidus | 50 | | | |
| Opacus | 98 | | | |
| **CIRRUS** | | 38 | 82 (9/11) | -15, -10, +5 |
| Thin | 0 | | | |
| Thick | estimated 40 | | | |
| **CIRROCUMULUS** | estimated 20 | 0 | - | - |
| **CIRROSTRATUS** | | 91 | 83 (10/12) | -15– 0, +10 |
| Thin | 0 | | | |
| Thick | 70 | | | |

Shown in parenthesis are values of the ratio of the number of radar and visual cloud observations for each cloud type. Although the numbers are illustrative, it must be noted that the amount of observations is quite limited. All altostratus cases were observed during only two days, for instance. Table 3.13 also indicates observed values for equivalent radar reflectivity factor ($dBZ_e$) maximums for each cloud type. In their determination both values directly above the ceilometer and the maximum $dBZ_e$ value of the corresponding stratiform echo were considered. For precipitating clouds (cumulonimbus and nimbostratus) findings are in good agreement with earlier studies. Likelihoods for altocumulus and low-cloud detection are mostly lower. Reasons for this are disturbing effects of other non-precipitating echoes in the atmosphere and backscatter from greater distances as compared to the earlier studies. Although older radars were less sensitive, measurement distances with vertically pointing radars were significantly shorter than for the presented observations, especially in case of low clouds. The distance of 10 km away from the radar reduces the smallest detectable radar reflectivity factor approximately by 20 dBZ (figure 3.67).

Altostratus and high clouds were usually detected better in the presented than in the earlier studies. Non-precipitating low clouds were observed in 5% of all cases, middle clouds 57% and high clouds 83%, respectively. It is worth to note that during the study cumulus congestus or cirrocumulus were not observed at all above the ceilometer. It is evident from table 3.13 that the Finnish Meteorological Institute's weather radars are able to observe significant fractions of clouds at close distance.

In future, similar studies at night and in winter would be interesting because one may expect disturbing insect echoes to be weaker or entirely absent. Lower temperatures and more frequent existence of ice crystals might result in stronger non-precipitating cloud echoes. In order to maximize detection sensitivity, close observation distances would be important.

**3.8.5.2 Cloud height determination with radar.** The second objective was to inspect whether cloud heights could be deduced from radar observations. In this context the cloud was assumed to exist starting from the height where the ceilometer backscatter signal was distinguishable from background noise, and to end at the height where the ceilometer backscatter signal fell back to the noise level. Therefore, it is more precise to discuss starting and ending heights of backscatter, rather than cloud base and top heights.

Low cloud observations with radar were so limited in number and ambiguous that low clouds had to be neglected in the cloud-height determination. This was also the case for clouds above the ceilometer measurement range. Precipitating clouds had to be rejected as well. In the end, those altostratus, altocumulus and high clouds remained for inspection which had been observable simultaneously with radar and ceilometer. Results are shown in figure 3.70 and table 3.14. The figure shows vertical starting and ending heights of radar

and ceilometer backscatter. It consists of 15 cloud observations which is 16 % of the visual cloud observations in table 3.13.

Generally, radar and ceilometer detected the backscatter start approximately at the same heights. Discrepancies are much clearer in case of backscatter ending heights. Ceilometer backscatter ends always at lower height because its shorter wavelength signal attenuates over smaller distances within clouds. In addition, the ceilometer backscatter is restricted to 7,5 km detection height. Table 3.14 gives statistical measures for the data. In the most extreme cases, the radar gave 1300 m higher, and 500 m lower backscatter starting height. Considering backscatter ending heights, the radar gave 200-4100 m higher values.

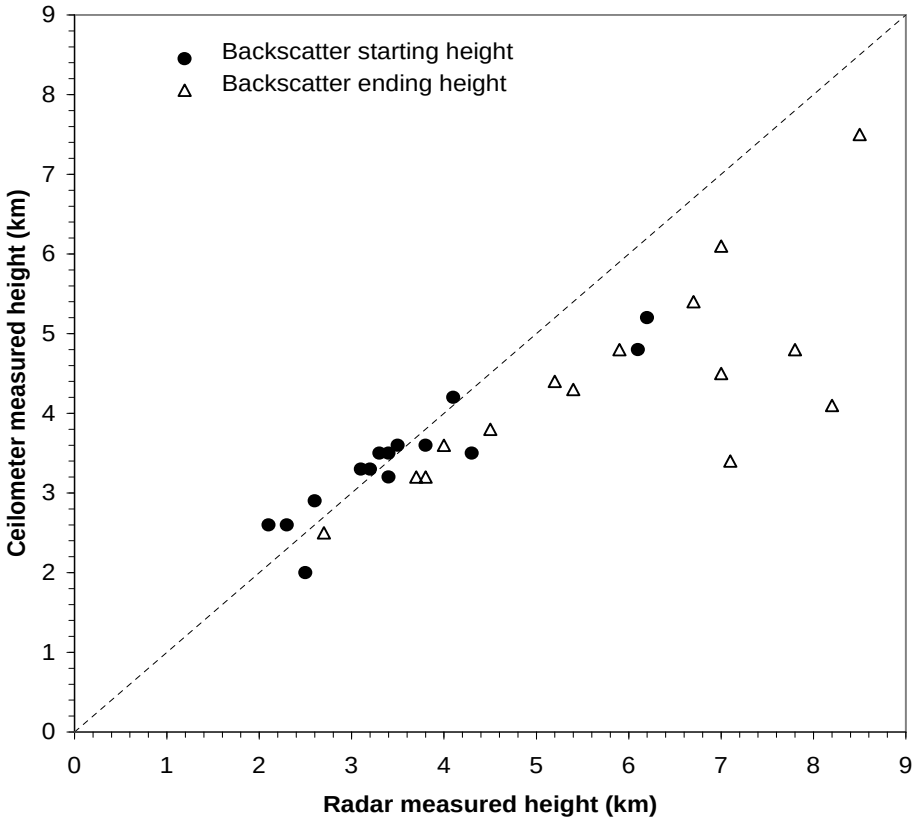


*Figure 3.70.* Comparison of radar and ceilometer backscatter profiles. Full circles represent heights at which backscatter started and open triangles represent heights at which the backscatter ended

## 3.8.6 SUMMARY

Clouds were observed with a 5,6 cm wavelength weather radar. Traditionally weather radars have not been used for this purpose, because they have not been considered sensitive enough for the detection of non-precipitating

*Table 3.14.* Comparison of backscatter starting and ending heights with radar and ceilometer. Ceilometer values subtracted from radar values

| | Backscatter starting (m) | Backscatter ending (m) |
|---|---|---|
| Average difference | 100 | 1500 |
| Standard deviation of difference | 500 | 1200 |
| Range of difference | -500, +1300 | 200, 4100 |

clouds. In Finland there exists an operational, modern weather radar network with good spatial coverage, whose feasibility for cloud observations was to be verified.

The likelihood of radar observations to detect a cloud was determined for each cloud type. This was based on observations during summer in the areas of Helsinki and Vantaa, Finland. Radar observations were verified with ceilometer and visual cloud observations. Table 3.13 summarises the detection percentages and shows that modern weather radars are capable of observing clouds at short distances, but they are not trustworthy in systematic cloud observations. The ability to detect clouds was strongly dependent on cloud type. Considering non-precipitating clouds, low clouds were harder to observe than middle and high clouds. The low detectability of low clouds resulted from their small radar reflectivity, but also from the detection distance. Based on drop size distributions and radar properties, also low clouds would be expected to be seen at close distance from the radar. An important problem in their detection was caused by clear air radar echoes, which were mixed with non-precipitating cloud echoes. Good detection of high clouds can be explained with the existence of relatively large ice particles within these clouds. Precipitating clouds were detected in all cases. Of the non-precipitating low clouds 5 %, middle clouds 57 %, and high clouds 83 % were observed, respectively.

Weather radar was often able to reveal more information about cloud layers, their heights and structures than the ceilometer alone. As compared to weather radar, an important weakness of a ceilometer was its poor transmission through the cloud. On the other hand, the radar was often too insensitive to detect small cloud droplets. By simultaneous inspection of measurements at different wavelengths it was possible to expand the knowledge about cloud-layer amounts, heights and vertical dimensions. In situations in which both instruments detected the same cloud layer, the backscatter started roughly at same height. However, backscatter ending heights were consistently lower in ceilometer observations. This was due to stronger attenuation of the ceilometer signal.

## Bibliography

Bartnoff, S. and D. Atlas, 1951: Microwave determination of particle-size distribution. *J. Meteor.*, **8**, 130-131.

Battan, L. J., 1973: Radar Observation of the Atmosphere. The University of Chicago Press, revised edition, Chicago.

Collis, R. T. H., 1969: Lidar for routine meteorological observations. *Bull. Am. Met. Soc.*, **50**, no. 9, 688-694.

Doviak, R. J. and D. S. Zrnic, 1984: Doppler Radar and Weather Observations. Academic Press, second edition, San Diego.

Gossard, E. E. and R. G. Strauch, 1983: Radar Observation of Clear Air and Clouds. Elsevier Science Publishers, Amsterdam.

Harper, W. G., 1964: Cloud detection with 8,6-millimetre wavelength radar. *Meteor. Mag., London*, **93**, 337-345.

Marshall, J. S. and K. L. S. Gunn, 1952: Measurement of snow parameters by radar. *J. Meteor.*, **9**, 322-327.

Plank, V. G., D. Atlas and W. H. Paulsen, 1955: The nature and detectability of clouds and precipitation determined by 1,25 centimeter radar. *J. Meteor.*, **12**, 358-378.

Sauvageot, H., 1992: Radar Meteorology. Artech House, Norwood.

# 3.9 METEOROLOGICAL APPLICATIONS OF THE GPS-SYSTEM WATER-VAPOUR MEASUREMENTS

M. Mauprivez[1], V. Klaus[2], and P. Hereil[1]
✉ Michel.Mauprivez@meteo.fr

[1]*Météo France, DSO Toulouse, France*

[2]*Météo France, CNRM Toulouse, France*

## 3.9.1 INTRODUCTION

The Global Positioning System is a network of high altitude ($\sim$ 20000 km) orbit satellites and ground stations which allows a very fine spatial location. It is particularly efficient in a relative reference using at least two ground stations.

Due to the difficulty to estimate the propagation time in the troposphere between the satellite and the ground station, the vertical component of this positioning is less accurate than the horizontal one.

This propagation time is by itself a very interesting parameter for meteorological applications, because it can provide the global humidity data in all weather conditions: Clear air, cloudy or rainy situations.

## 3.9.2 GPS WATER-VAPOUR MEASUREMENT

### 3.9.2.1 General principles.

An electromagnetic wave transmitted from a satellite crosses the atmosphere along an optical path $S$. This path is not exactly a straight line because of the atmospheric refractivity, and consequently, a delay $\Delta L$ can be observed, corresponding to the path increase relatively to the straight-line path in the zenith direction. It is called the Zenith Total Delay (ZTD), which is often expressed as:

$$\Delta L = 10^{-6} \int_S N \cdot dS + S - G \quad , \tag{3.83}$$

where $G$ is the straight-line distance of this path in the void, and $N$ is the refractivity of the crossed environment, defined as $N = 10^6 \cdot (n-1)$, with $n$ as refraction index.

A good approximation of $N$ can be written as (Smith and Weintraub, 1953)

$$N = 77,6\frac{P}{T} + 3,73 \cdot 10^5 \frac{e}{T^2} \tag{3.84}$$

where $P$ means air pressure (hPa), $T$ is air temperature (K), and $e$ is partial water-vapour pressure (hPa) .

Close to the zenith, it is $S - G \cong 0$, but at lower elevations, when modelling the total excess path, $S - G$ generally becomes significant and is included through a modified elevation dependence of the first term.

As illustrated in Fig. 3.71, the delay $\Delta L$ is the sum of two components:

- a hydrostatic component $\Delta L_h$, called the Zenith Hydrostatic Delay (ZHD), which represents the complete atmospheric contribution. Its value is around 230 cm, and

- a wet component $\Delta L_w$, called the Zenith Wet Delay (ZWD), which represents the water vapour contribution. It varies from near 0, in cold and dry conditions, to about 40 cm in a warm and wet atmosphere.

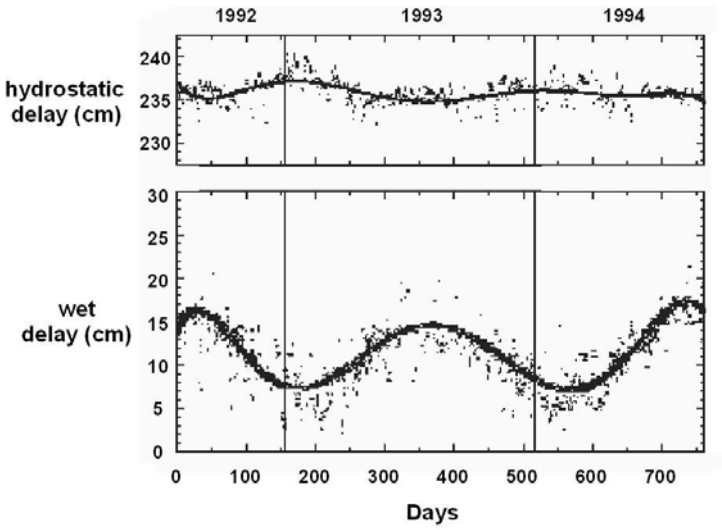


*Figure 3.71.* Example of the two delay components, as calculated from 2-year radio-sounding data at the Nîmes – Courbessac's meteorological station (Dörflinger, 2001)

### 3.9.2.2 The hydrostatic component.

The approximate formula of the hydrostatic component at each measurement point is:

$$\Delta L_h = \frac{(0.0022768 \pm 0.0000024) \cdot P_S}{f(\Phi, H)} \tag{3.85}$$

with $P_S$ air pressure (hPa), $\Phi$ latitude, $H$ altitude, and $f(\Phi, H) \approx 1$ (depending on gravity variations, altitude, and latitude). The accuracy of the hydrostatic component largely depends on the ground pressure measurement quality (Akyüz et al., 1991).

#### 3.9.2.3 The humidity component.

The wet delay caused by atmospheric humidity, is expressed as

$$\Delta L_w = \left[1 + (6 \pm 3) \cdot 10^{-5} \cdot T_m\right] \cdot (0{,}3754 \pm 0{,}003) \cdot \int_S \left( e \cdot \frac{Z_w^{-1}}{T^2} \right) dS \quad , \quad (3.86)$$

with $T$ air temperature (K), $e$ partial water-vapour pressure (hPa), $T_m$ mid-atmosphere temperature (K), and $Z_w^{-1}$ compressibility factor.

The equation can be solved only, if the distribution of water-vapour from the ground up to the upper atmosphere is known. Therefore, this component is generally derived indirectly by subtracting the hydrostatic component $\Delta L_h$ (see 3.85) from the global delay $\Delta L$ (see 3.83):

$$\Delta L_w = \Delta L - \Delta L_h \quad (3.87)$$

Three methods are then available to calculate the humidity component:

- The standard atmosphere model method (SM),
- direct measurements of the wet delay (DM), and
- the wet delay numerical estimation (NE).

**The standard atmosphere model method (SM)**

The SM method gives a first approximation of the wet delay using either meteorological ground measurements in the area (pressure $P$, temperature $T$ and relative humidity $U$, or standard atmospheric parameters (generally $P$ = 1013 hPa, $T$ = 18$^o$C and $U$ = 50% at the sea level).

The accuracy of this method is not very high (Saastamoinen, 1972).

**Direct measurements of the wet delay (DM)**

The implementation of the DM method is generally expensive and not very simple. It consists of a direct measurement of the integrated content of the atmospheric water vapour with different systems like radiometer, radiosounding, lidar, etc. ....

This method can be used for example to calibrate the instruments or to obtain the $\Delta L$ (or $\Delta L_w$) parameter in small networks (see 3.9.2.3) from a direct measurement at a given reference station with an already installed system.

**The wet delay numerical estimation (NE)**

The NE method has the best ratio of quality to price (Bock and Dörflinger, 2001), but several values must be known or calculated in order to estimate $\Delta L$. These values are provided by the international GPS Service (IGS), a worldwide network including between 200 and 300 receivers:

- Satellite orbits,
- Earth rotation parameter (ERP),

- station coordinates,
- antenna type,
- satellite and receiver clock, and
- the phase ambiguities.

Generally, a $\Delta L$ (or $\Delta L_w$) accuracy better than 10 mm can be obtained, depending strongly on the quality of these parameters.

Two different strategies can then be used to extract the $\Delta L$ value:

- The network approach and
- the precise point-positioning (PPP) approach.

**The network approach** The parameter is calculated in several stations. Here, the estimation of $\Delta L$ at a given point depends on the network size:

- In a large network with at least two points, having uncorrelated measurements from the same satellite, all the parameters and absolut values for $\Delta L$ can be calculated. Then, a single least-square adjustment method or Kalman-filter provides the final value.
- In a small network with a strong correlation between measurements from the same satellite on all the ground stations, the calculation becomes very difficult. Only the relative global delay between two stations can be estimated and another reference system is necessary (radiometer, radiosounding, etc...) to calculate the absolute delay $\Delta L$ at a given point.

Two different methods exist for this approach:

- The zero method, and
- the double difference method.

Theoretically, they give identical results, but the software implementation may result in small differences.

**The precise point positioning (PPP) approach** To implement the precise point positioning (PPP) method, satellite orbits, ERP and satellite clock parameters are necessary (a priori data). The main advantages are:

- direct availability of absolute value of $\Delta L$ at a given point,
- possibility of station by station processing, and
- no need to process a whole regional network.

However, this approach also demands special care for some other issues like for example:

- The difficulty to estimate integrated phase ambiguities,
- the need to have excellent quality of orbits, ERP and satellite clock parameters coming from the same source, and
- a very high correlation of the above parameters, which may be a problem for near-time applications (The IGS ultra-fast products cannot provide an accurate clock prediction).

**Comparison of the different methods and accuracy of the water vapour measurement**

On Fig. 3.72 below, some results obtained with each of the three methods are plotted from measurement campaigns between two French stations. We notice that NE and DM give similar results, but SM is obviously quite different (Dörflinger, 2001).

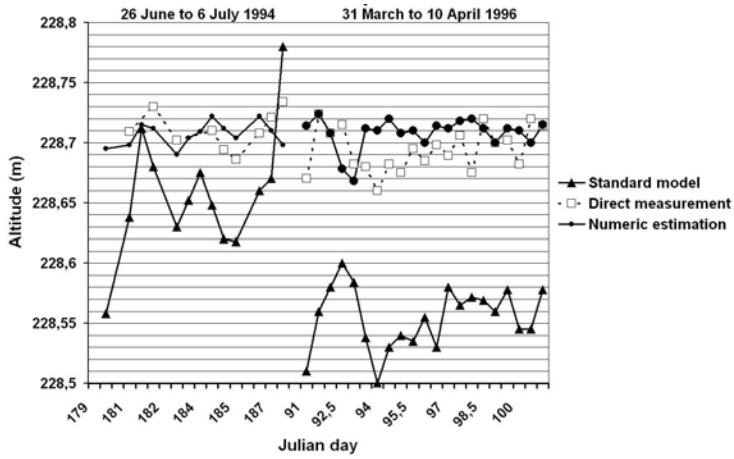


*Figure 3.72.* Comparison of relative delay estimation $\Delta L$ (or $\Delta L_w$) using 3 different methods: Standard model (SM: pink), direct measurements (DM: green), and wet delay numeric estimation (NE: brown). Data were obtained between two French stations (Mont Aigoual and Aniane) during two measurement campaigns (left: 26/06-06/07/1994, right 31/03-10/04/1996) (Dörflinger, 2001)

### 3.9.2.4 Integrated Water Content.

The wet delay value in the zenith direction easily provides the integrated water content $C$ using the following approximation (Davis et al., 1985):

$$C = \frac{\Delta L_w}{\kappa} \quad ,$$

where $\kappa$ is a dimensionless constant ($\kappa \cong 6.5$). $C$ can be estimated from temperature measurements in the surrounding with an error better than 1% (Bevis

et al., 1992). As an example, Fig. 3.73 shows a comparison of the precipitable water quantity between radiosoundings at the meteorological station Brest and a little French pilot GPS network (Dörflinger, 2001). We notice a very good agreement, showing that humidity data from GPS are quite reliable.

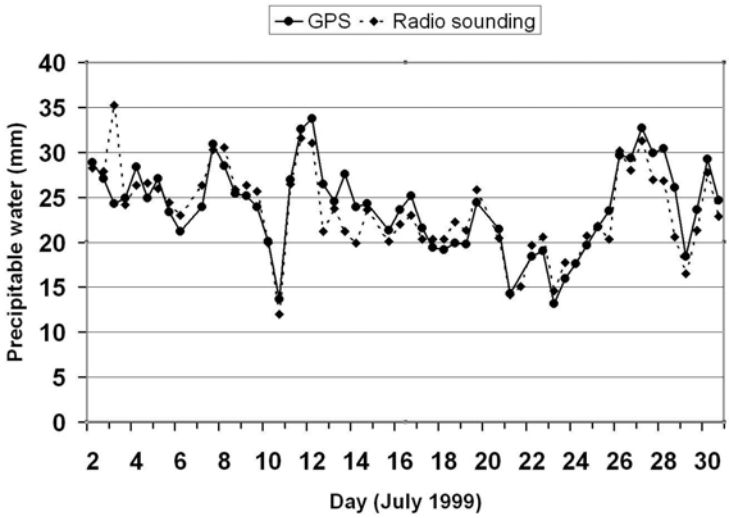


*Figure 3.73.* Comparison of precipitable water at Brest station between radiosoundings and a GPS station during a one-month experiment in July 1999 (Dörflinger, 2001).

### 3.9.3 RADIO-OCCULTATION TECHNIQUE

The Radio occultation technique uses the curvature of the GPS wave propagation path in the atmosphere between a GPS satellite and a non-GPS satellite moving at a lower-altitude orbit in the opposite direction (Fig. 3.74). This technique, based on atmospheric refractivity, provides humidity and temperature profiles with high time and space resolution from all points of the globe (see description of the method e.g. in (Steiner et al., 1999)). Recently, a measurement campaign with two low-altitude near-polar-orbit satellites (CHAMP and GRACE) has shown excellent agreement with meteorological analyses. No refractivity bias and a standard deviation between 1% and 2% from 5 km to 30 km have been observed (Wickert et al., 2005). An example from application of the radio occultation technique to the Northern Europe is given in figure 3.75. The results are particularly accurate above 8 km for temperature and above 5 km for humidity. Further GPS occultation missions with other low-altitude satellites were realized in 2006.

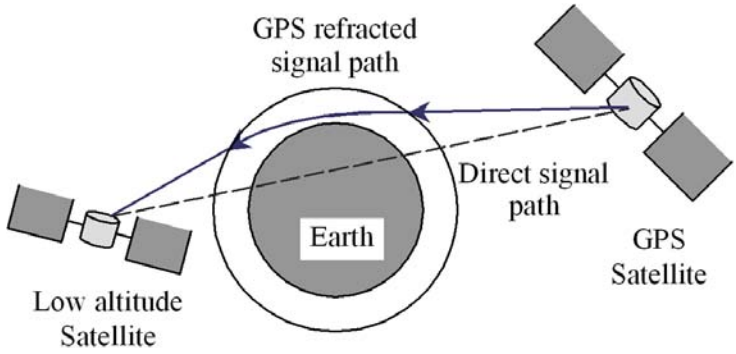


*Figure 3.74.* Principle scheme of the radio occultation technique.

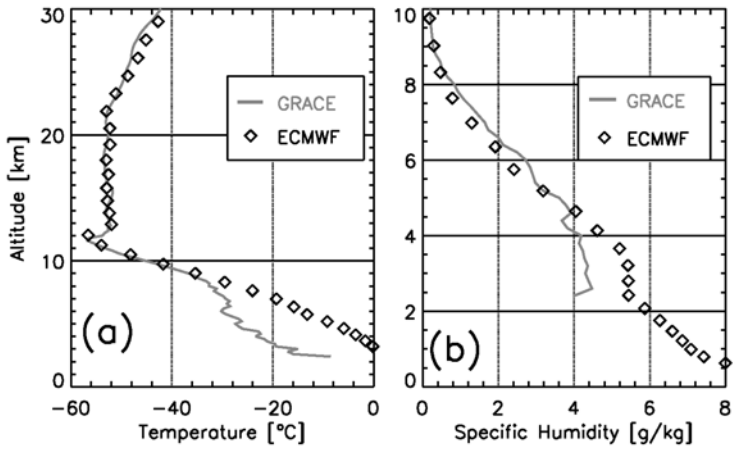


*Figure 3.75.* Example of a comparison of dry temperature (a) and specific humidity profiles (b) between the ECMWF analysis and the GPS occultation technique from GRACE (Gravity Recovery And Climate Experiment) (Wickert et al., 2005).

## 3.9.4 RESULTS OF THE COST-716 ACTION

A brief summary of main results obtained by the action COST-716 is exposed here without going into extensive details.

One of the main purposes of this action was to test real-time processing of total water vapour from a network of GPS receivers in Western Europe (NRT). These data were processed by up to eight geodesic institutes interested in GPS research and forwarded to a central meteorological data base, maintained by the UK Met Office in NRT. The network finally achieved a quality suitable for numerical weather prediction.

At the end of the COST-716 action, about 450 GPS sensing sites were available for research purposes with an unequal distribution among European coun-

tries. Spatial horizontal resolution of the GPS measurements is generally better than the existing radio sounding network. However, due to the very sharp decrease of the water-vapour pressure with temperature, the GPS technique primarily senses water vapour in the lower troposphere (3 km in winter and 5 km in summer); though it can be completed with other satellites measurements using for example the GPS radio occultation technique (see 3.9.3), providing a fairly accurate horizontal distribution of the water vapour in the upper and middle troposphere.

#### 3.9.4.1 GPS Data Usefulness.

GPS measurements have already shown their usefulness in identifying day-night variations in the performance of radiosonde humidity sensors. GPS data can also be used to evaluate the spatial representativity of the radiosondes' humidity measurements in the lower atmosphere. Besides, the GPS water-vapour network can replace some empirical relationships between vertical structure, surface and surface-cloud observations still in use in several countries.

The GPS data can help to improve the quality of water vapour measurements provided to operational meteorologists. Most of the processing centres can provide NRT observations with even higher accuracy to meet the needs of climatological applications. To this purpose yet, a longer processing time may be required in order to take into account for example the orbit corrections for GPS satellites.

Further applications may also be mentioned:

- Improvement of short-term forecasts during extreme rainfall events (6 to 24 hours ahead),
- summer convection nowcasting,
- identification of forecast errors in operational models, or
- evaluation of improvements of NWP model forecasts obtained by inclusion of water-vapour measurements from new satellites.

GPS meteorological data are available in the BUFR code format.

#### 3.9.4.2 COST-716 Recommendations.

The main recommendations of COST-716 are:

- Spatial resolution:
  - from 10 to 100 km for nowcasting;
  - from 10 to 250 km for NWP and climatological needs.
- Availability delay:
  - from 5 to 30 minutes for nowcasting;

  - from 30 minutes to 2 hours for numerical forecast and climatology needs.

- Accuracy/stability of the measurement of the integrated water-vapour content:
  - 2 kg/m$^2$ for nowcasting;
  - from 0.5 to 2 kg/m$^2$ for numerical forecasts (3.25 mm $\leq$ ZTD or $\Delta L \leq$ 13 mm);
  - better than 0.5 kg/m$^2$ for climatological needs.

#### 3.9.4.3 Possible use in the context of COST-720.

The integration of the GPS technique with ground-based remote-sensing instruments may represent a significant contribution in several aspects:

- The well-tested capabilities to provide precipitable water values above an integrated remote-sensing station helps to crosscheck the data provided e.g. by a radiometer and to serve as a suitable input to humidity profile integration with UHF and VHF radars,
- GPS radio occultation also represents a promising contribution, as it can provide humidity and temperature profiles over large and/or oceanic areas. These data may be particularly useful for higher-atmosphere measurements, where data from ground-based stations are either less accurate (e.g. radiometers) or influenced by optically thick clouds inhibiting to get data from that region (e.g. FTIR, Lidar).

### 3.9.5 CONCLUSION

In this brief section, it was shown that GPS-based measurements have capabilities which may contribute positively to ground-based integrated remote-sensing stations, as defined in the frame of COST-720. Their present state-of-art is already a significant asset for the automatic measurement of integrated humidity above a site. Additionally, promising contributions can be expected for improvements in quality and availability of full profiles of humidity and temperature, although GPS-based techniques with show here an emphasis on the upper troposphere as well as the stratosphere.

## Bibliography

Akyüz, F. A., H. Liu, and T. Horst, 1991: Wind tunnel evaluation of PAM II pressure ports. *J. Atmos. Ocean. Technol.*, **8,** 323-330.

Bevis, M., S. Businger, T. A. Herring, C. Roken, R. A. Anthes and R. H. Ware, 1992: GPS meteorology: Remote sensing of atmospheric water vapour using the Global Positioning System. *J. Geophys.*, **97**, 15787-15801

Bock O. and E. Dörflinger, 2001: Atmospheric processing methods for high accuracy positioning with the Global Positioning System. *Phys. and Chemistry of the Earth*

Davis J. L., T. A. Herring, I. I. Shapiro, A. E. Rogers and G. Elgered, 1985: Geodesy by radio interferometry: Effect of the atmospheric modelling errors on estimates of baseline length. *Radio Sci.*, **20**, 1593-1607.

Doerflinger E., 2001: Les applications météorologiques du système de positionnement satellitaire GPS. *La Météorologie*, **34,** 21-37.

Egered G., H.-P. Plag, H. van der Marel, S. Barlag and J. Nash, 2005: Final report of COST 716 Action – Exploitation of ground-based GPS for operational numerical weather prediction and climates applications

Saastamoinen J., 1972: Atmospheric correction for the troposphere in radio ranging of satellites. *Use of Satellites for Geodesy*, S. W. H. e. al., Ed.

Smith E. K. and S. Weintraub, 1953: The constants in the equation for atmospheric refractive index at radio frequencies. *Proc. IEEE*, **41,** 1035-1037.

Steiner A. K., G. Kirchengast, and H. P. Ladreiter, 1999: Inversion, error analysis, and validation of GPS/MET occultation data. *Ann. Geophysicae*, **17,** 122-138.

Wickert J., G. Beyerle, R. König, L. Grunwaldt, G. Michalak, C. Reigher, and T. Schmidt, 2005: GPS radio occultation with CHAMP and GRACE: A first look at a new and promising satellite configuration for global atmospheric sounding. *Ann. Geophysicae*, **23,** 653-658.

# APPENDIX

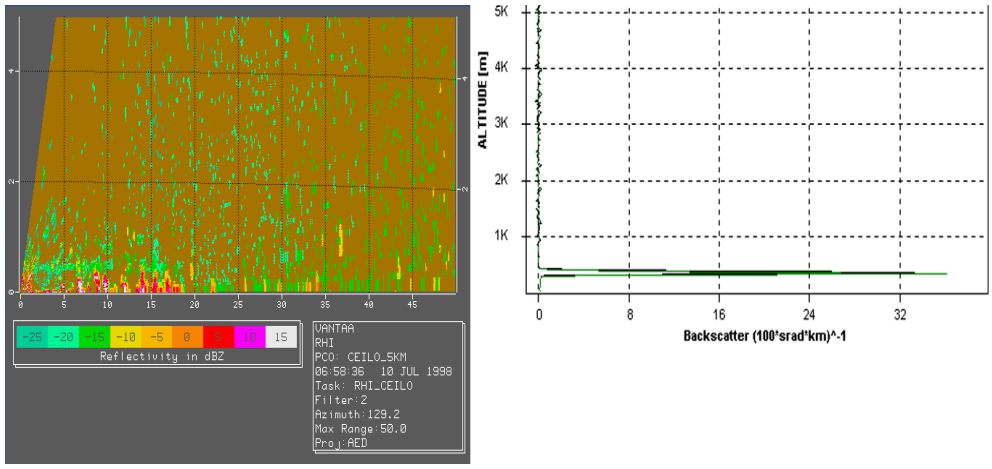


*Figure 3.A.1.* Radar range height scan and ceilometer backscatter profile in Stratocumulus case

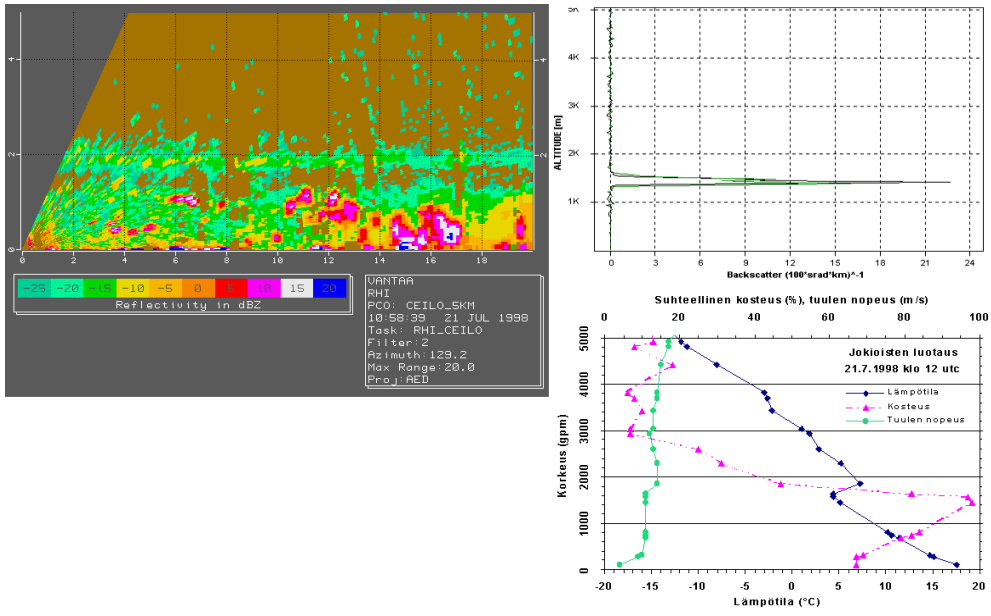


*Figure 3.A.2.* Radar range height scan, ceilometer backscatter profile and Jokioinen radio sounding in Stratocumulus case. In sounding image, temperature is marked in blue on primary x-axis, relative humidity in purple and wind speed in green on secondary x-axis. Y-axis is height in gpm

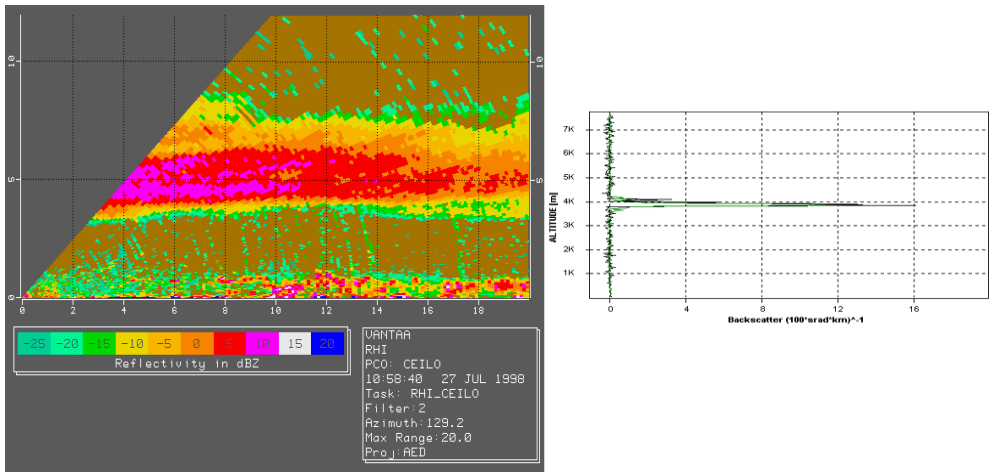


*Figure 3.A.3.* Radar range height scan and ceilometer backscatter profile in Altostratus case

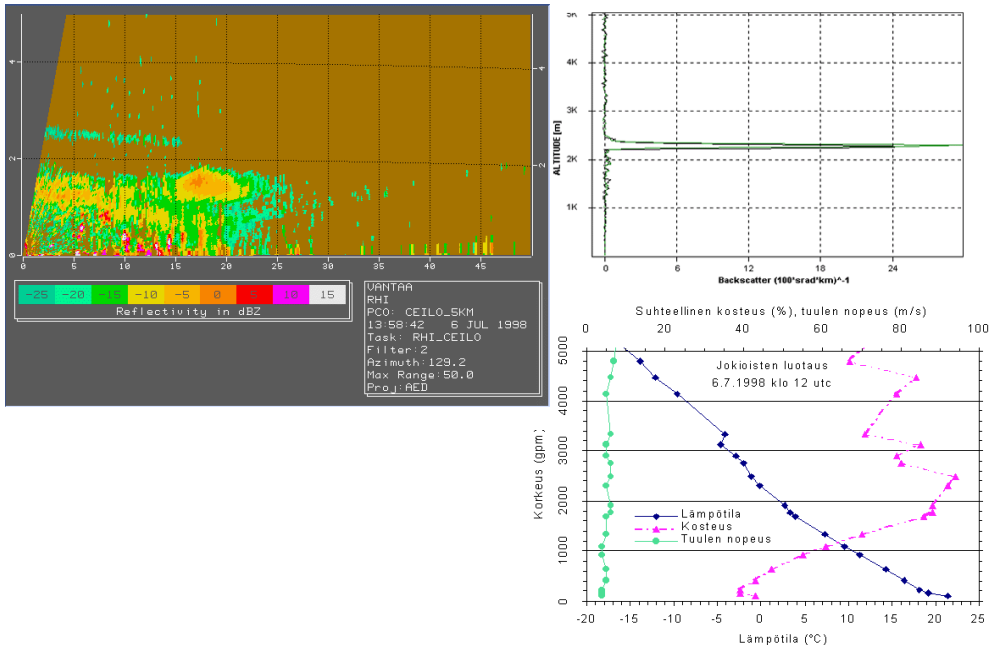


*Figure 3.A.4.* Radar range height scan, ceilometer backscatter profile and Jokioinen radio sounding in Altocumulus case. In sounding image, temperature is marked in blue on primary x-axis, relative humidity in purple and wind speed in green on secondary x-axis. Y-axis is height in gpm

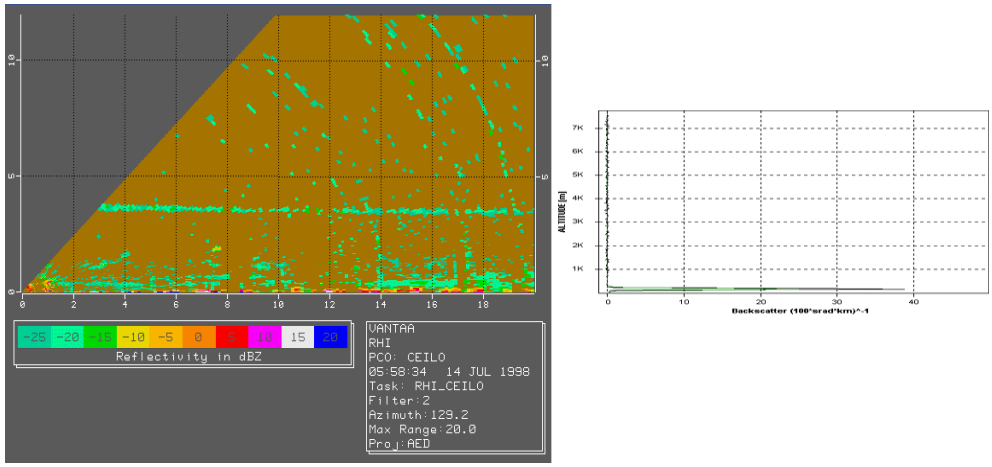


*Figure 3.A.5.* Radar range height scan and ceilometer backscatter profile in Stratus case

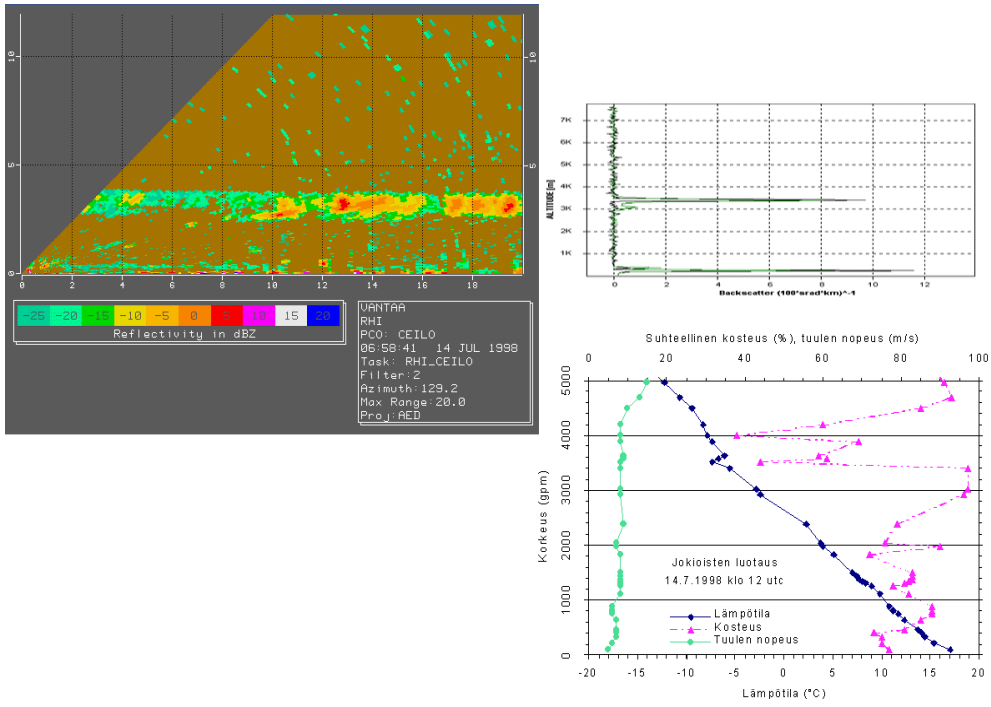


*Figure 3.A.6.* Radar range height scan, ceilometer backscatter profile and Jokioinen radio sounding in Stratus, Stratocumulus and Altocumulus case. In sounding image, temperature is marked in blue on primary x-axis, relative humidity in purple and wind speed in green on secondary x-axis. Y-axis is height in gpm

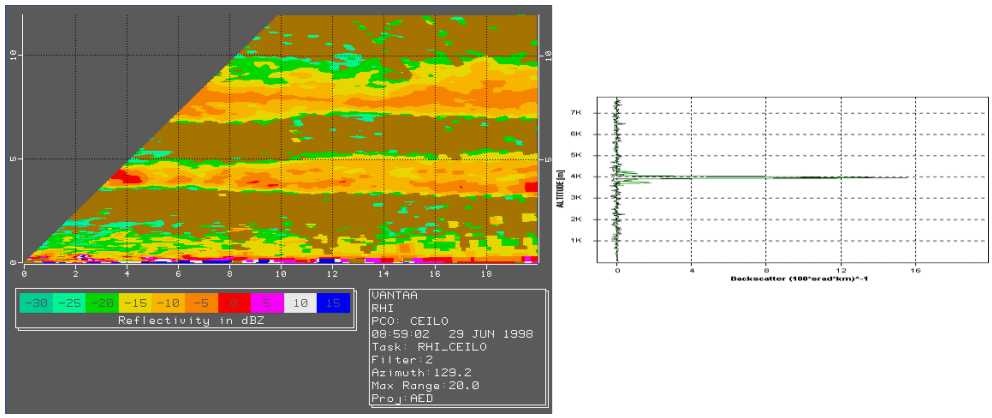


*Figure 3.A.7.* Radar range height scan and ceilometer backscatter profile in case which ceilometer signal attenuated in lower cloud

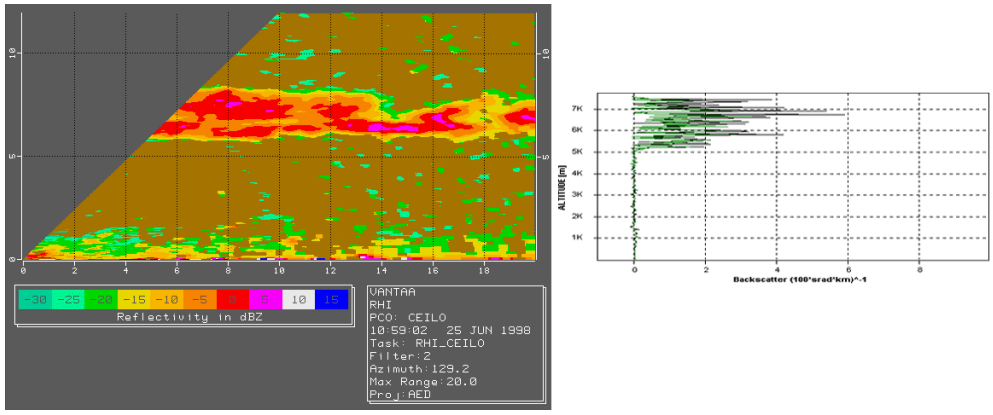


*Figure 3.A.8.* Radar range height scan and ceilometer backscatter profile in Cirrus case

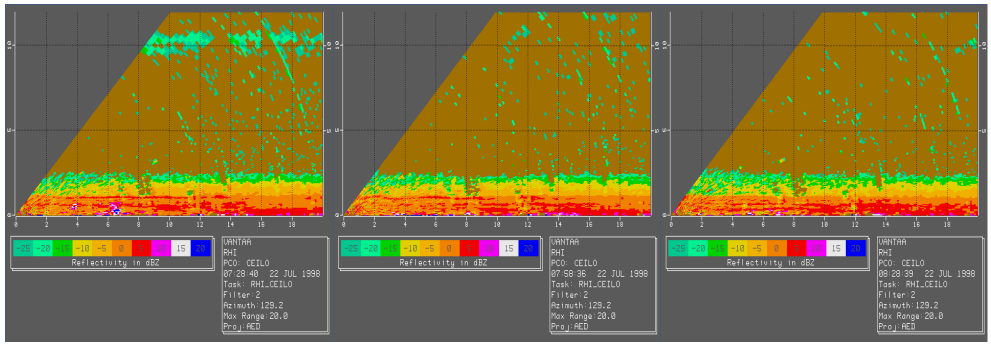

*Figure 3.A.9.* Radar range height scan sequence in Cirrostratus case. Image interval is 30 minutes, starting at 07:28 UT

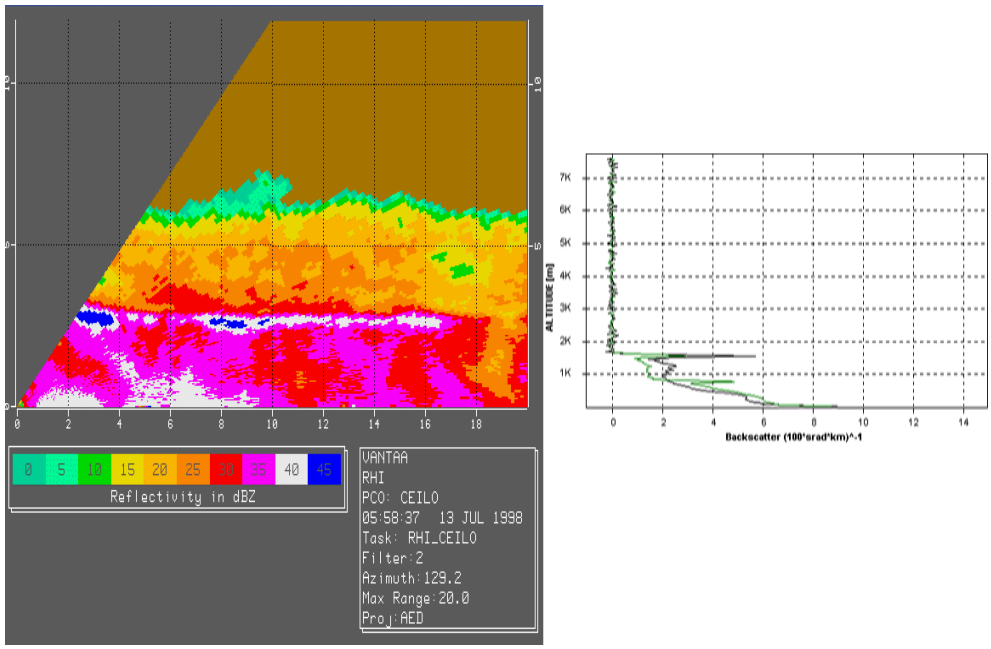


*Figure 3.A.10.* Radar range height scan and ceilometer backscatter profile in precipitating Nimbostratus case

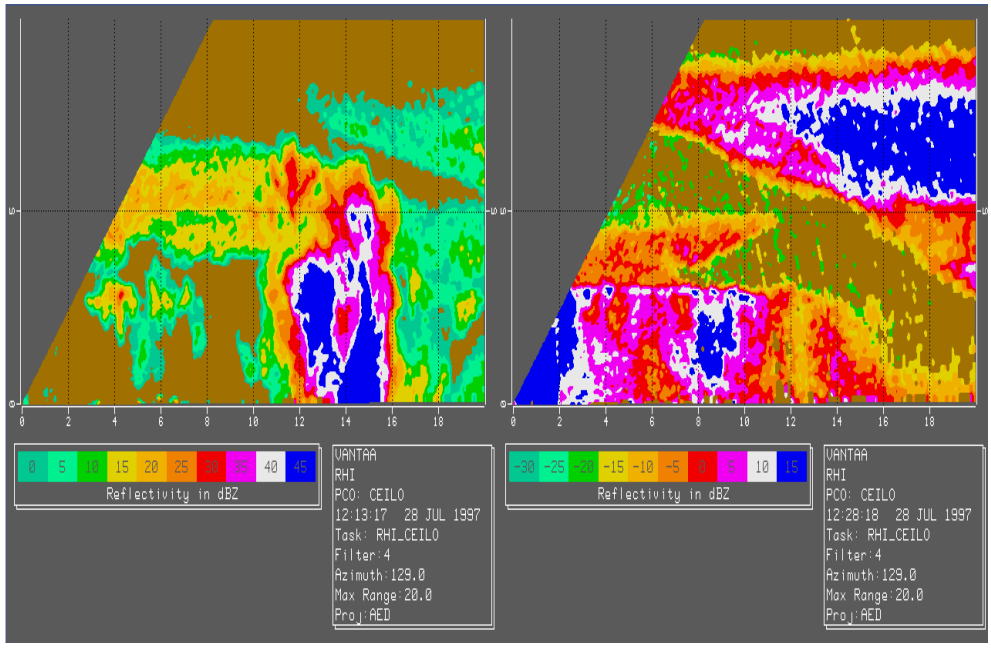


*Figure 3.A.11.* Radar range height scans in Cumulonimbus case

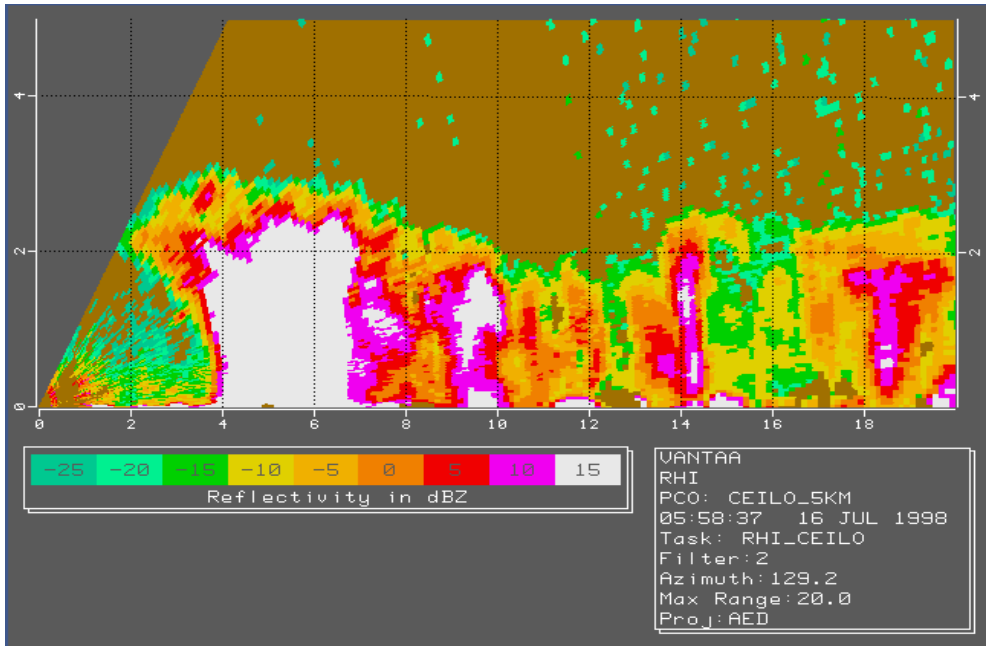


*Figure 3.A.12.* Radar range height scan showing convective cells embedded in stratiform cloud

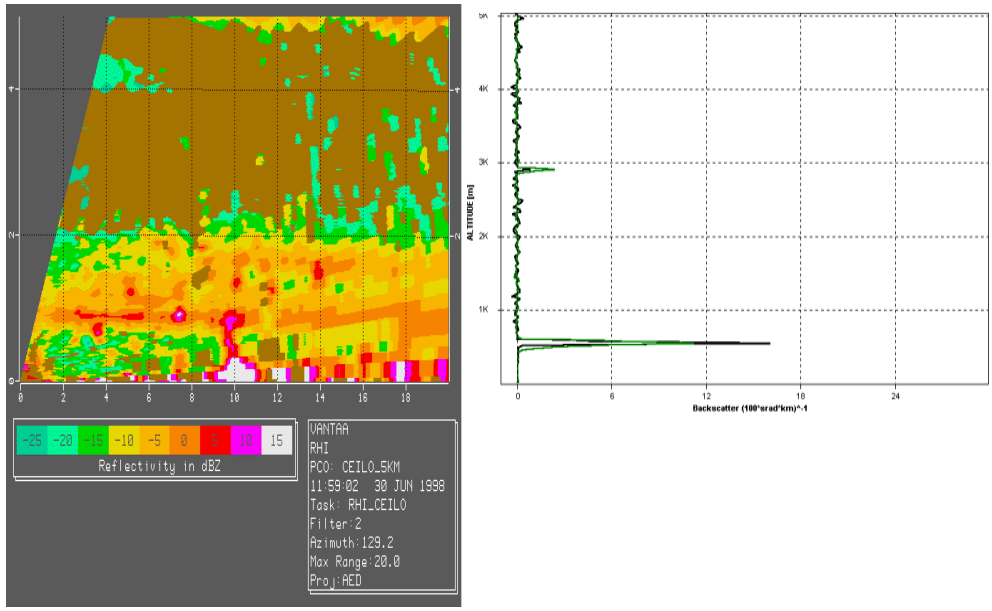


*Figure 3.A.13.* Radar range height scan and ceilometer backscatter profile in a situation illustrating radar image interpretation ambiguity

Chapter 4

# INTEGRATED PROFILING TECHNIQUES AND RELATED ALGORITHMS

## 4.1 RADAR-LIDAR SYNERGY FOR THE RETRIEVAL OF THE LIQUID-WATER CONTENT OF WATER CLOUDS

Oleg A. Krasnov and Herman W. J. Russchenberg

*Delft University of Technology – IRCTR, Delft, The Netherlands*
✉ H.W.J.Russchenberg@irctr.tudelft.nl

### 4.1.1 INTRODUCTION

The parameterisation of the microphysical characteristics for low-level stratiform water clouds can be developed in terms, among others, of the *effective radius of droplets* and the *liquid water content*. In principle, these parameters can directly be measured with in-situ probes mounted on board of aircrafts. These instruments, however, have an extremely small sample volume. Remote sensing methods, although less direct, have a much better spatial and temporal coverage and they allow for routinely monitoring of clouds. In this chapter the focus is put on water clouds. As explained in Section 3.1, no single instrument is sufficient to completely measure liquid water clouds, because:

- lidar signals do not reach the cloud top and are therefore not representative for the whole cloud;

- radars are not always sensitive enough to detect the cloud base, and suffer from the 'large droplet issue', where a few small drizzle-like droplets dominate the radar signal and obscure reflections of smaller cloud droplets;
- standard microwave radiometers are not range-resolving and can only give estimates of the integrated liquid water path of a cloud – details of the vertical distribution of the cloud water are not resolved.

As a consequence, only a combination of sensors can lead to satisfying results. In this section the combination of radar and lidar to retrieve the liquid water content will be discussed in more depth. Other techniques, using different combinations of instruments, were introduced in Section 3.1.

### 4.1.2 PRINCIPLE OF THE RADAR-LIDAR TECHNIQUE

The technique of the radar-lidar technique is best explained with figure 4.1(left). The left panel shows the radar reflectivity factor Z versus the liquid content. It is clear that with radar alone, no realistic estimate of the liquid water content can be made. The scatter is huge, because of drizzle droplets inside the clouds. The right panel shows the ratio of the radar reflectivity factor

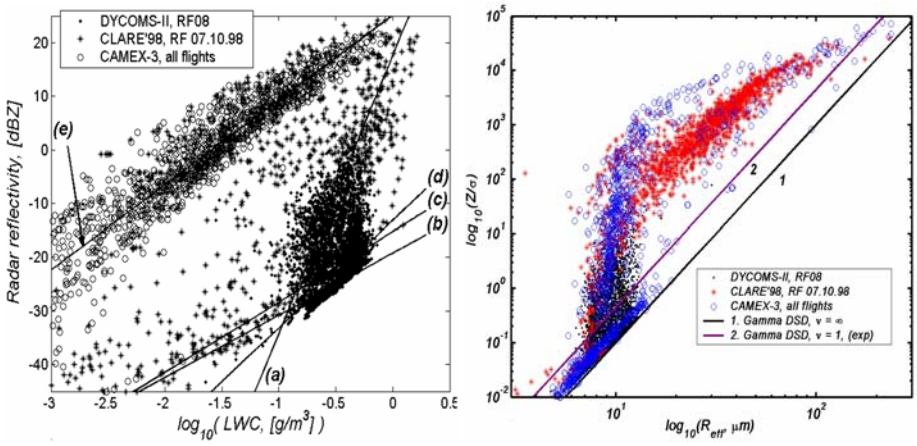


*Figure 4.1.* Left panel: Simulated relationships between the radar reflectivity factor $Z$ and the liquid water content LWC. The solid lines are best fit regression curves relating the liquid water content to the radar reflectivity for different parts of the plot. – Right panel: Simulated radar-lidar ratio versus the effective radius. Both plots are based on in-situ data taken during the CLARÉ98, DYCOMS-II, and CAMEX - 3 campaigns

and extinction of the lidar signal in the radar volume. The observed tendency reflects the process of drizzle formation in the cloud. The region between the

two diagonal lines corresponds to what can be expected from a mono-modal drop size distribution. Deviations from this are due to bi-modalities. We can see that around an effective radius of 10 micron the drop size distribution starts to become bimodal. Initially, the lidar extinction remains more or less constant (the radar reflectivity is much more sensitive to changes in the drop size), but later, when the drizzle component of the drop-size distribution starts to dominate, also the lidar extinction is affected. The drop size distribution is approaching the mono-modal shape, and the radar-lidar ratio curve starts to follow the diagonal lines again. This behaviour of the radar-lidar ratio can be

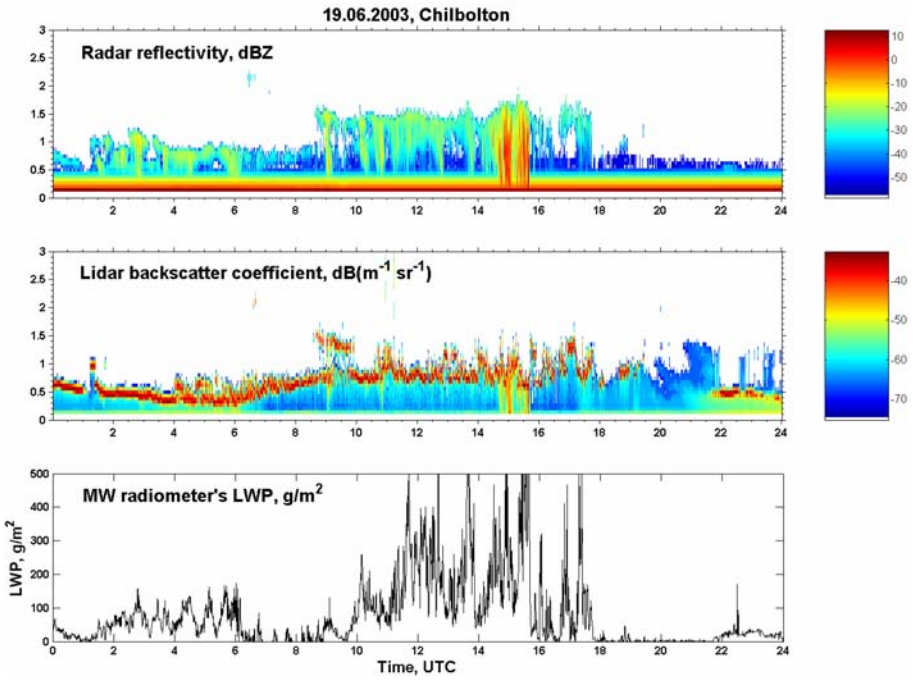


*Figure 4.2.* Radar, lidar, and microwave radiometer observations of sometimes drizzling water clouds. Data is taken at Chilbolton

used to classify the cloud into three regimes: non-drizzling clouds, clouds-in-transition in which drizzle is being formed, and clouds containing mature drizzle. These regimes can be matched with the appropriate relationship between the radar reflectivity factor and the liquid water content derived from the left panel in figure 4.1:

**Clouds-in-transition:** (a) Baedi et al. (1999):

$$Z = 57.54 \cdot LWC^{5.17} \tag{4.1}$$

**Non-drizzling clouds:** (b) Fox and Illingworth (1997):

$$Z = 0.012 \cdot LWC^{1.16} \tag{4.2}$$

(c) Sauvageot and Omar (1987):

$$Z = 0.03 \cdot LWC^{1.31} \tag{4.3}$$

(d) Atlas (1954):

$$Z = 0.048 \cdot LWC^{2.0} \tag{4.4}$$

**Drizzling clouds:** (e) Best fit of all data for the CAMEX-3 and CLARE'98 campaign:

$$Z = 323.59 \cdot LWC^{1.58} \tag{4.5}$$

To select the appropriate relationship, the following thresholds are used with the radar-lidar ratio:

- *Non-drizzling clouds*: radar-lidar ratio $< -1$;
- *Clouds-in-transition:* $-1 <$ radar-lidar ratio $< 1.8$;
- *Drizzling clouds:* radar-lidar ratio $> 1.8$.

Large values of the optical extinction in water clouds usually cause situations when the ground-based lidar backscattering profile (and derived optical extinction) does not cover the whole cloud depth. Consequently, the radar-lidar ratio can not be retrieved for the upper part of the cloud. In such cases only the radar reflectivity is used to classify the cloud regime. It requires two threshold values of the radar reflectivity factor. A lower value of -30 *dBZ* can be used for the classification of the "non-drizzling clouds" class. This value was estimated from the CLARE'98 in-situ measured cloud particles size spectra and has good agreement with others campaigns data for stratiform clouds. The second threshold value for differentiation the clouds with "light" and "heavy" drizzle fractions using the similar procedure was selected to be equal to -20 *dBZ*. The latter is however very variable: during application of the algorithm to remote sensing data it can be used as an additional free parameter in the retrieval algorithm to optimize the results.

The algorithm produces vertical profiles of the liquid water content. These profiles can be integrated over the height to get the liquid water path. This can be compared with retrievals from a microwave radiometer for validation.

### 4.1.3 THE APPLICATION TO CLOUDNET DATA

CloudNet is a research project supported by the European Commission under the Fifth Framework Programme. The project, from April 2001 – September 2005, aimed to collect data obtained quasi-continuously for the development and implementation of cloud remote sensing synergy algorithms. A network of three cloud remote sensing stations: Chilbolton - UK, Cabauw – the

Netherlands, and Palaiseau – France, were operated continuously, their data formats were harmonized and a joint data analysis was performed to evaluate the representation of clouds in major European weather forecast models. Remote sensing synergy techniques for the retrieval of ice- and water-cloud parameters were developed in the framework of the project and applied to measured data to produce different product levels. The detailed description of the CloudNet project, available data and products can be found on the internet site http://www.cloud-net.org.

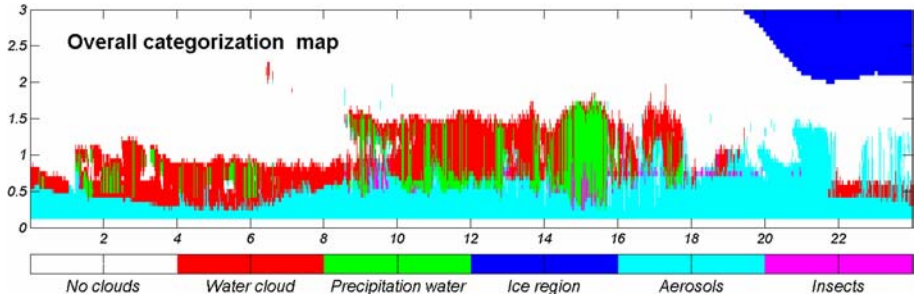


*Figure 4.3.* Categorization of the clouds with the standard CloudNet classification scheme

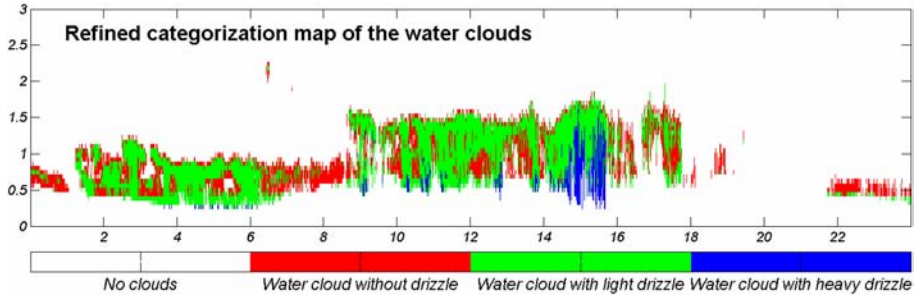


*Figure 4.4.* Refined categorization of water clouds with the radar-lidar technique

Performing the radar-lidar algorithm on the CloudNet data base requires a selection tool for the identification of water clouds in, usually complex, atmospheric situations with water, mixed and ice clouds occurring simultaneously. To this end, dedicated categorization algorithms were developed and implemented in the CloudNet data base (Hogan and O'Connor, 2004).

Figure 4.1 shows temporally and spatially matched radar, lidar and radiometer measurements for one observational day, June 19, 2003, at Chilbolton. This day is quite interesting, as a combination of different water-cloud types and precipitation occurs. In the time interval, 01.00 - 06.00 UT, thin-drizzling stratiform clouds with cloud top around 1000 m above see level can be seen, followed by non-precipitating clouds, and between 09.00 – 18.00 UTC thick drizzling and rain clouds with cloud top up to 1500 m above see level are

present. For the whole day the cloud top is well below the zero-C isotherm. In figure 4.1.3 the CloudNet categorization map is shown. This map was used

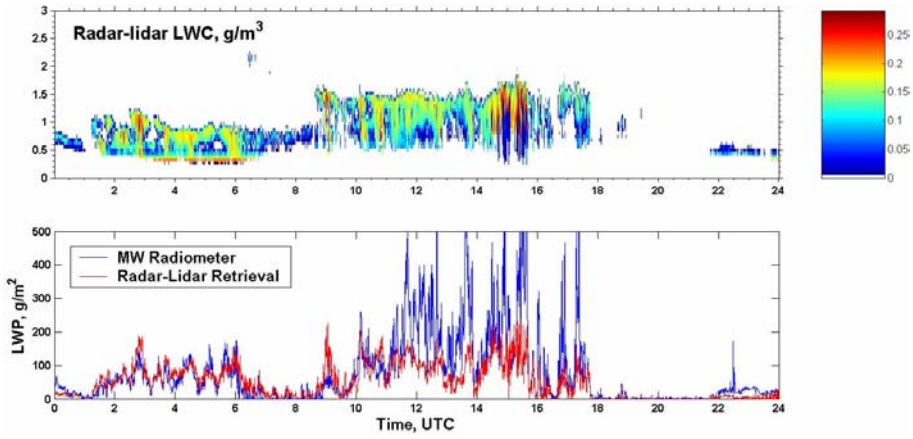


*Figure 4.5.* Retrieved liquid water content profiles with the radar-lidar technique and the liquid water path obtained with the microwave radiometer

to select liquid water clouds. On the remaining data the radar-lidar algorithm was applied to refine the classification into the three earlier mentioned cloud regimes. The resulting liquid water categorization map is presented in figure 4.3. It shows a quite natural and physically understandable drizzle distribution within the clouds.

This liquid water categorization map was used for the selection of the appropriate relationship between the liquid water content and radar reflectivity. The resulting profiles of liquid water content are presented in the upper panel of figure 4.4. The vertical integration of the resulting LWC gives the liquid water path, which can be compared with independent measurements with microwave radiometer: see the lower panel of figure 4.4. Figure 4.4 shows good correlation and agreement. For the interval 09.00 – 18.00 UTC, with precipitation reaching the ground, the agreement is not so good, although some correlation is still visible. To exclude such rainfall, all cases when the microwave radiometer's liquid water path was larger than 400 g/m$^2$ are subsequently excluded from further consideration. The scattering diagram of the radar-lidar retrievals versus radiometer data is presented in figure 4.5, left panel, showing good agreement in retrievals up to 150 g/m$^2$. Above this value the relation becomes non-linear. The histogram of the difference between the microwave radiometer derived LWP and the one of the radar-lidar technique is presented in figure 4.5, right panel. It demonstrates a quite reasonable statistical bias of 12 g/m$^2$ and standard deviation of 44.5 g/m$^2$, which has practically the same order as the random error of the microwave radiometer's LWP itself.

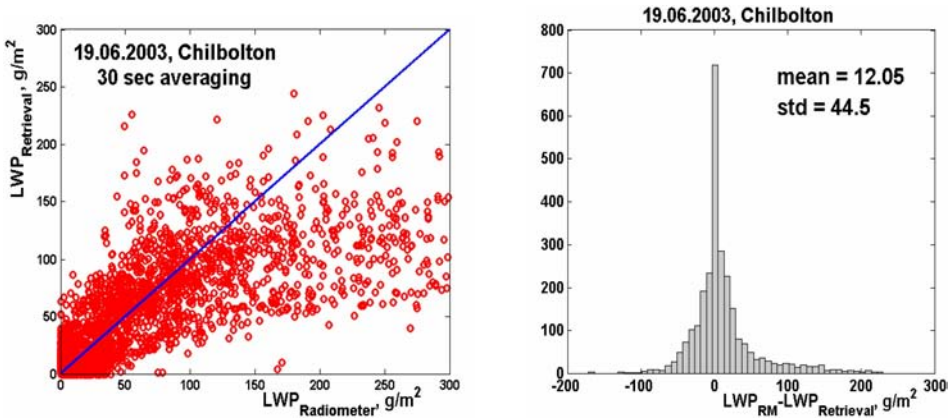


*Figure 4.6.* Comparison of the liquid water path obtained with the radar-lidar technique and the radiometer

The order magnitude of these statistical moments for the difference in LWPs from the radar-lidar technique and microwave radiometer is the same for the whole CloudNet database. For the cases without precipitation, when the microwave radiometer's liquid water path is less then 400 g/m$^2$, the statistical difference between the integrated liquid water contents derived from the radiometer and from the proposed technique is on the order of 50 g/m$^2$.

### 4.1.4 CONCLUSIONS

The combination of radar and lidar is very beneficial for the operational observation of liquid water clouds. It is useful for:

- The detection and parameterization of the drizzle fraction in water clouds,
- the classification of water clouds into three types – "non-drizzling clouds", "clouds-in-transition" and "drizzling clouds", and / or for
- the retrieval of profiles of the liquid water content.

The proposed technique for the *LWC* retrieval has been applied to the dataset collected in the framework of the CloudNet project on three European remote-sensing sites: Chilbolton – UK, Cabauw – the Netherlands, and Palaiseau – France. In total it includes 1784 days of observation. The *LWC* comparison between the radar-lidar technique and microwave radiometer technique shows good correlation and agreement. In the absence of precipitation, when radiometer *LWC* is less than 400 g/m$^2$, the statistical difference between radiometer and proposed technique is on the order of 50 g/m$^2$.

## Bibliography

Atlas, D., 1954: The estimation of cloud content by radar. *J. Meteor.*, **11**, 309–317.

Baedi, R.J.P., J.J.M. de Wit, H.W.J. Russchenberg and J.P.V. Poiares Baptista, 1999: Alternative algorithm for correcting FSSP measurements. *Proc. Int. Workshop CLARE'98*, ESA-ESTEC, 123–127.

Fox, N.I. and A.J. Illingworth, 1997: The retrieval of stratocumulus cloud properties by ground-based cloud radar. *J. Appl. Meteorol.*, **36**, 485–492.

Hogan, R.J. and O'Connor, E.J., 2004: Facilitating cloud radar and lidar algorithms: the Cloud-Net Instrument Synergy/Target Categorization product. *CloudNet Project Documentation.* – avail. on-line: http://www.met.rdg.ac.uk/∼swrhgnrj/publications/categorization.pdf

Sauvageot, H. and J. Omar, 1987: Radar reflectivity of cumulus clouds. *J. Atmos. Oceanic Technol.*, **4**, 264–272.

# 4.2 DETECTION OF FOG AND STRATUS BY COMBINING CEILOMETER AND CLOUD RADAR INFORMATION

Daniela Nowak

*Institute for Atmospheric and Climate Science, EHT Zürich, Switzerland*
✉ Daniela.Nowak@meteoswiss.ch

## 4.2.1 INTRODUCTION

Precise forecasting of the formation, evolution, and erosion of fog and/or low stratus is a major challenge in meteorology, especially in complex topography. Frequent and detailed information about the meteorological conditions are important for weather forecasters. Especially during nighttime, automatic weather reports are becoming important as human observations are continuously more difficult to organize (Aviolat et al., 1998). One of the high-priority duties of observers is the description of the evolution of clouds, especially within the planetary boundary layer.

One of the goals of the COST720 Temperature, hUmidity and Cloud (TUC) wintertime experiment, undertaken in Switzerland in 2003-2004 (Ruffieux et al., 2006) and described in section 5.1, was to provide a dataset for determining base and top of low clouds using a simple combination of ground-based remote sensing instruments. This section describes a method to identify fog situations and low stratiform cloud layers from cloud radar and ceilometer data (Nowak et al., 2008). During wintertime stable episodes, fog and low stratiform cloud layers often occur in the Swiss Mittelland, a relatively flat region between the hills of he Jura mountains to the N-NW (1000-1500 m asl) and the Alps to the S-SE (2000-4400 m asl). Among profiling systems set during the TUC experiment, a Vaisala CT25K ceilometer and a 78GHz FMCW cloud radar were installed and operated at Payerne from mid of November 2003 to mid of February 2004.

## 4.2.2 INSTRUMENTATION AND METHOD

The aerological station of Payerne is an official World Meteorological Organisation (WMO) site for synoptic weather observations, including cloud information, which are performed every 3 hours, starting at 0 UTC. Cloud cover, type, and base height are reported for the three main cloud levels (low, middle, high clouds) as well as the ground visibility (Müller, 1982). However, a limitation of these observations is the restriction to the lowest cloud layer in the case of multi-layer clouds with full sky coverage of the lowest layer.

Even if these observations are subjective and may vary from one observer to another, they are generally of excellent quality and give regular and important information to meteorologists about the state of the sky, the meteorological conditions (fog, snow, rain etc.), and the visibility. Balloon-borne meteorological radiosoundings including pressure, temperature and humidity profiling are performed twice a day at 12 and 0 UTC (launched at 11 and 23 UTC respectively). In addition, a wind profiler is operated continuously.

In the presented method, cloud base is detected by a Vaisala ceilometer CT25K. This light detection and ranging (lidar) system is able to detect three cloud layers simultaneously and to retrieve cloud heights every 30 s with a vertical resolution of 15 m. The minimum visibility that can be measured is 15 m (e.g. in case of fog). A 78GHz Frequency-modulation continuous wave (FMCW) cloud radar, designed at the Rutherford Appleton Laboratory, retrieves backscatter information at a time interval of 30 s. It is sensitive to clouds and precipitation up to 8 km above the ground and with a vertical resolution of around 15 m. It is used to retrieve cloud top information. The lowest detected cloud top height is 65 m above the radar.

Human eye observations (synops) were used to estimate the efficiency of cloud detection by the ceilometer and cloud radar combination. The fog situations were defined as either fog being reported or mist with a code 9 for the parameter "total cloud cover" (sky not visible because of fog, snow or other meteorological phenomena). Cases with fog, in combination with other clouds or more than one cloud layer were discarded. Low level stratus cloud situations were selected if a total coverage of 8 octas (*stratus nebulosus*) was reported. Cases with more than one cloud type or more than one cloud layer (full cloud coverage not in the first detected cloud layer) were not considered. This allowed testing the detection of fog or stratus boundaries with the ceilometer and cloud radar in simple and clearly identified cases.

Wind profiler signal-to-noise ratio time series measured simultaneously were used in two case studies (Gossard et al., 1999). The refractive-index structure function parameter $C_n^2$ profile depends mainly on temperature and humidity gradients in the atmosphere as well as turbulence. At the top of a well defined stratus layer, the strong change in humidity and temperature with height as well as a possible increase of turbulence initiated by wind shear between the two distinct layers can be used as information to detect it.

In order to determine the fog and cloud base height, only the first detected signal from the ceilometer was taken into account. To determine the fog or cloud top from the FMCW cloud radar data, a simple empirical method was applied (Ruffieux et al., 2006).

### 4.2.3 RESULTS

Out of 720 human eye reports (synops) recorded during the TUC campaign 200 stratus cloud or fog situations were stated. These cases are divided into

110 stratus cloud and 90 fog observations (Table 4.1). The ceilometer was operational for all cases and the FMCW radar for 143 of them. For the rest of this section only cases where both remote sensing systems were in operation (143 cases) are analyzed: 83 low stratus clouds cases (including 25 cases with precipitation), and 60 fog cases (including 9 cases with precipitation).

| | Total obs. | CR & CM operative | CR (top) | CM (base) | CR & CM simult. |
|---|---|---|---|---|---|
| Stratus all | 110 | 83 | 34 (41%) | 74 (89%) | 34 (41%) |
| Stratus dry | 79 | 58 | 34 (59%) | 56 (97%) | 34 (59% |
| Fog all | 90 | 60 | 38 (63%) | 59 (98%) | 38 (63%) |
| Fog dry | 80 | 51 | 35 (69%) | 50 (98%) | 35 (69%) |

*Table 4.1.* Rate of cloud base and top detection, relative to the total observed situations for both systems operative during TUC in Payerne, 15 November 2003 – 15 February 2004 (obs. = observations, CR = cloud radar, CM = ceilometer, simult. = simultaneous detection). The total observations correspond to the number of stratus or fog situations reported during the TUC campaign.

For the stratus situations, the ceilometer retrieved cloud bases in 89% of the situations (74 of 83 cases, see Table 4.1), while the cloud radar retrieved the cloud top in 41% of the cases (34 out of 83). All the 34 latter cases were also in the 74 cases when cloud based was retrieved by the ceilometer. Furthermore, it was not possible to retrieve cloud top with the FMCW radar in the low stratus cloud situations with precipitation, and consequently all 34 cases were dry low stratus situations. Considering only dry situations, the ceilometer retrieved cloud base in 97% of the cases (56 out of 58), and the cloud radar also detected the cloud top in 59% of the cases.

In 59 of the 60 fog situations, the vertical visibility could be retrieved by the ceilometer (98%), leading to the detection of a lower boundary, while the cloud radar detected the cloud top in 63% of the situations (38 of 60 cases). In fog situations also, precipitation again made cloud top detection with the cloud radar more difficult. Three situations with drizzle were detected by the cloud radar out of 9 fog situations with precipitation. When cases with any form of precipitation are disregarded, the fog detection with both systems worked for 69% of the observed fog situations (35 of 51 cases).

Two single-day case studies are chosen to demonstrate possibilities and limitations of such ground-based remote sensing in determining low clouds. The first case on 9 December 2003 is a typical day with fog and low stratus changing with time but remaining present the entire day. It represents an example where the stratus and fog determination with both systems in parallel performed reasonably well (figure 4.7). A low level stratus cloud layer was reported in the synops at 0, 9, 12, 15, 18 and 21 UTC and at 0 UTC the following day. At 3 and 6 UTC, fog with visibility below 1 km was observed. Good determination of the fog and low stratiform cloud situation was possible over

24 hours. A few measurement points of the cloud radar (cloud top) retrieval are detected crossing or going below the ceilometer (cloud base) signal (after 9 UTC and between 12 and 18 UTC). This may be explained either by the instruments pointing in slightly different directions, or by a height measurement error in one or both instruments. The determination of cloud base and top was compared with the temperature and humidity profiles measured with radiosoundings from Payerne at 0 UTC (8 December 2003), at 12 UTC and at 0 UTC (see the three boxes in figure 4.7 upper panel). At 12 UTC and 0 UTC on 9 December there is an excellent agreement between the top of the cloud as detected with the cloud radar and the bottom of the thermal inversion, indicated by a sharp decrease of the humidity (grey line), and temperature (magenta line)

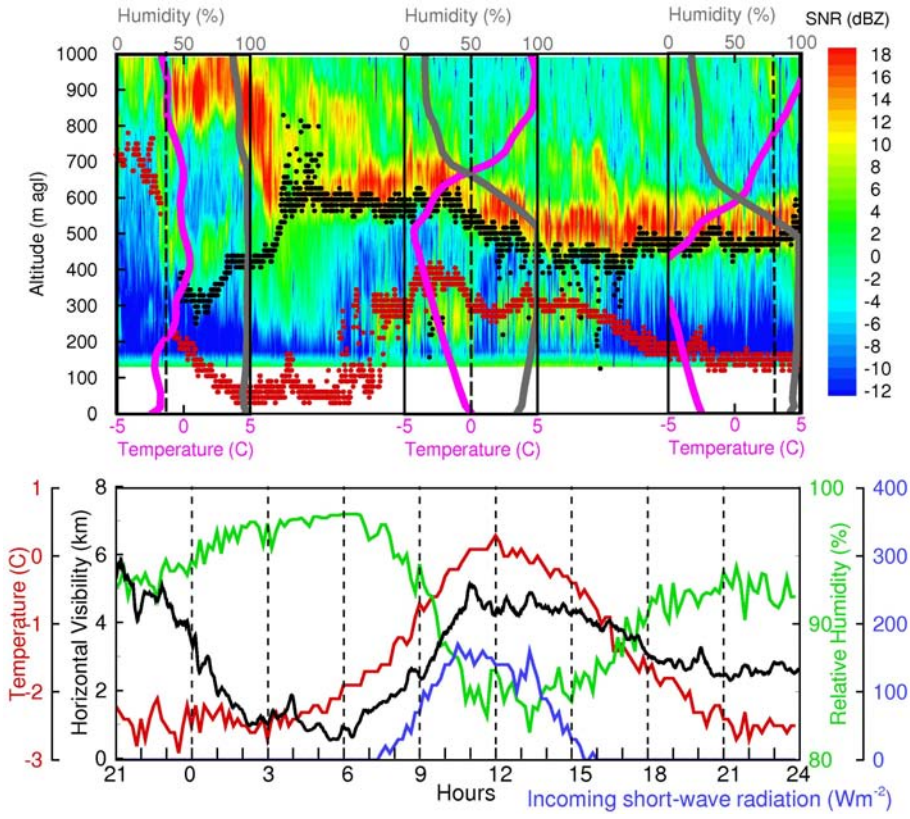


*Figure 4.7.* Upper panel: time series of cloud base (ceilometer, red dots), cloud top (cloud radar, black dots), and 2-D color time series of windprofiler signal-to-noise ratio, 9 December 2003, starting at 21 UTC of the previous day. The three rectangles with grey and purple lines correspond to the profiles measured with the radiosounding at 11 and 23 UTC (dashed line = time of sounding, purple line = temperature with a horizontal scale of 10 K, green line = humidity with a horizontal scale of 100%). Lower panel: time series of surface relative humidity (green), temperature (red), incoming short-wave radiation (blue), and horizontal visibility (black)

starting to increase with altitude. Confirmation of the cloud top determination is also obtained by overlaying the data with the Payerne wind profiler signal-to-noise ratio profiles (colored background in figure 4.7): the intensity of the returned signal depends mainly on humidity gradients and turbulence, producing an intensity maximum just above the cloud layer (Dibbern et al., 2003). On the other hand, when comparing with the first radiosonde profile (8 December 0 UTC), or with the wind profiler SNR between 21 and 3 UTC, the cloud radar seems to give an erroneous cloud top height. Close inspection of the upper panel of figure 4.7 reveals the reason for this discrepancy. First, between 0 and 3 UTC, the wind profiler shows higher SNR at two altitudes separated by one region of lower SNR. This may indicate multiple layers in the first 1000 m, of which the cloud radar would have picked the lowest one. Second, the temperature inversion was at 1500 m above ground level (AGL) (not shown), which is out of the limit chosen for the cloud radar top height detection algorithm. Finally, the ceilometer shows a transition period from a higher cloud layer to well detected low stratus cloud between 21 and 0 UTC. Thus, it can be assumed that there was a transition period until 4 UTC from a multilayer cloud situation in the lower troposphere to a well defined low stratus cloud situation for the rest of the day. Surface information (lower panel, figure 4.7) is consistent with a day constantly overcast with a low cloud layer or fog. The relative humidity (green) was high all day long ($> 80\%$), the temperature (red) shows only a modest increase during daytime, and the incoming shortwave radiation (global radiation, blue) is very low even at noon. Similarly, the horizontal visibility was low all day corresponding well with the low visibilities reported in the synops, even though the correspondence is not perfect (synops indicate $>$ 10 km of visibility at 0 UTC, then visibility $< 2$ km until 15 UTC, then again $> 10$ km).

The second case, 19th November 2003, represents a more complex situation where fog and cloudy conditions alternated. Fog was reported in the synops at 6, 15, 18 and 21 UTC, as well as 0 UTC. Figure 4.8 displays the data retrieved from ceilometer and cloud radar for that day. The cloud radar was unable to detect the fog top corresponding to observations at 18, 21 and 0 UTC, but the fog base was well detected with the ceilometer. At 6 UTC the cloud top was not detected, but the cloud base and top of a layer of fog was detected during the previous hour, while at noon, the base and top of a cloud layer was detected by the ceilometer and cloud radar, even though the observation at that time did not report fog. In the period between 10 and 15 UTC conditions were unstable with fog setting and clearing, which explains the apparently contradictory results. Radiosounding temperature and humidity profiles recorded at 0, 12 and 0 UTC the next day are consistent with the reported intermittent fog situations. The two radiosoundings at 0 UTC show a high relative humidity (grey line) with a sudden decrease between 200 and 400 m AGL. At 12 UTC, the humidity is high but not as much as expected in a foggy situation, and the drop at around 300 m is less marked. The humidity at this time may have been too low for

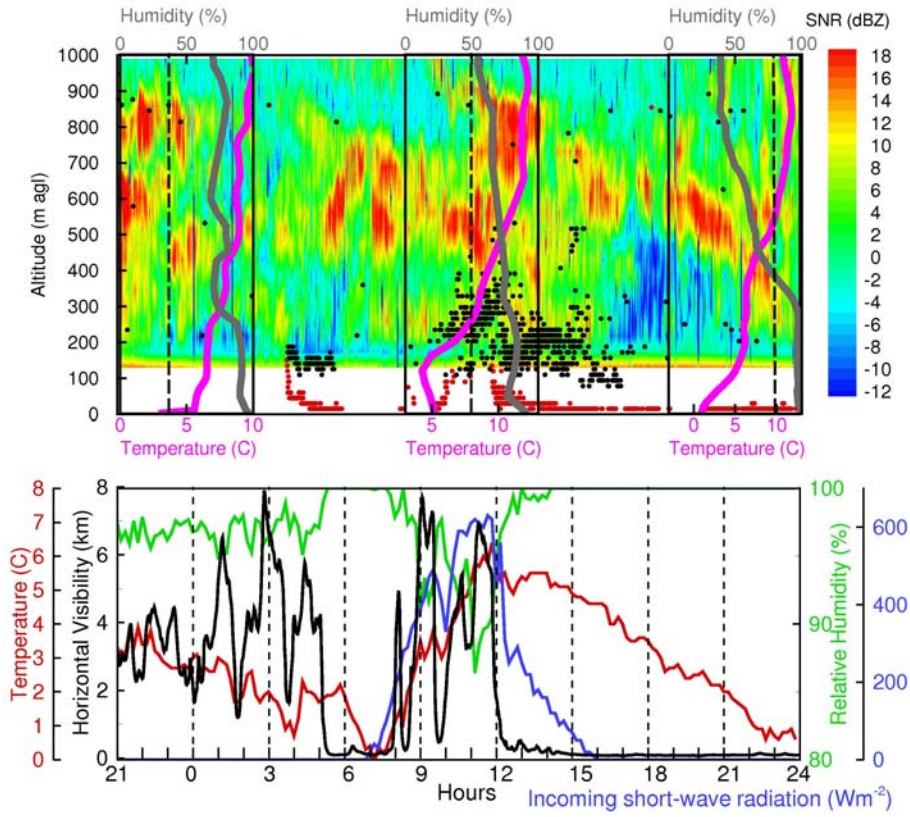


*Figure 4.8.* Same as figure 4.7, but for 19 November 2003

a dense fog to set up, and fog and mist episodes alternated. This explains the fog detection by the ceilometer and cloud radar while the observation at noon did not report fog, and the relative humidity from the profile being below the selected threshold. Wind profiler signal-to-noise ratio profiles also show patchy layers which indicate variable hydrolapse and temperature inversion height and strength. This is likely to be associated with alternate presence and absence of fog or cloud. The surface information (figure 4.8, lower panel) is consistent with such a situation, as well. The relative humidity (green) was above 80and 100% when fog was reported. The horizontal visibility varied between 0 and 8 km. The very low visibility observed at 18, 21 and 0 UTC also confirms the presence of fog. Temperature (red) and shortwave radiation (global radiation, blue) are as expected for such conditions.

### 4.2.4 DISCUSSION AND CONCLUSION

The intention of the study was to test an automatic detection algorithm of fog and low stratus using both ceilometer and cloud radar data. The ceilometer

showed excellent efficiency as 98% of the fog situations and 89% of the low stratus situations could be determined. Restricting the stratus cases to situations without precipitation allows an overall detection efficiency $> 95\%$. The lower efficiency in case of precipitation is explained by the laser light of the instrument being scattered back by the hydrometeors. In the case of the FMCW radar, precipitation (snow and rain) produces artifacts in the reflectivity signal. It was thus not possible to determine the cloud top when precipitations occurred, using the algorithm for cloud top detection. However under fog conditions with drizzle, the determination of the top of the cloud was still possible.

In this study, about 60% of the stratus cloud tops and 70% of the fog tops could be determined under dry (without precipitation) conditions. In the remaining cases, the cloud top may sometimes have been outside the detection range of our algorithm, which was set to 1200 m AGL. Another possibility for cases when the FMCW cloud radar did not detect the cloud top in dry situations may be its lack of sensitivity to small droplets, or to saturation in the first range gates in presence of very thin fog layers. Finally, further improvement of the cloud top retrieval algorithm would probably result in better scores (e.g. in the case of multilayer clouds).

The two case studies demonstrated the capabilities and limitations of the cloud radar and ceilometer combination. In the case of 9 December 2003 verification with the radiosounding confirmed the altitude of the cloud top. The comparison with the wind profiler SNR confirmed that the highest SNR is normally found just above the cloud radar-determined upper boundary.

A combination of both ceilometer and cloud radar could be a good alternative to human observations to monitor low clouds evolution on airports for example. In addition, cloud amount (sky coverage in octas) could automatically be estimated using incoming long-wave radiation and surface parameters (Dürr and Philipona, 2004).

## Bibliography

Aviolat, F., T. Cornu and D. Cattani, 1998: Automatic clouds observation improved by an artificial neural network. *J. Atmos. Oceanic Technol.*, **15**, 114–126.

Dibbern J., W. Monna, J. Nash, and G. Peters (Ed.), 2003: COST Action 76: Development of VHF/UHF wind profilers and vertical sounders for use in European observing systems - Final report, 2003. European Commission, EUR 20614, 352pp.

Dürr, B. and R. Philipona, 2004: Automatic cloud amount detection by surface longwave downward radiation measurements. *J. Geophys. Res.*, **109**, D05201.

Gossard E.E., D.E. Wolfe, and B.B. Stankov, 1999: Measurement of humidity profiles in the atmosphere by the Global Positioning System and radar wind profilers. *J. Atmos. Oceanic Technol.*, **16**, 156–164.

Müller, G., 1982: Handbuch für Beobachter des automatischen Beobachtungsnetzes. Schweizerische Meteorologische Anstalt (SMA), 121p.

Nowak D., D. Ruffieux, J. L. Agnew, and L. Vuilleumier, 2008: Detection of fog and low cloud boundaries with ground-based remote sensing systems, *J. Atmos. Oceanic Technol.*, In Press.

Ruffieux ,D., J. Nash, P. Jeannet and J. L. Agnew, 2006: The COST 720 temperature, humidity and cloud profiling campaign. *Meteorol. Zeitschr.* (TUC Special Issue.), **15**(1), 5–10.

## 4.3 AN EXAMPLE OF INTEGRATION OF UHF WIND PROFILER AND MICROWAVE RADIOMETER

Laura Bianco[1,2], Domenico Cimini[3], Frank Marzano[4], Randolph Ware[5]

[1] *Corporative Institute for Research in Envoironmental Sciences (CIRES), University of Colorado, Boulder, Colorado(USA)*

[2] *NOAA/Earth System Research Laboratory (ESRL) / Physical Sciences Division (PSD), Boulder, Colorado, (USA)*
Laura.Bianco@noaa.gov

[3] *Center of Excellence CETEMPS, University of L'Aquila, Italy*

[4] *Dipartimento di Ingegneria Elettrica, University of L'Aquila, Italy*

[5] *Radiometrics Co. and University Consortium for Atmospheric Research, Boulder, Colorado, USA*

### 4.3.1 ABSTRACT

An algorithm to compute atmospheric humidity high-resolution profiles by synergetic use of MicroWave Radiometer Profiler (MWRP) and Wind Profiler Radar (WPR) is illustrated. The focal point of the proposed technique is based on the processing of WPR data for estimating the potential refractivity gradient profiles and their optimal combination with MWRP estimates of potential temperature profiles in order to fully retrieve humidity gradient profiles. The combined algorithm makes use of recent developments in WPR signal processing, computing the zeroth, first, and second order moments of WPR Doppler spectra via a fuzzy logic method, which provides quality control of radar data in the spectral domain. On the other hand, the application of neural network to brightness temperatures, measured by a multichannel MWRP, can provide continuous estimates of tropospheric temperature and humidity profiles. Performance of the combined algorithm in retrieving humidity profiles is compared with simultaneous in situ radiosonde observations (RAOB). The empirical sets of WPR and MWRP data were collected at the Atmospheric Radiation Measurement (ARM) Program's Southern Great Plains (SGP) site. Combined microwave radiometer and wind profiler measurements show encouraging results and significantly improve the spatial vertical resolution of atmospheric humidity profiles. Preliminary results are shown and advantages and limitations related to this technique are discussed.

## 4.3.2 INTRODUCTION

The role of ground-based remote sensors in boundary layer research is currently well established due to the ability of remote sensors to monitor important meteorological parameters continuously in height and time. In the past few years, ground-based microwave radiometry has proven very reliable for accurately measuring atmospheric integrated water vapour content. More recently, the development of multispectral microwave radiometers has opened the possibility of humidity-profile estimates by passive instruments, thanks to the differences in the height dependence of weighting functions at different frequencies. However, the inversion of humidity profiles from passive observations is an ill-posed problem. Thus, the vertical resolution of estimated profiles is limited by the small number of frequencies carrying independent information. Therefore, ground-based passive retrievals usually tend to smooth elevated sharp humidity gradients, although providing good estimates of the main water vapour profile, especially near the surface. On the other hand, active instruments, such Radar Wind Profilers (RWP), are able to detect changes in atmospheric refractivity related to humidity gradients. The aim of this work is to show the results of an algorithm for the computation of high-resolution atmospheric humidity profiles by synergetic use of ground-based remote sensors, such as a Micro-Wave Radiometer Profiler (MWPR) and a RWP. Potential refractivity gradient profiles are computed from radar data, and in combination with radiometer estimates of potential temperature profiles, humidity gradient profiles can be retrieved. The algorithm makes use of recent developments in radar and radiometer signal processing applied to simultaneous observations collected in June 2002 at the ARM SGP site, Lamont/OK, USA (Lat.: $36^o$ 37' N, Lon.: $97^o$ 30' W, altitude: 313 m above sea level). The combined algorithm performances in retrieving humidity profiles are tested with simultaneous radiosonde measurements. The synergy of microwave radiometer and wind profiler measurements shows potential for significantly improving the vertical resolution of humidity profiles. Preliminary results are shown and advantages and limitations related to this technique are discussed.

## 4.3.3 BASIC PRINCIPLES

Most atmospheric boundary layer parameters currently obtained by RWP systems are derived from the first three moments of the measured Doppler spectra. The mean velocity profile, obtained by the first moment of the Doppler spectrum, was one of the earliest quantities extracted from remote sensing observations. Unfortunately, radar signals often show contamination from other sources, such as ground clutter, intermittent clutter, radio frequency interference, and sea clutter. For this reason, signal-processing techniques have been developed to identify the true atmospheric signal from the spectra (Wilczak et al., 1995; Cornman et al., 1998; Jordan et al., 1997). Proper identification of the first moment in the spectrum is very important for further applications,

since it allows for more accurate computation of the area under the signal peak, or zeroth moment, that can be related to the Signal-to-Noise Ratio (SNR) of the backscattered power and to other parameters. On the other hand, the second moment of the Doppler spectrum (when the radars are pointing vertically) has not been widely exploited, and its use is still in the research and evaluation stage. It is a measure of the broadening of the Doppler spectrum due to a variety of factors, including velocity variance resulting from atmospheric turbulence on scales smaller than the pulse volume. It has the potential to provide profiles of turbulence quantities, such as eddy dissipation rate and structure parameters, continuously in time. Over the last two decades several attempts have been made to use spectral width from profilers to measure the turbulence intensity without much success (Gossard et al., 1990; Cohn, 1995). The principal problem is related to the fact that contamination by unwanted targets is especially detrimental to second-moment calculations. Other non-turbulent processes also contribute to the broadening. In order to be able to use the spectral width to measure turbulence intensities, it is necessary to be certain that the entire broadening is due to turbulence. To obtain accurate moments, an algorithm that makes use of recent developments in RWP signal processing for computing the zeroth, first, and second moments of RWP Doppler spectra using a fuzzy logic method (Bianco and Wilczak, 2002) was used to provide quality control of radar data in the spectral domain. Once the RWP data have been re-processed, the zeroth, first, and second moments, computed by the fuzzy logic algorithm can be employed to compute the structure parameter of potential refractivity $(C_\phi^2)$, the horizontal wind $(V_h)$, and the structure parameter of vertical velocity $(C_w^2)$, respectively (Stankov et al., 2003). $C_\phi^2$, $V_h$, and $C_w^2$ can then be combined together to retrieve the potential refractivity gradient profiles $(d\phi/dz)$. Measurements from a multi-channel MWRP, operating in the 20-60 GHz range, can provide tropospheric temperature profiles and thus estimates of potential temperature gradient profiles $(d\Theta/dz)$. Profiles of $d\phi/dz$ and $d\Theta/dz$ are needed to fully retrieve humidity gradient profiles $(dQ/dz)$ as suggested by (Stankov et al. 1996). The advantage of such a technique is to retrieve humidity profiles from RWP and MWRP measurements, independently from radiosonde observations. Humidity profiles from the combined algorithm have been compared with simultaneous radiosonde observations to test their validity.

## 4.3.4 INSTRUMENTS AND DATA PROCESSING

The empirical sets of RWP and MWRP data were provided by the ARM Program and collected at the ARM SGP site. The RWP is a 915 MHz five-beam phased-array system manufactured by Radian Corp. (now Vaisala). The antenna is approximatively 4 m square and is oriented in a horizontal plane so the in-phase beam travels vertically. Only the 60 m mode, sampling the boundary layer from 90 m to 2500 m AGL (Above Ground Level) in the ver-

tical, is used for this study. Figure 4.9 is the time-height cross section of range corrected SNR obtained by the RWP on 7 June 2002. The MWRP, manufactured by Radiometrics, observes radiation at 12 frequencies in the 20-60 GHz spectrum. The system includes a vertically pointing infrared sensor, and surface-temperature, humidity and pressure sensors. Observation frequencies (22.035, 22.235, 23.835, 26.235, 30.00, 51.250, 52.280, 53.850, 54.940, 56.660, 57.290, 58.800 GHz) were chosen by eigenvalue analysis to optimize the profile retrieval accuracy (Solheim et al., 1998). The retrieval algorithm is based on a neural network trained with a synthetic data set produced from historical radiosondes launched at the same site. The radiometer 22-30 GHz channels are calibrated by tipping (Han and Westwater, 2000). The 51-59 GHz channels calibration uses a cryogenic blackbody target. Figure 4.10 shows the time-height cross section of temperature $T(K)$ and humidity $Q(gkg^{-1})$ obtained by the MWRP on 7 June 2002.

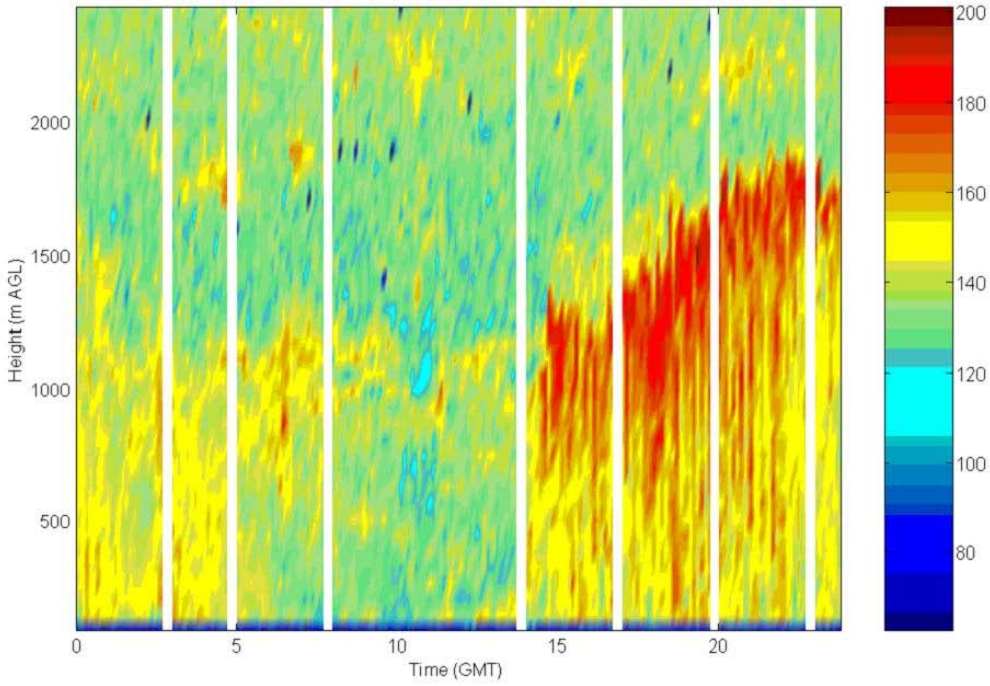


*Figure 4.9.* Time-height cross section of range-corrected SNR obtained by the RWP located at SGP on 7 June 2002.

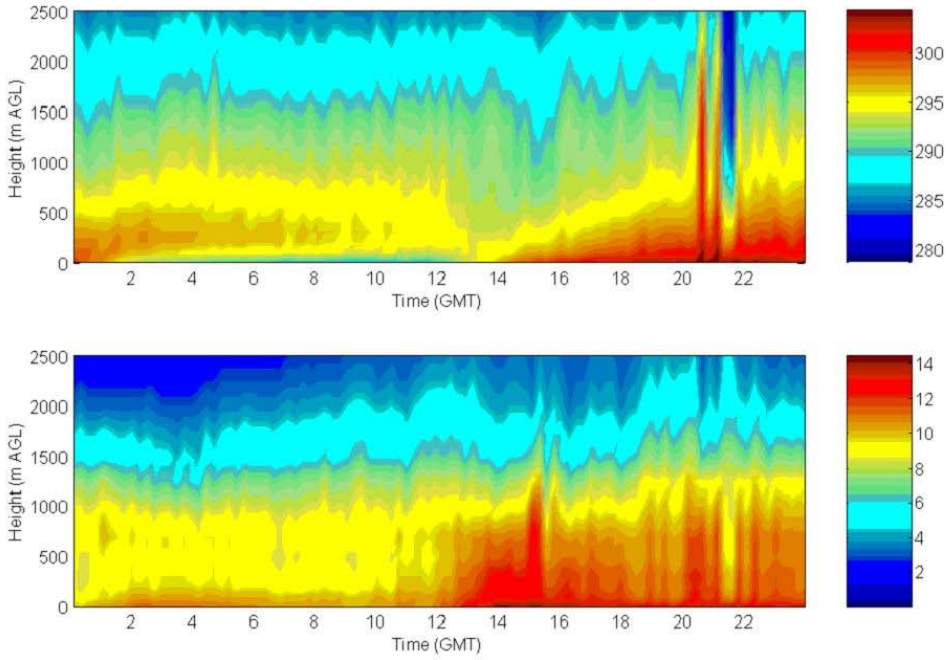


*Figure 4.10.* Upper panel: Time-height cross section of temperature $T(K)$. Lower panel: Time-height cross section of humidity $Q(gkg^{-1})$. Estimates were obtained by the MWRP located at SGP on 7 June 2002.

### 4.3.5 CASE STUDY

To test the potential of this technique, simultaneous measurements from a radiosonde and ground based instruments on 23:30 GMT, 7 June 2002, were processed.

$C_\phi^2$, $C_w^2$ and $dV_h/dz$ profiles are computed from RWP measurements using the vertical beam only. For the computation of $C_w^2$ the algorithm uses an approximate formula (White et al., 1999) for correcting Doppler spectral width for the spatial and temporal filtering effects. For the same hour the profile of $d\Theta/dz$ is obtained from temperature and pressure profiles estimated by MWRP. Introducing the constants $a_0 \approx 1$ and $b_0 \approx 6$ and the outer length scales for potential refractive index ($L_\phi$) and shear ($L_w$) as defined in Gossard et al. (1982), the following equations are valid (Stankov et al., 2003; Gossard et al., 1982; White, 1997):

$$(d\phi/dz)^2 \approx (L_w/L_\phi)^{4/3}(dV_h/dz)^2 C_\phi^2/C_w^2 \tag{4.6}$$

$$dQ/dz = (b_0)^{-1}[d\phi/dz + a_0 d\Theta/dz] \tag{4.7}$$

Ground-based estimates of $C_\phi^2$, $C_w^2$, $dV_h/dz$ and $d\Theta/dz$ profiles are input in Equations (4.6) and (4.7) to retrieve humidity gradient profiles, which are finally compared with in-situ measurements made by radiosondes. Results are presented in figure 4.11. In the upper left panel we show $d\phi/dz$ measurements from radiosonde (red line), estimates from RWP (black line) and MWRP (blue line). In the upper right panel is the vertical gradient profile of potential temperature as obtained by the MWRP (blue) and by the radiosonde (red).

In the lower left panel, the red line is the $dQ/dz$ profile from the radiosonde, the blue line is from the MWRP, while the black line is obtained with the proposed technique (MWRP-RWP), in which the sign ambiguity of $d\phi/dz$ has been resolved looking at the profile of the same quantity estimated by MWRP. Finally, in the lower right panel, vertical profiles of $Q$ as obtained by MWRP (blue), the combined technique (black), and the radiosonde (red) are compared. The case study shows that the combined technique improves substantially the vertical resolution of $dQ/dz$ profiles with respect to the MWRP only. The height of the peak in the MWRP-RWP $dQ/dz$ profile is consistent with the fact that the refractive index structure parameter $C_w^2$ has a local maximum at the inversion, as visible in figure 4.9 at approximately 1650 m AGL, around hour 23:30 GMT.

### 4.3.6 SUMMARY AND FURTHER DEVELOPMENTS

We explored the possibility to improve the vertical resolution of tropospheric humidity profiles using only ground-based remote sensors. The proposed technique is advantageous with respect to previous work (Stankov et al., 2003) because it is completely independent of radiosonde measurements, which are used only for validation. The case study shows the potential of the proposed technique in retrieving continuous humidity profiles and in detecting sharp humidity gradients. The proposed technique requires a well developed turbulence as found in convective situations. This explains why the case study analyzed in this work happened around 23:00 GMT. However, in a following work (Bianco et al., 2005), even limiting our sample to these hours, we experienced several unsatisfactory cases in which the combined technique did not outperform MWRP estimates. In a deeper analysis we found out that the use of vertical gradients of the horizontal wind as computed by standard consensus algorithms strongly influences the quality of the humidity profile retrieval. Therefore, generating consensus files from the raw-moment data, as computed on the post-processed spectra, can limit this undesired aspect.

Possible improvements of the proposed technique concern both data processing and experimental setup. On the first side, we could use a statistical, rather than analytical, approach to derive the absolute humidity profile from the remote observations (Stankov, 1998). Although other investigators (Gossard et al., 1999) found a good agreement comparing the two methods, the statistical approach provides tools for making the estimate possibly more robust.

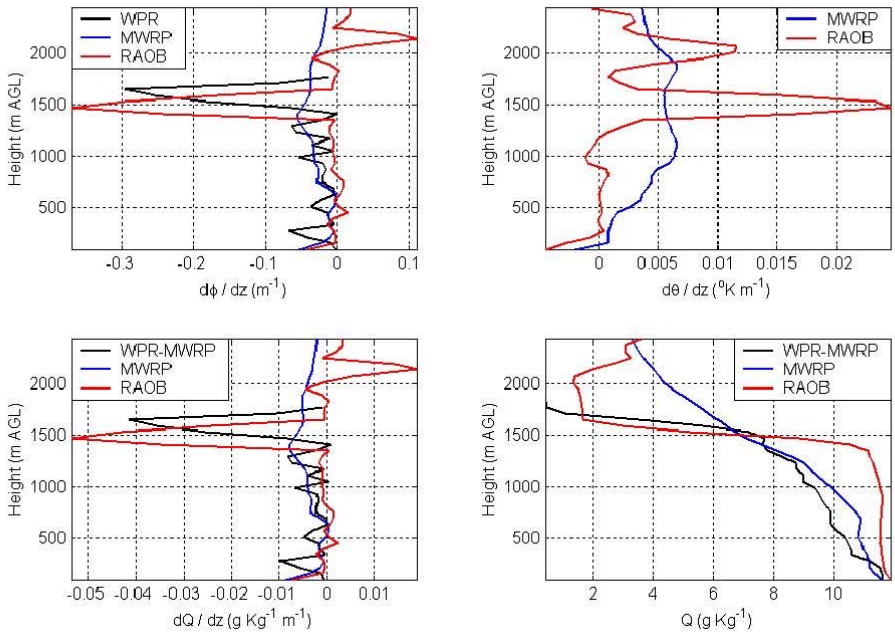


*Figure 4.11.* Comparison of the RWP-MWRP, MWRP, and radiosonde observed profiles on 7 June 2002, 23:30 GMT. Upper left panel: $d\phi/dz$ measurements. Upper right panel: Vertical gradient profiles of potential temperature. Lower left panel: $dQ/dz$ profiles. Lower right panel: Vertical profiles of $Q$.

On the other hand, we have to consider that the present experimental setup was not designed for this purpose, and much shrewdness could be adopted for the purpose. As pointed out by Stankov et al. (2003), the more powerful 449 MHz radar system performs better than the 915 MHz one, due to its narrower beam. Also, by increasing the number of points in the spectral domain of the WPR acquisition, we would obtain a better resolution on the vertical radial velocity computation which could improve the retrieval of the structure parameter of vertical velocity. Further improvements might come from the optimization of other settings, such as the dwell time. Moreover, ground-based MWRP estimates of temperature and humidity profiles could be further improved by coupling these measurements with those available from other sensors, such as satellite radiometers and ground-based Raman lidars. Further research (Bianco et al., 2005) was performed to look at a statistical analysis from a larger dataset comparing MWRP-RWP technique results and radiosonde observations.

**Acknowledgements** The work presented in this paper was partially sponsored by the Environmental Sciences Division of the Department of Energy as

a part of their Atmospheric Radiation Measurement Program.

## Bibliography

Bianco, L., and J. M. Wilczak, 2002: Convective Boundary Layer Mixing Depth: Improved Measurement by Doppler Radar Wind Profiler Using Fuzzy Logic. *J. Atmos. Oceanic Technol.,* **19** , 1745-1758.

Bianco L., D. Cimini, F. S. Marzano, and R. Ware, 2005: Combining microwave radiometer and wind profiler radar measurements for high-resolution atmospheric humidity profiling. *J. Atmos. Oceanic Tech.,* **22** , 949-965.

Cohn, S. A., 1995: Radar Measurements of Turbulent Eddy Dissipation Rate in the Troposphere: A Comparison of Techniques. *J. Atmos. Oceanic Technol.,* **12** , 85-95.

Cornman, L. B., R. K. Goodrich, C. S. Morse, and W. L. Ecklund, 1998: A Fuzzy Logic Method for Improved Moment Estimation from Doppler Spectra. *J. Atmos. Oceanic Technol.,* **15** , 1287-1305.

Gossard, E. E:, R. R. Chadwick, W. D., W. D. Neff, and K. P. Moran, 1982: The Use of Ground Based Doppler Radars to Measure Gradients, Fluxes and Structure Parameters in the Elevated Layers. *J. Appl. Meteorol.,* **21** , 211-226.

Gossard, E. E., D. C. Welsh and R. G. Strauch, 1990: Radar-Measured Height Profiles of $C_n^2$ and Turbulence Dissipation Rate Compared with Radiosonde Data During October 1989 at Denver. NOAA Tech. Report ERL 442-WPL 63, Environmental Research Laboratories, 115 pp. [*Available from:* NOAA/ERL/ETL Broadway, Boulder, Co, 80305].

Gossard, E. E., S. Gutman, B. B. Stankov, and D. E. Wolf, 1999: Profiles of radiorefractive index and humidity derive from radar wind profilers and the Global Position System. *Radio Science,* **34** , 371-383.

Han Y. and E. R. Westwater, 2000: Analysis and improvement of tipping calibration for ground-based microwave radiometers. *IEEE Trans. Geosci. Remote Sensing,* **38** (3), 1260-1276.

Jordan, J. R., R. J. Lataitis, and D. A. Carter, 1997: Removing Ground Clutter and Intermittent Clutter Contamination from Wind Profiler Signal Using Wavelet Transforms. *J. Atmos. Oceanic Technol.,* **14** , 1280-1297.

Solheim, F., J. Godwin, E. Westwater, Y. Han, S. Keihm, K. Marsh, and R. Ware, 1998: Radiometric Profiling of Temperature, Water Vapor, and Liquid Water using Various Inversion Methods. *Rad. Sci.,* **33** , 393-404.

Stankov, B. B., E. R. Westwater, and E. E. Gossard, 1996: Use of Wind Profiler Estimates of Significant Moisture Gradients to Improve Humidity Profile Retrieval. *J. Atmos. Oceanic Technol.,* **13** , 1285-1290.

Stankov, B. B., 1998: Multisensor retrieval of atmospheric properties. *Bull. Amer. Meteor. Soc.,* **79** (9), 1835-1854.

Stankov, B. B., E. E. Gossard, B. L. Weber, R. J. Lataitis, A. B. White, D. E. Wolfe, and D. C. Welsh, 2003: Humidity Gradient Profiles from Wind Profiling Radars Using the NOAA/ETL Advanced Signal Processing System (SPS). *J. Atmos. Oceanic Technol.,* **20** , 3-22.

White, A. B., 1997: Radar remote sensing of scalar and velocity microturbulence in the convective boundary layer. *NOAA Tech. Memo. ERL ETL-276*, Environmental Technology Laboratory, Boulder, Co, 127 pp. [*Available from:* NOAA/ERL/ETL Broadway, Boulder, Co, 80305].

White, A. B., R. J. Lataitis, and R. S. Lawrence, 1999: Space and Time Filtering of Remotely Sensed Velocity Turbulence. *J. Atmos. Oceanic Technol.,* **16** , 1967-1971.

Wilczak, J. M., R. G. Strauch, F. M. Ralph, B. L. Weber, D. A. Merritt, J. R. Jordan, D. E. Wolfe, L. K. Lewis, D. B. Wuertz, J. E. Gaynor, S. A. McLaughlin, R. R. Rogers, A. C. Riddle, and T. S. Dye, 1995: Contamination of Wind Profiler Data by Migrating Birds: Characteristics of Corrupted Data and Potential Solutions. *J. Atmos. Oceanic Technol.,* **12** , 449-467.

## 4.4 INTEGRATION OF MICROWAVE AND THERMAL-INFRARED RADIOMETERS

Christian Mätzler[1], Domenico Cimini[2], Jürgen Güldner[3], and Tim Hewison[4]

[1] *Institute for Applied Physics, University of Bern, Bern, Switzerland*
matzler@iap.unibe.ch

[2] *IMAA, National Research Council, Italy, and CIRES, University of Colorado, Boulder(USA)*

[3] *Richard-Aßmann-Observatory Lindenberg, German Meteorol. Service, Lindenberg, Germany*

[4] *UK MetOffice, University of Reading, United Kingdom*

Microwave radiometers were discussed in detail in Section 3.2. This text concentrates on thermal-infrared radiometers, followed by examples describing the potential of integrating the two radiometer types to sensor systems.

### 4.4.1 INFRARED RADIOMETERS

Infrared radiometers remotely sense the thermal radiance emitted by absorbing objects hosted in transparent media. The distance between object and sensor may be very short as in medical and industrial applications, or large, as in astronomy and earth observation. In the latter case it is important to properly select the spectral range to achieve the required range requirement.

For thermal-infrared radiometers, the received power is proportional to the radiance integrated over a wavelength range near the peak of the black-body function. As the power strongly increases with temperature (proportional to about $T^5$ for the terrestrial temperature range from 250 to 300 K and wavelength range from 8 to 14 $\mu$m), infrared radiometers are very sensitive thermometers (Rees, 2001). Broadband instruments cover this full wavelength range, corresponding to the frequency (inverse wavelength) range of 1250 to 710 $cm^{-1}$. The interval coincides with a main atmospheric window of the cloud-free atmosphere. Emission and absorption by atmospheric gases ($CO_2$ and $H_2O$) limit the transmission at the border of the window with some lines also within the window. At the centre, near 1000 $cm^{-1}$, there is a band of ozone lines whose emission originates mainly in the stratosphere (bottom curve of figure 4.12). Its main effect is to reduce the potential contrast of the cold background with respect to tropospheric emission, as shown for the cirrus clouds.

### 4.4.2 INFRARED RADIOMETERS FOR CLOUD MONITORING

Main applications of surface-based infrared radiometry are for cloud observations and temperature measurements. Furthermore, thermal-infrared radiometers respond to trace gases, such as water vapour, $CO_2$ and ozone. In contrast to the main components of clear air, ice and liquid water have strong continuum absorption in the entire thermal-infrared range. A typical cloud gets optically thick whenever its Integrated Liquid Water (ILW) reaches or exceeds 20 to 30 g/m$^2$ (Bloemink et al., 1999). Infrared radiometers are even slightly more sensitive to ice clouds as shown by the spectra of the imaginary refractive index of ice and water in figure 4.12 (ice data from Warren (1984) and revised by personal communication, water data from Segelstein (1981)). In the thermal infrared, optically thick clouds are good black bodies because backscattering is nearly negligible, scattering is small and mostly in the forward direction and significantly smaller than absorption.

For observations from the earth surface, infrared radiometry is a very sensitive tool to monitor clouds within atmospheric windows by observing the downwelling radiation. In the absence of clouds, the radiance is very small due to the high atmospheric transmission and negligible extraterrestrial radiation. Measured spectra from 600 to 1500 cm$^{-1}$ of downwelling radiation are shown in figure 4.13 for cloud-free sky, thin cirrus and stratus clouds, respectively. The largest differences between the three curves appear in the spectral range 800 to 1000 cm$^{-1}$, corresponding to the wavelength range from 10 to 12.5 $\mu$m. Radiometers optimised for cloud detection often concentrate on this part of the atmospheric window.

The main information on clouds obtained from infrared radiometers is the cloud temperature within the lowest decameters within the cloud; this temperature is usually called the cloud-base temperature. The measurement is limited to sufficiently thick clouds. Very thin clouds (liquid or ice water column $<$20 g/m$^2$) may not be optically thick, and thus would require a correction for non-black body radiation.

With sufficient spectral resolution, infrared radiometry can provide profiles of humidity and temperature in the cloud-free atmosphere. This is the topic of section 3.4 on Fourier-Transform IR (FTIR) spectrometry.

### 4.4.3 SYNERGIES BETWEEN MICROWAVE AND INFRARED RADIOMETER DATA

Integrating microwave and infrared radiometers extends the observations to a very large frequency range of thermal radiation. Multiband systems,

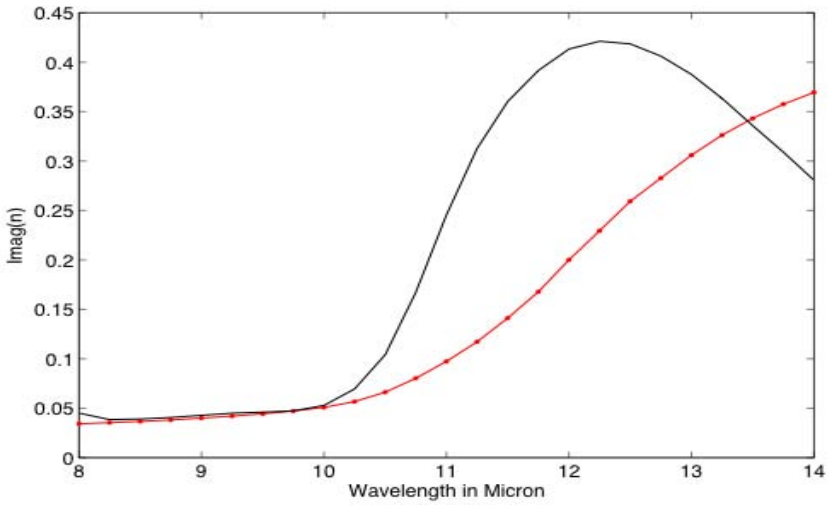


*Figure 4.12.* Imaginary refractive index in the 8 to 14 $\mu$m range of ice (line with points) and water (single line), data from Warren (1984) and Segelstein (1981)

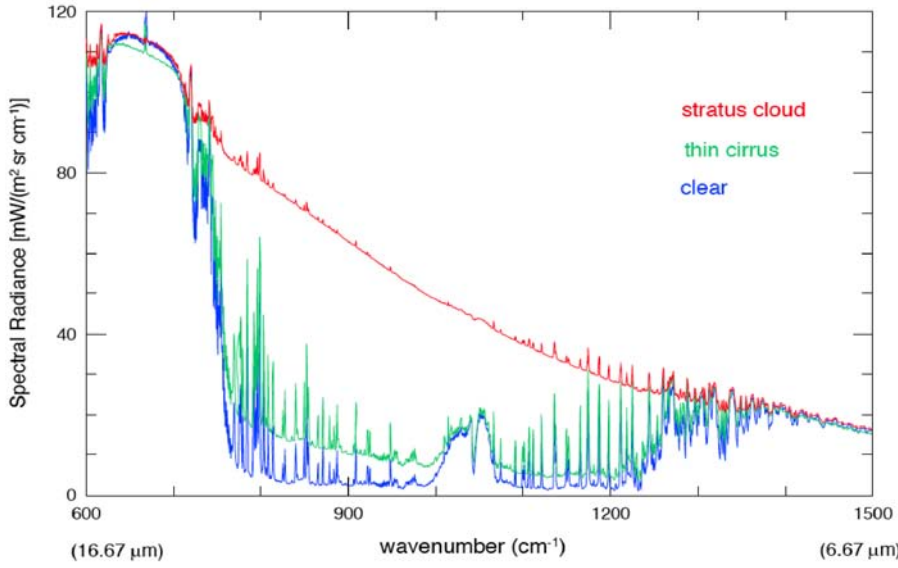


*Figure 4.13.* Measured spectra of downwelling atmospheric radiance for clear, dry atmosphere (bottom curve), thin cirrus clouds (middle), and stratus clouds (top). The baseline level of window emission also varies with water-vapour content and temperature. From Shaw et al. (2005)

covering this wide spectrum, are able to yield significantly more independent information than either system alone. This is the main reason for the existence of synergies. Unfortunately, so far, there have not been many investigations on this topic, partly because of the complex links between the two methods. Nevertheless, the following examples reveal interesting feasibilities.

**1. Potential to measure cloud-base height**

From the temperature profile obtained with the microwave radiometer and the cloud-base temperature obtained from the infrared radiometer we can determine the height of the cloud base. This method was tested with ASMUWARA supported by cloud-radar, laser-ceilometer and radiosonde data during the TUC Campaign (Schneebeli et al., 2005). In a further test, made at the DWD test site in Lindenberg, Germany, with a laser ceilometer, it was found that the cloud-base heights agree well for periods of low IR temperature variability when measured at short (5s) intervals.

**2. Potential to detect very thin and high clouds**

Although infrared radiometers are very sensitive to clouds, it is difficult to accurately determine the radiation level of the cloud-free atmosphere. A high accuracy is required if we want to sense very thin clouds, especially high cirrus clouds. The required accuracy can be achieved if atmospheric profiles of temperature and humidity are at least approximately known (Thurairajah and Shaw, 2005). This information can be obtained from microwave radiometers. For thin clouds, infrared radiometers can be used to estimate the amount of integrated liquid water (ILW) or integrated ice water (IIW).

**3. Separation between liquid-water, ice clouds and supercooled liquid-water clouds**

The combination of microwave and infrared radiometry allows to classify ice and liquid-water clouds. Especially it is possible to identify supercooled water clouds if ILW is non zero and if the cloud-base temperature is $< 0^o$C. For this purpose it is important to have the same view direction at all channels as realised for instance by ASMUWARA (Martin et al., 2006). The microwave radiometers determine the amount of cloud-liquid water, and the presence of clouds and their cloud temperature (at the cloud base) are determined by the infrared radiometer. Ice clouds are identified if ILW=0 with a non-negligible cloud signal in the infrared.

**4. Boundary-layer and air-sea temperatures**

Over a surface with a well-defined emissivity, the combination of microwave and infrared radiometers allows the monitoring of surface temperature and atmospheric boundary layer. An example was described by Cimini et al. (2003) for the marine boundary layer temperature profile and air-sea temperature difference measured with ship-based radiometers at wavelengths

of 5 mm and 14 $\mu$m. The data are important for the determination of latent and sensible heat flux and of the atmospheric stability.

**5. Model physics and sensor validation**

Synergisms also help in the validation of instruments. An example with ground-based microwave and thermal-infrared radiometer observations, and with radiosonde-based simulations in the tropics was the investigation of a dry bias, affecting the radiosonde humidity sensors (Westwater et al., 2003). The work contributed to the evaluation of techniques for reducing this problem.

Furthermore, microwave and infrared radiometers are combined to address the need for more accurate measurements of microphysical properties of clouds with low liquid water paths. Examples of evaluations of existing methods, development of new integrated approaches, and recommendations for automated techniques providing these microphysical properties routinely with the required accuracy are given by Turner et al. (2005).

### 4.4.4 ON THE TECHNICAL REQUIREMENTS FOR INTEGRATING MICROWAVE AND INFRARED RADIOMETERS

In order to realise the synergies in a useful integration of microwave and thermal-infrared radiometers, the observation directions, beam widths and observation times must be the same for all channels. This can be achieved if all optical systems (mirrors, lenses, radomes) cover the entire frequency range. Polished and degreased aluminium mirrors, or gold-plated mirrors, are suitable for both wavelength ranges with IR emissivity of $\leq 0.03$ (http://www.infrared-thermography.com/material.htm). It is, however, more difficult to find dielectrics suitable for well transparent lenses and radomes. Therefore the optics of ASMUWARA consists of a single flat aluminium mirror used to direct all beams simultaneously in the requested direction.

## Bibliography

Bloemink, H.I., A.C.A.P. van Lammeren, A.J. Feijt and S.C.H.M. Jongen, 1999: Active-passive sensor synergy for cloud observation; IR cloud properties and cloud liquid water. in: *Remote Sensing of Cloud Parameters*, Proceed., Symposium, 21-22 Oct. 1999, IRCTR, Delft University of Technol., ISBN 90-804551-6-4, The Netherlands.

Cimini, D. J. A. Shaw, Y. Han, E. R. Westwater, V. Irisov, V. Leuski and J. H. Churnside, 2003: Air temperature profile and air-sea temperature difference measurements by infrared and microwave scanning radiometers. *Radio Sci.*, **38**(3), 8045, doi:10.1029/2002RS002632.

Martin, L., M. Schneebeli and C. Mätzler, 2006: ASMUWARA, a ground-based radiometer system for tropospheric monitoring. TUC special issue, *Met. Zeitschr.*, **15**, 11–17.

Rees, W.G., 2001: *Physical Principles of Remote Sensing*. 2$^{nd}$ Edition, Cambridge Univ. Press.

Schneebeli, M., J. Cermak, L. Martin, D. Ruffieux and C. Mätzler, 2005: Assessment of cloud amount and cloud properties with ground-based remote sensing systems during the TUC campaign, EGU General Assembly - April 2005.

Segelstein, D.J., 1981: The complex refractive index of water. Thesis (M.S.), Department of Physics. University of Missouri-Kansas City.

Shaw, J.A., P.W. Nugent, N.J. Pust, B. Thurairajah and K. Mizutani, 2005: Radiometric cloud imaging with an uncooled microbolometer thermal infrared camera. *Optics Expr.*, **13**(15), 5807–5817.

Thurairajah, B., and J.A. Shaw, 2005: Cloud Statistics Measured With the Infrared Imager (ICY). *IEEE Trans. Geosci. Rem. Sens.*, **43**(9), 2000–2007.

Turner, D.D., C. Flynn, C. Long, S. McFarlane, A. Vogelmann, K. Johnson, M. Miller, C. Chiu, A. Marshak, W. Wiscombe, S.A. Clough, P. Heck, P. Minnis, J. Liljegren, Q. Min, W. O'Hirok and Z. Wang, 2005: Microphysical Properties of Clouds with Low Liquid Water Paths: An Update from Clouds with Low Optical (Water) Depth. 15th ARM Sci. Team Meeting, Proceed., Daytona Beach, Florida, March 14–18, 2005.

Warren, S.T., 1984: Optical constants of ice from the ultraviolet to the microwave. *Appl. Opt.*, **23**, 1206–1225.

Westwater, E.R., B. B. Stankov, D. Cimini, Y. Han, J. A. Shaw, B. M. Lesht and C. N. Long, 2003: Radiosonde Humidity Soundings and Microwave Radiometers during Nauru99. *J. Atmosph. Ocean. Techn.*, **20**(7), 953–971.

# 4.5 COMBINING UHF RADAR WIND PROFILER AND MICROWAVE RADIOMETER FOR THE ESTIMATION OF ATMOSPHERIC HUMIDITY PROFILES (*KLAUS ET AL., 2006*)

Vladislav Klaus
*Météo France, CNRM Toulouse, France*
✉ Vladislav.Klaus@meteo.fr

## 4.5.1 INTRODUCTION

Over the last 20 years many works have been addressed to show that ground-based microwave radiometers can be used to measure temperature and humidity profiles in the lower troposphere (Westwater, 1993; Stankov, 1996; Cimini et al., 2006a). However, the main weakness of this instrument is found to be in the lack of vertical resolution. Radiometers are not able to reproduce sharp hydrolapses. On the other side, wind profiling radars are very sensitive to changes in the humidity. Taking advantage of the complementary characteristics of each instrument, the idea of combining the two instruments to improve the vertical resolution of the humidity profile seems an attractive prospect, as shown by Stankov et al. (1996). Several works showed that wind profilers can be used to measure humidity profiles (Gossard et al., 1999; Tsuda et al., 2001) or at least to their improvement through the use of GPS integrated water vapor (Stankov et al., 2003) or radiometer data, in a combined sensor approach (Stankov et al., 2003; Bianco et al., 2005).

Here we try to adapt the method developed by Tsuda et al. (2001) in a combined sensor approach. In section 4.5.2 we describe and discuss the Tsuda technique. Section 4.5.3 shows how this method can practically be implemented. In section 4.5.4 the experimental site and instrumentation are introduced. The results are presented in section 4.5.6. The discussion of the results and the conclusions are given in the final section.

## 4.5.2 THE TSUDA TECHNIQUE

This study is based on the remote-sensing technique developed by Tsuda et al. (2001) for measuring the humidity profile directly from the wind profiler data. This technique consists in solving the humidity equation in the following form:

$$q(z) = \theta^2 \left[ \int_{z0}^{z} \left( 1{,}652 \frac{T^2}{P} M + \frac{T}{7800} \frac{N^2}{g} \right) \theta^{-2} dz + \frac{q_0}{\theta_0^2} \right] \quad , \qquad (4.8)$$

with

$$N^2 = g\frac{d\ln\theta}{dz} = \frac{g}{T}\left(\frac{dT}{dz} + \Gamma\right) \quad . \tag{4.9}$$

In the previous equations $\theta$ (K) is the potential temperature, $T$ (K) the absolute temperature, $P$ (hpa) the atmospheric pressure, $M(m^{-1})$ the refractive index gradient, $N$ (rad $s^{-1}$) the Brunt-Väisälä frequency, $g$ ($ms^{-2}$) the acceleration of gravity, and $z$ (m) the altitude. $q_0$ and $\theta_0$ are respectively humidity and potential temperature at the boundary height, while $\Gamma$ is the dry adiabatic lapse rate (9.8 K $km^{-1}$).

As suggested by Hooper et al. (2004), $P/T$ can be approximated as $\rho_0 \exp\left(-z/\overline{H}\right)$, where $\rho_0$ is the mean density at sea level, and $\overline{H}$ the mean scale height which may be considered as constant. Consequently, eq. (4.8) can be solved, if only $M$ and $T$ profiles, ground data $\rho_0$, and boundary conditions ($q_0$ and $\theta_0$) are known at a given range.

In this study $T$ is deduced from both radiometer and rawinsonde measurements available during the campaign, and $M$ is computed from the wind profiler signals according to the following method:

$$|M| = \varepsilon^{-1/3} F^{1/2} \eta^{1/2} N \quad , \tag{4.10}$$

(Tsuda et al., 2001), where (Hocking, 1985)

$$\varepsilon \approx 0{,}5 N \sigma^2 \quad . \tag{4.11}$$

$\varepsilon$ ($m^2$ $s^{-3}$) is the turbulence dissipation rate provided by $\sigma$ (the width of the turbulence echo on the Doppler spectrum, in $ms^{-1}$), $F$ is the filling factor of turbulence layers assumed constant (around 0.1 to 0.2), and $\eta$ ($m^{-1}$) is the radar volume reflectivity deduced from the turbulence echo power.

In the same way as above, this equation can be simplified as follows:

$$|M| \propto K\, \sigma^{-2/3} N^{2/3} z \sqrt{P_r} \tag{4.12}$$

Alternative expressions do not make explicit use of the signal width $\sigma^{--2/3}$ and the static stability $N^{2/3}$ (VanZandt et al., 1978; Gage and Balsley, 1980).

### 4.5.3 PRACTICAL IMPLEMENTATION

Several steps are necessary for an accurate resolution of the humidity equation (eq. (4.8)). Figure 4.14 illustrates the block diagrams of this method. As indicated by the initial boxes, 3 data inputs are required beside the wind profiler measurements:

- The temperature profile. In the absence of a VHF+RASS capability to reach at least 6 km height on an operational basis (Furumoto et al., 2003; Klaus et al., 2002), we use either the rawinsonde or the radiometer data according to the experimental set-up described in section 4.5.4.

- The air density at the surface, which allows an estimation of the pressure at various range gates according to the already available temperature profile. We

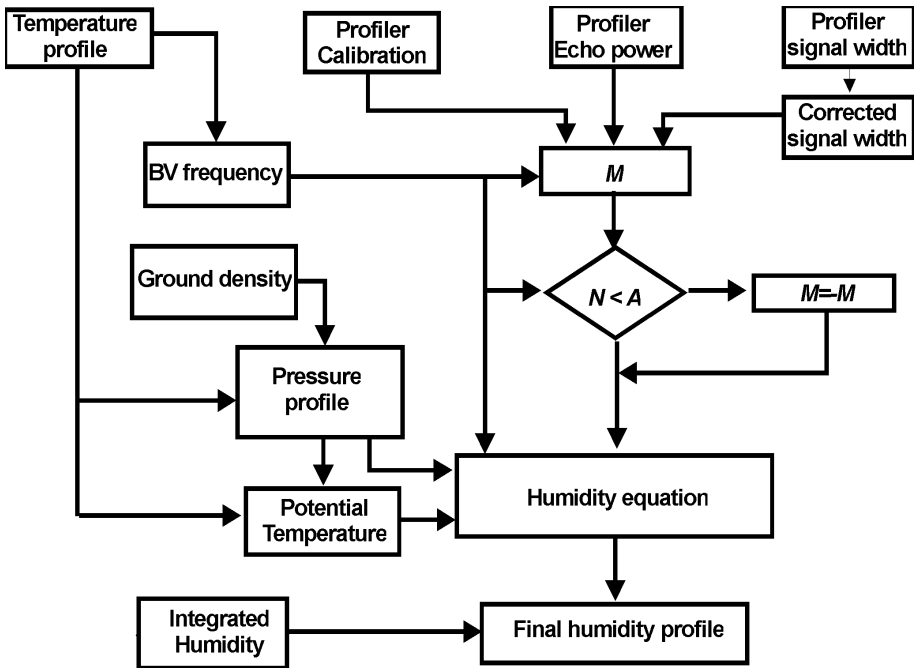


*Figure 4.14.* Block diagram of the method for evaluating the $q$ profile with the wind profiler data.

can then easily deduce the potential temperature needed to solve the humidity integration equation.

- An integrated humidity value, necessary to adjust the humidity integral equation. This parameter was extracted either from radiometric (sections 4.5.5.1 and 4.5.5.2) or from rawinsonde measurements (section 4.5.5.3).

The radar data also need to be well checked:

- The correct estimation of the signal power return $P_r$ needs a good calibration of the profiler, which is not always available. Consequently, empirical value of $K$ in eq. (4.12) was calculated. In sections 4.5.5.2 and 4.5.5.3 they were estimated for each profile to fit the radiometric values using the mean square method. In section 4.5.4, unique constants $K$ and $K'$ were used for the whole experiment. They were deduced from a match with $M$ profile calculated from a rawinsonde, specially selected to display important variations with altitude to facilitate a more accurate calibration.

- The $\sigma$ values provided by the profiler need to be corrected because of possible wind shear (ex. Jacoby-Koaly et al. (2002)). When horizontal wind, vertical wind shear, or wind time variation is significant, the correction may become quite important and consequently, lower accuracy is observed for $\sigma$.

Once these initial boxes have been implemented, automatic calculation of humidity is possible, but attention should be paid in eq. (4.8) to the sign of $M$, which can become positive in 10 to 20% of cases. However, as

already observed by Tsuda et al. (2001), a good correlation generally exists between $N^2$ and $M$ when horizontal advection is not very important (Mapes and Zuidema, 1996). Practically, $M$ becomes positive when $N^2$ is low, with a threshold of about $3\text{x}10^{-5}$ rad$^2$s$^{-2}$.

### 4.5.4 EXPERIMENTAL SITE AND INSTRUMENTATION

The dataset used for this study was collected during the international COST-720 Temperature, hUmidity and Cloud (TUC) profiling experiment (Ruffieux et al., 2006). This experiment was organised during 3 months (November to February) in winter 2003-2004 at Payerne, Switzerland. Various *in situ* and active/passive ground-based remote sensing systems, including three microwave radiometers, a cloud radar, a wind profiler and rawinsondes were operating at the same location.

The wind profiler used in this work is a LAP-3000 manufactured by Vaisala (ex Radian). The operating frequency is 1290 MHz. This radar operates in pulse mode, using 3 beams (1 vertical and 2 oblique). It is configured to operate in two modes (thereafter called "low mode" and "high mode") which differ by the vertical resolution (respectively 45 and 210 m) and the vertical ranges (respectively from 135 to 1035 m, and from 675 to 4975 m). The wind profiler dataset used for this experiment is formed by 51 30-minute measurement cases (25 for the low mode and 26 for the high mode) which have been subjected to a validation study already described in this Issue (Gaffard et al., 2006). Several *advanced* post-processing methods have been tested (introduced in Gaffard et al. (2006)) showing only very slight variations in the results obtained for humidity calculation.

The rawinsondes used in this comparison are the corrected operational Swiss rawinsonde SRS400 (Ruffieux et al., 2006). They report temperature, humidity and wind vector measurements. The height sampling is variable, 10-30 m for temperature and humidity, 40 m to a couple of hundred meters for the wind.

The radiometric data were obtained from a Radiometrics TP/WVP-3000 (Ware et al., 2003). This ground-based microwave radiometer is designed to allow retrieval of temperature and humidity in the lower troposphere. It is configured to sample sequentially 5 channels in the water-vapour band between 22.235-30 GHz and 7 channels along the edge of the oxygen complex between 51.25-58.8 GHz. It can use also elevation angle in addition to vertical pointing to increase the information content. The manufacturer's software uses a neural network method to retrieve temperature and humidity profiles. For the neural network retrieval, we used profiles from vertical pointing only. 37 radiometric profiles were available over the period covered by the wind profiler data set.

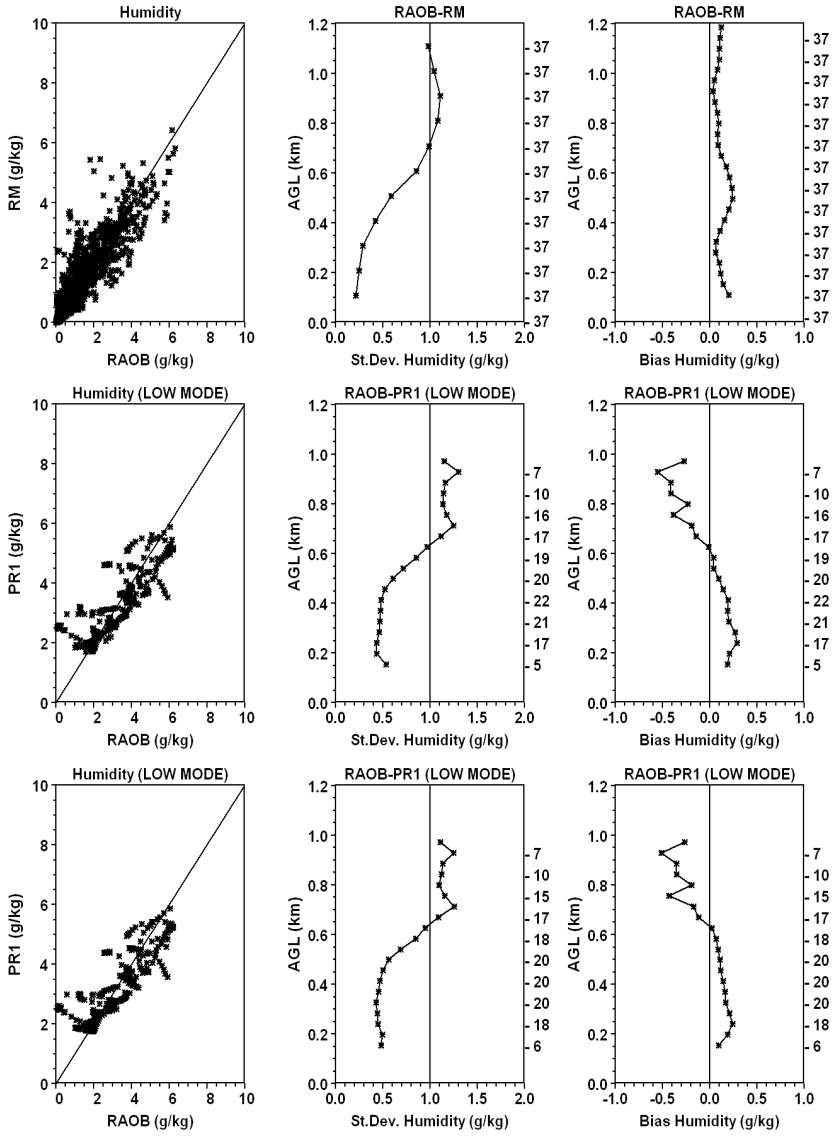


*Figure 4.15.* Statistical comparison of the humidity data versus those measured by rawinsondes (RAOB) from the Radiometrics profiler (RM) (top), low mode with profiler data using temperature from RM (middle), and using temperature data from radiosoundings (below). In each case, the figures show scatterplot of humidity values (left), standard deviation with height (middle), and bias with height (right). The numbers at the right of middle and right figures represent the number of cases taken for the statistics at each range. Heights are given above ground level (AGL). *M*was adjusted by least mean square method to the *M*(RM) values and *Q*(RM) data integrated over a height covering the 5 first profiler range gates was used for the integral constant

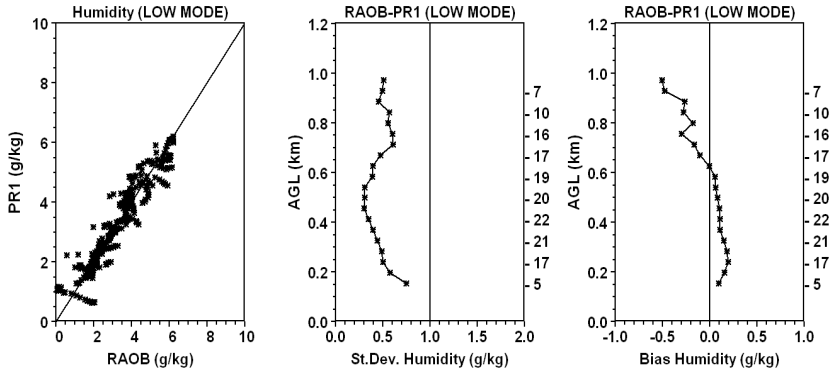


*Figure 4.16.* Same as in figure 4.15, but using a fixed coefficient for $M$ and estimating the integrated humidity over the profiler range from rawinsonde

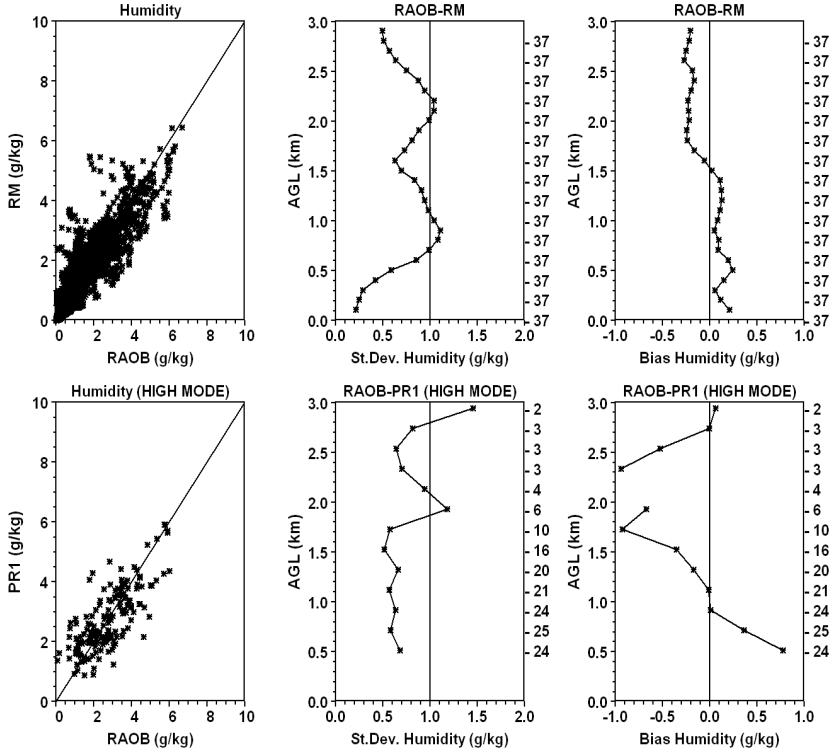


*Figure 4.17.* Same as in figure 4.16, but for high mode

## 4.5.5 RESULTS

**4.5.5.1 Radiometer vs. rawinsonde.** In order to evaluate the level of accuracy to be reached in this study, we started with the performance of the ra-

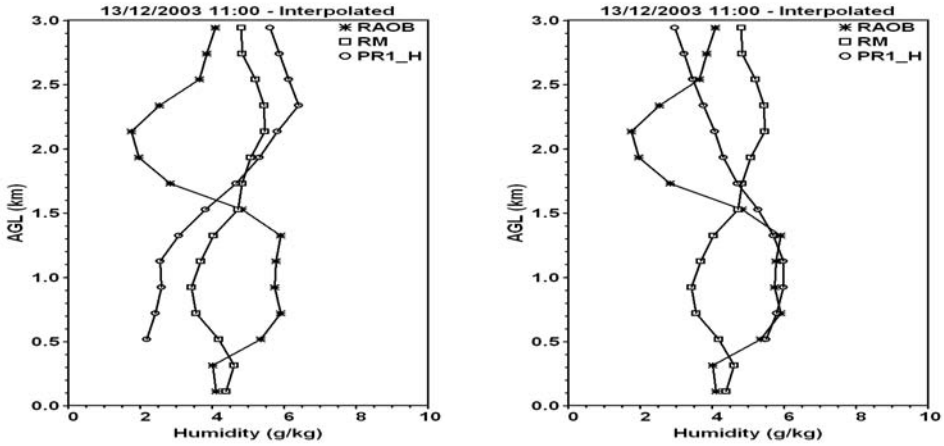


*Figure 4.18.* Examples of humidity profile obtained with the rawinsonde (RAOB), the radiometer (RM), and the profiler in high mode (PR1_H) calculated respectively by method 1 [left] and 2 [right] for 13/12/2003 at 11:00

diometer alone, because it is already an operational sounding instrument. From this result, considered as the state of art of automatic sounding of upper level humidity, we try to quantify the contribution of the wind profiler in term of data quality improvement. Figure 4.15a shows the scatterplot (left), standard deviation (middle), and bias (right) of the humidity profiles given by the radiometer compared to the rawinsonde observations. We notice a general good agreement where the standard deviation does not extend much above 1 g $kg^{-1}$ with a bias less than $\pm$ 0.4 g $kg^{-1}$ showing slight variations with height.

**4.5.5.2 Profiler calibrated by radiometer and integrated humidity from radiometer.** In the first step, the profiler data need to be calibrated in order to extract the $M$ values in eqs. (4.12). To this purpose, $M$ profiles deduced from radiometer data ($M$(RM)) were calculated to serve as a reference for determining at each time the coefficients $K$ in equation (4.12). To this purpose, $M$(PR) profile from profiler was estimated using a mean square method to globally fit the $M$(RM) profile. Then, humidity equation (4.8) is solved using the temperature data from radiometer and the boundary conditions extracted from integrated values of humidity from radiometer over a range containing identified atmospheric signals from the profiler. The results in figure 4.15b for the low mode, compared to the radiometer alone (figure 4.15a) show that in the lowest layers, no improvement is detected.

Using accurate $T$ profiles from rawinsonde data, little improvement in the data accuracy was reached by this method (figure 4.15c), confirming the fact that higher quality $T$ measurements are not required, as already demonstrated by Tsuda et al. (2001), who simply uses the virtual temperature profiles pro-

vided by the RASS (Radio Acoustic Sounding System) instead of an original $T$ profile.

**4.5.5.3 Profiler calibrated separately, temperature from radiometer, integrated humidity from rawinsonde observations.** So far, we tried to dynamically adjust the coefficients for the $M$ value according to the $M$(RM) curve. This approach showed some limitations due to the fact that any error related to radiometer is transferred to the profiler calculations. In order to avoid this interference, we decided to use a fixed coefficient for the calculation of $M$(PR). The integral for $Q$ (eq. (4.8)) is then solved by using the $T$(RM) profiles and the integrated values of humidity provided by radiometer over a range containing identified atmospheric signals from the profiler. This method did not bring much better results. Finally, the integrated value of humidity was calculated in the same way from rawinsonde observations. The results presented in figure 4.15 respectively for low and high mode show significant improvements.

In the low mode, the lowest height gives a little higher standard deviation (STD) of about 0.5 g $kg^{-1}$, but it stays at this level up to 700 meters AGL (Above Ground Level) with even a slight decrease between 400 and 600 m. The bias is quite stable, not exceeding 0.3 g $kg^{-1}$ on the whole profile except for the lowest range. In the high mode, STD is kept under 0.7 g $kg^{-1}$ up to 2 km height, but the bias can exceed 0.5 g $kg^{-1}$ in the lower range and above 1.7 km height.

The results obtained on this data set show that an independent method, using a general calibration and a good estimation of integrated humidity, is the best way to give accurate humidity profiles.

## 4.5.6 DISCUSSION AND CONCLUSIONS

Several methods were tested to combine the humidity information from independent observations by a wind profiler and a radiometer.

The first important result shows that the integrated humidity data measured by the radiometer over the range covered by the profiler is not a reliable parameter for solving the integral in the humidity equation (eq. (4.8)). Besides, the $M$ values calculated from radiometer are not the best way to calibrate the profiler, and no major improvement in the quality of humidity profile was obtained by this method. Large discrepancies observed sometimes between the radiometer and the rawinsonde humidity measurements were mainly due to the radiometer smoothing effect, and more rarely to the sensing volume distances in a rapidly changing weather pattern (examples are given in Fig. 4.18). A once-for-all calibrated profiler appears as a much better solution for this integration task.

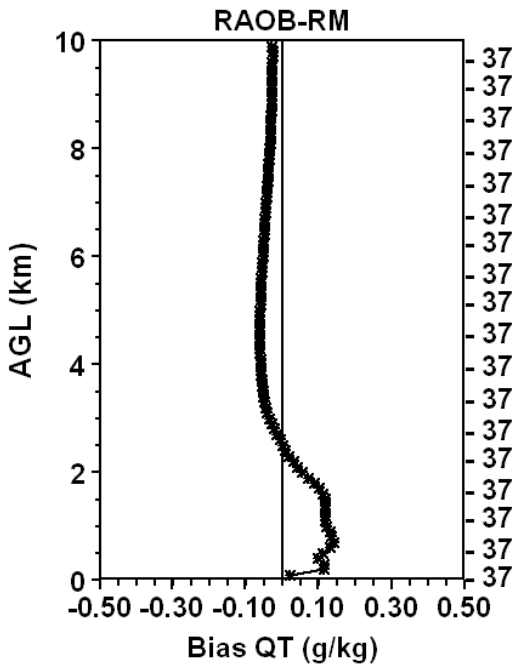


*Figure 4.19.* Bias in specific humidity integrated from the surface to different heights from rawinsonde (RAOB) relative to radiometer (RM)

Several prospects can thus be drawn:
First, humidity measurement techniques of radiometer can still be perfected with more constraints, provided for example by a wind profiler.

Second, radiometer integrated humidity values seems to be more reliable over a larger altitude range, due to their poor vertical resolution. This is illustrated in figure 4.19, which shows the radiometer's specific humidity integrated from the surface becomes closer to that from the rawinsondes after 3 km height. Such range coverage is within the reach of conventional VHF and UHF radars operating at few kW peak power, especially in summer. In these conditions, new tests could improve the contribution from the radiometric humidity.

Third, a VHF reaching the tropopause combined with a low layer UHF could cover practically the whole humidity range which makes it possible to cross-check with the GPS derived integrated humidity as already implemented on the MU radar in Japan (Furumoto et al., 2003). Such a method could also benefit from using surface humidity measurements to account for the humidity below the lowest usage UHF range gate. Moreover, neglecting humidity at the higher boundary will provide by itself the integration constant (equation (4.8)) without the need of external input (Klaus et al., 2003).

The temperature data from the radiometer were quite useful to solve the profiler equations without any significant distortion. This confirms previous stud-

ies (Tsuda et al., 2001) where virtual temperature profiles provided by RASS were used to solve the profiler equations.

In conclusion, sounding techniques using wind profiler radars can significantly improve the automatic estimation of humidity in the lowest kilometers. The only conditions are a temperature profile, which need not be accurate, and a good estimate of humidity either at a single point or on a given integrated layer not exceeding the profiler range coverage. For the analyzed data set, except for temperature profile, we cannot conclude that a radiometer can provide a definite contribution to this retrieval technique. However, many prospects still exist not only in the evolution of the radiometric measurements, but also in a more complete instrumental set-up with instruments such as VHF, RASS and GPS which will further help to provide significantly improved high-resolution humidity measurement in the upper atmosphere by only remote sensing technique.

## Bibliography

Bianco, L., D. Cimini, F. S. Marzano and R. Ware, 2005: Combining microwave radiometer and wind profiler radar measurements for high-resolution atmospheric humidity profiling, *J. Atmos. Oceanic Technol.,* 22, 949-965.

Cimini, D., T. J. Hewison, L. Martin, J. Gueldner, C. Gaffard and F. Marzano, 2006: Temperature and humidity profiles retrievals from ground-based microwave radiometers during TUC, *Meteor. Z.* , **15,** 45-56.

Fukao, S., M. D. Yamanaka, N. A., W. K. Hocking, T. Sato, M. Yamamoto, T. Nakamura, T. Tsuda and S. Kato, 1994: Seasonal variability of vertical eddy diffusivity in the middle atmosphere 1. Three-year observations by the middle and upper atmosphere radar, *J. Geophys. Res.*, 99, 18973-18987.

Furumoto, J., K. Kurimoto and T. Tsuda, 2003: Continuous observations of humidity profiles with the MU radar-RASS combined with GPS and radiosonde measurements, *J. Atmos. Ocean. Technol.*, 20, 23-41.

Gaffard, C., L. Bianco, V. Klaus and M. Matabuena, 2006: Evaluation of moments calculated from wind profiler spectra: A comparison between five different processing techniques, *Meteor. Z.*, *same Issue*, **15,** 73-85.

Gossard, E. E., D. E. Wolfe, and B. B. Stankov, 1999: Measurement of humidity profiles in the atmosphere by the Global Positioning System and radar wind profilers, *J. Atmos. Oceanic Technol.*, **16,** 156-164.

Greisser, T. and H. Richner, 1998: Mutiple peak processing alogorithm for identification of atmospheric signal in Doppler radar wind profiler spectra*, Meteor. Z.,* **7,** 292-302.

Hocking, W. K., 1985: Measurements of the turbulent energy dissipation rates in the middle atmosphere by radar techniques: A review, *Radio Sci.*, **20,** 1403-1422.

Hooper, D. A., J. Arvelius and K. Stebel, 2004: Retrieval of atmospheric static stability from MST radar return signal power, *Ann. Geophysicae*, **22,** 3781-3788.

Jacoby-Koaly, S., B. Campistron, S. Bernard, B. Bénech, F. Ardhuin-Girard, J. Dessens, E. Dupont and B. Carissimo, 2002: Turbulent Dissipation Rate in the Boundary Layer via UHF Wind Profiler Doppler Spectral Width Measurements, *Boundary-Layer Meteor.*, **103,** 361-389.

Klaus, V., G. Cherel, P. Goupil, and N. Penetier, 2002: RASS developments on the VHF radar at CNRM/Toulouse height coverage optimization, *J. Atmos. Ocean. Technol.*, **19,** 967-979.

Klaus, V., J. Van Baelen, J.-P. Aubagnac and G. Chérel, 2003: Humidity Profiling using Wind Profilers and GPS, *6th International Symposium on Tropospheric Profiling: Needs and Technology*, Leipzig, Germany, 53-55.

Klaus, V., L. Bianco, C. Gaffard and T. Hewison, 2006: Combining UHF radar wind profiler and microwave radiometer for the estimation of atmospheric humidity profiles. *Meteor. Zeitsch.*, **15,** 87-97

Mapes, B. E. and P. Zuidema, 1996: Radiative-dynamical consequences of dry tongues in the tropical troposphere, *J. Atmos. Sci.*, **53,** 620-638.

Morse, C. S., R. K. Goodrich and L. B. Cornman, 2002: The NIMA Method for Improved Moment Estimation from Doppler Spectra, *J. Atmos. Ocean. Technol.*, **19,** 274-295.

Ruffieux, D., J. Nash, P. Jeannet and J. L. Agnew, 2006: The cost 720 Temperature, hUmidity, and Cloud profiling campaign: TUC, *Meteor Z.*, **15,** 3–4.

Stankov, B. B., 1996: Ground- and space-based temperature and humidity retrievals: Statistical evaluation, *J. Appl. Meteor.*, **35,** 444-463.

Stankov, B. B., E. R. Westwater and E. E. Gossard, 1996: Use of wind profiler estimates of significant moisture gradients to improve humidity profile retrieval, *J. Atmos. Ocean. Technol.*, **13,** 1285-1290.

Stankov, B. B., 1998: Multisensor retrieval of atmospheric proprieties, *Bull. Amer. Meteor. Soc.*, **79,** 1835-1854.

Stankov, B. B., E. E. Gossard, B. L. Weber, R. J. Lataitis, A. B. Withe, D. E. Wolfe, and D. C. Welsh, 2003: Humidity gradient profiles from wind profiling radars using the NOAA/ETL advanced Signal Processing System (SPS), *J. Atmos. Oceanic Technol.*, **20**, 3-22.

Tsuda, T., M. Miyamoto and J. Furumoto, 2001: Estimation of a humidity profile using turbulence echo characteristics, *J. Atmos. Ocean. Technol.*, **18,** 1214-1222.

VanZandt, T. E., J. L. Green, K. S. Gage and W. L. Clark, 1978: Vertical profiles of refractivity turbulence structure constant: Comparison of observation by the Sunset radar with a new theoretical model, *Radio Sci.*, **13,** 819-829.

Ware, R., F. Solheim, R. Carpenter, J. Gueldner, J. Liljegren, T. Nehrkorn and F. Vandenberghe, 2003: A multi-channel radiometric profiler of temperature, humidity and cloud liquid, *Radio Sci.*, **38**, 8079, doi:10.1029/2002RS002856

Westwater, E. R., 1993: Ground-based Remote Sensing of Meteorological Variables. *Chapter 4 in Atmospheric Remote Sensing by Microwave Radiometry*, *M. A. Janssen (Ed.), J. Wiley & Sons, Inc.*, 145–213.

# 4.6 INVESTIGATION OF THE RELATIONSHIP BETWEEN WINDPROFILER SIGNAL TO NOISE AND TEMPERATURE, HUMIDITY, AND CLOUD PROFILES

Catherine Gaffard[1] and John Nash[2]

[1] *UK Met Office, Reading University, Reading, UK*
✉ catherine.gaffard@metoffice.gov.uk

[2] *UK MetOffice, Exeter, United Kingdom*

## 4.6.1 INTRODUCTION

This section describes basic investigations of the origins and characteristics of signal to noise and spectral width measurements from UHF boundary layer wind profilers. Tests have been performed in the UK since 1999 with a 915 MHz wind profiler and in the temperature and humidity comparison (TUC) test in Switzerland with a 1.29 GHz wind profiler (see section 5.1). Wind profilers were primarily designed to provide measurements of wind; but wind profiler signals also contain information about the vertical distribution of temperature, water vapour and clouds, see Stankov et al. (1996, 2003), Bianco (section 4.3), or Klaus (4.5).

A description is provided of all the scattering mechanisms known to contribute to the signal to noise measured by wind profilers i.e. Bragg, Fresnel and Rayleigh scattering. The theoretical considerations by which the signal to noise ratio should be related to the mean gradient of the refractive index (see equations 4.13, 4.15, and 4.18) are given and the possibility of using the spectral width to quantify the turbulence observed is considered (see equations 4.19 and 4.20). Precautions to ensure that a wind profiler reports valid atmospheric signals and valid spectral widths are summarized. Inherent limitations in the reproducibility of wind profiler signal to noise and spectral width measurements are identified and the origins of these limitations discussed.

The variation of refractive index in the vertical derived from the radiosondes will be compared with observations of signal to noise from the various experiments. Finally, recommendations on utilizing wind profiler signal to noise in quantitative manner to improve the accuracy of relative humidity profiles will be presented.

## 4.6.2 SCATTERING MECHANISMS

**4.6.2.1 Clear air echo.** A detailed summary of the scattering mechanisms can be found in chapter 4 of the COST-76 Final Report (COST Action 76, 2003). Here, we review the scattering mechanisms which may be responsible for the return signal from boundary layer wind profilers.

In clear air condition, two mechanisms are generally used to describe the returned signal, Bragg scattering and Fresnel scattering. In the absence of cloud, the return signal for UHF radars is mainly the result of Bragg scattering from turbulent irregularities of the refractive index. The refractive index at microwave frequency in the troposphere depends on pressure, temperature and water vapour, through the following equation,

$$n = 1 + 10^{-6}(C_1 \frac{p}{T} + C_2 \frac{e}{p} + C_3 \frac{e}{T^2}) \quad , \tag{4.13}$$

where $n$ is the refractive index $C_1 = 77.6$ K hPa$^{-1}$, $C_2 = 71.6$ K hPa$^{-1}$, $C_3$ =3.7 $10^5$ K$^2$ hPa$^{-1}$, $P$ and $e$ (in hPa) are air and water vapour pressure, respectively, and $T$ is temperature in degrees Kelvin.

If the distribution of refractive index irregularities of size $\lambda/2$ ($\lambda$ is the incident wave length) is random, homogeneous and isotropic, the profiler return power is not aspect sensitive. Doviak and Zrnic (1993) described the volume scattering by an ensemble of sub-volumes i.e. blobs of a refractive index irregularity of $\lambda/2$, where the blob size is defined by the correlation length of the $\lambda/2$ irregularities. For each sub-volume the Fraunhofer approximation can be used to describe the scattering as long as the correlation length of the $\lambda/2$ irregularities is smaller than the Fresnel length $(\lambda r/\pi)^{0.5}$, ($r$ is the distance from the radar to the scattering volume). For example for a 1 GHz radar and 1km distance, the Fresnel length would then be $\sim$ 20m. Then, the signals scattered from blobs add incoherently and hence the average received power is an integral of the power contributed by each. Backscattered radar echo power is proportional to the 3-dimensional spectrum of the refractive index fluctuation field, $\Phi_n(\vec{r}, 2k)$, for twice the incident radial wave number. Then, atmospheric Bragg scattering has associated with a volume reflectivity (i.e. backscattering cross section per unit of volume) given by

$$\eta \approx 8\pi^2 k^4 \Phi_n(\vec{r}, 2k) \quad . \tag{4.14}$$

For isotropic turbulence in the inertial regime, the 3D spectrum has a wave number dependency of $k^{-11/3}$ and is proportional to the turbulence structure parameter for the refractive index $C_n^2$ (Tatarskii, 1961). The backscattering cross section per unit volume is then given by

$$\eta \approx 0.38 C_n^2 \lambda^{-1/3} \quad . \tag{4.15}$$

When the spatial correlation of a blob is not negligible compared to the Fresnel length, the far field approximation is not valid, the scattering is affected by the

orientation of the blob and is aspect sensitive. This aspect sensitive scattering is known as Fresnel scattering. The formulation of such process is more complex and the volume reflectivity is not simply related to $\Phi_n(\vec{r}, 2k)$. Fresnel scattering leads to anisotropy in VHF radar observations at longer wavelengths but on average anisotropic scattering has not been reported for UHF.

**4.6.2.2 Particle scattering.** In the presence of randomly distributed particles (droplets, ice crystals, insects), the radar signal is incoherently backscattered. The wavelength $\lambda$ used for the wind profiler is several orders of magnitude larger than the particle diameter D and the Rayleigh approximation can always be applied. The backscattering cross section per unit volume in this case is given by

$$\eta \approx \pi^5 |K|^2 Z.\lambda^{-4} \quad , \tag{4.16}$$

where $[(K = [(\varepsilon - 1)/(\varepsilon + 2)]^2$ (for water at $20^o$C $|K|^2$ is equal to 0.93 at a wavelength of 10 cm), $\varepsilon$ is the relative permittivity of the particle, and $Z$ the radar reflectivity from particles given by

$$Z = \frac{1}{V} \sum_{i=1}^{N} D^6 \quad , \tag{4.17}$$

and $V$ is the scattering volume with $N$ particles.

Figure 4.20 shows the relative efficiency versus the radar wavelength of the two scattering mechanism (Bragg against Rayleigh) for moderate turbulence ($C_n^2 = 10^{-14}$ to $10^{-15}$) in clear air, and values of $Z$ ranging from precipitation to cloud. Bragg scattering in clouds may be significantly smaller than Bragg scattering in clear air, if the air within the cloud is saturated and refractive index changes induced by vertical velocities are smaller than in clear air.

At VHF frequency (meter wavelength) backscattered signals from hydrometeors will be much smaller than clear-air Bragg scattering indicated here, but may be similar to the much lower VHF Bragg scattering found within some types of clouds. However, the Rayleigh scattering is larger relative to clear air for UHF radars near 1 GHz. UHF radars will see rain and drizzle ($Z = 10^{-1}$), with the Rayleigh signals as strong as the Bragg signal for drizzle and much stronger for rain. Insects may have a reflectivity similar to drizzle.

For clouds with a reflectivity $Z < 10^{-2}$, the Rayleigh scattering in the UHF becomes negligible compared to the Bragg scattering, which may also be lower than for clear air indicated here in some types of clouds. For ice clouds, the UHF reflectivity is much stronger and hence a UHF profiler will see ice cloud.

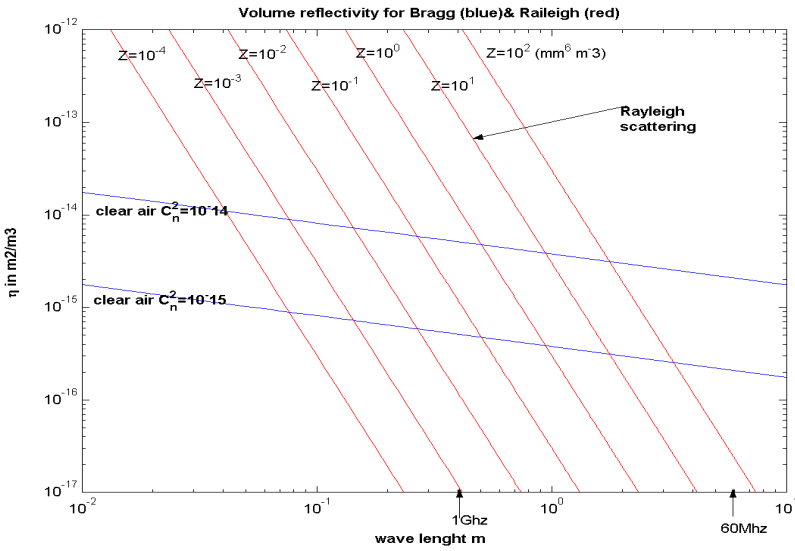


*Figure 4.20.* Wavelength dependence of scattering mechanisms. Red lines: Rayleigh scattering for different values of $Z$, Blue lines: Bragg scattering for different values of $C_n^2$

### 4.6.3 RELATING VERTICAL STRUCTURE IN REFRACTIVE INDEX TO TURBULENT STRUCTURE PARAMETERS

**4.6.3.1 $C_n^2$ and mean property.** Following Tatarskii (1961), Gossard et al. (1982) derived a relationship between the turbulent structure parameters of the refractive index $C_n^2$, the turbulent structure parameter of the vertical speed $C_w^2$ and the mean property of the layer where it can be assumed that the turbulence is homogeneous and isotropic

$$\begin{aligned} \left(\frac{dn}{dz}\right)^2 &= \left(\frac{L_w}{L_n}\right)^{4/3} \left(\frac{dv_h}{dz}\right)^2 \frac{C_n^2}{C_w^2} \\ C_w^2 &= B_w \varepsilon^{2/3} \quad , \end{aligned} \tag{4.18}$$

where $n$ is the potential refractive index, $v_h$ the horizontal velocity, $\varepsilon$ the eddy dissipation rate, $L_w$ and $L_n$ are the mixing length scales for vertical speed and potential refractive index. $L_w$ and $L_n$ are not constant and depend on stability. In 1982 Gossard et al. (1982) suggested that the ratio$L_w/L_n$ should be nearly constant because the same eddy ensemble mixed both quantities. Nevertheless, by 1998, it was recognized that the ratio can vary with values ranging from 2 to 6 in very stable conditions.

The spectral width should be related to $C_w^2$ but this assumes a radar volume filled with turbulence. The extent to which the beam is filled can be judged to some extent by comparing measurements of a layer at different vertical reso-

lutions. From recent tests in the UK it would appear that on some occasions a vertical resolution of about 50m or better is required to ensure beam filling e.g. in a strong inversion over stratocumulus cloud see figure 4.21 and it is possible that in some situations even finer structure is present vertical resolution towards 10 m is required using FM-CW radars.

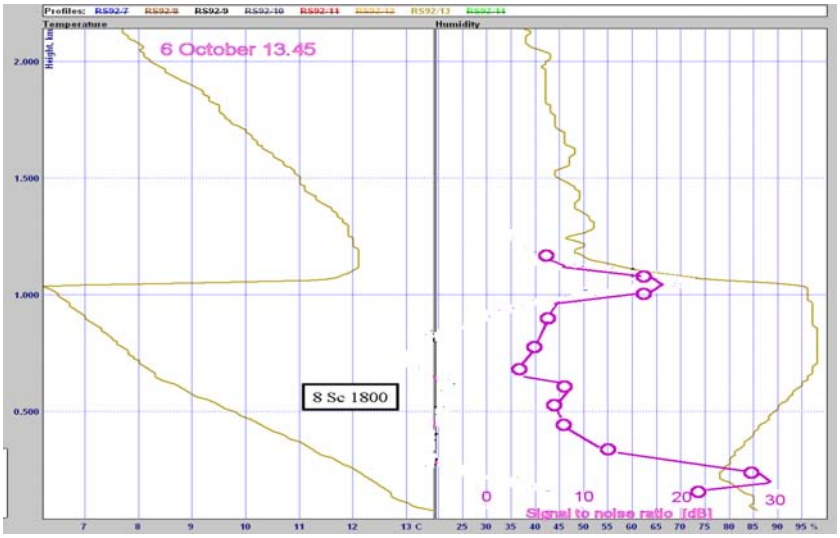


*Figure 4.21.* Temperature (left) and humidity profile (light brown) from radiosonde showing strong inversion above stratocumulus cloud. To capture the signal to noise variation associated with this inversion seems to require a resolution of less than 50 m

### 4.6.3.2 $C_w^2$ and Doppler width.

**Estimation of turbulent broadening from measured spectral width.** Scattering elements within the pulse volume move with different radial velocities, so the spectrum of the backscattered signal is spread about the mean radial velocity. Part of the spread is purely geometrical and linked to the beam aperture or beam width of the profiler. Wind shear within the observed volume increases the observed spectral width further, see Doviak and Zrnic (1984).

Each individual turbulent eddy is independent of the mean wind, therefore the broadening due to the turbulence ($\sigma^2_{turb}$) is independent of the broadening ($\sigma^2_{shear}$) due to wind shear, and their contribution to the total width ($\sigma^2_{spec}$) is simply additive. Therefore:

$$\sigma^2_{spec} = \sigma^2_{turb} + \sigma^2_{shear} \tag{4.19}$$

The formulation of $\sigma^2_{shear}$ given in Doviak and Zrnic has been adapted to wind profiler geometry by Jacoby-Koaly et al. (2002) and will be used in this study to correct the width from the non-turbulent effect (the typographic error

existing in the paper of Jacoby-Koaly et al. (2002) has been corrected in the version given below):

$$\begin{aligned}
\sigma^2_{shear} &= k^2_\beta + k^2_\theta + k^2_r \\
k_\beta &= \frac{\sigma_\beta}{r}(u\cos\beta - v\sin\beta) \\
k_\theta &= \frac{\sigma_\theta}{r}\,[r\cos^2\theta(\sin\beta\ \delta u/\delta z + \cos\beta\ \delta v/\delta z) - u\sin\beta\sin\theta - \\
&\quad v\cos\beta\sin\theta + r\cos\theta\sin\theta\ \delta w/\delta z + w\cos\theta] \\
k_r &= \sigma_r[\cos\theta\sin\theta(\sin\beta\ \delta u/\delta z + \cos\beta\ \delta v/\delta z) \\
&\quad + \sin^2\theta\ \delta w/\delta z]
\end{aligned} \tag{4.20}$$

where $k_\beta$, $k_\theta$, $k_r$ are the components of the radial shear in a spherical coordinate system, where $\beta$ is the azimuth of the antenna (relative to north), $\theta$ the elevation angle from the ground (90 degrees for the vertical beam), and $r$ is the range of the target, $\sigma^2_\beta$ , $\sigma^2_\theta$ are the second moments of the arc length of the two-way antenna power angular pattern in the indicated direction ($\beta$, $\theta$), $u$, $v$, and $w$ are the easterly, southerly, and vertical velocities, and $\sigma^2_r$ is the second moment of the range-weighting power function in the radial direction, which is a function of the pulse shape and the receiver characteristics, respectively.

For a circular symmetric Gaussian pattern,

$$\sigma_\beta = \sigma_\theta = r\Phi\left(4\sqrt{\log(2)}\right)^{-1} \quad , \tag{4.21}$$

where $\Phi$ is the one-way half-power width.

$\sigma^2_r$ is the second moment of the range weighting power function in the radial direction which is a function of the pulse shape and the receiver characteristic. For a rectangular impulse and a Gaussian receiver under matched conditions (Doviak and Zrnic, 1984),

$$\sigma_r = (0.35c\tau/2) \quad , \tag{4.22}$$

where $\tau$ is the pulse length.

Once the width of the spectrum has been corrected for shear broadening due to the non-turbulent flow, it can be used to estimate the intensity of the turbulence. The corrected width, $\sigma^2_{turb}$ is an estimate of the radial velocity variance for the unresolved turbulent scale for time scales less than the acquisition time and spatial scales less than the dimension of the resolution volume.

**Relating turbulent spectral width to the eddy dissipation rate.** Under the hypothesis that the outer scale of turbulence, $L_0$, is larger than the dimension of the equivalent volume observed by the radar during the acquisition time $T$, White et al. (1999) derived a relation between the broadening $\sigma^2_{turb}$ and the

eddy dissipation rate $\varepsilon$

$$\begin{aligned}
\varepsilon &= \sigma_{turb}^3 (4\pi/\alpha_e)^{3/2} J^{-3/2} \\
J &= 12\Gamma(2/3) \int_0^{\pi/2} \int_0^{\pi/2} (\sin^3\theta)(\sigma_r^2 \cos^2\theta + \sigma_\beta^2 \sin^2\theta + \\
&\quad (L^2/12)\sin^2\theta\cos^2\phi)^{1/3}\, d\theta d\phi \\
L &= vT \quad , \qquad (4.23)
\end{aligned}$$

where $v$ is the horizontal wind speed, $T$ the acquisition time, and $\alpha_e = 1.6$ is a Kolmogorov constant.

In theory, the turbulence can be extracted from the spectral width, but in practice evaluation of the spectral width needs the use of several correcting factors like the horizontal speed, vertical speed, wind shear, beam width and illumination pattern. Estimates of the turbulent part of the spectral width may often be limited by errors in these correction procedures.

## 4.6.4 EXPERIMENTAL DATA

Experimental data used come from operational wind profilers with two data sets from Camborne (UK), and the third from the TUC experiment, Payerne. The first test was used to identify layers in the signal to noise ratio associated with change in the refractive index computed from radiosondes. In the second, the evolution of the signal to noise ratio was compared with hourly radiosondes, collocated radiometer measurement and ceilometer data. A systematic study of the estimated moments (signal to noise ratio, spectral width) from the TUC shows some of the limiting factors in the observations, allowing recommendations for future use to be developed.

**4.6.4.1 Camborne data 1999: Layer identification.** The 915 MHz wind profiler located at Camborne, Cornwall (UK) has a 500 W peak power, uses 3 beams of 6 degrees width and works in 2 interlaced modes: a high mode that reaches 8 km with a 200 m vertical resolution, and a low mode configuration that reaches 2 km with a 58 m vertical resolution. The signal to noise ratio used here was an average of the 3 beams over 30 minutes for the low mode. Values have been range corrected. During this test there was no precipitation, only few clouds and no strong winds, but many temperature inversions.

31 radiosondes were launched at the site during the period from 26 July 1999 until 31 July 1999. Temperature and humidity with a 10 m vertical resolution were used to compute the gradient of the refractive index after Tatarskii (1961). The square of the gradient was averaged over 120 m and weighted with a Gaussian of 60m width and an overlap of 50% in order to simulate the vertical resolution of the radar. Refractive index profiles were always adjusted by the same empirical calibration factor.

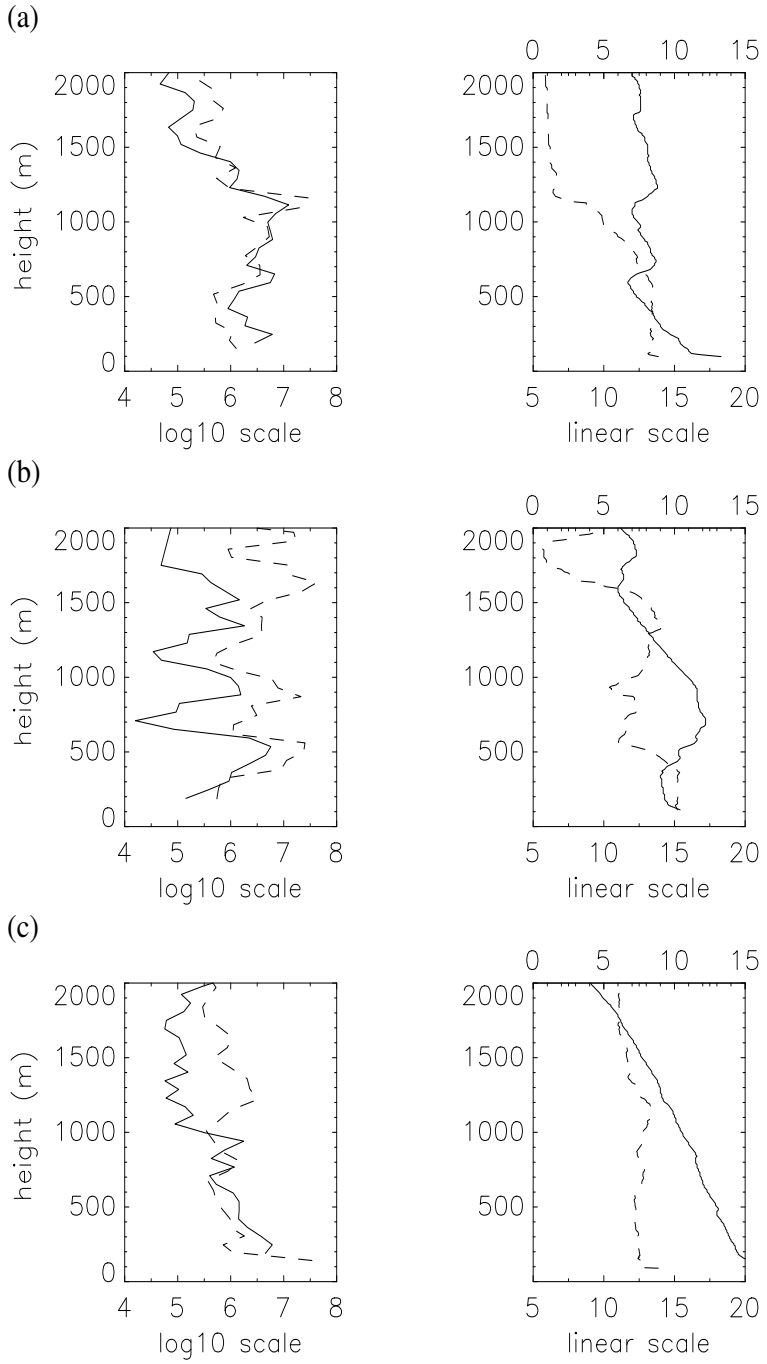


*Figure 4.22.* Left comparison of range corrected signal to noise ratio profiles above sea level (continuous line) with the gradient of the refractive index computed from the radiosonde measurements (dashed line) for (a) 19-07-99/20 UTC, (b) 28-07-99/11UTC (c) 26-07-99/17 UTC. Right, temperature in deg Celsius, continuous line bottom scale in degree, specific humidity (dashed line) upper scale in g/kg from radiosonde measurement

In general the agreement between radar and the refractive index gradients from the radiosonde measurements was good. Three examples of comparisons are shown on the left side of figures 4.22(a), (b), and (c). The continuous line represents the range-corrected signal to noise ratio, and the dashed line represents the square of the fluctuation of the refractive index from the radiosonde. The right side of figures 4.22(a), (b), and (c) show the associated temperature (continuous line) and humidity (dashed line) profile. Nearly all the variations in the radar signal to noise ratio are reproduced by in the refractive index computed from the radiosonde, except in the third example. Identifying the reason for this exception required more supporting evidence than was available in this first test.

Figure 4.23 shows a comparison between the locations of the maxima found in the radar signal and in the computed fluctuations of the refractive index for the whole period. The significant maxima were selected automatically by algorithms specially developed for this test. The final results show good agreement between the locations of the maxima in both profiles. The bias between the height locations was negligible (0.12 m), and the value of the standard deviation between both quantities (130 m) was comparable to the vertical range resolution of the radar measurements. Thus, in clear air conditions wind profiler signal to noise can be used to identify the height of significant levels in vertical profiles, such as capping lids.

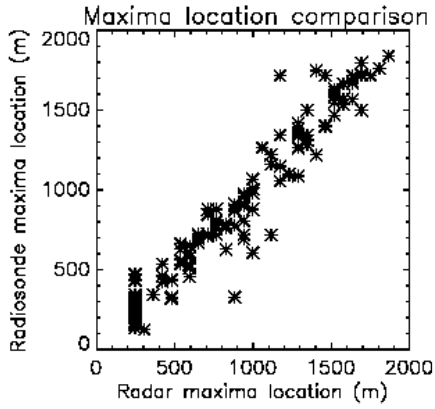


*Figure 4.23.* Scatter plot of maxima location of the range corrected signal to noise ratio profile and the corresponding maxima found on computed gradient of refractive index from the collocated radiosonde for the whole period. 129 pairs of maxima were identified, the bias between them is 0.12 m, and the standard deviation 130 m

**4.6.4.2 Camborne data 2002: Hourly comparison.** Three intensive observation periods of hourly radiosonde were conducted at Camborne in May 2002, in support of the activities of the Working Group on Integration of COST-720. A ceilometer and a 12-channel microwave radiometer were op-

erated on the site during the observing periods. Conditions differed between the three days including the development of the convective boundary layer, a stable day with variable cloud, and lastly a clear-air situation.

**Developments in the Convective Boundary Layer Case Study.** Figure 4.24 shows the time-height evolution of the range corrected wind profiler signal to noise ratio (SNR) at high time resolution (5 minutes) for the vertical beam on 14 May 2002. Each point represents 30 s of acquisition time. The layer of stronger signal between 200 and 300 m is the result of ground clutter contamination and measurements at these heights should be ignored. The cloud base detected by the ceilometer was superimposed in white circles. Cloud base varied from about 800 m up to 2000 m and was usually in the middle of a variable region of higher signal to noise ratio. Low level winds were not weak. The large variability of the profiler signals on this day implied that atmospheric conditions were very variable and radiosonde measurements were unlikely to have good representativeness. The upper limit of the highest

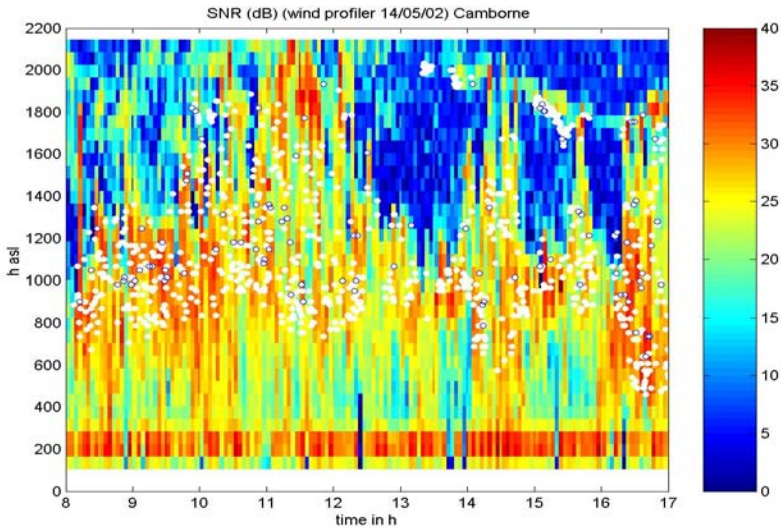


*Figure 4.24.* Signal-to-noise ratio of wind profiler (dB scale) on 14.05.02 at Camborne. White and blue circles show cloud base reported by ceilometer

signals increased from 1000 m at 08:00 to a maximum of 2150 m at around 11:30 UT. Radiosondes showed convection was possible throughout the day with capping lids mostly at heights of 800 m and near 2000 m. The upper lid capped the convection at around 11.30 UT. Between 13 UT and 17 UT the base of the clouds near 2000 m was steady in the short term, and the signal to noise in the upper lid was lower than associated with the lids near 800 m.

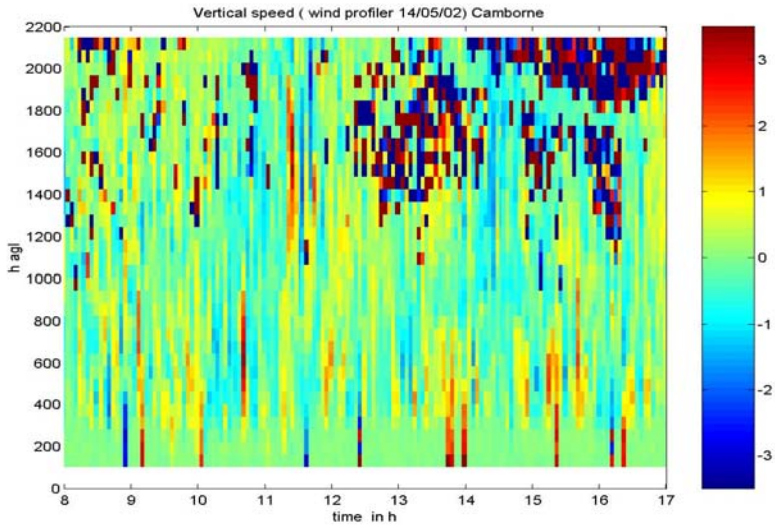


*Figure 4.25.* Time-height cross section of vertical speed measured by the wind profiler for the 14.05.02 at Camborne

The time height evolution of the square of the gradient of the potential refractive index, figure 4.26, computed from the radiosondes clearly reflects the discontinuity associated with the capping lid at 2 km. However at lower levels ,the $< (dn/dz)^2 >$ computations from the radiosondes did not reproduce the stronger signal to noise observed between 500 m and 100 m. Thus, the basic theory fails to represent the difference between the turbulence and convective structures in this region and the conditions that existed near 200 m and with more stable capping lids or inversions

The vertical speed measured by the wind profiler is shown in the figure 4.25. The time resolution in this test ($\sim$5 min) was insufficient to capture the variation of vertical velocities that have been observed in later tests with a temporal resolution of about 1 minute. However several periods of strong positive vertical speed are noticeable at heights above 400 m. Those with vertical extent to around 1 km and under the cloud base were likely to be updrafts feeding the cloud. Radiometer measurements showed drizzle falling from some clouds, between 10.30 UT and 12 UT. So, whilst most of the regions of negative vertical speed could be interpreted as downdraft, the stripes between 10.30 UT and 12 UT above 1000m may be the result of drizzle. For the future, drizzle detection techniques using ceilometer and cloud radar, as described by Ruschenberg in section 4 would be helpful and perhaps essential for operational applications observed on other days at Camborne. In the CSIP experiment in 2005, see section 5.3, observations were obtained using a wind profiler that was set up to perform a full cycle of three beams within a minute. An example of

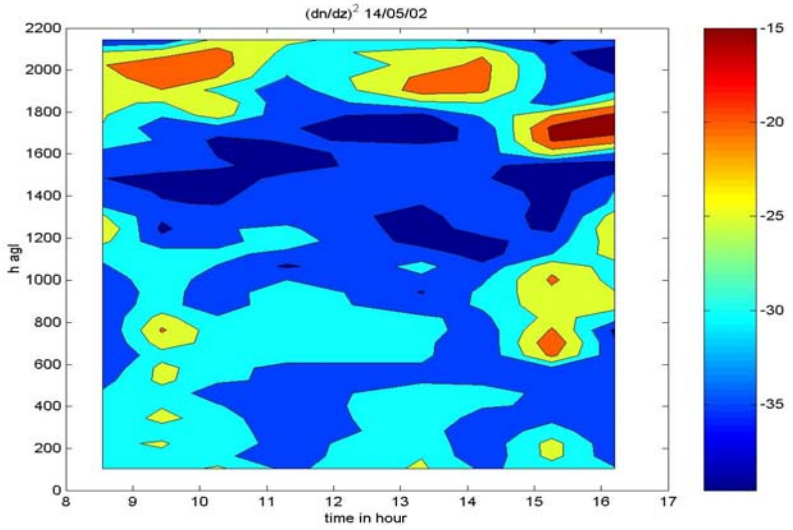


*Figure 4.26.* Time-height series of square gradient of the refractive index (dB scale) computed from hourly radiosonde on 14/05/02, Camborne

updrafts feeding the cloud in a convective situation is shown in figure 5.27. With the higher time resolution, the updraft feeding the cloud and penetrating a downdraft were more reliably defined. The associated signal-to-noise ratio plot shown in figure 5.30 shows that signals are very weak within the updraft but strong at the intersection between the updraft and downdraft where the downdraft is likely to be drier than the updraft.

**Cloud Evolution Case Study.** On the 15 May 2002, strong signal to noise was mostly limited to the region between 200 m and 600 m, with variable signal to noise structure above 1000 m, see figure 4.27. Strong signals between 200 m and 300 m were again influenced by ground clutter. During the morning low stratus broke up into convective cumulus of moderate extent. Thus, from 08:00 UT to 11:00 UT the cloud base was variable in the short term, with strong wind profiler signals extending to about 150 m above the cloud base, where the capping inversion was located , see figure 4.28. By the afternoon, an extensive sheet of less convective stratocumulus appeared at 1000 m and the cloud base was more stable in the short term between 12.30 UT and 15 UT. The cloud base was located at different heights, with weak signals between the cloud base and a layer with strong wind profiler signal that rose from 1200 m up to 1900 m where there was another stable layer above the cloud. The maximum in signal to noise definitely represents the height of the inversion on top of the cloud between 13.30 UT and 14.30 UT, see the radiosonde measurements in figure 4.29 and 4.30.

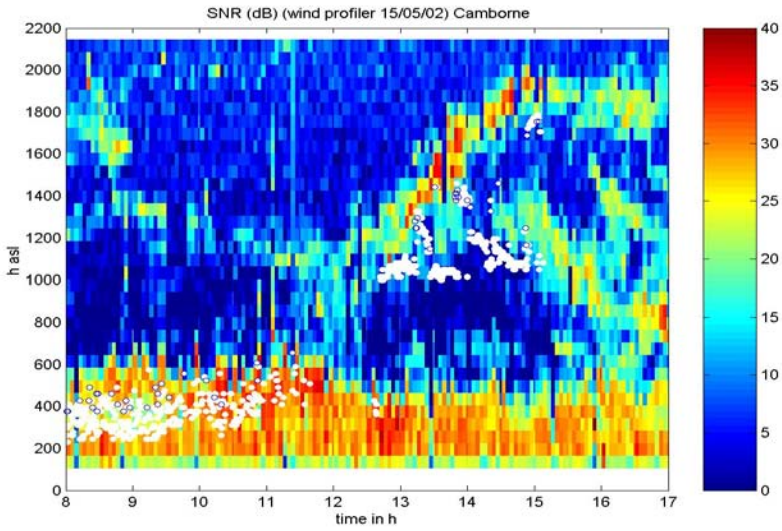


*Figure 4.27.* Signal-to-noise ratio of wind profiler (dB scale) on 15/5/02 at Camborne. White and blue circles show cloud base reported by ceilometer

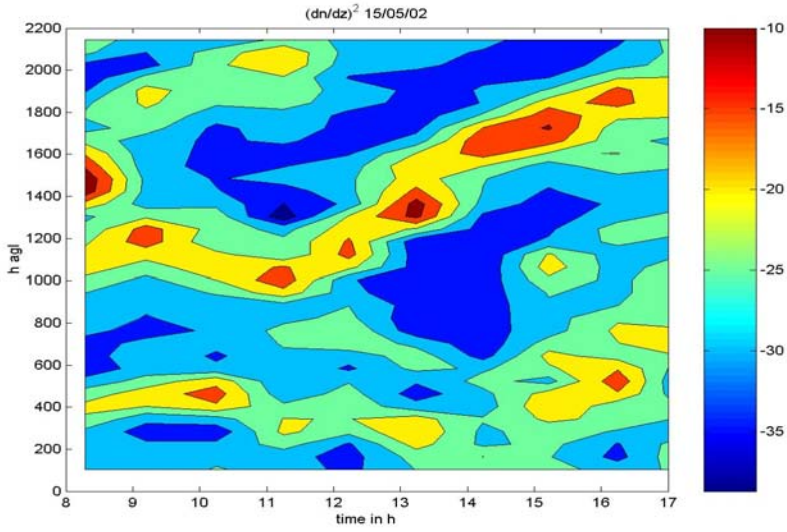


*Figure 4.28.* Time-height series of square gradient of the refractive index (dB scale) computed from hourly radiosonde on 15/5/02., Camborne

The wind profiler did not see strong signals from within this cloud, because the relative humidity within the cloud was probably at saturation and so refractive index fluctuations from relative humidity were smaller than in clear air. Also the size of the water drops within the cloud was probably not large enough to give Rayleigh scattering larger than the clear air Bragg scattering.

The evolution of $(dn/dz)^2$ from the radiosondes during the day shown in figure 4.28 is in very good agreement with the evolution of range-corrected signal-to-noise ratio. The radiosonde temperature profiles showed a stable atmosphere, so most of the vertical structures in the wind profiler signals on this day were adequately described by the basic theory. The microwave radiometer reported a similar tendency to the radiosondes for the temperature, see figure 4.29, and the humidity, see figure 4.30, but could not resolve the temperature inversion and the associated dry layer shown by the radiosondes. In this case, incorporation of information from the wind profiler signal-to-noise should improve the vertical structure reported from the radiometer.

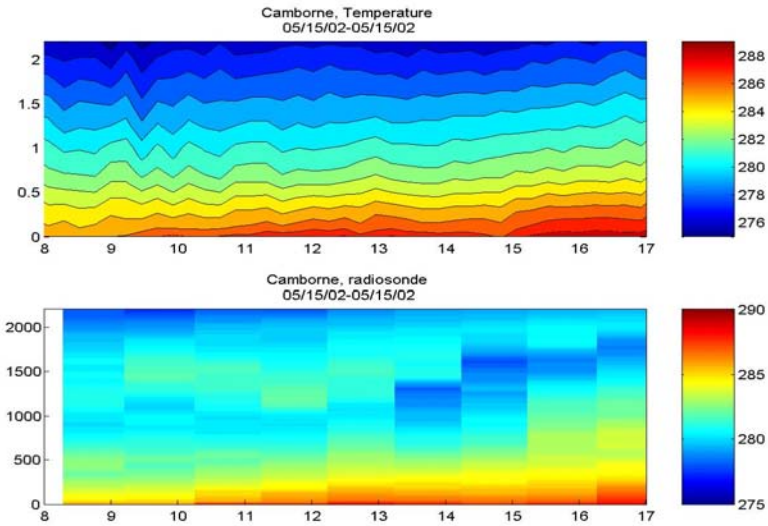


*Figure 4.29.* Time-height series of temperature profile from radiometer (upper panel) and radiosonde (lower panel) Camborne, 15 May 2002, 08.00–17.00 UT

**Clear air situation.** On the 16 May 2002, figure 4.31, there was no low-level cloud. However, the laser ceilometer did show the presence of two layers with different aerosol scattering properties, see figure 4.32 where the top of the first layer corresponds to a large temperature inversion. The top of the second layer fits underneath the first local maximum of the lowest wind profiler signal to noise in the vertical and corresponds to a strong decrease in the humidity but a weak temperature inversion The evolution of $(dn/dz)^2$ from the radioson-

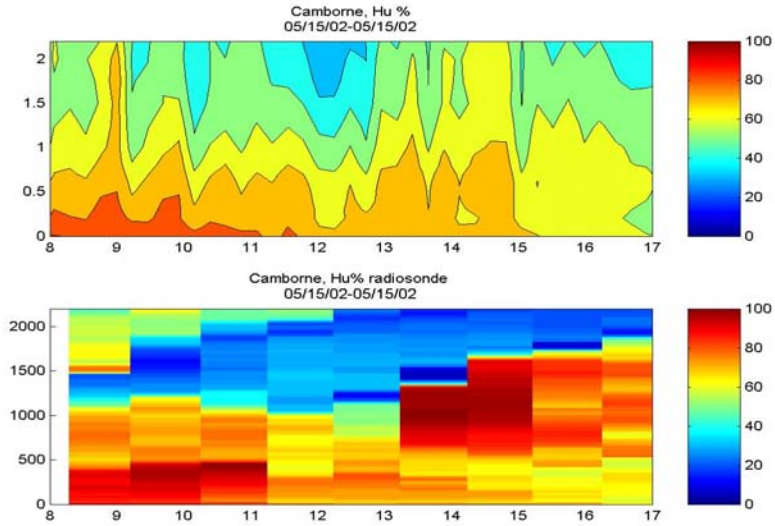


*Figure 4.30.* Time-height series of humidity profile from radiometer (upper panel) and radiosonde (lower panel) Camborne, 15 May 2002, 08.00-17.00 UT

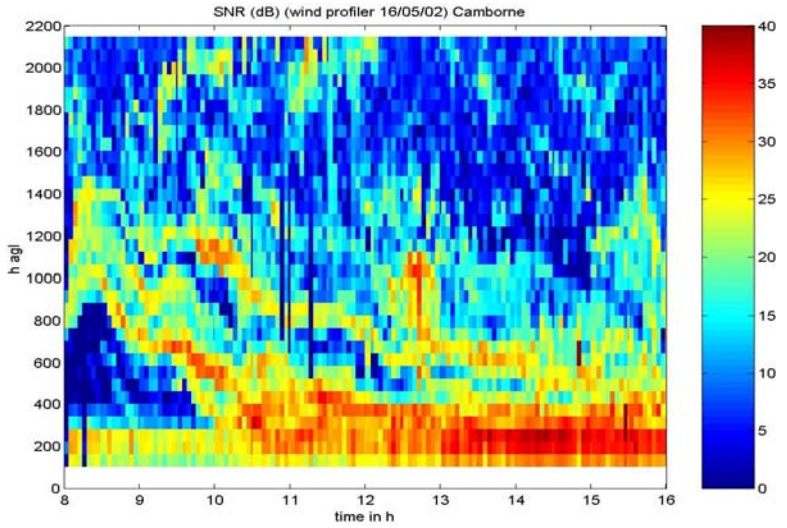


*Figure 4.31.* Signal-to-noise ratio of wind profiler (dB scale) on 16/05/02 at Camborne

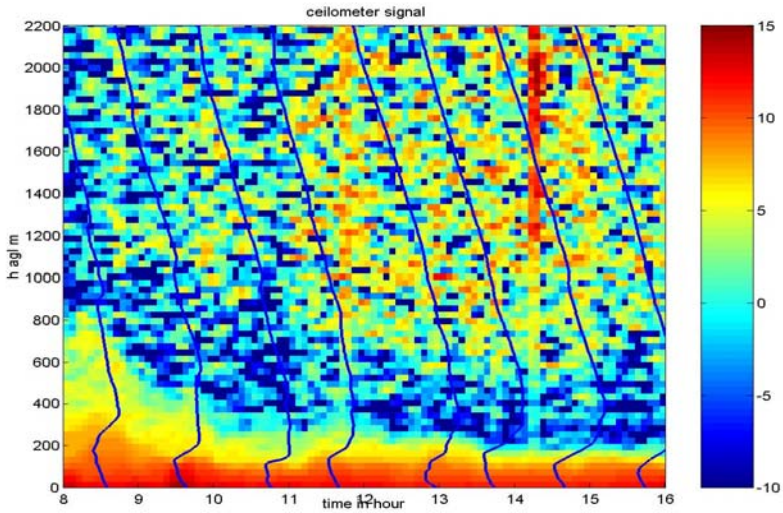


*Figure 4.32.* Ceilometer signal averaged over 5 min for 16/05/02. Blue curves are temperature profiles

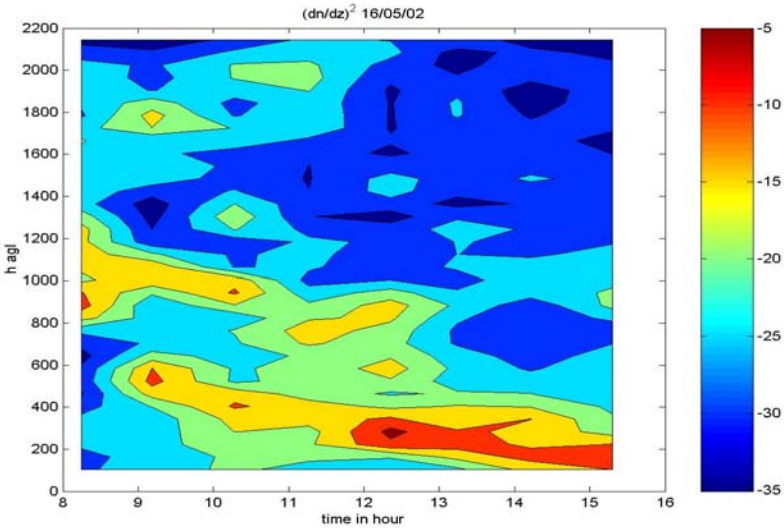


*Figure 4.33.* Time-height series of square gradient of the refractive index (dB scale) computed from hourly radiosonde on 16/05/02 08.00–15.15 UT

des shown in figure 4.33 reproduces the evolution of the signal to noise ratio between 300 m and 1200 m in the vertical and as for the 15 May the basic theoretical treatment was adequate.

**Discussion.** For the two non convective situations the agreement between the gradient of the potential refractive index and the signal to noise was excellent. The time height cross section of the signal to noise ratio followed in fine detail the evolution of discontinuity in the refractive index associated with temperature inversion and hydro lapse. Such information added to the radiometer retrieval should improve the vertical resolution of the retrieved profile.

For the convective day, the vertical structure in the signal to noise ratio differed from the refractive gradient index computation from radiosondes, with signals much higher near 800 m than expected from the radiosondes using the basic theory. This suggests that strong signals associated with convection may need different theoretical treatment compared to the theory for layered structures in more stable conditions. On inland sites, convection is very common in summertime conditions in the UK, and this was the reason that the Met Office contribution to CSIP was initiated (see section 5.3).

On the convective day, drizzle contamination might explain some unexpectedly strong signals above 1000 m. Collocated cloud radar would allow a complete discrimination between clear-air echo and drizzle echo and may prove essential for observing the boundary layer in UK conditions, where clear days are relatively rare. On this day, atmospheric variability was high, and combination of cloud radar, ceilometer, radiosondes and microwave radiometer was probably necessary to present an adequate description.

### 4.6.5 MOMENTS ANALYSIS OF THE TUC DATA, 2003/2004

**4.6.5.1 Introduction to TUC data.** The observations used in this moments analysis were made by the Meteo-Suisse 1290 MHz wind profiler at Payerne, [see section 6.1], again as part of work packages for the COST-720 Working Group on Integration. This wind profiler differed from Camborne in its operating frequency (1290 MHz). So the beam width of the antenna was slightly narrower than for Camborne (5˚ instead of 7˚). Low mode and high mode measurements were interlaced in time, using vertical resolutions of 45 m and 210 m and vertical ranges of 1 km and 5 km respectively. The total integration time or dwell time for each spectrum was around 30s, so it took around 3minutes to do a full measurement cycle. The profiler was upgraded to digital signal processing in early January 2004. The dwell times were then reduced to about 20 s, giving a higher rate of sampling but lower signal to noise ratios.

Signal processing software was similar to Camborne except that the spectra were averaged with the ICRA averaging method. This method checks that

the spectrum follows a Gaussian distribution for each spectral bin, if not, the value is taken out of the average, hence, removing intermittent interference. The side effect of the ICRA method is introduction of higher variability to the spectrum and therefore to the signal to noise ratio and to the width. As at Camborne, Payerne spectral moments were estimated using a simple peak-tracking algorithm together with a ground clutter removal algorithm.

The magnitude of clear air scattering in wintertime conditions in the TUC experiment was relatively low compared to the tests at Camborne. In clear air conditions complete profiles of reliable signals in the low mode were rare and high mode measurements were rarely complete above 1 km in the high mode. For instance in 4.34, time-height cross-sections of the signal to noise in the high and low modes are shown for a transition from dry conditions at low levels to a situation dominated by precipitation. Signals were only received from structures in the atmosphere that gave the largest scattering, e.g. the strongest hydrolapses. The operational signal processing recorded a value for the signal to noise ratio, the Doppler shift and the width with no quality flag or confidence value in all possible areas of the data files. So for analyses to be based on reliable signals, a quality control system was needed. The methods used to determine reliability will be discussed in the next sections. The quality controlled signal to noise data set was also used in the work of Klaus (see section 4.5).

**4.6.5.2 Use of a signal-to-noise threshold and vertical wind speed for quality control.** Signal-to-noise thresholds for satisfactory measurements were derived by monitoring the occasions when vertical winds were clearly spurious. Positive vertical wind speed greater than 3 $ms^{-1}$ averaged over 30 s was considered unrealistic, in Payerne, although occasionally vertical speeds close to 3 $ms^{-1}$ were associated with wave activities triggered by hills to the west of Payerne.

Figure 4.35 shows the ratio of unrealistic vertical speed measurements to the total number of measurements for positive speeds, as a function of the signal to noise in the low mode. Very few unrealistic values of vertical speed occurred when the signal to noise ratio was greater than –15 dB. The high mode showed a similar distribution.

Unusually high values of the signal-to-noise ratio were often caused by scattering from rain or ice crystals (see section 4.6.2.2). However, in light drizzle the signal-to-noise from precipitation can be much closer to the clear-air signal. Thus, a check on the persistence of negative wind speed in the vertical was used to try and improve discrimination between Bragg and Rayleigh scattering. Precipitation was flagged if five consecutive gates in the vertical had a negative vertical speed greater or equal to 0.5 m/s. When the precipitation data were removed by this method the distribution of vertical velocities was biased towards positive values, so this precipitation check probably removed some valid measurements from descending parcels of clear air. On some occa-

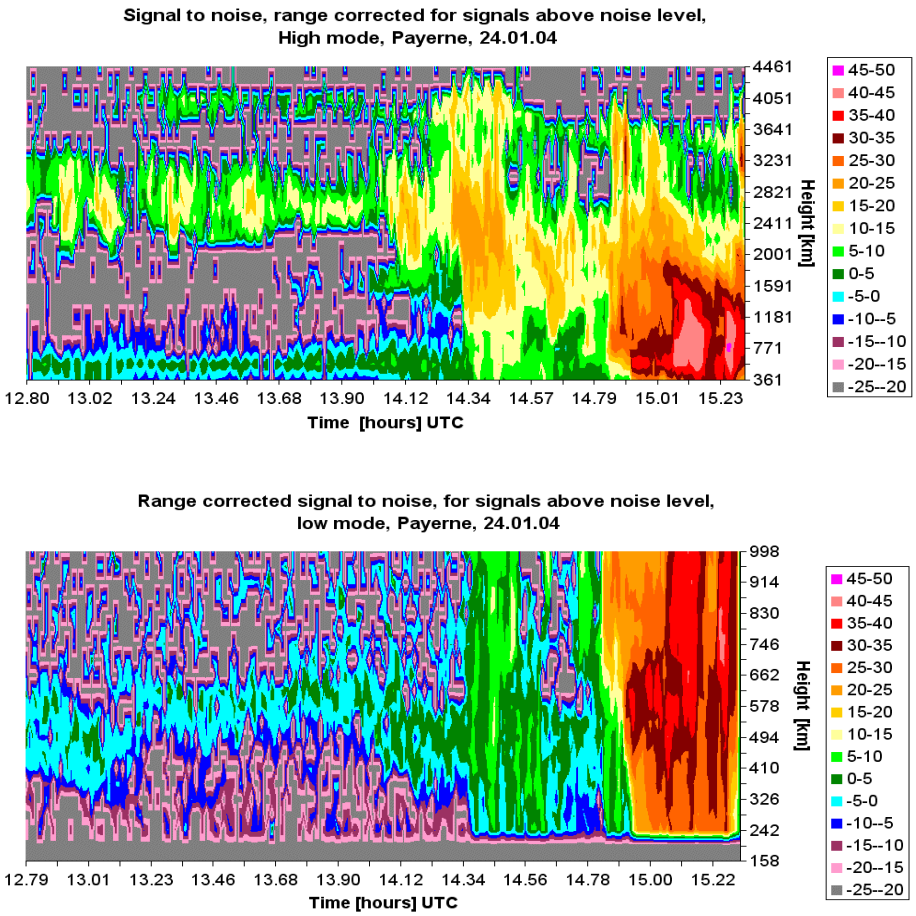


*Figure 4.34.* High mode and low mode time-height cross-section of signal-to-noise on 24/01/2004 with signals lower than a signal-to-noise threshold of about -16 dB excluded and set to a value below -20 dB. Conditions were relatively free of precipitation/drizzle before 14.00 UT apart from layers in the high mode at about 2.8 km. Drizzle/precipitation reaching the surface started just after 14.34 UT

sions with ascending parcels of air at around 1 $ms^{-1}$, this precipitation check would also fail to identify signals from drizzle. Thus, for future operational use of wind profiler signal-to-noise, a more reliable method of rejecting Rayleigh scattering is required, probably using cloud radars and laser ceilometers to identify precipitation and drizzle events more reliably.

**4.6.5.3 Use of spectral width for quality control.** As already mentioned in section 4.6.3.2.0, the beam width broadening effect causes the width of each spectrum to be larger than a minimum value which is function of the horizontal wind speed. A scatter plot of the spectral width against wind speed is shown in figure 4.36 for one of the oblique beams of the Payerne profiler.

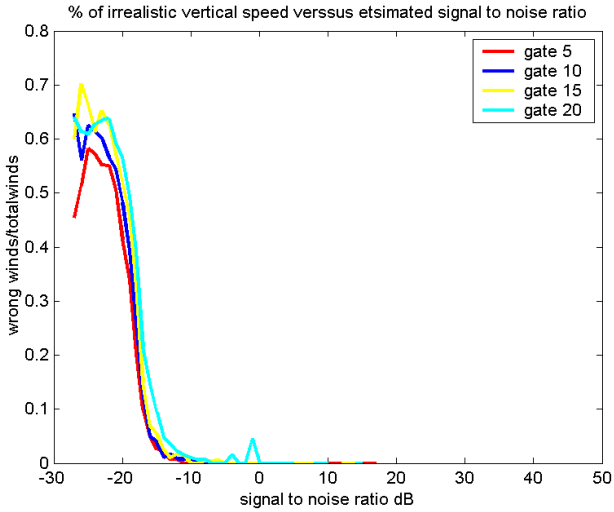


*Figure 4.35.* Percentage of unrealistic vertical speed plotted against signal-to-noise ratio for different gates for the low mode

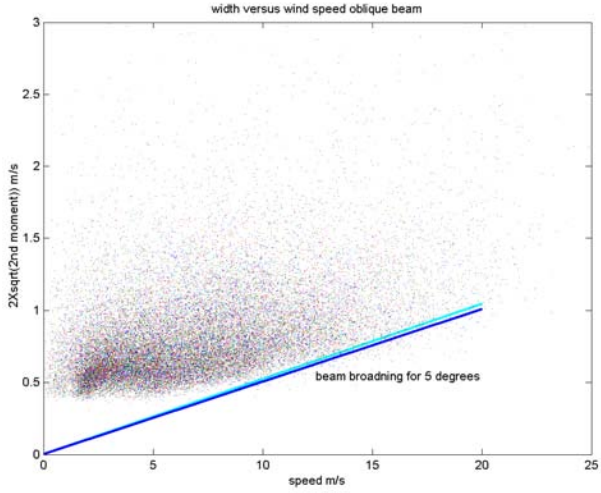


*Figure 4.36.* Spectral width versus wind speed for one of the oblique beams; the blue and cyan lines are the minimum and maximum beam width broadening for a 5 deg beam width

Figure 4.36 was derived from a data set limited to occasions where vertical wind shear was unlikely to lead to increased the spectral width. The minimum envelope of the scatter plot corresponds very well at speeds greater than 10 m/s with the expected value for the nominal beam width in all 3 beams, confirming the beam width quoted by the manufacturer. Spectra with a width smaller than the minimum beam broadening width can be rejected as spurious. The resolution of the FFT used to determine the spectrum limits minimum values to 0.4 m/s and a higher-order FFT would be necessary to resolve smaller values at wind speeds lower than about 8 m/s.

Very wide spectral width can be due to bird or precipitation contamination or the presence of anomalous signals [e.g. internal interference or spurious signals received in the antenna side-lobes.] To establish a maximum acceptable spectral width, spectral widths estimates were derived from observations of dissipation rate in the UK [0.005 m $s^{-3}$ in stratocumulus] using the White formula (see section 4.6.3.2.0) and the beam broadening effect for the low and high mode. The results are shown in figure 4.36 for the low mode (left) and high mode (right) respectively. In both figures maximum values for a given wind speed were used as the upper limit for reasonable broadening in clear air for the two profiler modes.

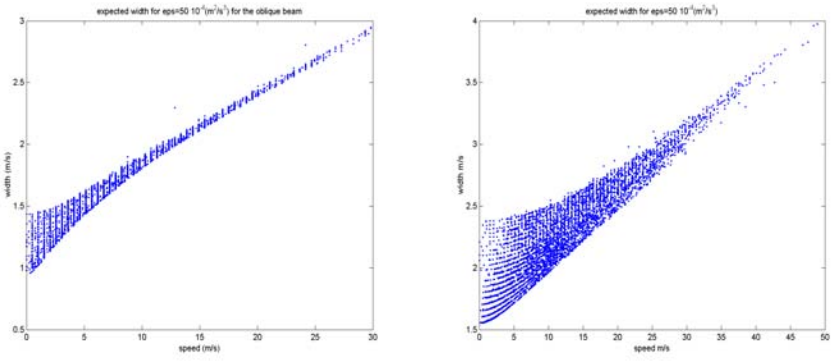


*Figure 4.37.* Expected spectral width for $\varepsilon = 0.005$ m $s^{-3}$ versus wind speed, low mode (left) and high mode (right)

The application of quality control using spectral width proved effective in removing significant numbers of poor spectral width observations that had been allowed through by quality checks on signal-to-noise and vertical wind speed.

**4.6.5.4 Exclusion of other anomalous signals.** During the TUC experiment, a building site was in operation around 300 m from the radar site. As the cranes on the sites moved during operations, direct reflections from the

cranes were received in the side lobes of all three beams. These spurious signals had non-zero Doppler shift and caused errors in the wind profiler signal to noise measurements in the lowest range gates of the low mode.

Figure 4.38 is a time-height cross section of the signal-to-noise ratio of the vertical beam showing the impact of the crane during working hours. Increased low-level signals started at 07 UT and finished at 16 UT, with a gap of 1 hour starting at 11 UT, coincident with lunch break on the building site. Data below 400 m during working time were always likely to be contaminated by the crane signal. Apart from the fact that this increased signal coincided with working hours, it was rather difficult to identify. There was no obvious discontinuity in the wind field, (the crane was only working in low-wind conditions) nor special spectral characteristics.

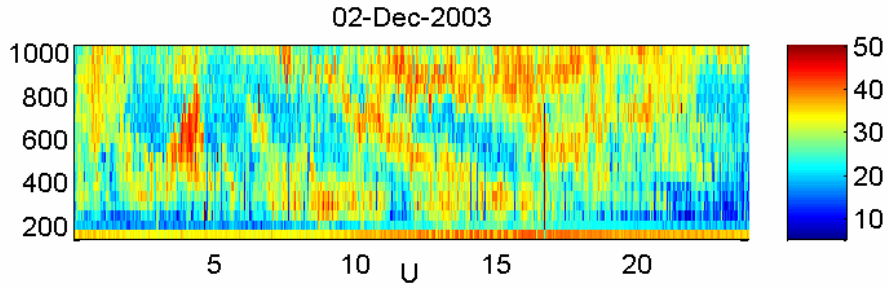


*Figure 4.38.* Time-height cross section of range-corrected signal-to-noise ratio. The signal inside the box is due to direct reflection from the crane, the signals stopped during the lunch break from 11 UT to 12 UT

If correct values of wind profiler signal-to-noise will be critical in an experiment it is essential to check very carefully for sources of spurious signals, especially those that can enter through side-lobe reception, e.g. ground clutter from trees, etc., or objects moving consistently such as tracking-radar antenna.

A second source of spurious signal to noise that occurred on a significant number of the TUC days was range aliasing of strong signals from about 3 or 4 km into the low mode. Here the upper signals from cloud/precipitation were much stronger than the weak clear air signals in the low mode, and appeared as the dominant signal at false heights in the low mode. When there was strong wind shear with height, as was usually the case, the range aliasing was most readily identified by very abrupt changes in horizontal wind velocities.

#### 4.6.5.5 Variability and consistency between the 3 beams.

**Signal to noise ratio (SNR).** A scatter plot of the comparison in signal to noise ratio between oblique beams in the low mode of the Payerne profiler is plotted in figure 4.39 There was a small bias between the two oblique beams (-0.2 dB) and the standard deviation of the comparison was 3.4 dB. However,

the vertical beam had a bias of -2.8 dB relative to the oblique beams. The significant negative bias in the vertical beam was probably the result of the ground-clutter removal algorithm and also the direct-current algorithm which removed the energy at zero Doppler shift.

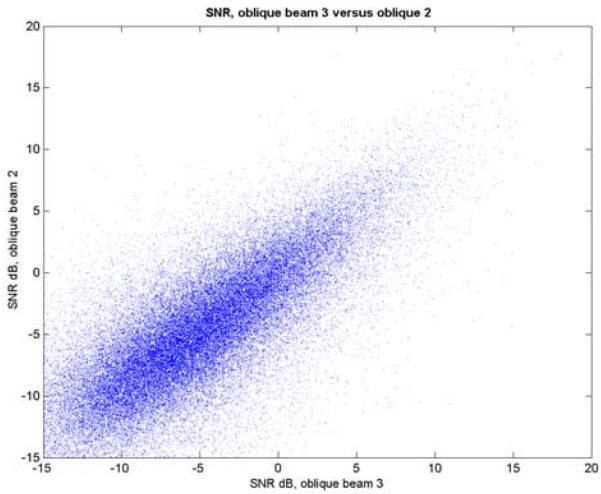


*Figure 4.39.* Oblique beam-3 signal-to-noise ratio (x-axis) versus oblique beam-2 signal-to-noise ratio (y-axis). Values are in dB and are not range corrected, low mode

The standard deviation between the values obtained from two different beams was quite high. Part of this variability may be due to variation in the instrument noise, but for values well above the noise level, the scatter plot between the 2 oblique beams remained wide suggesting that there was variation in the atmospheric scattering between the two beam directions. Examination of 915 MHz profilers in the UK also showed similar standard deviations between oblique beams. Whether this is purely because the atmospheric structure is different between the two beam directions, or whether the scattering may have some variation in aspect sensitivity caused by limited Fresnel scattering is unclear. For the high mode the standard deviation between the 2 oblique beams was slightly smaller (3.09 dB) and the correlation better (0.83 compared to 0.77) than for the low mode.

When these basic signal to noise ratios were averaged over increasing time windows the standard deviation between the beams decreased sharply down to 20 min averages (see figure 4.40). The correlation between the signal-to-noise ratio in different beams see figure 4.41 increased rapidly as the time averaging increased to 20 minutes, and then less sharply as the averaging time increased further.

The correlation between the value from the vertical beam and the oblique beam is much smaller than the correlation between the oblique beams and

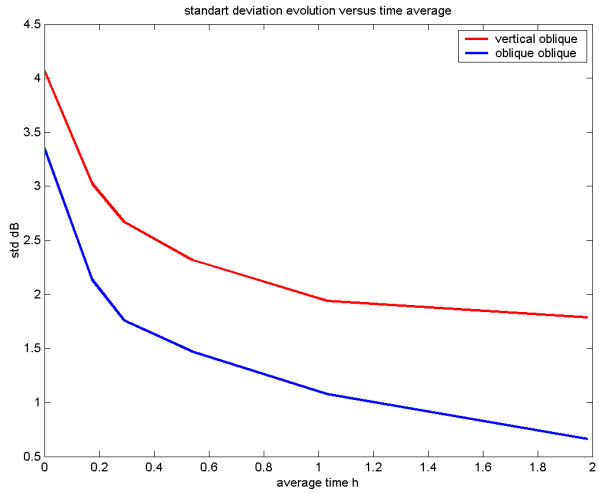


*Figure 4.40.* Standard deviation of signal to noise ratio between beams, evolution versus time averaging. Red curve vertical against oblique, blue curve oblique against the other oblique (low mode)

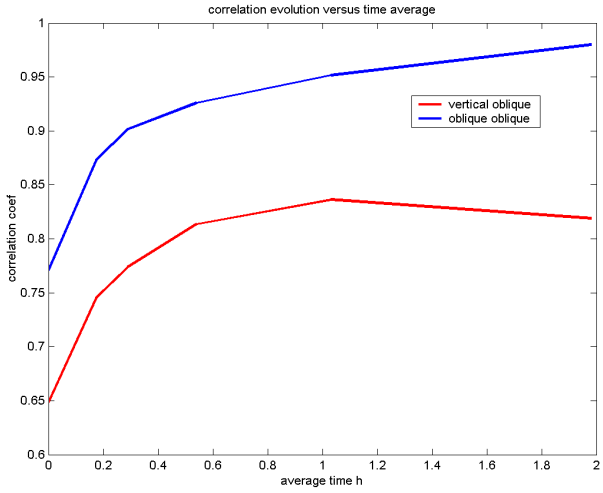


*Figure 4.41.* Correlation of signal-to-noise ratio between beams, evolution versus time averaging. The red curve shows vertical beam versus oblique, and blue curve oblique versus the other oblique (low mode)

clearly indicates a problem with the vertical beam measurements. Thus, representative samples of signal-to-noise data for quantifying refractive index gradients seems to require averaging for at least 20 minutes. However, identifying the mechanisms involved in producing the profiler signal-to-noise data, e.g. the type of turbulence or thermal structures, is best performed at high temporal resolution [1 minute],

**Spectral Width.** Once corrected for shear broadening, the Doppler width for the 3 beams should represent the turbulent broadening and ought to be similar for the 3 beams. The scatter plot of $\sigma^2_{turb}$ between the 2 oblique beams is shown in figure 4.42.

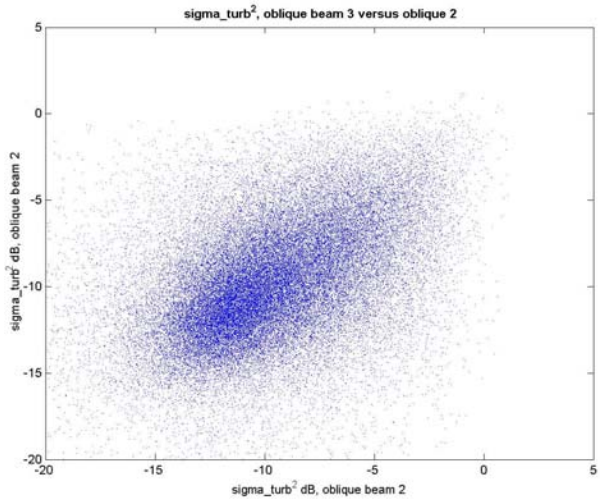


*Figure 4.42.* $\sigma^2_{turb}$ from oblique 3 beam (y-axis) versus $\sigma^2_{turb}$ from oblique 2 beam (x-axis)

The standard deviation between two oblique beams was 3.87 dB, whilst the range of variability in turbulent broadening was around 15 dB. This led to a poor correlation of 0.42 between the individual samples of $\sigma^2_{turb}$ for the 2 oblique beams. Variation in instrument noise, possible variation introduced by anomalous signals only affecting one beam, and variation in atmospheric scattering between the beam directions will have contributed to the variability of $\sigma^2_{turb}$.

The use of a simple correcting factor which took into account only the beam broadening compared to the full correcting factor marginally degraded the correlation in spectral width for the low mode and marginally improved the correlation for the high mode. Thus, poor estimation of shear broadening did not appear to be the main factor limiting the correlation in figure 4.42. As the averaging time increased to about 20 minutes, the correlation between beams for

the spectral width increased and the standard deviation decreased sharply see figures 4.43a and 4.43b.

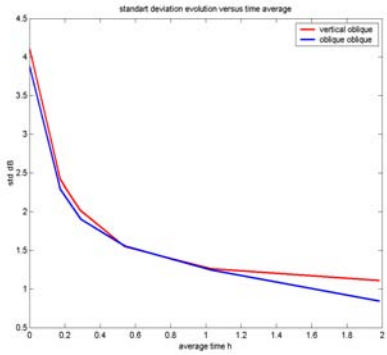


*Figure 4.43a.* Standard deviation evolution versus time averaging for spectral width: Red curve is vertical against oblique, blue curve oblique against the other oblique (low mode)

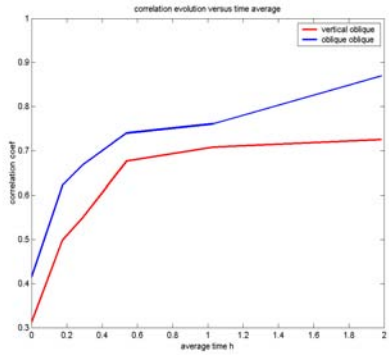


*Figure 4.43b.* Correlation evolution versus time averaging for spectral width: Red curve is vertical against oblique, blue curve oblique against the other oblique (low mode)

The correlation of $\sigma^2_{turb}$ between the vertical and oblique beam was much smaller than for the 2 oblique beams, indicating there were some problems with the vertical beam measurements. Thus, for evaluation of $C_n^2$ and of $\sigma^2_{turb}$, it was better to use the oblique beams than the vertical beam at Payerne. This is probably the case for most wind profilers, although the beam performance of each profiler needs to be checked for each instrument. An average over 20 to 30 minutes significantly reduces the dispersion between the 2 oblique beams. However, the correlation between different beams at Payerne for the width using the available software remained low even with 30 minute averages.

#### 4.6.5.6 Comparison with radiosondes [TUC].

**Gradient of refractive index versus SNR.** For the TUC, the wind profiler data were collocated with radiosonde measurements within a time window of 0.5 h centered on the launch time of the radiosonde. The potential temperature and the potential water vapour were averaged at the radar resolution, and the potential refractive index gradient $(dn/dz)$ was computed from the mean values following Gossard et al. (1998). Most of the radiosonde samples were 6 or 12 hours apart, so comparisons were more fragmented than in the Camborne tests. This has the disadvantage that if the radiosonde and wind profiler estimates were not in agreement it was much more difficult to identify whether this was caused by:

- a collocation problem, i.e. the radiosonde and profiler observing different parts of the atmosphere in a region with large atmospheric variation in the horizontal, or where structure was changing rapidly with time,
- scattering conditions which were unlikely to be represented by the theoretical treatment, e.g. enhanced signals because of the convective structures near the top of unstable layers, or layers with unusually low turbulence in stable conditions at night,
- radar malfunction, including interference or temporary loss of sensitivity, e.g. if snow falls into the clutter screen.

As in the Camborne tests, the radar signals in layers above thermal convection sometimes gave higher signal to noise than expected by up to about +20 dB. On other occasions, significant inversions measured by the radiosonde were linked with very low radar values, values low by at least 20 dB, at the actual observation time, even though there may have been much higher radar signals at the expected level within $\pm$ 3 hours.

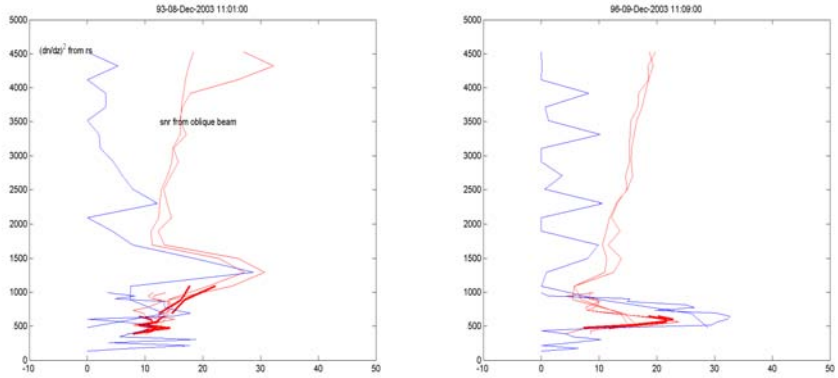


*Figure 4.44.* Profile of $(dn/dz)^2$ from radiosonde (blue line), signal-to-noise ratio from wind profiler averaged for half an hour (red lines) for both, low mode (up to 1000 m), and high mode (up to 4500 m) on Dec 8, 2003 / 11 UT (left) and Dec 9, 2003 / 11 UT (right)

Figure 4.44(left) shows an example of a comparison between the signal-to-noise ratio from the oblique beam (red line) and the $(dn/dz)^2$ (blue line), computed from the radiosonde. The thick line was obtained from the data that have past the full quality control, and the thin line obtained from data flagged as not rain. The values are expressed in decibel and the radiosonde curve has been empirically shifted by the same amount for all the comparisons in the data set. Here, the agreement between the radiosonde and wind profiler was good, taken from a day with a steady, strong layered signal, which coincided

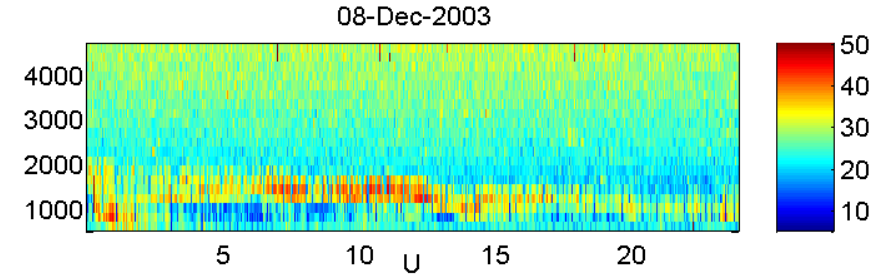


*Figure 4.45.* Time-height cross section of the range corrected signal-to-noise ratio observed in high mode. Time axis is in hours (x axis), height in m (y axis): 24 h plot from 8/12/03

well with the discontinuity in the refractive index (see figure 4.45). However, the resolution of the high mode looks inadequate to resolve small shifts in the vertical position of the refractive index gradients associated with the inversion on this day, so the strength of signals in the layered structure fell when the layer was centred between adjacent range gates.

Figure 4.44(right) shows another refractive index against radar comparison from a similar inversion on 9th December 2003. Here, the radar signal was at least 7 dB lower than that expected from the low mode radiosonde comparison. This inversion structure again persisted for most of the day, see figure 4.46. When all the comparisons from the TUC were considered the inversion level shown by the radiosonde was always close to the maximum in the radar signal. However, the signal to noise ratio associated with a given midrange refractive index gradient often varied by up to $\pm$ 10 dB from the radiosonde computation. Better correlation between wind profiler and radiosonde requires a method of identifying the reasons for the outliers. For this to happen, it seems essential to have a higher density of radiosondes when the outliers are occurring.

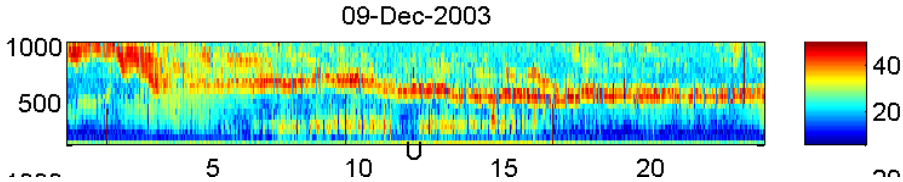


*Figure 4.46.* Time-height cross section of the range-corrected SNR from the low mode. Time axis is in hours (x axis), and height in m (y axis): 24 h plot from 9/12/03

**Gossard formulation.** The relation between $C_n^2$ and $(dn/dz)^2$ given in equation 4.18 should be improved, if variation in the corrected spectral width is taken into account in the comparison between radiosonde and radar. However, the use of this full Gossard formulation didn't improve the comparison with the refractive index gradient computed from radiosonde. The lack of correlation

in the turbulence portion of the spectral width observed between the different beams might indicate problems with the spectral width observations that may have limited the application of spectral width from Payerne. On many occasion the higher spectral widths were associated with regions of low signal-to-noise values, possibly because it is necessary to have good signal-to-noise data to get a good spectral width measurement, and the limiting signal-to-noise value for spectral width may be much higher than for the basic signal-to-noise application. Thus, boundary-layer wind profilers with improved signal-to-noise data relative to current designs may be required to progress this type of study in wintertime conditions. However, it is also possible that the turbulence, giving enhanced wind profiler signals on top of thermals may not be isotropic. Pursuit of investigations, where the isotropy of the turbulence can be identified may also improve understanding of the outliers in the comparison between radar and radiosonde and show if a removal of observations at near-zenith angles may be helpful.

### 4.6.6 FURTHER WORK AND RECOMMENDATIONS

(1) If a maximum can be identified in the clear air wind profiler signal in stable conditions, it is possible to get good agreement with refractive index gradients computed from a radiosonde measurement. In all these tests, discontinuity in the refractive index gradient could be followed over long periods throughout the day using the wind profiler signal. For the future, data assimilation tests for numerical weather prediction models should be used to see whether the models represent the changes in the height of these layered structures with time. Then the impact of assimilation of the observed profiler signal to noise ratio in improving the forecast of atmospheric conditions in the lower troposphere will need to be assessed. This would be expected to include cases associated with fog forecasting, or the forecasting of conditions associated with sever weather in the summer.

(2) In order to ensure that the information supplied for data assimilation tests is valid, the operation of the wind profiler should be checked in detail, as was done for the system at Payerne. Discrepancies caused by ground clutter contamination will need to be identified and mitigated if possible, especially for problems in individual beam directions. Also potential sources of short terms spurious signals, for instance, light aircraft/helicopters passing the site, or birds will require suitable quality control.

(3) In addition, better discrimination between drizzle and light rain and clear air signals is probably necessary, and the cost effectiveness of ceilometers and cloud radars in helping with this problem needs to be evaluated.

(4) In future field experiments it will be necessary to take account of the large rates of change in atmospheric structure with time , even in foggy situations. The patterns of radiosonde deployment need to be designed to help identify the reasons for the discrepancies between radiosonde and profiler radar refractive index gradients.

(5) A better understanding of the origin of wind profiler signals is obtained when looking at high time resolution data. Thus, wind profilers for researching these phenomena need to have sufficient power to observe at a temporal resolution of a minute, even in layers in the lower troposphere where expected signal to noise will be low, e.g. winter in Payerne.

(6) Future studies will benefit from the use of advance processing techniques like the multi peak algorithm or fuzzy logic e.g. see section 5.6. These advanced methods may be tuned to reject ground clutter and radiofrequency interference more efficiently and in case of rain contamination, will attempt to separate the rain echo from the clear air echo. A comparison of these different methods was performed on the TUC data (Gaffard et al, 2006).

(7) Further studies need to be performed to assess the factors limiting estimation of turbulence from wind profiler spectral width. This should be pursued with profilers that have better signal to noise than was found in the conditions at Payerne.

(8) Improved understanding of the relationship between radiosonde and profiler refractive index gradients, and the possible classification of the meteorological conditions associated with different turbulent scattering mechanisms may be obtained from further dedicated field experiments. Classification of short term variability in the atmosphere using tethered balloons can be investigated. The use of radar and lidar observations at high angles from zenith as well as near zenith can be used to test when assumptions of homogeneity and isotropy are valid for the turbulence in the layer being observed. Collocated wind profilers operating in the UHF and VHF may also aid understanding of remote sensing of cloud.

(9) The use of the variation in signal to noise measurements between beams as an indicator of the quality of the resultant wind measurements should be investigated, since the variability between the beams is not totally random with the variability much higher in certain conditions than in others.

(10) The quality of operational wind profiling software has improved to the extent that observations of corrected spectral width can also prove useful in identifying contamination from spurious signals, or when e clear air and precipitation echoes are of similar magnitude. Thus, more work is

recommended to improve the reliability and use of spectral width and the consistency between the methods of calculating and reporting spectral width from the different types of software in operational use.

## Bibliography

COST Action 76: Development of VHF/UHF wind profilers and vertical sounders for use in European observing systems - Final report. European Commission, EUR 20614, 2003.

Doviak, R. J. and D. S. Zrnic: Reflection and scatter formula for anisotropically turbulent air. *Radio. Sci*, **19**, 325–336, 1984.

Doviak, R. J. and D. S. Zrnic: Doppler radar and weather observations, $2^{nd}$ ed.. *Acad. Press*, San Diego, 458 pp., 1993.

Gaffard,C., L. Bianco, V. Klaus, and M. Matabuena: Evaluation of moments calculated from wind profiler spectra: A comparison between five different processing techniques. *Meteorol. Zeitschr.*, **15**, 73–86, 2006.

Gossard, E. E., R. B. Chadwick, W. D. Neff, and K. P. Moran: The use of ground-based Doppler Radars to measure gradients, fluxes and structure parameters in elevated layers. *J. Appl. Meteorol.*, **21**, 211–226, 1982.

Gossard, E. E., D. E. Wolfe, K. P Moran, R. A.Paulus, K. D. Anderson, and L.T Rogers: Measurement of clear-air gradients and turbulence properties with Radar wind profilers. *J. Atmos. Ocean. Technol.*, **15**, 321–342, 1998.

Jacoby-Koaly, S., B. Campistron, S. Bernard, B. Benech, F. Ardhuin-Girard, J. Dessens, E. DuPont, and B. Carissimo: Turbulent dissipation rate in the boundary layer via UHF wind profiler Doppler spectral width mesasurements. *Bound.-lay. Meteorol.*, **103**, 361–389, 2002.

Stankov B. B., E. R. Westwater, and E. E. Gossard: Use of wind profiler estimates of significant moisture gradients to improve humidity profile retrieval. *J. Atmos. Ocean. Technol.*, **13**, 1285–1290, 1996.

Stankov B. B, E.. E. Gossard, B. L. Weber, R. J. Lataitis, A. B. White, D. E. Wolfe, D. C. Welsh, R. G. Strauch: Humidity gradient profiles from wind profiling radars using the NOAA/ETL advanced signal processing system (SPS). *J. Atmos. Ocean. Technol.*, **20**, 3–22, 2003.

Tatarskii, V. 1961: *Wave propagation in a Turbulent medium*. McGraw–Hill, New York, 285pp., 1961.

White A. B., R. J. Lataitis, and R. S. Lawrence: Space and time filtering of remotely sensed velocity turbulence. *J. Atmos. Ocean. Technol.*, **16**, 1967–1972, 1999.

# 4.7 1D-VAR RETRIEVAL OF TEMPERATURE AND HUMIDITY PROFILES FROM GROUND-BASED MICROWAVE RADIOMETERS

Tim J. Hewison

*UK Met Office, Reading University, Reading, UK*
✉ tim.hewison@metoffice.gov.uk

## 4.7.1 INTRODUCTION

Numerical Weather Prediction (NWP) and *nowcasting* applications have a requirement for observations of temperature and humidity profiles of increasing accuracy, frequency and resolution. It is anticipated that these requirements may be addressed by integrating observations from different ground-based remote sensing instruments, including a microwave radiometer, to supplement the radiosonde network and to complement satellite data over land. These *Integrated Profiling Systems* offer the potential to provide information on vertical profiles of temperature, humidity and cloud at a high temporal resolution, which could be assimilated into the next generation of convective scale NWP models. This paper demonstrates that a one dimensional variational (1D-VAR) retrieval method can be used to combine observations from multiple instruments with background information from an NWP model to provide retrievals of temperature, humidity and cloud profiles. The performance of these retrievals can be compared with the user requirements.

The retrieval of temperature and humidity profiles from passive ground-based sensors is an *ill-posed* problem, because there are an infinite number of atmospheric states that can produce a given observation vector within its uncertainty. This can be resolved by the addition of *background* data. Variational retrievals provide an *optimal* method of combining observations with a background in the form of a short-range forecast from an NWP model, which accounts for the assumed error characteristics of both. For this reason they are often referred to as *Optimal Estimation* retrievals. The 1D-VAR retrievals presented here are similar to the *Integrated Profiling Technique* Loehnert et al. (2004), but takes its background from an NWP model instead of radiosondes and uses different control variables to concentrate on retrieving profiles of atmospheric temperature and humidity.

The 1D-VAR retrieval is performed by adjusting the atmospheric state vector, $\mathbf{x}$, from the background state, $\mathbf{x}^b$, to minimize a cost function of the form

Rodgers (2000):

$$J(\mathbf{x}) = \left[\mathbf{x} - \mathbf{x^b}\right]^T \mathbf{B}^{-1} \left[\mathbf{x} - \mathbf{x^b}\right] + \left[\mathbf{y} - H(\mathbf{x})\right]^T \mathbf{R}^{-1} \left[\mathbf{y} - H(\mathbf{x})\right] \tag{4.24}$$

where **B** and **R** are the error covariance matrices of the background, $\mathbf{x}^b$, and observation vector, **y**, respectively, $H(\mathbf{x})$ is the forward model operator and $^T$ and $^{-1}$ are the matrix transpose and inverse, respectively, using the standard notation of Ide et al. (1997).

## 4.7.2 BACKGROUND DATA AND STATE VECTOR

The mesoscale version of the Met Office Unified Model is used to provide background data for the retrievals in the form of profiles of temperature, humidity and liquid water. The model grid points are interpolated to the position of the observations. This model is initiated every six hours, including data from radiosonde stations. A short-range forecast (T+3 to T+9 hr) is used for the background, as would be available to operational assimilation schemes. This is independent of any radiosondes launched at observation time, which may be used to validate the retrievals.

The state vector, **x**, used in the retrievals is defined as the temperature and total water on the lowest 28 model levels. These extend up to 14 km, but are concentrated near the surface, where most of the radiometer's information is.

In this study the humidity components of the state vector are defined as the natural log of total water, $\ln q_t$. ($q$ is the specific humidity.) This control variable is a modified version of that suggested in Deblonde and English (2003), with a smooth transfer function between water vapor for $q_t / q_{sat} < 90\%$ and liquid water for $q_t / q_{sat} > 110\%$ (where $q_{sat}$ is $q$ at saturation.) The condensed part of the total water is further partitioned between liquid and ice fractions as a linear function of temperature, producing pure ice at -40°C. The choice of total water has the advantages of reducing the dimension of the state vector, enforcing an implicit super-saturation constraint and correlation between humidity and liquid water. The logarithm creates error characteristics that are more closely Gaussian and prevents unphysical retrieval of negative humidity.

The background error covariance, **B**, describes the expected variance at each level between the forecast and true state vector and the correlations between them. In this work, $\mathbf{B}_{ATOVS}$ was taken from that used to assimilate data from satellite instruments operationally at the Met Office. **B** could also be calculated by the *NMC* method (Parrish and Derber, 1992), which estimates $\mathbf{B}_{NMC}$ as the covariance of the state vectors taken from sequential runs of the forecast model, valid at the same time – e.g. the 6 h forecast and the 12 h forecast from the previous model run, 6 h earlier. For the temperature components of **x**, $\mathbf{B}_{NMC}$ has much smaller diagonal terms and correlations than $\mathbf{B}_{ATOVS}$. However, for humidity, $\mathbf{B}_{NMC}$ increases with height rapidly. The diagonal components of $\mathbf{B}_{ATOVS}$ are shown for reference in Figure 4.49.

### 4.7.3 OBSERVATIONS

This study uses observations from a Radiometrics TP/WVP-3000 microwave radiometer (Ware et al., 2003). This has 12 channels: seven in the oxygen band 51-59 GHz, which provide information primarily on the temperature profile and five between 22-30 GHz near a water vapor line, which provide humidity and cloud information. This radiometer includes sensors to measure pressure, temperature and humidity at ∼1 m above the surface. The pressure is taken as a reference from which geopotential height is calculated at other pressure levels via the hydrostatic equation. The instrument's integral rain sensor is used to reject periods which may be contaminated by scattering from precipitation, as this is not included in the forward model and emission from raindrops on the radome, which may bias the calibration. This instrument incorporates a zenith-viewing infrared radiometer (9.6-11.5 $\mu$m) to provide information on the cloud base temperature.

In this study the observation vector, **y**, is defined as a vector of the zenith brightness temperatures ($T_b$) measured by the radiometer's 12 channels, with additional elements for the surface temperature ($T_{AMB}$) and humidity (converted to $\ln q_{AMB}$) and the infrared brightness temperature ($T_{ir}$):

$$\mathbf{y} = [T_{b1}, T_{b2}, ..., T_{b12}, T_{AMB}, \ln q_{AMB}, T_{ir}] \tag{4.25}$$

The observation error covariance, **R**, has contributions from the radiometric noise (**E**), forward model (**F**) and representativeness (**M**) errors ( **R = E + F + M** ).

The radiometric noise, **E**, can be evaluated as the covariance of **y** measured while viewing a stable scene (such as a liquid nitrogen target) over a short period (∼30 min). This term is approximately diagonal – i.e. the channels are independent – with diagonal terms ∼(0.1-0.2 K)$^2$, except the 57.29 GHz channel of this particular instrument, as shown in Table 4.2.

The forward model error, **F**, includes contributions from uncertainties in the spectroscopy and errors introduced by the profile discretization, FAP model and monochromatic equivalent frequency (see section 4.7.4). The spectroscopic component was estimated as the covariance of the difference in zenith $T_b$ calculated using two absorption codes (Rosenkranz (1998) and Liebe et al. (1993)). The other terms were calculated as the covariance of the difference between $T_b$ calculated using the full line-by-line model at high vertical resolution and the approximations. **F** contains significant off-diagonal terms, and is largest for the channels most sensitive to the water vapor continuum (26 – 52 GHz), where it reaches ∼(1.1 K)$^2$.

The representativeness error, **M**, allows for the radiometer's sensitivity to fluctuations on smaller scales than can be represented by the NWP model. It is possible to estimate **M** by studying the fluctuations in the radiometer's signal on typical time scales taken for atmospheric changes to advect across the horizontal resolution of the NWP model. In the case of the mesoscale model with a

| Channel | Measurement Noise, $E$ in K | Modeling Errors, $F$ in K | Representativeness Error, $M$ in K | Total Uncertainty, $R$ in K |
|---|---|---|---|---|
| 22.235 GHz | 0.17 | 0.83 | 0.65 | 1.07 |
| 23.035 GHz | 0.12 | 0.84 | 0.67 | 1.08 |
| 23.835 GHz | 0.11 | 0.82 | 0.69 | 1.08 |
| 26.235 GHz | 0.13 | 0.67 | 0.78 | 1.04 |
| 30.000 GHz | 0.21 | 0.61 | 1.00 | 1.19 |
| 51.250 GHz | 0.18 | 1.10 | 1.70 | 2.04 |
| 52.280 GHz | 0.15 | 0.88 | 1.35 | 1.62 |
| 53.850 GHz | 0.17 | 0.35 | 0.32 | 0.50 |
| 54.940 GHz | 0.18 | 0.06 | 0.10 | 0.14 |
| 56.660 GHz | 0.19 | 0.05 | 0.10 | 0.22 |
| 57.290 GHz | 0.54 | 0.05 | 0.40 | 0.67 |
| 58.800 GHz | 0.18 | 0.06 | 0.11 | 0.22 |
| $T_{AMB}$ | 0.24 | 0.00 | 0.15 | 0.28 |
| $\ln q_{AMB}$ | 0.02 | 0.00 | 0.01 | 0.02 |
| $T_{ir}$ | 2.50 | 0.59 | 8.77 | 9.14 |

*Table 4.2.* Diagonal components of Observations Error Covariance Matrix, $R^{1/2}$ evaluated for clear and cloudy conditions

12 km grid, 1200 s was chosen to represent a typical advection timescale. The r.m.s. difference (divided by $\sqrt{2}$) in **y** measured over this time interval was used to calculate **M**, after subtracting the contribution from the radiometric noise, **E**. This showed strong correlation between those channels sensitive to liquid water, water vapor and temperature, respectively. The liquid water and humidity terms were found to vary by an order of magnitude, depending on the atmospheric conditions. The average values calculated over a 7 day period of dry conditions with variable cloud amounts were taken to be typical. This period was later sub-divided into clear and cloudy samples and **M** re-evaluated for each. The representativeness term evaluated in this way dominates the observation error covariance of some channels, with terms $\sim$(0.1-1.7 K)$^2$. **M** can also be evaluated dynamically, based on time series of observations within 1 hour window of each observation. This technique allows the errors to be reduced in periods of atmospheric stability, when more confidence can be placed that the radiometer observations are representative of the model's state.

The magnitude of the diagonal components of each term of $\mathbf{R}^{1/2}$ is shown in Table 4.2 for the 12 channels of the microwave radiometer, surface temperature and humidity sensors (as dimensionless $\ln q$) and infrared radiometer.

### 4.7.4 FORWARD MODEL AND ITS JACOBIAN

A forward model, $H(\mathbf{x})$, is needed to transform from state space to observation space. For the microwave radiometer, each channel's $T_b$ is calculated at an

equivalent monochromatic frequency (Cimini et al., 2006a) using the radiative transfer equation to integrate down-welling emissions from each atmospheric layer between model levels using a standard absorption model (Parrish and Derber, 1992), which was found to have small biases in these channels (Hewison et al., 2006). The forward model for the surface temperature and humidity sensors is trivial – a 1:1 translation to the lowest level of the state vector, **x**. A simple forward model defines $T_{ir}$ as the temperature of the lowest level with any cloud. A more sophisticated radiative transfer model is used here to calculate $T_{ir}$ which accounts for extinction by atmospheric water vapor and liquid water cloud, assigning extinction coefficients of 0.02 Np/km.(kg/kg)$^{-1}$ and 33.3 Np/km.(kg/m$^3$)$^{-1}$ respectively. This model gives more Gaussian error characteristics, due to having less abrupt transitions at cloud boundaries. Examples of the forward model and its Jacobian are shown in Figure 4.47 and 4.7.5.

The *Jacobian* is the matrix of the sensitivity of the observation vector, **y**, to perturbations of each element of the state vector, **x**, $\mathbf{H}=H'(\mathbf{x})=\nabla_x\mathbf{y}$. It is needed to minimize the cost function (see section 4.7.6). In this study, **H** is calculated by *brute force* – each level of the state vector, **x**, is perturbed by 1 K in temperature or 0.001 in $\ln q_t$. The magnitude of these perturbations was selected to ensure linearity of **H**, while preventing numerical errors due to truncation.

However, to speed up the calculation, a *Fast Absorption Predictor* model is used to calculate the absorption in each level between the surface and the 100 hPa level as a third-order polynomial function of pressure, temperature and $q$ following Loehnert et al. (2004). This introduces an additional error in the calculation of $T_b$ described above. **H** is only calculated for levels between 0-8 km, corresponding to the maximum range of likely impact from the radiometer data. For levels above this, $\mathbf{H}=0$.

### 4.7.5 ERROR ANALYSIS

An estimate of the uncertainty on the retrieved profile can be derived by assuming the errors are normally distributed about the solution and that the problem is only moderately non-linear. In this case, the error covariance matrix of the analysis, $A$, is given (Rodgers, 2000) by:

$$\mathbf{A} = \left(\mathbf{H}_i^T \mathbf{R}^{-1} \mathbf{H}_i + \mathbf{B}^{-1}\right)^{-1} \tag{4.26}$$

where $\mathbf{H}_i$ is evaluated at the solution (or final iteration).

It is also possible to express the information content of the observations with respect to the background as the *Degrees of Freedom for Signal*, *DFS*. This represents the number of layers in the retrieved profile which are retrieved independently. It can be calculated (Rodgers, 2000) as:

$$DFS = \mathrm{Tr}\left(\mathbf{I} - \mathbf{A}\mathbf{B}^{-1}\right) \tag{4.27}$$

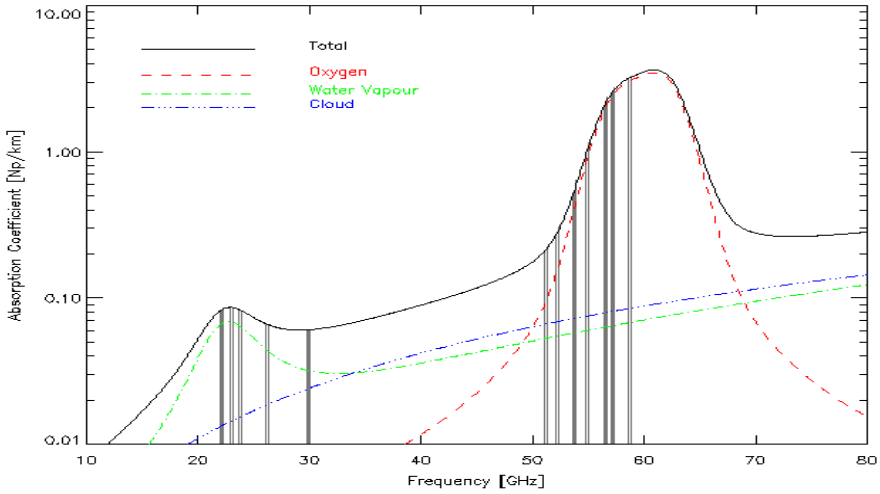


*Figure 4.47.* Atmospheric absorption spectrum for typical surface conditions: $T$=288.15 K, $p$=1013.25 hPa, $RH$=100 %, $L$=0.2 g/m$^3$ following Parrish and Derber (1992). Line styles show total absorption coefficient and contributions from oxygen, water vapor and cloud according to the legend. Grey vertical bars indicate the passbands of the Radiometrics TP/WVP-3000 microwave radiometer

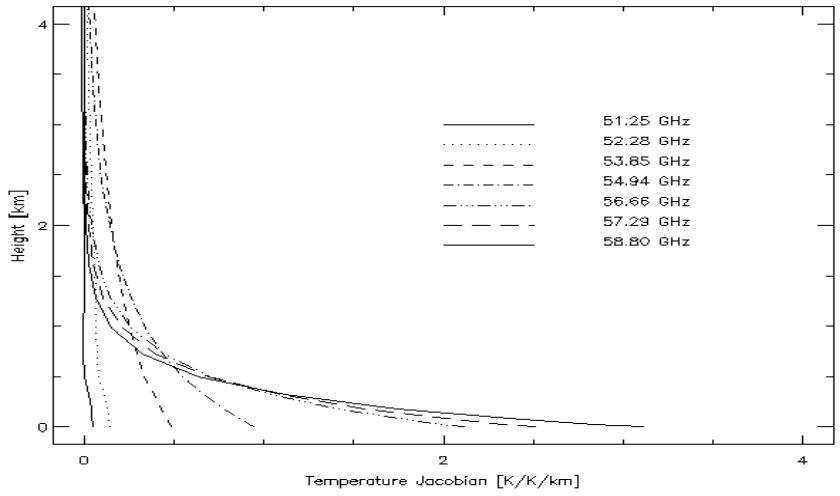


*Figure 4.48.* Temperature Jacobians of 51–59 GHz channels of Radiometrics TP/WVP-3000, scaled by model layer thickness,$\Delta z : H/\Delta z = (\partial y/\partial x)/\Delta z$

where **I** is the identity matrix and Tr() is the trace operator.

**A** has been evaluated for different combinations of instruments for a *clear* US standard atmosphere in Figure 4.49, although it depends on the reference state through $\mathbf{H}_i$. This shows error in the temperature profile retrieved from the radiometer is expected to approach 0.1 K near the surface, but increases with height, to exceed 1 K above 5 km and includes 2.8 degrees of freedom. For the humidity profile, **A** varies greatly with **x**. In this example the retrieval's ln$q$ error increases from 0.05 ($\sim$5%RH) near the surface to 0.4 ($\sim$40%RH) by 3 km and includes 1.8 degrees of freedom, increasing by $\sim$1.0 in cloudy conditions. This presents a substantial improvement on the background and the surface sensors alone, which only influence the lowest 500 m, but falls short of the radiosonde's accuracy above $\sim$1 km for both $T$ and ln$q$. Figure 4.49 also shows the analysis error resulting from the errors assumed in the assimilation of radiosonde data in the Met Office NWP models. Their **R** is a diagonal matrix, dominated by representativeness errors and may not be perfect. However, the radiometer provides much more frequent observations than radiosondes can, reducing errors of representativeness applying their data to analysis at arbitrary times.

When $B_{NMC}$ is used instead of $\mathbf{B}_{ATOVS}$, **A** gives more limited improvements up to 3 km, providing 2.6 degrees of freedom for temperature, but only 1.2 for humidity – fractionally more than a surface sensor.

However, **A** only tells part of the story. The other important aspect of the retrieval's performance is the vertical resolution – its ability to resolve a perturbation in state space. One simple, robust definition of the vertical resolution is the inverse of the trace of the *averaging kernel matrix* (Rodgers, 2000). This is evaluated in Figure 4.50, which shows that the vertical resolution of temperature profiles degrades with height, from $\sim$1 km near the surface, approximately linearly as twice the height from 0.5-4 km. For ln$q$, it degrades very rapidly above 1.5 km, from $\sim$1.5 km near the surface, but this is critically dependent on the reference state, **x**, due to non-linearity in **H**. However, this definition tends to produce estimates of vertical resolution a factor of $\sim$2 times poorer than other methods (Collard, 1998; Liljegren et al., 2005).

### 4.7.6 MINIMIZATION OF COST FUNCTION

Variational retrievals are performed by selecting the state vector that minimizes a cost function in the form of (4.24). For linear problems, where **H** is independent of **x**, this can be solved analytically. However, the retrieval of temperature profiles above $\sim$1 km and humidity profiles is moderately non-linear, so the minimization must be conducted numerically. This has been achieved using the Levenberg-Marquardt method (Rodgers, 2000) (which was found to improve the convergence rate in cloudy conditions compared to the classic Gauss-Newton method) by applying the following analysis increments

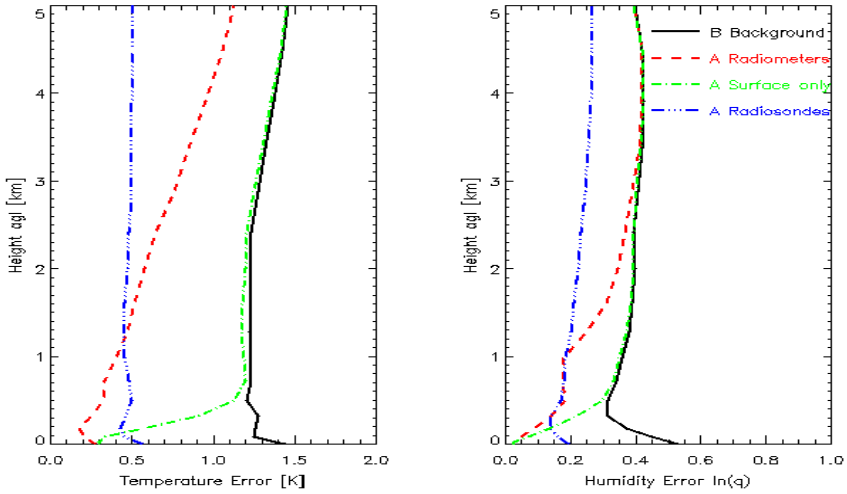


*Figure 4.49.* Background error covariance from mesoscale model, $\mathbf{B}^{1/2}_{ATOVS}$ (black) and analysis error covariances, $\mathbf{A}^{1/2}$ with surface sensors only (green), radiometers and surface sensors (red), and radiosonde only (blue). Plotted as square root of the matrices' diagonal components for the lowest 5km of temperature [K] and humidity (ln $q$) [dimensionless]

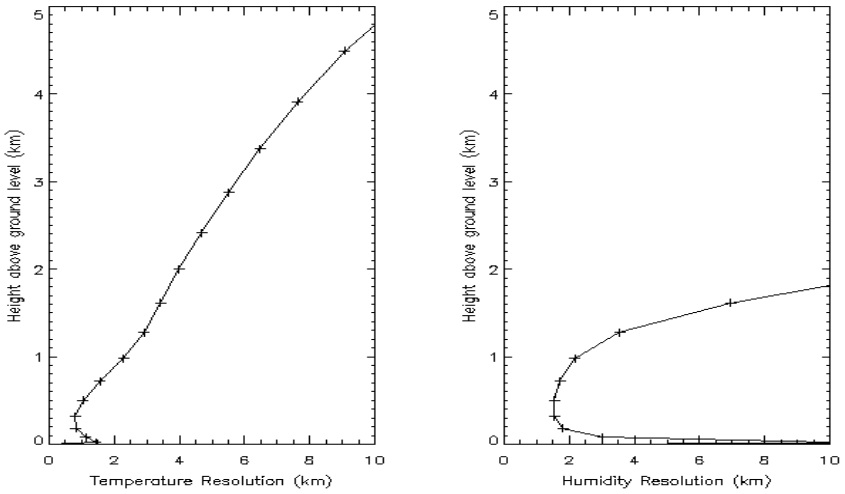


*Figure 4.50.* Vertical Resolution of temperature and humidity $(lnq)$ retrievals

iteratively:

$$\mathbf{x}_{i+1} = \mathbf{x}_i + \left((1+\gamma)\,\mathbf{B^{-1}} + \mathbf{H}_i^{\mathbf{T}}\mathbf{R^{-1}}\mathbf{H}_i\right)^{-1} \cdot \left[\mathbf{H}_i^{\mathbf{T}}\mathbf{R^{-1}}\left(\mathbf{y} - H(\mathbf{x}_i)\right) - \mathbf{B^{-1}}\left(\mathbf{x}_i - \mathbf{x^b}\right)\right] \tag{4.28}$$

where $\mathbf{x}_i$ and $\mathbf{x}_{i+1}$ are the state vector before and after iteration $i$, and $\mathbf{H}_i$ is the Jacobian matrix at iteration, $i$.

This is iterated until the following convergence criteria (Rodgers, 2000) is satisfied, based on a $\chi^2$ test of the residuals of [**y**-$H$(**x**)]:

$$\left[\left(H(\mathbf{x}_{i+1}) - H(\mathbf{x}_i)\right)\right]^T \mathbf{S}_{\delta\mathbf{y}}^{-\mathbf{1}} \left[\left(H(\mathbf{x}_{i+1}) - H(\mathbf{x}_i)\right)\right] << m \tag{4.29}$$

where $\mathbf{S}_{\delta y}$ is the covariance matrix between **y** and $H(\mathbf{x}_i)$ and $m$ is the dimension of **y** ($m$=15 in this case).

This typically takes 3-10 iterations, each requiring ~0.25 s of CPU time on a 2.4 GHz Pentium IV using the *Fast Absorption Predictor* model.

Upon convergence the retrieved state vector,$\hat{\mathbf{x}}$, is tested for statistical consistency with **y** and **R** by calculating the value:

$$\chi^2 = \left[H(\hat{\mathbf{x}}) - \mathbf{y}\right]^T \mathbf{R^{-1}} \left[H(\hat{\mathbf{x}}) - \mathbf{y}\right] \tag{4.30}$$

Retrievals with a $\chi^2 > 100$ were rejected. The choice of $\chi^2$ threshold was found not to be critical, as it had a small influence on the statistics of the retrievals.

## 4.7.7 EXAMPLE 1D-VAR RETRIEVALS

4.7.8 shows an example of 1D-VAR retrievals using synthetic observations, generated to be consistent with **R**. These are based on a real radiosonde profile for Camborne (UK) at 11:21 on 9/12/2004 and NWP background profile from a 5 hr forecast, valid 21 minutes earlier. This case was selected because the model had forecast the inversion ~200 m too low and overestimated the humidity by a factor of ~2 over the whole profile. The retrieval was repeated for 100 such sets of observations, all of which converged within 4 iterations on average. The retrieved profiles are closely clustered with typical standard deviations of 0.2-0.4 K in temperature and 0.05-0.10 in ln$q$, showing they are relatively robust in the presence of observation noise. In all cases, the retrieval thins the cloud and gives profiles closer to the truth than the background. However, the correlation between temperature at adjacent levels of **B** makes it impossible for the retrieval to move a misplaced feature in the vertical.

## 4.7.8 CLOUD CLASSIFICATION SCHEME

Examination of the performance of the retrieval scheme showed there were often problems when the humidity approaches the threshold of cloud formation – the residuals often oscillate without reaching convergence. This was partially improved by the implementation of the Levenberg-Marquardt method of minimization, which adjusts the size of the increment at each iteration to

### 5.1.2 IN-SITU AND REMOTE-SENSING SYSTEMS INVOLVED

During TUC, both active and passive ground-based remote sensing systems were deployed in Payerne. Table 5.1 describes the systems involved in the ex-

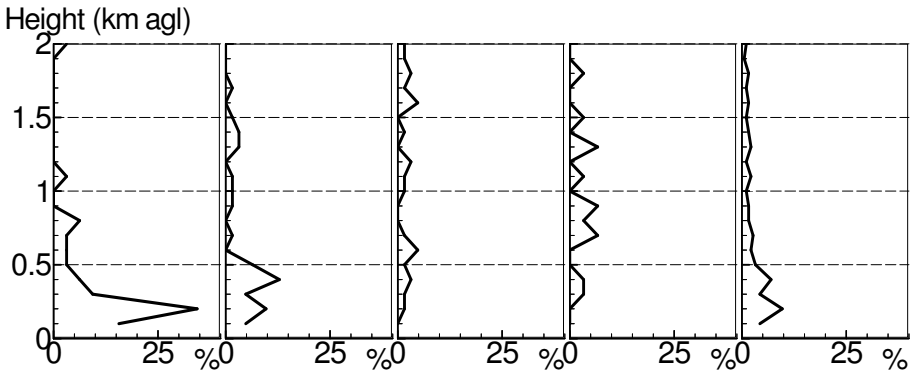


*Figure 5.2.* Percentage of cases, from radiosoundings data, with fog or stratus and temperature inversions stronger than 2K, as a function of height. From left to right: November 2003, December 2003, January 2004, February 2004, total TUC period.

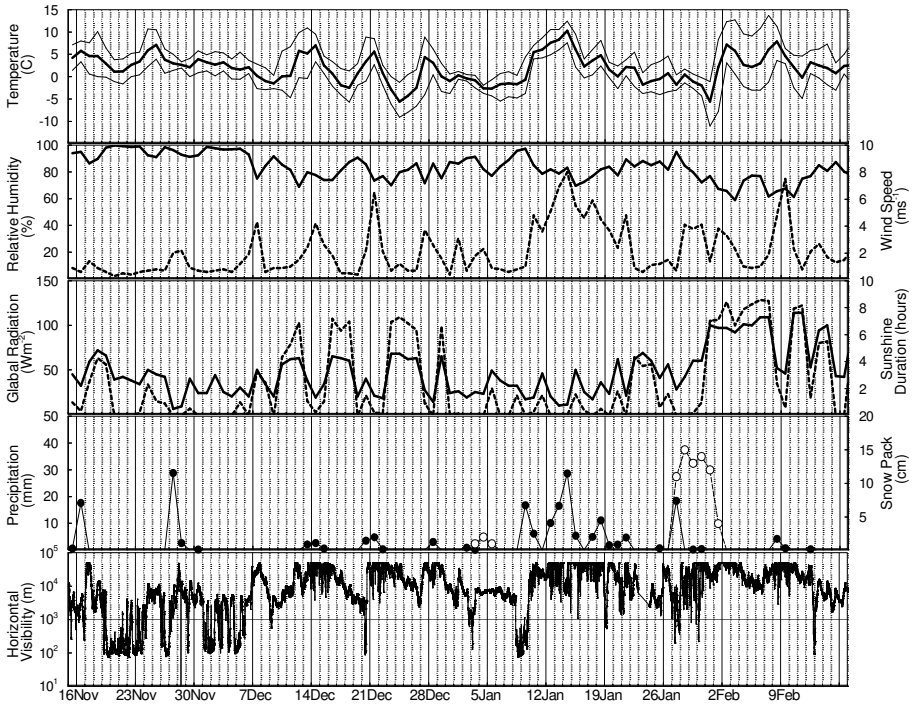


*Figure 5.3.* Time series of meteorological parameters measured at Payerne during TUC. From top, 2m temperature and standard deviation, relative humidity (solid line) and wind speed (dashed line), global radiation (solid line) and sunshine duration (dashed line), precipitations (solid line) and snow pack (dashed line with open circles), and horizontal visibility.

### 5.1.2 IN-SITU AND REMOTE-SENSING SYSTEMS INVOLVED

During TUC, both active and passive ground-based remote sensing systems were deployed in Payerne. Table 5.1 describes the systems involved in the ex-

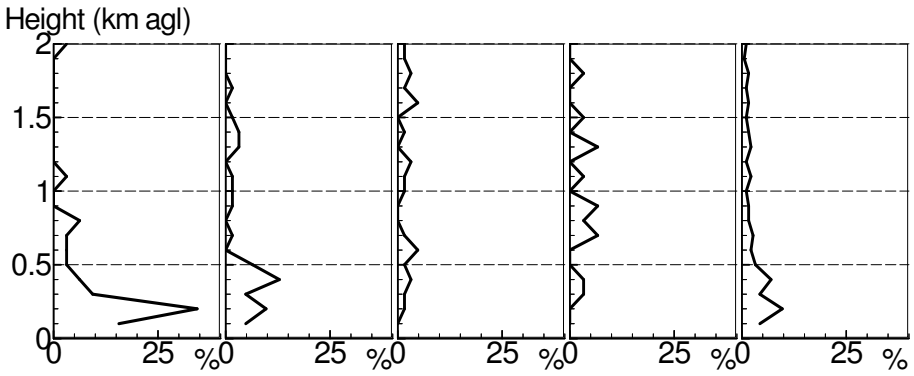


*Figure 5.2.* Percentage of cases, from radiosoundings data, with fog or stratus and temperature inversions stronger than 2K, as a function of height. From left to right: November 2003, December 2003, January 2004, February 2004, total TUC period.

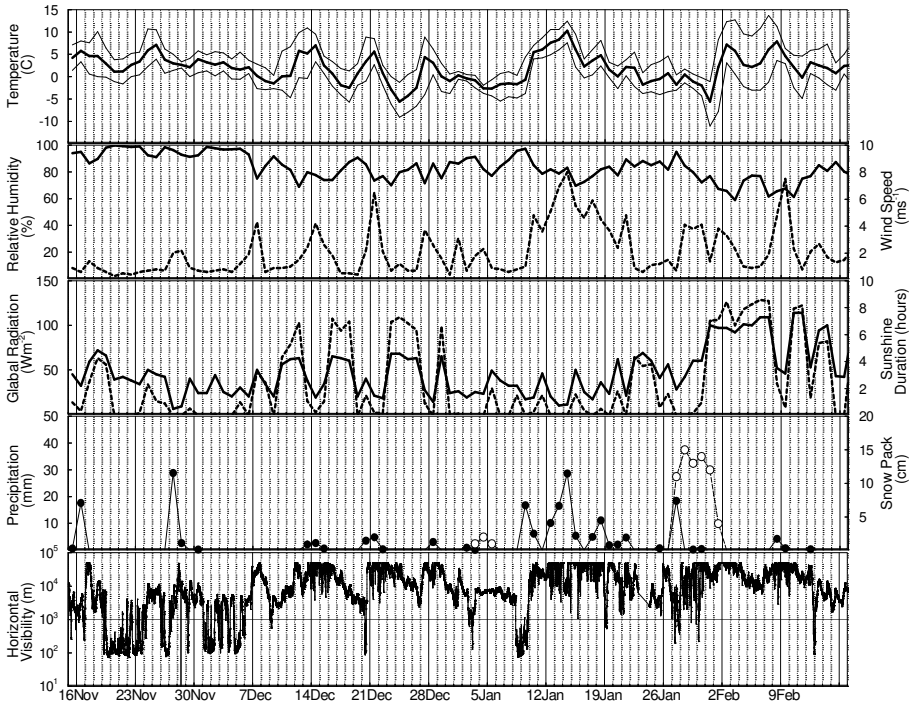


*Figure 5.3.* Time series of meteorological parameters measured at Payerne during TUC. From top, 2m temperature and standard deviation, relative humidity (solid line) and wind speed (dashed line), global radiation (solid line) and sunshine duration (dashed line), precipitations (solid line) and snow pack (dashed line with open circles), and horizontal visibility.

### 5.1.3 SUMMARY

During the TUC experiment, a significant amount of data were collected by various in-situ and ground-based remote sensing systems. A significant effort was made to produce a quality controlled dataset available for scientific studies related to winter conditions in central Europe.

A series of analyses have already been performed using the data from the TUC experiment (Ruffieux et al., 2006). The ASMUWARA microwave radiometer is presented in Martin et al. (2006a) and Martin et al. (2006b). Comparison of brightness temperature measured by the different microwave radiometers can be found in Cimini et al. (2006b), while retrieved profiles are analyzed in Cimini et al. (2006a). The validation of the absorption models used for calculating temperature and humidity profiles is presented in Hewison et al. (2006). GPS integrated water vapor time series are compared in Martin et al. (2006c). Methods of determining cloud characteristics using both satellite information and ground-based remote sensing techniques are described in Cermak et al. (2006). A comparison of various processing algorithms for wind profiler spectral data is presented in Gaffard et al. (2006). Finally, an integration method of wind profiler and microwave radiometer data to obtain improved humidity profiles can be found in Klaus et al. (2006).

The TUC experiment gave the opportunity for scientists from Europe and USA to work together on the same dataset but with different viewpoints. The complementarity between researchers and scientists responsible for operations was very interesting. Co-location of all systems at Payerne gave a good homogeneity to the dataset. However, data from some of the systems such as the wind profiler were occasionally contaminated, which sometimes made the data analysis and integration more difficult. Finally, a well-calibrated radiosounding system is mandatory, especially for humidity profiling, in order to obtain a valuable reference for comparisons and validation purposes. The planetary boundary layer was the centre of investigation of TUC; therefore a special attention needed to be put on the measurements close to surface. A tethered sounding system would be a good complement to the operational soundings performed on a routine basis only four times per day.

**Acknowledgements** The authors wish to acknowledge the valuable support from the Aerological station of Payerne, especially Mr. Heinz Berger and the radiosounding team.

## Bibliography

Cermak, J., M. Schneebeli, D. Nowak, L. Vuilleumier, and J. Bendix, 2006: Characterization of low clouds with satellite and ground-based remote sensing systems. Meteorol. Z., Vol 15, No. 1, 65-72.

Cimini, D., T. J. Hewison, L. Martin, J. Güldner, C. Gaffard, and F. S. Marzano, 2006a: Temperature and humidity profile retrievals from ground-based microwave radiometers during TUC. Meteorol. Z., Vol 15, No. 1, 45-56.

Cimini, D., T. J. Hewison, and L. Martin, 2006b: Comparison of brightness temperatures observed from ground-based microwave radiometers during TUC. Meteorol. Z., Vol 15, No. 1, 19-25.

Clothiaux E.E, T. P. Ackerman, G. G. Mace, K. P. Moran, R. T. Marchand, M. A. Miller and B. E. Martner, 2000: Objective Determination of Cloud Heights and Radar Reflectivities Using a Combination of Active Remote Sensors at the ARM CART Sites. J. Appl. Meteor., 39, 645–665.

Crewell S, H. Bloemink, A. Feijt, S. G. García, D. Jolivet, O. A. Krasnov, A. Van Lammeren, U. Löhnert, E. Van Meijgaard, J. Meywerk, M. Quante, K. Pfeilsticker, S. Schmidt, T. Scholl, C. Simmer, M. Schröder, T. Trautmann, V. Venema, M. Wendisch and U. Willén, 2004: The Baltex Bridge Campaign, an integrated approach for a better understanding of clouds. Bull. Amer. Meteor. Soc., 85, 1565-1584.

Dabberdt W.F., T.W. Schlatter, F.H. Carr, E.W.J. Friday, D. Jorgensen, S. Koch, M. Pirone, F.M. Ralph, J. Sun, P. Welsh, J.W.. Wilson, and X. Zou, 2005: Multifunctional mesoscale observing networks. Bull. Amer. Meteor. Soc., 86, 961-982.

Gaffard C., L. Bianco, V. Klaus, and M. Matabuena, 2006: Evaluation of moments calculated from wind profiler spectra: A comparison between five different processing techniques. Meteorol. Z., Vol 15, No. 1, 73-85.

Hewison T.J., C. Gaffard, D. Ruffieux, J. Nash, R. Nater, and B. Andrade, 2004: Monitoring Inversions from Ground-based Remote Sensing instruments during Temperature, Humidity, and Cloud profiling campaign (TUC). Proceedings of the $8^{th}$ Specialist Meeting on Microwave Radiometry and Remote Sensing Applications, 24-27 February, 2004, Roma, Italy, ISSN 1824-2383, 4pp.

Hewison T. J., D. Cimini, L. Martin, C. Gaffard, and J. Nash, 2006: Validating clear air absorption models using ground-based microwave radiometers and vice-versa. Meteorol. Z., Vol 15, No. 1, 27-36.

Klaus V., L. Bianco, C. Gaffard, M. Matabuena, and T. J. Hewison, 2006: Combining radar wind profiler and microwave radiometer for the estimation of atmospheric humidity profiles. Meteorol. Z., Vol 15, No. 1, 87-97.

Loehnert U, S. Crewell, and C. Simmer, 2004: An integrated approach toward retrieving physically consistent profiles of temperature, humidity, and cloud liquid water. J. Appl. Meteor., 43, 1295–1307.

Martin, L., M. Schneebeli, and C. Mätzler, 2006a: ASMUWARA, a ground-based radiometer system for tropospheric monitoring. Meteorol. Z., Vol 15, No. 1, 11-17.

Martin, L. and C. Mätzler, 2006b: Tropospheric water and temperature retrieval for ASMUWARA. Meteorol. Z., Vol 15, No. 1, 37-44.

Martin, L., C. Mätzler, T. J. Hewison, and D. Ruffieux, 2006c: Intercomparison of integrated water vapour measurements. Meteorol. Z., Vol 15, No. 1, 57-64.

Nash J., 2005: Review of progress in the development of operational upper air technology. WMO Technical Conference on Meteorological and Environmental Instruments and Methods of Observation (TECO-2005), Bucharest, Romania, 4-7 May 2005, 14pp.

Revercomb, H. E., D. C. Turner, D. D. Tobin, R. O. Knuteson, W. F. Feltz, J. Barnard, J. Bösenberg, D. Cook, R. Ferrare, J. Goldsmith, S. Gutman, R. Halthore, B. Lesht, J. Liljegren, H. Linné, S. Melfi, J. Michalsky, V. Morris, W. Porch, S. Richardson, B. Schmid, M. Splitt, T. Van Hove, E. Westwater, and D. Whiteman, 2003: The Atmospheric Radiation Measurement (ARM) Program's Water Vapor Intensive Operational Periods: Overview, Accomplishments, and Future Challenges. Bull. Amer. Meteor. Soc., 84, 217-236.

Richner H. (Editor) 1999: Grundlagen aerologischer Messungen speziell mittels der Schweizer Sonde SRS 400. Veröffentlichungen der SMA-MeteoSchweiz, 61, ISSN 1422-1381, 140pp.

Ruffieux D., J. Nash, P. Jeannet, and J.L. Agnew, 2006. The COST 720 temperature, humidity, and cloud profiling campaign : TUC. Meteorol. Z., Vol 15, No. 1, 5-10.

Ruffieux D., and J. Joss, 2003: Influence of radiation on the temperature sensor mounted on the Swiss radiosonde. J. Atmos. Oceanic Technol, 20, 1576-1582.

Turner D.D., B. M. Lesht, S. A. Clough, J. C. Liljegren, H. E. Revercomb and D. C. Tobin, 2003: Dry Bias and Variability in Vaisala RS80-H Radiosondes: The ARM Experience. J. Atmos. Oceanic Technol, 20, 117–132.

Voemel H., M. Fujiwara, M. Shiotani, F. Hasebe, S.J. Oltmans, J.E. Barnes, 2003: The Behavior of the Snow White Chilled-Mirror Hygrometer in Extremely Dry Conditions. J. Atmos. Oceanic Technol, 20, 1560–1567.

Wang J., D.J. Carlson, D.B. Parsons, T.F. Hock, D. Lauritsen, H. C. Cole, K. Beierle, and E. Chamberlain, 2003: Performance of operational radiosonde humidity sensors in direct comparison with a chilled mirror dew-point hygrometer and its climate implication. Geophys. Res. Letters, 30, doi:10.1029/2003GL016985.

# 5.2 LAUNCH-2005 - INTERNATIONAL LINDENBERG CAMPAIGN FOR ASSESSMENT OF HUMIDITY AND CLOUD PROFILING SYSTEMS AND ITS IMPACT ON HIGH-RESOLUTION MODELLING

Dirk A. M. Engelbart[1] and Edwin Haas[2]

[1] *German Met. Service DWD, Richard-Aßmann-Observat., Lindenberg, Germany*
✉ Dirk.Engelbart@dwd.de

[2] *Karlsruhe Research Center – Inst. for Meteorology & Climate Research, Garmisch-Partenkirchen, Germany*

## 5.2.1 INTRODUCTION

Within the frame of the European Research Action COST-720, "Integrated Ground-based Remote-Sensing Stations for Atmospheric Profiling", and in connection with the WMO GEWEX Working Group on Cloud and Aerosol Profiling "GEWEX CAP", the Richard-Aßmann-Observatory of the German Meteorological Service (DWD) at Lindenberg (Germany) organized the international campaign LAUNCH-2005 from 29th August to 31st October 2005. LAUNCH-2005 had been designed to accomplish four major scientific objectives:

(1) Assessment of new or improved profiling systems like water-vapor lidars, cloud-radar systems, various microwave profiler systems, a Doppler wind lidar, a new single-photon counting high-range ceilometer, and the re-designed FTIR spectrometer EISAR (see also section 3.4),

(2) assessment of various algorithms, combining different techniques for profiling of cloud parameters,

(3) provision of a data set, designed for validation and comparisons between measurements and NWP output, and

(4) provision of a data set for data assimilation experiments using high-resolution water-vapor profiling systems in regional NWP modelling.

In this section, special emphasis is put on the assessment of the fully autonomous new water-vapour Raman lidar at Lindenberg, Germany, which was used for the first time during LAUNCH-2005. With respect to the combination of profiling techniques in integrated algorithms, the so-called "*integrated profiling*", we will furthermore summarize the intercomparison of various algorithms for improved liquid-water content profiling, being a highly important variable for forecast-model validation demanded by the NWP community. Finally, a brief overview is given on Observation System Experiments (OSEs) using small networks of water-vapour lidars in 3D-VAR and 4D-VAR data assimilation schemes.

### 5.2.2 ASSESSMENT OF BASIC TECHNIQUES AND ALGORITHMS

Current remote-sensing techniques for atmospheric profiling have individual advantages but also deficits with respect to accuracy, resolution (time and height), all-weather capabilities, cost and/or maintenance. It is therefore important to assess new or improved techniques with regard to their capabilities and potential deficits. Therefore, several new profiling systems have been investigated during LAUNCH-2005. Apart from a number of profiling systems already mentioned in the introduction, the campaign here made particular use of various water-vapour lidars and microwave profiler systems, both during simultaneous measurements for independent validation purposes side by side, and by using these techniques in small networks.

*Figure 5.6.* The Raman lidar system RAMSES at the Richard-Aßmann Observatory of the DWD in Lindenberg, Germany

During LAUNCH-2005, e.g. the new, fully-autonomous water-vapour Raman-lidar system RAMSES of the German Meteorological Service at the Richard-Aßmann-Observatory Lindenberg, Germany, has proven its nighttime capabilities in a first campaign. Figure 5.6 shows the system, which is housed in a standard 20ft container. The external chillers and heat exchangers for air conditioning and laser cooling are installed in a shed attached to the container. The container's interior is divided into a temperature-stabilized instrument cabin and a room for the operators. In the instrument cabin, the optical bench with the laser and the transmitter optics, the thermally insulated telescope hall, and the optical bench with the lidar receivers are mounted on a solid three-leg structure to avoid vibrations of the measurement system. The telescope hall is covered with an autonomously-operating hatch which, inde-

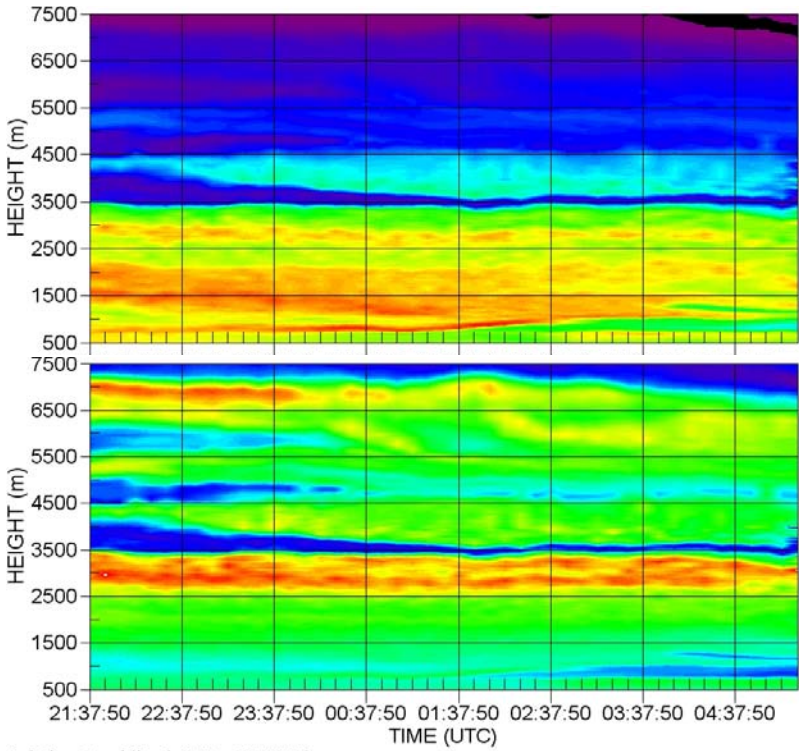


*Figure 5.7.* Time series of mixing ratio (0 –6 g/kg, top) and relative humidity (0 – 85%, bottom) observed over Lindenberg, Germany, in the night of 30–31 October 2005. The time resolution is 10 minutes, the height resolution ranges from 67.5 m to 307.5 m.

pendently of the system control computer, terminates lidar operation and seals the container in case of precipitation or unacceptably high levels of sunlight. This approach ensures that the lidar is protected from adverse ambient conditions even if the computerized system control fails.

| **Receiver** | **near field** | | | **far field** | | |
|---|---|---|---|---|---|---|
| **Channel wavelength** | 354.7nm | 386.5nm | 407.5nm | 354.7nm | 386.5nm | 407.5nm |
| Dichroic beamsplitter **1 reflectivity** | 1.6% | 0.7% | >99% | 1.6% | 0.7% | >99% |
| Dichroic beamsplitter **2 reflectivity** | 0.3% | >99% | – | 0.3% | >99% | – |
| Interference filter **bandwidth** (FWHM) | 1.95 nm | 2.08 nm | 1.78 nm | 1.98 nm | 2.08 nm | 1.74 nm |
| Interference filter **transmission** | 58% | 78% | 84% | 60% | 86% | 88% |

*Table 5.2. RAMSES* beamsplitters and filters.

Figure 5.7 gives a measurement example from LAUNCH-2005, with system-generated time-height cross sections of atmospheric humidity from sunset to sunrise on 30–31 October 2005 as observed with *RAMSES*. During LAUNCH-2005 it turned out that the new lidar system is capable to provide automatically and reliably atmospheric humidity profiles of reference quality for validation of other systems, e.g. ground-based passive sensors or satellite sensors.

Apart from the assessment of the water-vapour Raman lidar, also intercomparisons of a Doppler wind lidar of the Institute for tropospheric research (IfT), Leipzig versus an 482 MHz wind profiler of the German Meteorological Service (DWD) was conducted. Summarizing this intercomparison, both systems agreed, expressed by their bias to within 0.2 m/s and 5 deg at the campaign.

Another objective with respect to basic techniques referred to an improved microwave profiling. The emphasis here was laid on a direct side-by-side intercomparison of two identical microwave profilers (MWP) of the same type at Lindenberg and on a long-term test of the regression-based retrieval algorithm for water-vapour and temperature profiling developed at Lindenberg Observatory prior to the campaign. As a result of these microwave-related objectives, the data from LAUNCH-2005 helped to clarify in which range of accuracy brightness temperatures from MWP can be interpreted and which differences are caused by statistical, hardware-related inaccuracies. A special report summarizing the results of this direct intercomparison is currently under preparation, while results of the regression-based retrieval technique can be found in the microwave section of this report (section 3.2.10). While microwave

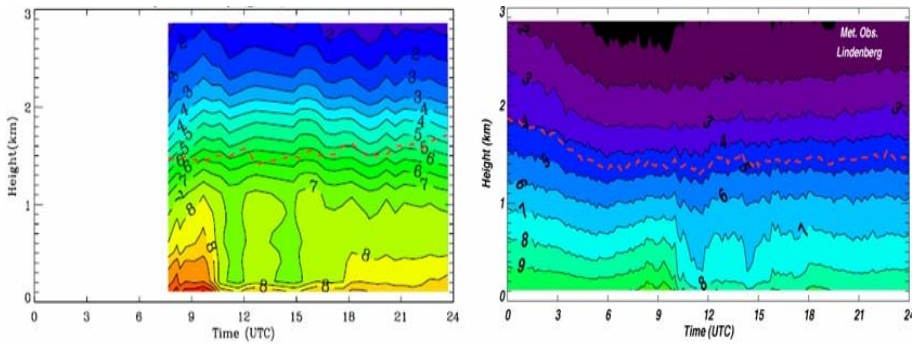


*Figure 5.8.* Time-height cross sections of water-vapour density for FTIR (left) and MWP (right) data from 22 Sep, 2005 at Lindenberg Observatory. Color shading has been defined similarly. The dashed red line defines the column content of integrated water vapour

profiler systems (MWP) are qualified to all-weather conditions (with the only exception of strong rain events), optically-sensing Fourier-transform infrared spectrometers (FTIR) may have advantages in vertical resolution over MWP systems due to their considerably higher spectral resolution. First investigations on intercomparing both passive remote-sensing systems have also been

performed during LAUNCH-2005. An impression on the performance of FTIR systems is given in figure 5.8. It shows a time-height cross section of the water-vapour density at 22nd September 2005, where color scaling for both systems has been defined similarly.

A final example for investigations on basic techniques refers to an intercomparison of high-range ceilometers, where an analog-detection system (VAISALA LD-40) and an single-photon-counting system (JENOPTIK CHM-15k) have been compared with respect to their capabilities in cirrus detection, depending on the optical depth of the respective cirrus clouds. During the intercomparison, a "*real*" lidar system (DWD-RAMSES, see above) has served as a reference for the presence of clouds using the elastic backscatter signal of the frequency-tripled ND:YAG laser of the RAMSES system. It turned out that the single-photon-counting JENOPTIK system is reliably able to continuously monitor cirrus clouds down to optical depths (OD) of less than 0.03, while the analog-detecting VALSALA system was only capable of detecting thick cirrus clouds of $OD > 0.45$ (see also figure 5.9).

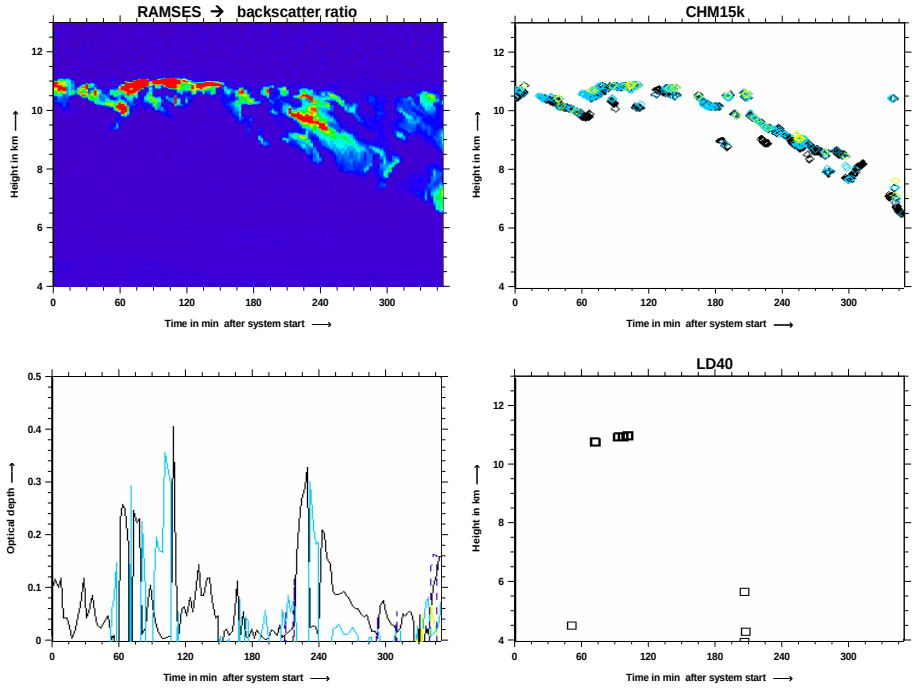


*Figure 5.9.* Detectability of cirrus clouds using ceilometers: (top-left) Time-height cross section of the lidar backscatter signal using the DWD RAMSES system at Lindenberg for the supply of a cloud reference. (bottom-left) Optical depth of cirrus layers; each layer is represented by different colors. (top-right) Cirrus clouds as detected by the JENOPTIK CHM15k. (bottom-right) Cirrus clouds as detected by the VAILSALA LD40.

### 5.2.3 ASSESSMENT OF ALGORITHMS FOR INTEGRATED PROFILING

Vertical profiling with improved resolution or data quality may be realised by using combinations of single (basic) profiling techniques like e.g. microwave profilers, cloud radars, or lidar systems. During LAUNCH-2005, special attention in this field was focussed to profiles of the liquid-water content (LWC) of thin water clouds by intercomparison and evaluation of methods using a standalone microwave profiler together with an infrared pyrometer, a combination of microwave profiler and ceilometer, an adiabatic approach proposed by Boers et al. (2000), a dual-system retrieval using a combination of cloud radar and lidar according to Krasnov and Russchenberg (2006), and the so-called "*integrated profiling technique*" (IPT) according to Löhnert et al. (2004). It resulted, that both cloud radar - lidar and the IPT perform best, in particular when looking at the standard deviation (STD) of the LWC (see table 5.3). According to evaluations from LAUNCH-2005, the STD for this micro-

*Table 5.3.* Results from an intercomparison of the liquid water path in thin water clouds using various instruments and retrieval techniques: The table shows mean values (Mean) and standard deviations (STD) for (a) Microwave profiler (MWP), (b) Microwave profiler plus ceilometer (MWP-Cei), (c) Adiabatic method, (d) Radar-Lidar retrieval, and (e) Integrated Profiling Technique (IPT)

| | MWP | MWP-Cei | Adiabat. | Radar-Lidar | IPT |
|---|---|---|---|---|---|
| Mean, g/m$^2$ | 9.0 | 11.9 | 58.0 | 4.6 | 15.3 |
| STD, g/m$^2$ | 15.34 | 23.82 | 19.31 | 5.57 | 7.36 |

physical cloud parameter shows a range of about 50-70% of the mean when the IPT algorithm or the retrieval for combination of cloud radar and lidar (ceilometer) is applied. However, as there is no absolut reference yet for real LWC data, it remains still unclear which of the two methods will supply more realistic results, although arguments may perhaps vote for the IPT as measurement infomation and physical base is highest at the IPT technique, which not only combines radar and lidar but additionally data e.g. from radiosonde and microwave radiometer.

A different investigation for integrated profiling during LAUNCH-2005 was dedicated e.g. to an improved rain-rate profiling: The experimental setup during the campaign for this objective comprised of a cheap x-band radar for rain detection combined by several micro rain radars, chained up in a line in order to assess stationarity of drop size distributions (DSD) in space and time. Figure 5.10 shows the complete data set of all rain situations during LAUNCH-2005 ($> 30h$ of rain), viewed in terms of reflectivity $Z$ versus rain rate $R$. The averaged $Z-R$ relation for the full data set was then $Z = 200 \cdot R^{1.6}$. When MRR drop size distribution data are now used to make a distinction into droplet modes according to size classes, and a recalculation of $Z-R$ relations for each

mode is performed it resulted that a considerable improvement of measured rain rates can be reached. From the example figure an easy distinction into

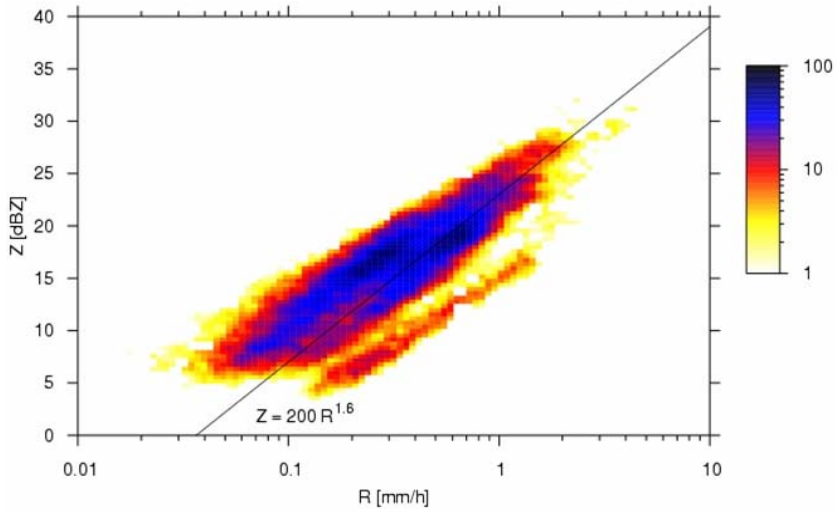


*Figure 5.10.* Summary of rain events (30 hours) during LAUNCH-2005 showing radar reflectivity $Z$ versus rain rate $R$ from evaluation of x-band radar and MRR: Distinction of modes according to classes of drop sizes may improve rain rate detection when $Z-R$ relations are determined in real-time from integrated profiling using x-band radar and MRR. The figure clearly shows a bi-modal distribution where smalller droplets are represented in the lower right part

situations with large droplets (8 hours data) and those with small droplets (2 hours data) at the lower right part of the $Z-R$ display can be seen. Already from regression by eye of these two distributions it becomes obvious, that a considerable improvement in the resulting $Z-R$ relations will follow. Hence, the combination of x-band radar together with MRR for DSD detection can amend the remote measurement of rain rates considerably.

### 5.2.4 OBSERVATION SYSTEM EXPERIMENTS (OSES) USING NETWORKS OF WATER-VAPOUR LIDARS

In order to get a picture of what a small network of stationary, short-period but high-quality, and high time-resolution profiling systems is capable to provide to NWP, two NWP modeling groups made first Observation System Experiments (OSEs) with LAUNCH-2005 data. First and preliminary investigations show, that a positive impact on the NWP model output has resulted. The results from comparisons of vertical humidity profiles with or without lidar data assimilation imply that a considerable improvement in model output is achieved (see also section 6.3 or section 6.2). However, more detailed studies of LAUNCH-2005 data have still to be done in order to confirm and generalize this preliminary result.

### 5.2.5 MODEL VALIDATION USING HIGH-PRECISION REMOTE SENSING

High-precision ground-based remote-sensing systems like windprofiler radars, cloud radars, or lidars may beneficially act as a good reference for comparison and validation or verification of NWP model output. During LAUNCH-2005 this has been realized with an emphasis on water vapour and cloud information from the operational mesoscale NWP model "*LM*" of the German Meteorological Service DWD. A qualitative example for this comparison between measurement and model is given in figure 5.11. With the above

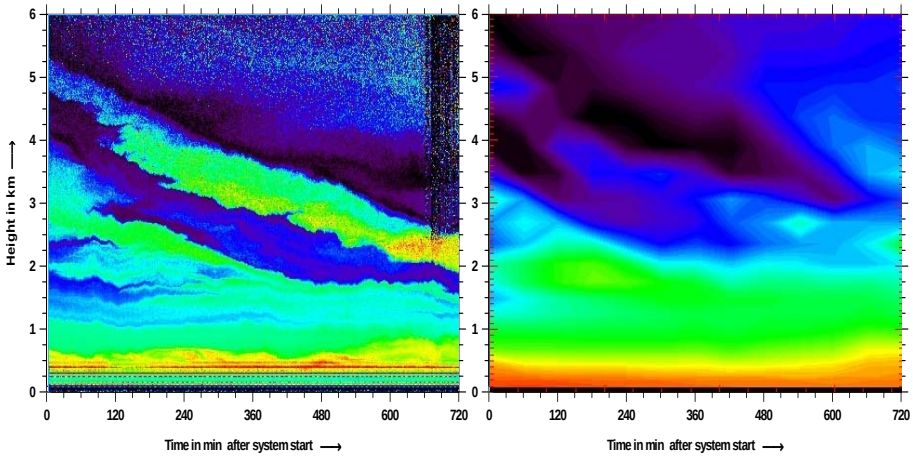


*Figure 5.11.* Time-height cross section of the water-vapour mixing ratio over Lindenberg for Oct 14/15, 2005. The measurement was started at sunset on Oct. 14th. The left figure shows reference data from the RAMSES lidar, while the right figure represents NWP forecast data from 14th October 2005, 12 UT

figures it can be made strikingly obvious whether the NWP model output still shows deficits or not. In the example, the 00 UT forecast was quite precise with respect to water vapour; however, strong deficits on a number of different situations not shown here demonstrate that NWP still exhibits problems with the operationally correct description of the water-vapour field in the atmosphere. High-precision water-vapour lidar systems with typical resolutions of up to 7.5m in the vertical and 30s in time can here contribute to improved NWP parametrization and forecasting when these systems are operated continuously at one or several reference locations as a means for steady model validation. With LAUNCH-2005, and for the operational models of the DWD, the RAMSES lidar system at Lindenberg was tested to act as a long-term reference in this respect and quasi-operational NWP model validation for the reference site at Lindenberg Observatory has continued to be active since then.

### 5.2.6 EVALUATION OF A NEW MOISTURE ADVECTION AND TIME INTEGRATION SCHEME IN MM5

The fifth-generation Penn State / NCAR Mesoscale Model MM5 was developed as a non-hydrostatic model in the early nineties, based on the hydrostatic model MM4. The development team was formulating the model equations in such a way that they could re-use as much of the numerics of MM4 as possible. Due to this, the governing equations are numerically integrated using the leapfrog-scheme, which was quite popular and widely used in the eighties due to its second-order accuracy. To overcome some disadvantages of the leapfrog scheme, like the introduction of artificial non-physical waves in the numerical solutions, an Asselin time filter is applied to avoid splitting of the numerical solution and to suppress the generation of oscillations. The new filtered quantity $Q$ at the time level $t$ is according to Grell et al. (1994) computed by a convex combination of the non-filtered quantities $q$ at the three time levels $t-1$, $t$ and $t+1$ by

$$Q^t = (1-\nu)q^t + \nu(q^{t+1} + q^{t-1}) \tag{5.1}$$

In MM5, the filter coefficient $\nu$ is set to 0.1 for all. The time filter smoothes the numerical solution.

**5.2.6.1 Problem addressed by LAUNCH.** Within the Institute of Meteorology and Climate Research, the MM5 model is used for a variety of applications, like real-time regional weather prediction, simulation of meteorological input data for air quality studies, long-term regional climate simulations and others. Using four-dimensional data assimilation techniques to feed data into the MM5, and comparing the resulting distributions of water vapour with the data obtained by radiosondes, one can observe in most cases a clear trend that MM5 predicts too much moisture in the upper regions above the planetary boundary layer. Comparing simulations with different parameterisations for the boundary layer in MM5, this effect is present for all parameterisations. One hypothesis is that the numerical integration scheme combined with the Asselin time filter is responsible for this effect.

**5.2.6.2 Solution.** To address this problem, a new time integration scheme for the moisture conservation equations was developed and integrated in MM5 V3.6. The explicit scheme is based on three time levels $t-1$, $t$ and $t+1$ to guaranty consistency with the MM5 moisture physics. Advection is treated with a new scheme based on the convex combination of the upstream- and the centered-difference scheme

$$q^{t+1} = \alpha \cdot \text{ upstream } + (1-\alpha) \cdot \text{ centered difference} \tag{5.2}$$

The weighting coefficient $\alpha$ determines the influence of the strongly diffusive, but monotone and positive definite upstream advection scheme with respect the

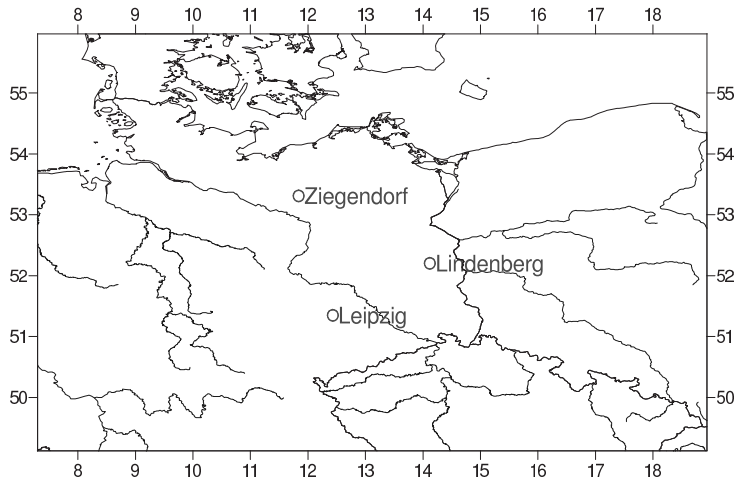


*Figure 5.12.* Domain D2 with the locations of the observation sites; horizontal grid resolution: 6 km

non-diffusive, but neither monotone- nor positive-definite centered-difference advection scheme. Parameter $\alpha$ can either be set to a fixed value or adaptively determined depending on local gradients of the advected quantity. Using this formulation for the numerical treatment of the advection problem, one obtains an advection scheme with only little diffusion which can suppress the evolution of non-physical waves and oscillations in the numerical solution. The resulting scheme is much less complex than the popular MPDATA-scheme of Smolarkiewicz and Margolin (1998) or the advection schemes of Bott (1989).

**5.2.6.3 Results of validations using LAUNCH-2005 data.** In the following subsection, preliminary results of an evaluation study of the new time-integration and advection scheme for the moisture conservation equation and an inter-comparison with temporal and spatial high-resolution lidar observations are presented. In addition to that, a journal publication with a detailed discussion of the results is in preparation.

The episode under investigation consists of a nested simulation of two domains with 18 and 6 km grid resolution. A one degree FNL analysis is combined with radiosonde data for the simulation in the coarse domain D1. The simulation for domain D2 is nested into the domain D1 and starts 12 hours after the simulation for D1. The simulation for the high-resolution domain D2 starts at October 26$^{th}$ at 12:00 UTC and lasts 24 hours. 3D output is available every 10 minutes. The domain D2 and the location of the observation sites is shown in figure 5.12. Observations for the inter-comparison are available for the lidar sites at Lindenberg, Leipzig, and Ziegendorf (all in Germany), supplied by DWD Lindenberg, see table 5.4.

| *Site* | *System* | *Vertical resolution [meter]* | *Observation time [UTC]* | *Data resolution [minutes]* |
|---|---|---|---|---|
| Lindenberg | Raman-Lidar | 67.5, 127.5, 307.5 (800 - 10000m) | 26/10/05 19:26 27/10/05 4:00 | 10 |
| Leipzig | Raman-Lidar | 180, 300, 600 (210 - 10000m) | 26/10/05 17:45 27/10/05 5:15 | 30 |
| Ziegendorf | Raman-Lidar | 180, 300, 600 (210 - 10000m) | 26/10/05 18:18 27/10/05 5:16 | 30 |

*Table 5.4.* Data of the observation sites for inter-comparison

As the data for the inter-comparison between lidar profiles and simulations are not defined on a common grid, the data had to be interpolated onto a common grid in height and time for the three different validation sites. As the lidar data for the sites Leipzig and Ziegendorf is defined on a much coarser spatial and temporal resolution, the resulting common grid is defined for this coarse resolution. To evaluate differences between simulated and the lidar-observed water-vapour distributions, differences between the results of the original MM5 and the lidar observations were evaluated on this coarse inter-comparison grid.

For the investigation, MM5 simulations were realized using version 3.6 with the following model configuration:

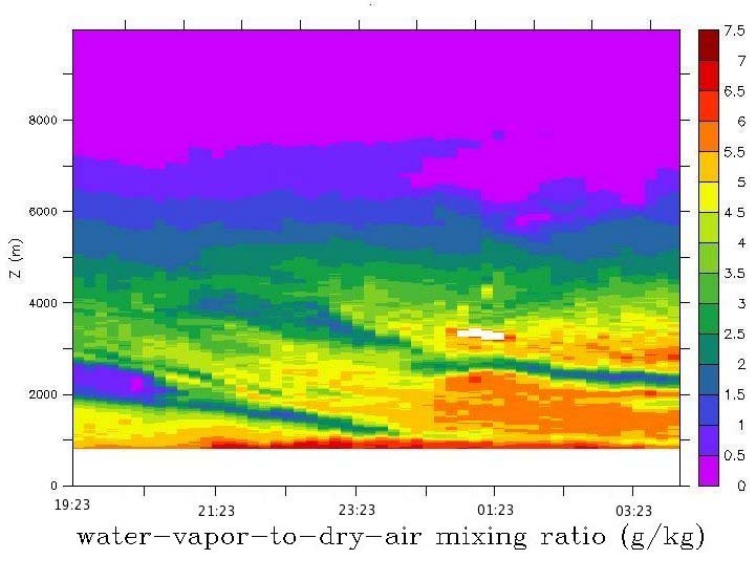


*Figure 5.13.* Raman-Lidar site Lindenberg: Water-vapour mixing ratio (g/kg), 26/10/05, 19:26 to 27/10/05, 04:00 (UTC)

- Reisner mixed-phase explicit moisture scheme
- Grell cumulus parameterisation
- Simple soil model

A sensitivity study was carried out to determine the effect of the different parameterisations for the planetary boundary-layer physics on the simulated water-vapour distribution. As a result, the effects of the different boundary-layer parameterisations are much smaller than the differences caused by the new time integration and advection scheme. Therefore, all simulations finally used the MM5-Eta-M-Y boundary-layer parameterisation, which has proved to be suitable for central European domains within many studies such as e.g. DEKLIM (www.deklim.de) or BerliOZ (Berlin Ozone Experiment).

The figures 5.13 and 5.14 for the site Lindenberg show the Lidar observations and the corresponding MM5 simulation. Differences between the simulations with the original MM5 and the modified MM5 are presented in figure 5.15 and figure 5.16 shows the difference between the MM5 simulation and the Lindenberg lidar observations. The corresponding results for the site Leipzig are presented in figures 5.17 to 5.20 and for the site Ziegendorf in figures 5.21 to 5.24.

**5.2.6.4 Discussion of the preliminary results.** The inter-comparison of the simulations of the original MM5 with the corresponding ones with

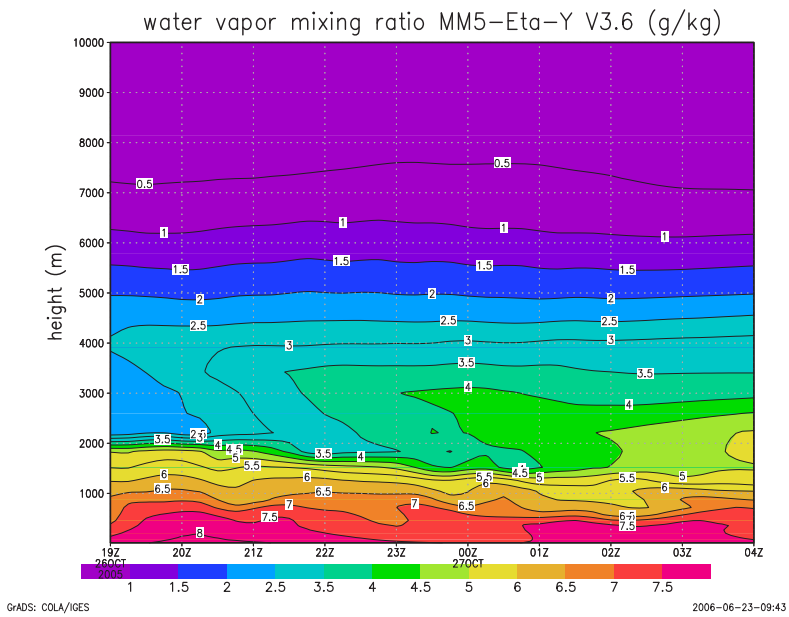


*Figure 5.14.* MM5 Simulation: Vertical profile water-vapour mixing ratio (g/kg) at observation site Lindenberg, 26/10/05, 19:15 to 27/10/05, 04:00 (UTC)

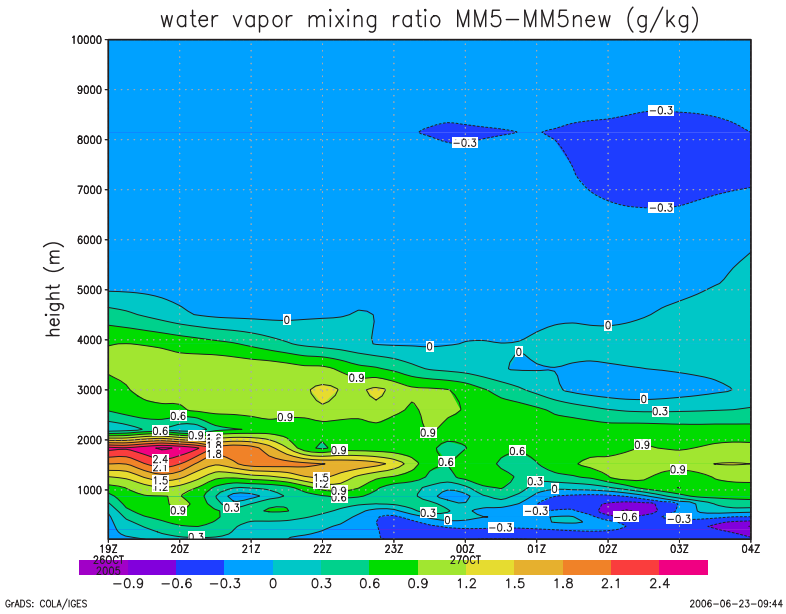


*Figure 5.15.* Differences in MM5 Simulations: Original MM5 minus modified MM5: Vertical profile water-vapour mixing ratio (g/kg) at site Lindenberg, 26/10/05, 19:15 to 27/10/05, 04:00 (UTC)

the modified MM5-numerics approved the hypothesis that the MM5 leapfrog scheme is largely responsible for the differences in the three-dimensional distribution of water vapour. The simulations with the modified numerical schemes result in more water vapour within the boundary layer but less in the region above it. Here, the original MM5 in general over-predicts the water-vapour content.

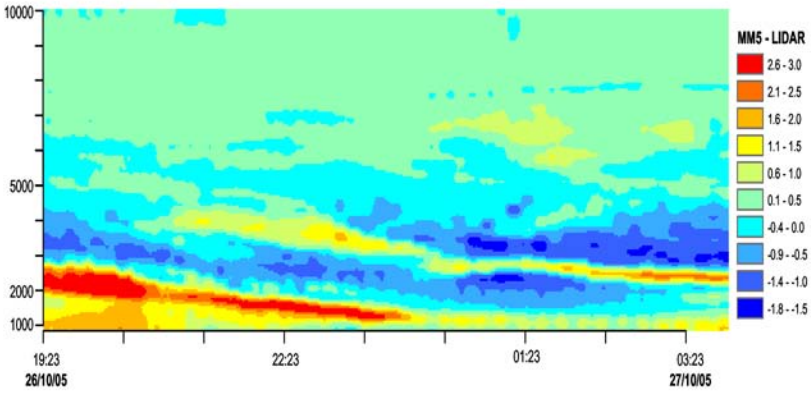


*Figure 5.16.* Difference between MM5 Simulation and Lidar Observation: Vertical profile water-vapour mixing ratio (g/kg) at site Lindenberg, 26/10/05, 19:15 to 27/10/05, 04:00 (UTC)

For the Lindenberg site, the positive difference between results of the simu-

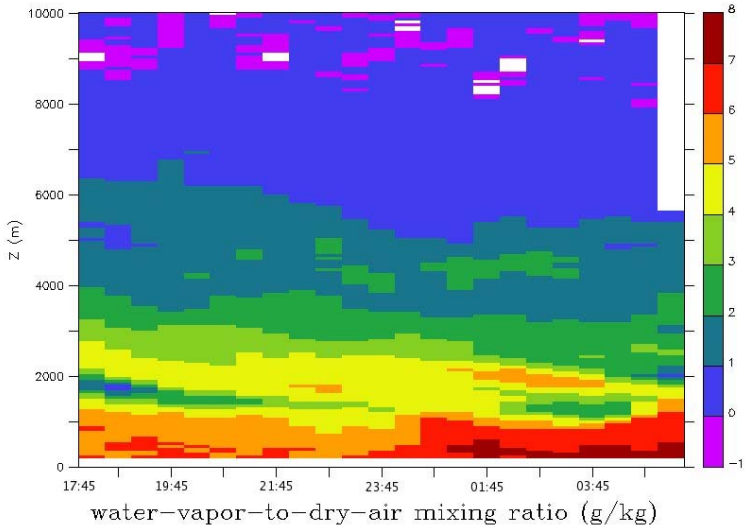


*Figure 5.17.* Raman-Lidar site Leipzig: Water-vapour mixing ratio (g/kg), 26/10/05 17:45 to 27/10/05 5:15 (UTC)

lation and observational data (see figure 5.16) for the first hours in the lower region (0 to 3000 m) corresponds to a positive difference in the model inter-comparison (difference between simulations with original MM5 and the modified MM5) in figure 5.15 for the same spatial and temporal position. This effect can be observed later as a negative difference in the simulation – observation inter-comparison as well as in the corresponding model – model inter-comparison.

The same effects and correlations can be observed for the sites Leipzig (see figures 5.20 and 5.19) and Ziegendorf (see figures 5.23 and 5.24) as well.

Generally, the assumption, that the modified MM5 yields more accurate distributions of water vapour than the original MM5 has to be confirmed with respect to precipitation effects by subsequent studies and inter-comparisons with precipitation observations. This LAUNCH-2005 study will also have be extended to further simulations with grid resolutions of 2 km in order to obtain small-scale simulation results for the inter-comparison. Additionally, an inter-comparison of the simulation results with radiosonde data might further approve the conclusions of this study. Nevertheless, the study clearly outlines the importance and usefulness of high-quality ground-based remote-sensing data for the validation of new and/or improved numerical model simulations.

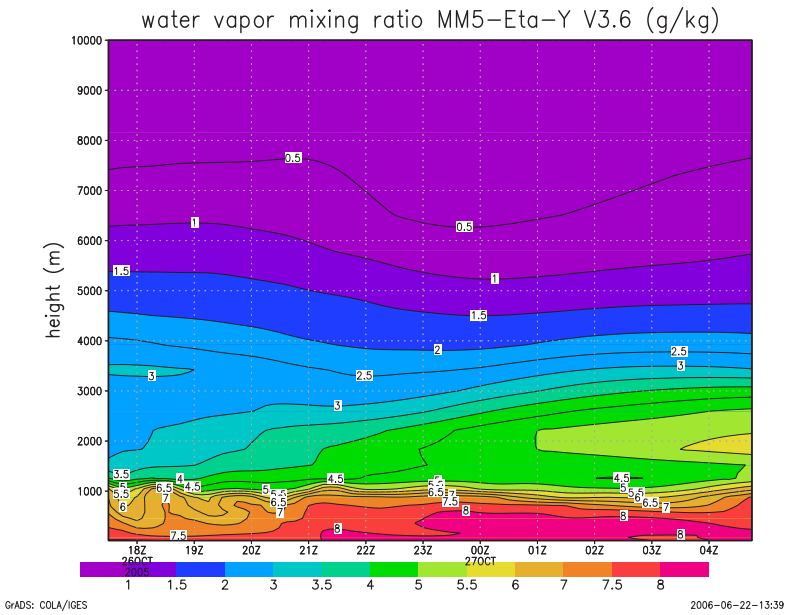


*Figure 5.18.* MM5 Simulation: Vertical profile water-vapour mixing ratio (g/kg) at observation site Leipzig, 26/10/05 17:45 to 27/10/05 5:15 (UTC)

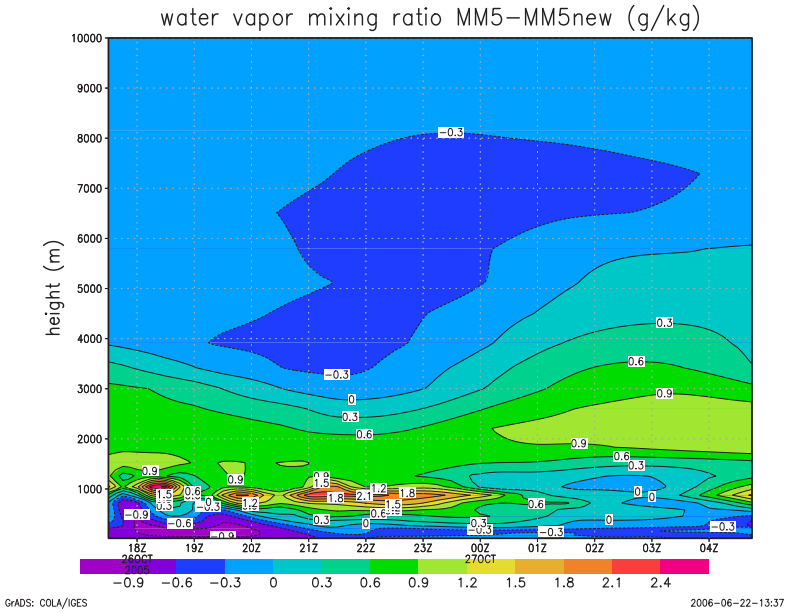


*Figure 5.19.* Difference in MM5 Simulations: Original MM5 minus modified MM5: Vertical profile water-vapour mixing ratio (g/kg) at site Leipzig, 26/10/05 17:45 to 27/10/05 5:15 (UTC)

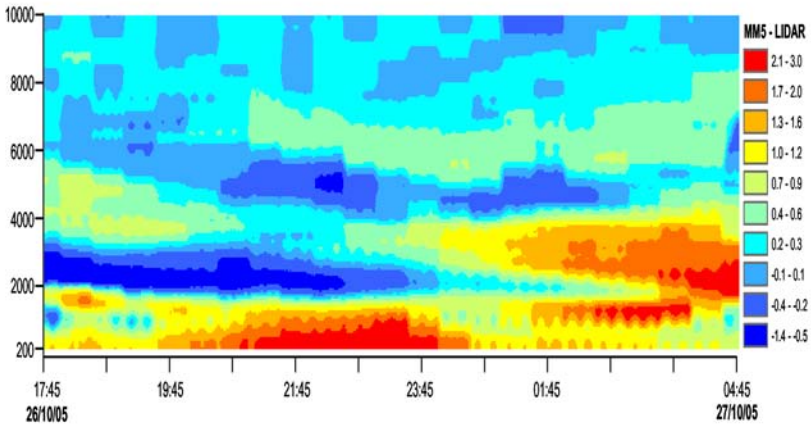


*Figure 5.20.* Difference between MM5 Simulation and Lidar Observation: Vertical profile water-vapour mixing ratio (g/kg) at site Leipzig, 26/10/05 17:45 to 27/10/05 5:15 (UTC)

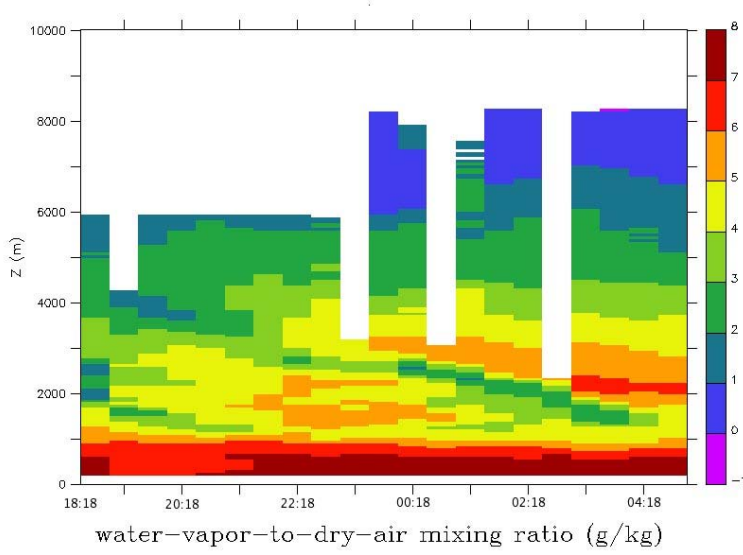


*Figure 5.21.* Raman-Lidar site Ziegendorf: Water-vapour mixing ratio (g/kg), 26/10/05 18:18 to 27/10/05 5:16 (UTC)

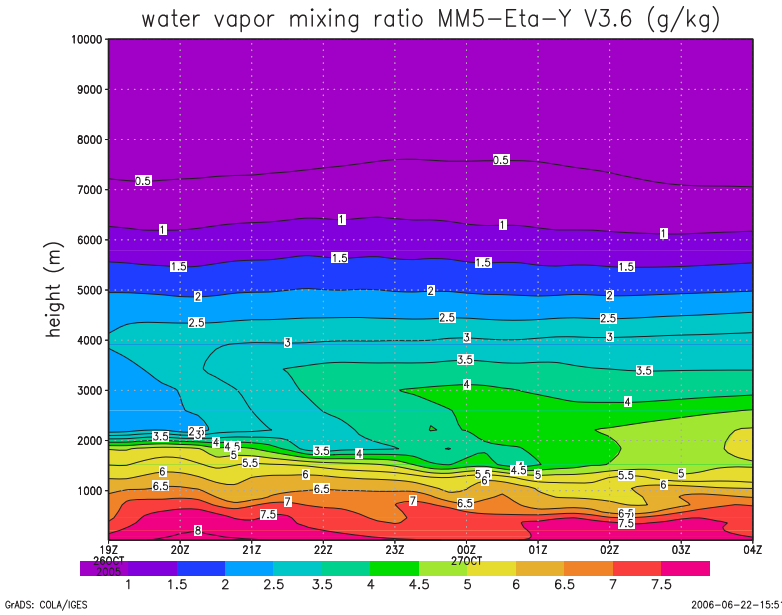


*Figure 5.22.* MM5 Simulation: Vertical profile water-vapour mixing ratio (g/kg) at observation site Ziegendorf, 26/10/05 18:18 to 27/10/05 5:16 (UTC)

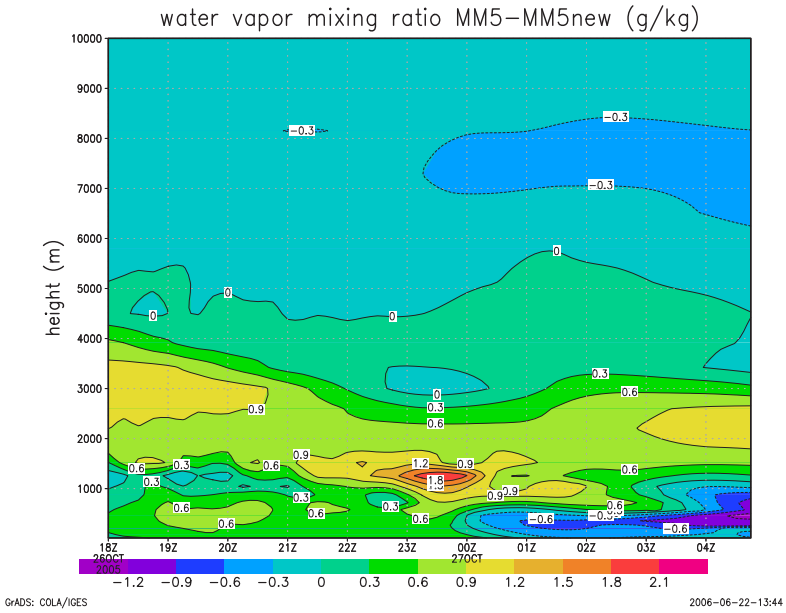


*Figure 5.23.* Difference in MM5 Simulations: Original MM5 minus modified MM5: Vertical profile water-vapour mixing ratio (g/kg) at site Ziegendorf, 26/10/05 18:18 to 27/10/05 5:16 (UTC)

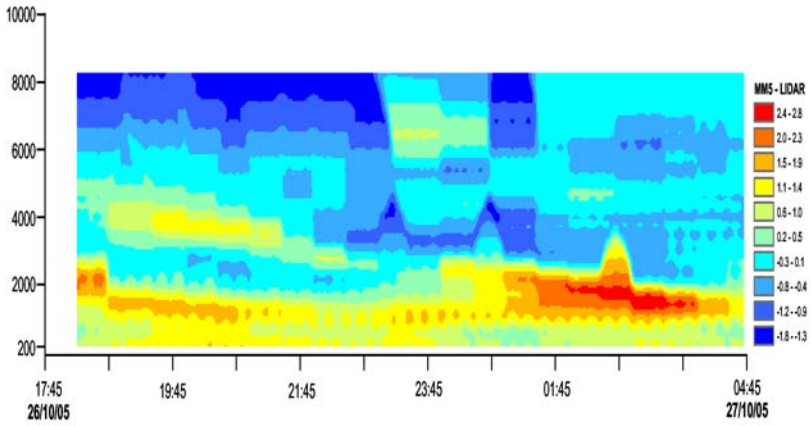


*Figure 5.24.* Difference between MM5 Simulation and Lidar Observation: Vertical profile water-vapour mixing ratio (g/kg) at site Ziegendorf, 26/10/05 18:18 to 27/10/05 5:16 (UTC)

## Bibliography

Grell, G., J. Dudhia, and D. Stauffer, 1994: A Description of the Fifth-Generation Penn State/NCAR Mesoscale Model (MM5). *Techn. Rep.*, NCAR Technical Note NCAR/TN-398.

Boers, R., H. Russchenberg, J. Erkelens, V. Venema, A. van Lammeren, A. Apituley, and S. Jongen, 2000: Ground-Based Remote Sensing of Stratocumulus Properties during CLARA, 1996. *J. Appl. Meteor.*, **39**, 169–181.

Krasnov, O. A. and H. W. J. Russchenberg, 2006: A synergetic Radar-Lidar technique for the LWC retrieval in water clouds. *ISTP - 7th International Symposium on Tropospheric Profiling: Needs and Technologies*, 11–17 June 2006, NCAR, Boulder(CO), USA, pp. 1–16.

Löhnert, U., S. Crewell, and C. Simmer, 2004: An integrated approach towards retrieving physically consistent profiles of temperature, humidity, and cloud liquid water. *J. Appl. Meteor.*, **43**, 1295–1307.

Smolarkiewicz, P. and L. Margolin, 1998: MPDATA: A finite-difference solver for geophysical flows. *Journ. Computat. Phys.*, **140** (2), 459–480.

Bott, A., 1989: A positive definite advection scheme obtained by non-linear renormalization of the advective fluxes. *Month.Wea.Rev.*, **117**, 1006–1015.

## 5.3 THE CONVECTIVE STORM INITIATION PROJECT (CSIP)

Judith Agnew

*CCLRC Rutherford Appleton Laboratory, UK*
J.L.Agnew@rl.ac.uk

Although current NWP models have skill in forecasting the regional location of convective rainfall, they are unable to predict the precise timing and location of convective initiation. The *Convective Storm Initiation Project* (CSIP) was designed to understand precisely, where and how convective clouds form and develop into showers. Forecasting of convective precipitation is important because of the potential risks to people and property. The experimental period of the campaign occurred in two phases: A pilot study in July 2004 and the main measurement period June to August 2005. As is common with such long-duration field campaigns, weather forecasts were used to identify days of particular interest. These were then declared as Intensive Operation Periods (IOPs). The project was a collaboration between groups within several UK

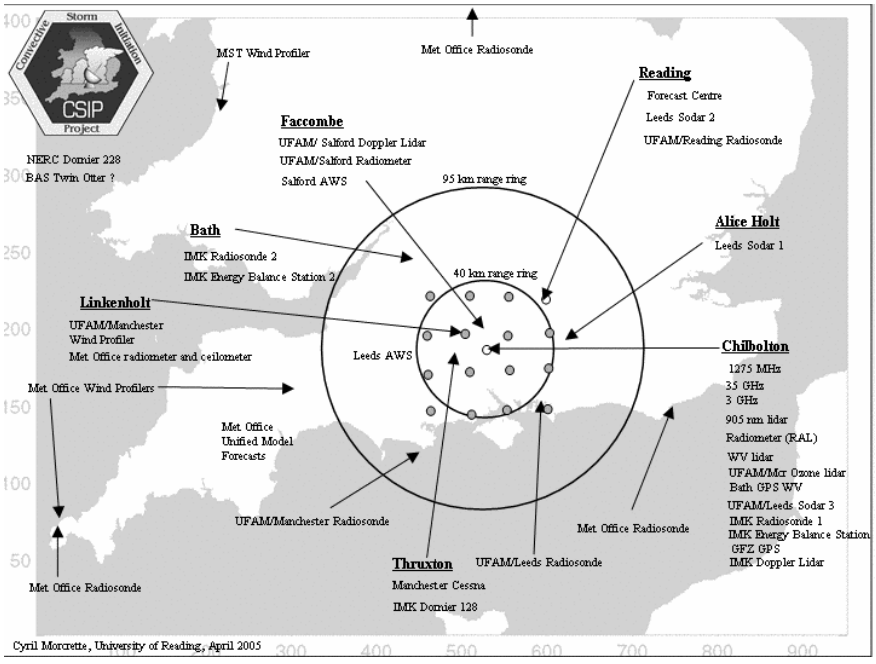


*Figure 5.25.* Locations of instruments during the CSIP campaign

universities (Aberystwyth, Bath, Leeds, Manchester, Reading, and Salford), the Met Office (UK), and the CCLRC Chilbolton Observatory, the "Institut für Meteorologie und Klimaforschung" (IMK, Germany), and finally the "Geoforschungszentrum Potsdam". The information obtained by the project will be used in a variety of studies on different aspects of convective initiation, including the validation and development of high-resolution versions of the UK MetOffice's NWP models. Currently, data analysis is ongoing, and a wide variety of papers is planned.

Figure 5.25 shows a map of southern England indicating the positions of the instruments involved. Many instruments are operated by the NERC UniversitiesŕFacility for Atmospheric Measurements (UFAM). The measurement area was centred on the Chilbolton Observatory, where a large number of instruments, including some fixed high-power radar and lidar systems were located. Of particular interest for convection studies is the 1275 MHz ACROBAT radar which is used for clear air observations. It can detect convective cells using scattering from discontinuities in temperature and humidity at their boundaries. A large number of radiosondes were launched from 5 sites in addition to the existing Met Office radiosonde sites. Two aircraft, the UFAM Cessna and a Dornier 128, operated by IMK, also made measurements during IOPs.

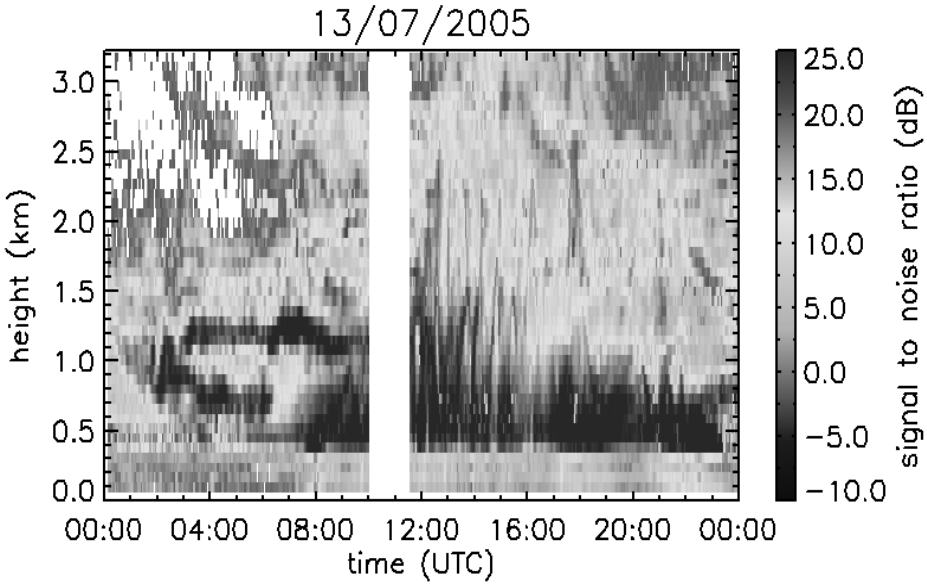


*Figure 5.26.* The minimum signal-to-noise ratio measured by a vertical-pointing 1290 MHz wind profiler on 13 July 2005

The UFAM Degreane 1290 MHz wind profiler (operated by the University of Manchester) (Norton et al., 2006) was located at Linkenholt, 19km north-

west of Chilbolton, to be in the line of sight of the ACROBAT 1275 MHz scanning radar. The Met Office deployed a microwave radiometer (Hewison and Gaffard, 2006), a ceilometer and radiosondes to this site. The collocation of these instruments allowed tests on both their individual performance and the benefits of their integration at one site. The measurements provide datasets for validating algorithms for identifying the top of the boundary layer and integrating wind profiler and radiometer measurements in the convective boundary layer. They also test the ability of the microwave radiometer to resolve the temperature/humidity structure of individual convective eddies and the ability of the wind profiler to provide quantitative information on turbulence.

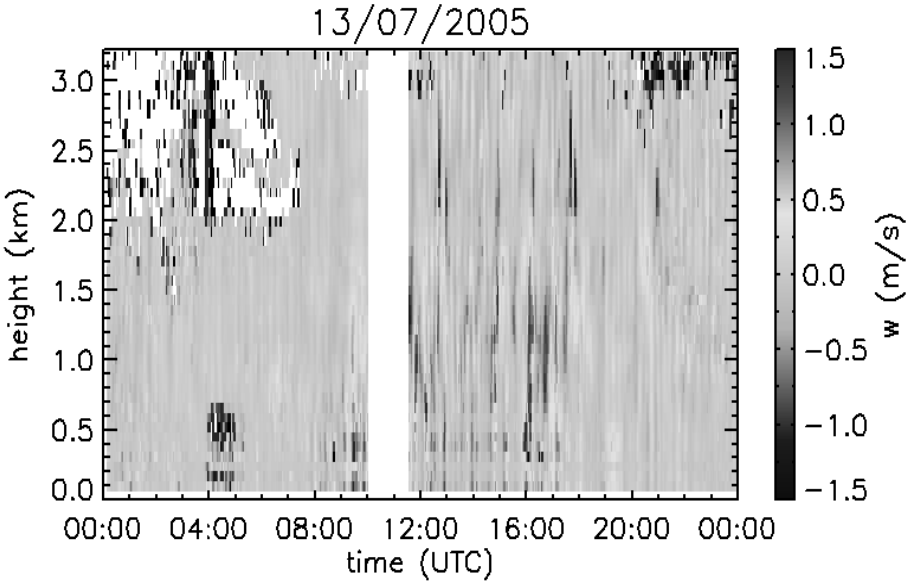


*Figure 5.27.* Vertical wind speed measured by a vertical-pointing 1290 MHz wind profiler on 13 July 2005

Figures 5.26 to 5.31 show a selection of data from July 13, 2005. This day was chosen as an IOP due to the convection which developed in the area as a result of solar heating. There was a large amount of cumulus congestus but only a few clouds produced precipitation. Figure 5.26 shows the minimum signal-to-noise ratio (SNR) of the three beams recorded by the vertical-pointing Degreane 1290 MHz wind profiler based at Linkenholt. The development of the convective boundary layer is shown by the higher values of SNR. The boundary-layer thickness increased from around 1 km to about 2 km as convection increased during daylight hours. Below approximately 0.25 km, the measurements are not reliable. Figure 5.27 shows measurements of the vertical wind speed using the same instrument. The larger variability in verti-

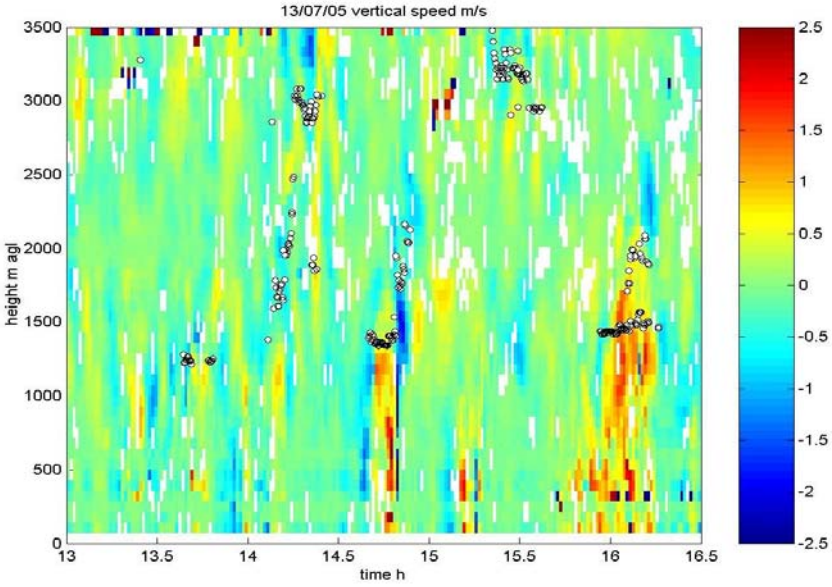


*Figure 5.28.* Vertical wind speed measured by a vertical pointing 1290 MHz wind profiler on 13 July 2005. Superimposed in black dots are cloud base data detected by a ceilometer

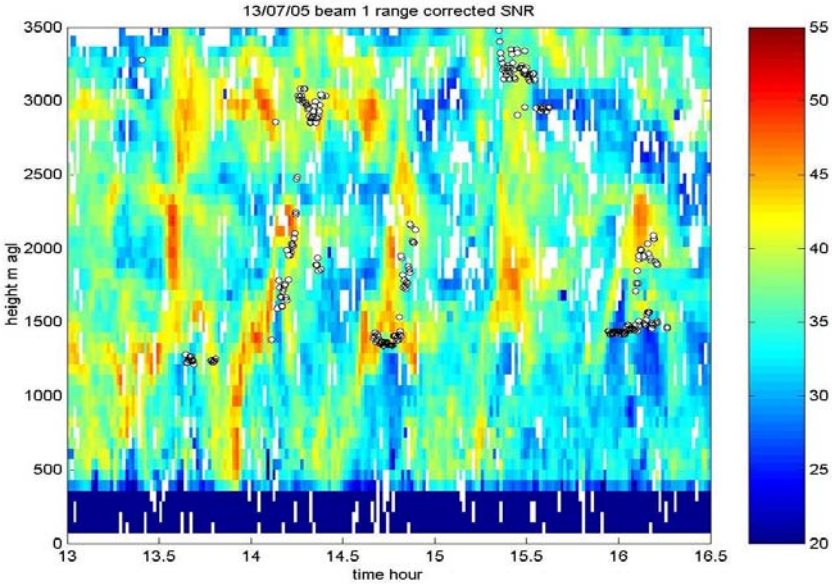


*Figure 5.29.* Range-corrected signal-to-noise ratio measured by a vertical-pointing 1290 MHz wind profiler on 13 July 2005 using an oblique beam. Superimposed in black dots are cloud-base data detected by a ceilometer

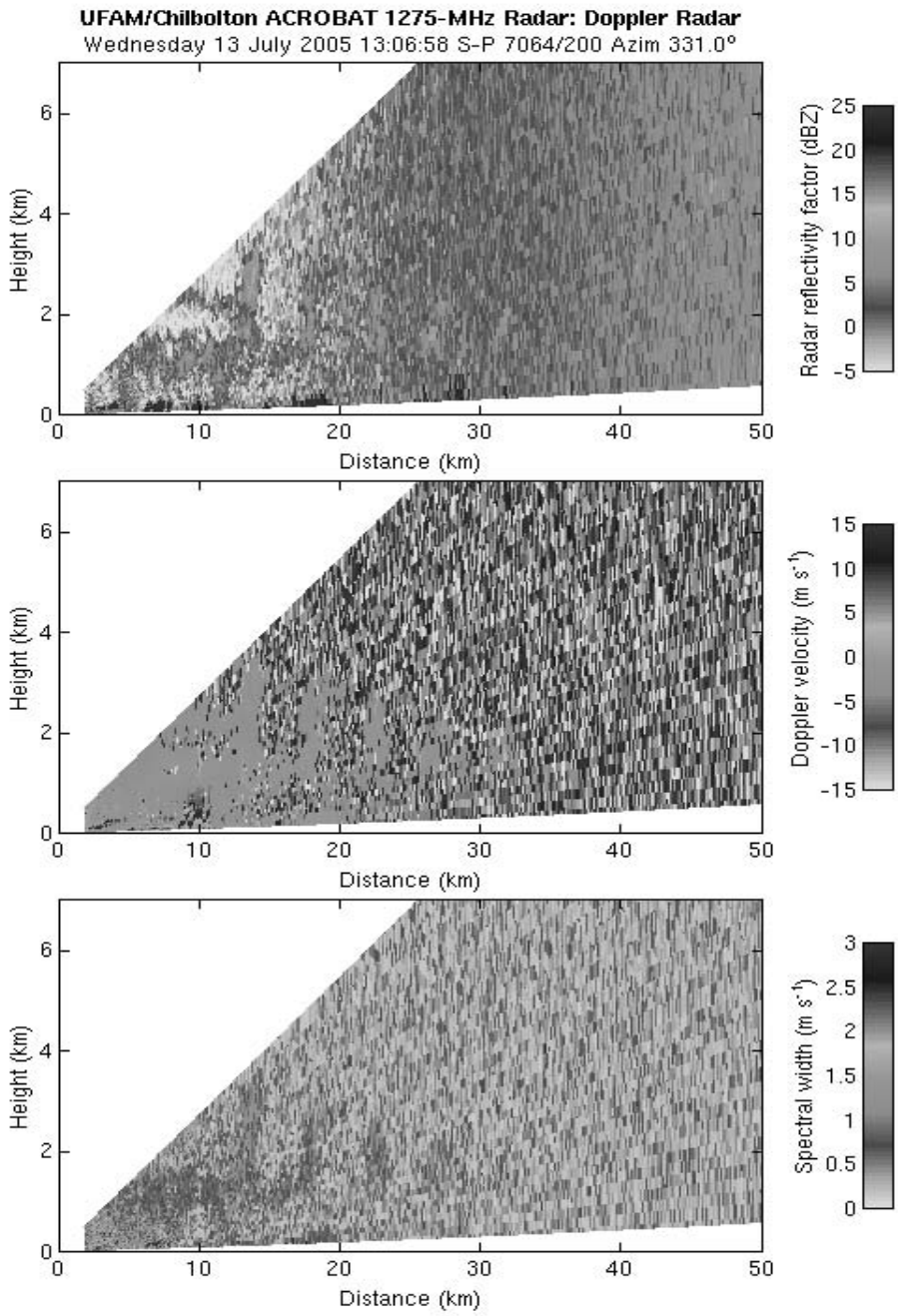


*Figure 5.30.* Radar reflectivity, radial (Doppler) velocity and spectral width measured by 1275 MHz ACROBAT scanning radar at 13:06 UT on 13 July 2005

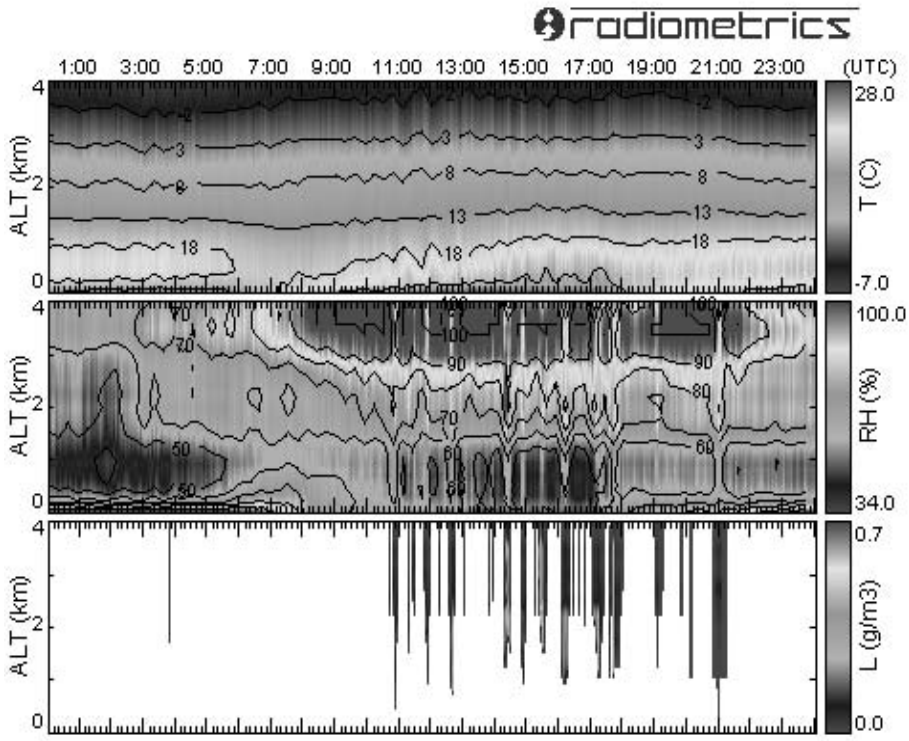


*Figure 5.31.* Radiometrics TP/WVP-3000 microwave radiometer measurements on 13 July 2005

cal wind speed from approximately 09 UT to 18 UT indicates increased convection. Furthermore, the figure shows that on this day individual convective cells were identified by the wind profiler. Figure 5.28 reveals that individual updrafts and downdraft were associated with convective cells. The cloud base measured by the ceilometer is indicated by black dots. Around 14:45 UT, there is a remarkable example of an updraft penetrating a cloud. Within this updraft, the range-corrected signal-to-noise ratio is rather weak, (figure 5.29) while it is strong at the edges of the updraft and of the downdraft. The downdrafts typically consist of dryer air than the updrafts, resulting in reduced turbulence. Enhanced turbulence however, can may occur on the other hand in the vertical speed discontinuity area. This leads to a large variation in the refractive index within this zone and corresponds to a strong signal-to-noise ratio.

Figure 5.30 shows measurements of radar reflectivity, radial velocity and spectral width recorded using the ACROBAT 1275 MHz scanning radar at Chilbolton Observatory. This was recorded using a scan with fixed azimuth in the approximate direction of the 1290 MHz wind profiler at 13:06 UT. The radar reflectivity shows the boundaries of convective cells up to heights of around 3 km. The strong signals near the lower range of the measurement

are due to clutter. Note that the wind speed shown is a radial measurement in the direction of the beam, rather than a vertical measurement. The spectral width of the signal gives a measure of turbulence within the convective cells. It can only be determined for regions showing sufficient radar reflectivity and has to be wind-shear corrected. Figure 5.31 shows vertical profile retrievals of temperature, relative humidity and liquid-water content, made using the Met Officeś Radiometrics TP/WVP-3000 profiling microwave radiometer. The radiometer measurements show general agreement with the radiosondes, but do not resolve sharp features such as are commonly seen in relative humidity measurements.

## Bibliography

Hewison, T. J. and C. Gaffard: 1D-VAR Retrieval of Temperature and Humidity Profiles from Ground-based Microwave Radiometers. Proceedings of MicroRad'06, Puerto Rico, 28 February - 3 March 2006, 2006.

Norton, E. G., G. Vaughan, J. Methven, H. Coe, B. Brooks, M. Gallagher, and I. Longley: Boundary layer structure and decoupling from synoptic scale flow during NAMBLEX. *Atmos. Chem. Phys.*, **6**, 433-445, 2006.

# 5.4 HELSINKI TESTBED: A NEW OPEN FACILITY TO TEST GROUND-BASED INSTRUMENTATION TECHNOLOGY FOR ATMOSPHERIC PROFILING

Jani Poutiainen[1], E. Saltikoff[3], W. Dabberdt[2], J. Koistinen[1], and H. Turtiainen[3]

[1] *Finnish Meteorological Institute, Helsinki, Finland*
Jani.Poutiainen@fmi.fi

[2] *Vaisala Inc., Boulder/Colorado, USA*

[3] *Vaisala Inc., Helsinki, Finland*

## 5.4.1 DESCRIPTION OF HELSINKI TESTBED

The Finnish Meteorological Institute (FMI) and Vaisala meteorological measurements company have initiated a mesoscale observational network in a coastal high-latitude environment in Southern Finland. Figure 5.32 shows the location of the testbed domain. The broad scope of this project is to provide input and experience for mesoscale weather research, forecast and dispersion model development and verification, information systems integration, end-user product development and data distribution for public and the research community.

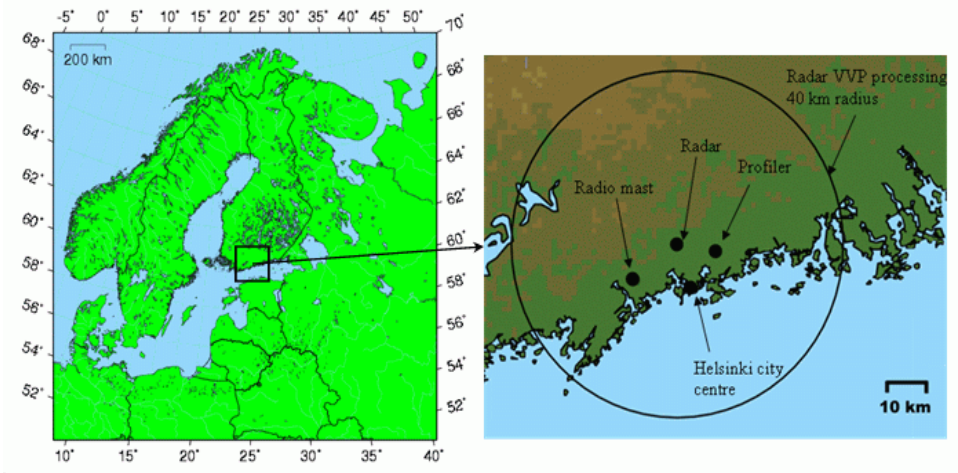


*Figure 5.32.* The main domain of the Helsinki Testbed is shown with black rectangle (left) and sites of interest in this article (right). Table 5.32 lists the most essential testbed measurements

A testbed can be defined as a working relationship in a quasi-operational framework among measurement specialists, forecasters, researchers, private-sector, and government agencies, aimed at solving operational and practical regional problems with a strong connection to the end-users (Dabberdt at al., 2005). Outcomes from testbeds are more effective observing systems, better use of data in forecasts, improved services, products, and economic/public safety benefits. Testbeds accelerate the translation of research and development findings into better operations, services, and decision-making. The Helsinki Testbed is open to researchers around the world to test measurement and modeling systems. The Helsinki Testbed core project has funding from the Tech-

| No. | Site type |
|---|---|
| 46 | FMI weather stations |
| 34 | FMI precipitation stations |
| 13 | Off-line temperature loggers in greater Helsinki area |
| 8 | Weather transmitters in greater Helsinki area |
| 191 | Road weather stations |
| 292 | Surface weather stations, total |
| 42 | Pairs of weather transmitters in masts |
| 5 | Optical backscatter profilers (new ceilometers) |
| 6 | FMI ceilometers |
| 4 | C-band Doppler radars |
| 1 | Dual polarization Doppler radar |
| 3 | RAOB sounding stations |
| 1 | UHF wind profiler with RASS |
| - | Total lightning network |
| 3 | Visiting research instruments:<br>2 POSS precipitation occurrence sensor systems (Met Service Canada)<br>1 Doppler lidar (University of Salford, UK) |

*Table 5.5.* Weather stations in Helsinki Testbed

nology Agency of Finland and partners from many sides of the society: e.g. Finnish Road Enterprise, Road Administration, Radiation and Nuclear Safety Authority, Helsinki Metropolitan Area Council (Air Quality Authority) and some partners from industry.

FMI and Road Administration have reasonably good existing observation networks in the area. For the Helsinki Testbed campaigns, these have been supplemented with numerous new sites. A dense network of stations has been equipped with Vaisala WXT510 weather transmitters. Of these stations, 42 consist of cell phone base-station masts, converted to meteorological towers by installing weather transmitters on them. Two or three transmitters exist at different heights to derive stability and bulk profiles of temperature and humidity. Additional weather transmitters have been installed at ground level in urban areas.

The number of radio soundings, wind profiler and RASS (radio acoustic sounding system) observations have been increased. A network of new laser ceilometers has been established to map both cloud base and boundary-layer structure. The existing precipitation stations have been supplemented with several automatic weighing gauges, capable of measuring both liquid and solid precipitation. Satellite and C-band weather radar data will be extracted from FMI and research equipment.

This section illustrates many of the testbed observations and presents examples on combining information from ground based remote sensing instruments. It shows simultaneous measurements of weather radar and wind profiler with RASS option, but considers also *in-situ* data from radio soundings, a radio mast, and a surface weather station. A primary interest is focused here on measurements of vertical profiles of wind speed, temperature, and backscatter (e.g. from precipitation).

## 5.4.2 MEASUREMENT CAMPAIGNS IN HELSINKI TESTBED AND CLIMATE SUMMARY

The Helsinki Testbed focuses on meteorological observations and forecasting directed towards meso-$\gamma$ scale phenomena that typically last from a few minutes to several hours. The most intense activities concentrate on specific, usually month-long measurement campaigns. For convenience, each of the campaigns has been named with a typical mesoscale phenomena or activity of that season: August 2005 Nowcasting, November 2005 Precipitation type, January-February 2006 Stable boundary layer, May 2006 Sea breeze, and August 2006 Convection. The observational network is expected to be continued as a long-term pseudo-operational platform after the above campaign periods.

All four seasons can be distinctly separated in this northern environment. Weather is dominated by transient eddies connected to the polar front, arriving to Finland from south-west usually in a rather late phase of the occlusion process. Snow cover lasts around 100 days. Climatological statistics for the testbed campaign months in Helsinki are given in the table 5.4.2. The Gulf of Finland freezes on average on 1$^{st}$ of February, and 2-4 weeks earlier (Leppäranta et al., 1998) along the coasts.

In the testbed region yearly variation of possible sunshine hours is pronounced, the sun is above horizon about five hours during the shortest daylight time, and nearly 20 hours in mid-summer, respectively. The best chance of having clear days is in May-June while the lowest corresponding possibility is in November-December. In Helsinki, water phase of precipitation can often change quickly, both in space and time. In an average November, temperature drops below zero at about half of the days near the coastline (table 5.4.2). In most cases, the water phase is obvious: Rain occurs when temperatures are well above the freezing point, and snow when temperatures are below -10°C. However, at temperatures near 0°Call precipitation types are possible. Precip-

| Month | T (°C) mean | T (°C) max; average | T (°C) min; average | T (°C) max; absolute | T (°C) min; absolute | Days $T_{max}$ >25 (°C) | Days $T_{min}$ <0 (°C) | RR (mm) mean | RR (mm) max |
|---|---|---|---|---|---|---|---|---|---|
| Jan | -4.2 | -1.7 | -6.9 | 8.5 | -34.3 | | 26 | 47 | 85 |
| Feb | -4.9 | -2.2 | -7.7 | 10.3 | -26.0 | | 24 | 36 | 101 |
| May | 9.9 | 14.0 | 6.0 | 26.3 | -3.1 | | 1 | 32 | 68 |
| Aug | 15.8 | 19.3 | 12.6 | 31.2 | 3.4 | 2 | | 78 | 174 |
| Nov | 1.4 | 3.6 | -0.8 | 11.6 | -18.6 | | 15 | 68 | 160 |

*Table 5.6.* Climatological statistics of some weather parameters in Helsinki Kaisaniemi, for the months of Helsinki Testbed campaigns (Drebs et al., 2002)

itation type is not determined only by near-surface temperature, but also by humidity and temperature profiles aloft (Saltikoff et al., 2000). In very-dry weather, snow can fall at +4°C. In inversion situations, it is not uncommon to see liquid rain fall at -2°Cand drizzle at even colder temperatures. In the following analysis(see 5.4.4), data from the *November-precipitation-type* campaign have been used and a case study with near-zero temperatures has been chosen.

### 5.4.3 INTEGRATION OF TECHNOLOGIES

In observation production and information integration, joining different measurement systems touches upon many technical as well as data content issues. One of the key goals of the Helsinki Testbed is the demonstration of technology integration of meteorological instruments, observation systems, and ICT-technologies, not forgetting end-user interfaces. It is anticipated that meteorological information systems are likely to further develop towards automated information processes. These include dynamic process logic thus enabling more efficient resource utilization. Both fully automated and human intervened processes will autonomously interact with other processes, examples being adaptive sampling strategies responsive to current and predicted weather patterns, as well as advanced control engineering methods in data quality control and respective network-maintenance processes.

To some extent emphasis in measurements design has been shifted from individual sensors or networks towards systems and information integration at a higher level of planning. It is worth to consider all measurements and other information sources as a whole, thus representing uniform meteorological information architecture. Fastly developing and changing technologies are likely to lead to a mixture of solutions, including e.g. sensor, data transmission and processing technologies. Integration of meteorological measurement systems to other information technologies can not be avoided. However, from

a combined meteorological and ICT-technological perspective, available standardization does not always keep up with the pace of technological progress.

Goals of a testbed include pursuing solutions for large-scale infrastructures and efficient measurement networks maintenance. In the course of history, many separate networks and other data sources have come to existence, and in many cases data producers represent different organizations and different countries. In search of both meteorologically and economically optimal solutions in continuously evolving requirement space, data content from different sources should be combined. Modularity and well defined open data interfaces are crucial from product development and network management viewpoints.

Yet another idea behind the testbed is to provide tools to tune operational system cost levels so that data quality issues can be treated in a credible way for the varying foci of meteorological measurements. For example, cost-quality optimized requirements of global, climatologically representative research data are likely to be different from respective requirements of data input for operational mesoscale nowcasting. Finally, data accessing and visualization is where all the previous efforts are realized or information potential is missed.

During the Helsinki Testbed campaigns free real-time and past data have been provided on the project web site (http://testbed.fmi.fi), as well as non-profit mobile products such as WAP observation maps with color graphics and weather data software clients for new mobile operating systems. In the Helsinki Testbed, a freely distributable XML scheme has been defined in meteorological data exchange for heterogeneous data sources. In the current approach, open protocols, multi-tier and service-oriented architecture (SOA) together with generic data interfaces set the basis for future expansion and integration of systems.

The discussion above closely relates also to ground-based remote-sensing instruments. In data integration, the following choices characterize the issue. When assuming two remote-sensing methods of observation, both existing at the same moment in time, and both representing the same measurement volume in the atmosphere, the combination of both leads to two different major alternatives although intermediate situations may occur in practice:

(1) Both methods measure the same atmospheric property in the volume: In this case, one method can be principally replaced with the other, or use one to verify results of the other.

(2) Both methods measure entirely different atmospheric properties in the volume: In this case, due to synergy between the methods, the combination of the results, gives a considerably improved knowledge of the situation.

The following comparisons on the different remote sensing data will shed empirical light, which of the preceding choices characterizes their relation.

Both of the alternatives may yield beneficial new information, but only when the nature of relations between pairs of instruments are well known.

### 5.4.4 DATA ANALYSIS

This subsection outlines some examples from a November-2005 measurement campaign. The emphasis is laid on simultaneous observations of various remote-sensing techniques, in order to illustrate their differences and potential in fusing information. Although primary motivation comes from integration of ground-based remote sensing, from practical view it is tempting to expand this target towards more general integration of meteorological profile data.

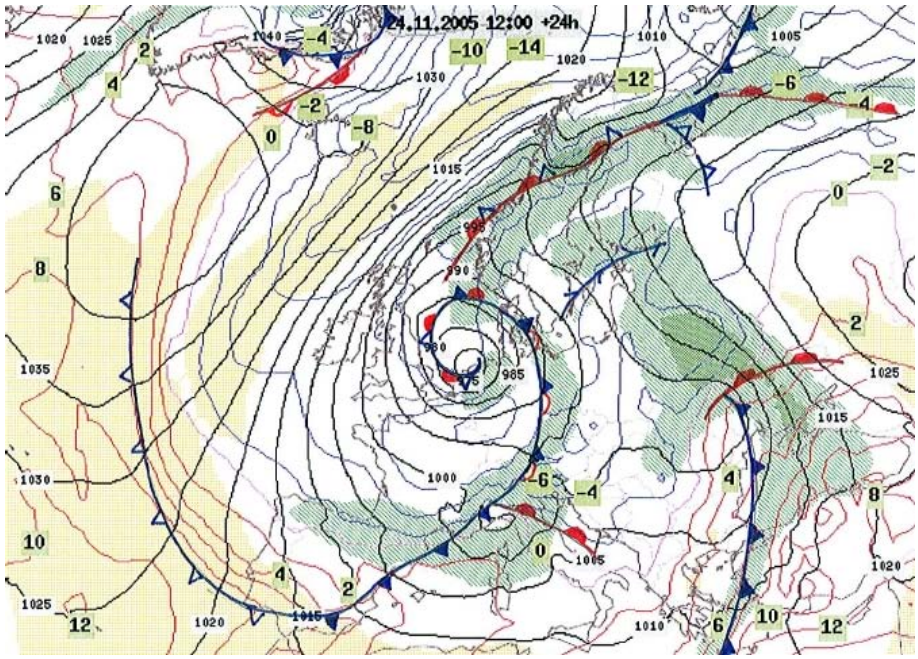


*Figure 5.33.* ECMWF 24h forecast with frontal analysis, valid at 25.11.2005 12:00 UTC. Solid black lines represent surface pressure and colored lines 850 hPa temperature. Green (moist) and yellow (dry) shadings show humidity at 700 hPa level

This leads to incorporating also other available data, especially near surface below 150 meter height where many variables are not available with remote sensing methods, at least not with high resolution, high all-weather performance, temporally continuous manner and operationally. Therefore, the following cases include *in-situ* measurements at four levels in 327 m high radio mast. Sites of interest are illustrated in figure 5.32. Radio soundings are made about 1 km north-east of the radar site. Wind profiler is Vaisala model LAP3000 with RASS feature. Radar measurements are made with FMI's operational C-band weather radar, whose horizontal wind fields are produced with

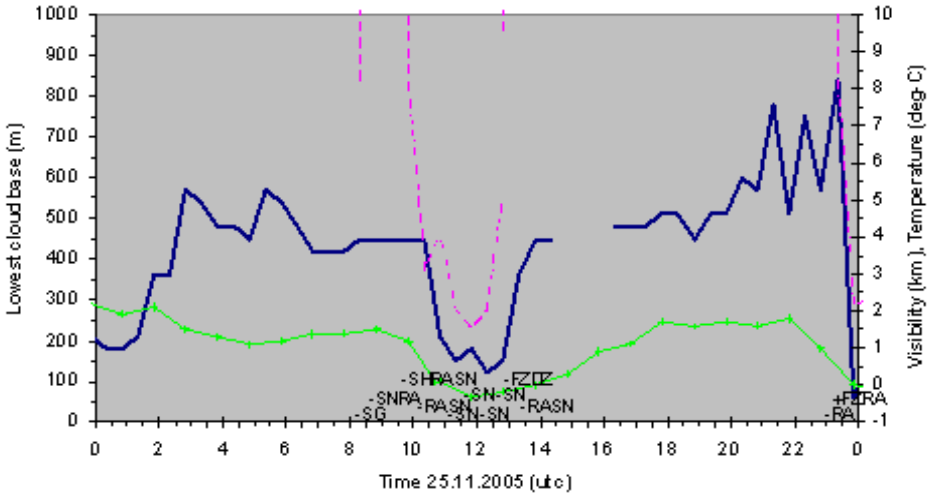


*Figure 5.34.* Cloud base (solid blue curve), visibility (broken red curve), temperature (green curve) and precipitation occurrence (METAR codes) in Malmi

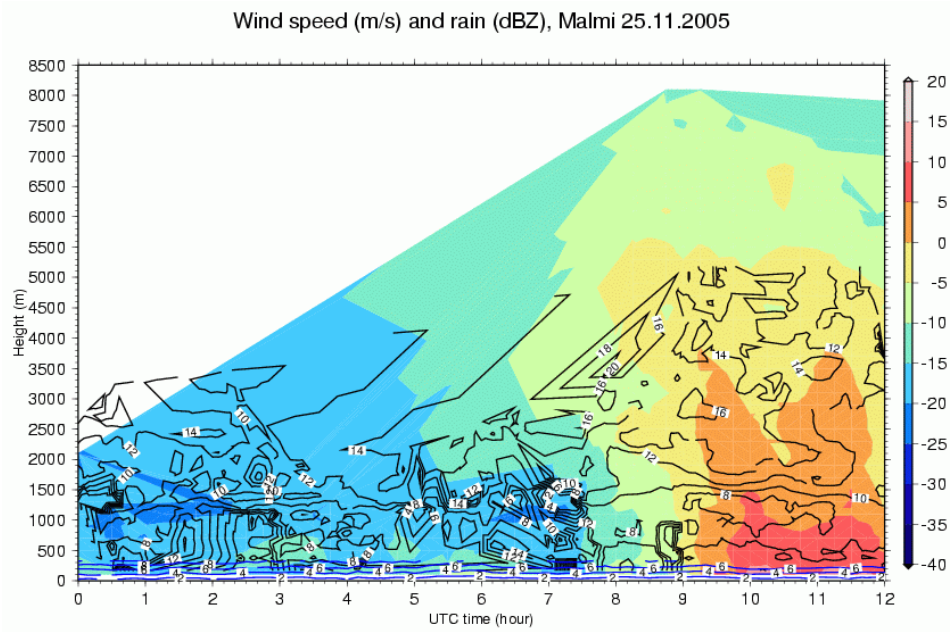


*Figure 5.35a.* Radar reflectivity factor (dBZ, color scale), profiler wind speed (m/s, black contours) and mast observations (m/s, blue contours) of wind speed

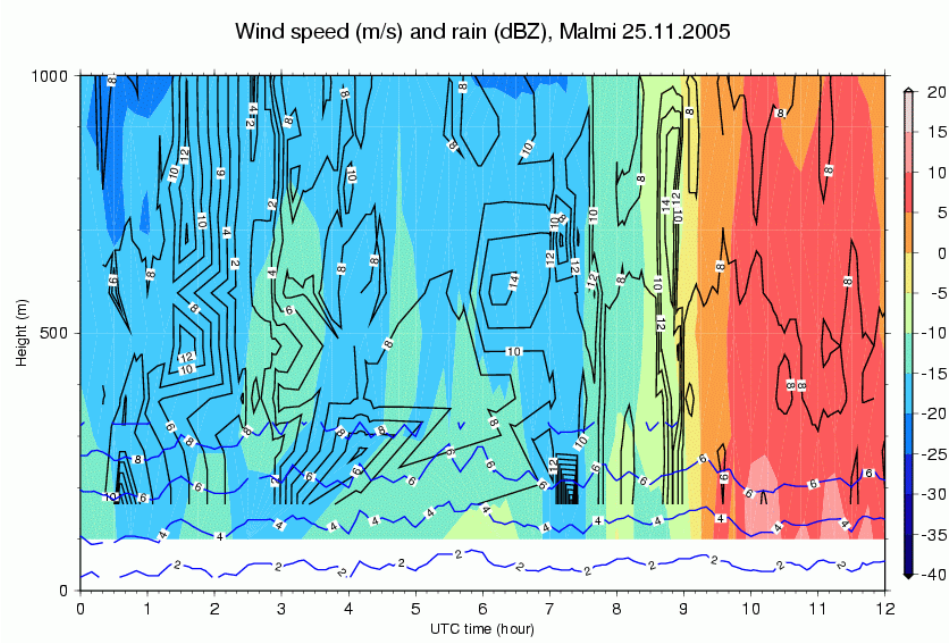


*Figure 5.35b.* The same as figure 5.35a but in the height range of 0-1 km

the VVP (Volume Velocity Processing) method and a processing radius of 40 km. In profile data contouring, optimal Delaunay triangulation is used.

As the wind profiler with RASS is located on the site, Helsinki Malmi airport was chosen as a ground reference on 25th of November 2005. On that day, various precipitation types were observed. Figure 5.33 shows the synoptic weather chart for the respective day.

The following closer look (figure 5.34) is based on METARs from Malmi. The solid blue line marks the cloud base while the broken red line represents visibility and the green line temperature. Present weather is shown with METAR codes at respective times during precipitation. The cloud base lowered from about 10:00 to 13:30 UT. Sleet was observed from 09:20 to 10:50 UT and again at 13:50 UT, while the whole precipitation episode started with snow grains at 08:20 and 08:50 UT and ended with sleet at 13:50 UT. The starting time of sleet closely agrees with weak precipitation echoes (0-5 dBZ) from radar (see figure 5.35a).

Figure 5.35a illustrates the complementing combination of radar, wind profiler, and mast data. The idea is to seek an optimal mix of observations in a data product in order to maximize the all-weather accuracy in rain and wind detection. The inclusion of mast data shows a significant improvement in the lowest 300 meters of the atmosphere above ground, which may be seen better in figure 5.35b. Mast observations and profiler data seem to include very few

exactly similar features at overlapping heights. Especially, the wind speed field is much more continuous in mast data.

Figure 5.36 presents an attempt in height range maximization for vertical motion measurement. For the profiler, positive values represent movement towards the instrument, and vice versa for the radar. In this picture, the structure of vertical motion from profiler data is more meaningful, although the radar's observation range principally extends higher during precipitation. Figure 5.37 shows a combination of temperature observations from mast and RASS. Again, this illustrates maximization of height coverage for continuously available temperature profile data. In comparing the sources, the shapes of profiles fit quite well. However, when looking e.g. at the -1°Cisotherm from mast, it is seen that it closely corresponds to the 0°Cisotherm of the RASS (*note that within the image different temperature measures are used*). The virtual temperature would equal normal temperature only in a water-vapour-free atmosphere. Also, in a 4-year intercomparison of virtual temperatures between a balloon-borne sounding system and RASS (BBSS-RASS) mean and standard deviations of -0.64°Cand 0.95°Cwere found (Coulter and Lesht, 2001). Reasons for RASS's virtual temperature discrepancy have been thought to include vertical motion of the atmosphere, turbulent inhomogeneities, and inaccuracies in temperature retrieval. In this study, RASS had 3 minute averaging time. Figure 5.38a

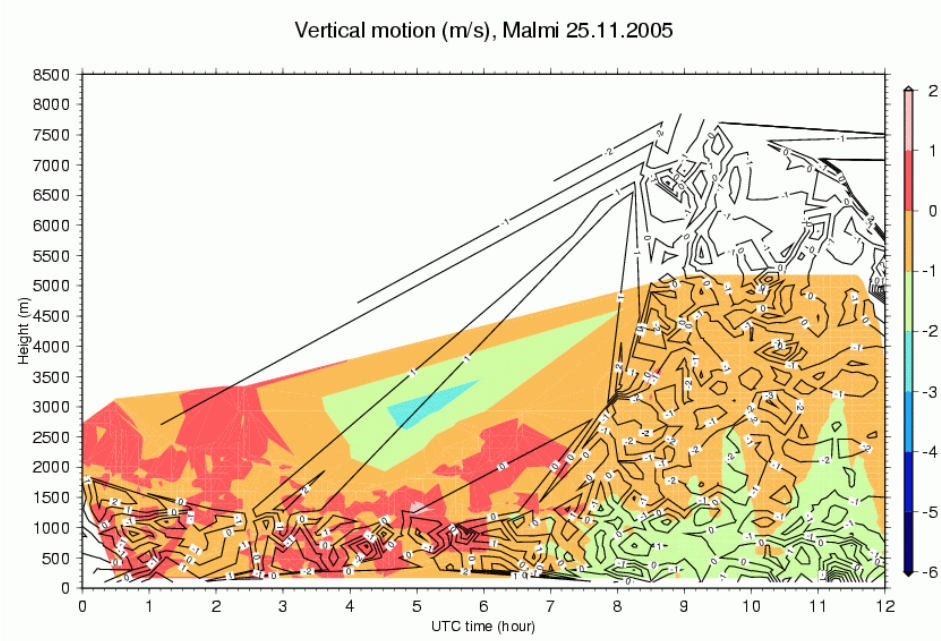


*Figure 5.36.* Vertical motion (m/s) measured with radar (black contours) and profiler (color scale)

shows that both profiler and radar reveal a number of similar features in wind

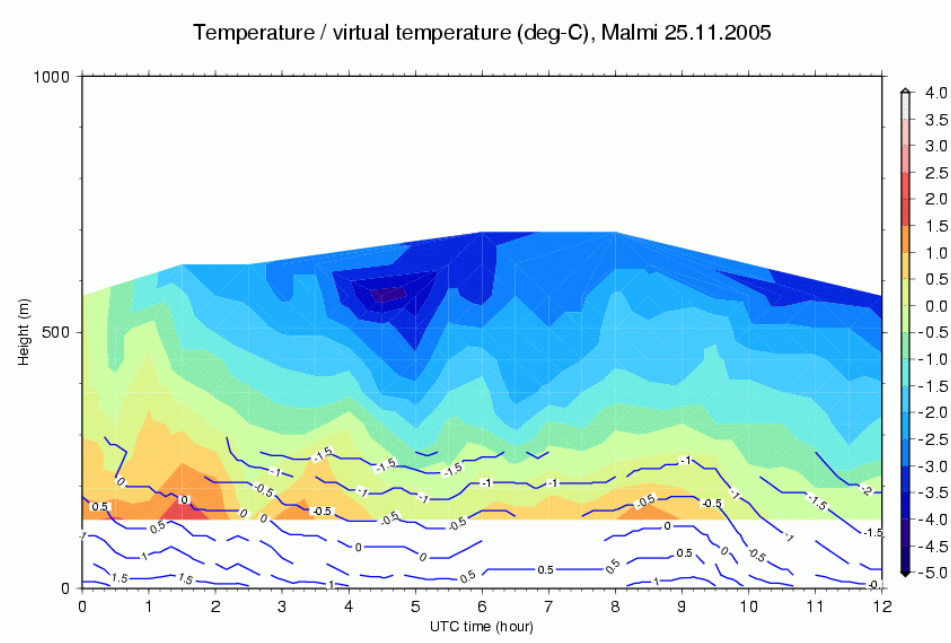


*Figure 5.37.* Virtual temperature from RASS (color scale) and temperature from radio mast (blue contours)

speed. This can be seen especially during precipitation events, although radar data are processed for a horizontal range up to 80 km due to low elevation angles of the weather-radar antenna. On the other hand, also non-meteorological structures at some isolines are apparent in some parts of the figure because of threshold values in backscatter detection (from vertical), partly noisy data, and/or the interpolation method. This is most striking in weather-radar data before 08 UT and above 1500 meters. To have a closer look at sensor agreement near the surface, figure 5.38b presents only the lowest 1 km. Irregularities as in the remote-sensing data are absent in mast observations. Interestingly, the profiler shows a nearly calm period from 02:00 to 03:00 UT and gusty episodes e.g. at about 07:30 and 08:50 UT. Radar instead, shows minimum peaks for wind speed from 03:00 to 06:30 UT, and no maximum peaks at all. Wind profiles (Figs. 5.38a and 5.38b), and temperature profile (figure 5.37) can be compared to more infrequent sounding data (Figs. 5.39a and 5.39b).

The sounding shows a sharp increase in wind speed at about 1-1.5 km level around 06:00 UT, from 8 to 17 m/s. A weak signal of this can be seen with remote sensing instruments as well. When temperature inversion dissolves, the greatest winds in the sounding diminish to about 13 m/s below 5 km at the last two soundings, which is almost exactly the same as observed with both remote sensing instruments at the respective times.

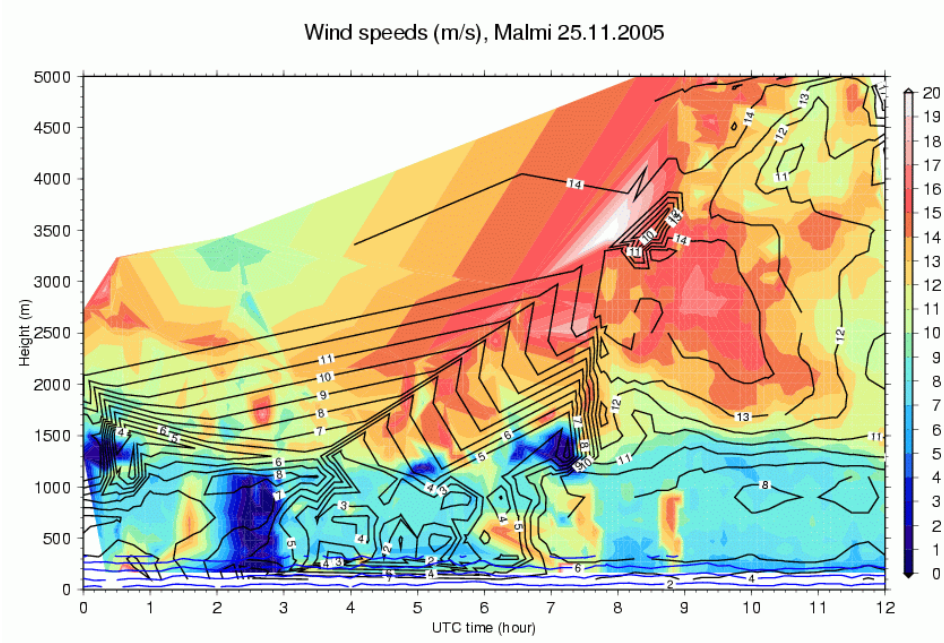


*Figure 5.38a.* Wind speeds (m/s) from radar (black contours), profiler (color scale) and mast (blue contours)

As for the temperature comparison in the lowest 450-500 m, all the observation methods confirm general cooling of surface temperature and temperature profile. In the first two soundings temperature drops from about 1,5°Cnear surface to about -4°Cat 600 m. In the last two, temperature drops from slightly above 0°Cto about -4°C. Qualitatively these observations are in agreement with mast and RASS data. In the layer of 500-1000 m, soundings generally show a warming trend towards noon in UTC time. Obviously, this can not be verified with mast data, but the profiler data give indication of a weak warming in the 500-600 m layer between 06:00 and 08:00 UT. In figure 5.39b, the right image is shown to illustrate a high-resolution temperature sounding in the Helsinki Testbed and the evolution of an inversion layer. The data are equally spaced at 2-second intervals.

Figure 5.40 has been created by the system computer of the profiler unattended, and it is that kind of product that most readily is available to end-users. This wind-barb display has a 30-minute update interval with 27-minute averaging. Another routine product in the Helsinki Testbed measurement configuration has a 5-minute update interval with 15-minute averaging. In the previous product, temporal resolution is lower, but temporal coverage is much better. Obviously, compromises in product generation need to be made between configuration and representativity of each data product.

Finally, figure 5.41 presents an intercomparison of profiler and weather-radar backscatter. Although part of the rain was in liquid form, the bright band (melting layer) is absent due to near zero surface temperatures during the precipitation period. During precipitation, soundings and mast data reveal

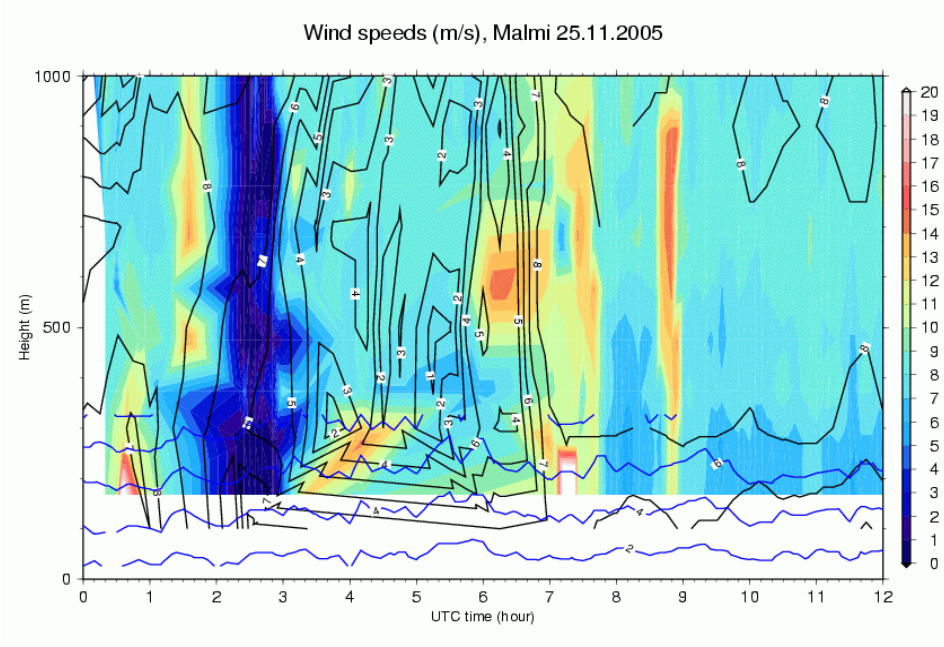


*Figure 5.38b.* The same as figure 5.38a but in the height range of 0-1 km

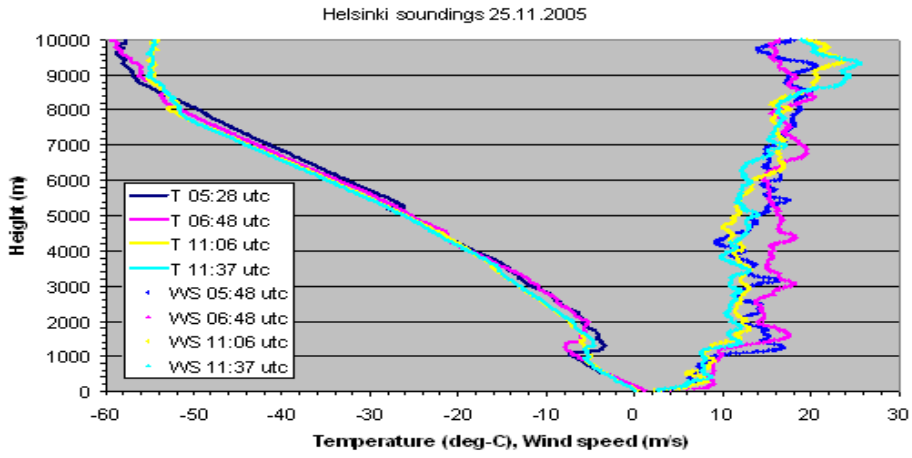


*Figure 5.39a.* Soundings made in Helsinki Testbed during the first 12 hours on November 25th, in greater Helsinki area

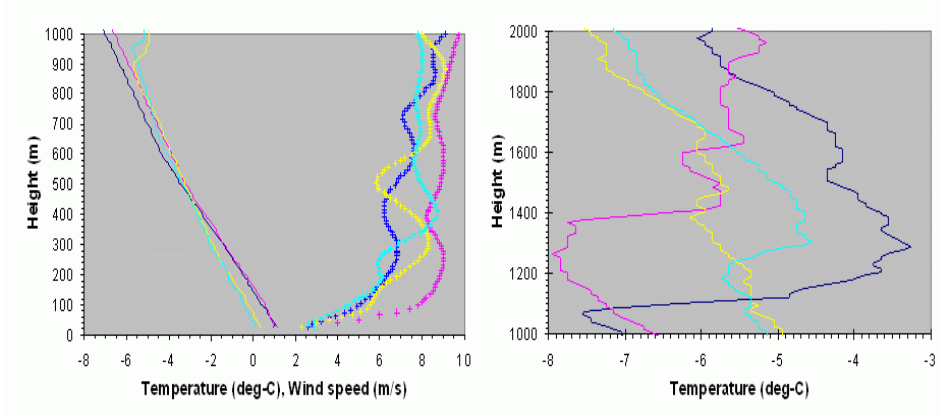


*Figure 5.39b.* The same as figure 5.39a, but with different scales in order to see more detailed features of soundings

that the 0°Cisotherm was below 150 m height, which practically can not be detected from profiler or radar data. Precipitation started at 09:20 UT, when echo patterns in radar and profiler strikingly resemble each other, although the radar had an about 3 km higher maximum vertical range of its observations.

In the hours before precipitation (00:00-09:20 UT), the profiler interestingly reveals a well-defined echo layer at about 800 m altitude. This is most likely due to effects of a temperature inversion and a cloud layer below the inversion itself, both observable in the sounding data. Although not shown, humidity profiles reached 100% in the first two soundings at an altitude between 500-600 m. The same feature can also be seen in figure 5.34.

## 5.4.5 CONCLUSIONS

This section described the Helsinki Testbed mesoscale weather-measurement project along with discussions on technology integration, and examples of various combinations of data sources. In line with the November-2005-measurement-campaign goal of detecting different types of rain, a case study for near-zero-temperature precipitation period was chosen. In this event, different available remote-sensing observations were examined to get atmospheric vertical profiles of temperature, wind speed and backscatter signal. In addition, *in-situ* observations of surface weather station, mast and radio soundings were utilized. It is clear that the best height coverage and information content of observations is obtained when these *in-situ* data are incorporated. Each of the different remote sensing or *in-situ* profiling methods has their strengths and weaknesses. This is particularly true when aiming at integrated observation systems and continuous all-weather performance with high temporal and vertical resolutions, good height coverage, and high accuracy. Therefore, combining all the relevant and available data sources

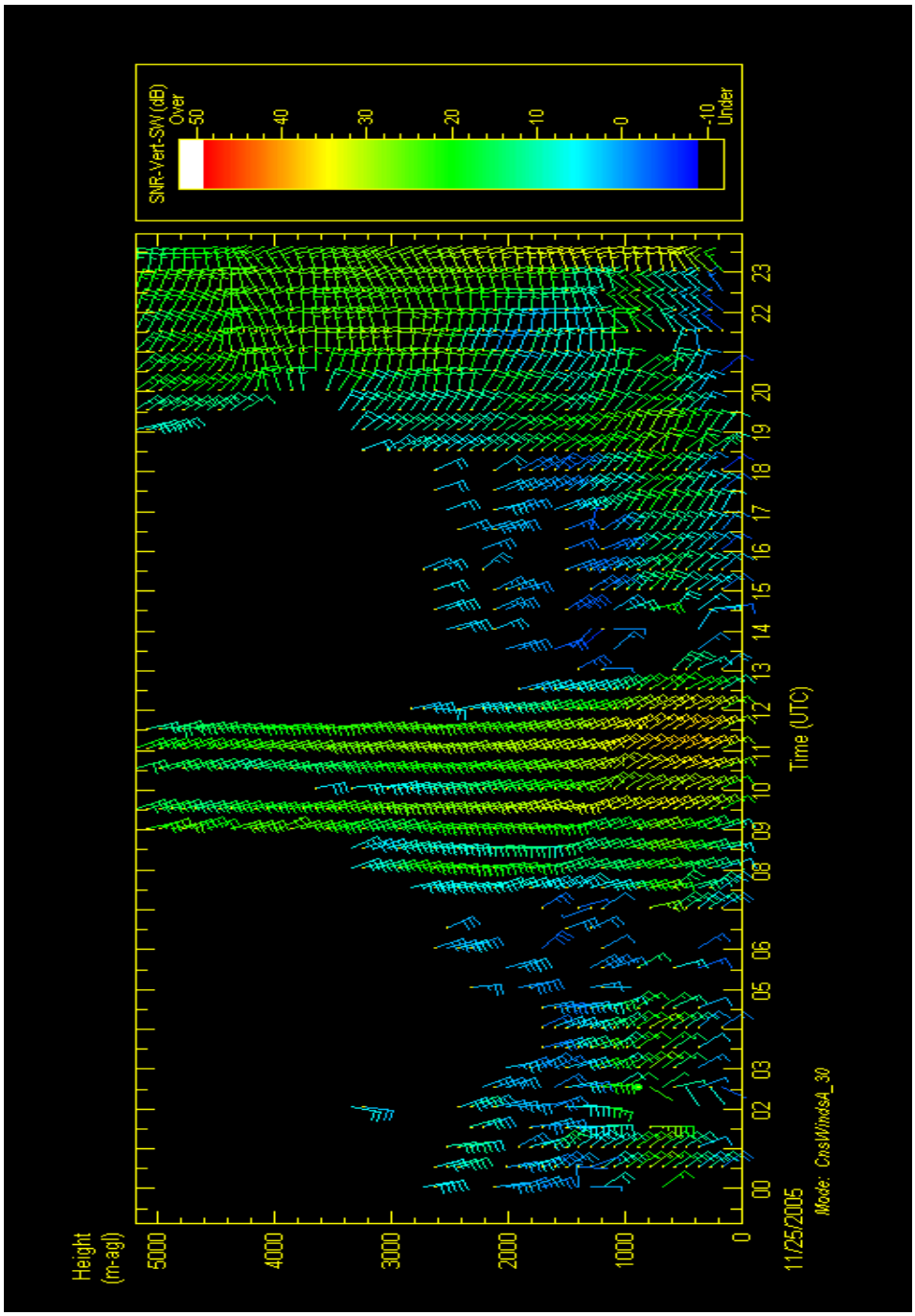


*Figure 5.40.* Profiler's wind barb time series generated in profiler computer

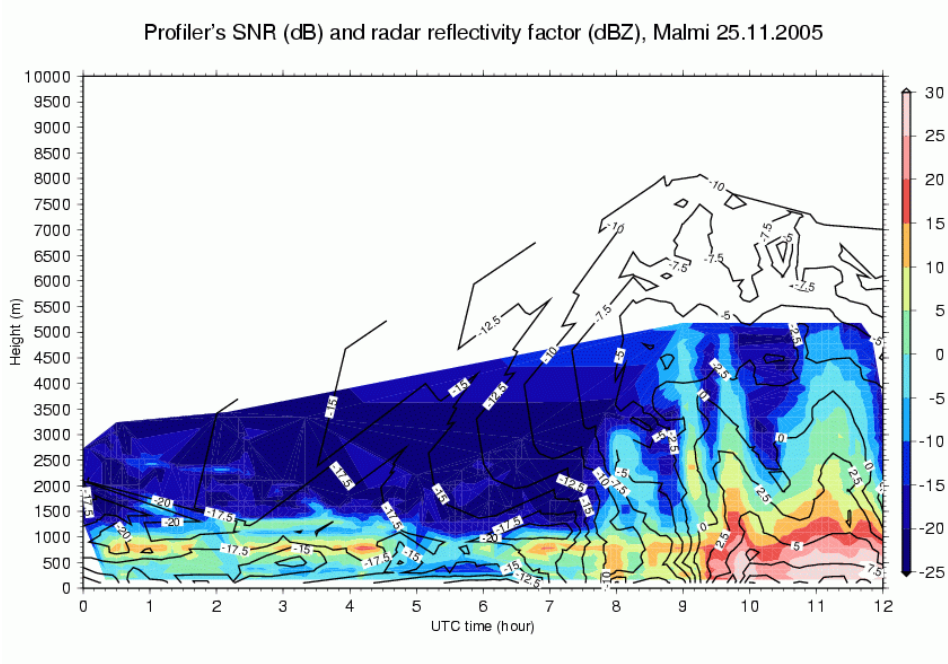


*Figure 5.41.* Combined backscatter product of radar (dBZ, black contours) and profiler (dB, color scale)

should be pursued. In doing so, all remote-sensing instruments currently present (weather radar, wind profiler, RASS) complemented each other in a beneficial way.

## Bibliography

Coulter, R. L. and B. M. Lesht, 2001: A 4-Year Study of the RASS Temperature Bias. Eleventh ARM Science Team Meeting Proceedings, Atlanta, Georgia, March 19-23, 2001, online at: *http://arm.gov/publications/proceedings/conf11/extended_abs/coulter_rl.pdf* referred on 8.1.2006.

Dabberdt, W. F., T. W. Schlatter and F. H. Carr with E. W. J. Friday, D. Jorgensen, S. Koch, M. Pirone, M. Ralph, J. Sun, P. Welsh, J. Wilson and X. Zou, 2005: Multifunctional Mesoscale Observing Networks. *Bull. Amer. Meteor. Soc.*, ***86*** (7).

Drebs, A., A. Nordlund, P. Karlsson, J. Helminen and P. Rissanen, 2002: Climatological statistics of Finland 1971-2000. Finnish Meteorological Institute, Helsinki, Finland.

Leppäranta M., E. Palosuo, H. Grönvall, S. Kalliosaari, A. Seinä and J. Peltola, 1988: Phases of the ice season in the Baltic Sea (North of latitude 57' N), Finnish Institute of Marine Research, No. 254.

Saltikoff, E., H. Hohti and J. Koistinen, 2000: Operational experience of adjustment of Z-R according to water phase. *Phys. Chem. Earth (B)*, **25**, 1017-1021.

# 5.5 WMO INTERCOMPARISON OF HIGH-QUALITY RADIOSONDE SYSTEMS

John Nash

*UK MetOffice, Exeter, United Kingdom*
✉ John Nash@meto.gov.uk

## 5.5.1 INTRODUCTION

The WMO Intercomparison of High Quality Radiosondes was organized in 2005 because a new generation of radiosondes was being introduced into most of the global upper air network. These radiosonde designs can be expected to be in use for the next 10 to 20 years. The test was performed in Vacoas, Mauritius from 2 to 25 February 2005. The test and results are described in detail in Nash et al. (2006). Five new operational radiosonde systems from Europe, Japan and the US were intercompared. None of them had been intercompared previously in earlier WMO Radiosonde Intercomparisons. Two additional working references were flown within the intercomparison to provide additional evidence on the accuracy of the operational radiosondes. The intercomparison was intended to identify any significant flaws in the new radiosonde designs, so that these could be rectified before use became widespread in the operational radiosonde networks.

Information on the accuracy that can be achieved with these new operational radiosondes was required by COST 720 for experimental validation of ground based remote sensing measurements. Referencing the quality of radiosonde relative humidity measurements between daytime and night conditions is difficult without independent observations of water vapour. In recent years both microwave radiometer and/or GPS measurements of integrated water vapour have proved useful in identifying discrepancies in radiosonde measurements. WMO requested that COST 720 recommend a suitable set of ground-based remote-sensing systems to be deployed for this purpose at the test site in Mauritius. Given the difficulties of shipping systems to Mauritius at short notice, COST 720 suggested that GPS water vapour measurements be used as a reference, and that a combination of 78GHz fmcw cloud radar and laser ceilometer is used to record the clouds conditions associated with the radiosonde measurements. Subsequently, COST provided funding to contribute to the test, including collection and archiving of the remote sensing observations and to the scientists supporting the remote sensing equipment.

### 5.5.2 RESULTS FROM EQUIPMENT SUPPORTED BY COST 720

The remote sensing systems deployed at Vacoas to support the intercomparison were:

- Vaisala CT75K laser ceilometer, provided by Vaisala, with data logging supported by the Finnish team, see figure 5.42
- Rutherford Appleton Laboratory (RAL) 78 GHz FM-CW cloud radar, supported by M. Oldfield (RAL) and D. Lyth (Met Office), see figure 5.42
- GPS water vapour sensor, installed by R. Smout (UK) and processed subsequently in the UK by J. Jones (Met Office), see figure 5.43

In addition, Hans Richner [ETH, Switzerland] assembled a database from the radiosonde measurements to compare with collocated CHAMP GPS occultation measurements of temperature and humidity profiles over Mauritius. Twenty seven temperatures and humidity profiles based on GPS occultation measurements from the CHAMP satellite were provided by J. Wickert, GeoForschungsZentrum (GFZ), Potsdam, Germany].


*Figure 5.42.* Vaisala CT75K lidar ceilometer plus Rutherford Appleton Laboratory 78 GHz fmcw cloud radar (centre of picture) operating in the wet towards the end of the intercomparison

The lidar ceilometer and GPS water vapour sensors were operational throughout the test. However, there were some periods when problems occurred with data logging. The cloud radar was only available from 16 February until the end of the intercomparison. The cloud radar suffered some system

failures in shipment to Mauritius, and the Mauritius Meteorological Services provided energetic support to Mr. Oldfield in solving the problems.


*Figure 5.43.* GPS water vapour sensor installed on the handrails of the staircase to the roof, Vacoas

Despite some problems with the availability of GPS water vapour measurements, there were sufficient to estimate day-night differences in the radiosonde relative humidity measurements, see figures 5.44 and 5.45.

The GPS water vapour antenna was installed at an early stage of the test, and by some other radiosonde antenna were installed afterwards interrupting the field of view to the GPS satellites in some directions and causing multipath problems under some conditions. Thus, certain parts of the GPS water vapour record were not reliable enough to be used. It would have been better if the sensor had been installed away from the other antenna. The number of GPS water vapour sensors in the Indian Ocean area was very limited and the quality of the GPS solutions would have benefited from one or two more receivers on Mauritius and possibly one on Rodriguez. An example of GPS measurements processed at 15 minute resolution, using Met Office/University of Nottingham processing suite is shown in figure 5.44.

The sensitivity of both the laser ceilometer and the cloud radar at Vacoas proved inadequate for observing upper ice clouds in tropical conditions. Both systems reported cloud in the lower and middle troposphere, but rarely (ceilometer) and never (cloud radar) at heights above 7 km. This type of instrumentation has rarely been thoroughly tested in the wet conditions encountered in Vacoas. Rain reaching the ground and wetting the cloud radar antenna can decrease the sensitivity by as much as 10 dB. There may have also been problems with ingression of water internally into the radar. Thus, the cloud radar

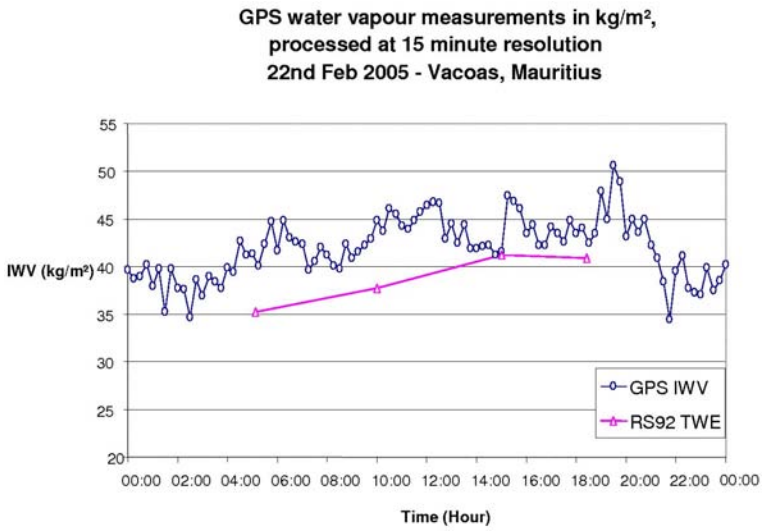


*Figure 5.44.* Example of 24 hours of GPS water vapour measurements processed at 15-minute resolution, Vacoas , Mauritius compared with IWV from Vaisala radiosonde measurements. Time is UT so that the radiosonde ascent just before 16.00 UT was in the dark

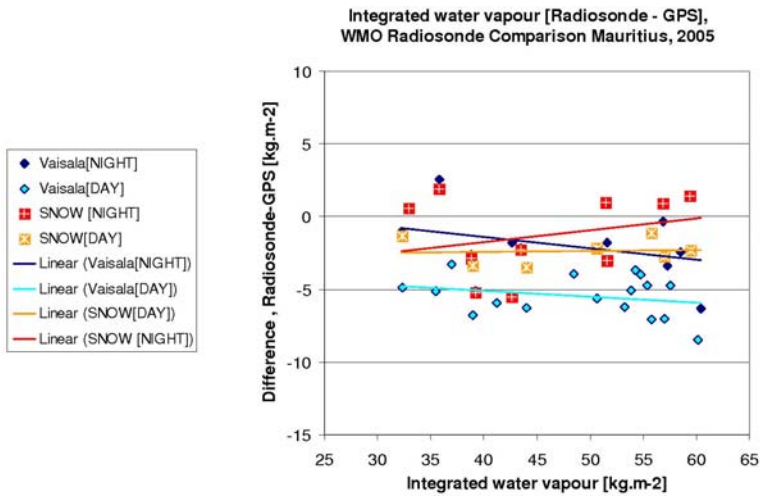


*Figure 5.45.* Results of all daytime and night-time comparisons of integrated water vapour from radiosondes and GPS water vapour (Radiosonde-GPS) for Snow White and Vaisala, WMO Radiosonde Intercomparison Mauritius

measurements in Mauritius were probably less sensitive than the equivalent measurements in the TUC experiment. The CT75K ceilometer may not have been sensitive enough to detect high cirrus clouds especially in daytime.

An example of the different information available from laser ceilometer and cloud radar in the lower troposphere is shown in figures 5.46 to 5.48. Fig-

ure 5.46 shows a time versus height plot of basic laser ceilometer output (signal +noise) from 16 February 2005. Figure 5.47 shows range corrected signal power output from the 78 GHz cloud radar. The cloud radar is extremely sensitive to back scattering from drizzle size drops. In the cloud shown here, the drizzle rate was probably just high enough to feel intermittent drops impacting an observer stood outside. This was towards the edge of a light shower passing over Vacoas, not heavy rain. In figure 5.48, data from the radiosonde test flight at 10.16 UT has been superimposed on the cloud radar plot. The cloud top and base were probably as shown. The three relative humidity measurements on this test flight indicate some fluctuations in relative humidity within the cloud layer. Meisei relative humidity increased with time in the cloud, as chemical contamination started to outgas from the sensor, whereas both Modem and Vaisala relative humidity reduced as the radiosondes moved close to the cloud top. As this was a daytime ascent, it is probable that solar heating started to introduce a negative bias of 2 to 3 per cent in relative humidity for Modem and Vaisala in the upper part of the cloud. However, given the small-scale variability in cloud structure in the horizontal, this conclusion can only be validated if this type of pattern occurred on a large number of daytime ascents through cloud.

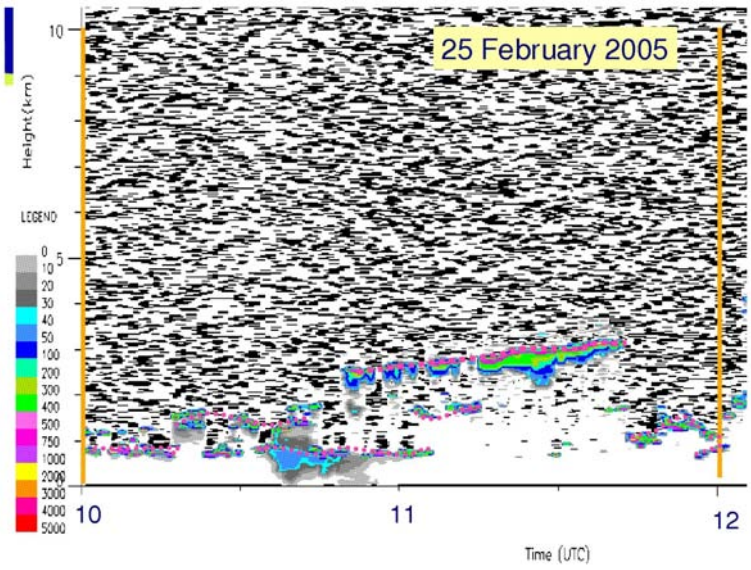


*Figure 5.46.* Time vs. height cross-section, CT75K signal output, dotted and dashed on 25 February 2005, purple lines are for referencing position of ceilometer signals to cloud radar output in figure 5.47

In figure 5.49, GPS water vapour measurements at 15 minute intervals are superimposed on cloud radar measurements for 24 February 2005. Information from the laser ceilometer on cloud base and the lowest level of precipi-

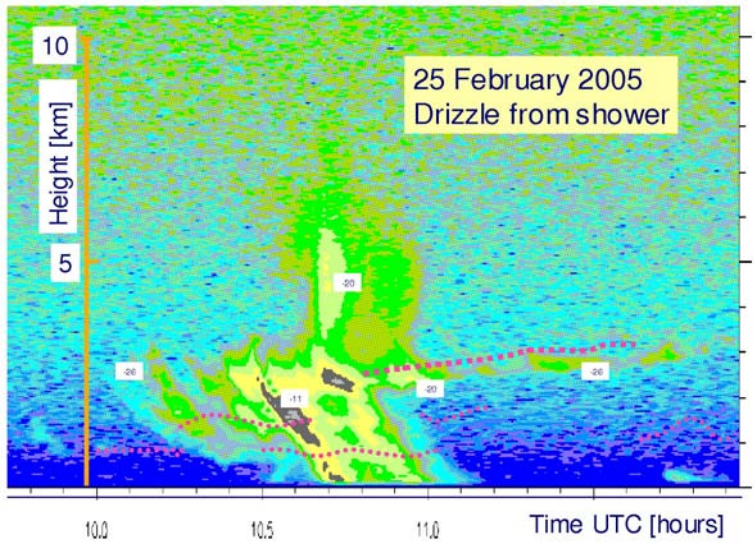


*Figure 5.47.* Time vs. height of range-corrected 78 GHz cloud radar output, backscatter contoured at 3 dB power intervals, absolute values are arbitrary, since the cloud radar appeared to have different sensitivity from earlier tests in Switzerland and UK

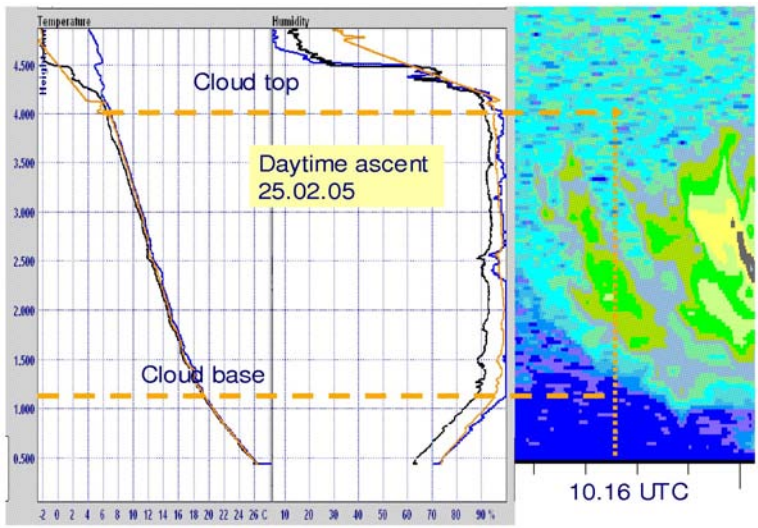


*Figure 5.48.* Relationship between radiosonde test data from flight 67, 10.16 h on 25 February 2005 and cloud radar output

tation falling from the cloud is also plotted. In this example the cloud radar measurements have not been range corrected.

Both cloud radar and ceilometer show precipitation falling from the cloud to the ground for much of the time from a succession of small showers. At around

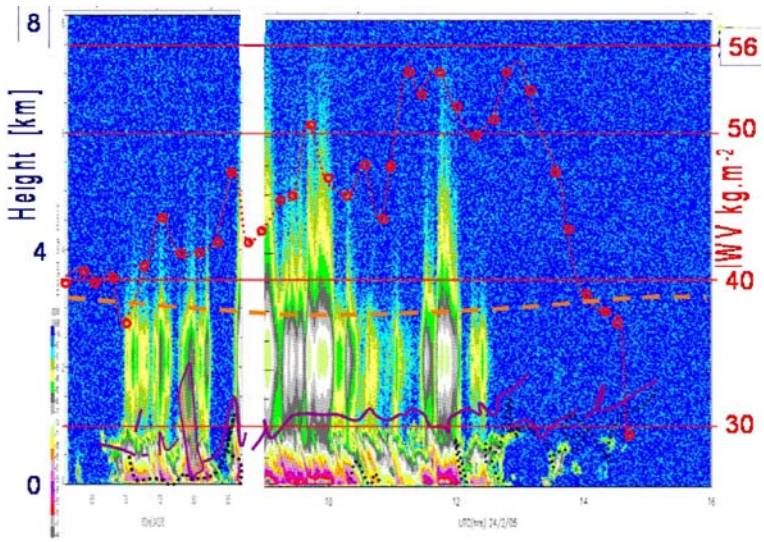


*Figure 5.49.* Integrated water vapour from GPS superimposed on cloud radar measurements on 24 February 2005, showing the water vapour increasing with time during the day until the showers stop in the evening. The solid purple lines are strongest signals from the ceilometer (cloud base); the dotted block lines are the bottom of precipitation falling from the clouds as seen by the laser ceilometer. *Dashed orange line estimated bottom of extremely dry layer from radiosondes which persisted all day*

07.00 UT, the cloud radar sensed the precipitation near the ground earlier than the ceilometer. Drizzle near the ground was probably advected over the cloud radar from an adjacent shower. At other times, e.g. 8.30 UT and 13.00 to 15.00 UT, the cloud radar did not sense low cloud that was detected by the ceilometer. This would be expected if there were very few drizzle size drops in the low cloud.

The dashed orange line in figure 5.49 indicates the bottom of a very dry layer with the position derived from the radiosonde ascents. Thus, in the regions where the cloud radar shows signal extending above this level, the cloud radar signals were likely to be anomalous. This type of artifact where strong signals from showers generate anomalous signals in range gates above the real showers was observed in showery weather in England and in the TUC test in Switzerland.

The cloud radar signals near the ground are very strong relative to any upper signals between 09.00 and 11.00 UT and around 12.00 UT. This led to suspicions that the optics in the cloud radar had become misaligned during shipment.

Figure 5.50 shows the radiosonde test flight results from 10 UT towards the end of the strong cloud radar signals near the surface. All the radiosonde types show that there was a dry layer under the cloud. Near the ground a shallow layer, about 200 m thick, had much higher relative humidity than the layers

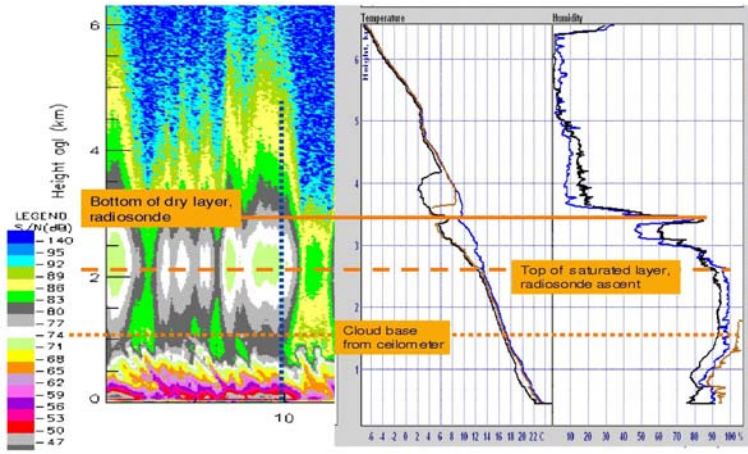


*Figure 5.50.* Radiosonde test flight results from 10.00 h on 25.02.05 superimposed on cloud radar measurement. Radiosondes reporting were Vaisala (blue), Meisei (black) and SRS (brown) but the SRS relative humidity became totally contaminated on entering the cloud and subsequent SRS measurements have been eliminated from the data set

above. This layer corresponded to the levels at which the cloud radar had very strong signals. Thus, the very strong signals in this layer relative to the upper signals were probably correct, with raindrops falling through a dry layer from a cloud higher up enhancing light drizzle near the ground.

When collocated remote sensing and radiosonde measurements were available, potential problems with the radiosondes and with the remote sensing instrumentation could be identified. The combination of the radiosondes and remote sensing gave a very much more comprehensive picture of the upper air conditions above Mauritius, than is usually available from the individual observing systems.

The main success of this first attempt to utilize remote sensing directly in WMO radiosonde tests, was the use of GPS water vapour measurements in identifying day- night differences in radiosonde relative humidity.

## 5.5.3 RADIOSONDE TEST RESULTS RELEVANT TO COST 720

**5.5.3.1 Errors in geopotential height / pressure.** In this section, results from Mauritius relevant to temperature and water vapour profiles in the lower troposphere are discussed.

Firstly, the Intercomparison in Mauritius demonstrated that modern GPS radiosondes provide very reproducible height measurements, from near the surface to heights of 35 km above the ground, see figure 5.51 for the systematic differences. For the lower troposphere the heights of the better radiosonde systems probably fell on average in the range of systematic errors from -10 m to

+10 m Estimates of the reproducibility of the GPS height measurements were in the range 5 to 10 m [1 standard deviation] for the better GPS radiosondes.

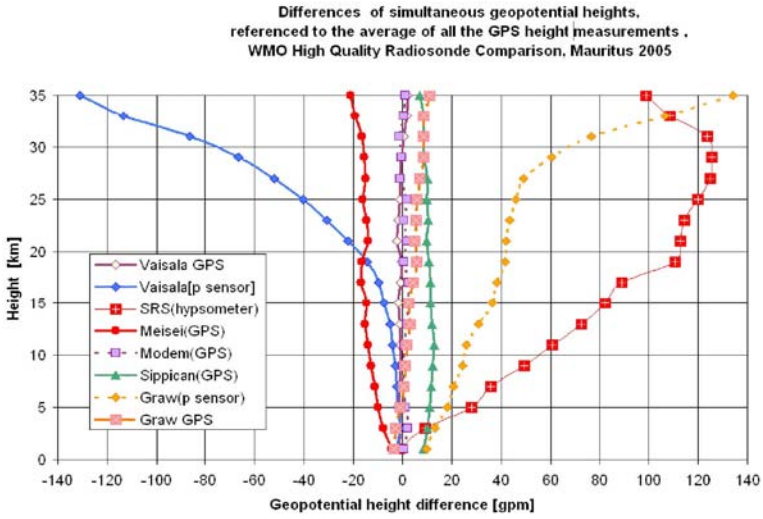


*Figure 5.51.* Systematic difference between geopotential height measurements (gpm), Vaisala, SRS and Graw heights derived from high quality pressure sensors, others from GPS height measurements

These height errors correspond to a range in systematic errors of pressure from + 1 to -1 hPa, with the reproducibility of pressure measurements in the lower troposphere between 0.5 and 1 hPa [1 standard deviation].

**5.5.3.2 Errors from water contamination.** The WMO Intercomparison was performed during the rainy season so that the radiosondes often became wet during the ascents. If the radiosondes passed into dry air after passing through rain/cloud, then the temperature sensors would often disagree by more than $1^oC$, whilst the liquid water evaporated from the sensors, see figure 5.52.

The relative humidity sensors can also become contaminated by liquid water in these conditions and in figure 5.52, most of the radiosondes have indicated cloud top 15 to 20 s later than the true cloud top, i.e. about 100 m higher than the true cloud top. The true cloud top was taken as the level just before the differential cooling of the temperature sensors started.

**5.5.3.3 Errors in temperature and relative humidity measurements.** Systematic differences between all the simultaneous radiosonde temperature measurements in the lower troposphere were small and not greater than $0.3^oC$. The reproducibility of the measurements was in the range 0.1 to $0.2^oC$ [1 standard deviation]. Thus, it might be expected that the absolute accuracy of the temperature measurements was better than or equal to $0.3^oC$, apart from the

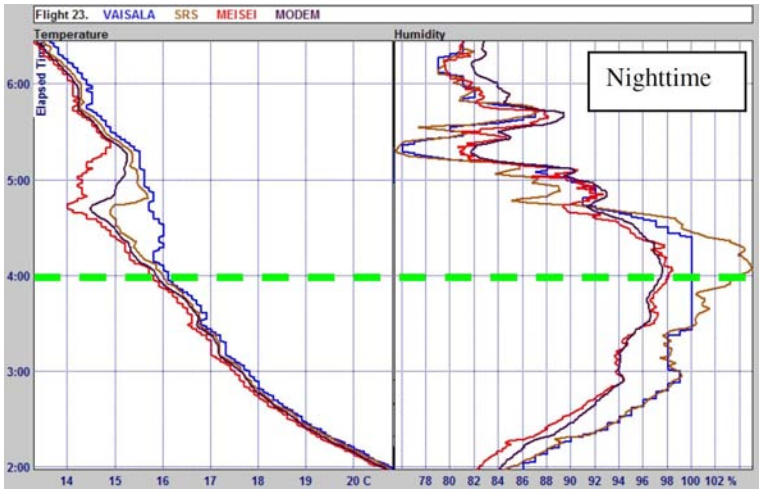


*Figure 5.52.* Detailed second-by-second intercomparison of radiosonde temperature and relative humidity from Flight 23 in the Mauritius intercomparison. The temperature sensors have become wet in passing through the cloud. Then, the temperatures differ above the cloud top (green dashed line) due to the different amounts of water evaporating from the sensors in the drier air above the cloud top

conditions when the sensors were wet. The vertical resolution [2·time constant of response] of the temperature profiles in the lower troposphere would usually be better than 15 m.

The situation with respect to errors in relative humidity in the lower troposphere was more complex, and for COST 720 only the performance of the Vaisala RS92 radiosonde and the Swiss Snow white dewpoint sensor will be considered.

- Daytime and night Snow white water vapour measurements are judged to have little day-night difference in the lower troposphere and also showed similar small day and night differences from simultaneous GPS water vapour measurements, see figure 5.45;

- at night Snow white measurements at high relative humidity showed a positive bias relative to Vaisala-RS92 measurements of 3 per cent. Here, it is possible that the Snow white measurements are too high because the system warms the saturated air to prevent deposition of liquid water around the chilled mirror, and so may give a dewpoint that is higher than truth;

- at night Snow white measurements at low relative humidity [25 per cent] showed a negative bias relative to Vaisala RS92 measurements of 3 per cent. In this case, it is possible that the Vaisala measurements were too high on average because of hysteresis effects in the system;

- in the day time the Snow white measurements were higher than Vaisala by 10 per cent relative humidity at high humidity and 3 per cent at low relative humidity.

The comparisons with GPS water vapour measurements in figure 5.45 confirm that the Vaisala relative relative humidity measurements have a significant negative bias in daytime measurements.

In the lower troposphere, the reproducibility [1 standard deviation] of the relative humidity measurements from these two sensors were close to 2 per cent relative humidity at high relative humidity and 4 per cent relative humidity at about 25 per cent relative humidity.

Thus at night, typical absolute accuracy of both relative humidity sensors was probably better than 4 per cent relative humidity , but the daytime Vaisala measurements were less accurate than this. In situations where solar heating of the relative humidity sensor was significantly smaller than in the tropics, the daytime quality of Vaisala measurements may be closer to the night measurements.

### 5.5.4 LESSONS LEARNED

The main lesson learned in Mauritius was that the remote sensing equipment needed to be established on the site for the intercomparison well before the radiosonde test began. It was too much work for the project team to concentrate on setting up both types of system at the same time. This work requires dedicated specialists to be made available before the test starts.

With the systems established well in advance it also allows anomalies in the remote sensing systems to be identified in advance, so that rectification or supporting experiments to understand limitations can be put in place before the test starts.

In a situation such as in Mauritius where the people supporting the test were not familiar with remote sensing technology, it would also be helpful to provide improved documentation describing how the systems work.

The support received from Mauritius Meteorological Services was invaluable to the scientists working on the test. Thus, Mauritius is to be recommended as a suitable test site for further development of remote sensing in the tropics and subtropics.

## Bibliography

Nash, J., R. Smout, T. Oakley, B. Pathack, and S. Kurnosenko, 2006: WMO Intercomparison of High-Quality Radiosonde Systems, Vacoas, Mauritius, 2-25 February 2005 (2006). WMO IOM Report No. **83**, WMO TD-1303.

Chapter 6

# DATA ASSIMILATION

Hans-Stefan Bauer[1], Matthias Grzeschik[1], and Rossella Ferretti[2]

[1] *University of Hohenheim, Institute of Physics and Meteorology, Hohenheim, Germany*
Stefan.Bauer@physik.uni-hohenheim.de

[2] *University of L/Aquila, L/Aquila, Italy*

## 6.1 INTRODUCTION

Numerical weather prediction depends on an accurate representation of the initial state of the atmosphere. Errors the initial state will be amplified during the simulation and cause large errors in the predicted state (Toth et al., 1997; Hamill et al., 2002, e.g.).

The quality of today's weather forecast is mainly determined by two factors: The quality of the initial conditions and the representation of the physical processes by the model. However, the specification of the initial conditions was, in early days regarded as a cumbersome auxiliary task. The main focus was on the numerical and physical formulation of the model. Today, the situation has changed. Both parts are of the same importance and data assimilation developed into a main research field in meteorology in recent years.

Under the term data assimilation in meteorology, one understands the adjustment of a model run to the real development of the atmosphere, as described by available observations. Thereto, the observations will be assimilated into the model by taking the observed values and their error characteristics into account.

Data assimilation is an integral part of our daily life (Wergen, 2003). When we cross a street, at first we need observations about the approaching vehicles. From that we can determine if the cars are speeding or slowing down. Then we can apply our knowledge about the behaviour of an "average car driver" (our forecast model) to decide whether it is possible or not for us to cross the street without danger. But this process can also fail. Either because our observation or our forecast model ("average car-drivers") are incorrect. Similarly, these are the two most important causes for erroneous weather forecast ( errors in initial conditions or errors in the forecast model).

The size and difficulty of the problem becomes apparent, when the amount of required initial information is calculated. A typical domain for MM5 forecasts has about 200x200 grid points and 36 vertical levels. This number of grid points has to be multiplied by the number of prognostic variables, e.g eight depending on the used physical packages. The model needs therefore about $1 \cdot 10^7$ initial values.

Hence, it is obvious that the number of available observations is by far not sufficient (and will not be in the foreseeable future) to provide all the grid points of the model with the necessary initial conditions. Furthermore, the available observations are very irregularly distributed on the globe with many observations on the Northern Hemisphere continents and nearly no observations over the ocean. Numerical weather prediction is therefore an underdetermined initial value problem. This disparity between required and available information is especially large in limited area models such as MM5 (Grell et al., 1994) used in this project, due to its high temporal and spatial resolution. It is therefore all the more important to use the data of todays and future observing systems in data assimilation to narrow the gap between the available and the needed number of observations, thus improving the initialization of numerical weather prediction models.

So, the first task of an assimilation system is to eliminate this underdetermination with the help of additional information. As first source of information the previous data is used. For temporal extrapolation in data assimilation, the forecast model itself is used, mostly in the form of a short-term forecast from the most recent analysis date. The model equations represent the summarized knowledge about the processes occurring in the atmosphere. The forecast model allows the correlation of different variables and thus a reduction of the degree of under-determination. It is also an important ability of the model to link space and time scales together and from that obtain temporal tendencies of the prognostic variables. The wind and pressure field e.g. have a physical dependency from each other. This allows to close data gaps in regions where no observations are available. In addition, the information from the past can be used for the analysis of the current situation. The assumption of the initial state, provided by the short-term forecast, is called ‟first guess“. When observations exist, the first guess will be corrected. On the other hand, when there are no observations available, the first guess is identical to the final analysis. The second task of the assimilation system is to filter the information relevant for the model initialization out of the available observations. The third task is the interpolation of the observations onto the model grid.

At the end of the assimilation process, a three-dimensional picture of the atmosphere and the surface emerges, the so called analysis. It is used as initial condition for a new weather forecast. It provides the best possible compromise between the new observations and the ‟model history“, is as consistent as possible with the model equations, and is available on the regular model grid.

The second most important tool for data assimilation is the statistics. It is very fundamental for the appraisal of the volume affected by an isolated observation. For instance, a temperature measurement of a weather station is valid not only for that point but also for a certain surrounding area. Statistics helps to improve our knowledge about the structure in the atmosphere which is used to further reduce the degree of under-determination. This knowledge will be summarized in the covariance matrix B of the background error, which is of fundamental importance for every assimilation system.

Statistical methods are furthermore necessary for the current analysis to properly weight both information sources (model and observations) and for data quality control. For every single observation, it must be decided whether it is plausible or better not be used it in the final analysis.

The mesoscale data assimilation problem resembles in many aspects its synoptic-scale counterpart. The same governing equations apply. However, mesoscale models are only integrated over a part of the globe. Hence, correctly formulated lateral boundary conditions are very important to keep the model in balance (Gustafsson et al., 1998). In addition, the smaller time and space scales on the mesoscale require additional data, i.e. high time-resolution data as e.g. from lidars and/or wind profilers (Daley, 1991). Furthermore, the reduced grid size forbids the use of simplifications that can be used on larger scales, as e.g. the geostrophic and hydrostatic approximations.

# 6.2 DATA ASSIMILATION EXPERIMENTS USING LIDAR DATA - 3D VAR RESULTS FROM CASE STUDIES OF LAUNCH-2005

Rossella Ferretti and Claudia Faccani

*University of L'Aquila, L'Aquila, Italy*
✉ rossella.ferretti@aquila.infn.it

Recently, the scientific community put a lot of effort to improve numerical weather forecasts by using standard and new-generation observations e.g. from radar, various satellite sensors or windprofiler (Xiao et al. (2000), De Pondeca and Zou (2001), Liu et al. (2001), and Cucurull et al. (2004)). The most-usual technique is the variational assimilation (1-3 or 4DVAR). Indeed, the variational technique allows to assimilate all kind of data, as long as they can be expressed by model variables. To evaluate the impact of high-density observations, Liu and Rabier (2002) performed a simple one-dimensional study. Their results showed that additional good-quality observations can improve the accuracy of the analysis. They further examined these results using 4DVAR (Liu and Rabier (2003)) and a simulated data set of observations. This investigation confirmed the results of Liu and Rabier (2002). They also studied the impact of the assimilation of a high-vertical-resolution data set. Since the simulated observations were placed on all model levels, the vertical resolution was perfect. To assess the impact of the vertical resolution, they assimilated observations with a lower density in the vertical direction. The results showed that it is necessary to have a balance of observations in vertical and horizontal direction.

The water vapour as recorded by lidar has a very high vertical resolution. Therefore, to respect the condition of the necessary balance between vertical and horizontal resolution, a high-density network of lidars has to be made available. This opportunity was e.g. given by those data which were recorded by the Italian lidar network during LAUNCH-2005 (see section 5.2), which was set up as a regional 'high-resolution' water-vapour network. The water vapour measurements from the lidar have been used now to improve the initial condition (ic) of the MM5 mesoscale model (see below) and some preliminary results of a case study using these data are reported here in terms of an improved IC and its impact on the precipitation forecast.

### 6.2.1 VARIATIONAL ASSIMILATION TECHNIQUE: 3DVAR

Briefly, the variational method is an optimization problem: the three Dimensional Variational Data Assimilation 3DVAR (Courtier et al. (1998), Lorenc et al. (2000)) allows to find the optimal Initial Condition fitting an initial background field, called First Guess, with scattered observations. The best fit is obtained minimizing the so called *Cost Function* $J$, defined as

$$J = J^b + J^o = \frac{1}{2}(x^b - x)^T B^{-1}(x^b - x) + \frac{1}{2}(y^o - H(x^b))^T (F)^{-1}(y^o - H(x^b)) \tag{6.1}$$

where $x^b$ is the background term, $y^o$ is the generic observation, $H(x^b)$ is the corresponding value evaluated by the operator $H$ used to transform the gridded analysis to the observation space. The solution of this equation $x = x^a$ is the *a posteriori* maximum likelihood estimate of the true state of the atmosphere. $B$ and $F$ are the covariance error matrices for the background and the observations respectively.

The 3DVAR used in this study has recently been developed by for the MM5 model Barker et al. (2004). The main characteristics are as follows:

- incremental formulation of the model-space cost function
- quasi-Newtonian minimization algorithm
- geostrophic and cyclostrophic balance

For further details see Barker et al. (2004).

Moreover, a newly developed high resolution background error covariance matrix (Faccani (2005)) is estimated *ad hoc* for these experiments using the NMC-method. This matrix is specifically designed for the Mediterranean area, with a horizontal resolution of 27km.

### 6.2.2 METEOROLOGICAL EVENT

During the LAUNCH campaign the Italian lidar network was operational most of the time. The case analyzed is associated to a cold-air intrusion from N-NE starting on the late afternoon of Sep 30, 2005 and moving south-eastward. The cold and dry tongue is entering from the North in the eastern part of the centre of Italy, and is moving quickly south-eastward. The deep surface low is well in phase with the upper-level cut-off low (figure 6.1a), advecting cool and dry air from NE over central-eastern Italy. The ECMWF analysis clearly shows the tongue of dry air west of Italy (figure 6.1b) at 1800 UT Oct 1, but the WV satellite imagery (figure 6.2) shows the tongue of dry

air already in the east side of Italy at 1800 UT Oct 1, 2005 (the dark band crossing Italy and curling over Greece). The lidar data at most of the stations (UNIRM, UNIAQ, UNINA, and UNIBAS, figure 6.4) recorded the dry air already by 1800 UT (Ferretti et al. (2006)), confirming the wrong location of the dry tongue given by the ECMWF analysis. This meteorological structure caused heavy precipitation both in the North and in the center of Italy as the 12h-accumulated precipitation shows (figure 6.3).

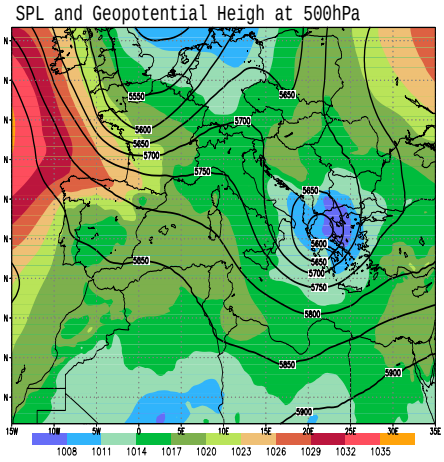


*Figure 6.1a.* Surface pressure and geopotential height in 500 hPa at 1800 UT Oct 1, 2005

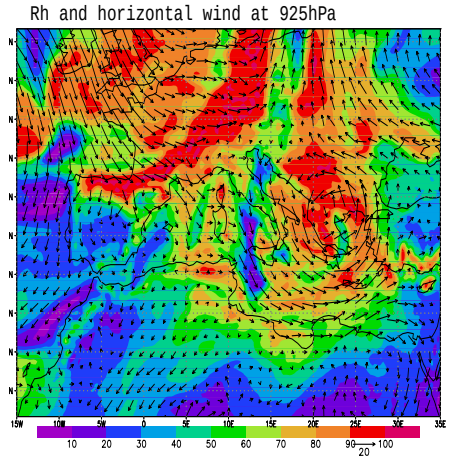


*Figure 6.1b.* Horizontal wind field and relative humidity at 925 hPa on Oct 1, 2005 at 1800 UT

## 6.2.3 MODEL SET UP AND EXPERIMENTS

The MM5 model (Version-3) from PSU/NCAR (Grell et al., 1994; Dudhia, 1993) is used for this study. The MM5 is a non-hydrostatic model at the primitive equations with a sigma terrain following vertical coordinate. The model has multiple-nesting capabilities to enhance the resolution over the area of interest: the configuration is chosen to improve the forecast over central Italy using 3 domains two way-nested (figure 6.4). The mother domain has a grid size of 27 km and it is centered over the Mediterranean region. The grid resolution of domain 2 is 9 km, and the one of domain 3 is 3 km. The model configuration is basically the one used operationally at CETEMPS (http://cetemps.aquila.infn.it): The Troen and Mahrt (1986) planetary boundary-layer (PBL) parametrization is used; an explicit moisture scheme (Reisner et al. (1998)) for all domains is associated to the Fritsch and Kain (1993) cumulus convection parametrization for D1 and D2 only. In ad-

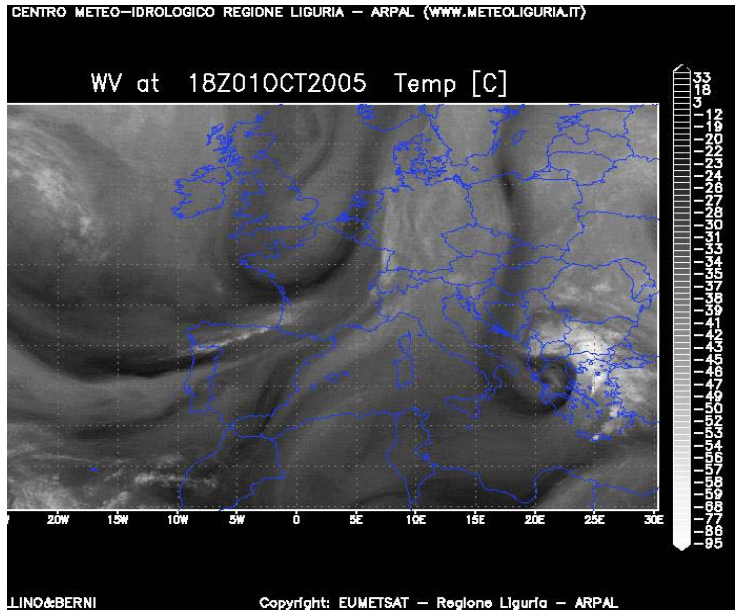


*Figure 6.2.* Water-vapour satellite imagery

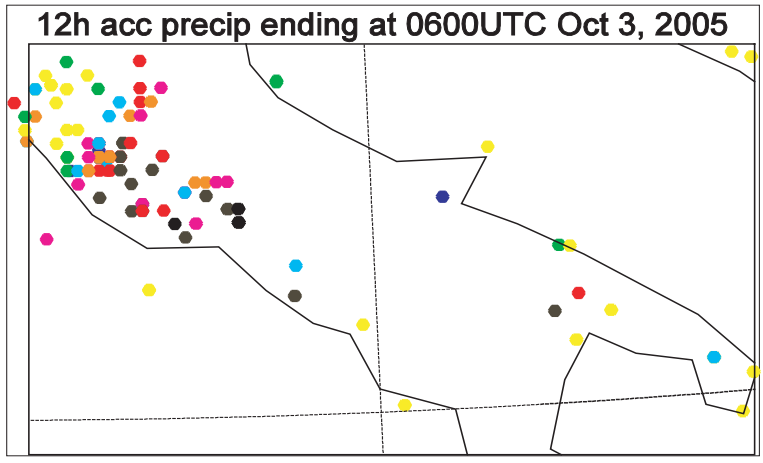


*Figure 6.3.* 12hours accumulated precipitation ending at 0000 UT on October 3, 2005: Black and red colors indicate high precipitation, blue and green colors low precipitation

dition, 29 unequally-spaced vertical sigma levels are used.[1]

[1] 1.00, 0.999, 0.995, 0.99, 0.98, 0.97, 0.96, 0.95, 0.94, 0.93, 0.92, 0.9, 0.85, 0.80, 0.75, 0.70, 0.65, 0.60, 0.55, 0.50, 0.45, 0.40, 0.35, 0.30, 0.25, 0.20, 0.15, 0.10, 0.05, 0.00

The MM5 is initialized using the *European Center for Medium-Range*

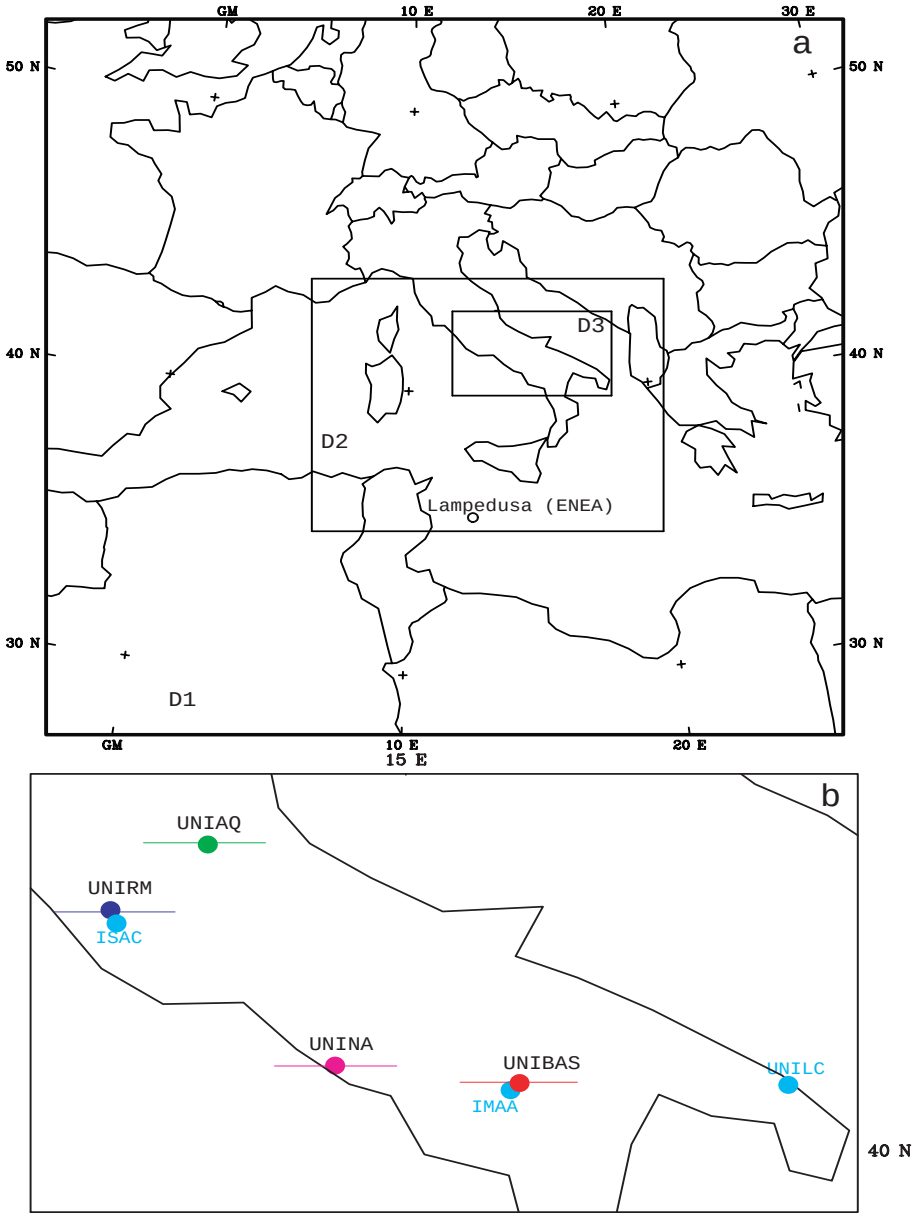


*Figure 6.4.* (top) Model domains: Domain1 at 27 km; domain 2 at 9 km and domain 3 at 3 km. (bottom) Lidar network and cross-sections. The cyan color indicates those stations which were not used for the assimilation

*Weather Forecast* (ECMWF) data analysis and the data assimilation of lidar

data is applied to the ECMWF analysis: the ECMWF analysis, used as if it was a *first guess*, is combined with the high-resolution data from the lidar network, to generate the new mesoscale field for initial condition. Therefore, the following experiments are performed:

(1) A simulation performed without assimilation (CNTR) used as reference

(2) The assimilation of water vapor by 4 Lidar stations (UNIRM, UNIAQ, UNINA, and UNIBAS, figure 6.4) at the start time only by 3DVAR

All the experiments performed are in table 6.4. All the model simulations are initialized using the corresponding ECMWF data analysis on the pressure levels and they all start at 1800 UT Oct 1, 2005 and last for 48 hours.

| *MM5 experiments* | *Assimilation* | *IC* | *stations* |
|---|---|---|---|
| CNTR | no | ECMWF | no |
| 3DVAR | wv | ECMWF+lidar | 4 |

*Table 6.1.* MM5 Experiments

### 6.2.4 RESULTS

The comparison between the model experiments at the start time will allow for evaluating the impact of the assimilation by 3DVAR of the water vapour from lidar. To this aim the investigation of the vertical water-vapour distribution is performed on the high-resolution domain only. The vertical structure is analyzed along the 4 stations used for the assimilation as shown in figure 6.4 (UNIRM,UNIAQ, UNINA, and UNIBAS). The cross-sections (figure 6.5) clearly show the large correction introduced by the assimilation of the water-vapour from lidars around the area of any station. The dry intrusion from east is now clearly visible, reducing the water-vapour content of CNTR (figure 6.5) at UNIRM. The assimilation of UNIAQ produces an increase of water vapour at approximately 600 hPa and a reduction between 700 and 600 hPa. The UNINA site produces a correction of the ECMWF analysis on the sea side, into the right direction slightly increasing the water-vapour content. The UNIBAS clearly produces a tightening of the water-vapour stratification in the lower layers, turning into a dryer atmosphere above 750 hPa. The overall impact of the assimilation of lidar data is a better distribution of the water-vapour content in the free atmosphere and especially in the PBL. The large impact on the water-vapour distribution does not lead to a comparable impact on the precipitation forecast (figure 6.6). This is in agreement with previous studies (Faccani and Ferretti (2005), Ferretti and Faccani (2005)), where a large impact on the IC was found by assimilating surface and upper-air observations, but no remarkable improvement was found on the precipitation forecast. Nevertheless,

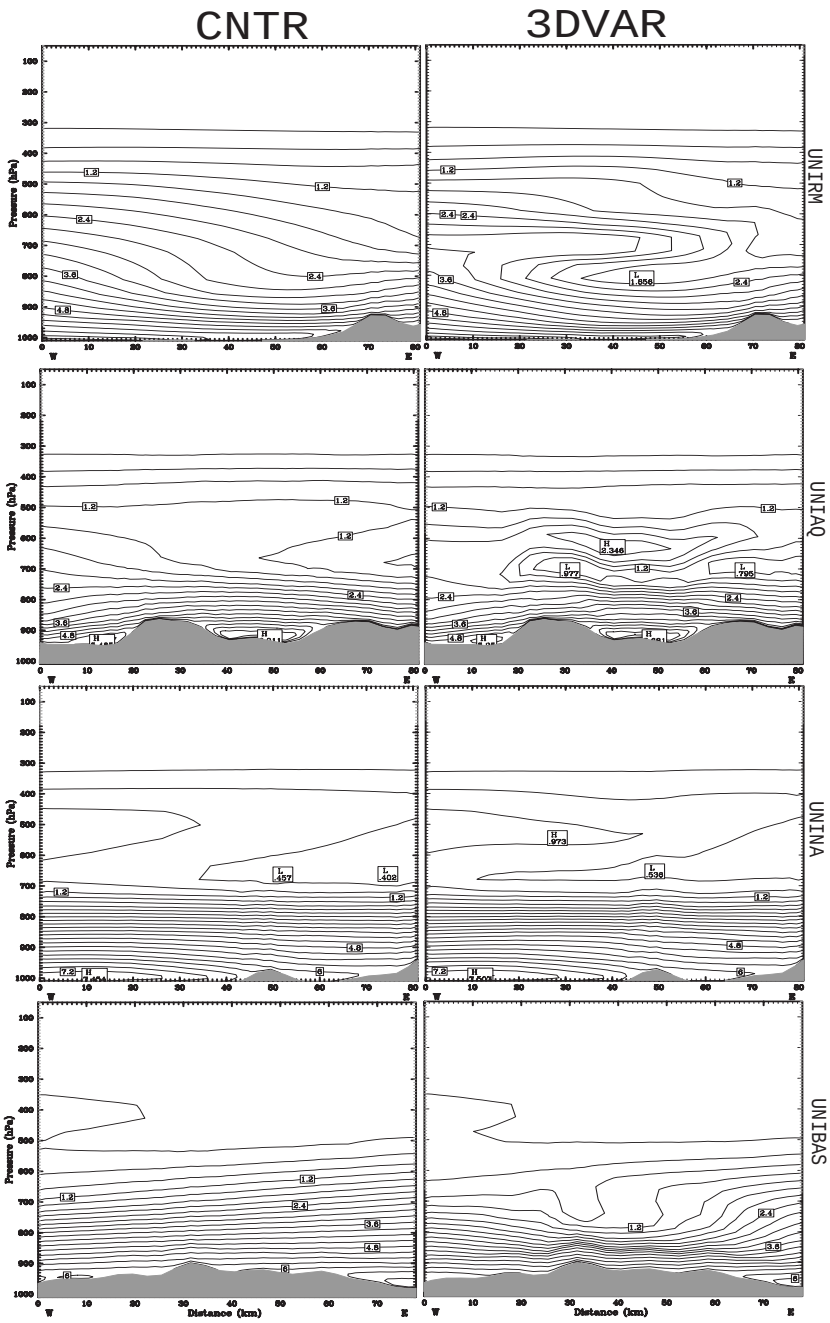


*Figure 6.5.* Water vapor vertical distribution along 4 cross-sections (see figure 6.4)

the assimilation of water-vapour profiles from lidar clearly improves the high-resolution rainfall distribution by separating the precipitating cells (figure 6.6). Also, by reducing the amount of the available moisture it makes the simulation drier. Therefore, a small reduction of the total amount of precipitation is obtained by assimilating the lidar-network data. Hence, although the CNTR run already underestimates the total amount of rainfall (compare figure 6.3 with figure 6.6), this amount of precipitation is even slightly more underestimated when water-vapour lidar profiles are assimilated into the forecast system.

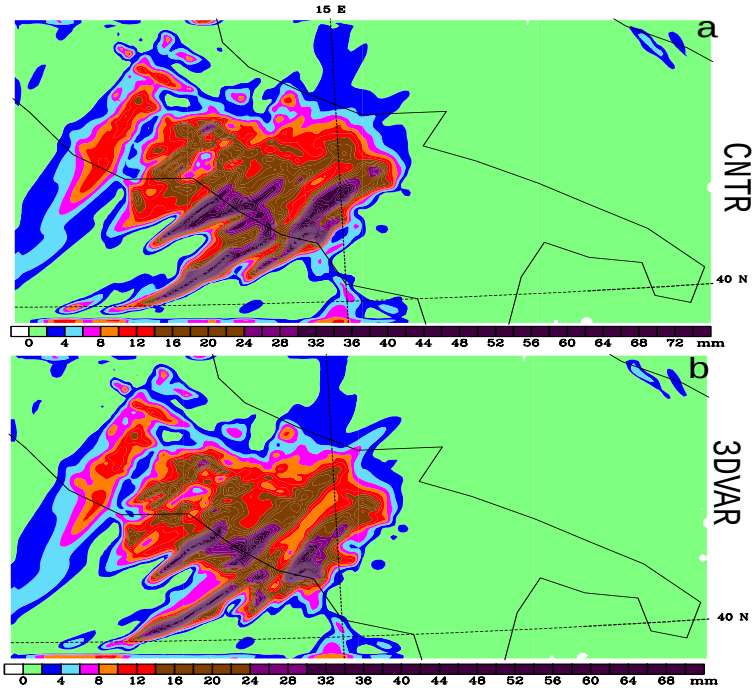


*Figure 6.6.* 12hours accumulated precipitation ending at 0600UTC Oct 3, 2005: a) CNTR,; b) 3DVAR

## 6.2.5 CONCLUSIONS

The impact of the assimilation of profiles from a small network of water-vapour lidar has been evaluated using the 3DVAR technique. The high vertical resolution of the lidar data allows to considerably correct the vertical distribution of tropospheric water vapour as given by ECMWF analysis on the standard pressure levels. This is a remarkable result, because it shows how the lidar measurements enable a considerable improvement of the high-resolution initial fields. Moreover, the assimilation of vertical profiles from water-vapour lidars obviously produces a small impact on the quan-

titative precipitation forecasts, but this result has still to be further investigated.

**Acknowledgments** NCAR is deeply acknowledged for the MM5 model and the 3DVAR algorithm. CETEMPS is acknowledged for supporting this research by computing time.

## Bibliography

Barker, D. M., Y.-R. Guo, A. J. Bourgeois, and W. Huang, 2004: A Three-Dimensional Variational Data Assimilation System for MM5: Implementation and Initial Results. *Mon. Wea. Rev.*, **132**(4)), 897–914.

Courtier P., E. Anderson, W. Heckley, J. Pailleux, D. Vasiljeric, M. Hamrud, A. Hollingsworth, F. Rabier, and M. Fisher, 1998: The ECMWF implementation of three-dimensional variational assimilation (3D-Var). I: Formulation. *Q. J. Roy. Meteorol. Soc.*, **124**, 1783–1807.

Cucurull, L., F. Vandenberghe, D. M. Barker, E. Vilaclara, and A. Rius, 2004: Three-Dimensional Variational Data Assimilation of Ground-Based GPS ZTD and Meteorological Observations during the 14 December 2001 Storm Event over the Western Mediterranean Sea. *Mon. Wea. Rev.*, **132**(3), 749–763.

Daley, R., 1991: *Atmospheric Data Analysis*. Cambridge University Press, 475pp.

De Pondeca, M.S.F.V. and X. Zou, 2001: A case study of the variational assimilation of GPS zenith delay observations into a mesoscale model. *J. Appl. Meteorol.*, **40**, 1559–1576.

Dudhia, J., 1993: A nonhydrostatic version of the Penn-State-NCAR Mesoscale Model: Validation, Tests and simulation of an Atlantic cyclone and cold front. *Mon. Wea. Rev.*, **129**, 1493–1513.

Ferretti R., C. Faccani, M. Cacciani, F. Cardillo, F. Congeduti, C. Cornacchia, K. De Sanctis, F. De Tomasi, P. Di Girolamo, T. Di Iorio, A. di Sarra, G. Fiocco, M. G. Frontoso, M. Iarlori, F. Madonna, D. Meloni, G. Pappalardo, M. R. Perrone, S. Piacentino, G. Pisani, V. Rizi, D. Sabatino, P. Sanò, D. Summa, A. M. Tafuro, X. Wang, 2007: LAUNCH - 2005 Assimilation of LIDAR data from the Italian network: Impact on the high resolution precipitation forecast during the LAUNCH campaign. in preparat. for: *J. Atm. Ocean. Techn.*

Faccani, C., 2005: A high resolution Background error covariance matrix for the 3D-VAR data assimilation system *PhD Thesis*, 2005.

Faccani C. and R. Ferretti, 2005: Data assimilation of high density observations: Part I. Impact on Initial Conditions for the MAP SOP IOP2b. *Q. J. Roy. Meteorol. Soc.*, **131A**, 21–42.

Ferretti R. and C. Faccani, 2005: Data assimilation of high density observations: Part II. Impact on the forecast of the precipitation for the MAP SOP IOP2b. *Q. J. Roy. Meteorol. Soc.*, **131A**, 43–62.

Fritsch, J. and J. Kain: 1993, Convective parametrization for mesoscale models: The Kain-Fritsch scheme. The Representation of Cumulus in Numerical Models. *Meteorol. Monogr.*, **46**, Amer. Meteorol. Soc., 165–177.

Grell, G., J. Dudhia, and D. Stauffer, 1994: A description of the fifth-generation Penn-State/NCAR mesoscale model (MM5). Techn. Rep. NCAR/TN-389+IA, Nat. Cent. for Atm. Res., Boulder/CO, USA.

Gustafsson, N., E. Källén, and S. Thorsteinsson, 1998: Sensitivity of forecast errors to initial and lateral boundary conditions. *Tellus*, **50A**, 167–185.

Hamill, T.and M., Snyder, C., 2002: Using improved background error covariances from an ensemble Kalman filter for adaptive observations. *Mon. Wea. Rev.*, **130**, 1552-1572.

Liu, Z.-Q. and F. Rabier, 2002: The interaction between model resolution, observation resolution and observation density in data assimilation: A one-dimensional study. *Q. J. Roy. Meteorol. Soc.*, **128**, 1367–1386.

Liu, Z.-Q. and F. Rabier, 2003: The potential of high-density observations for numerical weather prediction: A study with simulated observations. *Q. J. Roy. Meteorol. Soc.*, **129**, 3013–3035.

Liu, H., X. Zou, H. Shao, R.A. Anthes, J. C. Chang, J.-H. Tseng and B. Wang, 2001: Impact of 837 GPS/MET bending angle profiles on assimilation and forecast for the period June 20-30, 1995. *J. Geophys. Res.*, **106**, 31771–31786.

Lorenc, A.C., S. P. Ballard, R. S. Bell, N. B. Ingleby, P. L. F. Andrews, D. M. Barker, J. R. Bray, A. M. Clayton, T. Dalby, D. Li, T. J. Payne and F. W. Saunders, 2000: The Met. Office global three-dimensional variational data assimilation scheme. *Q. J. Roy. Meteorol. Soc.*, **126**, 2991–3012.

Reisner, J., R. Rasmussen, and R. Bruintjes, 1998: Explicit forecasting of supercooled liquid water in winter storms using the MM5 mesoscale model. *Q. J. Roy. Meteorol. Soc.*, **124**, 1071–1107.

Toth, Z., E. Kalnay, S. M. Tracton, R. Wobus and J. Irwin, 1997:A synoptic evaluation of the NCEP ensemble. *Weather and Forecasting*,**12**, 140–153.

Troen, I. and L. Mahrt, 1986: A simple model of the atmospheric boundary layer; sensitivity to surface evaporation. *Bound.-Lay. Meteorol.*, **37**, 129–148.

Wergen, W., 2003: Datenassimilation - Ein Überblick. *Promet*, **27**(3/4), 142–149.

Xiao, Q., X. Zou and Y.-H. Kuo, 2000: Incorporating the SSM/I-derived precipitable water and rainfall rate into a numerical model: A case study for the ERICA IOP-4 cyclone. *Mon. Wea. Rev.*, **128**, 87–108.

# 6.3 4DVAR RESULTS FROM CASE STUDIES OF LAUNCH-2005

Hans-Stefan Bauer and Matthias Grzeschik

*University of Hohenheim, Institute of Physics and Meteorology, Hohenheim, Germany*
Stefan.Bauer@physik.uni-hohenheim.de

## 6.3.1 THE 4DVAR METHOD FOR LAUNCH-2005

During the last decades, more and more complex assimilation techniques have been developed. However, even the most complicated technique can not replace observations. It only contributes to the optimal use of the available observations. A detailed introduction into data assimilation methods is given in Bouttier and Courtier (1999).

Here, the variational method, more specific, 4DVAR is used for the assimilation. The variational method was developed in the 70th. The problem of data assimilation is considered as a minimization task of the variation calculus, which in similar form can be formulated for 1-, 3-, and 4- dimensional analysis. The basis of this assimilation is the definition of a cost-function, which quantifies the differences of measured data to the model solution. The special solution is searched which leads to a minimum value of the cost function. An important advantage of the variational method is that it allows complicated associations between the observed and analysed variables, which is necessary for the increasingly important remote sensing data.

In variational data assimilation a so-called assimilation window is defined. It represents the time window from which the observations are used to create the analysis for the next forecast. In the different types of variational assimilation the observations are differently used in space and time (e.g. 3DVAR and 4DVAR).

In 3DVAR the whole 3D distribution of observations is to taken into account. However, as compared to 4DVAR, the temporal variation of the variables within the assimilation window is neglected by merging all observations within the assimilation window as collected at one fixed time. This makes the 3DVAR computationally much cheaper than 4DVAR, maintaining the advantages of the variational technique mentioned above. However, for data of a high temporal resolution, much information is lost due to the neglection of the differences of observation times. In an attempt to cope with this problem, versions of 3DVAR exist which are more adapted to temporally high-resolution data (e.g. 3DVAR FGAT as used in WRF (Barker et al., 2004; Wu et al., 2003). Another way to reduce the loss of information is to use shorter assimilation windows. The investigation of these methods and the search for the

"happy optimum" between accuracy and computational demands is still part of ongoing investigations.

3DVAR is the logical first step on the way to develop a 4DVAR system, since all of the techniques used in 3DVAR are also necessary in 4DVAR. Furthermore, there are many ways to improve variational assimilation systems in addition to including the varying time dimension in 4DVAR. This includes a better description of background and observation errors, and improved balance constraints. A large part of the recent developments focuses on a better determination of the covariance matrix **B** of the background errors, which mainly determines, how information of an isolated observation are vertically and horizontally distributed.

The essential difference between 4DVAR and 3DVAR is that the measured data must no longer be made on prescribed moments in time. For modern observing system as lidar, this is important since they observe in very high temporal resolution. Then the solution for one observing system is searched for which the following cost-function gives a minimum value in the data assimilation window.

$$J(\vec{x}) = (\vec{x}-\vec{x}_b)^T \mathbf{B}^{-1}(\vec{x}-\vec{x}_b) + \sum_{i=0}^{n} [\vec{y}_i - \mathbf{H}_i(\vec{x}_i)]^T \mathbf{R}_i^{-1} [\vec{y}_i - \mathbf{H}_i(\vec{x}_i) \ \ ,] \qquad (6.2)$$

where $\vec{x}$ and $\vec{x}_b$ are the state vectors of the model and background field variables, respectively. **B** is the background error covariance matrix. $\vec{y}_i$ are the observations and $\vec{x}_i$ the model forecasts both valid at times i. $\mathbf{H}_i$ is the corresponding model forward operator and $\mathbf{R}_i$ is the observation error covariance matrix.

During one assimilation cycle only data from the assimilation window is accepted to correct the initial state. Figure 6.7 shows an optimization step in this 4DVAR procedure.

Due to the complexity of the problem, it is not possible to do the minimization analytically. Therefore, the solution can be derived with iterative mathematical minimization methods. This generally requires the gradient of the function to be minimized in terms of the control variables (here the prognostic variables X (T,u,v, ...)). In order to calculate the gradient of the cost-function, the so-called adjoint model approach was developed in the mid 80th. The advantages of adjoint models compared to other methods of gradient calculation are the higher accuracy and the short calculation time. If we carry out one model run with the method of finite difference to calculate every component of the gradient, one model forecast is necessary for each parameter, resulting in $10^6$ to $10^7$ necessary forecast. On the other hand, one run of the adjoint model is enough for the calculation of the whole gradient.

On the basis of the calculated gradients, a direction is determined in every iteration step through the minimization method to search for the new initial value for which the cost-function provides a smaller value. The search will be continued until an adequately small value is reached.

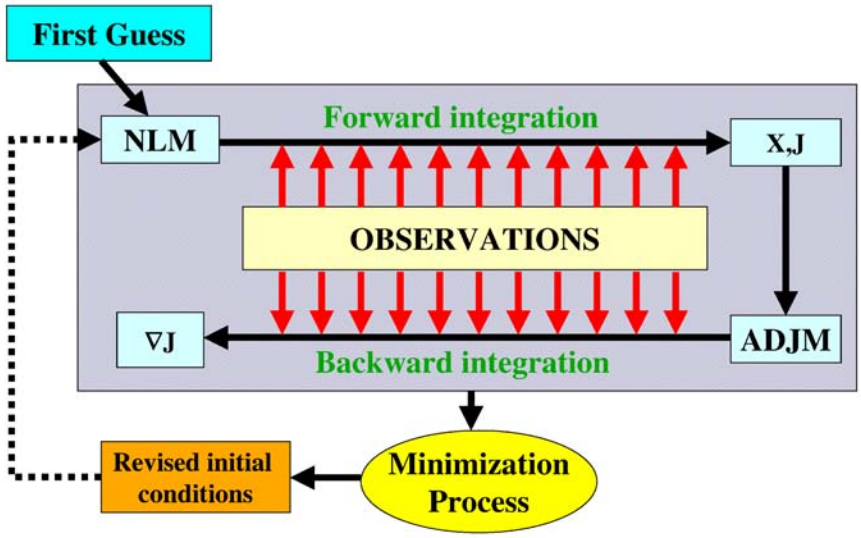


*Figure 6.7.* Steps to work through during 1 iteration of the 4DVAR (Image Source: Zupanski and Park (2003)). The observations are used to calculate the cost function $J$. Afterwards the adjoint model uses the observations again to calculate the gradient of the cost function $\nabla J$. Afterwards the minimization is checked and the cycle is repeated when the cost value is too large.

## 6.3.2 INTRODUCTION TO MM5 AND ITS 4DVAR SYSTEM

**6.3.2.1 The mesoscale model MM5.** The model used for the assimilation experiments is the PSU/NCAR mesoscale model (MM5). It is a limited-area, nonhydrostatic, terrain-following sigma-coordinate model designed to simulate or predict mesoscale and regional-scale atmospheric circulations. It has been developed at Penn State and NCAR as a community mesoscale model and is continuously being improved by contributions from users at several universities and national laboratories.

The Fifth-Generation NCAR / Penn State Mesoscale Model (MM5) is the latest in a series that developed from a mesoscale model used by Anthes at Penn State in the early 70's that was later documented by Anthes and Warner (1978). Since that time, it has undergone many changes designed to broaden its usage. These include

- a multiple-nest capability (1-way, 2-way, moving nests)
- nonhydrostatic dynamics, which allows the model to be used at a few-kilometer scale
- multitasking capability on shared- and distributed-memory machines

- different methods for data assimilation (3DVAR, 4DVAR, and FDDA)
- various physics options of different complexity

The model is supported by several auxiliary programs, which are referred to collectively as the MM5 modeling system. Terrestrial and isobaric meteorological data are horizontally interpolated (programs TERRAIN and REGRID) from a latitude-longitude mesh to a variable high-resolution domain on either a Mercator, Lambert conformal, or polar stereographic projection. Since the interpolation does not provide mesoscale details, the interpolated data may be enhanced (program little_r) with observations from the standard network of surface and rawinsonde stations using either a successive-scan *Cressman* technique or a *multi-quadratic* scheme. Finally, the program INTERPF performs the vertical interpolation from pressure levels to the sigma coordinate system of MM5 resulting in the initial files necessary to start the model simulation. Sigma surfaces near the ground closely follow the terrain, while the higher-level sigma surfaces tend to approximate isobaric surfaces. Since the vertical and horizontal resolution and domain size are variable, the modelling package programs employ parameterized dimensions requiring a variable amount of core memory. Some peripheral storage devices are also used.

Since MM5 is a regional model, it requires an initial condition as well as lateral boundary conditions to run. To produce lateral boundary conditions for a model run, one needs gridded data to cover the entire time period for which the model is integrated. For our experiments the ECMWF analysis provides the necessary data.

The MM5 model has been chosen for data assimilation, as it provides convenient tools for ingesting measurements of different observation systems, which is a good starting point for lidar data assimilation. An overview of the MM5 model is given in Grell et al. (1994). The different data assimilation schemes are described in Barker et al. (2004) (3DVAR), Ruggiero et al. (2001) (4DVAR), and Stauffer and Seaman (1994) (FDDA). We started with 4DVAR, as we expected here the major impact of a data assimilation effort. 4DVAR takes advantage of the high temporal and spatial resolution of ground-based Raman lidar data. This is particularly important in regions with high spatial/temporal variability in the water-vapour field such as near frontal boundaries. 4DVAR considers in a reasonable way the error characteristics of each instrument. Additionally, this continuous data assimilation technique considers the physics of the atmospheric processes while minimizing the cost function.

In its current release the MM5 4D-VAR data assimilation system only offers diagonal background error covariance matrices **B**. This approximation, however, has proven to work well for most studies conducted with the system (Zou et al., 1995; Xiao et al., 2000). This can probably be explained by the ability of 4D-VAR systems to generate physically consistent structure functions as the model integration goes on. The specification of **B** at the initial time seems therefore not crucial. For each control variable, the background error

variances (diagonal elements of the matrix) were specified by constructing the differences between the 3-hour forecasted and the initial values at each grid point. At each vertical level, the maximal value of the differences is found and assigned to all grid points on that level. This creates a vertical profile of forecast errors valid at all geographical locations of the model. The forecast errors are then squared to produce the diagonal elements of the background error covariance matrix.

The system was used in a recent study by Wulfmeyer et al. (2006) to assimilate data of airborne DIAL measurements on a convectively active day during the IHOP_2002 field campaign. The assimilation study shows that the inclusion of the water vapour profiles in a 3 hour assimilation window clearly improves the prediction of precipitation. As in the raman lidar study described here, the changes in the water vapour field remain in the forecast even hours after the end of the assimilation window.

### 6.3.3 ASSIMILATION EXPERIMENTS DURING LAUNCH-2005

**6.3.3.1 Observing systems used for the assimilaton.** For the assimilation experiments presented here only the data from 4 ground based Raman lidar stations were used. All systems sensed the atmosphere in a vertically pointing mode using different vertical resolutions and averaging times. The stations used were Lindenberg, Leipzig, Ziegendorf, and Potenza shown in figure 6.10. Apart from the Potenza site, where temperature and water vapour-mixing ratio were used for the assimilation, only water-vapour mixing ratio is assimilated. Since the Raman lidar observations took place during night, the time window used for the assimilation was chosen from 23 UT on Oct 26th to 02 UT on 27th of October 2005. The observations and observational errors of all stations were provided to the LAUNCH ftp server in an agreed NetCDF format. The first step necessary to use the data sets is a pre-processing, so that the MM5 4DVAR system is able to use them. During the assimilation, the available radiosonde operator function determined the observational part of the cost function.

The Raman Lidar sites provided observations of water-vapour mixing ratio and temperature, which are at the same time the prognostic variables used in MM5. Therefore, no transformations using additional assumptions were necessary, and the observations can directly be ingested in the existing radiosonde operator function. However, the averaging times to reduce noise were different for the different data sets. From the Lindenberg site e.g., one profile every 10 minutes was available while Leipzig used an averaging time of 30 minutes. Table 6.2 summarizes the temporal and vertical resolutions of the different lidar systems used for the assimilation. Figure 6.8 shows the development of the cost function as a function of the iteration number.

| Lidar system | Vertical resolution [m] | Temporal resolution [min] |
|---|---|---|
| RAMSES (Lindenberg) | 8 | 10 |
| Leipzig | 60 | 30 |
| Ziegendorf | 60 | 30 |
| Potenza (water vapour) | 30 | 10 |
| Potenza (temperature) | 30 | 10 |

*Table 6.2.* Vertical and temporal resolutions of the lidar systems used for the assimilation

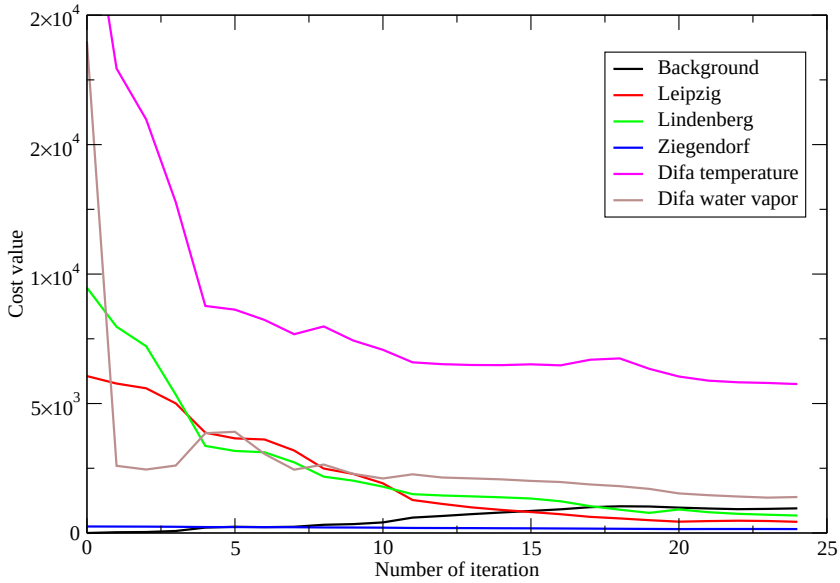


*Figure 6.8.* Development of the cost function for the different observations during the course of the minimization.

**6.3.3.2 Experimental setup.** The lidar data preprocessor and MM5 4D-VAR software were installed on the NEC supercomputer of the German Climate Computing Center (DKRZ) in Hamburg. So far, the minimization was carried out on one CPU only, since the parallelization technique used does not work well with the 4DVAR, yet.

The assimilation experiments split up into two major steps. First the assimilation is done using a coarse horizontal resolution and simplified physics. The two restrictions are necessary for the following reasons. The 4DVAR system needs a tremendous computational effort which is mostly consumed by the adjoint runs to determine the gradient of the cost function. To allow a sufficient number of iterations for determination of the minimum of the cost function, re-

| Physical process | Assimilation | Forecasts 27, 9, and 3 km | Forecasts 1 km |
|---|---|---|---|
| Radiation | simple | RRTM LW / Dudhia SW | RRTM LW / Dudhia SW |
| Convection | Kuo | Khain Fritsch 2 | no parameterization |
| Shallow convection | no | no | no |
| Boundary Layer | MRF | MRF | MRF |
| Cloud microphysics | simple | Reisner 2 | Reisner 2 |
| Land surface | | 5-layer soil model | 5-layer soil model |

*Table 6.3.* Parameterization schemes used for the assimilation run as well as the free forecasts using the different horizontal resolutions.

strictions in the horizontal resolution used are necessary to reduce the computation time. The restriction to a simplified physical package is necessary since adjoint versions of the parameterizations are necessary for 4DVAR, which are only available for the simplest ones. For our assimilation run, a horizontal resolution of 27 km is used in a model domain with 82 x 74 grid points and 36 vertical levels. Result of the assimilation is an optimal initial condition at the beginning of the assimilation window in the course model domain.

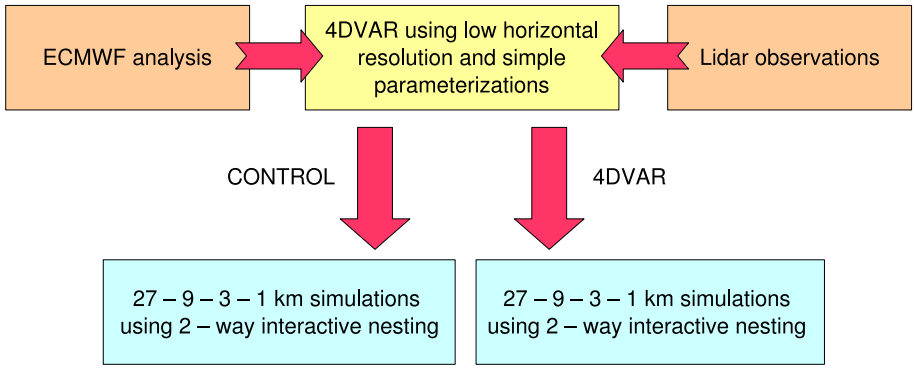


*Figure 6.9.* Schematic illustrating the experimental setup

Subsequently, free forecasts in 7 different domains are done in a 2-way interactive nesting mode using most sophisticated parameterizations available, and horizontal resolutions from 27 km down to 1 km. The forecasts started from initial conditions only created with ECMWF analysis data (CONTROL) and from initial conditions crated from ECMWF analysis data and optimized by 4DVAR of the lidar data. Table 6.3 summarizes the used physical parameterizations for the assimilation run as well as for the free forecasts in the different model domains, figure 6.9 summarizes the experimental setup, and figure 6.10 shows the domain configurations for the experiments.

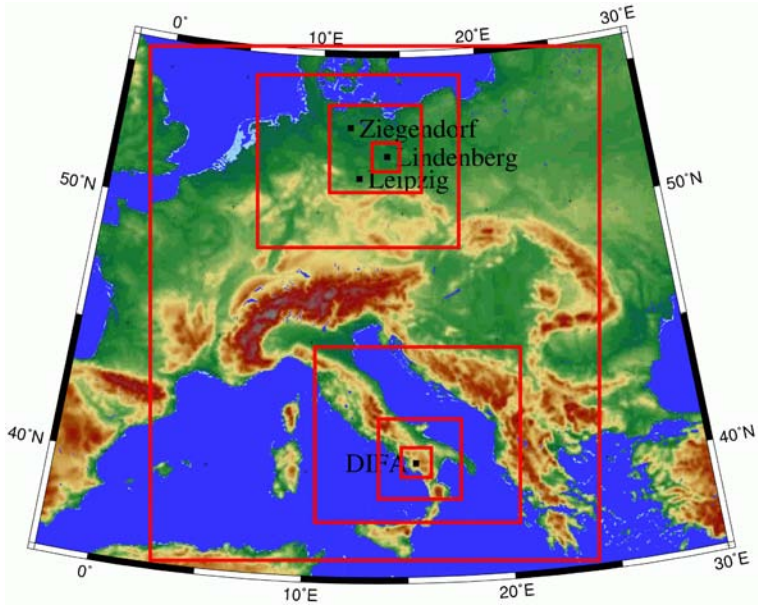


*Figure 6.10.* Map showing observational sites and the MM5 domain configuration. The assimilation is done in the large domain. Afterwards refinement is done into the two smaller regions with 2-way nesting down to a horizontal resolution of 1 km

The German domain refines to eastern Germany and contains the three sites Lindenberg, Leipzig, and Ziegendorf. The Italian domain, on the other hand, refines to southern Italy to contain the Potenza site. The following section shows first comparisons of the assimilated and non-assimilated forecasts for the coarse resolution domain, and vertical cross sections for the Lindenberg and Potenza sites extracted from the high-resolution 1 km simulations. More detailed comparisons also of the high resolution domains are planned for the future.

**6.3.3.3 Results IOP-7 (October 26-27, 2005).** Figure 6.11 shows the surface analysis map provided by the German Weather Service at 00Z, 27th October, 2005. Figure 6.12 shows the MSG (Meteosat-8) visible satellite image from 12Z, 27th October, 2005. It is clearly seen, that the synoptic situation is quite different in the two refinement regions in Eastern Germany and Southern Italy. While the region centering around Lindenberg resides in the cold air following a cyclone moving from eastern Poland to the east, the Italian region is influences by a weak high pressure system and only small pressure gradients. Therefore, it is expected that a signal induced by the lidar data assimilation is transported over longer distances from the sites located in Eastern Germany as compared to the measurements at the Potenza site. Figure 6.13 shows for the initial state (beginning of the assimilation window) 23Z, 26 October 2005 dif-

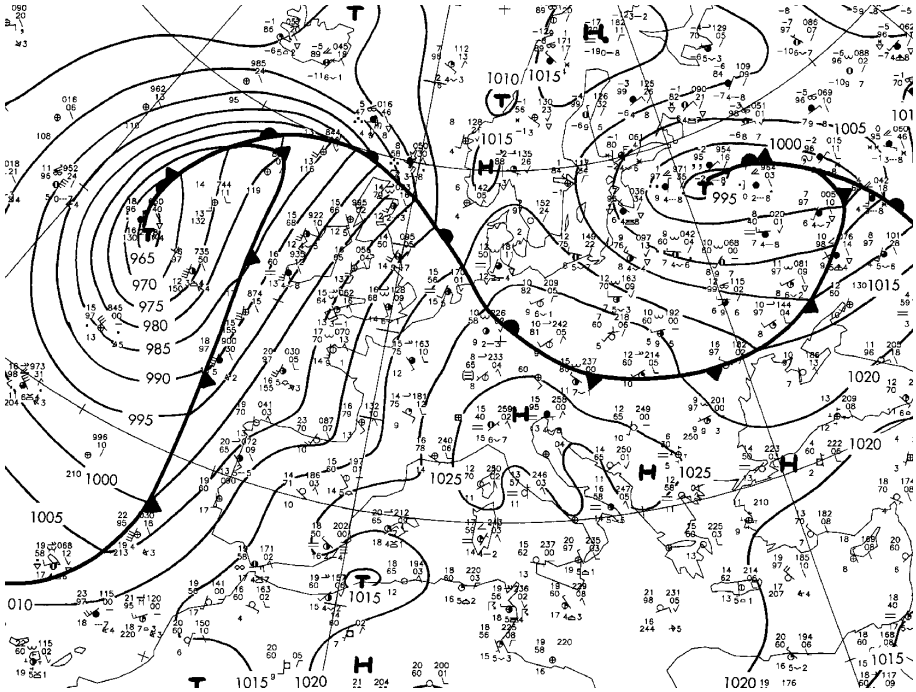


*Figure 6.11.* Surface analysis provided by the German Weather Service at 00Z, 27th of October 2005

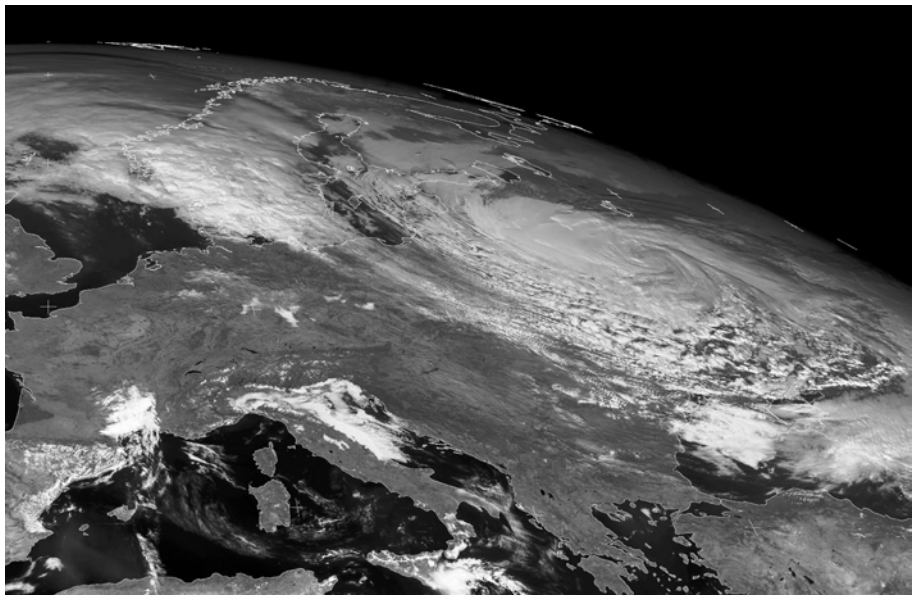

*Figure 6.12.* Visible satellite image of MSG (Meteosat 8) at 12Z, 27th October, 2005

ferences in the water vapour mixing ratio for different levels in the troposphere below 500 hPa. This is the only time step that is changed by the 4DVAR. As expectec changes are introduced to the atmospheric state nearby the measurement sites. Since data of 3 distributed stations were assimilated in Eastern Germany, a larger region is influenced here. In addition, the stronger circulation on the rear side of the cyclone over eastern Poland and western Russia expands the region influenced by the observations.

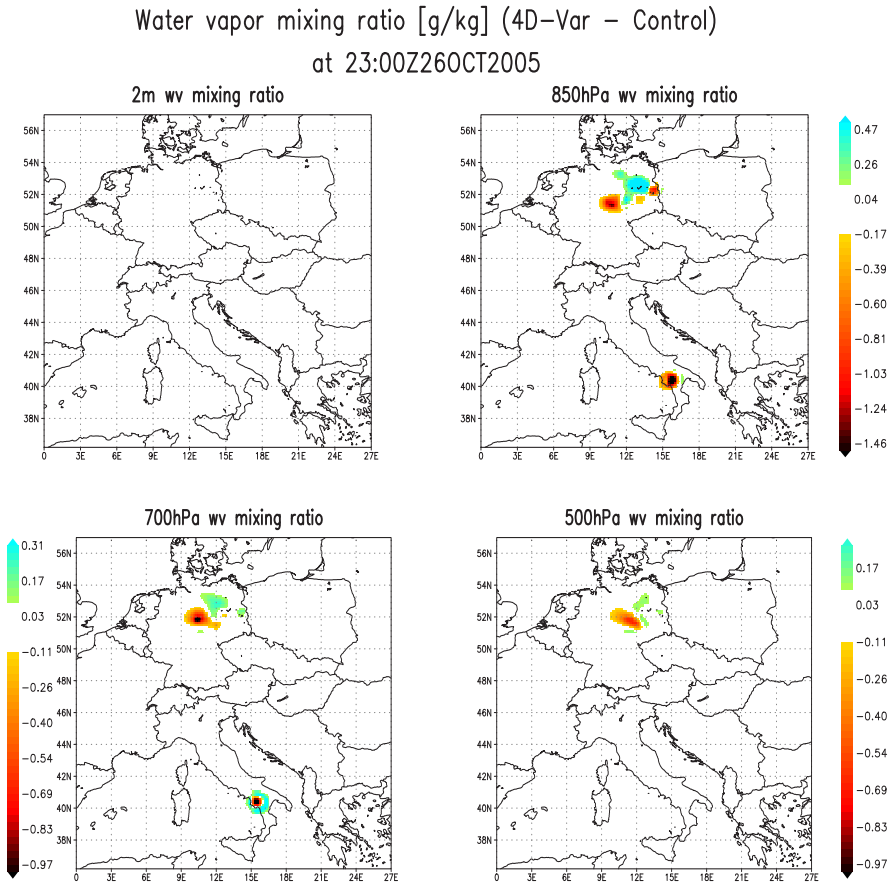


*Figure 6.13.* Difference of water-vapour mixing ratio [g/kg] (4DVAR − CONTROL) for different levels of the troposphere at the beginning of the assimilation window

The tendency is clearly seen that strongest changes are introduced at the 850-hPa level, roughly corresponding to the top of the boundary layer. The surface layer is not influenced at the beginning of the assimilation window, since the 4D-Var only changes the model levels, and not the diagnosed 2-m fields. Furthermore, no lidar observations are available in the lowest few hundred meters for technical reasons.

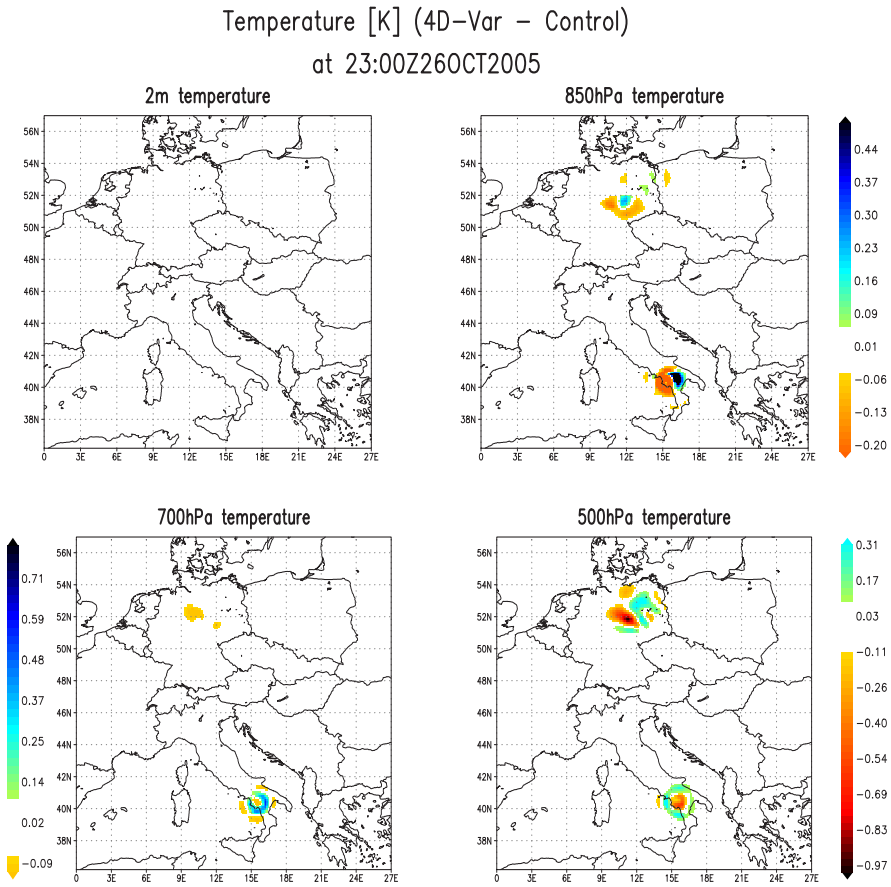


*Figure 6.14.* Same as figure 6.13, but for temperature differences (in K)

Another point influencing the area affected by the assimilation is the synoptic situation. This also determines the vertical spread of the region of influence. In the cold air behind the cold front in eastern Germany much stronger vertical mixing is present as compared to the high pressure influenced Italian region. Therefore, higher levels of the troposphere are influenced in Eastern Germany and the 500-hPa level is not influenced in Italy.

Figure 6.14 shows the temperature difference at the same time for the same levels. Again, no changes are introduced into the near-surface field. Here, the temperature field is more strongly influenced in the Italian region. This is not surprising since the Raman lidar at Potenza also provides temperature profiles for the assimilation. However, even in Eastern Germany, where only water vapour mixing ratio profiles are assimilated, changes are introduced into the temperature field, especially at higher levels in the troposphere. This nicely

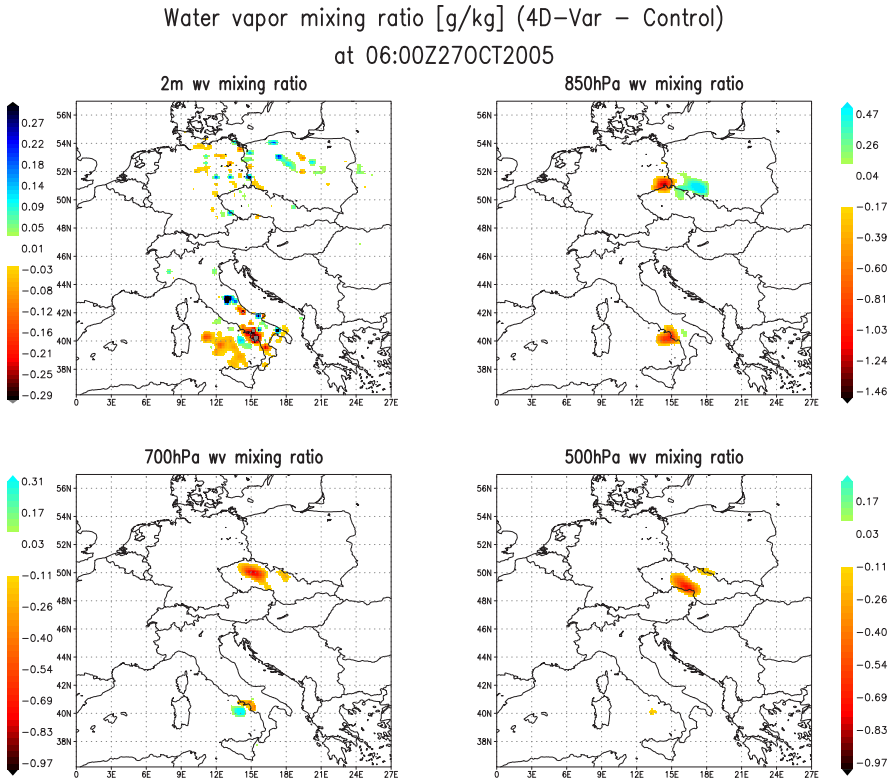


*Figure 6.15.* Difference of water-vapour mixing ratio [g/kg] (4DVAR − CONTROL) for different levels of the troposphere 4 hours after the end of the assimilation window

illustrates the dynamical coupling of the humidity and temperature fields in the assimilation system.

The next sequence of plots shows the same differences at the same levels, but 4 hours after the end of the assimilation window, corresponding to a 7-hour forecast. Figure 6.15 shows the differences in the water vapour field, whereas figure 6.16 shows the differences for the temperature.

A clear transport of the region influenced by the assimilation corresponding to the synoptic situation is seen. The region changed by the assimilation of the eastern Germay lidar sites Lindenberg, Leipzig, and Ziegendorf is transported to the southeast, the more the higher in the troposphere due to increasing wind speeds with height in the strong north-westerly flow behind the cold front of the cyclone.

On the other hand, the changes are restricted to lower levels and the horizontal spread is much smaller in the Italian region which is influenced by a weak high pressure system.

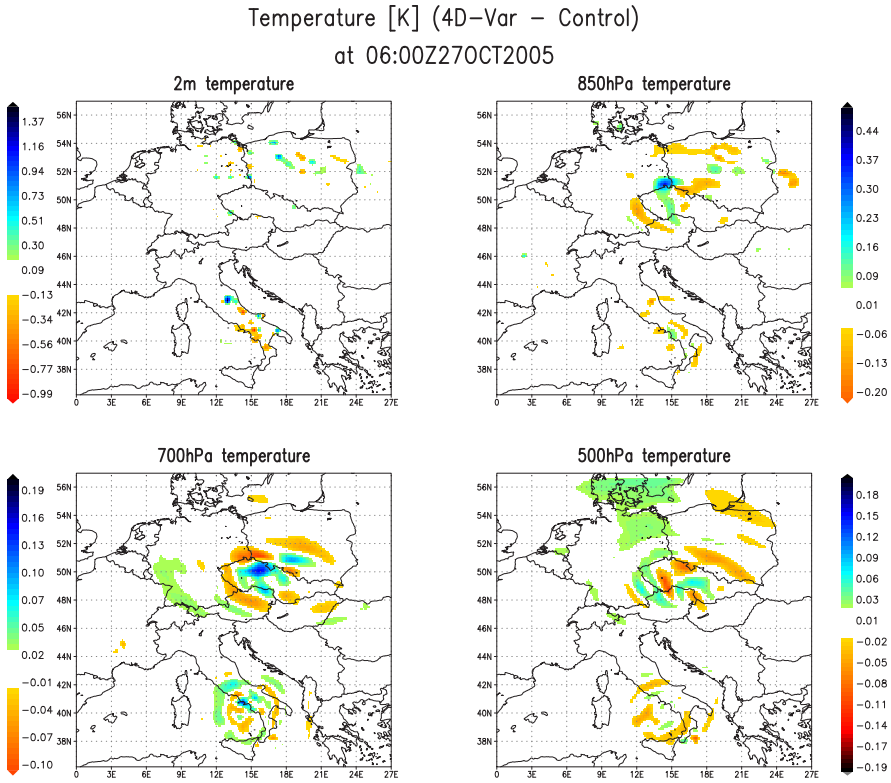


*Figure 6.16.* Same as figure 6.15, but for temperature differences

The temperature differences, shown in figure 6.16, indicate a larger spread of the information in the temperature field. However, on the other hand, the changes are relatively small and are removed much faster than it is the case for the water vapour field.

Figures 6.17 show vertical cross sections of the water-vapour mixing ration over time for the Lindenberg and Potenza sites. The differences shown so far were from the coarse 27-km domain. The cross sections, on the other hand, were extracted from the high resolution 1-km domains. On each plot the top panel is the lidar observation, the middle panel a MM5 forecast initialized only with the ECMWF analysis, and the bottom panel a MM5 forecast initialized by ECMWF and optimized by 4DVAR.

For the Lindenberg site it is nicely seen, that the forecast initialized with ECMWF only cannot reproduce the observed small-scale structure in the lower troposphere. Apart from that, the forecast is quite good, since ECMWF already provides a good background field. The forecast, initialized with ECMWF and 4DVAR of the lidar observations show much more of the small-scale structure, namely the observed dry layers.

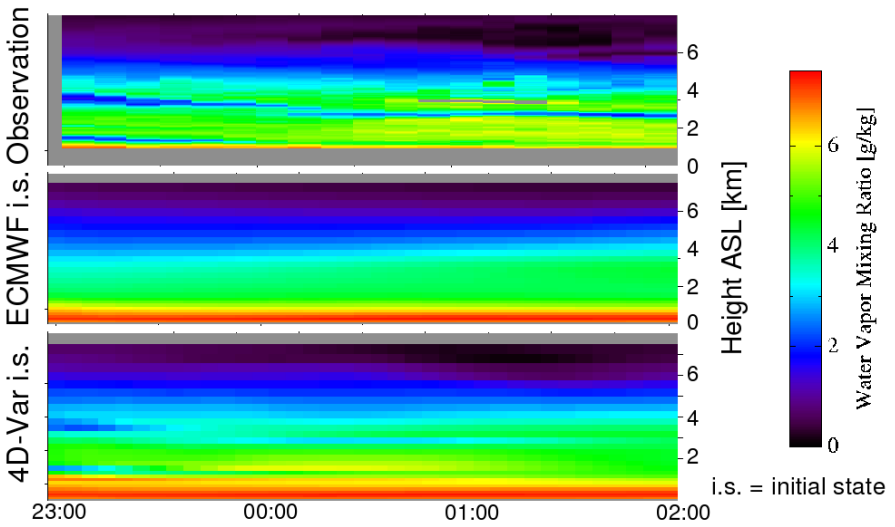


*Figure 6.17.* Vertical cross section of the water vapour mixing ratio [g/kg] over time for the Lindenberg station. Top panel: observation; Middle panel: CONTROL simulation; Bottom panel: Forecast using initial condition optimized by 4DVAR.

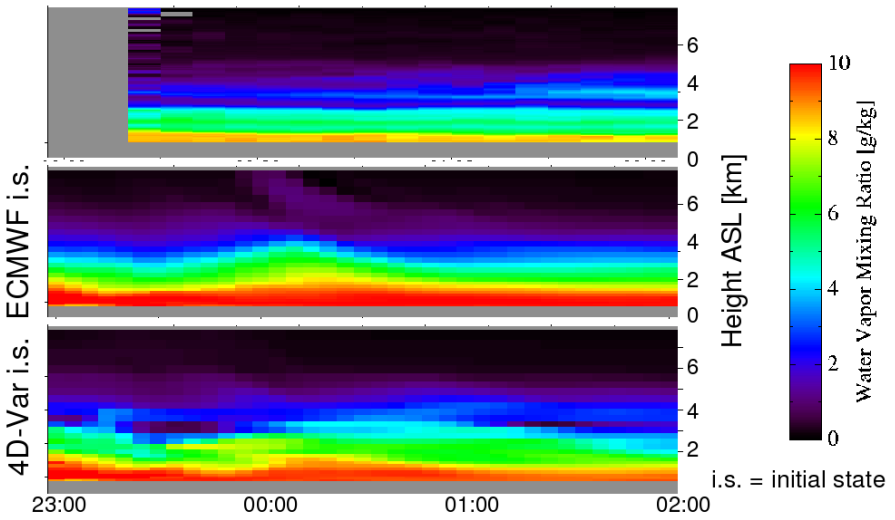


*Figure 6.18.* Same as Figure 6.17, but for the Potenza site

For the Potenza site, things are a little bit different. Here, the 4DVAR performes not so well. However, this is likely not a problem of the 4DVAR, but is instead caused by the much worser background provided by ECMWF. By comparing the upper and middle panel of figure 6.18, it becomes clear that ECMWF induces a wave-like structure that was not observed by lidar. 4DVAR tries to correct this error with little success. Therefore, one important conclusion is, that 4DVAR is capable to clearly improve the initial state, when the background, provided by ECMWF, is already a good representation of the observed situation. However, one has to keep in mind that we only assimilated information from few Raman lidars. An assimilation of additional observations from other observing systems (e.g. standard observations from GTS) at different locations is expected to lead to a much better performance of 4DVAR even in situations where the first guess is bad. But, this has the be investigated in more detail in future experiments.

### 6.3.4 OUTLOOK

So far, the technical work necessary to assimilate Raman lidar data was done, and first assimilation experiments show a clear impact on the water-vapour mixing ratio and temperature fields even 8 hours and more after the end of the assimilation window. This is true although only data from 4 stations were included into the assimilation. Nevertheless, it is still necessary to investigate the performance of the assimilation in more detail by comparing the results of the free forecasts, using the assimilated and non-assimilated initial condition, with observations. This gives rise to possible optimizations of the assimilation strategy and the influence of the observation system of the forecast. Similar experiments should also be carried out for the other two IOPs defined during the LAUNCH campaign.

Another important task, not tackled so far, is model validation. For this purpose, high resolution simulations with 1 km horizontal resolution done for a region centering around Lindenberg (see figure 6.10) shall be compared with observations. During the LAUNCH campaign dense observations were collected at the two sites Lindenberg and Falkenberg and provide the opportunity for a detailed validation of the representation of the boundary layer in the model.

To summarize, the following tasks should be tackled in a follow-up or new research activity:

- Assimilation experiments for the other IOPs
- Detailed comparisons with observations to capture the effect of the assimilation on the quality of forecasts.
- Assimilation of observations from additional observing systems (e.g. GPS, radiometers, or wind profilers).

- Validation of high resolution simulations (1 km horizontal resolution) in the Lindenberg area. Here, dense observations were collected at two sites (Lindenberg and Falkenberg) during the LAUNCH campaign.

## Bibliography

Anthes, R. A. and T. T. Warner, 1978: Development of hydrodynamic models suitable for air pollution and other mesometeorological studies. *Mon. Weath. Rev.*, **106**, 1045–1078.

Barker, D. M., Y.-R. Guo, A. J. Bourgeois, and W. Huang, 2004: A Three-Dimensional Variational Data Assimilation System for MM5: Implementation and Initial Results. *Mon. Wea. Rev.*, **132**(4)), 897–914.

Bouttier, F. and P. Courtier, 1999: Data assimilation concepts and methods. *Technical report*, ECMWF, Reading/UK.

Daley, R., 1991: *Atmospheric Data Analysis*. Cambridge University Press, 475 pp.

Grell, G., J. Dudhia, and D. Stauffer, 1994: A description of the fifth-generation Penn-State/NCAR mesoscale model (MM5). Techn. Rep. NCAR/TN-389+IA, Nat. Cent. for Atm. Res., Boulder/CO, USA.

Gustafsson, N., E. Källén, and S. Thorsteinsson, 1998: Sensitivity of forecast errors to initial and lateral boundary conditions. *Tellus*, **50A**, 167—185.

Hamill, T.and M., Snyder, C., 2002: Using improved background error covariances from an ensemble Kalman filter for adaptive observations. *Mon. Wea. Rev.*, **130**, 1552–1572.

Stauffer, D. R. and N. L. Seaman, 1994: Multiscale four-dimensional data assimilation. *J. Appl. Met.*,**33**,3, 416–434.

Toth, Z., E. Kalnay, S. M. Tracton, R. Wobus and J. Irwin, 1997: A synoptic evaluation of the NCEP ensemble. *Weather and Forecasting*,**12**, 140–153.

Ruggiero, F. H., G. D. Modica, T. Nehrkorn, M. Cerniglia, J. Michalakes, and X. Zou, 2001: Development of an mm5-based fourdimensional variational assimilation system for distributed memory multiprocessor computers. Prepr. *HPCMP 2001 User's Group Conf.*, Biloxi, MS, U.S. Naval Oceanographic Office.

Wergen, W., 2003: Datenassimilation - Ein Überblick. *Promet*, **27**(3/4), 142–149.

Wu, W. S., R. J. Purser, and D. F. Parrish, 2003: Three-dimensional variational analysis with spatially inhomogenous covariances. *Mon. Wea. Rev.*, **130**, 2905–2916.

Wulfmeyer, V., Bauer, H. S., M. Grzeschik, A. Behrendt, F. Vandenberghe, E. V. Browell, S., Ismail, and R. A. Ferrare, 2006: Four-dimensional variational assimilation of water-vapour differential absorption lidar data: The first case study within IHOP-2002. *Mon. Wea. Rev.*, **134**, 209–230.

Xiao, Q., X. Zou, and B. Wang, 2000: Initialization and simulation of a land-falling hurricane using a variational bogus data assimilation scheme. *Mon. Wea. Rev.*, **128**, 2252–2269.

Zou, X., H-Kuo, Y., and Guo, Y. R., 1995: Assimilation of atmospheric radio refractivity using a non-hydrostatic adjoint model. *Mon. Wea. Rev.*, **123**, 2229–2249.

Zupanski, D., and S. K. Park, 2003: Four-dimensional variational data assimilation for mesoscale and storm-scale applications. *Meteorol. Atmos. Phys.*, **82**, 173–208.

Chapter 7

# CONCLUSIONS

John Nash[1] and Catherine Gaffard[2]

[1] *UK MetOffice, Exeter, United Kingdom*
✉ John Nash@meto.gov.uk

[2] *UK Met Office, Reading University, Reading, UK*

## 7.1 MANAGEMENT AND ACTION STRUCTURE ISSUES

Whilst the original memorandum of understanding proposed three working groups to cover five Scientific Programme topics, this did not prove feasible in practice. Experts did not wish to commit to a working group purely based on algorithm development, or one based on impact studies and quality assessment where data was not readily available on the time-scale necessary for progress.

An incorrect assumption had been made about the maturity and reliability of the individual remote-sensing systems available in 2000. These individual systems required much more work than was envisaged before they could be brought into the state where they could be expected to be of reliable operational standard and provide large amounts of data for data assimilation experiments.

High short term variability in cloud cover requires short integration times for ground-based remote sensing of temperature, water vapour and cloud. Many of the systems proposed for integrated profiling were incapable of sampling with this temporal resolution in 2000.

Thus, the work of the Action was split into only two working groups concentrating on improving the basic systems identified as useful for integrated profiling and a second working group performing initial investigations into integration. Chapters 3 and 4 of this report illustrate the progress made by each of these two working groups.

The cooperation between experts in the project became much more efficient once cooperative field experiments were initiated, see chapter 5. This led to development of new international areas of cooperation and the scientific output improved once the groups began to produce scientific papers together, more than 10 papers were published in the Meteorologische Zeitschrift after

the field experiment organised in Payerne. Workshops also led to improved co-operation and were clearly cost-effective in furthering the work of the Action. On the Final Symposium held in Toulouse from 15 to 18 May 2006 about 60 papers were presented with a large fraction concerning

– *the integration of complementary remote-sensing techniques*,
– *data assimilation and modelling* and to
– *networking issues*.

This weighting of topics differs strongly from the first symposium held in L'Aquila in June 2002, which was still more focused to individual sounding techniques, and underlines the progress which has been achieved during the COST Action.

The development of the new working relationships was clearly facilitated by the availability of funds to perform short term scientific missions in various locations.

## 7.2 PROGRESS WITH BASIC TECHNIQUES AND ALGORITHMS

### 7.2.1 MICROWAVE RADIOMETERS

Microwave radiometers were identified as a component of many proposed integration methods. However, when deployed together for part of the field experiments associated with COST-720, the different radiometers showed discrepancies larger than expected from the nominal error characteristics of the systems. Recommendations were developed as to the best adjustment methods for using the radiometer measurements in subsequent comparisons with theoretically modelled radiances produced from radiosonde observations. These studies identified limitations in the models for microwave radiances between 51 and 52 GHz.

The microwave radiances were then used for various studies of retrieval methods/ data assimilation techniques, showing that the quality of the resultant atmospheric variables was still being limited by:

- atmospheric inhomogeneity [caused by clouds and rain] when using elevation scanning,
- uncertainties in the absorption models
- mechanical limitations in the radiometers

As COST-720 progressed the design of commercially available radiometers progressed so that observations were available at a high temporal resolution necessary to resolve cloud structure adequately. The designs were modified to

allow the radiometers to be built more cheaply. Facilities were added to improve the capability of observing in light rain, drizzle and fog, thus increasing the availability of useful operational measurements. This new generation of radiometers now seems ready for more extensive testing and the development of associated integration techniques.

COST-720 field tests also led to the improvement of newly developed scientific radiometers, with the interaction between the scientists and more operationally oriented instrumentation experts beneficial to both groups.

### 7.2.2 LIDARS [WATER VAPOUR, WIND, CLOUD AND AEROSOL]

Within the LAUNCH campaign, a large number of lidars contributed high temporal resolution water vapour measurements to the campaign data set and for use in subsequent data assimilation experiments. The Action was briefed on progress with the system at Lindenberg which had been designed for continuous operational water vapour measurements.

The Action was also briefed on progress with atmospheric aerosol measurements and the lidar systems suitable for making these measurements, and manufacturers contributed in the Final COST Workshop.

### 7.2.3 WIND PROFILER RADARS

For high time resolution data, the estimation of the atmospheric signal is a challenge because of interference, noise contamination and ground clutter. During the period of the Action the use of complex signal processing has improved the detection of the atmospheric signal and the reliability of the reported winds.

### 7.2.4 CLOUD RADAR [PULSED AND FM-CW]

During the period of the Action cloud radars were purchased and evaluated at several of the potential integrated profiling sites. Cloud radar measurements from the CLOUDNET sites were utilised in testing much of the integrated profiling for cloud profiles from the CLOUDNET group, and would seem to be an important component of future integrated profiling sites, particularly if the purchase price can be reduced.

### 7.2.5 C-BAND WEATHER RADAR

In Finland, the use of C-Band weather radar measurements for deriving vertical profiles of cloud layers was investigated and quantified.

## 7.3 PROGRESS WITH INTEGRATION OF INDIVIDUAL SYSTEMS INTO ONE PROFILING STATION

### 7.3.1 DERIVATION OF ADDITIONAL PARAMETERS

**7.3.1.1 Drizzle fraction and cloud liquid water content.** Good progress in developing remote sensing of water cloud has been facilitated by COST-720 in association with scientific developments in the CLOUDNET project. Here, Doppler cloud radar [observing either at 35 GHz or 94 GHz], laser ceilometer or Doppler Lidar measurements are combined to determine the amount of drizzle in the water cloud, and hence the liquid water content of the clouds as a function of time. Liquid Water content cannot be reliably inferred from the measurements of the individual systems.

In addition, the Integrated profiling technique for profiles of temperature, humidity and cloud developed in Germany, see Löhnert, et al.[2004] has integrated measurements of microwave radiometer, laser ceilometer, cloud radar and the closest available radiosonde.

Within COST-720, a combination of these two techniques has also been developed and the results from the various algorithms evaluated.

**7.3.1.2 Cloud top and base.** Methods of combining measurements from a cloud radar with high vertical resolution and laser ceilometer to determine the vertical extent of cloud have been tested. It has been demonstrated that in many cases, a cloud radar can reliably measure the top of low clouds or fog, as long as there are larger water drops [towards drizzle size] towards the top of the fog or cloud. This type of technique was used to verify satellite measurements of the depth of fog/low cloud, and it has been proposed that combination of measurements from the two types of system would be beneficial for future operational observing systems.

**7.3.1.3 Heights of layers associated with maximum refractive index gradient.** The heights of layers associated with maximum refractive index gradient in the vertical in clear air conditions can be identified from maxima in the signal to noise of UHF or VHF profilers. With UHF profilers it is essential to identify clear air conditions, as precipitation/drizzle can also give large signal to noise. As the change in refractive index is mostly associated with changes in water vapour in the vertical, it has been proposed that these heights be assimilated directly into numerical weather prediction models to improve the heights of inversions in the lower troposphere, or alternatively used as an additional element in integrated profiling techniques associated with microwave radiometer measurements.

The reproducibility of wind profiler signal to noise and spectral width measurements has been examined and recommendations produced as to the best sampling periods for quantitative estimates of signal to noise and spectral

width, and also the higher temporal sampling necessary to identify the atmospheric processes associated with the signals. Quality control of the wind profiler signals was also examined in detail, including the effects of different algorithms on the moment estimation from the wind profiler spectra, with recommendations for future application of these algorithms.

**7.3.1.4 Temperature and humidity profiles inferred from wind profiler signals.** Initial tests were performed on combining UHF wind profiler signals with measurements of vertical temperature and water vapour profiles to produce more reliable retrieval of atmospheric structure than could be obtained from the microwave radiometer alone. This work was performed with data obtained during the winter in Switzerland when the wind profiler signals were not really strong enough to allow humidity to be constrained over a very deep layer. Using radiosonde measurements to constrain the radar signals provided improvement to vertical profiles, but the vertical resolution of the microwave radiometer measurements was not good enough to constrain the radar measurements over the relatively shallow layer. It was expected that the proposed technique would work better in summer when the vertical extent of reliable signal to noise measurements would have a better match with the vertical resolution of the microwave radiometer. As a result, proposals for future combinations of systems were generated.

In a similar technique, proposals for combining layers of high wind profiler signal to noise identified with a fuzzy logic algorithm with microwave radiometer measurements were also demonstrated on cases study.

The results obtained during this action are encouraging but long time series of integration should be performed to evaluate the real improvement brought by the wind profiler.

## 7.3.2 DATA RETRIEVAL/ ASSIMILATION TECHNIQUES

Data assimilation for numerical weather prediction and retrieval techniques for combining information from microwave radiometers with various other sources of information, including the infrared radiometer channel normally deployed with modern multi-channel microwave radiometers were investigated. Further work in this area is clearly required if integrated profiling based around the techniques suggested above is to be fully exploited in future.

## 7.3.3 INITIATION OF A EUMETNET OBSERVATORY-TYPE NETWORK PROJECT

The work performed in COST-720 and CLOUDNET, mainly on improving or implementing various new observing systems into a level of reliability, where they can be operated at sites where staff are available to support system operation, has led to a proposal for an EUMETNET network project called *OB-*

*SNET* which bases on a network of stations for integrated profiling in Europe, with systems initially located in Finland, France, Germany, Italy, Netherlands, Switzerland and the UK. This was not implemented yet but further cooperation has also been sought within EU Framework Programmes.

### 7.3.4 COST EFFECTIVE PROFILING FOR OPERATIONAL NETWORKS

Understanding of the potential of the integrated profiling techniques has reached a stage where potential combinations of systems for unmanned operation can be identified. The most cost-effective combinations of systems to be used in the operational integration have yet to be identified, since this also requires a better knowledge of the atmospheric processes that need to be observed at high temporal resolution. The observing systems generated for the future will need to satisfy both the requirements of operational meteorology [where observations that improve forecasting of weather which has large societal impacts will be required] and the requirements of more generalised cross-cutting environmental monitoring activities. Thus, a proposal to co-ordinate future operational developments and associated scientific studies and data assimilation activities in a new *COST Action*, EG-CLIMET, European Ground-based observations of essential variables for CLImate and operational METeorology has been prepared. This proposal was accepted, and the action has been started in May 2008.

# LIST OF TABLES

# LIST OF FIGURES

COST Office

**EUR 24172 — COST Action 720 — Integrated Ground-Based Remote-Sensing Stations for Atmospheric Profiling**

Luxembourg: Publications Office of the European Union

2008 — xxiii, 398 pp. — 17.6 × 25 cm

ISBN 978-92-898-0050-1

doi:10.2831/10752